Experimental and numerical study of Jupiter's dynamics: jets, vortices and zonostrophic turbulence

Daphné Lemasquerier

THÈSE

présentée en vue de l'obtention du grade universitaire de

DOCTEUR DE L'UNIVERSITÉ D'AIX-MARSEILLE

Délivré par : *Aix-Marseille Université (AMU)*

Présentée et soutenue le *13/10/2021* par :

Daphné LEMASQUERIER

Étude expérimentale et numérique de la dynamique de Jupiter : jets, tourbillons et turbulence zonostrophique

Experimental and numerical study of Jupiter's dynamics: jets, vortices and zonostrophic turbulence

---

JURY

PHILIPPE CARDIN	DR CNRS, ISTerre, Grenoble	Rapporteur
PAUL BILLANT	DR CNRS, LadHyX, Palaiseau	Rapporteur
CLAUDIA CENEDESE	*Professor, WHOI, Woods Hole*	Examinatrice
PETER READ	*Professor, University of Oxford*	Examinateur
RAFFAELE MARINO	CR CNRS, LMFA, Lyon	Examinateur
FREDDY BOUCHET	DR CNRS, ENS Lyon	Examinateur
BENJAMIN FAVIER	CR CNRS, IRPHE, Marseille	Co-directeur de thèse
MICHAEL LE BARS	DR CNRS, IRPHE, Marseille	Directeur de thèse

École doctorale et spécialité :
ED 353 : Sciences pour l'ingénieur : Mécanique, Physique, Micro et Nanoélectronique
Spécialité : Mécanique et Physique des fluides

Unité de Recherche :
Institut de Recherche sur les Phénomènes Hors Équilibre (UMR 7342)

Directeurs de Thèse :
Michael LE BARS et *Benjamin FAVIER*

Numéro national de thèse/suffixe local :
2021AIXM0439/027ED353

Je soussignée, Daphné Lemasquerier, déclare par la présente que le travail présenté dans ce manuscrit est mon propre travail, réalisé sous la direction scientifique de Michael Le Bars et Benjamin Favier, dans le respect des principes d'honnêteté, d'intégrité et de responsabilité inhérents à la mission de recherche. Les travaux de recherche et la rédaction de ce manuscrit ont été réalisés dans le respect à la fois de la charte nationale de déontologie des métiers de la recherche et de la charte d'Aix-Marseille Université relative à la lutte contre le plagiat.

Ce travail n'a pas été précédemment soumis en France ou à l'étranger dans une version identique ou similaire à un organisme examinateur.

Fait à Marseille le 21 Juin 2021

« Mais puisque je ne peux pas m'arracher à l'objectivité qui m'écrase, ni à la subjectivité qui m'exile, puisqu'il ne m'est pas possible de m'élever jusqu'à l'être, ni de tomber dans le néant, il faut que j'écoute. Il faut que je regarde autour de moi plus que jamais… Le monde… Mon semblable… Mon frère… »

JEAN-LUC GODARD – *Deux ou trois choses que je sais d'elle*

Résumé

Jupiter fait partie des planètes les plus dynamiques de notre système solaire, faisant ainsi l'objet d'études dans une variété de disciplines, incluant la planétologie, la météorologie, et la mécanique des fluides. Son atmosphère est cisaillée par des vents est-ouest intenses appelés jets zonaux, au sein desquels coexistent d'immenses vortex, dont la Grande Tache rouge. Aux hautes latitudes, la sonde Juno a révélé la présence de cyclones organisés en polygones autour des pôles. Ces structures à grande échelle, jets et vortex, sont extrêmement robustes, bien qu'elles interagissent avec un intense écoulement turbulent à plus petite échelle.

Cette dynamique soulève des questions fondamentales, portant sur les mécanismes qui forcent et dissipent les jets et les vortex, leur auto-organisation en termes d'échelles et d'intensités, et leur stabilité. Le couplage entre l'atmosphère superficielle et la dynamique convective profonde de Jupiter est également une question cruciale, toujours non résolue. Pour y répondre, les données des missions spatiales sont précieuses, mais elles sont discontinues, restreintes à la couche de nuages, et cumulent une multitude d'effets physiques difficiles à isoler. Des modélisations idéalisées sont nécessaires, et c'est dans ce cadre qu'a été entreprise la présente thèse. Nous conjuguons ainsi des approches expérimentale, numérique et théorique pour mieux comprendre les mécanismes physiques sous-jacents à la dynamique jovienne.

Dans un premier temps, dans la continuité de Aubert et al. (2012) et Facchini et al. (2016), nous étudions la forme d'équilibre d'anticyclones au sein d'un écoulement tournant, stratifié et cisaillé, reproduisant la situation des vortex de Jupiter aux moyennes latitudes. Ces expériences, complétées par des analyses théorique et numérique, montrent que l'on peut prédire la profondeur des vortex joviens qui est pour l'instant hors de portée des mesures de surface. Ces vortex sont très superficiels, et notre modèle prédit que la Grande Tache rouge a gardé une épaisseur constante malgré sa récente contraction.

Dans un second temps, nous avons conçu un dispositif expérimental améliorant celui employé par Cabanes et al. (2017) pour étudier la dynamique des jets zonaux. Nous forçons une turbulence à petite échelle à la base d'une couche d'eau homogène en rotation rapide. La forme paraboloïdale de la surface libre résultant de la rotation génère un effet β topographique, analogue à la variation de la force de Coriolis avec la latitude à la surface d'une planète. Nous complétons nos expériences par des simulations numériques idéalisées dites quasi-géostrophiques, et nous étudions l'émergence, la saturation non-linéaire et la stabilité à long terme des jets zonaux obtenus. Nous mettons en évidence une transition et une bistabilité entre deux régimes de jets, que nous modélisons par une résonance d'ondes de Rossby advectées par l'écoulement zonal. Cette transition pourrait aider à expliquer l'observation de différents régimes de jets à l'échelle planétaire. Dans le régime obtenu à haute intensité de forçage, nous retrouvons les propriétés de la turbulence dite zonostrophique, pertinente pour les géantes gazeuses, et nous montrons que l'état final obtenu fait partie d'un ensemble d'états multistables. Enfin, nous confirmons un effet de suppression du transport turbulent par l'écoulement zonal, qui peut se révéler important dans les modèles de circulation océanique ou atmosphérique où la turbulence est paramétrisée.

Dans un troisième temps et en guise d'ouverture, nous présentons des expériences préliminaires permettant d'étudier la dynamique proche des pôles. Nous formons plusieurs cyclones simultanément au sein d'une fine couche d'eau douce flottant sur une couche épaisse d'eau salée en rotation. La migration des cyclones sous l'effet β couplée à un phénomène de répulsion entre cyclones peut conduire à leur organisation autour du centre de la cuve, analogue au pôle, sans fusionner.

Mots-clés : Jupiter, jets zonaux, vortex, turbulence zonostrophique, ondes de Rossby, écoulement quasi-géostrophique

Abstract

Owing to the multiple processes at play, Jupiter's intense dynamics draw the interest of scientists from many disciplines, including planetology, meteorology and fluid mechanics. The atmosphere of Jupiter supports strong east-west winds, so-called zonal jets, in which large vortices are embedded; the most striking example being the Great Red Spot. At high latitudes, Juno revealed the presence of cyclones organized in polygonal patterns around the poles. These two types of large-scale structures, jets and vortices, are robust despite their interaction with the intense underlying turbulence.

This complex dynamic raises fundamental questions regarding the mechanisms that drive and dissipate jets and vortices, their self-organization in terms of scale and intensity, their feedback on the small-scale turbulence and their stability. How the shallow atmosphere is coupled with the deep convective interior of the planet is also a long-standing issue. Spacecrafts' observations are important to tackle these questions. However, they are discontinuous, mostly limited in depth at the cloud level, and they result from multiple coexisting physical processes which are difficult to disentangle. The present thesis aims at developing idealized physical modelling to better identify the basic physical mechanisms at play on Jupiter.

Firstly, building upon Aubert et al. (2012) and Facchini et al. (2016), we studied the quasi-static equilibrium shape of anticyclones embedded in a rotating and stratified shear flow. These ingredients aim at reproducing the situation of the large-scale vortices embedded in Jupiter's zonal jets at midlatitudes. By combining experiments, numerical simulations and theoretical analyses, we show that we can predict the depth of Jovian vortices, inaccessible to direct measurements. Jovian vortices are very shallow structures, and our model predicts that the Great Red Spot has kept a constant thickness despite its recent horizontal shrinkage.

Secondly, following Cabanes et al. (2017), we built an improved experimental setup to study barotropic zonal jets formation and evolution. We force small-scale turbulent motions at the bottom of a rapidly rotating homogeneous layer of water. Due to rotation, the paraboloidal shape of the free-surface leads to a topographic β-effect, analogous to the variation of the Coriolis force with latitude at the surface of a planet. We complement these experiments by idealized, quasi-geostrophic numerical simulations. We study the spontaneous emergence, non-linear saturation and long-term stability of the obtained zonal jets. In particular, we identify a transition between two zonal jets regimes, associated with bistability. We model the transition in a quasi-geostrophic framework by a resonance of Rossby waves, due to their advection by the zonal flow. Such transition may help explain the different regimes of jets observed in various planetary flows. In the regime obtained with a strong forcing, we show that the flow shares the properties of the so-called zonostrophic turbulence, relevant to the gas giants, and that the final zonal flow profile is multistable. Finally, we confirm the so-called suppression effect of the zonal flow on the turbulent transport efficiency, which underlines the importance of accounting for the effect of zonal flows on turbulent transport in global oceanic or atmospheric circulation models, where small-scale turbulence must be parametrized.

Thirdly, we present preliminary experiments which aim at studying the dynamics of cyclones close to the poles. We generate multiple cyclones in a thin layer of fresh water floating on a deeper denser layer of salt water. Because of the β-effect, cyclones drift towards the centre of the tank, corresponding to the pole. A repelling mechanism between cyclones then allows for their organization around the pole without merging.

Keywords: Jupiter, zonal jets, vortices, zonostrophic turbulence, Rossby waves, quasi-geostrophic flow

Remerciements

Le travail de thèse présenté dans ce manuscrit n'aurait pu aboutir sans la contribution et le soutien de multiples personnes, de près comme de loin. Je tiens à les en remercier sincèrement ici.

Michael, Benjamin, d'abord. Rencontrés sur un malentendu, notre premier contact s'est résumé à des attracteurs d'ondes inertielles et à une sombre histoire d'instabilité elliptique. Qui aurait cru alors que je succomberais ! Et pourtant, après plus de trois années à vos côtés, je réalise chaque jour un peu plus la chance que j'ai eu d'être encadrée par vos personnes. Merci, pour ce magnifique sujet de thèse, et pour la confiance que vous m'avez accordée en me le confiant. Merci, pour avoir mis à ma disposition des moyens matériels quasiment illimités et pour m'avoir fait participer à d'innombrables conférences et écoles autour du monde, malgré le tacle du Covid. Merci, Michael, pour avoir guidé le navire d'une main de maître, pour m'avoir transmis ton recul, ton ambition, ta soif de toujours plus, ton ingéniosité, mais aussi ta clairvoyance dans ce monde académique où naviguer à vue ne se fait pas sans rencontrer d'écueil. Merci, Benjamin, pour m'avoir transmis si naturellement et si généreusement ton immense savoir, pour ton entrain inébranlable, ta pédagogie, ta rigueur, tes remises en question permanentes et bien sûr, pour ce laser, qui finalement ne m'aura jamais tranché la tête ! Merci à tous les deux pour avoir donné corps, doigts, yeux et âme à ces cent vingt-huit tuyaux récalcitrants. Des personnalités bien différentes, mais ô combien complémentaires ; vous êtes pour moi de vrais exemples à suivre, et vous resterez un duo de choc pour quiconque aura la chance de travailler à vos côtés.

Je tiens aussi à remercier l'ensemble des membres de mon jury de thèse. Merci à Paul Billant et Philippe Cardin d'avoir endossé les rôles de rapporteurs et de s'être plongés dans ce manuscrit de thèse. Merci à Claudia Cenedese, Peter Read et Raffaele Marino d'avoir examiné mon travail. Merci à Freddy Bouchet d'avoir présidé ce jury et orchestré la séance de questions lors de ma soutenance. Les discussions que vous avez soulevées, par leur diversité et leur pertinence, ont été pour moi extrêmement enrichissantes et m'ont permis de pousser la réflexion sur les limites mais aussi la portée de mon travail.

I also want to personally thank Jon Aurnou, for introducing me to geophysical fluid dynamics in Los Angeles, for getting me in touch with Michael and Benjamin, and for initiating the Jacuzzi experiment project a few years back. A huge thank also to Bruce Sutherland, for sharing his precious time with me during his visit to Marseille, around rotating plumes experiments, and for his constant generosity and support.

Une thèse ne se mène pas seule, et encore moins quand il s'agit de monter des expériences. Je souhaite donc exprimer mon immense reconnaissance envers l'équipe technique du laboratoire, qui a toujours été disponible pour me prêter main forte. Merci à toute l'équipe de l'atelier, Mathieu, Adrien, et Léo. Merci, William, pour les montages électroniques, pour ta patience, pour avoir pris le temps de me transmettre ton savoir. Merci, Jean-Jacques, pour ta disponibilité, tes trucs et astuces pour gérer les soubresauts de Dynamic Studio, mais aussi pour ton souci permanent de s'assurer que tout va bien. Un immense, mais vraiment immense merci à Eric, pour avoir toujours été là, pour t'être plié en quatre au moindre problème, pour ton expertise et ton inébranlable volonté d'aider. Sans l'ombre d'un doute, je sais que je n'aurais pas vécu mes séries de manip de la même manière sans ton accompagnement.

Un grand merci, ensuite, à tous les doctorants et post-doctorants de l'IRPHE. Merci aux anciens, pour leur accueil, leur amour de Marseille et pour avoir montré l'exemple, et merci aussi aux nouveaux, face auxquels on endosse le rôle de doyen sans comprendre où le temps a bien pu filer. Merci Giulio, pour les heures passées à mes côtés à me former devant les manip *Revival*, et pour m'avoir traînée à Malmousque, Basile, pour les barbecues dans les square marseillais et ton sens de l'humour lumineux, JB, pour ta personnalité excentrique irremplaçable, les débats alambiqués sans fin au RU, et tes falafels, Amélie, pour ton souci permanent des autres quelles que soient les circonstances et pour notre maligne alliance contre l'ennemi mauricien, Teri, pour ta bonne humeur contagieuse et les origamis de Noël, Thomas, pour avoir été ce co-bureau de rêve, incarnation humaine d'une encyclopédie (sisi!), pour les concerts privés de basson le matin en salle de manip, et pour ton amour du Mont St Helens, Fab', pour les débats éclairés et ton partage de savoir, pour les après-midi jeux en entente cordiale, et les parties de 0 A.D. pour mieux supporter le confinement, Pierre, pour ton expertise en salle de manip, ton soutien discret, pour toujours savoir relativiser et pour ton malin plaisir à semer la zizanie autour de la chocolatine, Keshou, pour être ce rayon de soleil même quand tout ne va pas fort, ta bonne humeur, tes blagues dignes des plus grands et tes leçons de billard et d'échecs, Fatma, pour les pâtisseries tunisiennes à se damner, Ludo, pour tes coups de main musclés en montage de manip, pour ta passion pour la rotation de ma cuve et pour avoir été ce chauffeur doux et patient de la Corse jusqu'au Mont Rainier, Mathieu, pour ton empathie et les discussions à cœur ouvert... Merci Romain, pour ton sens de l'écoute, ton calme olympien, ta tolérance et ta présence rassurante, et pour m'avoir initiée au bloc (mieux vaut tard que jamais !), Sarah, pour l'énergie et la gnaque que tu dégages, Rémi, pour ta bienveillance au Baraka, tes expériences de fermentation inspirantes et pour avoir toléré de rester en vie jusqu'ici, Tommy, pour ton entrain débordant, qui flirte avec la folie joyeuse, Raul, pour partager les randos dans la brume, Ahmed pour ta générosité et ton sens du partage, Marc, pour ton amour des Calanques, Lucas, pour ton sourire du Sud, Quentin, pour m'avoir supportée en salle de manip, pour avoir le cœur sur la main, pour ta générosité et ta perspicacité... J'ai rencontré durant ces trois années des personnalités extrêmement diverses, mais toutes accueillantes, sincères et généreuses. La cohésion, l'esprit de soutien et de partage qui règne au laboratoire est une force immense au quotidien, et pour cela je vous remercie toutes et tous individuellement.

Ces remerciements s'adressent aussi bien sûr à tous les chercheurs et chercheuses du laboratoire qui par un sourire, un échange autour d'une pause café – ou chicorée - , une attention, une remarque cynique bien placée, ou une partie de pétanque rondement menée (ils se reconnaîtront !) ont contribué de près ou de loin à l'aboutissement de ces trois années de travail.

Naturellement, je voudrais clore ces remerciements par une pensée pour ma famille. Papa, maman, pour votre soutien permanent, humble et discret mais ô combien sincère. Pour m'avoir fait sillonner le monde et découvrir ses richesses avant d'avoir à l'affronter. Pour m'avoir encouragée dans mes choix avant de me demander de les justifier. Pour m'avoir donné les armes pour avancer avant de me jeter dans la mêlée. J'ai puisé en vous la patience de l'instit' et l'émerveillement du physico-chimiste, l'exigence de la maîtresse expat et la soif d'apprendre du prof agrégé. On ne se construit pas seul, et encore moins sans fondations, alors merci de m'avoir accompagnée jusqu'ici, et pour encore longtemps j'espère. Max, Rodolphe, les frérots, un grand merci aussi. Que serais-je aujourd'hui sans les cours de maths un tantinet autoritaires de ce modèle de grand-frère. Sans Max pour me programmer le Kid-Kala qui a tout explosé à l'oral d'info, et pour son affinité sans faille pour l'α-D glucopyranose. Le canard taïwanais aura sa place dans ma valise pour les périples à venir.

Elles ne sont pas de la famille, mais c'est tout comme. Une immense merci aux copines Zembrokal de la Réunion, pour cette amitié qui dure malgré les aléas de la vie, les coups de stress et les absences. Merci Lauren, Méliane et Maureen pour cette cohésion sincère alors que chacune fait son bonhomme de chemin et pour se serrer les coudes sans jugement dans les hauts comme dans les bas.

Enfin, un dernier merci et pas des moindre pour ma moitié, Aristée. Merci pour ta patience et ton abnégation. Pour avoir supporté sans sourciller mes remises en question et mon acharnement intellectuel sur des modèles qui n'aboutissent pas. Pour avoir su rester le chêne dans cette jungle pourtant sacrément envahissante. Pour avoir enjambé les montagnes russes émotionnelles avec un flegme et une lucidité désarmantes. Pour être là, solide, malgré la distance, merci.

Contents

Résumé **5**

Abstract **6**

Remerciements **9**

Contents **9**

List of Figures **13**

List of Tables **17**

1. An overview of Jupiter's structure and fluid dynamics **19**
1.1 A gas giant planet: global features and specificities of Jupiter 20
1.2 Jupiter's dynamics: fundamental physical effects 22
1.2.1 Governing equations 23
1.2.2 Flows with rotation 23
1.2.3 Flows with density inhomogeneities 28
1.2.4 Flows with a β-effect 31
1.2.5 Some fundamental concepts of 3D and 2D turbulence 39
1.3 Jupiter's dynamics: vortices 43
1.4 Jupiter's dynamics: zonal jets 45
1.4.1 Observations 45
1.4.2 Modelling of barotropic jets 48
1.5 Global scale, multi-processes simulations of Jupiter's dynamics 55
1.6 Zonal jets and vortices: ubiquitous features 57
1.6.1 Jovian and oceanic vortices 57
1.6.2 Zonal jets in atmospheres, oceans, liquid cores and tokamaks 57
1.7 Objectives and methods of the present work 60

2. Depth of Jovian vortices: remote determination from laboratory experiments **62**
2.1 Introduction 64
2.2 Equilibrium shape 66
2.2.1 Governing equations 66
2.2.2 Theoretical shape 68
2.3 Experimental and numerical methods 70
2.3.1 Experimental methods 70
2.3.2 Numerical methods 74
2.3.3 Non-dimensional parameters 77
2.4 Equilibrium shape of the vortices: experimental and numerical validation 77
2.4.1 Observations and dominant balances 77
2.4.2 Comparison with theoretical laws 79
2.5 Equilibrium shape of the vortices: application to Jovian vortices 80
2.5.1 Relevant parameters for application to Jovian vortices 80
2.5.2 Three-dimensional instantaneous shape of the GRS (1979) and the Ovals DE, BC (1997) and BA (2007) 85
2.5.3 Shape evolution of the GRS since 1979 86
2.5.4 Roots of the vortex 87

2.6 Long-term evolution of the vortex . . . 89
2.6.1 Advection-diffusion of the density anomaly . . . 90
2.6.2 Decay of the vortex . . . 90
2.7 Conclusions . . . 93

3. Zonal jets in the laboratory: a bistability due to Rossby waves resonance 96
3.1 Introduction . . . 98
3.2 Experimental methods . . . 100
3.3 Experimental results . . . 105
3.3.1 Regime I: Low-amplitude, locally forced jets . . . 105
3.3.2 Regime II: High-amplitude large scale jets . . . 110
3.3.3 Nature of the transition: a first-order subcritical bifurcation . . . 110
3.4 Theoretical model for the transition: a Rossby waves resonance . . . 115
3.4.1 Linear model for the Reynolds stresses . . . 116
3.4.2 Comparison of the linear model with experimental results . . . 118
3.4.3 Resonance of the Reynolds stresses and associated feedback . . . 120
3.4.4 Stationary solutions and linear stability . . . 122
3.4.5 Comparison of the experimental to theoretical transition . . . 124
3.5 Conclusions and discussion . . . 127
3.5.1 Robustness of the transition with the forcing pattern: insights from quasi-geostrophic numerical simulations . . . 127
3.5.2 Conclusions and future work . . . 129
3.5.3 Modelling and relevance for planetary systems . . . 133

4. Non-linear saturation into the zonostrophic regime of zonal jets: turbulence statistics and transport properties 137
4.1 Introduction . . . 139
4.2 List of experiments and non-dimensional parameters . . . 141
4.2.1 Characteristic length scales . . . 141
4.2.2 Non-dimensional parameters . . . 143
4.2.3 List of experiments . . . 143
4.3 Spectral analysis of experimental measurements: signature of the zonostrophic regime . . . 145
4.3.1 Zonal and residual kinetic energy spectra . . . 145
4.3.2 Rate of upscale energy transfer . . . 151
4.3.3 Discussion on the zonostrophic theory . . . 151
4.4 Potential vorticity mixing . . . 154
4.5 Effective turbulent diffusivities and zonal jets as transport barriers . . . 158
4.5.1 Finite scale Lyapunov exponent (FSLE) analysis . . . 158
4.5.2 Direct measure of effective diffusivity and its anisotropy . . . 164
4.6 Conclusions and discussion . . . 170
4.6.1 Advantages and drawbacks of different methods for estimating the turbulent energy transfer rate . . . 170
4.6.2 A zonal-flow dependent diffusivity for planetary transport and modelling . 171

5. Non-linear saturation into the zonostrophic regime of zonal jets: long-term stability and multistable states 175
5.1 Introduction . . . 177
5.2 Methods . . . 178
5.2.1 Experimental approach . . . 178

5.2.2 Numerical approach . . . 179
5.3 Observed multistable jets configurations in experiments and QG simulations . . . 179
5.4 Seeking transitions between multistable states . . . 185
5.4.1 Search for spontaneous transitions . . . 185
5.4.2 Experimentally forced transitions . . . 186
5.5 Discussion . . . 189
5.5.1 Origin of the multistability . . . 189
5.5.2 Non-zonal features . . . 190

6. Collective drift of floating cyclones towards the pole and clustering: a preliminary experimental study 194
6.1 Introduction . . . 196
6.2 Experimental set-up . . . 199
6.2.1 Non-dimensional parameters . . . 199
6.2.2 Description of the setup . . . 204
6.3 Results . . . 208
6.3.1 Single cyclone drift towards the pole . . . 208
6.3.2 Interaction of multiple cyclones generated simultaneously . . . 212
6.4 Discussion and future directions . . . 218
6.4.1 Conclusions . . . 218
6.4.2 Future work . . . 220

7. Conclusions and future prospects 222
7.1 Main results . . . 223
7.2 Complementarity of experimental and numerical approaches for studying gas giants' dynamics . . . 224
7.2.1 Advantages of experimental approaches . . . 224
7.2.2 Limitations of experimental approaches . . . 225
7.3 Future lines of work . . . 226
7.3.1 Future work on midlatitude and polar vortices . . . 226
7.3.2 Jets forcing mechanisms: local or non-local energy transfers? . . . 227
7.3.3 Sensitivity of the Rossby waves resonance to a more realistic forcing . . . 227
7.3.4 Zonal jets equilibration in regime II: a wave-mean flow WKB model. . . . 229
7.3.5 Coupling between deep barotropic jets and a stratified layer . . . 231

APPENDICES 234
A Table listing the parameters of experimental studies of zonal jets . . . 234
B Forcing details and calibration in the Jacuzzi (zonal jets) experiment . . . 236
B.1 Forcing details . . . 236
B.2 Calibration of the first set of pumps . . . 243
B.3 Calibration of the second set of pumps . . . 244
B.4 Correction of optical distortion from the free surface . . . 245
B.5 Beta-effect for various rotation rates and a curved or flat bottom . . . 247
C Quasi-geostrophic modelling of the Jacuzzi (zonal jets) experiment . . . 248
C.1 Motivation . . . 248
C.2 Derivation of the quasi-geostrophic model . . . 249
C.3 Classical QG model used for theoretical modelling . . . 250
C.4 Advanced QG model used in numerical simulations . . . 251
D Bessel-Fourier decomposition for kinetic energy spectra . . . 255
D.1 Principle for continuous functions . . . 255

D.2 Discrete transform 257
E Very long time experiments in the Jacuzzi setup 259

Bibliography **261**

List of Figures

1.1 Giant planets of our Solar system . . . 20
1.2 Jupiter and Saturn interior models . . . 21
1.3 Jupiter temperature and density profile from Galileo . . . 22
1.4 Illustration of rotation and stratification effects on a fluid injected in a water tank 24
1.5 Illustration of the geostrophic balance . . . 27
1.6 Sketches of stable and unstable stratifications in incompressible or compressible fluids. . . . 29
1.7 Shallow and deep models of Jovian dynamics . . . 33
1.8 The β-effect and potential vorticity in the shallow and deep frameworks. . . . 35
1.9 Rossby waves mechanism and illustration . . . 39
1.11 Velocity field and profile for the GRS and Oval BA . . . 44
1.13 Jupiter zonal winds superimposed to the clouds . . . 47
1.15 Illustration of theories on zonal jets dynamics . . . 54
1.16 Floating vortices in the Atlantic ocean (meddies). . . . 58
1.17 Zonal flows in fluid layers of other planets (atmospheres, oceans, liquid cores) . . 59
2.1 Sketch of the *Revival* experimental setup. . . . 68
2.2 Pictures of the *Revival* experimental setup . . . 71
2.3 Visualisations of an anticyclone in the rotating stratified shear flow using Rhodamine B and PIV measurements. . . . 73
2.4 Cross-stream and stream-wise velocity profiles in the experimental and simulated anticyclones as a function of time. . . . 74
2.5 Typical experimental and numerical observations in the *Revival* experimental setup. . . . 76
2.6 Dominant terms in the Navier-Stokes equations and the advection-diffusion equation of the density anomaly. . . . 78
2.7 Numerical profiles of the pressure anomaly associated with the vortex . . . 78
2.8 Evolution of the vortex shape for five experiments and simulations with increasing shear. . . . 79
2.9 Images and velocity fields of three Jovian anticyclones to which is superimposed the measured horizontal aspect ratio and the calculated one using our model. . . 86
2.10 Measured and predicted evolution of the GRS horizontal aspect ratio since *Voyager*. Predicted GRS thickness during this evolution. . . . 87
2.11 Qualitative imaging of the density anomaly associated with the GRS with depth, from the microwave radiometer of Juno. . . . 88
2.12 Vertical structure of the winds and density anomaly of the vortex in the reference simulation. . . . 89
2.13 Evolution of the density anomaly of the vortex through time. . . . 90
2.14 Decay of the Rossby number of the vortex through time. . . . 91
2.15 Evolution of the vortex characteristic decay time when varying the Reynolds number, Schmidt number, Rossby number and shear rate. . . . 92
3.1 Location of planetary flows and zonal jets laboratory experiments in the non-dimensional parameter space (Re, E, R_β) . . . 100
3.2 Sketch of the *Jacuzzi* experimental setup . . . 101
3.3 Pictures of the *Jacuzzi* experimental setup at rest and rotating. Pictures of the forcing plate located inside the tank. . . . 103

3.4 Instantaneous velocity field of the flow on a horizontal plane, computed from PIV measurements. The two zonal flows regimes are shown. . . . 106
3.5 Space-time diagrams of the zonal flow evolution in regimes I and II. Associated zonally-averaged zonal flow and potential vorticity profiles . . . 107
3.6 Instantaneous maps of the zonal and radial components of the velocity and vorticity in regimes I and II. . . . 109
3.7 Space-time diagram of a single experiment illustrating the hysteresis associated with the transition between regimes I and II. . . . 111
3.8 Experimental hysteresis loop visualised by plotting the mean flow amplitude as a function of the forcing amplitude. . . . 113
3.9 Evolution of the total kinetic energy during transitions from regime I to regime II. 114
3.10 Comparison between the experimental flow above the forcing rings and the linear stationary quasi-geostrophic model. . . . 119
3.11 Comparison of the Reynolds stresses divergence (eddy momentum flux) between the experiment and the linear quasi-geostrophic model. . . . 120
3.12 Lorentzian shape of the stream-function amplitude as a function of the background zonal flow U due to the linear Rossby waves resonance . . . 122
3.13 Stationary solutions of the low-dimensional model for the zonal flow evolution equation, incorporating the Rossby waves resonance. . . . 123
3.14 Visualisation of the Rossby waves excited in the experiment at a given radius. . . . 125
3.15 Evolution of the bistable zone predicted by the model as a function of the friction rate, the forcing scale and the β-effect. . . . 126
3.16 Result of QG numerical simulations with the experimental forcing pattern, in regimes I and II. . . . 130
3.17 Results of QG numerical simulations forced at a scale twice smaller than in the experiment. Regimes I and II are retrieved. . . . 131
3.18 Results of QG numerical simulations forced on a cartesian pattern instead of a polar one, at a scale twice smaller than in the experiment. Regimes I and II are retrieved. . . . 132
3.19 Estimates of zonal flow velocities and Rossby waves phase speed for different planetary flows. . . . 135
4.1 Location of the experiments listed in Table 4.2 in the non-dimensional parameters space (E, Re, R_β). . . . 145
4.2 Instantaneous velocity fields measured from PIV in experiment J and A of Table 4.2. 146
4.3 Time-averaged zonal flow profiles in experiment N, J and A of Table 4.2. . . . 147
4.4 Residual and zonal kinetic energy spectra for an experiment in regime I, and two experiments in regime II. . . . 149
4.5 Superposition of the zonal kinetic energy spectra of the three experiments of Fig.4.4. 150
4.6 Comparison between the upscale energy transfers measured on the spectra, ϵ^S, estimated based on Ekman friction, ϵ^E, and deduced from the Thorpe scale measurements, ϵ^T. . . . 152
4.7 Instantaneous potential vorticity maps for experiments J and A of Table 4.2. . . . 155
4.8 Potential vorticity profiles in experiments J and A of Table 4.2, and associated Thorpe scale determined by sorting the PV profiles. . . . 156
4.9 Comparison between the Thorpe scale, the Rhines scale and the transitional scale for the experiments of Table 4.2. . . . 157
4.10 Typical Lagrangian trajectories computed from the measured Eulerian velocity fields from PIV. . . . 161

4.11 Total, radial and azimuthal finite-scale Lyapunov exponents for experiments N, A and B of Table 4.2. . . . 163
4.12 Space-time diagrams showing the radial dispersion of Lagrangian particles released at a single radius, far from or close to a zonal jet. . . . 165
4.13 Histograms of the radial dispersion of Lagrangian particles initially released at the southern edge of a zonal jet. . . . 166
4.14 Radial profiles of effective radial and zonal diffusivities, and correlation with the zonal flow profile. . . . 167
4.15 Measured radial diffusivity in experiments A, B and N, as a function of a theoretical prediction in the framework of anisotropic β-plane turbulence. . . . 167
4.16 Evolution of the radial distribution of the Lagrangian particles after integrating the trajectories over 375 rotation periods for Experiment A. . . . 169
4.17 Diffusivities estimates in the Southern Ocean from Klocker et al. (2012), after suppressing or not the effect of the zonal flow. . . . 173
5.1 Jupiter's zonal jets profile from 1979 to 2016 . . . 178
5.2 2D view of the multistable states observed in the *Jacuzzi* experiments . . . 182
5.3 Zonal flow for each multistable state . . . 183
5.4 Hovmöller diagrams of 3 QG simulations leading to 3 different final states despite the same forcing . . . 184
5.5 Long-time evolution of the zonal flow for three long-time experiments (tens of thousands of rotation times). . . . 185
5.6 Transition between two multistable states triggered by a spin-up of the flow from 70 to 75 RPM. . . . 187
5.7 Space-time diagrams of experiments with alternating forcing between rings C1/3/5 and C2/4/6 . . . 188
5.8 Multistable states with 3 jets obtained by Simonnet et al. (2021) in a barotropic channel flow . . . 190
5.9 Comparison of zonal winds profile in both hemispheres of Jupiter and Saturn . . . 190
5.10 Packets of vortices propagating at the edge of a prograde jet in a *Jacuzzi* experiment in regime II. . . . 191
5.11 Space-time diagram showing the long-term azimuthal propagation of Rossby wave-packets at the edge of a prograde jet . . . 192
6.1 Observations of Saturn's poles . . . 197
6.2 Observations of Jupiter's poles . . . 198
6.3 Illustration of the differences between the shallow and deep β-effects in the *Clusters* experimental setup. . . . 201
6.4 Theoretical velocity and vorticity profiles for different degrees of shielding . . . 202
6.5 Velocity profile measured inside Jupiter's polar cyclones . . . 203
6.6 Sketch of the *Clusters* experimental setup used to study cyclones drift and clustering under a polar β-effect. . . . 205
6.7 Pictures of the *Clusters* experimental setup used to study cyclones drift and clustering under a polar β-effect. . . . 206
6.8 Examples of velocity fields and profiles measured in the experimental floating cyclones from surface PIV. . . . 208
6.9 Visualisation of a single cyclone during its trajectory towards the centre of the tank (the pole). . . . 209
6.10 Comparison of the trajectory of a single cyclone in the deep and shallow configurations. . . . 211

6.11 Translational speed of the cyclones compared to the Rossby waves phase speed in the deep and shallow configurations. . . . 212
6.12 Trajectories of two opposite shallow cyclones. . . . 213
6.13 Trajectories of two adjacent shallow cyclones. . . . 214
6.14 Trajectories of three shallow cyclones. . . . 215
6.15 Trajectories of six shallow cyclones. . . . 216
6.16 Evolution of the distance to the pole and translational speed of 6 cyclones. . . . 217
6.17 Streamlines of the flow for the final configurations of the experiments with 6 cyclones. . . . 217
6.18 Distances and angles between two cyclones for each pair of vortices in one of the 6 cyclones experiments. . . . 218
7.1 Results of QG numerical simulations with a decreasing Ekman number. . . . 228
7.2 Results of QG numerical simulations with a stationary forcing or with a forcing pattern rotated azimuthally by a random angle every prescribed time step. . . . 229
7.3 Illustration of possible coupling between zonal jets in the molecular hydrogen envelope and stably stratified layers . . . 232
B.1 Schematics and pictures of the bottom plate and distributors for the *Jacuzzi* setup. 238
B.2 Pictures of the tubing and pumps below the bottom plate through which the forcing is performed in the *Jacuzzi* setup. . . . 239
B.3 Control box for the first set of pumps in the *Jacuzzi* setup. . . . 240
B.4 Control box for the second set of pumps in the *Jacuzzi* setup. . . . 241
B.5 Pictures of the connections between the drivers and the submersible pumps in the *Jacuzzi* setup. . . . 242
B.6 Webpage generated to remotely control the six pumps in the *Jacuzzi* setup. . . . 243
B.7 Calibration of the first set of pumps in the *Jacuzzi* setup. . . . 244
B.8 Calibration of the second set of pumps in the *Jacuzzi* setup. . . . 245
B.9 Pictures of the target for the optical calibration of the *Jacuzzi* setup. . . . 246
B.10 Curves of the topographic β-effect obtained for various rotation rates and a curved or flat bottom . . . 247
D.1 Structure of the basis functions used for the Bessel-Fourier spectral decomposition of chapter 4. . . . 257
E.1 Space-time diagrams of the zonal flow in a long-time experiment (30,000 rotation periods) with forcing set #1 . . . 259
E.2 Space-time diagrams of the zonal flow in a long-time experiment (30,000 rotation periods) with forcing set #2 . . . 260

List of Tables

2.1 Experimental and numerical non-dimensional parameters for chapter 2 (*Revival* experimental setup). 77
2.2 Parameters used for the prediction of the horizontal and vertical aspect ratios of the Great Red Spot (GRS) in 1979, the Oval BA in 2006 and the Oval DE and BC in 1997. 84
2.3 Parameters and references used to compute the GRS aspect ratios as a function of time since 1979. 85
3.1 Typical Rossby and Reynolds numbers for regimes I and II in the *Jacuzzi* experiments 108
4.1 Definition of the non-dimensional parameters used to characterize the experimental flow (Ekman, Reynolds, Rossby numbers and zonostrophy index). 144
4.2 Parameters of the *Jacuzzi* experiments used in chapter 4. 144
4.3 Parameters deduced from the spectral analysis of the turbulent flow in regime II, using the theory of zonostrophic turbulence. 152
5.1 Parameters of selected experiments performed to evaluate the long-term stability of regime II. 180
6.1 Non-dimensional parameters for Jupiter and previous studies of the dynamics of cyclones in a flow with a β-effect. 204
A.1 Dimensional and non-dimensional parameters of previous experimental studies of zonal jets. 235

Chapter 1.

An overview of Jupiter's structure and fluid dynamics

Jupiter has been observed and modelled for tens if not hundreds of years. After briefly describing the current – static – picture of Jupiter's interior, we focus on its intense dynamics observed in the weather layer. We begin this introductory chapter by presenting the main physical effects at play as well as the associated governing equations. Along with these effects, we underline the long-lasting distinction between deep and shallow models of gas giants dynamics. We then overview some observations of Jupiter's dynamics and associated modelling, focusing on large-scale structures such as vortices and zonal jets. We underline the fact that these structures are ubiquitous and also observed in oceans and atmospheres of other planets. We finally conclude by presenting the goals and approaches of the present thesis.

1.1. A gas giant planet: global features and specificities of Jupiter

Jupiter belongs to the giant planets of our Solar system, along with Saturn, Uranus and Neptune (Fig.1.1). Their striking difference with the smaller inner rocky planets is namely due to their larger distance to the Sun when they formed. According to the so-called core accretion scenario (Helled et al. 2014), at such distances, the temperature was sufficiently cold for volatiles (essentially water) to solidify. Hence, not only refractory materials were accreted but also icy pebbles such that the embryo planets became large enough to capture gas. Compared to the gas giants Jupiter and Saturn, the icy giants Uranus and Neptune grew more slowly, and did not have the time to accrete as much gas before it dissipates from the protoplanetary disk (Helled et al. 2014; Morbidelli 2018).

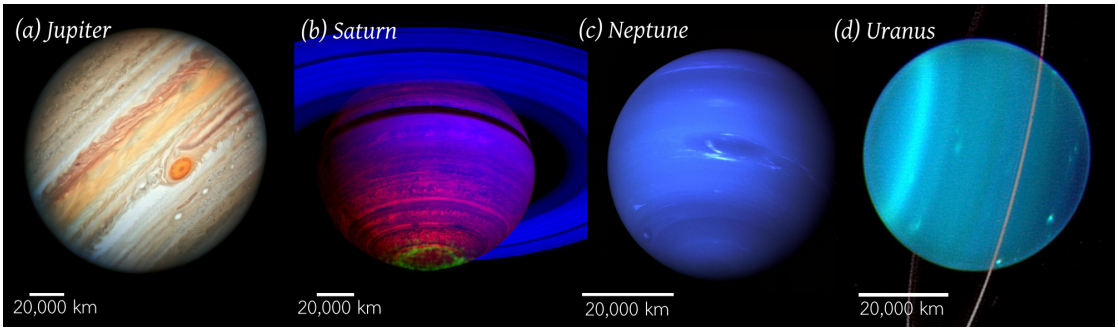

Figure 1.1. – *(a)* Jupiter view taken by the Hubble Space Telescope on June 27, 2019. Credits: NASA, ESA, A. Simon (Goddard Space Flight Center) and M.H. Wong (University of California, Berkeley) *(b)* Composite image of Saturn made from Cassini's visual and infrared mapping spectrometer on Nov. 1, 2008. Credits: NASA/JPL/ASI/University of Arizona/University of Leicester. *(c)* Neptune imaged by Voyager 2. Credits: NASA/JPL *(d)* Keck Telescope view of Uranus. Credits: Lawrence Sromovsky, University of Wisconsin-Madison/W.W. Keck Observatory.

At the end of Jupiter's formation, hydrogen (H) and helium (He) account for about 90% of the envelope by mass, and the remainder is composed of heavy materials, i.e. elements heavier than He (Helled et al. 2014). Gas giant planets are hence fluid planets, with no solid surface below the observed clouds contrary to terrestrial planets. In the following, when the "surface" of the planet's is mentioned, it corresponds to the 1 bar pressure level. The composition and distribution of heavy elements in the interior of the gas giants is currently unknown, and the relative distribution of H and He and their physical state are also poorly constrained. That being said, the recent measurements performed during the Cassini and Juno missions, combined with high-pressure experiments, *ab initio* calculations and theoretical models have allowed to make progress in our understanding of gas giants. Helled (2019) provides a description of the current picture of the gas giants interior, sketched in Fig.1.2. High-pressure experiments and *ab initio* equation-of-state calculations show that H should be insulating and molecular (H_2) in an outer envelope. At deeper levels, it becomes *progressively* a metallic-atomic hydrogen. In this metallic state, electrons are free and H becomes electrically-conducting. A second important phenomenon is that helium is expected to become immiscible with hydrogen, and begin to separate and settle at a given depth, a process referred to as "helium rain". Apart from H and He, the remaining of the planet consists in heavy elements, which are assumed to be mostly water, ammonia, iron and silicates, with unknown distribution. Finally, a central core may exist as a distinct region with a well-defined boundary or a simple progressive increase of heavy-elements concentration.

If Jupiter's interior remains mostly unknown, the picture is different for its atmosphere. The entire planet is covered by a layer of colourful clouds which is observable from Earth through

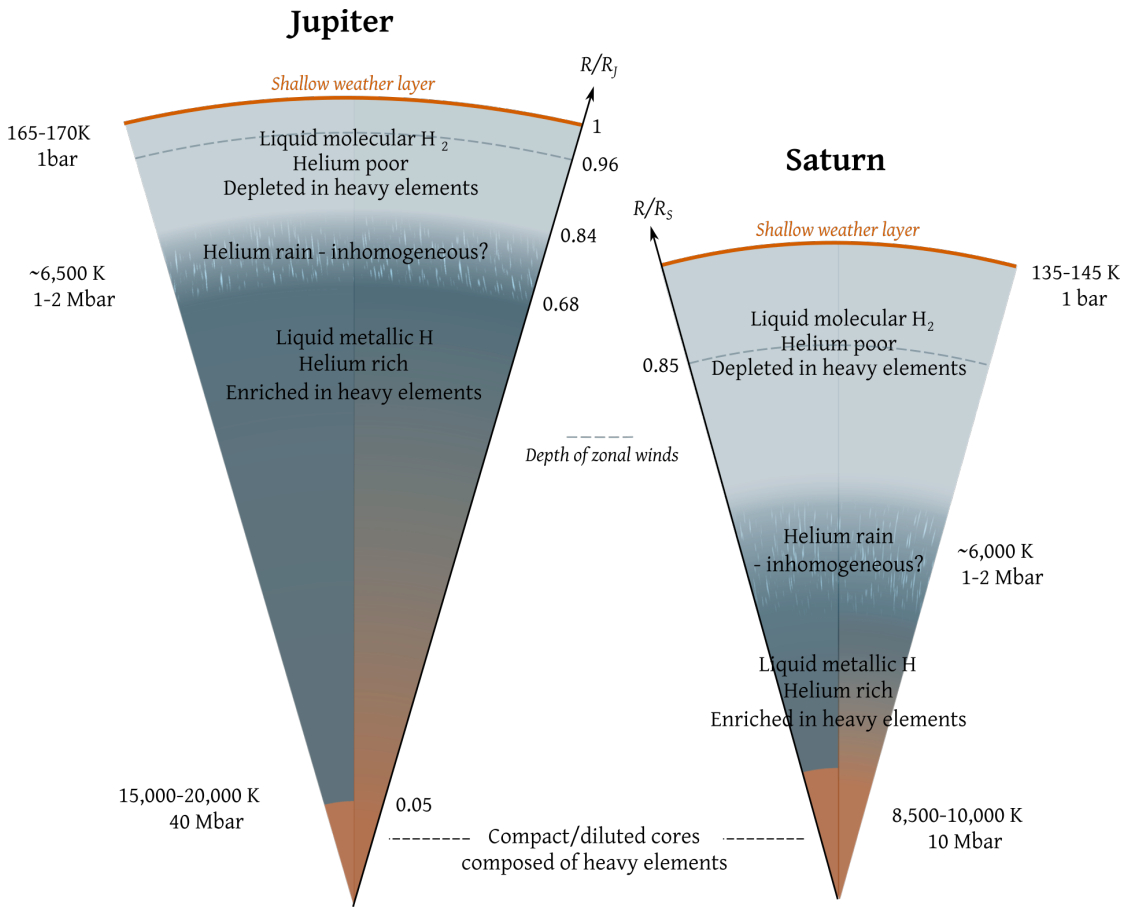

Figure 1.2. – Jupiter and Saturn interior models. Adapted from Fig.5 in Helled (2019). The fractions of Jupiter's radius are estimated by Brygoo et al. (2021) for the helium rain region and Debras et al. (2019) for the core. The region of He immiscibility in Jupiter corresponds to a distance between ~11,000 and 22,000 km below the cloud level. The depth of zonal winds are taken from Kaspi et al. (2018) for Jupiter and Galanti et al. (2019a) for Saturn. They correspond respectively to depths of 3,000 and 9,000 km below the cloud level. For both planets, this depth is where electrical conductivity of molecular hydrogen becomes within an order of magnitude of 1 $\mathrm{S\,m^{-1}}$ (Kaspi et al. 2020).

a simple telescope. Theoretical thermochemical models predict that the clouds structure is composed of an ammonia ice layer at about 700 mbar, an ammonium hydrosulfide cloud layer at about 2 bars, and a water cloud layer with a base near 6 bars, as represented in Fig.1.3*(b)* (Sindoni et al. 2017, and references therein). In 1998, the Galileo probe was voluntarily sent into Jupiter's atmosphere, and took measurements from 0.4 up to 22 bars (span of 150 km) providing an estimate of the atmosphere's stratification (Vasavada et al. 2005). The temperature and density profiles measured by Galileo are represented in Fig.1.3.

We have drawn the current "static" view of the gas giants. But in fact, due to their fluid nature, these planets are the most dynamic of the Solar System. In the gas giants deep interior, the main mechanism of energy transport is convection, which arises due to the excess of heat coming from the planet's interior. The deep convection is responsible for the generation of Jupiter's magnetic field by the dynamo process, i.e. by the motions of a conducting fluid. It should be noted that compositional gradients, due for instance to core erosion or immiscibility of elements in metallic H, may lead to double-diffusive convection, or even inhibit convection in the deep interior (Helled 2019). Compared to the deep interior, the thin outer atmosphere is additionally forced by solar insulation and dominated by moist convection and a radiative heat transport. An intense dynamic takes place in the weather layer, such as strong east-west winds –

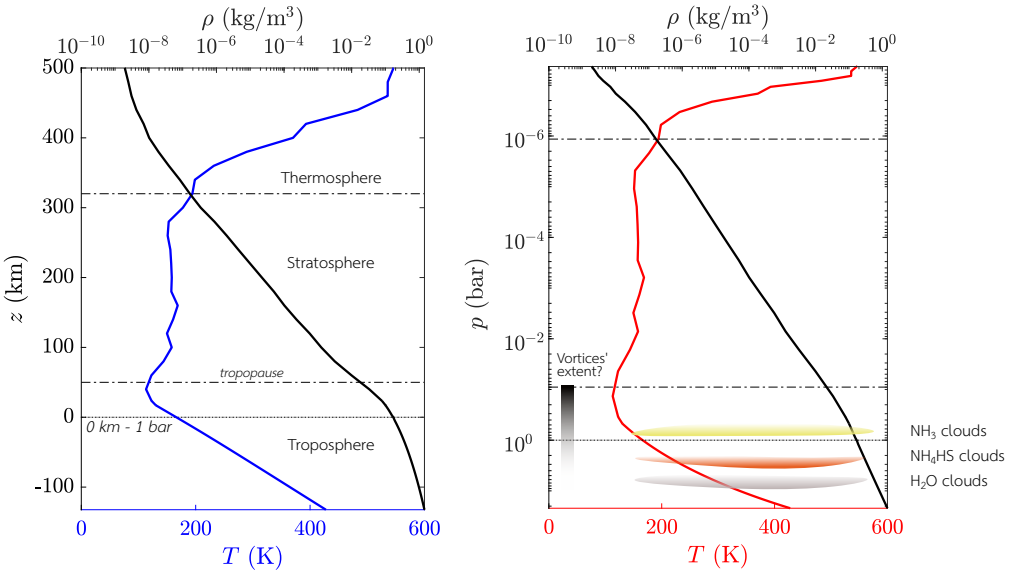

Figure 1.3. – Jupiter temperature and density profile as measured by *Galileo* during its descent in the atmosphere. The data used for these plots is provided in Seiff et al. (1998). Left: Profiles as a function of altitude. The "surface" (zero altitude) is arbitrarily chosen to coincide with the 1 bar pressure level. Right: Profiles as a function of pressure. The approximate position of the clouds in the weather layer is indicated in colour.

so-called zonal jets – or persistent large scale vortices, including the Great Red Spot (Vasavada et al. 2005). The degree of coupling between the weather layer and the deep convective dynamics is a very long standing question. In the present thesis, we do not question the deep interior structure of Jupiter, but focus on modelling the intense observed dynamics.

We start this introductory chapter by reviewing the basic physical effects at play in Jupiter's dynamics (§1.2): rotation, stratification, β-effect and quasi-bidimensional turbulence. The reader familiar with these notions can jump to §1.3 and 1.4 where we describe Jupiter's dynamics and idealized modelling with a focus on vortices and zonal jets. In §1.5 we briefly review global scale models proposed up to date to account for the properties of Jupiter's dynamics. Finally, in §1.6, we show that both features, vortices and zonal jets, are not specific to Jupiter but are generic features observable on other planets and physical systems. We conclude in §1.7 with the goals of the present thesis and the approaches employed to reach them.

1.2. Jupiter's dynamics: fundamental physical effects

In this section, we give an overview of the four main physical effects necessary to understand the dynamics observed on Jupiter, from the fluid dynamics point of view. The considered flows are rotating, stratified in density, subject to a β-effect and turbulent. We briefly explain the consequences of each of these effects on the flow properties. We do not discuss the compressible nature of the flows, neither the interaction between the motion of an electrically conducting fluid and the magnetic field, since these aspects are not explored in the present thesis. Note that the notions addressed in this section are the source of an extremely rich fluid dynamics. We make the choice to favour qualitative and intuitive physical reasoning that are sufficient to allow for a comprehensive lecture of the present manuscript. For thorough details and mathematical derivations, we refer the reader to classical textbooks such as Vallis (2017) or Pedlosky (2013).

1.2.1. Governing equations

In the following, we consider the motion of an *incompressible, non-electrically-conducting* fluid of constant kinematic viscosity ν and density ρ in a Galilean fixed frame of reference. We denote $\boldsymbol{u} = (u, v, w)_{\boldsymbol{e}_x, \boldsymbol{e}_y, \boldsymbol{e}_z}$ the velocity field in the Cartesian coordinate system (O, x, y, z) represented in Fig.1.4*(a)*. We assume that the only volumetric force applied to the fluid is the gravitational force (gravitational acceleration $\boldsymbol{g}$), and an external forcing $\boldsymbol{F}$. Let us denote Φ the gravitational potential per unit mass such that $\boldsymbol{g} = -\boldsymbol{\nabla}\Phi$. The Navier-Stokes and mass conservation equations read

$$\frac{\partial \boldsymbol{u}}{\partial t} + (\boldsymbol{u}\cdot\boldsymbol{\nabla})\boldsymbol{u} = -\frac{1}{\rho}\boldsymbol{\nabla} p + \nu\nabla^2\boldsymbol{u} - \boldsymbol{\nabla}\Phi + \boldsymbol{F}, \tag{1.1}$$

$$\boldsymbol{\nabla}\cdot\boldsymbol{u} = 0, \tag{1.2}$$

where the second equation accounts for the incompressibility of the flow (the volume of a fluid parcel cannot change). Alternatively to the velocity field, the flow can be described by its vorticity field, $\boldsymbol{\zeta} = \boldsymbol{\nabla}\wedge\boldsymbol{u}$. Taking the rotational of equation (1.5) leads to the vorticity evolution equation for an incompressible fluid:

$$\frac{\partial \boldsymbol{\zeta}}{\partial t} + (\boldsymbol{u}\cdot\boldsymbol{\nabla})\boldsymbol{\zeta} = \underbrace{-\boldsymbol{\nabla}\wedge\left(\frac{1}{\rho}\boldsymbol{\nabla} p\right)}_{\text{Baroclinic term}} + \underbrace{(\boldsymbol{\zeta}\cdot\boldsymbol{\nabla})\boldsymbol{u}}_{\text{Stretching term}} + \nu\nabla^2\boldsymbol{\zeta} + \boldsymbol{\nabla}\wedge\boldsymbol{F}. \tag{1.3}$$

The baroclinic term can be recast as

$$\boldsymbol{\nabla}\wedge\left(\frac{1}{\rho}\boldsymbol{\nabla} p\right) = -\frac{1}{\rho^2}\boldsymbol{\nabla}\rho\wedge\boldsymbol{\nabla} p. \tag{1.4}$$

It is only present in so-called *baroclinic* flows, where density and pressure gradients are not aligned, or, in other words, when the isopycnals are not parallel to isobars. In the opposite case, the flow is said *barotropic*.

The term $(\boldsymbol{\zeta}\cdot\boldsymbol{\nabla})\boldsymbol{u}$ is the vortex stretching-tilting term. It materializes how vorticity is modified by the velocity field variations in the direction of the vorticity vector. Tilting arises from variations of the velocity component orthogonal to the vorticity. Stretching arises from variations of the velocity component collinear to the vorticity: these variations stretch or flatten a given vorticity tube, thereby decreasing or increasing its section, and increasing or decreasing the associated vorticity magnitude, respectively. We will see in section 1.2.4.1 that Jovian flows are quasi-bidimensional. The quasi-2D nature of the flow alters the vortex stretching term and has important dynamical consequences, as will be discussed when introducing the β-effect (section 1.2.4).

1.2.2. Flows with rotation

Gas giants are fast rotators, and the motions observed at the planetary scale are only small deviations compared to the global solid-body rotation. In that case, rotation has a strong influence on the flows when observed in the frame rotating with the planet. To illustrate the effect of rotation, we first neglect density variations and consider a homogeneous fluid ($\rho = \rho_0 = \text{cst}$). The Navier-Stokes equation then reads

$$\frac{\partial \boldsymbol{u}}{\partial t} + (\boldsymbol{u}\cdot\boldsymbol{\nabla})\boldsymbol{u} = -\boldsymbol{\nabla}\left(\frac{p}{\rho_0} + \Phi\right) + \nu\nabla^2\boldsymbol{u} + \boldsymbol{F}. \tag{1.5}$$

Compared to flows described in an inertial frame, flows in a rotational frame are subject to

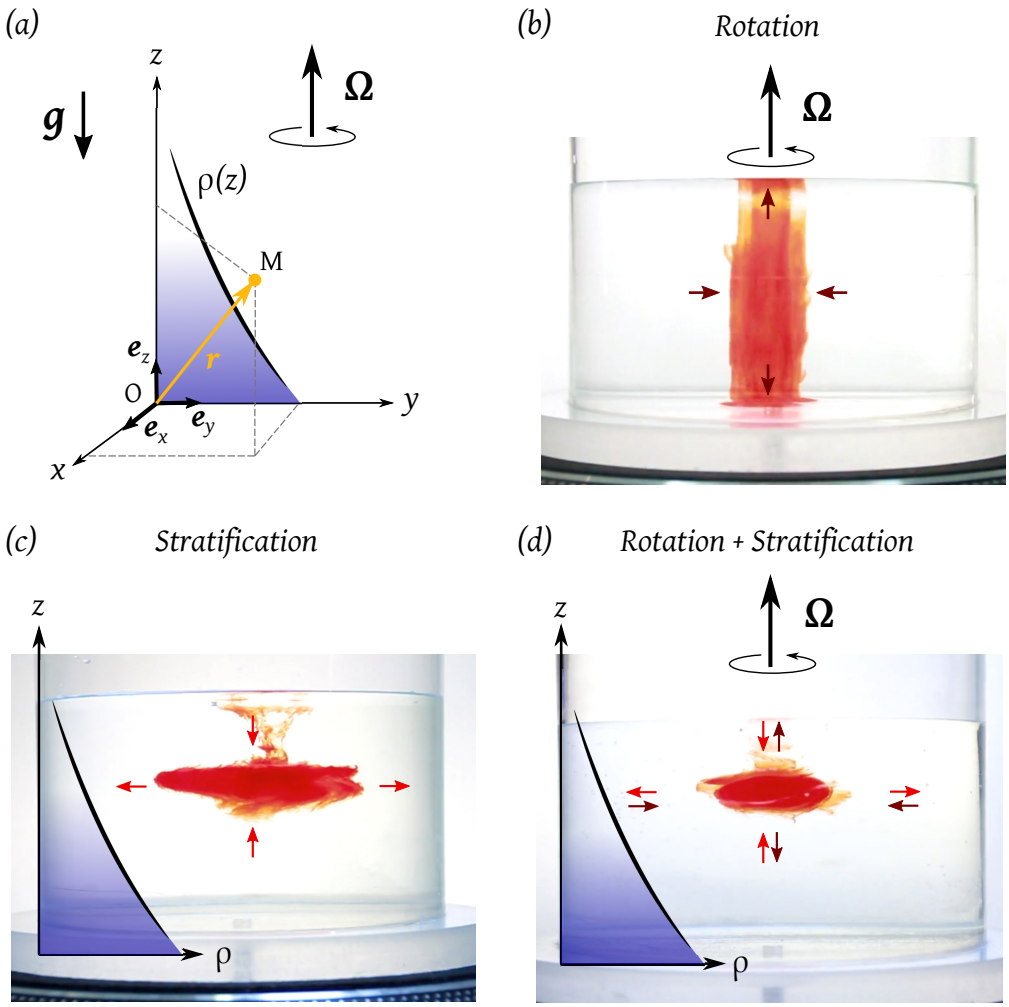

Figure 1.4. – *(a)* Cartesian frame of reference used in the present chapter. *(b,c,d)* Illustrations of rotation and stratification effects on a fluid injected in a water tank and dyed with red food colouring. *(b)* Rotation constraints invariance along the rotation axis (Taylor column). *(c)* Stratification acts against vertical displacements (the fluid spreads at its density level). *(d)* Combination of stratification and rotation. The injected fluid adopts an ellipsoidal equilibrium shape. Experiments realized by O. Aubert, J. Aurnou, A. Grannan, M. Le Bars, Spinlab, UCLA (movie).

two additional inertial "forces". The absolute velocity in the fixed Galilean frame $\boldsymbol{u}$ is related to the velocity in the rotating frame $\boldsymbol{u}_r$ by the expression $\boldsymbol{u} = \boldsymbol{u}_r + \boldsymbol{\Omega} \wedge \boldsymbol{r}$. $\boldsymbol{r}$ is the position vector, and $\boldsymbol{\Omega}$ is the rotation vector, which we chose to be aligned along the z direction and pointing upward (see the schematic in Fig.1.4*(a)*). Substitution in the Navier-Stokes equations (1.5) leads to the momentum equation in the rotating frame:

$$\frac{\partial \boldsymbol{u}_r}{\partial t} + (\boldsymbol{u}_r \cdot \boldsymbol{\nabla})\boldsymbol{u}_r = -\boldsymbol{\nabla}\left(\frac{p}{\rho_0} + \Phi \underbrace{-\frac{1}{2}(\boldsymbol{\Omega} \wedge \boldsymbol{r})^2}_{\text{Centrifugal pressure}}\right) \underbrace{-2\boldsymbol{\Omega} \wedge \boldsymbol{u}_r}_{\text{Coriolis force}} + \nu\nabla^2\boldsymbol{u}_r + \boldsymbol{F}, \tag{1.6}$$

The associated vorticity equation in the rotating frame is

$$\frac{\partial \boldsymbol{\zeta}_r}{\partial t} + (\boldsymbol{u}_r \cdot \boldsymbol{\nabla})\boldsymbol{\zeta}_r = ((\boldsymbol{\zeta}_r + \underbrace{2\boldsymbol{\Omega}}_{\text{Coriolis}}) \cdot \boldsymbol{\nabla})\boldsymbol{u}_r + \nu\nabla^2\boldsymbol{\zeta}_r + \boldsymbol{\nabla} \wedge \boldsymbol{F}. \tag{1.7}$$

Here $\boldsymbol{\zeta}_r$ is the vorticity in the rotating frame, called the *relative vorticity*, and $\boldsymbol{\zeta}_a = 2\boldsymbol{\Omega} + \boldsymbol{\zeta}_r$ is called the *absolute vorticity* because it incorporates the *planetary vorticity* $2\boldsymbol{\Omega}$ associated with the background rotation. In the following of the chapter, we remove the subscripts "r" for the relative velocity and vorticity fields, and instead clearly mention when the equations are written in the rotating frame. The Navier-Stokes and vorticity equations in the rotating frame exhibit two supplementary terms compared to the same equations in a fixed frame, described hereafter: the centrifugal and Coriolis terms.

1.2.2.1. Centrifugal force

Imagine a container filled with water rotating at a constant angular velocity. The fluid will progressively be entrained in solid-body rotation at the same velocity as the container, and will end up in a state with no relative velocity compared to the global rotation, $\boldsymbol{u}_r = \boldsymbol{0}$. The Navier-Stokes equation (1.6) then leads to

$$\frac{p}{\rho_0} + gz \underbrace{-\frac{\Omega^2 r_\perp^2}{2}}_{\text{Centrifugal term}} = \text{cst}. \tag{1.8}$$

where $r_\perp$ is the distance to the spin-axis, and we used $\Phi = gz$ since gravity is the only volumetric force. This equation shows that the centrifugal force acts as a volumetric force. It is commonly incorporated in a generalized pressure P by correcting the centrifugal effect from p. One important effect of the centrifugally induced pressure, particularly for rotating experiments, is that it leads to a deformation of the fluid free surface. Indeed, the free surface corresponds, if we neglect surface tension effects, to an isobar surface where $p = p_{\text{atm}}$. The level of the free surface as a function of the distance to the rotation axis, $z(r_\perp)$, then verifies $-gz(r_\perp) + \frac{\Omega^2 r_\perp^2}{2} = \text{cst}$. The free surface becomes paraboloidal, with a minimum height on the rotation axis. If we denote h_{min} the fluid height at $r_\perp = 0$, then the total fluid height as a function of radius in a rotating container is

$$h(r_\perp) = h_{\text{min}} + \frac{\Omega^2}{2g} r_\perp^2. \tag{1.9}$$

Rotation thus introduces a supplementary hydrostatic pressure term, compensated by a paraboloidal free-surface deformation. This deformation is frequently used in rotating fluid experiments to simulate topographies, and we will take advantage of it in our *Jacuzzi* and

Clusters experimental setups (chapters 3 and 6).

1.2.2.2. Coriolis force and geostrophic balance

The Coriolis force, $-2\boldsymbol{\Omega}\wedge\boldsymbol{u}_r$, is not hydrostatic and orthogonal to the fluid velocity. Since Jupiter viewed from its North Pole rotates in the anti-clockwise direction, the Coriolis force deviates the trajectory of a fluid parcel towards its right in the Northern hemisphere, and its left in the Southern hemisphere as sketched in Fig.1.5*(b,d)*. This force is responsible for the formation of large scale cyclones and anticyclones around low and high pressure regions, both in Earth's or Jupiter's atmospheres, through the geostrophic balance described in the next section. The importance of the Coriolis force relatively to inertial forces in the Navier-Stokes equations is represented by the so-called ***Rossby number***:

$$Ro = \frac{\text{advective term}}{\text{Coriolis term}} = \frac{|(\boldsymbol{u}\cdot\boldsymbol{\nabla})\boldsymbol{u}|}{|2\boldsymbol{\Omega}\wedge\boldsymbol{u}|} \sim \frac{V}{\Omega L}, \tag{1.10}$$

where V and L are typical velocity and lengthscale of the flow in the plane perpendicular to the spin axis. When $Ro \ll 1$, the flow is strongly affected by rotation. For Jupiter for instance, $V \sim 50$ ms^{-1}, $L \sim 10^3$ km and $\Omega \sim 10^{-4}$ rads^{-1}, leading to $Ro \sim 0.5$. The Coriolis force is then sufficiently dominant to affect large-scale motions. Note that strictly speaking, L should be the *local* scale of the considered structure (and V its velocity). For a given flow, large scale structures (e.g. large-scale vortices) can be dominated by rotation whereas small-scale motions are not (e.g. thunderstorms).

To evaluate the relative importance of the viscous and Coriolis forces, we introduce the ***Ekman number***

$$E = \frac{\text{viscous diffusion}}{\text{Coriolis force}} = \frac{|\nu\nabla^2\boldsymbol{u}|}{|2\boldsymbol{\Omega}\wedge\boldsymbol{u}|} \sim \frac{\nu}{\Omega H^2}, \tag{1.11}$$

where H is the typical depth of the flow. The coupling between viscous and rotational effects is particularly important close to boundaries perpendicular to the rotation axis (e.g. at the bottom of a rotating container), where they lead to the development of a so-called Ekman layer. In this layer, of depth $HE^{1/2}$, velocity goes to zero due to friction, but with a net divergence or convergence of fluid due to the Coriolis force. This divergence (convergence) is compensated by a downwelling (upwelling) of fluid coming from the bulk. This is the so-called Ekman pumping phenomenon. The Ekman number of the planets is always vanishingly small, meaning that the observed motion are insensitive to small-scale viscous diffusion in the bulk.

Geostrophic balance and Taylor-Proudman theorem The effect of the Coriolis force is best illustrated in the regime where $Ro \ll 1$ and $E \ll 1$, such that both inertial and viscous effects can be neglected. In this limit, if we further assume that the motions are slowly varying or quasi-stationary (we neglect the time derivatives), equations (1.6) and (1.7) reduces to

$$\mathbf{0} = -\boldsymbol{\nabla}\left(\frac{P}{\rho_0}\right) - 2\boldsymbol{\Omega}\wedge\boldsymbol{u}, \tag{1.12}$$

$$\mathbf{0} = (2\boldsymbol{\Omega}\cdot\boldsymbol{\nabla})\boldsymbol{u}, \tag{1.13}$$

where the centrifugal effects are incorporated in the generalized pressure term ($P = p + \rho_0 g z - \rho_0\Omega^2 r_\perp^2/2$). Equation (1.12) constitutes the so-called ***geostrophic balance***. In a flow in geostrophic balance, the force arising from pressure gradients is equilibrated by the Coriolis force. This equilibrium is illustrated in Fig.1.5*(e)* in the cases of a cyclone and an anticyclone. Equation

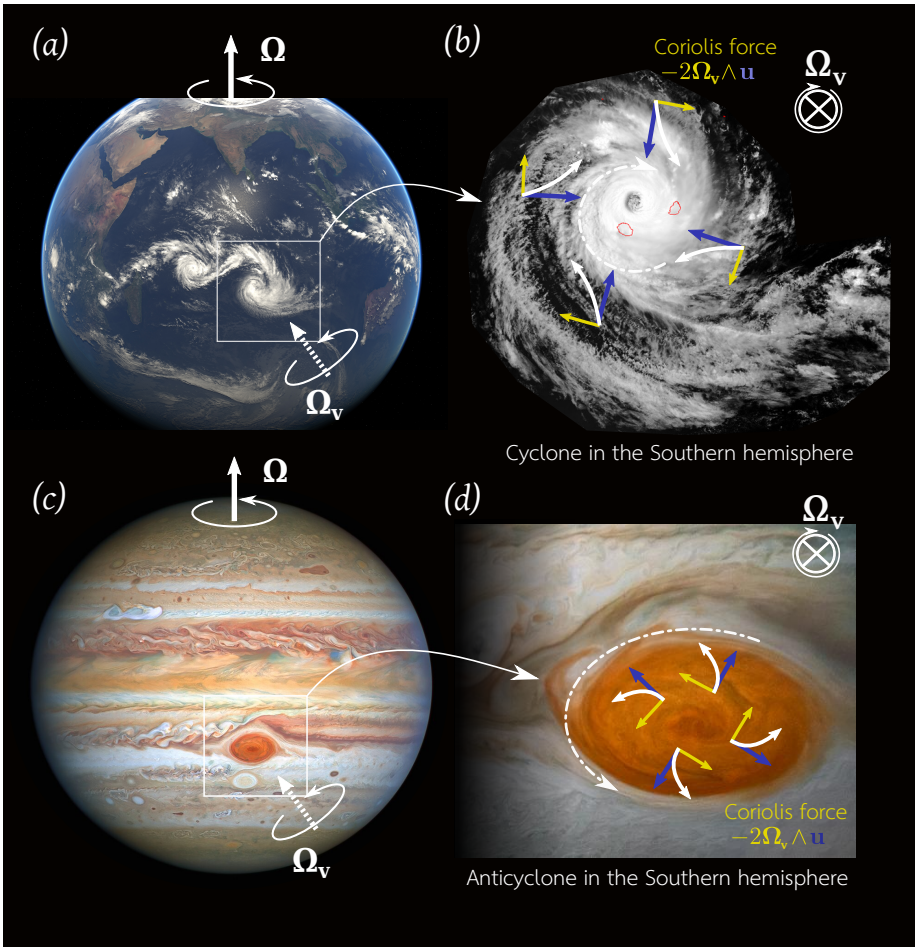

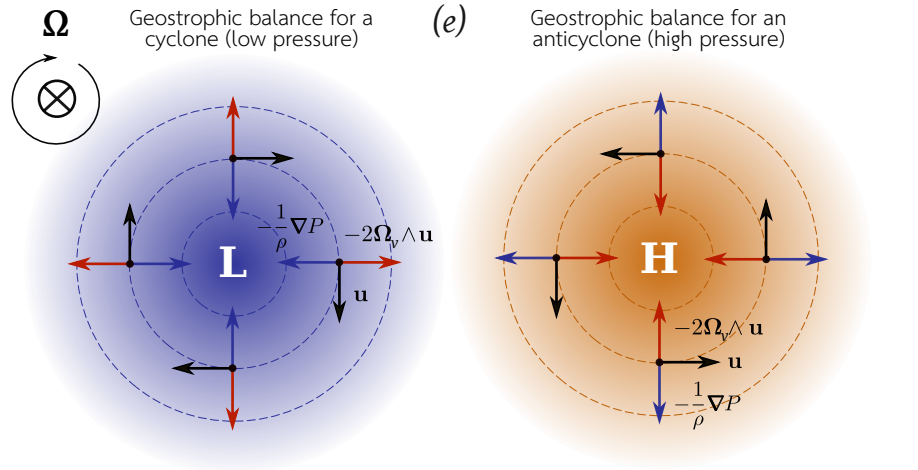

Figure 1.5. – Illustrations of the geostrophic balance on Earth and on Jupiter. $\mathbf{\Omega}$ is the planet rotation vector, and $\mathbf{\Omega}_v$ its component aligned with the local vertical (orthogonal to the surface of the planet). *(a)* Satellite view of two tropical cyclones in the Indian Ocean. Credits: Meteosat image Copyright EUMETSAT. *(b)* View of the cyclone DINA approaching Reunion island in January 2002 (Credits: Meteo France). Without rotation, the fluid would tend to flow towards the low pressure (blue arrows), but it is deviated on the left by the Coriolis force (yellow arrows). *(c)* Jupiter view from Hubble Space Telescope. Credits: NASA, ESA, A. Simon (Goddard Space Flight Center), and M. H. Wong (University of California, Berkeley) and the OPAL team. *(d)* Close-up view of the Great Red Spot. Credits: NASA/JPL-Caltech/SwRI/MSSS and Kevin M. Gill. *(e)* Schematics of the geostrophic balance for a cyclone and an anticyclone in the Southern hemisphere.

(1.13) constitutes the so-called ***Taylor-Proudman theorem*** and can be recast as

$$\frac{\partial u}{\partial z} = \frac{\partial v}{\partial z} = \frac{\partial w}{\partial z} = 0. \tag{1.14}$$

The geostrophic balance and Taylor-Proudman theorem physically imply that:

— The flow is invariant along the rotation axis. For instance, if a horizontal motion is imposed in the bulk of a rotating container filled with water, the fluid will be set in motion along a entire vertical column. The vertical columns which form due to this frozen-in property are called *Taylor columns* (see Fig.1.4*(b)*). Note that this theorem breaks close to the solid boundaries where $\partial_z \boldsymbol{u}$ cannot be null due to viscous effects.

— The flow is normal to the pressure gradient, or in other words, the streamlines follow the isobars. We are familiar with this consequence when interpreting meteorological maps, where the wind rotates around low and high pressure regions corresponding to concentric isobars (see Fig.1.5*(e)*).

— For an incompressible fluid, the continuity equation (1.2) also implies that $\partial_x u + \partial_y v = -\partial_z w$, leading to

$$\frac{\partial u}{\partial x} + \frac{\partial v}{\partial y} = 0. \tag{1.15}$$

The flow is thus horizontally non-divergent. In particular, the horizontal section of vorticity tubes remains constant.

Note that the geostrophic balance is not a prognostic equation, since the knowledge of the pressure field is required to determine the flow evolution, and vice-versa. The geostrophic balance is never perfectly verified by natural flows, but it gives a good zeroth-order balance to which more complex flows can be compared to. Invariance along the rotation axis is the reason why fast rotating flows are said to be quasi-bidimensional, as underlined in section 1.2.4.1.

1.2.3. Flows with density inhomogeneities

Natural flows, including those on Jupiter, are not homogeneous, and variations in their density, $\rho(x, y, z, t)$, are observed at global or local scales. Density differences can be due to difference in chemical composition such as the concentration of salt in the oceans, or to temperature differences. Compressibility can also influence the density of a fluid parcel. We neglect compressible effects in the present thesis, but weak density inhomogeneities can nevertheless be considered in an incompressible framework using the so-called Boussinesq approximation.

1.2.3.1. Vertical stratification

A vertical stratification refers to a density varying along the vertical direction (defined as the direction of the local gravitational acceleration). In a configuration where the gravity field is directed downward, if density decreases with depth, then the stratification is said unstable. Indeed, if a particle is displaced from its equilibrium position and in the absence of any diffusive process, it will naturally continue to move away from its initial position because it is less dense than the ambient fluid (see the first sketch in Fig.1.6). This configuration can give rise to instabilities but it is not considered in the present thesis. Instead, when the density increases with depth, the stratification is stable because a fluid parcel displaced from equilibrium will return to its initial position. The buoyancy force then acts as a restoring force opposed to any vertical displacement (second panel in Fig.1.6). When returning to equilibrium the fluid parcel

oscillates with an angular frequency N called the buoyancy or Brunt-Väisälä frequency:

$$N = \sqrt{-\frac{g}{\rho_0}\frac{\mathrm{d}\rho}{\mathrm{d}z}}, \tag{1.16}$$

where ρ_0 is the mean density.

Note that the aforementioned picture is true for an incompressible fluid. For a realistic, compressible fluid such as an atmosphere, a stratification with increasing density downward can be either stable or unstable. Indeed, when a parcel rises, its density changes even in the absence of heat or chemical diffusion because of its dilatation. If the fluid parcel is displaced without heat or chemical exchanges, this density variation due to dilatation follows an adiabatic (dashed line in the last two panels of Fig.1.6). The condition for stability is then that the density change due to dilatation is smaller, in absolute value, compared to the density change in the ambient environment between the two initial and final positions of the parcel. Said differently, the stratification is stable if the density gradient in the ambient is larger than the adiabatic gradient.

We know that Jupiter's atmosphere is stratified due to a combination of temperature, pressure and compositional effects, but the corresponding density profile has been measured only once when Galileo entered the weather layer (Fig.1.3). Galileo measurements are limited to a depth of 22 bars, representing only 0.2% of Jupiter's radius. In addition to the weather layer, stratification is also likely in Jupiter's deep interior because of the distribution of heavy elements and/or helium immiscibility with hydrogen, but very poorly constrained.

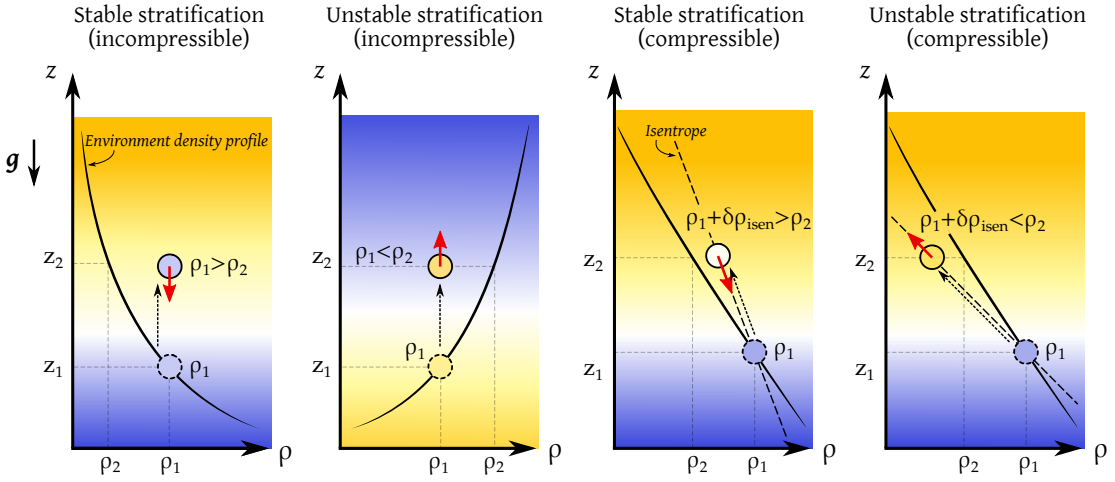

Figure 1.6. – Sketches of stable and unstable stratifications in incompressible or compressible fluids. The dashed arrow represents an initial vertical displacement of a fluid parcel. The colour of the parcel represent its density (blue is denser, yellow lighter). The red arrow represents the buoyancy force acting on the parcel following the displacement. If it points upward, the fluid parcel continues to rise (unstable configuration). In an incompressible fluid, a vertical stratification where density increases with depth is always stable. In a compressible fluid, this is not the case because when a deep (dense) fluid parcel is displaced upward, its density decreases because of the associated decompression ($\delta\rho_{\mathrm{isen}} < 0$). If this decrease is larger than the decrease of the ambient density ($\rho_2 - \rho_1$), the parcel becomes less dense than the ambient and rises.

1.2.3.2. Boussinesq approximation

The Boussinesq approximation allows to take into account first order density variations effects in a simple manner. The Boussinesq approximation is valid when the density variations

are small compared to the mean density, i.e. when

$$\rho(x,y,z,t) = \rho_0 + \tilde{\rho}(x,y,z,t), \text{ with } \frac{\tilde{\rho}}{\rho_0} \ll 1. \tag{1.17}$$

For a Boussinesq fluid, density changes are so small that they have negligible influence on the mass balance, and mass conservation reduces again to the incompressibility condition (1.2). The pressure field, with a reference pressure in hydrostatic balance with the mean density field, is $p = \text{cst} - \rho_0 g z + \tilde{p}(x,y,z,t)$. Substituting the expressions for p and ρ in the momentum equations (1.1) leads to

$$\frac{\partial \boldsymbol{u}}{\partial t} + (\boldsymbol{u}\cdot\boldsymbol{\nabla})\boldsymbol{u} = -\boldsymbol{\nabla}\left(\frac{\tilde{p}}{\rho_0}\right) + \underbrace{\boldsymbol{g}\frac{\tilde{\rho}}{\rho_0}}_{\text{Buoyancy}} + \nu\nabla^2\boldsymbol{u} + \boldsymbol{F}, \tag{1.18}$$

It is common to say that in the Boussinesq approximation, all density variations are neglected except those associated with the gravitational (or buoyancy) term. The Boussinesq approximation is generally valid for liquids, which have very small expansion coefficients associated with thermal expansion, salt concentration or compressibility. But it is generally not valid for gases and clearly not valid in Jupiter's atmosphere. An alternative to the Boussinesq approximation is then the so-called anelastic approximation, where the basic state compared to which deviations are considered small is not a mean constant density, ρ_0, but a mean density profile, $\rho_1(z)$. Large density variations in the basic density profile are then allowed. Anelastic models are however much more difficult to handle numerically and theoretically, and cannot be easily considered in the lab where water is used as a working fluid.

In addition to the momentum and mass conservation equations, an equation for the evolution of the density perturbation, $\tilde{\rho}$ is necessary to close the set of equations. In our experiments for instance, density only varies due to the mass concentration in sodium chloride, ρ_{NaCl}. This concentration follows an advection-diffusion equation:

$$\frac{\partial \rho_{\text{NaCl}}}{\partial t} + (\boldsymbol{u}\cdot\boldsymbol{\nabla})\rho_{\text{NaCl}} = \kappa\boldsymbol{\nabla}^2\rho_{\text{NaCl}}, \tag{1.19}$$

where κ is the salt diffusivity. The density is related to the mass concentration of salt through an equation of state. For liquids, empirical equations of state are employed. For small variations of density, a reasonable approximation of the equation of state is

$$\rho = \rho_0\left[1 - \beta_T(T - T_0) + \beta_S(S - S_0) + \beta_p(p - p_0)\right], \tag{1.20}$$

where β_T is a thermal expansion coefficient, β_S a saline contraction coefficient and β_p a compressibility coefficient (Vallis 2017, section 1.4). The salinity, S, is the mass of dissolved salt in a unit mass of solution. For a single chemical component, S coincides with the mass fraction of the component: $S = \rho_{\text{NaCl}}/\rho_0$. In the case where thermal and compressible effects are absent, there is a linear relationship between density and mass concentration in salt, and equation (1.19) leads to

$$\frac{\partial \rho}{\partial t} + (\boldsymbol{u}\cdot\boldsymbol{\nabla})\rho = \kappa\boldsymbol{\nabla}^2\rho, \tag{1.21}$$

which represents the advection-diffusion of the density field.

1.2.3.3. Relative importance of buoyancy and rotation

When both rotation and stratification are present, it is useful to introduce non-dimensional parameters that inform us about their relative importance. One way of doing so is to compare the characteristic scale of the observed dynamics to the Rossby radius of deformation. The radius of deformation is the typical scale over which a density perturbation can spread before being deflected by the Coriolis force. Said differently, it is the scale at which rotation and stratification effects become comparable. For a continuously stratified fluid of buoyancy frequency N, the internal Rossby radius of deformation is

$$R_{d,N} = \frac{NH}{f}, \tag{1.22}$$

where H is the vertical length scale of the stratification.

The simplest possible stratification is when two layers of different densities are superposed. In chapter 6, we will use the so-called $1-1/2$ shallow-water system where a shallow layer of thickness h rests hydrostatically on a denser quiescent and infinitely deep layer. The internal radius of deformation is then

$$R_{d,\Delta} = \frac{\sqrt{g'h}}{f} = \frac{\sqrt{gh\,\Delta\rho/\rho_0}}{f}, \tag{1.23}$$

where $g' = g\Delta\rho/\rho_0$ is the reduced gravity with $\Delta\rho/\rho_0$ the relative density difference between the two layers. R_d is then the distance travelled by an internal gravity wave propagating at the interface between the two layers, during one rotation period.

For a given structure, say a vortex, of length scale ℓ, the *local Burger number* $Bu = R_d^2/\ell^2$ can be used to estimate if it is dominated by buoyancy ($Bu > 1$) or rotational ($Bu < 1$) effects. On Jupiter, at midlatitudes, the Rossby radius of deformation is of about 1,500-3,000 km (see the Supplementary Information in Young et al. 2017). Large-scale vortices are of a comparable size, hence stratification is important to take into account along with rotation.

Baroclinic flows will be considered in chapters 2 and 6 which focus on midlatitude and polar vortices respectively. For zonal jets, we focus on purely barotropic processes by assuming $\rho = \rho_0 = \text{cst}$, i.e. neglecting stratification altogether (chapters 3 to 5).

1.2.4. Flows with a β-effect

Jovian flows are rotating and stratified. The third effect that we introduce is the so-called β-effect, responsible for the formation of zonal jets. In its essence, the β-effect arises from the variation of the Coriolis force with latitude. Historically, two different models have been considered to describe Jovian dynamics: one is shallow and the other one is deep. In these two frameworks, we show that the flow can be considered as quasi-bidimensional and provide the corresponding 2D governing equations (§1.2.4.1). We then show that the β-effect has two distinct physical origins in the shallow or deep models (§1.2.4.2 and 1.2.4.3).

1.2.4.1. Quasi-bidimensional flows: shallow and deep models

Historically, the quasi-bidimensionality of Jovian flows has been justified in two different ways, sketched in Fig.1.7*(a,b)*. These two models arose because of the uncertainty regarding how deep the observed atmospheric structures are, but also because of the different approaches employed by different scientific communities:

- The first model is a **shallow model**, adopted by the atmospheric sciences community, in which the dynamics observed at the cloud level is supposed to be confined in the thin

weather layer of thickness ~ 100 km (Vasavada et al. 2005). With typical lateral structures of ~ 1000 km, the atmospheric structures would have a vertical to horizontal aspect ratio of about 0.1 and are geometrically constrained to be bidimensional. This is analogous to what is assumed for Earth ocean and atmosphere, considered as thin spherical layers.

- The second model emerged from the deep Earth and thermal convection community (Busse 1976). It consists in a **deep model**, where dynamical features extend through the molecular hydrogen region of Jupiter's interior over several thousands of kilometres, leading to an aspect ratio $\gtrsim 1$. In this deep model, in the limit where the planet's rotation dominates inertia (i.e. small Rossby number), bidimensional motions are again expected because rotation imposes invariance along the spin axis, as demonstrated by the Taylor-Proudman theorem, presented in section 1.2.2.

In any of these two models, the bidimensionality is only partial, and three-dimensional motions are expected, particularly at small-scales for which geometrical or rotational constraints do not hold anymore. Nevertheless, the large-scale flows exhibit features reminiscent of purely 2D flows, in particular from the turbulent point of view, described later in §1.2.5. In this section, we will hence use the bidimensional form of the Navier-Stokes and vorticity equations. We consider that the 2D flow evolves in the (x,y) plane, with a rotation vector aligned along the z direction. In the shallow model, since the flow is quasi-2D at the surface of the sphere, this amounts to consider a local cartesian frame where the (x,y) plane is tangent to the sphere (see Fig.1.8, top panel). The rotation vector is then the component of $\boldsymbol{\Omega}$ which is aligned with the normal to the sphere, $\boldsymbol{\Omega}_v$. In the deep model, (x,y) is on the contrary perpendicular to the spin axis of the planet.

Let us consider a 2D velocity field, $\boldsymbol{u}_h = (u,v,0)_{\boldsymbol{e}_x,\boldsymbol{e}_y,\boldsymbol{e}_z}$. The 2D Navier-Stokes equations (1.6) for an incompressible and homogeneous fluid in the rotating frame are

$$\frac{\partial u}{\partial t} + (\boldsymbol{u}_h \cdot \boldsymbol{\nabla}_h) u = -\frac{\partial}{\partial x}\left(\frac{P}{\rho_0}\right) + 2\Omega v + \nu \nabla_h^2 u + F_x, \tag{1.24}$$

$$\frac{\partial v}{\partial t} + (\boldsymbol{u}_h \cdot \boldsymbol{\nabla}_h) v = -\frac{\partial}{\partial y}\left(\frac{P}{\rho_0}\right) - 2\Omega u + \nu \nabla_h^2 v + F_y, \tag{1.25}$$

where the subscript "h" indicates that we consider bidimensional motions. For a 2D flow, the vorticity has a single component orthogonal to the flow,

$$\boldsymbol{\zeta} = \zeta \boldsymbol{e}_z = \left(\frac{\partial v}{\partial x} - \frac{\partial u}{\partial y}\right) \boldsymbol{e}_z. \tag{1.26}$$

The vortex stretching-tilting term in the vorticity equation (1.3) naturally disappears, and the 2D vorticity equation reads

$$\frac{\partial \zeta}{\partial t} + (\boldsymbol{u}_h \cdot \boldsymbol{\nabla}_h)\zeta = \nu \nabla_h^2 \zeta + \boldsymbol{\nabla}_h \wedge \boldsymbol{F} \quad (-\alpha\zeta). \tag{1.27}$$

The last term in parenthesis is a linear friction of damping rate α, which is one way of avoiding energy accumulation at large scales in strictly 2D flows. It is also physically relevant to model Ekman or magneto-hydrodynamic drag on a bottom boundary or Rayleigh drag, as we will see later.

1.2.4.2. Shallow, atmospheric β-effect

In the shallow model, motions in the atmosphere feel a local rotation corresponding to the projection of the global rotation vector on the local normal to the planet's surface: $\Omega_v = \Omega \sin(\theta)$,

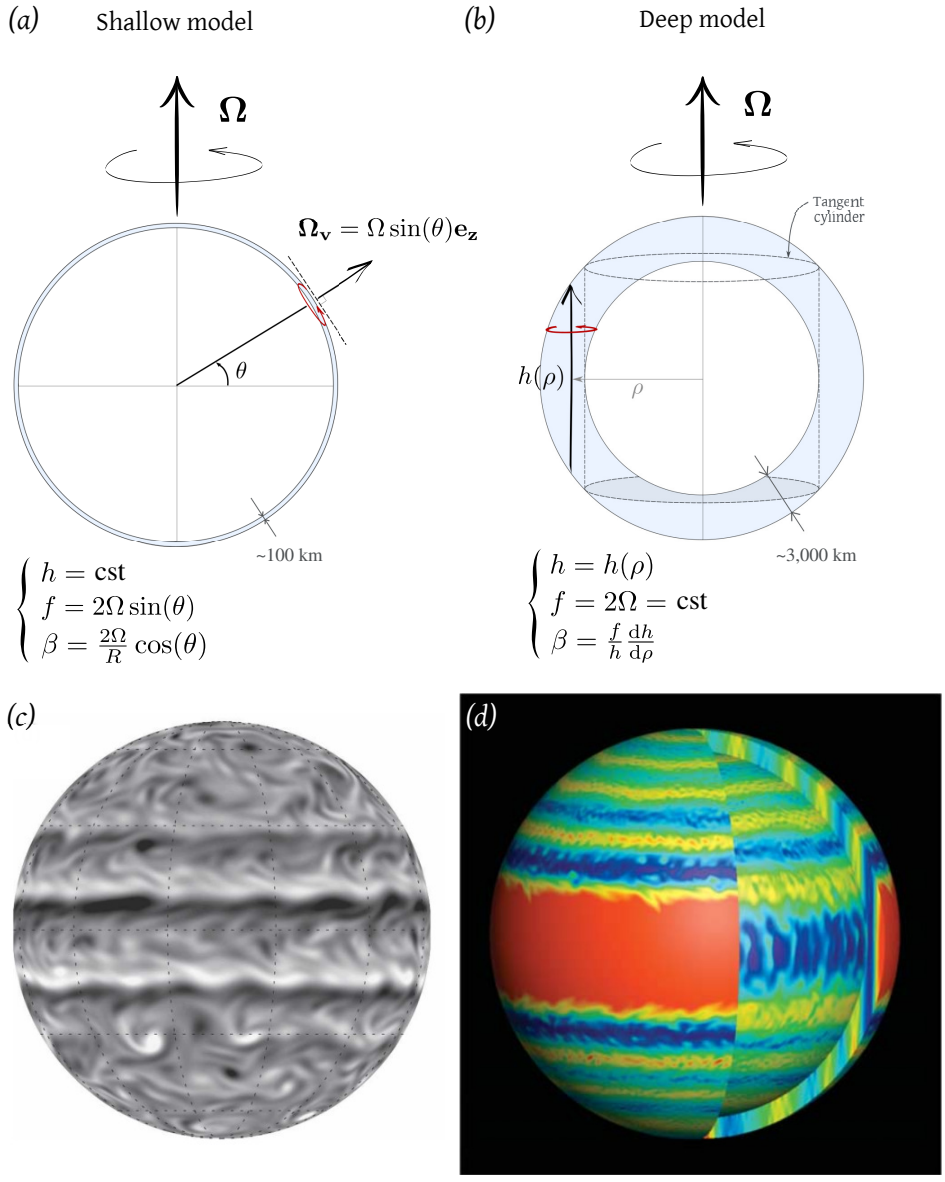

Figure 1.7. – Shallow and deep models of Jovian dynamics. *(a)* In the shallow model, the flow is quasi-2D because of geometrical confinement in a thin spherical shell and the β-effect arises from the variation of the Coriolis parameter with latitude (§1.2.4.2). *(b)* In the deep model, the flow is quasi-2D because of rapid rotation, and a β-effect arises from the variations of the fluid height with the distance to the spin axis (§1.2.4.3). Note that the depth of the dynamical region is not to scale, Jupiter has a mean radius of about 70,000 km. *(c)* Result of a numerical simulation solving the shallow-water equations on the sphere (shallow model). Figure taken from Scott et al. (2007). Shades of grey represent the relative vorticity (white: positive, black:negative). Sharp gradients correspond to prograde jets. *(d)* Result of a numerical simulation solving convective motions in a deep spherical shell. Colours represent the zonal component of the velocity (red: prograde, blue: retrograde). Figure taken from Heimpel et al. (2005).

where θ is the latitude (see Fig.1.8, top panel). The local coordinate system (x, y, z) is centred at a given latitude θ_0. x is the zonal coordinate (increasing towards the East), y the meridional one (increasing towards the North) and z the local vertical (aligned with $\mathbf{\Omega}_v$). The relation between y and the latitude is simply $y \approx R(\theta - \theta_0)$, where R is the planet's radius. In this local frame, the variation of the local rotation rate can be approximated by its Taylor expansion around the position $y = 0$:

$$\Omega_v(y) = \Omega_0 + \underbrace{\frac{\Omega}{R}\cos(\theta_0)}_{\beta/2}\ y\ +\ O\left(y^2\right). \tag{1.28}$$

The local rotation rate is $\Omega_0 = \Omega\sin(\theta_0)$. The β parameter, $\beta = 2\Omega/R\cos(\theta_0)$, represents the linear increase rate of the Coriolis parameter $f = 2\Omega$. This local, first-order description of the variation of the rotation rate is called the β-plane approximation (the motions are described on a plane tangent to the surface of the sphere). Note that at the pole, the same description leads to $\beta = 0$ since $\theta_0 = \pi/2$. To describe polar dynamics while taking into account the variation of the rotation rate, it is necessary to continue the expansion at second order:

$$\Omega_v(y) = \Omega_0 + \underbrace{\frac{\Omega}{R}\cos(\theta_0)}_{\beta/2}\ y\ \underbrace{-\frac{\Omega}{R^2}\sin(\theta_0)}_{\gamma/2}\ \frac{y^2}{2} + O(y^3) \tag{1.29}$$

This is the so-called γ*-plane approximation*.

Due to the variation along y of the rotation rate, a new term appears in the vorticity equation (1.27). Taking the curl of the 2D Navier-Stokes equations (1.24) and (1.25) leads to

$$\frac{\partial\zeta}{\partial t} + (\boldsymbol{u}_h\cdot\boldsymbol{\nabla}_h)\zeta = -2\frac{\partial\Omega_v}{\partial y}\ v + \nu\nabla_h^2\zeta + \boldsymbol{\nabla}_h\wedge\boldsymbol{F} \tag{1.30}$$

In the β-plane approximation, $\partial_y\Omega \approx \beta/2$, leading to the 2D barotropic vorticity equation on the β-plane:

$$\frac{\partial\zeta}{\partial t} + (\boldsymbol{u}_h\cdot\boldsymbol{\nabla}_h)\zeta + \beta v = \nu\nabla_h^2\zeta + \boldsymbol{\nabla}_h\wedge\boldsymbol{F}\quad(-\alpha\zeta). \tag{1.31}$$

Since the motions are bidimensional, it is convenient to define a streamfunction ψ such that $u = -\partial_y\psi$, $v = \partial_x\psi$ and $\zeta = \nabla^2\psi$ leading to

$$\frac{\partial}{\partial t}\nabla^2\psi + \mathscr{J}(\nabla^2\psi,\psi) + \beta\frac{\partial\psi}{\partial x} = \boldsymbol{\nabla}_h\wedge\boldsymbol{F}\quad(-\alpha\zeta), \tag{1.32}$$

where $\mathscr{J}$ is the Jacobian or Poisson bracket operator $\mathscr{J}(a,b) = \partial_x a\,\partial_y b - \partial_x b\,\partial_y a$. Compared to 2D-dynamics with a uniform rotation rate, the only additional term is the last one on the left-hand-side of (1.32), the so-called β-effect. This term acts as a source of negative vorticity for any northward motion ($v > 0$), and a source of positive vorticity for motions towards the equator ($v < 0$), as represented in the schematics of Fig.1.8.

1.2.4.3. Deep topographic β-effect and quasi-geostrophic model

We presented the origin of the β-effect in the framework of a shallow model for atmospheric motions, in the simplest case of a purely 2D flow. In the deep model, the aspect ratio of the structures cannot be considered as small, and the relevant rotation vector is the global one,

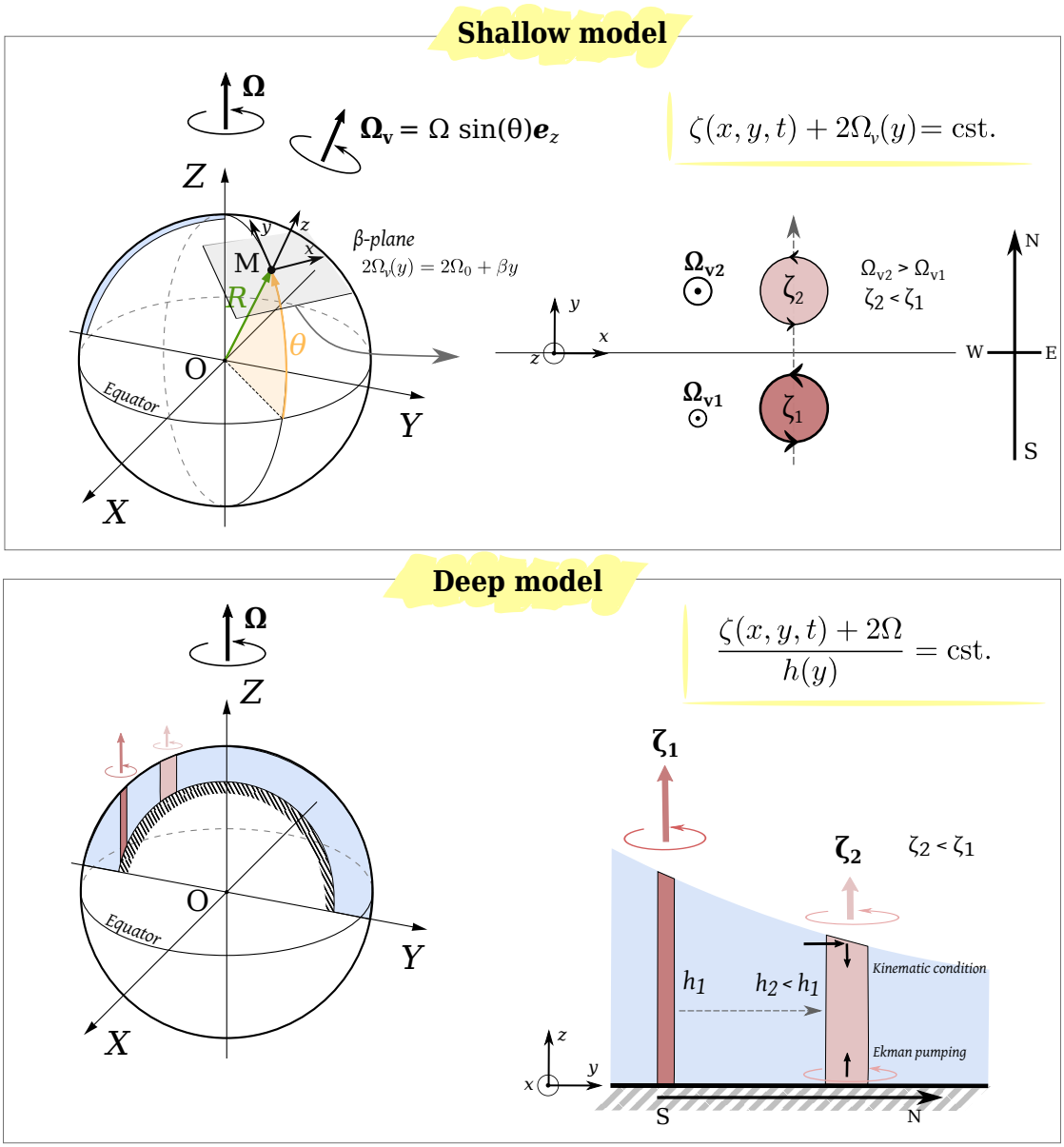

Figure 1.8. – The β-effect and conservation of potential vorticity in the shallow and deep frameworks. **Top row:** In a shallow model assuming a purely 2D flow on the surface of the sphere, β is the rate of increase of the local Coriolis parameter with latitude, $f = 2\Omega_v = 2\Omega\sin(\theta)$. In the β-plane approximation, this rate is considered constant, and motions are described in the vicinity of a reference latitude, θ_0. The schematic on the right explains the decrease of relative vorticity ζ when a fluid parcel is displaced towards the North, because the local rotation increases. **Bottom row:** In the deep model, the β-effect is topographic and due to variations of the fluid height with distance to the spin axis. The schematic on the right explains the decrease of relative vorticity ζ when a fluid parcel is displaced towards the North, because the fluid height decreases.

which is constant (see Fig.1.8). The bidimensionality arises from the fast rotation, which, as we saw previously, implies invariance of the flow in the direction parallel to the rotation axis. The flow would then resemble an ensemble of Taylor columns, aligned with the spin-axis of the planet. In this framework, one could think that the β-effect disappears because the rotation vector is constant, but in fact an analogous effect arises from the fact that the height of the fluid columns varies with distance to the spin axis, as sketched in Fig.1.8 (bottom panel). This is the so-called topographic β-effect. To demonstrate the analogy with the shallow β-effect, let us start again from the vorticity equation, assuming that we can neglect $\partial_z u$ and $\partial_z v$ thanks to fast rotation:

$$\frac{\partial \zeta}{\partial t} + (\boldsymbol{u}_h \cdot \boldsymbol{\nabla}_h)\zeta + (\zeta + f)(\partial_x u + \partial_y v) = \nu \nabla_h^2 \zeta + \boldsymbol{\nabla}_h \wedge \boldsymbol{F}. \tag{1.33}$$

The term involving the horizontal divergence is identically zero in a purely 2D flow like the one we considered before for the shallow β-effect. Here, we do not neglect it since variations in the height of a fluid column following meridional motions will induce horizontal divergence, and this is precisely where the topographic β-effect comes from. Integrating vertically the mass conservation equation (1.2) over the fluid depth gives an expression for the horizontal divergence:

$$\partial_x u + \partial_y v = -\partial_z w \tag{1.34}$$

$$\implies \frac{1}{h(y)} \int_{z=0}^{h(y)} (\partial_x u + \partial_y v) dz = -\frac{1}{h(y)} [w]_{z=0}^{z=h} \tag{1.35}$$

$$\implies \partial_x u + \partial_y v = \frac{w(z=0) - w(z=h)}{h(y)}. \tag{1.36}$$

The horizontal divergence is due to the vertical velocities at the top and bottom boundaries (see the schematic in the bottom right of Fig.1.8). The vertical velocity at the free surface, $w(z=h)$ can be expressed thanks to the kinematic boundary condition

$$w(z=h) = \frac{\partial h}{\partial t} + u\frac{\partial h}{\partial x} + v\frac{\partial h}{\partial y} \tag{1.37}$$

$$= v\frac{\partial h}{\partial y}, \tag{1.38}$$

where we neglect any perturbations of the free surface which are small compared to the large, stationary topographic variations (rigid-lid approximation). The vertical velocity at the bottom, $w(z=0)$, results from the no-slip boundary condition generating an Ekman pumping. According to linear Ekman theory, for a flat bottom and small Rossby number, the vertical velocity at the top of the boundary layer is proportional to the relative vorticity in the interior flow (see section 5.7 in Vallis 2017):

$$w(z=0) = -\frac{1}{2} E^{1/2} H \zeta, \tag{1.39}$$

where E is the Ekman number (equation (1.11)). The horizontal divergence is then

$$\partial_x u + \partial_y v = -\frac{v}{h}\frac{\mathrm{d}h}{\mathrm{d}y} + \frac{E^{1/2} H}{2h}\zeta. \tag{1.40}$$

The stretching of vorticity is hence due to the changes in the fluid depth and to the vertical velocity induced by the Ekman boundary layer. Substitution of the horizontal divergence in the

vorticity equation yields

$$\frac{\partial \zeta}{\partial t} + u\frac{\partial \zeta}{\partial x} + v\frac{\partial \zeta}{\partial y} \underbrace{-(\zeta + f)\frac{v}{h}\frac{\mathrm{d}h}{\mathrm{d}y}}_{\text{Topographic } \beta\text{−effect}} + \underbrace{\frac{E^{1/2}H}{2h}(\zeta + f)\zeta}_{\text{Ekman pumping}} = \nu\nabla^2\zeta + \boldsymbol{\nabla}_h \wedge \boldsymbol{F}. \tag{1.41}$$

We stand in the limit where the local Rossby number of the flow $Ro_\zeta = \zeta / f$ is small, hence $\zeta \ll f$. Retaining only the linear part of the β-effect and Ekman pumping, we retrieve the classical 2D barotropic vorticity equation in the β-plane approximation derived previously:

$$\frac{\partial \zeta}{\partial t} + (\boldsymbol{u}_h \cdot \boldsymbol{\nabla}_h)\zeta + \underbrace{\beta\, v}_{\beta\text{−effect}} + \underbrace{\alpha\zeta}_{\text{Ekman friction}} = \underbrace{\nu\nabla^2\zeta}_{\text{Bulk dissipation}} + \boldsymbol{\nabla}_h \wedge \boldsymbol{F} \quad , \tag{1.42}$$

with β the topographic β parameter resulting from the fluid height meridional variations and α the linear Ekman friction parameter:

$$\beta = -\frac{f}{h}\frac{\mathrm{d}h}{\mathrm{d}y}, \tag{1.43}$$

$$\alpha = \frac{E^{1/2} f H}{2h}. \tag{1.44}$$

Given the exact similarity of the two β-effect terms in equations (1.31) and (1.42), the physical effect is the same: any meridional motions are accompanied by a change in the relative vorticity of the fluid column. The only difference with equation (1.31) is the presence of a linear friction term due to Ekman pumping. This term is lacking when considering directly purely 2D dynamics, but in fact a linear friction term or a hypoviscous term is always added to the 2D vorticity equation to provide a way to dissipate energy at large scales. Otherwise, energy would accumulate at large scales, which is not physically relevant.

Equation (1.42) constitutes the simplest so-called *quasi-geostrophic* (QG) model. Indeed, we have taken advantage of the fact that the flow is almost in geostrophic balance due to fast rotation, but we have incorporated three-dimensional effects due to the curvature of the free-surface as well as the friction over the bottom (Ekman pumping). In chapter 3, the β-effect in the *Jacuzzi* experimental set-up is of topographic origin. We will use the basic quasi-geostrophic model (1.42) to analyse the emergence of the zonal flow. A QG model will also be used to perform idealized numerical simulations to complement the experiments. The main differences are that the numerical model is derived in cylindrical geometry to better represent the experiment, and that it incorporates higher order terms for the β-effect and Ekman friction (see Appendix C).

1.2.4.4. Potential vorticity

The evolution of the flow in the presence of a β-effect in the shallow (equation (1.31)) and the deep (equation (1.42)) models is often described in terms of potential vorticity. The potential vorticity q is a function of the relative vorticity ζ which is materially conserved in the absence of viscous dissipation. Its expression can be derived in the shallow or deep models by noticing that, in the absence of forcing and dissipation, equations (1.31) and (1.41) can be recast as

$$\frac{\mathrm{D}(\zeta(x,y,t) + \beta y)}{\mathrm{D}t} = 0, \text{ hence } \quad q \equiv \zeta(x,y,t) + \beta y \tag{1.45}$$

for the shallow model, and

$$\frac{\mathrm{D}}{\mathrm{D}t}\left[\frac{\zeta(x,y,t)+f}{h(y)}\right]=0, \text{ hence } \quad q\equiv\frac{\zeta(x,y,t)+f}{h(y)} \tag{1.46}$$

for the deep model, where $\mathrm{D}\cdot/\mathrm{D}t=\partial_t\cdot+(\boldsymbol{u}_h\cdot\boldsymbol{\nabla}_h)\cdot$ is the material derivative. The conservation of the potential vorticity along the trajectory of a fluid parcel helps to physically interpret the β-effect, as sketched in Fig.1.8. Let us assume a northward displacement $\delta y>0$ of a fluid parcel of initial cyclonic relative vorticity $\zeta_1>0$. In the shallow model, after this displacement, the ambient rotation is increased by $+\beta\delta y$, leading to a decrease of the parcel's relative vorticity such that q remains constant. In the deep model, a fluid column flattens while moving northward, because of the decreasing fluid height. Its relative vorticity then decreases such that q remains constant.

1.2.4.5. Rossby waves

Apart from source and sink of relative vorticity, the β-effect introduces an important new linear dynamics in the form of so-called *Rossby waves* or *planetary waves*. Qualitatively, Rossby waves can be understood as represented in Fig.1.9*(a)*. If we imagine a sinusoidal meridional displacement, then the conservation of potential vorticity implies that the vorticity of the parcels moved towards the north decreases ($\delta\zeta<0$), whereas the vorticity of parcels moved towards the south increases ($\delta\zeta>0$). Since $\partial_x v=\zeta$ (in the case $u=0$), the initial oscillation is transmitted towards the negative x direction, i.e. westward. This behaviour can be mathematically derived from the vorticity equation. The β-plane vorticity equation (1.32), inviscid, and linearised about a mean zonal flow U is

$$\frac{\partial}{\partial t}\nabla^2\psi+U\frac{\partial}{\partial x}\nabla^2\psi+\beta\partial_x\psi=0. \tag{1.47}$$

We seek solutions of this equation in the form of unbounded plane waves, $\psi\sim\exp(\mathrm{i}(\boldsymbol{k}\cdot\boldsymbol{x}-\omega t))$, where $\mathbf{k}=(k,l)$ is the horizontal wave vector and ω is the angular frequency. We obtain the dispersion relation of the Rossby waves:

$$\omega=Uk-\beta\frac{k}{k^2+l^2}=Uk-\beta\frac{k}{K^2}. \tag{1.48}$$

The associated phase and group velocities are

$$c_x=\frac{\omega}{k}=U-\frac{\beta}{K^2}, \qquad \text{(zonal phase speed)} \tag{1.49}$$

$$c_y=\frac{\omega}{l}=U\frac{k}{l}-\beta\frac{k}{K^2l}, \qquad \text{(meridional phase speed)} \tag{1.50}$$

$$c_{g,x}=\frac{\partial\omega}{\partial k}=U+\beta\frac{k^2-l^2}{K^4}=c_x+\frac{2\beta k^2}{K^4} \quad \text{(zonal group velocity)} \tag{1.51}$$

$$c_{g,y}=\frac{\partial\omega}{\partial l}=\frac{2\beta kl}{K^4} \qquad \text{(meridional group velocity)} \tag{1.52}$$

Rossby waves have a westward phase speed relatively to the mean flow ($c_x<U$), which increases with increasing wavelength (long Rossby waves are the fastest). They can become stationary in an eastward ($U>0$) mean flow. This is important for Earth's atmosphere, because Rossby waves can then be excited by stationary features such as topography. This property is also the basis of the mechanism described in chapter 3 for the transition between two regimes of zonal jets. Their zonal group velocity is equal to their zonal phase speed, plus a positive quantity. The zonal group velocity is hence eastward faster than the zonal phase speed. The

dispersion relation (1.48) is modified when taking into account surface and internal buoyancy effects, and involves in general the Rossby radius of deformation R_d (see Vallis 2017, section 6.5). Fig.1.9*(b,c)* show two real-world examples of long Rossby waves in a laboratory experiment and in Earth atmosphere.

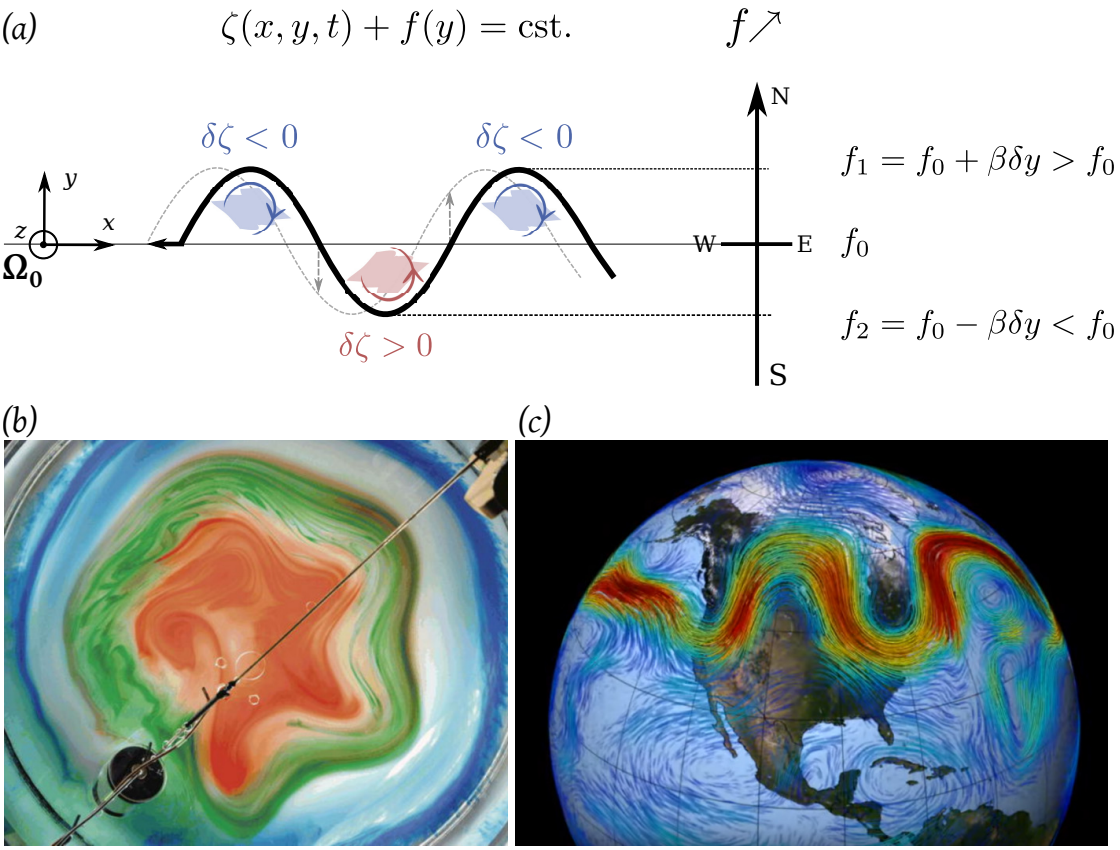

Figure 1.9. – *(a)* Schematic of Rossby waves propagation mechanism. *(b)* Rossby wave excited by the periodic oscillation of a plunger in a polar-β-plane experiment (figure from Rhines (2007)). *(c)* Long Rossby wave associated with the midlatitude jet stream undulations. Credits: NASA Goddard Space Flight Center.

1.2.5. Some fundamental concepts of 3D and 2D turbulence

Now that we have described basic properties and governing equations for rotating, stratified flows with a β-effect, we briefly expose the consequences of the turbulent nature of Jupiter's dynamics. We qualitatively present theories for three-dimensional and two-dimensional homogeneous isotropic turbulence. We will discuss later how the β-effect modifies these classical pictures and lead to zonal jets formation (§1.4.2.2).

1.2.5.1. Three-dimensional homogeneous and isotropic turbulence

Comparing the magnitude of the inertial to viscous terms in the Navier-Stokes equations (1.1) introduces the Reynolds number

$$Re \sim \frac{\text{advective term}}{\text{viscous diffusion}} \sim \frac{|(\boldsymbol{u}\cdot\boldsymbol{\nabla})\boldsymbol{u}|}{|\nu\nabla^2\boldsymbol{u}|} \sim \frac{VL}{\nu} \sim \frac{\tau_\nu}{\tau_i} . \tag{1.53}$$

The Reynolds number is also the ratio of the viscous timescale $\tau_\nu = L^2/\nu$ to a turnover timescale $\tau_i = L/V$, where L and V are typical length-scale and velocity of the flow respectively. The viscous time is the time for a structure of scale L to lose its momentum following viscous diffusion, and the turnover timescale is the time for an eddy of size L to perform a complete revolution. If $Re \gg 1$, viscous diffusion occurs on timescales much longer than the overturns, and the flow is said to be turbulent. In other words, inertial effects are dominant compared to viscous diffusion.

Three-dimensional turbulent flows are described by the famous self-similar Kolmogorov theory (Kolmogorov et al. 1991). Apart from the condition $Re \gg 1$, several strong assumptions lie behind this theory. First, eddies transfer energy to other eddies *locally* (i.e. only comparable scales speak to each other). Second, *isotropy* is assumed, meaning that the flow is (in a statistical sense) the same in all directions. Third, statistical *homogeneity* is assumed, meaning that the flow is the same everywhere in space. With these assumptions, the classical picture is that, if energy is injected at scales insensitive to viscous dissipation (scales for which $Re \gg 1$), then energy cascades locally to smaller and smaller eddies down to a scale where viscous dissipation becomes again efficient. Hence, despite the high Reynolds number of the flow, viscosity is crucial since it is responsible for removing the injected energy such that a statistical steady state can be achieved. The Kolmogorov theory namely allows to predict the behaviour of a statistical quantity, called the energy spectral density, which is the energy computed in the Fourier space. If we denote $\hat{\boldsymbol{u}} = (\hat{u}, \hat{v}, \hat{w})$ the Fourier transform of the velocity field, and $\boldsymbol{k} = (k_x, k_y, k_z)$ the associated wavenumber, then the Parseval relation ensures that the total kinetic energy can be computed in the physical or Fourier space indistinctly:

$$\mathscr{E} = \frac{1}{2}\iiint \|\boldsymbol{u}\|^2 \mathrm{d}V = \frac{1}{2}\iiint \|\hat{\boldsymbol{u}}\|^2 \mathrm{d}^3\boldsymbol{k}. \tag{1.54}$$

$\|\hat{\boldsymbol{u}}\|^2/2$ hence represents the kinetic energy per unit mass associated with the velocity components having a wavevector comprised in a volume $\mathrm{d}^3\boldsymbol{k}$ around $\boldsymbol{k}$ (in the spectral space). Given the isotropy and homogeneity assumptions, this energy depends on the wavevector modulus only ($\|\boldsymbol{k}\| = k$) and we can define the spectral energy density $E(k)$ such that

$$\mathscr{E} = \frac{1}{2}\iiint \|\hat{\boldsymbol{u}}\|^2 \mathrm{d}^3\boldsymbol{k} = \int \|\hat{\boldsymbol{u}}\|^2 \, 4\pi k^2 \mathrm{d}k = \int E(k)\mathrm{d}k. \tag{1.55}$$

$E(k)\mathrm{d}k$ is the kinetic energy contained by velocity components of wavenumber situated in an interval $\mathrm{d}k$ around k, i.e. the kinetic energy contained at a given scale $\sim 1/k$.

The key to Kolmogorov's theory is to state that there is an *inertial range* of scales comprised below the forcing scale, and above the viscous scale, where the transfer of energy between eddies is only sensitive to the energy input rate, ϵ, and to the considered scale or wavenumber, k, and is independent of both the forcing details and the viscosity. From dimensional analysis, with these two parameters, the only spectral energy density that can be constructed is

$$E(k) \propto \epsilon^{2/3} k^{-5/3}. \tag{1.56}$$

Energy decreases with decreasing scale, thereby illustrating the cascade mechanism. According to this theory, the proportionality constant known as Kolmogorov's constant should be universal, i.e. similar for any turbulent flow, even if they are forced by different mechanisms. The viscous scale, called the Kolmogorov scale, is the scale at which the local turbulent Reynolds number equals unity, i.e. when the viscous timescale $1/(k^2\nu)$ is equal to an eddy turnover timescale in the inertial range, $\epsilon^{-1/3}k^{-2/3}$, leading to $k_\nu \sim (\epsilon/\nu^3)^{1/4}$. The basic properties of 3D homogeneous isotropic turbulence are summarized in Fig.1.10*(a)*.

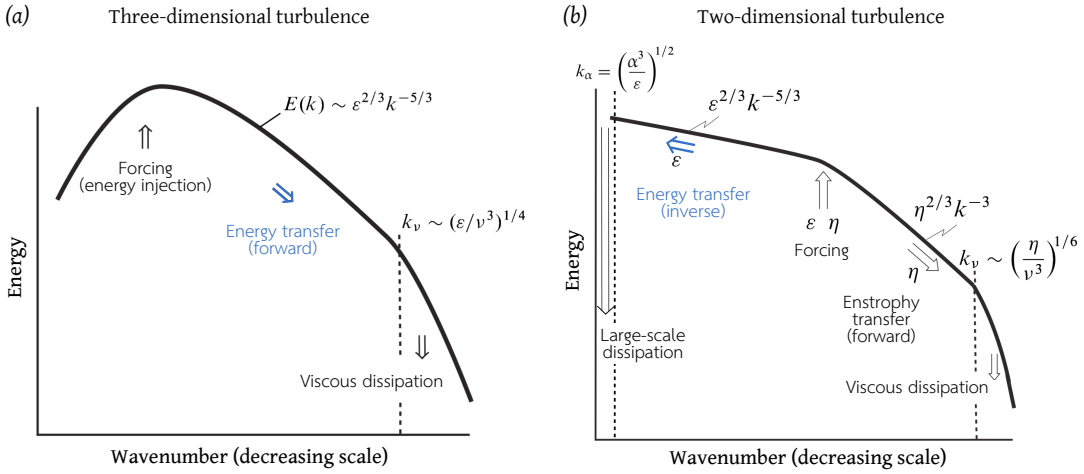

Figure 1.10. – Theoretical kinetic energy spectra of three-dimensional and two-dimensional turbulence. *(a)* 3D turbulence. Energy cascades towards smaller scales at a rate ϵ. *(b)* 2D turbulence. Energy cascades towards larger scales at a rate ϵ. Enstrophy cascades towards smaller scales at a rate η. k_ν is the viscous scale, k_α is the large dissipation scale, with α the frictional rate. Figures adapted from Vallis (2017).

To physically understand the origin of the energy cascade, the vorticity equation (1.3) is enlightening, and allows to readily feel the difference between 3D and 2D turbulence. The basic mechanism of turbulent forward cascade in 3D flows lies in the stretching-tilting term $(\boldsymbol{\zeta}\cdot\boldsymbol{\nabla})\boldsymbol{u}$: turbulent vorticity tubes are constantly stretched by velocity fluctuations. If on average they are more elongated that flattened, the vorticity increases in tubes of smaller section, thereby increasing the energy contained at smaller scales. Vorticity tubes are continuously elongated into tubes of smaller section, until they become small enough that the loss due to viscous diffusion compensates the vorticity increase due to stretching (Guyon et al. 2012).

1.2.5.2. Kolmogorov-Batchelor-Kraichnan theory of two-dimensional turbulence

In a 2D flow, the very basic physical mechanism by which energy is transferred to smaller scales is suppressed: velocity gradients (horizontal) are necessarily perpendicular to the vorticity axis (vertical), hence no vortex stretching can occur. Due to the absence of vortex stretching, a second quadratic invariant is present along with kinetic energy, called the enstrophy, $\mathcal{Z} = \frac{1}{2}\zeta^2$. Following the same assumptions as for 3D turbulence (locality, isotropy and homogeneity), the so-called Kolmogorov-Batchelor-Kraichnan theory predicts a double cascade: an *inverse* cascade of energy towards large scales (at a rate ϵ), and a *forward* cascade of enstrophy (at a rate η) towards small scales. Physically, the direct enstrophy cascade can be understood the following way: in the inertial range, the section of vorticity tubes is conserved. The corresponding area is deformed by velocity fluctuations, thereby concentrating vorticity in filaments of smaller transverse scale and hence transferring enstrophy at smaller scales. To allow for a steady state, these transfers should come along with a small-scale dissipation of enstrophy (viscous diffusion) at a scale k_ν and a large-scale dissipation of energy at a scale k_α. In classical models, the large-scale dissipation is represented by a linear friction. As seen previously, the drag term is a linear term $-\alpha\zeta$ in the vorticity equation, with α the friction rate (see equation (1.42)). If we assume that large-scale dissipation is entirely due to this linear friction, then the frictional scale L_α is

$$L_\alpha \propto \frac{1}{k_\alpha} \sim \left(\frac{\epsilon}{\alpha^3}\right)^{1/2}. \tag{1.57}$$

If the forcing scale is sufficiently separated from the two dissipation length scales, scaling laws are again expected for the spectral energy density in the two inertial ranges:

$$E(k) = C_K \epsilon^{2/3} k^{-5/3}, \text{ for } k_\alpha < k < k_f \tag{1.58}$$

$$E(k) = C_E \eta^{2/3} k^{-3}, \text{ for } k_f < k < k_\nu. \tag{1.59}$$

C_K and C_E are again universal constants. These properties are sketch in Fig.1.10*(b)*. Note that the theory of two-dimensional turbulence is not cast in stone, and that various aspects are still debated including the validity of the locality assumption in the forward enstrophy cascade. Numerical and experimental observations strongly support the $-5/3$ inverse cascade scaling, with $C_K \approx 6-7$, but the picture is less clear for the enstrophy cascade, namely due to the influence of coherent vortices, and the -3 scaling is not robustly obtained. These discussions are beyond the scope of the present chapter, we refer the reader to the review by Boffetta et al. (2012) for details regarding these matters.

The turbulence observed in Jupiter's atmosphere has features of bidimensional turbulence. In particular the fact that the largest scales of the flow are larger than the possible forcing scales (see section 1.4.1) implies an inverse transfer of energy. However, several assumptions underlying the Kolmogorov-Batchelor-Kraichnan (KBK) theory are very likely not fulfilled by planetary turbulence:

— Atmospheric flows are neither isotropic nor homogeneous. Isotropy is for instance broken by rotation (the meridional and longitudinal directions are not equivalent), and homogeneity is broken by large-scale jets and vortices.

— Jupiter's flows are only quasi-2D. The turbulent flow may lose bidimensionality at sufficiently small scale where geostrophy does not hold anymore (large local Rossby number) or, in the shallow model, when the scale becomes smaller than the fluid depth. We thus expect Jupiter's turbulence to share properties of both 2D and 3D turbulence.

— Rotation, stratification and the β-effect introduces restoring forces responsible for the existence of linear waves (inertial, internal and Rossby waves respectively). The turbulence is affected by these waves, and there is a subtle interplay between coexisting waves and turbulent eddies. We will see for instance in chapter 3 how linear Rossby waves strongly affect the final dynamics of turbulent zonal jets.

— The β-effect or the Rossby radius of deformation associated with a stratification can compete with the inverse cascade mechanism towards large scales and induce anisotropy. This interaction is detailed later in section 1.4.2.2.

We have presented the basic physical ingredients of Jupiter's dynamics: rotation, stratification, β-effect and turbulence – omitting compressibility and magnetohydrodynamical effects. We focused on the two simplest shallow and deep models to introduce the conceptual differences and similarities between the two frameworks. In both cases, more complete models are usually employed.

— In the shallow framework, we considered purely 2D flows. It is sufficient for the purpose of the present introduction, i.e. to understand the origin and consequences of the β-effect. But in reality, the atmospheric community uses more sophisticated models called shallow-water models where the fluid thickness is considered as thin, but deformations of the upper free surface are allowed introducing supplementary buoyancy effects (finite Rossby radius of deformation). More realistic two-layer shallow-water models are also employed in which the thin fluid layer representing the weather layer overlies a denser and much deeper layer. This is known as the $1-1/2$-layer equivalent barotropic, or reduced gravity model (Vallis 2017).

— In the deep framework, we have considered the rigid bottom boundary as flat. In reality, the bottom boundary is spherical and the associated Ekman pumping is modified by geometrical factors. There is also a discontinuity in the fluid height when crossing the tangent cylinder (Fig.1.7*(b)*). These geometrical effects are taken into account in QG models of rotating thermal convection in spherical shells (see e.g. Cardin et al. 1994; Gillet et al. 2006).

— Finally, some fully three-dimensional models are employed and allow to incorporate other relevant effects besides the β-effect, such as compressibility, via the anelastic approximation (e.g. Gastine et al. 2012; Heimpel et al. 2016; Yadav et al. 2020), or magnetohydrodynamical effects (e.g. Jones 2014; Dietrich et al. 2018; Gastine et al. 2021).

We now have the tools to guide our interpretation of Jupiter's dynamics. In the next two sections, we overview some observations, at the cloud level, of Jupiter's vortices and zonal jets, and associated modelling.

1.3. Jupiter's dynamics: vortices

Within Jupiter's zonal jets are observed hundreds of ovals of various colours. Bright colours, visible in Fig.1.11*(a)* in white ovals, are due to the scattering of the sunlight by the upper clouds and hazes condensed there. Reddish colours, seen in the GRS and Oval BA in the same figure, are attributed to chromophores which can coat ammonia particles (Sindoni et al. 2017). Cloud tracking reveals that these features are vortices of scales ranging from a few hundred kilometres up to the scale of the bands, 10,000 km (Fig.1.11). At midlatitudes, there is a preference for anticyclones over cyclones: 90% of the vortices are anticyclonic (Vasavada et al. 2005), i.e. rotating in the opposite direction compared to the planet's rotation: clockwise in the northern hemisphere, and anticlockwise in the southern hemisphere (see Fig. 1.5*(c,d)* for the GRS and Fig.1.11). Anticyclones are oval-shaped, whereas cyclones have a more irregular, lobed or filamentary structure. Anticyclones are located in anticyclonic shear zones, whereas cyclones are in cyclonic shear zones, suggesting that vortices rotating in the opposite direction compared to the shear are unstable and sheared apart (Marcus et al. 2000). The most well-known anticyclones are the GRS and Oval BA, because of their size and longevity.

In terms of longevity, the GRS is at least 150 years old, and could be much older and correspond to the large spot discovered in the seventeenth century (Rogers 1995). The Oval BA formed from the merger of three white ovals in 1998 and 2000, but before that, its parent white ovals survived for 60 years without merging (Choi et al. 2010). Smaller vortices have shorter lifetimes. Using the 70 days movie made by Cassini, Li et al. (2004) showed that the mean lifetime of spots exceeding 700 km in diameter is of 17 days. Morales-Juberias et al. (2002) found that large anticyclones (North-South extent between 1000 and 6000 km) have a lifetime of 1 to 3 years.

In terms of internal dynamics, Jovian vortices are free vortices with closed elliptical streamlines, and do not exchange a lot of fluid with the zonal jets (Vasavada et al. 2005). Large scale vortices have tangential velocities which increase roughly linearly with radial distance (Fig.1.11*(e)*). The GRS is the only Jovian vortex to display a quiescent centre where the winds seem to vanish (see Fig.1.11*(d)*). In 1996, the GRS had dimensions of $22,000 \times 11,000$ km. But for the past 40 years, the GRS has been shrinking in the longitudinal direction and the collar wind speeds have been increasing (Simon et al. 2018). This shrinking is accompanied by a reduction of the quiescent centre.

The main hypothesis is that Jupiter's largest vortices are formed by barotropic or baroclinic instabilities of the zonal jets (Read et al. 1983, 1984; Read 1986; Dowling et al. 1988a; Sommeria

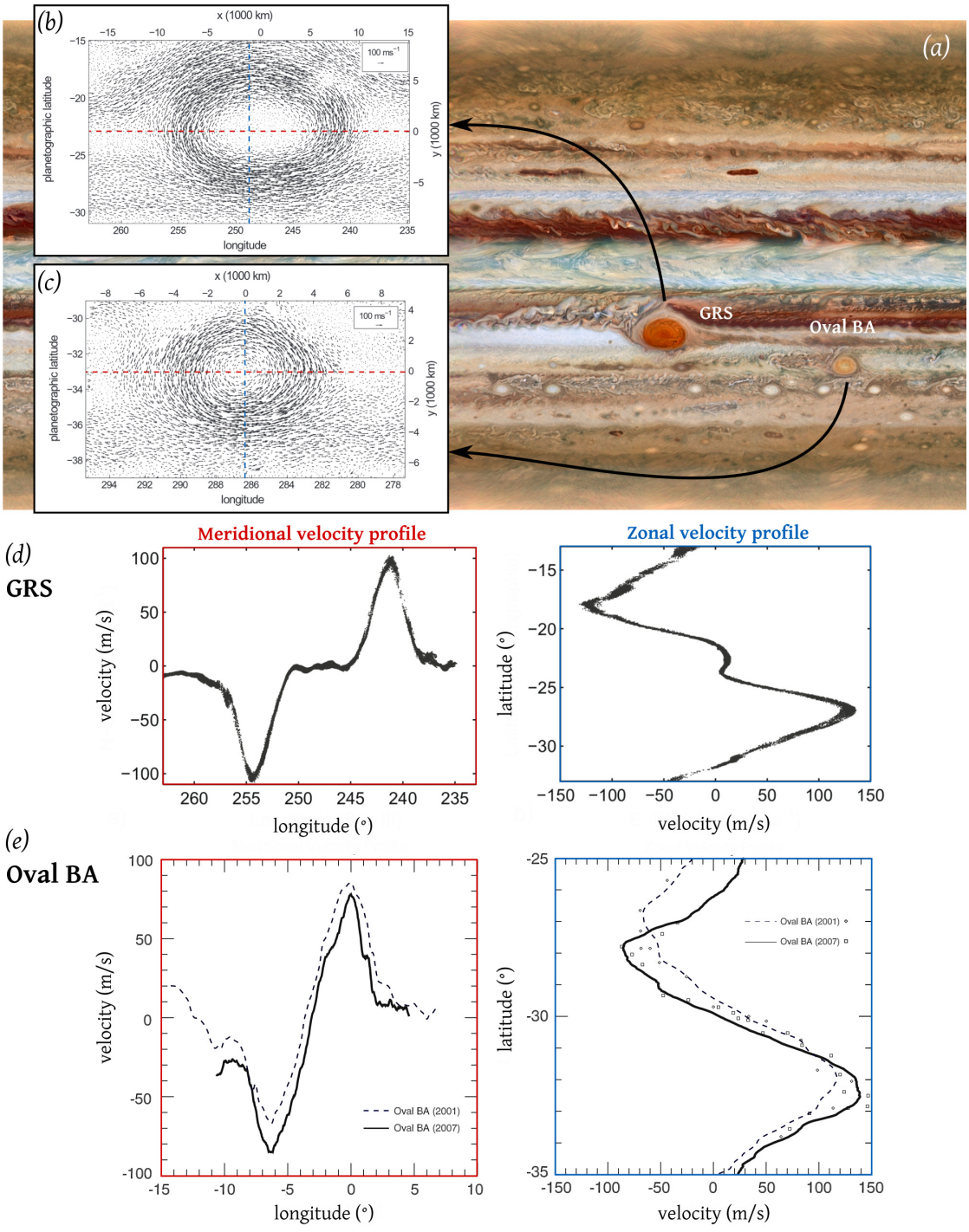

Figure 1.11. – Velocity fields and velocity profiles for two prominent anticyclones of Jupiter: the Great Red Spot (GRS) and the Oval BA. *(a)* Hubble Space Telescope, January 2015. *(b)* Velocity field in the GRS in 2006 (from Shetty et al. (2010)). *(c)* Velocity field in the Oval BA in 2006 (from Shetty et al. (2010)). *(d)* Velocity profiles through the GRS in 2006 (from Asay-Davis et al. (2009)). *(e)* Velocity profiles through the Oval BA in 2001 and 2007 (from Choi et al. (2010)).

et al. 1988; Williams 2002). In a given band, a chain of vortices forms following such instabilities, and the vortices merge when they approach each other and give rise to larger scale vortices. In the presence of a β-effect, vortices are expected to drift due to both the emission of Rossby waves and secondary circulations induced by the vortex itself (so-called β-gyres). Cyclones should migrate towards the north-west, and anticyclones towards the equator and the west. Midlatitude vortices are extremely stable in latitude, suggesting that zonal jets impede their meridional migration (Achterberg et al. 1994). In longitude, they mostly drift westward compared to the ambient flow, and this drift has been attributed to Rossby waves (Li et al. 2004). The emission of dispersive Rossby waves by vortices should lead to their progressive decay. An important degree of non-linearity is required to compensate for the tendency of vortices to be dispersed by this process. The source of energy maintaining the vortices against dispersion and dissipation is currently unknown, and could arise from heat latent release, merger with other vortices, exchange of energy with the zonal jets, etc. (Vasavada et al. 2005). Note that several properties of midlatitude Jovian vortices, such as the cyclone-anticyclone asymmetry, are only reproduced in shallow-water systems and not in purely 2D systems, underlying the importance of vortex columns stretching and of a finite radius of deformation (Polvani et al. 1994).

The vertical structure of Jovian vortices is unknown from direct measurements. Historically, Hide (1961) proposed that the GRS could be a Taylor column associated with a deep topography. The absence of any solid surface at depth, confirmed later by interior models, changed this initial picture into that of compact vortices floating in a stratified ambient, as in Fig.1.4*(d)*. This is an important difference with cyclones on Earth, which namely dissipate by friction on continents or oceans, and it is one of the keys to understand the longevity of Jovian vortices. Temperature measurements in the upper troposphere and lower stratosphere suggest that Jovian vortices extend at most up to 40 to 80 km above the cloud level (Conrath et al. 1981). Below the clouds, due to baroclinic instability, it has been suggested that the vortices depth should not exceed their width by a factor greater than f/N, leading to a maximum depth of 500 km below the clouds (Vasavada et al. 2005). The analysis of hot rings surrounding the periphery of ovals suggested that anticyclones could extend vertically from the water cloud (~ 5 bars) up to the tropopause (de Pater et al. 2010). The structure of midlatitude Jovian cyclones is the focus of chapter 2.

The dynamics of Jupiter at high latitudes is drastically different, as revealed recently by the Juno spacecraft (Fig.1.12). Whereas anticyclones are the dominant vortices at midlatitudes, Juno showed that the polar dynamics is dominated by cyclones measuring $\sim 2{,}500$ km in diameter, and with peak velocities of ~ 80 m/s. These cyclones are organized into striking polygonal patterns around each pole. They form a cluster of 5 cyclones at the North Pole, and a cluster of 8 cyclones at the South Pole, as seen in Fig.1.12. Corresponding imaging in the infrared is provided in chapter 6, Fig.6.2. In either case, there is an additional cyclone roughly centred at the pole (Adriani et al. 2018). These features have been remarkably stable for the past 2 years of observations (Adriani et al. 2020), and similarly to midlatitude vortices, we have no direct indication of how deeply-rooted polar cyclones are. Additional details on Jovian polar cyclones are provided in chapter 6 in which we discuss the dynamics of cyclones at the pole.

1.4. Jupiter's dynamics: zonal jets

1.4.1. Observations

1.4.1.1. Structure of Jovian zonal jets

Zonal jets are east-west winds of alternating direction. These winds are measured in the frame rotating with the planet, meaning that the flow in a zonal jet is rotating faster or slower

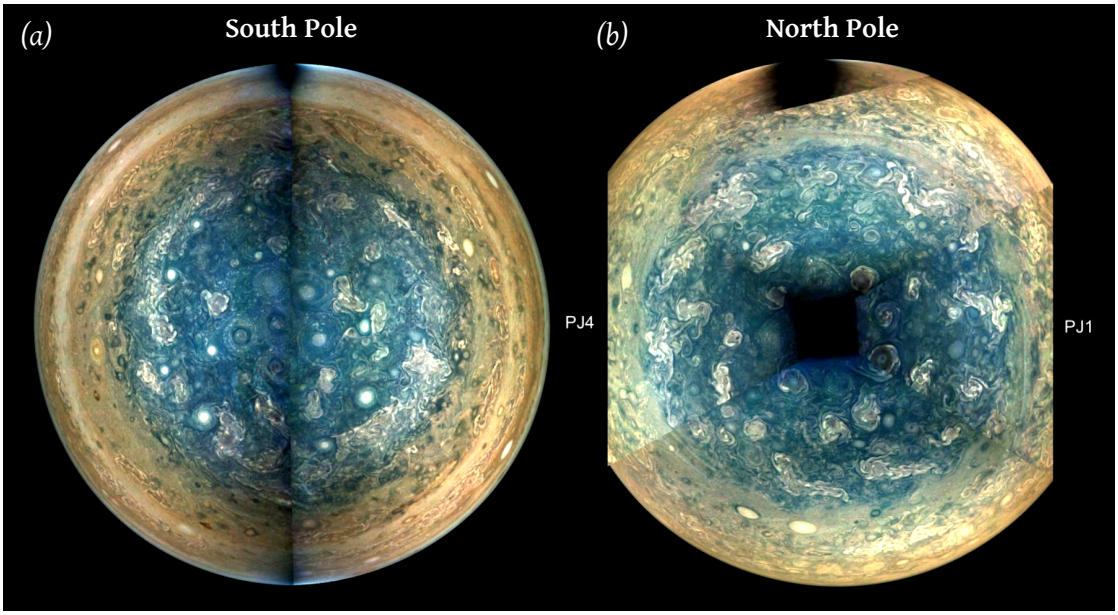

Figure 1.12. – *(a)* South polar view of Jupiter, composited from views directly above the pole at perijoves 1 and 4. *(b)* North polar view of the planet, composited from views directly above the pole at perijoves 1, 3, 4 and 5. Credits:NASA/SwRI/MSSS/Gerald Eichstädt/John Rogers.

than the underlying planet. Given the fluid nature of Jupiter, it is subtle to define a global solid-body rotation rate for the whole planet: differential rotation of concentric cylinders may a priori extend deep within the planet. Up-to-date, Jupiter's rotation period is assumed to be represented robustly by the rotation period of its magnetic field which is tilted from its spin pole (Helled 2019). The jets are called prograde when the corresponding wind is faster than the planet's rotation, i.e. when the wind is eastward in the frame rotating with the planet. In the opposite case where the winds are westward, jets are said retrograde. Zonal flows are ubiquitous in planetary fluid envelopes (see section 1.6), but they are particularly striking in the gas giant atmospheres, in the sense that they contain a large fraction of the total kinetic energy and that their dynamics is not complicated by topographic features or seasonal variations. On Jupiter, the zonal jets are famous because they are responsible for the banded appearance of the planet (Fig. 1.13), through the spreading of clouds of ammonia and water ices. The dark and light bands encircling Jupiter are respectively called belts and zones. The zones are defined as having anticyclonic vorticity (clockwise in the northern hemisphere) and the belts as having cyclonic vorticity (counter-clockwise in the northern hemisphere). About 30 zonal jets are present on Jupiter, up to latitudes of ~80° in each hemisphere, and the jets are located at the boundaries between belts and zones (see Fig.1.13). Near the equator, the zonal wind is prograde and reaches velocities up to 150 $\mathrm{m\,s^{-1}}$ (540 $\mathrm{km\,h^{-1}}$). The equatorial wind of Jupiter is qualified as super-rotating, because rotating faster than the planet. On Jupiter, it has been suggested that at the top of the clouds, the jets may contain more than 90% of the total kinetic energy (Galperin et al. 2014b). Apart from their strength, the remarkable stability of Jupiter's jets has been demonstrated by an almost continuous record of the zonal winds profile which varied very little over tens of years (Porco et al. 2003; Tollefson et al. 2017).

Similarly to vortices, observations and measurements of zonal winds are confined to the superficial weather layer, and very little is known about their three-dimensional structure. Up to recently, the only actual data about jets in Jupiter's interior were the measurements taken in 1995 by the Galileo atmospheric entry probe which sounded the gas giant's atmosphere from 0.4 up to 22 bars (Seiff et al. 1998). The winds measurements, performed at the northern edge of

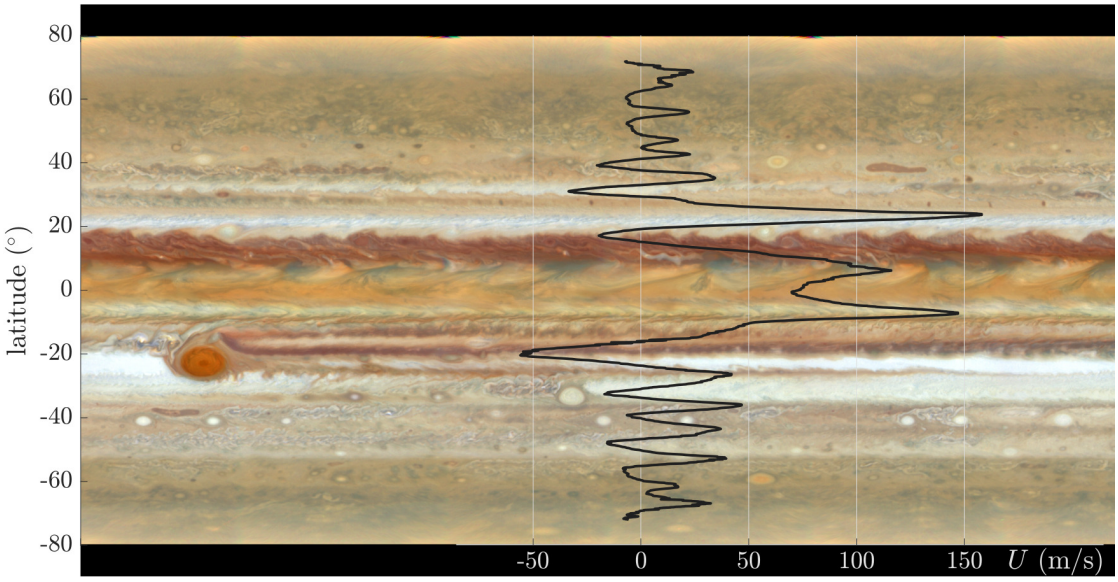

Figure 1.13. – Jupiter cloud-level zonal winds as a function of latitude. The winds velocity profile in 2015 is plotted from the data sets provided in Tollefson et al. (2017). The background image is a combination of Hubble Space Telescope images taken in 2019. Credits: NASA, ESA, A. Simon (Goddard Space Flight Center) and M.H. Wong (University of California, Berkeley).

the equatorial jet, indicated that the jet's speed increases from 90 to 180 $\mathrm{m\,s^{-1}}$ up to 5 bars, and then remains constant. Galileo measurements are nevertheless insufficient to assess anything about the vertical structure of the jets, given their local nature and the limited extent of the probing compared to the planet's radius (150 km vs. 70,000 km). Recently, the inversion of the gravity measurements of the Juno spacecraft (Bolton et al. 2017) answered this long-standing question by showing that the Jovian jets extend down to about 3,000 kilometres ($\sim 0.96 R_J$) beneath the clouds (Kaspi et al. 2018; Guillot et al. 2018), even if the use of the thermal-wind equation to perform the inversion is debated (Kong et al. 2018). This result is consistent with the predicted depth at which electrical conductivity becomes sufficiently large so that ohmic dissipation should suppress differential rotation between the jets (Liu et al. 2008; Cao et al. 2017). Another independent constraint on the jets behaviour at depth is provided by the Jovian magnetic field measurements. Moore et al. (2019) compared the structure of the magnetic field over a time span of 45 years (from Voyager to Juno spacecrafts). They show that the measured secular variation is consistent with an advection of the field by zonal jets having speed in a range of $\mathrm{cm\,s^{-1}}$ at a depth of $\sim 0.94 R_J$, where the magnetic field begins to matter for the jets dynamics. This velocity drop is consistent with the depth of the quenching of the jets determined from gravity measurements. The predicted depth is only a moderate fraction of the planet's radius (about 5%R_J, see the dashed blue line in Fig.1.2), but significantly exceeds the weather layer extent, thus supporting the deep model scenario. The same gravity field analysis performed on Saturn's gravity data obtained by Cassini led to a similar conclusions, with jets extending as deep as 9,000 km (Galanti et al. 2019a). The final picture of deep zonal jets dissipated by magnetohydrodynamical effects at their bottom is thus consistent for both gas giants (Kaspi et al. 2020).

The long-standing uncertainty in the jets vertical extent has led the community to be divided between the shallow and deep models mentioned in section 1.2.4.1 (Fig.1.7). In the shallow model, the jet streams are considered confined near the cloud level of Jupiter (Vasavada et al. 2005). The vertical aspect ratio of the jets (height/width) is $\ll 1$. In the deep model, the jet streams extend through Jupiter's interior as concentric cylinders parallel to the rotation axis

(Busse 1976), up to a depth of several thousands of kilometres, leading to an aspect ratio ~ 1.

1.4.1.2. Forcing of the jets

The physical nature of the jets forcing is not at all elucidated yet, and remains one of the long-standing questions of Jupiter's dynamics and jets formation in general. We focus here on the case of gas giants (the picture is different for terrestrial atmospheres and oceans). The shallow model community tends to see the forcing as arising from baroclinic instabilities. Such instabilities can be triggered by thermal contrasts due to the meridional gradient in solar heating (Sánchez-Lavega et al. 2019), or to local thermal contrasts in between bands due to latent heat release or albedo differences (Vasavada et al. 2005). In addition to baroclinic instabilities, valuable candidates for the shallow model are moist convection and active thunderstorms which could also act as forcing sources (Lian et al. 2010). On the contrary, the deep convection community usually assumes that the forcing is due to small-scale thermal convection in the deep interior of Jupiter. This hypothesis is reasonable given that Jupiter emits more total energy than it receives from the Sun, thus energy is dominated by thermal upwelling from below (Sánchez-Lavega et al. 2019). Finally, it is important to note that deep jets do not necessarily require a deep forcing: a shallow forcing may form jets which can extend vertically due to fast rotation. Conversely, jets could be formed at depth and extend upward through the troposphere.

After the source of energy for the jets, the second question is naturally how this energy is transferred to the jets. Turbulent cascades presented in section 1.2.5.2 are one possibility. Quantitative analyses of the Cassini 70-days movie of Jupiter's clouds support the picture of an inverse energy cascade in Jupiter's weather layer (Choi et al. 2011; Galperin et al. 2014b). Using the same data, Young et al. (2017) showed that there is indeed an inverse transfer of energy from scales of 2,000-3,000 km, up to 20,000 km. However, they also identify a direct transfer of energy from 2,000 km towards small scales, which is not expected in classical 2D turbulence. In addition, they show that most energy transfer occurs between eddies and the zonal flow directly, i.e. non-locally. The scale of transition between direct and inverse energy transfer is close to the first Rossby radius of deformation. This supports the idea that the forcing is due to baroclinic instabilities, and excludes the possibility of a forcing by moist convection, since thunderstorms have scales much smaller than 2,000 km. However, one should keep in mind that the velocity fields from which these conclusions are drawn are measured in the weather layer only. It is possible that the forcing of the jets at depth occurs via small scale convective motions, while baroclinic processes dominate in the shallow weather layer, with coupling mechanisms unexplored to date.

Observations alone are not sufficient to fully understand the jets forcing, origin and dynamics. Idealized modelling, focusing on few, well-identified physical processes have been developed, along with more complete, global scale simulations integrating a more complex dynamics. Both approaches improved our current understanding of zonal jets, as detailed below.

1.4.2. Modelling of barotropic jets

There is not yet a commonly accepted universal mechanism to explain the formation of zonal jets in planetary flows. The only consensus is that the β-effect is responsible for the anisotropisation of the turbulent flow. In his seminal paper, Rhines (1975) predicted that the β-effect would alter the inverse energy cascade expected in geostrophic turbulence, and redirect energy towards zonal modes at low wavenumbers. This work was however mainly heuristic, and since then, the dynamical process of jet formation has been the subject of intensive study. In a recent book, Galperin et al. (2019a) provide a survey of the latest theoretical, numerical

and experimental advancements focusing on zonal jets dynamics and their interactions with turbulence, waves, and vortices. Several processes can lead to zonal flows formation, such as anisotropic turbulent cascades, modulational instability and mixing of potential vorticity. Zonal flows also emerge as statistical equilibria from complex turbulent flows. In any of these theories, the same fundamental physical ingredients are invoked: the quasi-bidimensionality of the flow, the presence of a β-effect, and a forcing which supplies energy to sustain the zonal jets. In the present section, we briefly review the aforementioned theories, with an emphasis on their differences regarding the underlying physical hypotheses and mechanisms.

1.4.2.1. Eddy-driven jets

Zonal jets on Jupiter are considered as eddy-driven jets, i.e. that they are driven by the indirect cumulative effect of non-axisymmetric eddy motions, and not by a direct acceleration of the zonal velocity ($\langle F_x \rangle_x = 0$). The efficiency of eddies in accelerating the zonal flow can be formally expressed by performing a Reynolds decomposition of the flow into a zonally averaged component plus some fluctuations:

$$u = \langle u \rangle_x(y,t) + u'(x,y,t) \quad = \quad U + u', \tag{1.60}$$

$$v = \langle v \rangle_x(y,t) + v'(x,y,t) \quad = \quad v', \tag{1.61}$$

where $\langle \cdot \rangle_x = \frac{1}{L_x} \int_0^{L_x} \cdot \, \mathrm{d}x$ is the zonal mean. The zonal average of the zonal component of the Navier-Stokes equation (equation (1.24)) leads to the zonal flow evolution equation:

$$\frac{\partial U}{\partial t} = \underbrace{-\frac{\partial \langle u'v' \rangle_x}{\partial y}}_{\mathscr{R}(y,t)} + \mathscr{D}(y,t), \tag{1.62}$$

where $\mathscr{D}$ contains both the frictional and bulk dissipation of the zonal flow, and the source term $\mathscr{R}$ corresponds to the divergence of the Reynolds stresses – alternatively called the eddy momentum flux. To close equation (1.62), the Reynolds stresses divergence $\mathscr{R}$ needs to be modelled and expressed as a function of the zonal flow U itself.

For eddies to feed zonal jets, the eddy momentum fluxes should necessarily be directed along the mean momentum gradient. This is physically counter-intuitive given that for standard molecular diffusion processes, fluxes are directed against the mean gradient which is subsequently smoothed. The fact that momentum fluxes can be transferred upgradiently has been referred to as a "negative viscosity" phenomenon. More explicitly, using measurements of turbulence on Jupiter, Ingersoll et al. (1981), Ingersoll (1990), Salyk et al. (2006), and Galperin et al. (2014b) showed that the momentum fluxes $\overline{u'v'}$ are positively correlated to the zonal wind shear $\partial_y U$ ($\overline{u'v'} = D\,\partial_y U$, $D > 0$). Neglecting dissipation, the zonal flow evolution equation (1.62) becomes

$$\frac{\partial U}{\partial t} = -\frac{\partial \overline{u'v'}}{\partial y} = -D\frac{\partial^2 U}{\partial y^2}, \tag{1.63}$$

which is indeed a diffusion equation but with a negative diffusivity.

Saying that jets are forced by eddy momentum fluxes does not answer the question of the physical mechanism responsible for these fluxes. Said differently, the divergence of the Reynolds stresses is the only source term in the zonal flow evolution equation. The important point is to physically understand what mechanism leads to the correlation between fluctuating components of the velocity and thereby to positive or negative eddy momentum fluxes.

1.4.2.2. Zonal jets from local energy transfers: the theory of zonostrophic turbulence

Jets are the largest scales observed in Jupiter's flows. To energetically feed jets, an inverse transfer of energy from small scales (at which energy injection occurs) towards large scales is necessary. The inherent assumption behind the zonostrophic turbulence theory presented in this section is that this transfer occurs through a turbulent cascade, i.e. through *local* interactions, in a similar fashion than in purely bidimensional turbulent flows, except that anisotropy arise due to the β-effect.

β-plane turbulence: interplay between the inverse cascade and Rossby waves. Compared to traditional 2D turbulence, the β-effect adds complications in the form of a strong anisotropization of the inverse cascade of energy. Anisotropy is readily visible in the dispersion relation of Rossby waves (1.48). Because Rossby waves cause dispersive propagation, the nonlinear interactions arising from the advection operator are "detuned" and their efficiency is reduced. Since these nonlinear interactions are precisely the mechanism that allows the transfer of energy through the inverse cascade, the latter is thus slowed down. The question is then when or at which scale a significant decay in the inverse turbulent transfer rate occurs. One possibility is to seek the scale at which the advection and β terms are of same order in equation (1.32). Denoting L the characteristic length scale and using the total root-mean-square velocity $u_{\rm rms}$ for the velocity,

$$\mathcal{J}(\zeta,\psi) \sim u_{\rm rms}^2/L^2 \quad \text{and} \quad \beta\frac{\partial\psi}{\partial x} \sim \beta u_{\rm rms}, \tag{1.64}$$

and the two terms are comparable at a length scale

$$L_R \propto \frac{1}{k_R} = \left(\frac{u_{\rm rms}}{\beta}\right)^{1/2}. \tag{1.65}$$

Under this scale, the advective term dominates and above it the β-term is dominant. This scale is commonly known as the ***Rhines scale***, originally defined in Rhines (1975). It has often been associated either with the arrest scale of the inverse cascade or with the width of zonal jets that develop. Using the phenomenology of KBK two-dimensional turbulence (section 1.2.5.2), a second scale $L_\beta \sim 1/k_\beta$ can be obtained by equating a turbulent eddy turnover time to a Rossby wave period. This leads to

$$\epsilon^{-1/3} k_\beta^{-2/3} \sim k_\beta/\beta, \tag{1.66}$$

$$L_\beta \propto \frac{1}{k_\beta} = \left(\frac{\epsilon}{\beta^3}\right)^{1/5}. \tag{1.67}$$

This scale characterizes the threshold of turbulence anisotropisation under the action of the β-effect. When the inverse cascade of energy reaches scales of the order of L_β, the turbulent eddies begin to be affected by the β-effect. This scale is called the ***transitional scale*** (Vallis et al. 1993). However, such a scaling does not take into account the anisotropy of Rossby waves, and using (1.48) one should rather write

$$\epsilon^{-1/3} k^{-2/3} \sim \frac{k^2+l^2}{k\beta}, \tag{1.68}$$

where we recall that k and l are the zonal and meridional wavenumbers respectively. When $k \to 0$, i.e. for increasing scales in the zonal direction, the eddy-turnover time is always smaller

that the Rossby waves period so the eddies won't be affected by the waves propagation, whereas it is not the case for $l \to 0$. The condition (1.68) corresponds to a dumbbell shape in the wavevector space (Vallis et al. 1993), as represented in Fig.1.14. Coherent vortices are not spread by Rossby wave in an isotropic way and consequently the "halting" of the inverse cascade is directionally dependent. In other words, the inverse cascade can proceed more efficiently in the x direction, i.e. feed preferentially zonal flows. Note that this scale should not be seen as exclusive: both turbulent eddies and Rossby waves are present at all scales. The idea is that above L_β, the nonlinear interactions feeding the cascade are dominated by a sea of coherent Rossby waves (wave turbulence). Under L_β, Rossby waves are not predominant, and nonlinearities arise from incoherent turbulent eddies. In the case of wave turbulence, the fact that nonlinear interactions can only occur though waves is more selective, hence slowing down and introducing anisotropy in the inverse cascade.

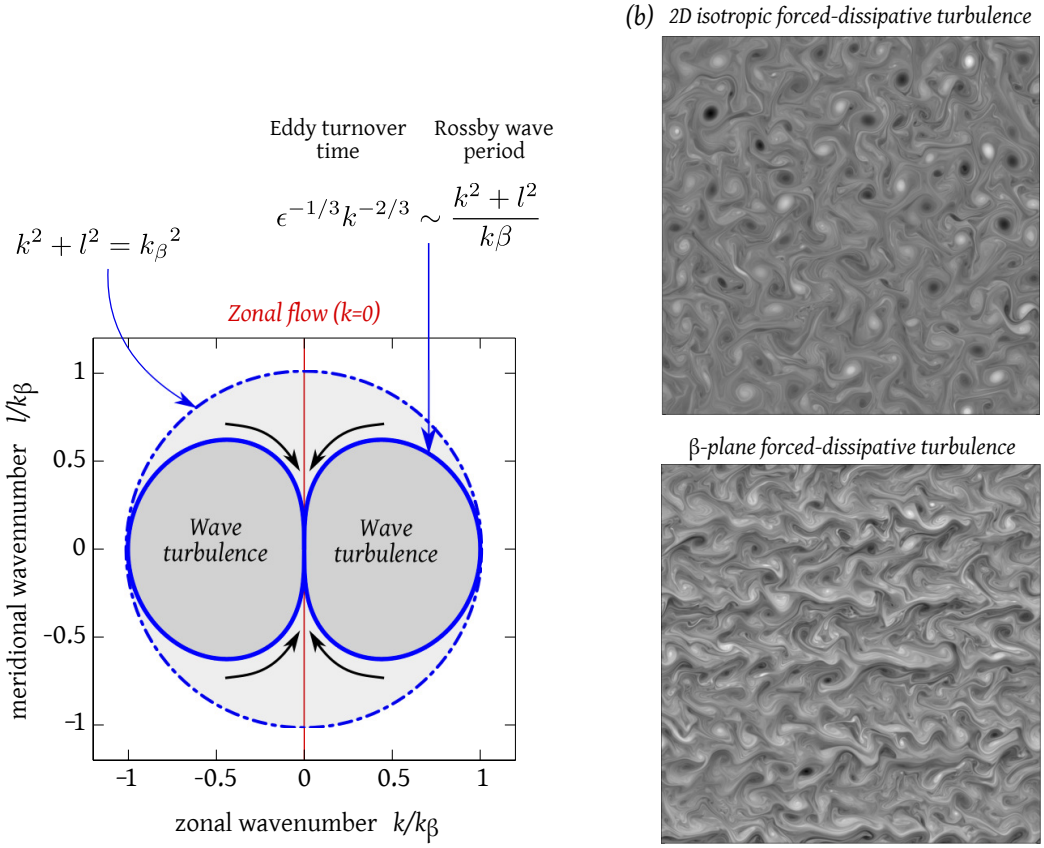

Figure 1.14. – *(a)* Theoretical boundary in the spectral space between isotropic and anisotropic turbulence on the β-plane. The dashed blue line represents the transitional wavenumber (1.67), i.e. the scale for which a Rossby wave period is equal to a turbulent eddy turnover time. The continuous blue line is the same boundary but taking into account the anisotropy of Rossby waves dispersion relation. It draws a dumbbell (Vallis et al. 1993) in which energy transfers are reduced because dominated by Rossby waves. Energy transfers proceed more efficiently towards the $k = 0$ axis (red line), i.e. towards zonal flows. *(b)* Vorticity snapshots of 2D turbulence numerical simulations without (top) and with a β-effect. Anisotropy and zonation in the turbulent flow develop in β-plane turbulence. Figures by Jeffrey Early.

Note that the phenomenology of a transitional scale above which turbulence becomes anisotropic is also relevant in purely rotating or stratified turbulence. L_β is indeed analogous the Zeman scale L_Z in rotating turbulence (Zeman 1994) and to the Ozmidov scale L_O in

stratified turbulence (Ozmidov 1965):

$$L_O = \left(\frac{\epsilon}{N^3}\right)^{1/2}, \quad \text{and} \quad L_Z = \left(\frac{\epsilon}{\Omega^3}\right)^{1/2}. \tag{1.69}$$

The important difference between the frameworks of rotating, stratified and β-plane turbulence is the nature of the waves causing anisotropy: inertial, internal and Rossby waves, respectively.

The zonostrophic regime of β-plane turbulence. The theory of zonostrophic turbulence predicts scaling laws and different regimes of β-plane turbulence depending on a single parameter called the zonostrophy index which compares the characteristic scales in β-plane turbulence. This theory will be described in more details in chapter 4 when it will be compared with our experiments, but let us briefly explain its principal features.

The ***zonostrophy index*** is defined as the ratio between the Rhines scale and transitional scale

$$R_\beta = \frac{L_R}{L_\beta} = \left(\frac{u_{\text{rms}}^5\,\beta}{\epsilon^2}\right)^{1/10}. \tag{1.70}$$

Galperin et al. (2006) and Sukoriansky et al. (2007) propose to use R_β as an indicator of how strongly zonal is the investigated turbulent flow:

— if $R_\beta \lesssim 1$, then the flow saturates at a scale smaller than the transitional scale, i.e. before that the turbulent eddies grow enough to feel the β-effect. In that case, one would expect the flow to remain nearly isotropic and show features of the classical KBK turbulence (section 1.2.5.2).

— if $R_\beta \gtrsim 1$, then the flow saturates at larger scales than L_β, and is expected to show profound anisotropy.

We will see in chapter 4 that the zonostrophy index can be alternatively expressed as a function of the frictional scale (equation (1.57)), leading to a perhaps more intuitive interpretation.

Given the anisotropy of the system, the kinetic energy spectra computed from the axisymmetric component of the flow E_Z can be separated from the residual non-axisymmetric component E_R. The zonostrophic theory predicts that in the inertial range of the zonostrophic regime, i.e. between k_β and k_α, E_Z and E_R follow different scalings (Huang et al. 2000; Sukoriansky et al. 2002, 2007; Galperin et al. 2006). Since high wave number modes are nearly isotropic, the residual spectra is expected to be the classical one of KBK theory of 2D turbulence (1.58):

$$E_R(K) \sim C_K \epsilon^{2/3} K^{-5/3}, \tag{1.71}$$

where $K = (k^2 + l^2)^{1/2}$ is the total wavenumber and $C_K \approx 6$ is the Kolmogorov-Kraichnan constant. On the contrary, the zonal spectrum follows a steeper slope:

$$E_Z(l) \sim C_Z \beta^2 l^{-5}, \tag{1.72}$$

where we recall that l is the meridional wavenumber, and C_Z is a constant of order unity (Rhines 1975; Chekhlov et al. 1996; Huang et al. 2000). The steepening of the spectrum for the zonal modes can be physically explained by the anisotropization of the inverse cascade. We have mentioned that the energy flux is redirected towards zonal modes. But even between zonal modes, the energy transfer rate is reduced compared to the purely 2D case. To conserve a constant total energy flux the spectral energy density of the zonal modes must increase and the spectrum steepens (Huang et al. 2000). These scalings are represented in Fig.1.15*(b)*. The

intersection of the zonal and residual spectra defines a spectral transitional wavenumber k_β^S, which can be expressed as

$$k_\beta^S = \left(\frac{C_Z}{C_K}\right)^{3/10} \left(\frac{\beta^3}{\epsilon}\right)^{1/5}. \tag{1.73}$$

Using 2D numerical simulations on the sphere, Galperin et al. (2006) and Sukoriansky et al. (2007) demonstrated that the regime of strong and rectilinear jets – so-called ***zonostrophic regime*** – is obtained when the scale at which the eddies start being deformed by the Rossby waves is well separated from the scale of the final jets ($R_\beta^S = k_\beta^S / k_R \gtrsim 2.5$), as shown in the regime diagram in Fig.1.15*(a)*. On the contrary, the regime is considered to be friction-dominated if $R_\beta^S \lesssim 1.5$ (dashed line in Fig.1.15*(a)*). Jupiter and Saturn midlatitude jets have $R_\beta \approx 5$ and are expected to be in the regime of zonostrophic turbulence (Galperin et al. 2014b). Earth's oceans and atmosphere are under the threshold with $R_\beta \approx 1.5$ (Galperin et al. 2019b, table 13.1). This index hence allows to estimate how a given flow is close to the regime relevant for gas giants. This is particularly useful to conceive and diagnose experimental studies of zonal jets, as will be discussed in chapter 3.

1.4.2.3. Zonal jets from non-local energy transfers

In its essence, the theory of zonostrophic turbulence relies of the assumption that the energy transfer from the small-scale forcing to the large-scale jets is local and proceed through a cascade. Other theories have been proposed and significantly differ from the phenomenology of turbulent cascades, namely by their non-local aspects.

Potential vorticity mixing. As seen in section 1.2.4 the potential vorticity (PV) is a scalar field which is materially conserved in the absence of dissipation. It has been proposed that jets formation can be described in terms of PV mixing (Dunkerton et al. 2008; McIntyre 2008; Dritschel et al. 2008; Scott et al. 2012a). In this framework, retrograde jets correspond to well-mixed regions of PV, whereas prograde jets would correspond to steep gradients of PV, thus defining a staircase-like profile in the meridional direction if multiple jets are present. An example of such a staircase is provided in Fig.1.15*(c,d)*. The mechanism of staircase formation was described in Dritschel et al. (2008) by analogy to what happens when a stratified fluid is mixed, the so-called "Phillips-effect" (Phillips 1972). The idea is that of a feedback mechanism: stratification is reduced in the mixed regions, the restoring force at the origin of gravity waves (buoyancy) is thus weakened, which allows for further mixing. Instead, where interfaces are forming, steeper stratifications locally develop, and the gravity waves restoring force is enhanced, thus inhibiting mixing across the interface. For a PV gradient instead of a density gradient, the mechanism is analogous but invokes Rossby waves elasticity which depends on how steep the local PV gradient is. The background PV gradient, β, is modified by the zonal flow itself and becomes $\beta - \partial_y^2 U$. This second, effective β, is reduced in a retrograde flow ($\partial_y^2 U > 0$), and enhanced in a prograde flow. The restoring force at the origin of Rossby waves is increased in prograde jets, and decreased in retrograde jets, and we retrieve the same positive feedback mechanism as in a stratified flow. That being said, subtleties arise from the fact that PV is different from density since there is a direct relationship between the flow dynamics and PV through the vorticity (see equations (1.45) and (1.46)). This theory predicts, for instance the relation between the jets spacing (the staircase width) and the jets intensity (the PV jump at the interfaces).

Modulational instabilities. From a totally different perspective, it has been proposed that zonal jets can arise from a nonlinear instability of Rossby waves. A basic flow, consisting of

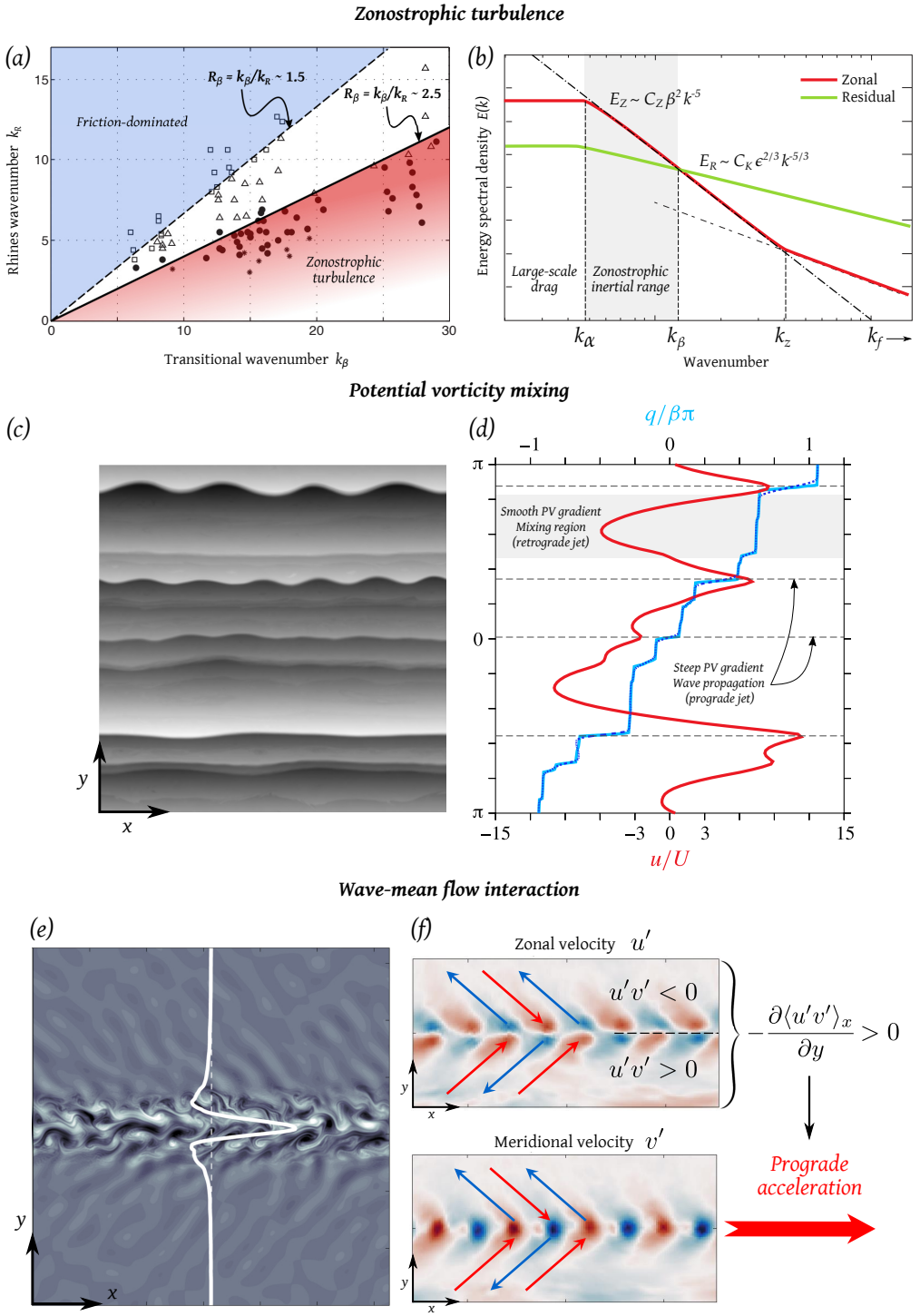

Figure 1.15. – Illustration of three theories on zonal jets dynamics: zonostrophic turbulence, potential vorticity mixing and wave-mean flow interaction. *(a)* Friction-dominated (squares) and zonostrophic (full circles) regimes in the space (k_β, k_R). The triangles correspond to a transitional regime. Adapted from Galperin et al. (2019b). *(b)* Expected spectral scalings in the zonostrophic regime. Adapted from Galperin et al. (2019b). *(c)* Vorticity map for a 2D flow on the β-plane with $L_R/L_\beta = 10.8$. *(d)* Corresponding zonal flow (U) and potential vorticity (q) profiles. Adapted from Scott et al. (2012b). *(e)* Vorticity field resulting from a localized stirring (gaussian in y) at a given length scale. The white line is the zonal flow. From Constantinou (2019). *(f)* Mechanism of zonal flow acceleration by Rossby waves. The zonal and meridional velocity maps are from the *Jacuzzi* experiments described in chapter 3. The forcing consists in a line of vortices (alternating cyclones and anticyclones). The jet is accelerated by the convergence of prograde eddy momentum flux towards the forcing region.

monochromatic Rossby waves, is unstable to a zonal jet perturbation. This mechanism is non-local by essence, since Rossby waves of wave vector $\boldsymbol{k} = (k, l)$ transfer energy to a zonal jet of wave vector $(k_J = 0, l_J)$, which can be seen as a zero-frequency Rossby wave (Lorenz 1972; Gill 1974). This instability was identified as a modulational instability by analogy with the Benjamin-Feir instability of gravity waves (see Quinn et al. 2019, and references therein).

Statistical approaches and quasilinear theories. Recently, statistical approaches have also been employed to describe zonal jets formation. Equilibrium statistical mechanics description of 2D turbulent flow is feasible in the inviscid limit. For quasi-geostrophic barotropic turbulent flows, zonal jets and large-scale vortices are shown to be the most probable structures (see the review by Bouchet et al. 2012). These theories are very appealing because they allow to reduce the complexity of the turbulent flow and focus on statistical properties and "macrostates". However, planetary flows are both strongly forced and strongly dissipated, and require out-of-equilibrium statistical theories, as proposed by Farrell et al. (2003). For instance, Constantinou et al. (2014) developed a quasi-linear statistical modelling to explain jets formation, and showed that jets can form even in a framework where eddy-eddy (local) interactions are ignored. Physically, the emergence of zonal jets is modelled as an instability of the statistical turbulent state where Rossby waves coexist. The modulational instability mentioned above is a special case of this more general statistical instability. In the end, both rely on a wave-mean flow description of jets formation.

According to wave-mean flow interactions, a local emission of Rossby waves can generate a zonal flow, provided that the waves are dissipated at a different location than where they are generated. In this case, prograde flow emerges in the wave-generating region while retrograde flows develop where Rossby waves dissipate. This mechanism is illustrated in Fig.1.15*(e,f)*, and further explored in chapter 3. It is analogous to the historic acoustic streaming process by which winds form due to acoustic waves dissipation (Lighthill 1978). In this framework, if the forcing is homogeneous and the dissipation is everywhere the same (i.e. there are no preferred regions of dissipation), no mean flow should emerge. But this is true as long as the retroaction of the mean flow on the waves propagation is neglected. However, the zonal flow itself modifies the local potential vorticity gradients from its initial value β to $\beta - \partial_y^2 U$. The presence of a zonal flow thus makes dissipation heterogeneous. In the quasilinear, statistical framework described in Constantinou (2019), this retroaction of the mean flow is naturally taken into account, and jets effectively emerge even in the case of a homogeneous forcing.

1.5. Global scale, multi-processes simulations of Jupiter's dynamics

In addition to the aforementioned idealized theories of barotropic zonal jets formation, the second type of modelling approach that has been employed in the past decades consists in designing global scale models trying to reproduce as accurately as possible Jovian processes. It is in these global scale models that the distinction between shallow and deep frameworks (section 1.2.4.1) is the most important.

Both shallow and deep models have had their successes and failures to reproduce zonal jets like those on Jupiter. In shallow numerical models, one or multiple-layer shallow water equations are solved on the sphere. Shallow models successfully explain the formation of multiple jets (e.g. Cho et al. 1996; Williams 2003; Scott et al. 2007; Showman 2007), but the main criticism is that they often predict the wrong direction of the flow at the equator, which should be strongly prograde, a regime called "super-rotation" (see Fig.1.7*(c)*). Some

shallow models produced prograde equatorial jets when inhomogeneous bottom drag (zero at low latitudes) and intrinsic heat fluxes are included to simulate deep interior effects, such as convective heat fluxes and magneto-hydrodynamic drag (Schneider et al. 2009). Super-rotation is also observed when latent heating due to water condensation is included (Lian et al. 2010) or when energy is removed by radiative relaxation rather than linear friction (Scott et al. 2008; Warneford et al. 2014). Producing super-rotation in shallow models hence seems a little bit too dependent on the model's parameters to be robust, and the simulated equatorial jets are still weaker than in observations. Deep convective models on the contrary robustly predict the formation of a strong prograde jet in the whole region outside the tangent cylinder as visible in Fig.1.7*(d)*. Note that to define a tangent cylinder, the presence of a core, or a boundary where the zonal flows vanish, has to be somewhat arbitrarily assumed (see the schematic in Fig.1.7*(b)*). The first deep convection models of zonal flows assumed a very deep lower boundary (at about $0.35R_J$): such models reproduce well super-rotation, but only few jets are obtained at higher latitudes, inside the tangent cylinder (Aurnou et al. 2001; Christensen 2002). Deep models where the jets are instead dissipated a few thousands kilometres deep ($\sim 0.95R_J$) provide the best numerical modelling of Jupiter's jets up to now: because of this moderate depth, the region inside the tangent cylinder is large, and multiple zonal jets can develop at midlatitudes (Heimpel et al. 2005, 2016; Yadav et al. 2020). These spherical shell simulations anticipated that the lower boundary of zonal jets would be located at about $0.95R_J$ due to MHD dissipation, and Juno confirmed this hypothesis, as mentioned earlier.

Most recently, global circulation models (GCM) have been developed, for both Jupiter (Young et al. 2019) and Saturn (Spiga et al. 2020; Cabanes et al. 2020b). In GCM, a dynamical core solves the dynamical, momentum equations, and idealized parametrisations are used to represent forcing and dissipation processes. However, these climate models cannot extend deep enough to take into account the jets coupling with interior convective fluxes (the bottom boundary is located at about 3 bar for Saturn's GCM and 18 bar for Jupiter). Deep effects are hence parametrized by an interior heat flux and weak bottom drag, whereas differential solar heating and radiative cooling account for shallow processes. Jupiter's GCM reproduce multiple jets and super-rotation when interior heating is added, but again the equatorial jet is too weak compared to observations (Young et al. 2019). In Saturn's GCM, super-rotation is enhanced by imposing that the bottom drag is zero as low latitudes. This approach, initiated by Schneider et al. (2009) is supposed to mimic the effect of the tangent cylinder, which is thought to cause the equatorial super-rotating jets in deep-convective models. By essence, these GCM remain up to now weather layer models and it can seem artificial to include deep jets effects such as inhomogeneous drag in simulations where the jets are necessarily confined to the weather layer.

Fully-consistent models coupling deep interior convection and weather layer processes still remain to be developed, but it represents a big technical challenge. For instance, most recent 3D convection models try to incorporate the presence of a stratification close to the surface by imposing a negative heat flux there, which generates a shallow stable (sub-adiabatic) stratification (Heimpel et al. 2016). These simulations suggest that the deep jets can penetrate through the stratified region, and that large-scale Jovian anticyclones can form when deep convective plumes impinge the shallow stratified layer. The lifetime of the formed vortices is however much shorter than on Jupiter, and important processes of the weather layer are absent, such as cloud physics, moist convection and radiative transfer.

1.6. Zonal jets and vortices: ubiquitous features

The physical ingredients listed in section 1.2 (rotation, stratification, β-effect and turbulence) are common to a variety of geophysical and astrophysical flows besides Jupiter. The same type of structures should then be observed in different planetary fluid layers. In this section, we briefly mention other systems where zonal jets and large-scale vortices like those of Jupiter are encountered. The idea is to underline that the basic fluid dynamics methods and results presented in this thesis are not restricted to applications to Jupiter, and may be generic and applicable to other physical systems.

1.6.1. Jovian and oceanic vortices

The oval midlatitude vortices encountered in Jupiter's weather layer have their equivalent in the terrestrial oceans. Earth's oceans are stratified due to variations in salinity and temperature, and of course they are rotating flows. Large-scale vortices analogous to Jupiter's ovals are the so-called Meddies (Medditerranean Eddies) found in the Atlantic Ocean. Meddies are large anticyclones made from saltier and warmer water flowing out of the Mediterranean Sea along the continental slope through the Strait of Gibraltar (Fig. 1.16*(a)*). When this Mediterranean water reaches the depth where its density is the same as the ambient density, it flows horizontally. The Coriolis force deviates the current and forms anticyclones. They have an average diameter of 80 km, a thickness of 600 to 1,000 m, and float at a depth of 1000 m below the ocean surface (Richardson 1993). Tangential velocities in meddies can reach 50 $\mathrm{cm\,s^{-1}}$ (Carton et al. 2010). They were discovered fortuitously in the late 1970s (McDowell et al. 1978), because the deep dynamics of our oceans is not readily observable. Once discovered, meddies were followed thanks to the sea surface displacement ($\sim$ 10 cm) that they generate, but also thanks to vertical profiles realised during sea campaigns, since they have a clear signature on temperature and salinity profiles as seen on the measurements reproduced in Fig.1.16*(b)* (Tychensky et al. 1998).

15 to 20 meddies form each year and they have a mean lifetime of 1.7 year. Some of them can disappear quickly because of their interaction with currents or collision with seamounts. Others manage to escape the Canary basin and travel in the Atlantic ocean at speeds of about 3.5 km per day, and finally collapse on South American east coasts after 4 to 5 years. Note that since the discovery of meddies, similar structures were discovered in other oceanic basins, including the Red Sea (Meschanov et al. 1998), near the Gulf Stream (Carton 2001), near Japan in the Ulleung Basin (Chang et al. 2004), as well as in the Bay of Biscay (Carton et al. 2013). Lenticular eddies have also been identified in the Arctic Ocean (Manley et al. 1985). Understanding their formation and evolution is important since they play a fundamental role in terms of energy and scalar transport (e.g. Olson et al. 1985; Kim et al. 2012). These vortices share a lot of properties with Jovian ovals, including their long lifetime, their floating structure, and their persistence in a chaotic environment.

1.6.2. Zonal jets in atmospheres, oceans, liquid cores and tokamaks

Besides Jupiter, zonal flows have been revealed on Saturn and on the icy giants, Uranus and Neptune (Ingersoll 1990; Vasavada et al. 2005; Sánchez-Lavega et al. 2019), as shown in Fig.1.17*(a)*. In the Earth's oceans, zonal jets have only been revealed recently, after a careful time-averaging (Maximenko et al. 2005) (see Fig.1.17*(e)*). Oceanic jets are much weaker, intermittent, and meandering (a regime sometimes referred to as "latent"), but they penetrate deep into the ocean (e.g. Cravatte et al. 2012). The strongest zonal current in the ocean is the Antarctic Circumpolar Current (ACC), presumably because it is not blocked by continental features. But this strong current seems in fact to be composed of multiple smaller jets (Fig.1.17*(c,d)*). In

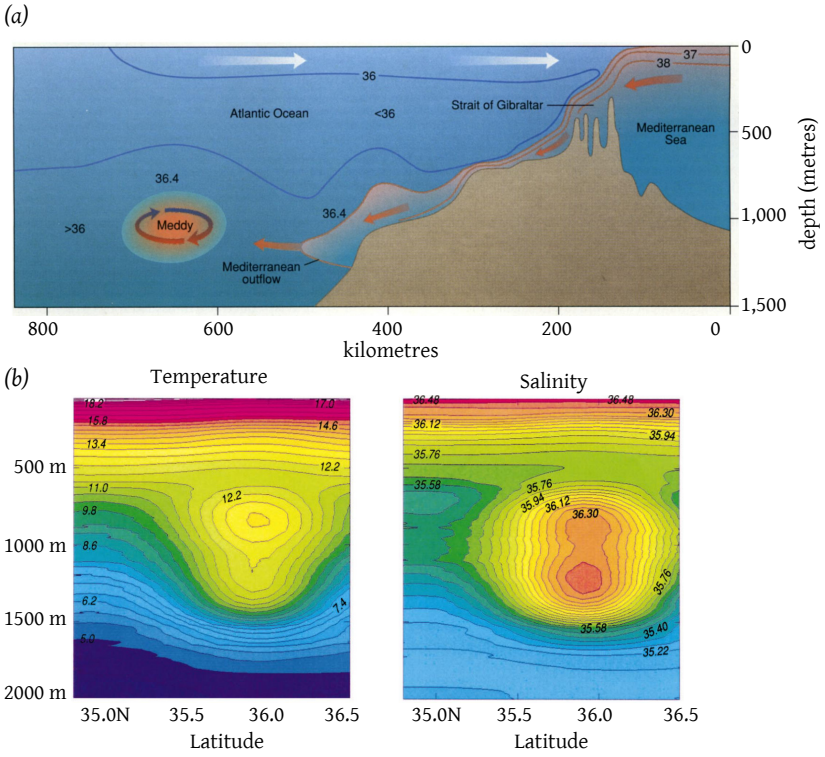

Figure 1.16. – *(a)* Schematic of meddies formation (figure from Richardson (1993)). *(b)* Temperature and salinity measured inside a meddy (figures from Tychensky et al. (1998)). The overall diameter of the meddy is around 120 km.

addition to gas, icy giants, and Earth's oceans, zonal jets are observed in the atmosphere of terrestrial bodies: the Earth, Mars, Venus and Titan (Mitchell et al. 2019). As seen in Fig.1.17*(b)*, two zonal jets – the subtropical and polar jet streams – are present in each hemisphere of Earth's troposphere, even if they are sometimes difficult to isolate from each other (Gallego et al. 2005). The global circulation on Mars is assumed to be very close to the Earth's case. Venus atmosphere is super-rotating, with clouds rotating about 60 times faster than its surface. Super-rotation has also been revealed on Titan despite the thick and opaque aerosol haze covering the moon of Saturn.

Besides superficial fluid envelopes, zonal flows very likely exist in the deep interior of terrestrial bodies. External liquid cores support rotating thermal convection with a topographic β-effect due to the spherical inner and outer boundaries of the liquid core. The associated turbulence is hence expected to feed zonal jets just like on the gas giants, and this is indeed what is observed in numerical simulations of core convection (see e.g. Guervilly et al. 2017, and Fig.1.17*(f)*).

Finally, zonal flows are also observed in magnetically confined plasmas, namely in tokamaks. Despite the huge differences between magnetically-confined plasmas and geophysical flows, both exhibit self-organized zonal flows emerging from turbulence. This similarity arises from the analogy between the Coriolis force and the Lorentz force, where the magnetic field breaks a symmetry just as rotation does (see the review by Terry (2000) and section IV in Galperin et al. (2019a)).

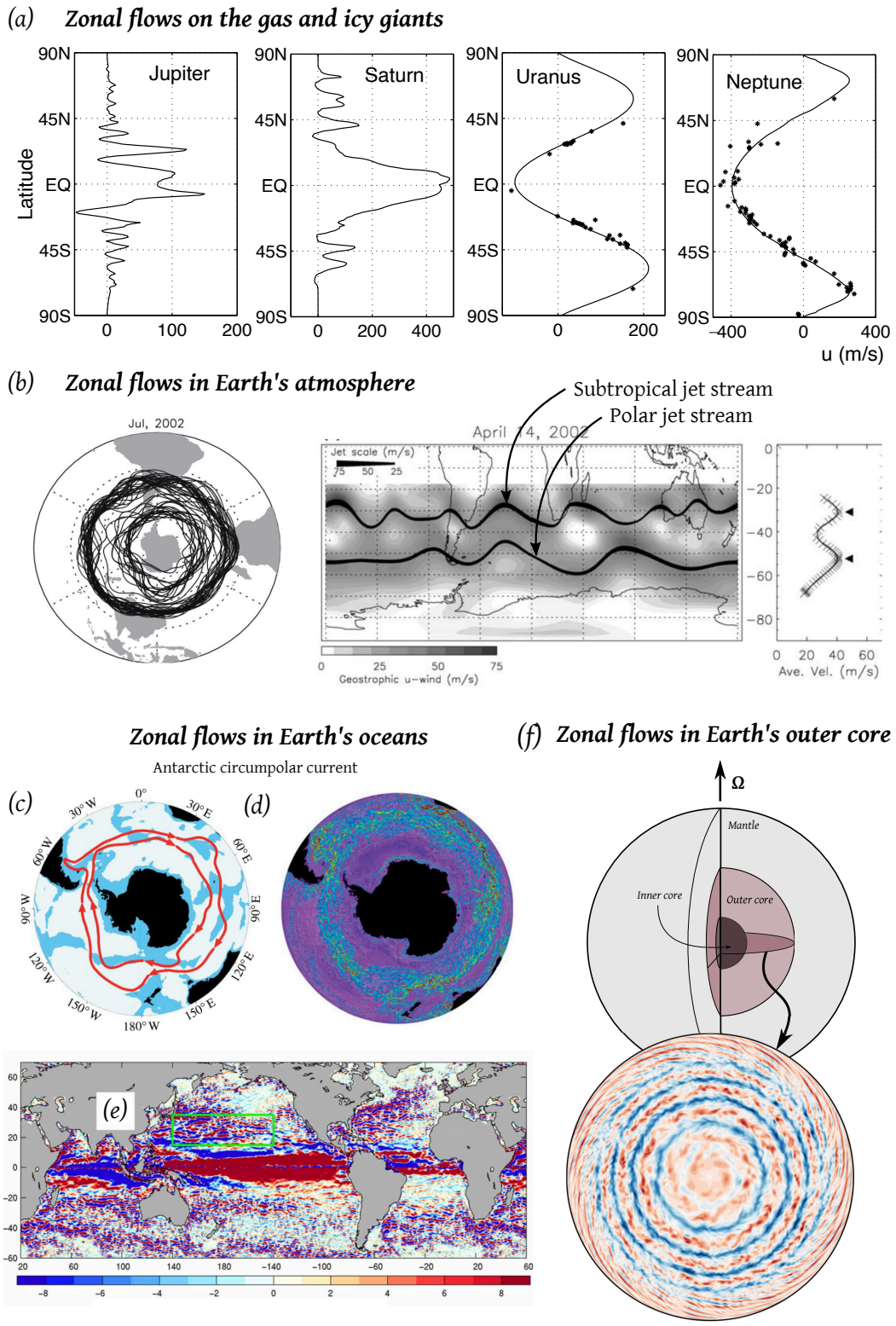

Figure 1.17. – *(a)* Zonal winds measured on the four giant planets. Figure reproduced from Sukoriansky et al. (2002). *(b)* Subtropical (~ 33°S) and polar (~ 50°S) jet streams in the southern hemisphere of Earth's atmosphere. Figure from Gallego et al. (2005). *(c)* Schematic path of the Antarctic Circumpolar Current (ACC). *(d)* Surface currents associated with the ACC. Figures from Thompson (2008). *(e)* Anomaly of zonal geostrophic velocities (cm/s). Figure from Maximenko et al. (2005). *(f)* Zonal component of the velocity in a numerical simulation of rotating thermal convection in a sphere. Azimuthal velocity map from Guervilly et al. (2017).

1.7. Objectives and methods of the present work

Jupiter's dynamics raise a lot of fundamental questions. The variety of theories which aim at explaining the formation and nonlinear saturation of large-scale zonal jets and vortices indicates by itself that this is still an intense subject of research and that no universal mechanism prevails yet. The results of the ongoing Juno mission have answered but also raised new questions, and continue to surprise the scientific community thereby motivating further exploration of these problematics. The main questions on which we focus can be summarized as follows:

— What is the dominant mechanism of jets formation and their source of energy?

— How to explain their final intensity and scale in the non-linear saturated regime?

— How to explain their long-term stability?

— What is the feedback between the jets and the underlying turbulence?

— Are the jets superficial or are they the manifestation of deep dynamics? How is the deep dynamics coupled with the weather layer?

— How are midlatitude large-scale vortices coupled with the jets? How to explain their longevity?

— What is the depth of Jovian vortices?

— How do cyclones self-organize into clusters at Jupiter's poles?

These questions combine long-standing planetary science issues and fundamental fluid mechanics topics, such as the emergence of large-scale structures in a turbulent flow. In the present thesis, we propose to tackle these questions using a multi-method approach which combines experimental models, idealized numerical simulations and theoretical modelling.

Experimental modelling is motivated by the limitations and uncertainties of gas giant numerical and theoretical models. For instance, current models cannot simulate the dynamics over the very long radiative and frictional timescales, necessary for the system to equilibrate. In addition, gas giants regimes are characterized by a vanishing Ekman number (1.11) and a very large Reynolds number (1.53). This regime is not achievable by realistic fully three-dimensional models, and can only be approached by simplified models relying on physical simplifications whose relevance needs to be systematically addressed. Experimental studies also complement the direct observations of Jupiter's flows, which are sparse and lack the possibility of repeatability. The ability of experiments to model Jovian phenomena relies on the zero-th order geostrophic balance of its flows (section 1.2.2), observed when $Ro \sim E \times Re \ll 1$. Rotating fluid experiments easily fulfil the low Rossby number constraint, and thereby respect the dominant balance. Even if they cannot reproduce the very small viscous effects of Jovian flows, experiments usually allow to reach more extreme regimes than numerical models, and study the dynamics of real, fully nonlinear and developed flows in a statistically steady-state. Of course, experiments come with their own limitations, such as necessary physical boundaries, and the difficulty in incorporating magneto-hydrodynamical or compressibility effects. All the aforementioned approaches, experimental, numerical and theoretical investigations guided by observations, hence strongly complement each other, and combining them is the key to a better understanding of Jovian dynamics.

In this thesis, we adopted two significantly different and complementary approaches. The first approach consists in trying to explain how large-scale structures *spontaneously* emerge from Jupiter's turbulence and how the system behaves once in the nonlinear saturated state.

This approach is used in chapters 3,4,5, which focus on barotropic zonal jets. A second approach consists in ignoring or simplifying the background turbulence, and focus on the quasi-equilibrium of the large-scale structures and the properties that we can deduce from this equilibrium state. This approach is used in chapters 2 and 6 in which we focus on midlatitude and polar large-scale vortices. More precisely, our research plan is the following:

- In chapter 2, following and expanding the work of Aubert et al. (2012) and Facchini et al. (2016), we study the quasi-equilibrium of vortices in a rotating stratified shear flow, three basic ingredients which aim at reproducing the situation of midlatitude Jovian vortices floating in Jupiter's stratified weather layer and sheared by the zonal winds. The goal is to predict the vertical extent of such vortices as a function of the ambient parameters, and apply our results to the most prominent Jovian anticyclones to complement observations limited to the weather layer. The experimental setup employed in this chapter is referred to as the *Revival* setup.

- In chapters 3 to 5, we study the emergence of deep barotropic zonal jets from a flow forced at small-scale. We built a new improved version of the experimental setup employed by Cabanes et al. (2017). This second setup is referred to as the *Jacuzzi* experiment in the following.
  - The first goal of this setup is to study the development of strong, barotropic zonal jets in the deep scenario, in the presence of bottom drag, and to reach particularly extreme regimes compared to previous experiments. In chapter 3, we will focus on explaining zonal jets formation in this setup, in two different regimes, and we will explain the transition towards the most extreme regime.
  - The second goal, developed in chapter 4, is to study the properties of the fully-developed, saturated turbulent flow in the second, most turbulent regime of zonal jets, and address the relevance of the theories mentioned in the present introduction.
  - The third goal is to address the long-term dynamics of turbulent zonal jets, such as drift, mergers, nucleations and stability. This long-term stability is the focus of chapter 5.
  - To reach these goals, the experiments are guided and complemented by an idealized quasi-2D (quasi-geostrophic, QG) numerical code. Once validated by comparing the results of the 3D experiment with 2D simulated flows, this QG code then allows to address, for instance, the sensitivity of the results to the forcing details.

- In chapter 6, we present a preliminary experimental study of the dynamics of multiple cyclones at the pole. The goal is to determine if we can experimentally reproduce the drift due to the β-effect and the equilibration of floating cyclones at the pole. This third experimental setup is referred to as the *Clusters* setup.

- In chapter 7, we summarise the main results and propose future possible lines of work.

The results of each chapter will be systematically analysed in light of possible relevance and application to Jupiter's dynamics. The associated fundamental conclusions, from the fluid dynamics point-of-view, are however generic and applicable to other physical systems exhibiting rotating turbulence, stratification or topographic effects, such as those mentioned in section 1.6.

Chapter 2.

Depth of Jovian vortices: remote determination from laboratory experiments

Chapter 2.

Jupiter's dynamics shapes its cloud patterns but remains largely unknown below this natural observational barrier. Unravelling the underlying three-dimensional flows is a primary goal for NASA's ongoing Juno mission that was launched in 2011. In this chapter, we address the dynamics of large Jovian vortices using laboratory experiments complemented by theoretical and numerical analyses.

Chapter aims

1. Address the quasi-static dynamics of large-scale midlatitude vortices by combining laboratory experiments and direct numerical simulations of vortices embedded in a rotating stratified shear flow.
2. Determine scaling laws for the three-dimensional shape of lenticular vortices as a function of the ambient physical parameters.
3. Use estimates of Jovian physical parameters and conditions to predict the three-dimensional shape of large-scale anticyclones.

Highlights

- The generic cyclo-geostrophic and hydrostatic balance is responsible for the three-dimensional shape of floating anticyclones. From this, we define scaling laws for their horizontal and vertical aspect ratios as a function of the ambient rotation, stratification and zonal wind velocity.
- The theoretical aspect ratios are verified against results of the laboratory experiments and direct numerical simulations.
- We apply our model to the most prominent anticyclones of Jupiter (GRS, Oval BA, Oval BC, Oval DE), and predict that they are very superficial structures, with thicknesses between 50 to 150 km.
- For the Great Red Spot in particular, our model reproduces well the decrease of its aspect ratio since the Voyager mission in 1979. We predict that the Great Red Spot's thickness, inaccessible to direct observation, would have remained constant despite the observed horizontal shrinking.

D. Lemasquerier et al. (2020a). "Remote Determination of the Shape of Jupiter's Vortices from Laboratory Experiments". *Nature Physics*, 1–6. DOI: 10.1038/s41567-020-0833-9

2.1. Introduction

Earth-based telescope observations and records from various spacecrafts have revealed Jupiter's rich tropospheric dynamics. Moreover, the ongoing Juno mission (Bolton et al. 2017) is providing the scientific community with accurate and puzzling observations and data (e.g. Li et al. 2017; Kaspi et al. 2018; Iess et al. 2018; Guillot et al. 2018; Adriani et al. 2018). Among others, observations reveal that up to several hundred vortices are present among Jupiter's zonal winds at any instant in time (Vasavada et al. 2005), including the famous Great Red Spot (GRS). Yet, a lot of their features are still not well understood: how did they form? What are the processes controlling their lifetime? How do they interact with Jupiter's zonal flows? What is their three-dimensional structure, and more specifically their thickness? Are they columns that penetrate through the molecular envelope (Hide 1961), or shallow vortices confined near the cloud level (Marcus 1988; Dowling et al. 1988a)? Idealized numerical models (e.g. Williams et al. 1988; Dowling et al. 1988b; Marcus 1990) and laboratory experiments (Read et al. 1983, 1984; Sommeria et al. 1988; Antipov et al. 1986) offered clues to understand vortices formation, interaction and longevity in Jupiter's atmosphere. Here, we address the question of their depth for which we have no answer despite decades of observations. As mentioned in the introductory chapter (section 1.6), the attention devoted to such vortices also arises from the observation of similar structures in the Earth's ocean (Carton 2001). For instance, in the Atlantic ocean are found the so-called "meddies", whose structure is more directly available through velocity, temperature and salinity measurements (Fig.1.16). Understanding their formation and evolution is important since they play a fundamental role in terms of energy and scalar transport (e.g. Kim et al. 2012).

From a dynamical point of view, vortices naturally arise in planetary flows which are subjected to rapid rotation. Let us denote Ω the spin rate of a planet, and $f = 2\Omega\sin(\theta)$ the local Coriolis parameter (θ is the latitude). If we consider a flow of very low Rossby number Ro (equation (1.10)) the so-called *geostrophic balance* takes place at first order. Neglecting viscous forces and looking for steady solutions, the Coriolis term in the momentum equations balances the horizontal gradient of pressure such that

$$f\boldsymbol{e}_z \times \boldsymbol{u} = -\frac{1}{\rho}\nabla_h p, \tag{2.1}$$

where $\nabla_h p$ is the horizontal gradient of pressure, ρ is the fluid density, $\boldsymbol{e}_z$ is the local vertical and $\boldsymbol{u}$ is the velocity field. In such an equilibrium, the flow rotates around low and high pressure zones, thus naturally forming vortices (see Fig.1.5). In the sole presence of rotation, the vortices are expected to extend vertically through the fluid in columns owing to the Taylor-Proudman theorem which is readily retrieved by taking the curl of equation (2.1), and states invariance of the velocity components along the direction of the spin axis (see chapter 1, section 1.2.2).

In planetary flows, a second feature comes into play besides rotation: stratification. Vortices in the Earth's ocean are embedded in a strong and stable thermohaline stratification. Similarly, Jupiter's vortices lie in its stratified weather layer above the convective zone and below the tropopause (Vasavada et al. 2005). We recall that stratified flows are characterized by their buoyancy or Brunt-Väisälä frequency N which is the natural frequency of oscillation of a fluid parcel displaced from equilibrium with buoyancy acting as a restoring force:

$$N = \sqrt{-\frac{g}{\rho_0}\frac{\partial \rho}{\partial z}}, \tag{2.2}$$

where g is the gravitational acceleration, ρ_0 the mean density. In a stratified flow, as visible in Fig.1.4, rather than columns vortices take the shape of thin pancakes (Billant et al. 2001,

and references therein). It would thus seem natural that the relative strength of stratification compared to rotation, or equivalently the ratio N/f, gives a prediction of their thickness. But if their vertical shape depended exclusively on N/f, then all the vortices embedded in the same flow would have the same vertical over horizontal aspect ratio, which is not what is observed (see for instance Shapiro et al. 1995; Biescas et al. 2008, in the case of meddies). It was shown experimentally (Aubert et al. 2012) and numerically (Hassanzadeh et al. 2012) that the aspect ratio of those vortices depends not only on the ambient parameters f and N, but also on their strength and their internal stratification of buoyancy frequency N_c:

$$\left(\frac{c}{a}\right)^2 = \left(\frac{c}{b}\right)^2 = \frac{-Ro(1+Ro)f^2}{N^2 - N_c^2}, \tag{2.3}$$

where $a = b$ are the semi-axes of the axisymmetric vortex in the horizontal plane and c is the vertical semi-axis. The Rossby number of the vortex, which we define as $Ro = \omega_c/2f$, is indicative of its strength (ω_c being the vertical component of the vorticity at the vortex centre). Rather than the ambient stratification, it is the *difference* between the vortex and the background stratification that is relevant. This law also gives constraints on the vortices interior: weak anticyclones ($Ro \in [-1,0[$) are less stratified than the ambient ($N_c^2 < N^2$) and conversely for cyclones ($Ro > 0$). This is consistent with oceanic observations which show that the isopycnals are pinched towards a cyclone centre whereas they are displaced away from an anticyclone centre (e.g. Manley et al. 1985, figure 3). Facchini et al. (2016) completed this work by focusing on the temporal evolution of a vortex. They showed that when rotation and stratification coexist, the vortex decay is ultimately due to the recirculations within the vortex and is slower than what is expected from classical viscous dissipation of the azimuthal kinetic energy, which is compatible with the observed long-lived duration of both oceanic and Jovian anticyclones.

In this chapter, we aim at extending these results by adding a linear shear to rotation and stratification. This work is specifically motivated by Jovian vortices which are embedded in strong zonal winds (Mitchell et al. 1981) and to a lesser extent by oceanic mesoscale eddies which might be sheared by interactions with other vortices or large-scale currents (e.g. Carton et al. 2013; Shi et al. 2018). Interpreting these vortices properties in a global planetary circulation model is difficult because of the complex multi-scale dynamics involved. Instead, we present an experimental setup which allows us to generate vortices in a flow with the three aforementioned ingredients – rotation, stratification and shear – and follow their temporal evolution both in terms of shape and intensity. Note that the vast majority (~90%) of Jupiter's vortices are anticyclonic (Vasavada et al. 2005). Besides, nearly all anticyclonic structures are circular or oval in shape, whereas many Jovian cyclones are filamentary or multi-lobed. Furthermore, all long-lived Jovian vortices have relative vorticity with the same sign as that of the jets in which they are embedded (Vasavada et al. 2005). For those reasons we focus on anticyclones embedded in an anticyclonic shear.

In §2.2 we derive theoretical laws to predict the three-dimensional (3D) shape of a vortex in quasi-static equilibrium in a rotating stratified shear flow. In §2.3 we describe the experimental setup and direct numerical simulations used to complement experimental results. In §2.4, the theoretical laws are validated against both experiments and simulations. We conclude in §2.5 with an application of these laws to Jovian vortices (GRS, Oval BC, DE and BA) and a comparison with available data for their horizontal dimensions. We further make predictions for their up-to-now inaccessible depth, which await comparison with the upcoming Juno observations. Finally, in §2.6, we briefly discuss the long-term evolution of our experimental and numerical vortices.

2.2. Equilibrium shape

2.2.1. Governing equations

Let us first set the theoretical framework in which we stand and define all the parameters and variables that will be used in the following. We consider the flow of an incompressible fluid of constant kinematic viscosity ν rotating around the vertical axis (oriented upward) at a constant rate $\boldsymbol{\Omega} = \Omega\, \boldsymbol{e_z}$. In cartesian coordinates, we denote the velocity field $\boldsymbol{u} = (u, v, w)_{\boldsymbol{e_x}, \boldsymbol{e_y}, \boldsymbol{e_z}}$. Note that the shear is applied along the x direction, so that coherently with the established plane Couette flow, we designate x and y as the *stream-wise* and *cross-stream* directions respectively (see Fig.2.1*(a–c)*).

We start from the continuity and Navier-Stokes equations as well as the advection-diffusion equation of the stratifying agent of constant diffusivity κ (e.g. salt concentration field in our experiments). The concentration field of this stratifying agent is linearly related to the density field, which hence follows the same advection-diffusion equation (see chapter 1, section 1.2.3.2). In the Boussinesq approximation and in the rotating frame these read:

$$\left.\begin{aligned} &\boldsymbol{\nabla}\cdot\boldsymbol{u} = 0, \\ &\frac{\partial \boldsymbol{u}}{\partial t} + (\boldsymbol{u}\cdot\boldsymbol{\nabla})\boldsymbol{u} + f\,\boldsymbol{e_z}\times\boldsymbol{u} = -\frac{1}{\rho_0}\boldsymbol{\nabla}\tilde{p} + \frac{\tilde{\rho}}{\rho_0}\boldsymbol{g} + \nu\boldsymbol{\nabla}^2\boldsymbol{u}, \\ &\frac{\partial \tilde{\rho}}{\partial t} + (\boldsymbol{u}\cdot\boldsymbol{\nabla})\tilde{\rho} = \kappa\boldsymbol{\nabla}^2\tilde{\rho}, \end{aligned}\right\} \tag{2.4}$$

where $f = 2\Omega$ is the Coriolis parameter and ρ_0 is the mean density. $\tilde{\rho} = \rho - \rho_0$ is the deviation of the density field compared to this mean density, including the linear stratification, and $\tilde{p} = p + \rho_0 g z$ is the pressure deviation compared to the mean hydrostatic pressure (see section 1.2.3.2). The stationary solution without any vortex nor plane Couette flow, i.e. the hydrostatic equilibrium of the rotating stratified flow, writes

$$\bar{\rho}(z) = \rho_0 \frac{N^2}{g} z, \tag{2.5a}$$

$$\bar{p}(z) = p_0 + \frac{N^2 \rho_0}{2} z^2, \tag{2.5b}$$

where $N = \sqrt{-g\partial_z\bar{\rho}/\rho_0}$ is the buoyancy frequency corresponding to the background linear stratification. Defining the density and pressure perturbations as $\delta\rho = \tilde{\rho}(x,y,z,t) - \bar{\rho}(z)$ and $\delta p = \tilde{p}(x,y,z,t) - \bar{p}(z)$ gives the following system of equations for the perturbations in the Boussinesq approximation:

$$\left.\begin{aligned} &\boldsymbol{\nabla}\cdot\boldsymbol{u} = 0, \\ &\frac{\partial \boldsymbol{u}}{\partial t} + (\boldsymbol{u}\cdot\boldsymbol{\nabla})\boldsymbol{u} + f\,\boldsymbol{e_z}\times\boldsymbol{u} = -\frac{1}{\rho_0}\boldsymbol{\nabla}\delta p - \frac{\delta\rho}{\rho_0} g\,\boldsymbol{e_z} + \nu\boldsymbol{\nabla}^2\boldsymbol{u}, \\ &\frac{\partial \delta\rho}{\partial t} + (\boldsymbol{u}\cdot\boldsymbol{\nabla})\delta\rho = \frac{\rho_0 N^2}{g} w + \kappa\boldsymbol{\nabla}^2\delta\rho. \end{aligned}\right\} \tag{2.6}$$

Both experimentally and numerically, the shear is added via the action of two rigid boundaries located at $y = (-d, d)$ moving at constant velocity in opposite directions parallel to x (Fig.2.1*(b)*). Using half the distance between the two shearing boundaries d as the length scale and $1/f$ as

the time scale gives the non-dimensional variables $(x', y', z', \boldsymbol{u}', \delta\rho', \delta p')$ such that

$$t = t'/f \tag{2.7a}$$

$$(x, y, z) = (x', y', z')d, \tag{2.7b}$$

$$(u, v, w) = (u', v', w')df, \tag{2.7c}$$

$$\delta\rho = \delta\rho'\rho_0 df^2/g, \tag{2.7d}$$

$$\delta p = \delta p'\rho_0 d^2 f^2. \tag{2.7e}$$

The corresponding non-dimensional set of equations for the perturbations writes

$$\boldsymbol{\nabla}' \cdot \boldsymbol{u}' = 0, \tag{2.8a}$$

$$\frac{\partial \boldsymbol{u}'}{\partial t'} + (\boldsymbol{u}' \cdot \boldsymbol{\nabla}')\boldsymbol{u}' + \boldsymbol{e}_z \times \boldsymbol{u}' = -\boldsymbol{\nabla}'\delta p' - \delta\rho'\ \boldsymbol{e}_z + \frac{1}{Re}\nabla'^2 \boldsymbol{u}', \tag{2.8b}$$

$$\frac{\partial \delta\rho'}{\partial t'} + (\boldsymbol{u}' \cdot \boldsymbol{\nabla}')\delta\rho' = N^{*2} w' + \frac{1}{ScRe}\nabla'^2 \delta\rho', \tag{2.8c}$$

where we introduce the Reynolds number $Re = d^2 f/\nu$, the Schmidt number $Sc = \nu/\kappa$ and the ratio of the Brunt-Väisälä frequency to the Coriolis frequency $N^* = N/f$. Consistently, we denote $\sigma^* = \sigma/f$ the non-dimensional shear rate. In the following, we drop the $'$ for the sake of clarity but all the variables are dimensionless except when explicitly stated.

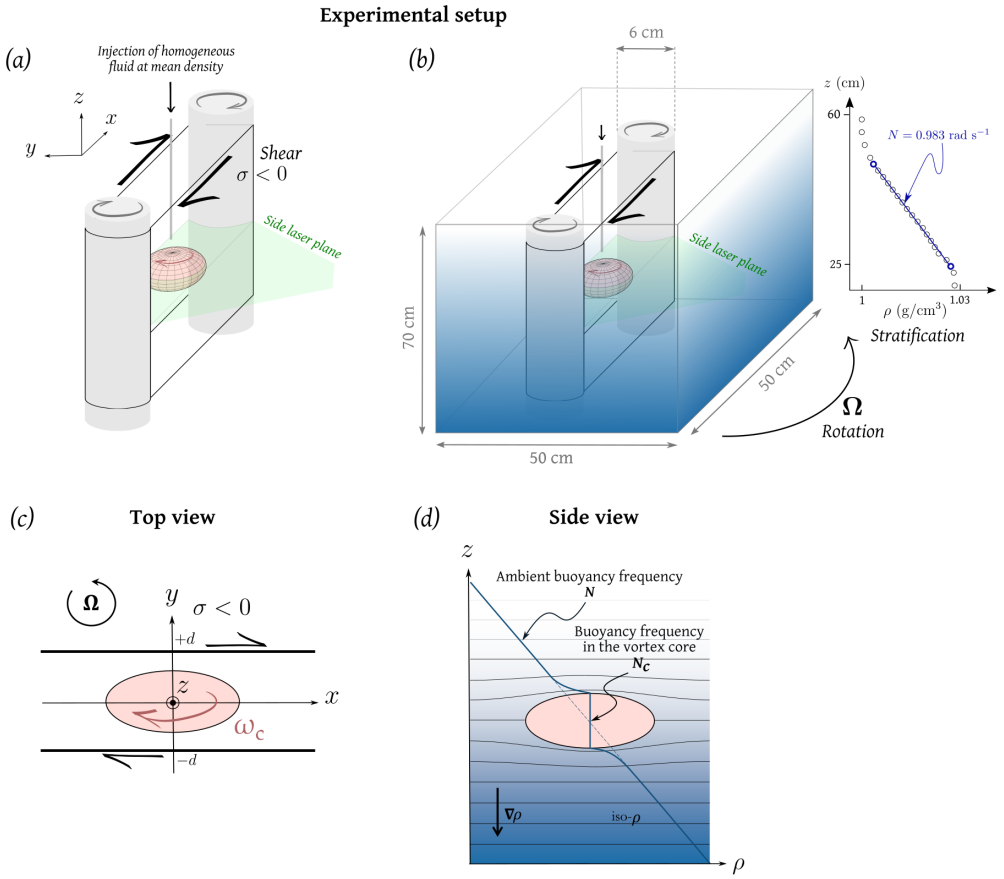

Figure 2.1. – Simplified sketch of the experimental set-up. *(a)* The shearing device is made of a PVC belt encircling two co-rotating cylinders. A capillary tube injects fluid in the gap between the membrane sides to create a vortex which is analysed by performing PIV in its equatorial plane. *(b)* The represented device is placed inside a bigger tank which rotates at a rate Ω. The fluid is stratified using salty water to achieve $N \approx 1$ rad s^{-1}. An example of a measured stratification is plotted, where ρ is the dimensional density. *(c)* Top-view schematic in the vortex equatorial plane. The ambient rotation is anti-clockwise, and both the vortex and the shear are clockwise (anticyclonic). *(d)* Side-view schematic. The ambient stratification has a buoyancy frequency N whereas the vortex core has a buoyancy frequency N_c. An anticyclone is under-stratified compared to the ambient ($N_c < N$).

2.2.2. Theoretical shape

Following the same method as Aubert et al. (2012), we discuss here the theoretical shape of a vortex in our setup. In the inviscid limit, we first derive the unperturbed pressure field corresponding to a rotating plane Couette flow, then we derive the pressure field inside a compact ellipsoidal vortex. We finally constraint pressure continuity between those two fields which leads to an ellipsoid equation for the vortex contour.

We start from the Navier-Stokes equation for the perturbations in the Boussinesq approximation, equation (2.8b), and neglect the viscous, non-linear and time-dependent terms since we search for a steady, weak, cyclo-geostrophic and hydrostatic equilibrium state. For a linear plane Couette flow, $\boldsymbol{U} = (-\sigma^* y, 0, 0)$, the pressure perturbation writes

$$\delta P = \delta P_0 + \frac{\sigma^*}{2} y^2, \tag{2.9}$$

where δP_0 is a constant. Neglecting diffusivity, viscosity and non-linearities allows to consider discontinuous velocity and density fields. We thus look for a compact triaxial ellipsoidal vortex and denote a, b and c its principal semi-axes ($a > b$ on the horizontal plane, and c along the

vertical). The constant vertical vorticity in the vortex is $\omega_c = 2Ro$ (Ro being the Rossby number of the vortex), and the corresponding velocity field in the vortex writes

$$\boldsymbol{u_v} = Ro \begin{pmatrix} -(1+\beta)\,y \\ (1-\beta)\,x \\ 0 \end{pmatrix}, \tag{2.10}$$

where $\beta = (a^2 - b^2)/(a^2 + b^2)$ is the equatorial ellipticity of the vortex which goes from 0 for an axisymmetric vortex to 1 for an infinitely stretched ellipse. The stratification inside the vortex is assumed to be linear with a buoyancy frequency N_c^* (see Fig.2.1*(d)*). The corresponding inviscid pressure field inside of the vortex, δp_v, writes

$$\begin{aligned} \delta p_v = \delta p_c \quad &+ \quad \frac{Ro}{2}(1-\beta)\left[Ro(1+\beta)+1\right]x^2 \\ &+ \quad \frac{Ro}{2}(1+\beta)\left[Ro(1-\beta)+1\right]y^2 \\ &- \quad \frac{N^{*2}-N_c^{*2}}{2}z^2, \end{aligned} \tag{2.11}$$

where δp_c is a constant – the pressure anomaly at the vortex centre. While the velocity and the density fields are discontinuous between the vortex and the background flow, we require the continuity of the pressure field between the vortex and the surrounding rotating plane Couette flow. Equality between equations (2.9) and (2.11) leads to ellipsoidal surfaces defined by

$$\begin{aligned} & Ro\,(1-\beta)\,\left[1+(1+\beta)Ro\right]\,x^2 \\ + \quad & \left(Ro\,(1+\beta)\,\left[1+(1-\beta)Ro\right]-\sigma^*\right)\,y^2 \\ + \quad & \left(N_c^{*2}-N^{*2}\right)\,z^2 = \text{cst}. \end{aligned} \tag{2.12}$$

Applying this relation at the points $(x,y,z) = (a,0,0)$ and $(0,b,0)$ gives a relation for the ellipticity β:

$$\beta^2\left(2\frac{Ro_x^2}{\sigma^*}+1\right)+2\beta\left(\frac{Ro_x^2}{\sigma^*}-1\right)+1=0, \tag{2.13}$$

where $Ro_x = (1-\beta)Ro$ is the stream-wise Rossby number (the slope of the cross-stream velocity v profile along x at the centre of the vortex). Knowing the strength of the vortex and the shear applied to it, this relation allows to predict the equatorial ellipticity of the vortex. From this equation, we select the root β that is positive and comprised between 0 and 1. The ellipticity then evolves intuitively: when $Ro_x^2/\sigma \gg 1$, the vortex does not "feel" the ambient shear and tends towards axisymmetry ($\beta \to 0$). On the contrary, when $Ro_x^2/\sigma \ll 1$, $\beta = 1$ meaning that the vortex is infinitely extended in the stream-wise direction ($a/b \gg 1$).

Similarly, applying relation (2.12) at $(x,y,z) = (a,0,0)$ and $(0,0,c)$ gives a relation for the vertical aspect ratio of the vortex

$$\left(\frac{c}{a}\right)^2 = \frac{Ro_x\left[1+Ro_x\,\frac{1+\beta}{1-\beta}\right]}{N_c^{*2}-N^{*2}}. \tag{2.14}$$

Interestingly, the shear does not directly appear in this relation since its influence is hidden in the ellipticity β. Thus, knowing only the horizontal aspect ratio, the strength of the vortex and its stratification allows to infer its vertical aspect ratio. For an axisymmetric vortex, i.e. without shear, $\beta = 0$ and we retrieve relation (2.3) in the sole presence of rotation and stratification. On the contrary when $\beta \to 1$, since $Ro_x = (1-\beta)Ro$, the vortex is infinitely sheared and flat ($c/a \to 0$).

Note that in terms of scaling analysis, the dimensionless parameters entering those laws are fully consistent with our assumptions. A dissipationless floating vortex is fully characterized by 8 dimensional parameters: its dimensions a, b and c, its physical characteristics given by its vorticity ω_c and the difference between its internal density gradient and the ambient one $N_c^2 - N^2$ and the environment physical characteristics given by the Coriolis frequency f, the buoyancy frequency N and the shear σ. According to the Π-theorem, the whole system is thus characterised by 6 dimensionless numbers, that we chose to be the geometrical parameters given by the equatorial ellipticity β and the aspect ratio c/a, and the dynamical parameters given by the Rossby number $Ro = \omega_c/2f$, the dimensionless shear $\sigma^* = \sigma/f$, the dimensionless buoyancy frequency $N^* = N/f$, and the dimensionless buoyancy anomaly $(N_c^2 - N^2)/f^2$. Note that the dimensionless buoyancy frequency alone does not appear in the scaling laws for the vortex aspect ratio, at least in the Boussinesq approximation considered here. Only the dimensionless buoyancy *anomaly* does.

The above parameters fully describe the quasi-static, inviscid and diffusion-less problem where our assumptions naturally lead us to neglect other dimensional parameters (the molecular viscosity ν and the stratifying agent diffusivity κ). In the full problem (equations (2.8a)–(2.8c)), two supplementary non-dimensional parameters are necessary: the Reynolds number $Re = d^2 f/\nu$ and the Schmidt number $Sc = \nu/\kappa$. These parameters (Re, Sc) are not relevant for determining the shape of the vortex, and they will only appear when we discuss the decay of the vortex through time (section 2.6), which is a completely different question.

2.3. Experimental and numerical methods

In this section, we describe the experimental and numerical methods that are used to validate the previously derived theoretical laws for the vortex shape.

2.3.1. Experimental methods

2.3.1.1. Experimental set-up

The experimental setup used in this chapter is the same as the one described in Facchini et al. (2018), except that we create a vortex within the established linear plane Couette flow. Details on the setup can be found in Giulio Facchini's doctoral dissertation (Facchini 2017). We recall briefly its principal features. A tank ($50 \times 50 \times 70$ cm) is filled with salty water linearly stratified in density using the double bucket method. The tank is mounted on a table that rotates around a vertical axis at a rate Ω (Fig.2.2*(a)*). The stratification is measured vertically by sampling the fluid at different heights and measuring the corresponding density with a density-meter. In all the experiments discussed here, we generated stratifications corresponding to a buoyancy frequency $N = 1 \pm 0.05$ rad s^{-1} with a rotation rate $\Omega = 0.5$ rad s^{-1} such that $N^* = N/f \sim 1$. An example of a measured stratification is plotted in Fig.2.1*(b)*. To impose a shear in the flow, we use a PVC belt encircling two co-rotating cylinders. Two additional pairs of cylinders allow to stretch out the membrane while keeping a constant gap $2d = 6$ cm between the two shearing sheets. Pictures of the principal tank and shearing device are provided in Fig.2.2.

After placing the shearing device inside the tank, we fill it with stratified salty water. We then gradually increase the rotation rate of the turntable to avoid disturbing the stratification during the spin-up. Note that we measure the stratification before and after each experiment to verify that it was not excessively modified both by the spin-up/spin-down processes and the studied vortices. Once solid body rotation is reached, we activate the shear and wait for the stationary plane Couette flow to establish (~ tens of minutes).

To create anticyclones in the gap, a one millimetre-diameter capillary tube is linked to a reservoir fixed above the tank. Using gravity fall only, we inject a volume of fluid having a constant density equal to the density at the injection height. In the experiments presented here, we typically inject fluid at mid-height during 6 seconds which corresponds to a volume $V \sim 40$mL. The parameters of the experimental cases discussed in this chapter are listed in Table 2.1. Fig.2.1 summarises the experimental setup and conventions.

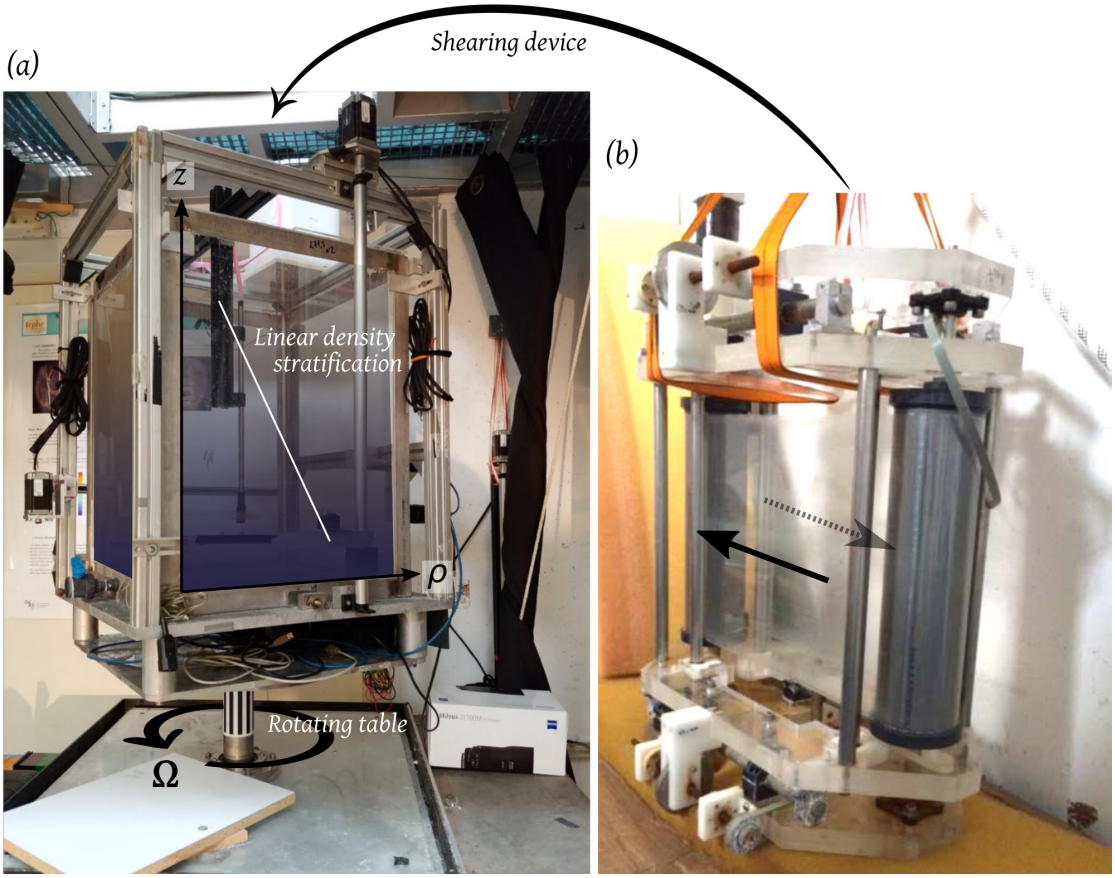

Figure 2.2. – *(a)* Rotating tank. The rotation is anti-clockwise. *(b)* Shearing device rotating in the clockwise direction (anticyclonic shear). The anticyclones are generated by injecting fluid of neutral density in between the walls of the shearing device (see also Fig.2.1).

2.3.1.2. Visualization and particle image velocimetry

Velocity field measurements are performed in the equatorial plane of the vortex using particle image velocimetry (PIV). We seed the fluid with 10 µm-diameter hollow glass spheres and their displacement is followed using a camera fixed in the rotating frame above the tank and looking downward. We use the Matlab software DPIVSoft2010 (Meunier et al. 2003) to extract velocity fields from these measurements. Typically, the field covers an area of 19×7 cm with a grid resolution of 210×52.

For some experiments we added Rhodamine B, a fluorescent dye, in the injected fluid to follow its evolution in a vertical plane. A second vertical laser plane aligned with the x-axis is thus present along with a camera fixed on the side of the tank to record corresponding movies. Note that the two laser sheets could not be switched on simultaneously since this would deteriorate the PIV measurements. For that reason, we do not have a continuous recording

of the vertical shape of the vortices but only a few instants per experiment during which we temporarily turned off the horizontal laser plane and switched on the vertical one. To compute the vertical aspect ratio, we binarize the images such that all pixels of intensity above an arbitrary threshold are equal to 1. We fill the holes inside the vortex that are due to PIV particles using the MATLAB *imfill* function. We then use the *regionprops* function to detect all the elliptic patches on the binary image. We extract from it the largest form detected as well as its long and short-axis a and c respectively.

Fig.2.3 shows the typical evolution of a vortex as observed during an experiment in the equatorial plane. We chose a case where Rhodamine B was added to the injection fluid for a better visualization. The corresponding velocity fields deduced from PIV are represented, keeping only one grid point out of three in both directions for clarity. As time increases, the vortex is stretched in the stream-wise direction by the linear shear and its intensity decreases. Fig.2.4*(a,b)* show velocity profiles along both x and y as a function of time during an experiment. We verify that, similarly to Facchini et al. (2016), along the x direction (parallel to the shear), the velocity profiles are close to that of a gaussian isolated vortex as defined by

$$\boldsymbol{u}_v(x,y,z,t) = Ro(t)\begin{pmatrix} -(1+\beta)y \\ (1-\beta)x \\ 0 \end{pmatrix}\exp\left(-\left[\frac{x}{a}\right]^2-\left[\frac{y}{b}\right]^2-\left[\frac{z}{c}\right]^2\right), \tag{2.15}$$

This is coherent with Kloosterziel (1990) who showed that when no net vorticity is introduced by the injection process, gaussian isolated vortices are a good approximation of laboratory vortices. In the y direction the effects of confinement are clearly visible, but the velocity field still resembles some gaussian profile superposed to the background shear. Note that the discontinuous linear model (equation (2.10)) exactly corresponds to the core of our experimental and numerical gaussian vortices.

To measure the horizontal ellipticity of our experimental vortices, we use a linear fit of the velocity profiles in the vortex core in the cross-stream and stream-wise direction. According to equation (2.10), the slope of the velocity profile in the cross-stream ($x = 0$) direction is $-Ro(t)(1+\beta(t))$, and $Ro(t)(1-\beta(t))$ in the stream-wise direction ($y = 0$). Fitting the two directions simultaneously thus allows to retrieve both $Ro(t)$ and $\beta(t)$.

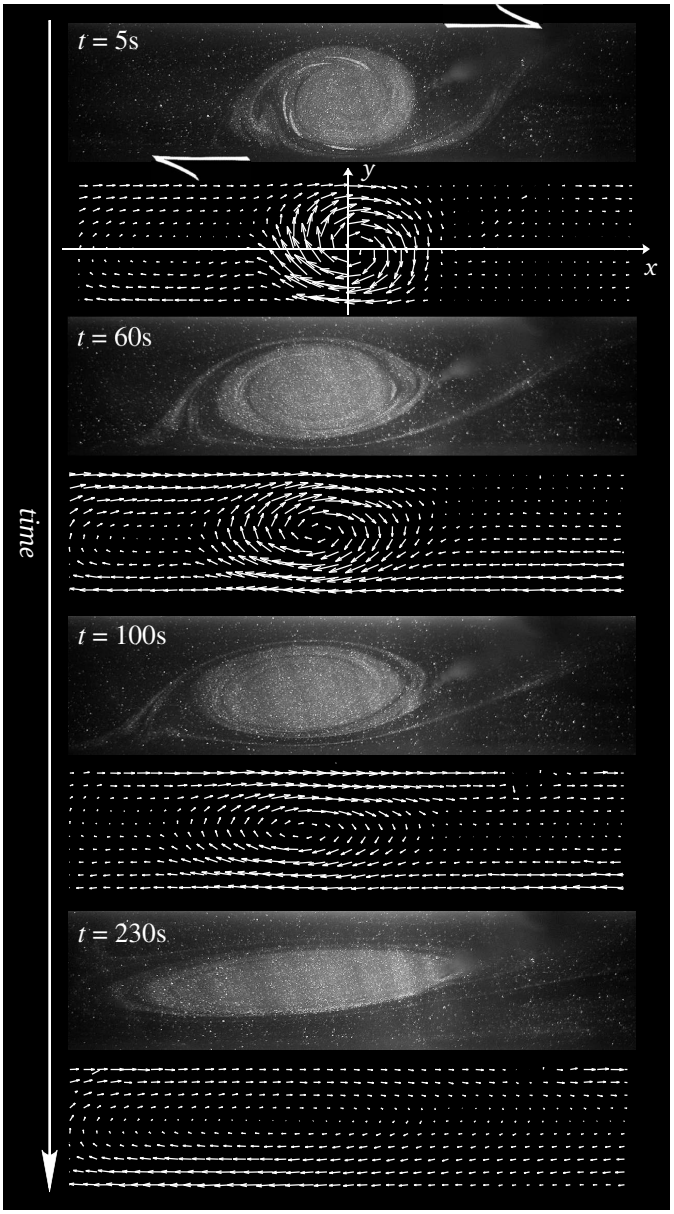

Figure 2.3. – Evolution of a sheared anticyclone as observed during our experiments on a horizontal plane. The Rhodamine B added to the injected fluid allows to follow the vortex shape evolution through time. The corresponding PIV vector fields are represented. The shearing boundaries are parallel to the x-axis and are located at the borders of the images and vector fields. The injected vortex is initially compact, stable and axisymmetric and evolves laminarily towards an elliptic shape under the action of shear. This shape evolution is accompanied by a decay of the strength of the vortex. Note that at $t = 230$ s, the vortex semi long-axis turns out to be $a \approx 2d$. The shear rate is $\sigma \approx 0.07$ s^{-1}. If the vortex was passively advected by the simple shear, it would have reached this extension at a much shorter time $a/(\sigma d) \approx 2/\sigma \approx 30$ s.

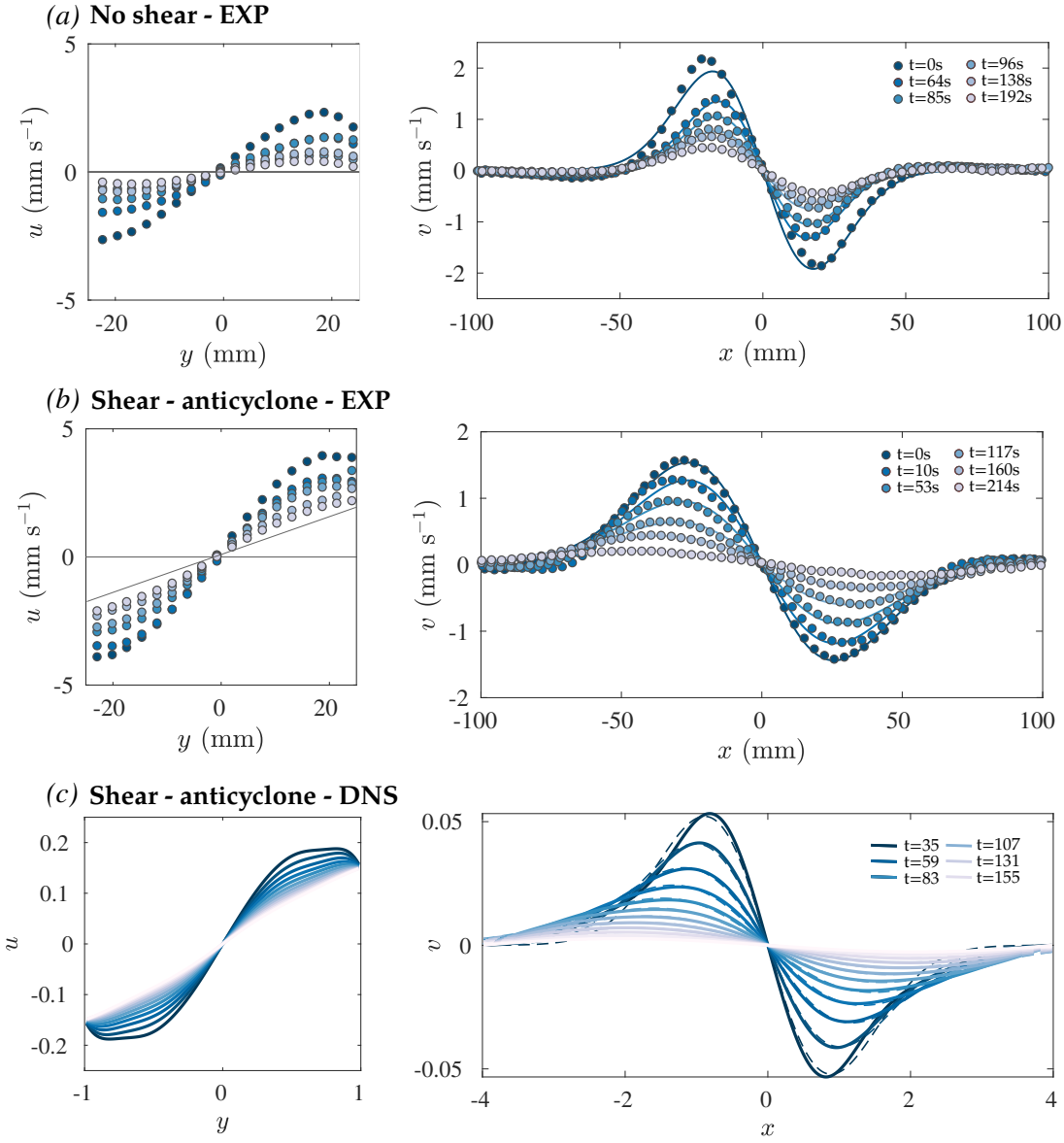

Figure 2.4. – *(a,b)* Measured velocity profiles for two anticyclones produced by a 6 seconds injection, *(a)* without shear but with the PVC belt installed so that the vortex is confined in the y direction, and *(b)* with a shear rate $\sigma \approx 0.07$ s^{-1} . The x direction is parallel to the shear direction whereas y is orthogonal to it. The dots are experimental measurements and the lines are the best-fitting Gaussian profiles (equation (2.15)). *(c)* Same velocity profiles extracted from the reference simulation (see Table 2.1). The dashed lines are the best-fitting Gaussian profiles.

2.3.2. Numerical methods

2.3.2.1. Numerical method

We performed direct numerical simulations (DNS) to compare with our experimental results and extend them to a wider range of parameters. To this aim, we solve the full system of equations (2.8a)-(2.8c) using the open-source spectral element solver Nek5000 (Fischer et al. 2008). These equations are solved in a rectangular box of dimensions (L_x, L_y, L_z)=(8,2,4) centred at the origin $(x, y, z) = (0, 0, 0)$ to mimic the experimental setup. The boundary conditions are periodic in both the stream-wise (x) and vertical (z) directions and rigid no-slip insulating

boundaries are imposed in the cross-stream (y) direction, i.e. $\boldsymbol{u} = \mp\sigma^* y\ \boldsymbol{e}_x$ and $\partial_y \delta\rho = 0$ at $y = \pm 1$. The global geometry is partitioned into $\mathscr{E}$ hexahedral elements. Inside each element, velocity, density and pressure perturbations variables are projected onto $\mathscr{N}$-th order Lagrange interpolating polynomials distributed on Gauss-Lobatto-Legendre nodes. For all the results discussed in this paper, the number of elements is $\mathscr{E} \sim 3000$ and we use Lagrange interpolating polynomials of order $\mathscr{N} = 15$ ($\mathscr{N} = 10$ after dealiasing) leading to $\sim 10^7$ grid points. Time integration is performed with a third-order explicit scheme for the advection and buoyancy terms while viscous and dissipative terms are integrated using an implicit third-order scheme.

2.3.2.2. Initial flow

The simulations are initialized with an established linear plane Couette flow $\boldsymbol{u}(t=0) = -\sigma y\ \boldsymbol{e}_x + \boldsymbol{u}_{v,0}$ where $\boldsymbol{u}_{v,0}$ corresponds to an axisymmetric ellipsoidal gaussian vortex centred at the origin

$$\boldsymbol{u}_{v,0}(x,y,z) = Ro_0 \begin{pmatrix} -y \\ x \\ 0 \end{pmatrix} \exp\left(- \left[\frac{\sqrt{x^2+y^2}}{a_0} \right]^2 - \left[\frac{z}{c_0} \right]^2 \right), \tag{2.16}$$

where a_0 and c_0 are respectively the initial horizontal and vertical dimensions of the vortex. For all the results discussed in this paper, we take $a_0 = 0.8$ for the vortex to fit between the two moving boundaries at $y = \pm 1$. The initial vertical extent c_0 is the one given by equation (2.14) with no initial ellipticity, $\beta_0 = 0$. The choice of starting with a gaussian vortex is first motivated by the experimental results which show that the velocity profiles are nearly gaussian. Second, when an initial discontinuous vortex with uniform density is considered, the very steep initial gradients in the density field require a too high numerical resolution, namely because the high Schmidt number of our simulations does not allow for the rapid regularization of the vortex edges by diffusion. Finally, $Ro_0 = \omega_{c,0}/2$ is the initial Rossby number of the vortex, ω_c being the vertical component of the vorticity at the centre of the vortex (divided by f). We explore the case where the shear and the vortex have the same vorticity sign hence we take $Ro_0 < 0$ and $\sigma^* < 0$. Finally, the initial density perturbation inside of the vortex relatively to the background linear stratification writes

$$\delta\rho_v(x,y,z,t=0) = \left[N^{*2} - {N^*_{c,0}}^2 \right] z \exp\left(- \left[\frac{\sqrt{x^2+y^2}}{a_0} \right]^2 - \left[\frac{z}{c_0} \right]^2 \right). \tag{2.17}$$

To be coherent with experiments where the injected fluid is well-mixed, we initialize anticyclones with no internal absolute stratification i.e $N^*_{c,0} = 0$. Thus, along the rotation axis ($(x,y) = (0,0)$) and in the vicinity of the vortex midplane, $z = 0$, the density anomaly writes $\delta\rho_{v,0} \sim N^{*2}\ z$. Fig.2.5 shows a qualitative comparison, in the equatorial plane, between experimental and numerical velocity fields.

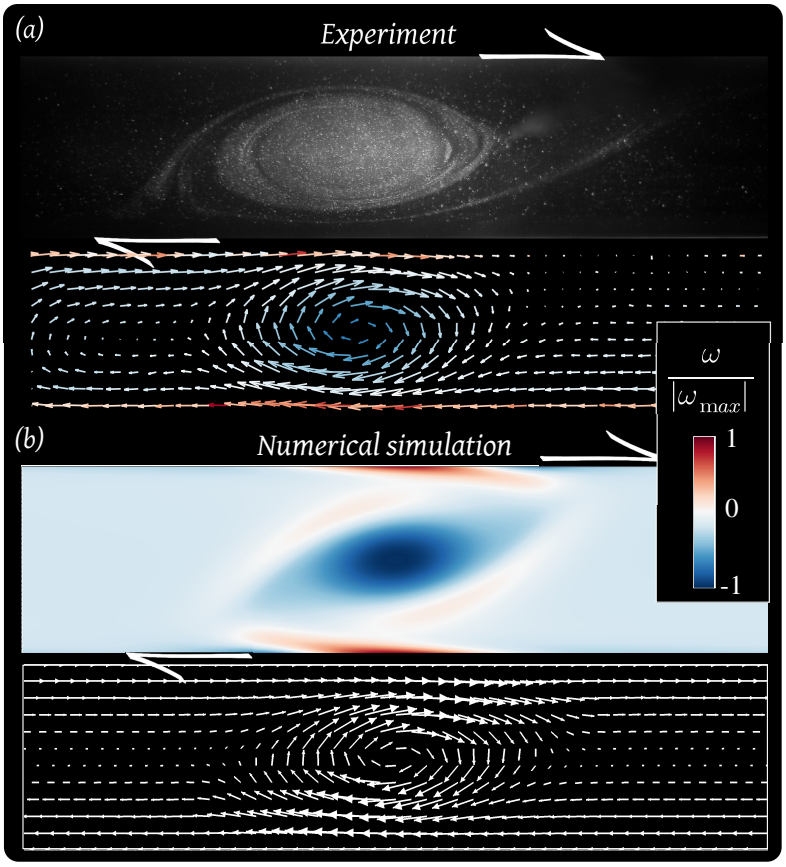

Figure 2.5. – *(a)* Top-view visualizations in the vortex equatorial plane during an experiment and corresponding velocity field. The vortex is brighter than the ambient because of Rhodamine B. On the PIV field, we represent only one grid point out of three in both directions for clarity. *(b)* Snapshot from a numerical simulation representing the vertical component of the vorticity ω and the velocity field in the vortex equatorial plane.

2.3.2.3. Vortex stability

All the cases discussed in this chapter and used to verify our model are cases where the vortex is stable. However, we want to mention that we numerically encountered unstable cases even if they are beyond the scope of our study. A wide variety of phenomena can destabilize an axisymmetric pancake-like vortex in a rotating-stratified flow, including gravitational, centrifugal, baroclinic and Gent-Mc Williams instabilities as well as combinations of them (see Yim 2015, and references therein). Such instabilities prevented us from exploring cases with strong stratifications, $N^* > 1$. Indeed, in those cases the core of the vortex becomes unstable. The study and the origin of this instability are beyond the scope of our study; however, we can locate our unstable cases in the maps of instabilities given in Yim et al. (2016). Using their dimensionless parameters definitions, our unstable cases typically have an aspect ratio $\alpha = c_0/a_0 \approx 0.25$, a Froude number $F_h = Ro/N^* \approx 0.23$, a Rossby number $\tilde{Ro} = 2Ro = -0.90$, a Reynolds number of the vortex $\tilde{Re} = RoRe \approx 259$ and a vertical Froude number $F_h/\alpha \approx 0.9$. The low Froude and Rossby numbers are consistent with the Gent-Mc Williams instability described in Yim et al. (2016). However our Reynolds number is considerably smaller than the one fixed in their study ($\tilde{Re}$ =10,000) and at such low Re, we would rather expect a displacement instability (see figure 5.18 in Yim 2015) which is not what we observed. We rather suspect that the observed instability finds its origin in the non-axisymmetric shape of the vortex. Due to the imposed strain field, the streamlines in the vortex core are elliptical which may lead to the so-called

	$Re = fd^2/\nu$	$N^* = N/f$	$Ro_0 = \omega_{c,0}/2f$	$\sigma^* = \sigma/f$	$Sc = \nu/\kappa$
Exp	900	~ 1	-0.5	-0.07	~700
Exp	900	~ 1	-0.5	-0.07	~700
Exp	900	~ 1	-0.5	-0.10	~700
Exp	900	~ 1	-0.5	-0.14	~700
Exp	900	~ 1	-0.5	-0.14	~700
Exp	900	~ 1	-0.5	-0.20	~700
Exp	900	~ 1	-0.5	-0.34	~700
DNS	900	1	-0.45	-[0.05:0.05:0.45]	35
DNS	1800	1	-0.45	-0.15	35
DNS	2700	1	-0.45	-0.15	35
DNS	3600	1	-0.45	-0.15	35
DNS	900	1	-0.45	-0.15	0.07
DNS	900	1	-0.45	-0.15	0.7
DNS	900	1	-0.45	-0.15	7
DNS	**900**	**1**	**-0.45**	**-0.15**	**35**
DNS	900	1	-0.45	-0.15	70
DNS	900	1	-0.45	-0.15	175
DNS	900	1	-[0.10:0.05:0.45]	-0.15	35
DNS	900	[0.50,0.75, *1.33,1.50 1.75,2.00]*	-0.45	-0.15	35

Table 2.1. – Experimental and numerical cases parameters. The bold parameters are those of the reference simulation to which we refer several times in the text. The blue parameters are the ones varied compared to the experiment. The parameters in italic are unstable ones, presumably because of an elliptical instability (see section 2.3.2.3).

elliptical instability via a parametric excitation of inertial waves in the core of the vortex (see Miyazaki 1993; Chomaz et al. 2010; Guimbard et al. 2010).

2.3.3. Non-dimensional parameters

Table 2.1 lists the non-dimensional parameters of the experiments and simulations discussed in the present chapter. The simulations were performed in the ranges $Re \in [900, 3600]$, $Sc \in [0.07, 175]$ and $N^* \in [0.5, 2]$. In the experimental conditions, $Re = 900$, $N^* = 1$ and $Sc \approx 700$. The large experimental value of the Schmidt number is the consequence of the small salt diffusion. To be in the same physical regime numerically without having to impose such a high Sc, we searched for the minimum Sc for which the vortex behaviour no longer depends on salt diffusion. As discussed in section 2.6, we show that this is the case as soon as $Sc \geq 35$. All the simulations discussed in this chapter are thus performed at $Sc = 35$.

2.4. Equilibrium shape of the vortices: experimental and numerical validation

2.4.1. Observations and dominant balances

In this section, we want to show that at zeroth-order, the dominant physical balances at play at any time during the vortex evolution are consistent with the hypotheses assumed to derive the equilibrium shape. We focus on the results of the reference simulation (bold line in Table 2.1) at time $t = 140$. In figure 2.6(*a,b*), the projections of the Navier-Stokes equations (2.8b) onto

$\boldsymbol{e}_x$ and $\boldsymbol{e}_y$ along the $(x,0,0)$ and $(0,y,0)$ directions show that the cyclo-geostrophic (or gradient wind) balance

$$\begin{aligned} v\,\partial_y u - v &\approx -\partial_x \delta p, \\ u\,\partial_x v + u &\approx -\partial_y \delta p, \end{aligned} \tag{2.18}$$

is indeed verified at zeroth order. Besides, the projection onto $\boldsymbol{e}_z$ (Fig.2.6*(c)*) is dominated by the hydrostatic balance $\delta\rho \approx -\partial_z \delta p$. We hence verify that the viscous and diffusive effects are negligible to determine the instantaneous shape of the vortex, as well as the vertical velocity w. As a consequence, the theoretical pressure anomaly at the core of the vortex given by equation (2.11) fits well those extracted from the numerical simulation, as shown in Fig.2.7. Outside of the vortex, the pressure field becomes the theoretical background pressure field given by equation (2.9), due to the rotating stratified plane Couette flow. Since the pressure perturbation inside the vortex is very close to parabolic in each direction, we compute the aspect ratios from our simulations using

$$\left(\frac{a}{b}\right)^2(t) = \frac{(\partial_y^2 \delta p)_c}{(\partial_x^2 \delta p)_c} \quad \text{and} \quad \left(\frac{c}{a}\right)^2(t) = \frac{(\partial_x^2 \delta p)_c}{(\partial_z^2 \delta p)_c}, \tag{2.19}$$

where the subscript c means that the derivatives are computed at the centre of the vortex.

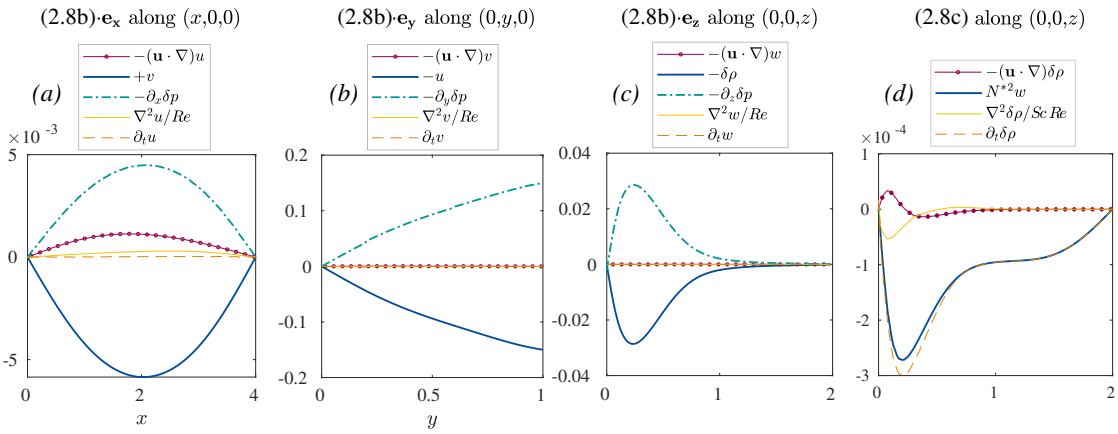

Figure 2.6. – Terms of equations (2.8b) and (2.8c) for different projections and along different directions. *(a)* First component of (2.8b) along x. *(b)* Second component of (2.8b) along y. These projections show that at zeroth order the system verifies a cyclo-geostrophic equilibrium where the Coriolis and centrifugal forces balances the pressure gradient. *(c)* Third component of (2.8b) along the z direction showing the predominance of the hydrostatic equilibrium $\delta\rho = -\partial_z \delta p$. *(d)* Density anomaly evolution equation (2.8c) along the z direction.

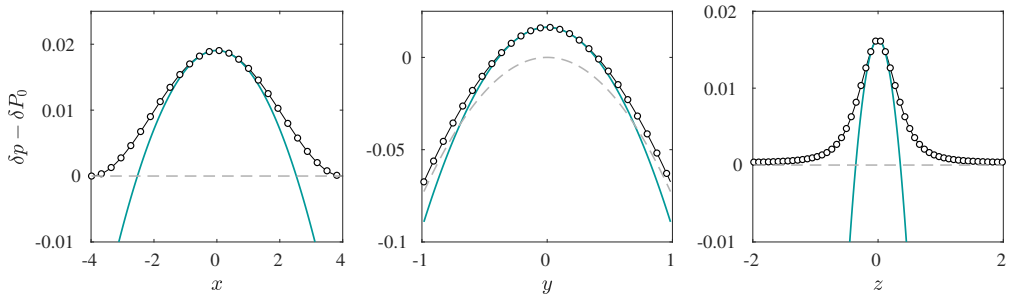

Figure 2.7. – Pressure perturbation profiles along $(x,0,0)$, $(0,y,0)$ and $(0,0,z)$. Dots represent results from the reference numerical simulation (parameters given in Table 2.1) at time $t = 140$. The bold green line is the theoretical pressure anomaly (2.11) inside of the vortex. The dashed grey line is the theoretical rotating plane Couette pressure field (2.9).

2.4.2. Comparison with theoretical laws

We have verified the basic hypotheses of our model: in our experiments and simulations, at zeroth order, the vortex is at any time ellipsoidal, and the cyclo-geostrophic and hydrostatic equilibria are dominant. In this section, we report the shape evolution of our laboratory and numerical vortices and confront it with the theoretical laws derived in section 2.2.2. We recall that in our model, this shape results from a quasi-static equilibrium and is independent of the processes that govern the vortex decay: all that is requested here is a time decoupling between the fast azimuthal motion that controls the equilibrium shape, and the slow dissipative processes that control the long-term evolution. This is indeed the case in both our experimental and numerical study, as well as for Jovian vortices.

The evolution of the measured horizontal aspect ratio (a/b) is represented as a function of $Ro_x/|\sigma^*|^{1/2}$ in Fig.2.8*(a)* for five simulations and five experiments with different shear rates. Additionally, we plot a line corresponding to the theoretical horizontal aspect ratio deduced from relation (2.13). These curves show that at any time during the simulations and experiments, there is a good agreement between the measured equatorial shape of the vortex and our prediction. We notice however that the higher the shear rate the better is the agreement. This is not surprising since we assumed that the vortex is at any time in a quasi-static equilibrium with the background plane Couette flow. If the vortex is stronger than the applied shear, it may impede the establishment of the plane Couette flow and the resulting quasi-equilibrium will not be the one expected from our model. Indeed, we recall that both numerically and experimentally, the shear is applied by two tangentially-moving rigid boundaries, thus through a purely viscous process. This effect may be suppressed numerically by implementing a shearing box, that is by solving the equations in a rotating and shearing frame of reference. This method is however beyond the scope of this study since the DNS are used to mimic the experiments.

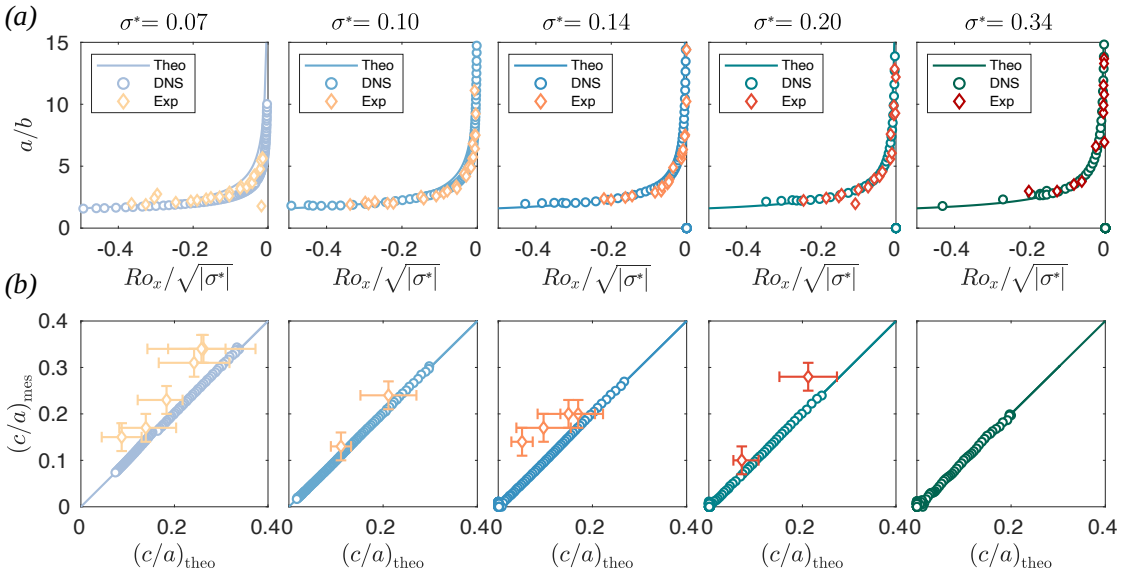

Figure 2.8. – Evolution of the vortex shape for simulations (dots) and experiments (diamonds). The colours distinguish different runs with different background shear rates. The continuous lines represent the theoretical laws (2.13) and (2.14). *(a)* Horizontal aspect ratio a/b of the vortices as a function of their Rossby number. Time increases from left to right since the Rossby number of a vortex decreases in absolute value by dissipation. *(b)* Measured vertical aspect ratio c/a as a function of its theoretical prediction. We recall that to measure c/a experimentally, we use a fluorescent dye and observe the vortex shape on a vertical laser plane. Since we cannot perform simultaneously PIV in a horizontal plane and visualizations on a vertical laser plane, only a few points are available for each experiment.

We now seek to verify the law on the vertical aspect ratio, equation (2.14). Fig.2.8*(b)* shows

the measured vertical aspect ratio c/a as a function of the theoretical one. To compute the theoretical vertical aspect ratio, $Ro_x(t)$ and $\beta(t)$ are measured at each time. Similarly, it is necessary to know the internal stratification of the vortex $N_c(t)$. We have access to it numerically, but not experimentally. Thus, we use the approximation that the stratification does not change inside the vortex, that is $\forall t,\ N_c(t) = 0$ (fully mixed interior). Fig.2.8*(b)* shows a very good agreement between the vertical aspect ratio of the simulated vortices and the theoretical one. The agreement is less good for the aspect ratio of the laboratory vortices, c/a being systematically a little bit underestimated by our theoretical prediction. This is probably the consequence of assuming $N_c^{*2} - N^{*2} = -N^{*2}$ constant whereas it significantly diminishes with time, as shown later by the numerical results (see Fig.2.13).

2.5. Equilibrium shape of the vortices: application to Jovian vortices

We showed that the quasi-static equilibrium on which is based our model is verified at each time in our experiments and simulations. We expect that it is also the case for the Jovian vortices since the quasi-static equilibrium does not depend on their temporal evolution nor on the causes of this evolution. The assumption here is that the time necessary to reach an equilibrium shape is short compared to the characteristic time of the vortices strength evolution. Keeping in mind that we neglect any compressible effect, we apply our laws to some of the most prominent Jovian anticyclones: the Great Red Spot (GRS) in 1979 (*Voyager 1* mission), the Oval DE and BC in 1997 before their merger (*Galileo*), and the Oval BA in 2007 (*New Horizons*). Note that contrary to the GRS, the Oval BA was created recently after the merger of three White Ovals (FA, BC and DE) between 1998 and 2000. In 2007, it was thus only 7 years old, and yet this was long enough for it to evolve from the triangular shape that followed the merging event (Choi et al. 2010) to a classical elliptical shape.

2.5.1. Relevant parameters for application to Jovian vortices

To apply our model to Jovian vortices, four dimensional parameters are required: the longitudinal Rossby number of the vortex Ro_x, the shear rate σ, the Coriolis frequency f and the stratification difference between the vortex and the surrounding atmosphere $N_c^2 - N^2$. The methods employed to estimate each parameter are provided in the next two paragraphs. The deduced parameters are reported in Tables 2.2 and 2.3.

2.5.1.1. Velocities and length scales estimations

We measure horizontal length scales of Jovian vortices based on wind velocities criteria for the GRS (Simon et al. 2018) and the Ovals BA and DE (Choi et al. 2010). For the Oval BC, we use a measurement based on cloud features(Mitchell et al. 1981). From these data, we deduce for each vortex a measured horizontal aspect ratio $(a/b)_{\text{mes}}$ and ellipticity β_{mes} to compare our predictions with (see Figs. 2.9 and 2.10 and Table 2.2).

To apply our model, the first quantity required is the longitudinal Rossby number Ro_x of these vortices, that is the slope of the meridional velocity along an East-West profile, divided by the Coriolis frequency f. For the Oval BA and DE, we compute it by a linear fit on their meridional velocity profile at the core of each vortex, with an uncertainty of $\pm$ 5 m/s on the velocities (Choi et al. 2010). For the Oval BC for which we could not find velocity profiles, we use estimates of the North-South peak velocities (Mitchell et al. 1981) and divide them by the

vortex semi-major axis length a. The resulting longitudinal Rossby numbers are given in Table 2.2.

For the GRS, we need to take into account the fact that it is a hollow vortex with a quiescent core (see Fig.1.11). The detail of the velocity profile does not invalidate our approach since in the dynamical collar of the GRS, we assume the same cyclo-geostrophic balance to hold, i.e. the pressure gradient compensates for the Coriolis and centrifugal forces arising from the non-zero azimuthal velocities. However, a correction needs to be added in the case of a hollow vortex to account for the fact that the distance from the core at which the velocity is maximal – the width of the vortex, a – is different from the characteristic distance of the pressure anomaly gradient – the width of the collar a_c – (Hassanzadeh et al. 2012). The longitudinal Rossby number measured in the collar is $Ro_x = \frac{V_{\max}}{a_c f}(1-\beta)$, where $V_{\max}$ is the mean peak meridional velocity along an East-West profile. In that case, a prefactor a_c/a should be added in our laws for the centrifugal term for which it is the radius of curvature of the trajectory, i.e. the distance to the centre that matters, not the size of the collar. Laws (2.13) and (2.14) are then modified as follow:

$$\beta^2\left(2\frac{a_c}{a}\frac{Ro_x^2}{\sigma^*}+1\right)+2\beta\left(\frac{a_c}{a}\frac{Ro_x^2}{\sigma^*}-1\right)+1=0, \tag{2.20}$$

$$\left(\frac{c}{a}\right)^2=\frac{Ro_x\left[1+Ro_x\,\frac{a_c}{a}\,\frac{1+\beta}{1-\beta}\right]f^2}{N_c^{*2}-N^{*2}} \tag{2.21}$$

where $Ro_x = \frac{V_{\max}}{a_c f}(1-\beta)$ is the stream-wise Rossby number measured inside the collar. For the GRS in 1996, 2000 and 2006, we measure the longitudinal Rossby number by fitting meridional velocity profiles in the East-West direction inside its anticyclonic collar. The corresponding measured values for a, a_c and Ro_x are reported in Table 2.3, along with corresponding references. When applying equation (2.21), rigorously speaking, the vertical aspect ratio (c/a) is the aspect ratio between the pressure anomaly's vertical and horizontal characteristic length scales. A complete and self-consistent model of the three-dimensional structure of a hollow vortex would be required, especially in terms of density anomaly, to conclude on the relevant scales. This lack of data and modelling leads us to use the simplest assumption, which is also the most consistent with our model, i.e. we assume that a and c are the semi-axes of the entire vortex. To conclude on this point, note that although the quiet centre of the GRS still remains today, it is significantly smaller than during the Voyager era (Table 2.3). Additionally, no other vortices on Jupiter are known to have this hollow structure. They are rather very close to solid body rotation with a linear increase of the velocity in their core (Choi et al. 2010) as assumed in our theoretical model, which hence seeks to be generic and applicable to the vast majority of Jovian anticyclones.

In addition to the Rossby number, our model requires estimates of the shear rate imposed by jets at the latitude of the vortices. Using linear fits on zonal winds profiles, we report those estimates and their errors for the GRS (Shetty et al. 2007), the Ovals DE and BC (Limaye 1986) and the Oval BA (Tollefson et al. 2017) in Table 2.2 with corresponding references.

2.5.1.2. Buoyancy and Coriolis frequencies estimations

The Coriolis parameter f, which is the amplitude of the vertical component of the rotation rate at the latitude of the vortices, is taken from Table 3 of Mitchell et al. (1981).

The last but crucial parameter that we need to estimate is the difference of stratification between the vortex and the surrounding atmosphere $N^2 - N_c^2$. To do so, we recall and discuss the method used by Aubert et al. (2012). The idea is to use temperature measurements that were performed in Jupiter's upper troposphere across the vortices and around them. Using the

ideal gas equation and the fact that the pressure anomaly is zero at the top of the vortex ($z = h$), the density anomaly with respect to the ambient fluid at the top of the vortex can be expressed as $\Delta\rho/\rho = -\Delta T/T$, hence

$$\frac{T_a(z=h) - T_v(z=h)}{T_a(z=h)} = -\frac{\rho_a(z=h) - \rho_v(z=h)}{\rho_a(z=h)}, \tag{2.22}$$

where T_a and ρ_a are the temperature and density in the surrounding atmosphere, and T_v, ρ_v within the vortex. At the core of the vortex ($z = 0$), the density anomaly is zero, and a Taylor expansion of the density profile leads to

$$\frac{T_a(z=h) - T_v(z=h)}{T_a(z=h)} \approx -h\frac{\left(\frac{\partial\rho_a}{\partial z}\right)_{z=0} - \left(\frac{\partial\rho_v}{\partial z}\right)_{z=0}}{\rho_a(z=h)} \approx \frac{h}{g}(N^2 - N_c^2). \tag{2.23}$$

A crude estimation of the stratification difference between the vortex and the ambient can thus be obtained using temperature differences measurements:

$$N^2 - N_c^2 \approx \frac{g}{h}\left(\frac{T_a - T_v}{T_a}\right)_{z=h}. \tag{2.24}$$

The temperature anomalies ($T_a - T_v$) associated with the vortices have been measured quite accurately (Conrath et al. 1981; Flasar et al. 1981; Fletcher et al. 2010). Additionally, we adopt the pressure-temperature profile derived from the Galileo probe data (Seiff et al. 1998) to obtain the mean atmosphere temperature T_a at the measurement level. For the GRS, Figure 2 in Flasar et al. (1981) shows a temperature anomaly of 8 ± 1 K at 50 mbar. With an atmospheric temperature at that level of $T_{a,50} = 121 \pm 4$ K, we obtain a relative temperature anomaly of $(T_a - T_v)_{50}/T_{a,50} = 0.0661 \pm 0.0104$. For the Ovals DE and BC, Figure 1 in Conrath et al. (1981) shows a temperature anomaly of 4 ± 1 K at 120 ± 20 mbar. With $T_{a,120} = 115 \pm 2$ K, we obtain a relative temperature anomaly of $(T_a - T_v)_{120}/T_{a,120} = 0.0348 \pm 0.0093$. Since no thermal measurements were performed across the Oval BA, we make the assumption that its stratification is the same as the vortices from which it formed, hence we use the same value as for the Ovals DE and BC.

Finally, the distance h between the measurement level and the vortex midplane where the temperature anomaly vanishes is also a poorly constrained parameter and should be considered with its uncertainties. Let us define a new vertical axis Z which origin is the 1 bar pressure level. The aforementioned anomalies are measured at 50 mbar ($Z \sim +58$ km) for the GRS and 120 mbar ($Z \sim +43$ km) for the Ovals. The coordinate of the vortices midplane now remains to be estimated. The cold anomaly of the GRS was observed up to 500 mbar (Flasar et al. 1981; Fletcher et al. 2010), at $Z \sim +16$ km, meaning that the midplane (zero-anomaly) is located at higher pressures. According to observers, it could extend up to 2 bar (de Pater et al. 2010), $Z \sim -20$ km. Consistently, in numerical modelling, the midplane of Jovian vortices is located between 400 to 1500 mbar (Morales-Juberıas et al. 2003; Legarreta et al. 2008). If we take into account this large uncertainty, we obtain $h = 60 \pm 18$ km for the GRS and $h = 45 \pm 18$ km for the Ovals. With a gravitational acceleration of $g = 23$ m s^{-2} based on the Galileo probe measurements (Seiff et al. 1998), we finally obtain $N^2 - N_c^2 = (2.53 \pm 1.16) \cdot 10^{-5}$ rad^2 s^{-2} for the GRS and $N^2 - N_c^2 = (1.78 \pm 1.19) \cdot 10^{-5}$ rad^2 s^{-2} for the Ovals. These values are reported in Table 2.2 with all the parameters required to apply our model.

Note that this method does not require an independent knowledge of the stratification in the atmosphere N and within the vortex N_c, which is an advantage since the stratification inside any of the Jovian vortices has never been measured. The drawback is that we use superficial measurements, and extrapolate them to deduce a density slope with the important assumption that this slope is constant. That being said, contrary to N_c, the stratification of

Jupiter's atmosphere has been measured and estimated (e.g. Galileo measurements (Seiff et al. 1998) and modelling estimates extrapolating Voyager data (Legarreta et al. 2008)). The result is that N is not constant in the range of pressure considered here for the vortex midplane. In the upper troposphere, both Voyager data (Legarreta et al. 2008, Figure 2) and estimates from inverse problems (Shetty et al. 2010) agree on $N \sim 0.02$ rad s^{-1}. At deeper levels in the atmosphere, this stratification is supposed to decrease and reach $N \sim 0.005$ rad s^{-1} for pressures between 1 to 7 bars (Legarreta et al. 2008). Unfortunately, we cannot rigorously take this stratification decrease into account without knowing how the vortex stratification varies along with it since the essential parameter in our model is the difference between the stratification within the vortex and the ambient one, not the stratification itself. As such, we cannot exclude that the vortices could ultimately reach the limit $N_c^2 \to N^2$ for which the vortex vertical extent would become infinite. Our results thus depend on a proper estimate of the stratification difference with depth, and provide lower bounds for the vortex depths rather than absolute values.

Table 2.2. – Estimation of the horizontal and vertical aspect ratios of the Great Red Spot (GRS) in 1979, the Oval BA in 2006 and the Oval DE and BC in 1997. The horizontal aspect ratios (a/b) are computed using equation (2.13) and the vertical ones (c/a) using equation (2.14).

	GRS *Voyager 1 (1979)* (Shetty et al. 2007) (Choi et al. 2007) (Simon et al. 2018)	**Oval BA** *New Horizons (2007)* (Choi et al. 2010)	**Oval DE** *Galileo (1997)* (Choi et al. 2010)	**Oval BC** *Galileo (1997)* (Simon et al. 1998) (Mitchell et al. 1981)
Rotation, stratification				
$f \cdot 10^4$ (rad s^{-1})	1.37	1.92	1.92	1.92
$N^2 - N_c^2 \times 10^5$ (rad^2 s^{-2})[a]	2.23 ± 1.16	2.17 ± 1.15	2.17 ± 1.15	2.17 ± 1.15
Vortex dimensions				
a (km)	9000	3350	2900	4890
b (km)	4667	2750	2200	2930
c (km)	**33-59**[a]	**34-60**[a]	–	–
$(a/b)_{\text{mes}}$	**1.93**	**1.22**	**1.34**	**1.67**
β_{mes}	0.58	0.20	0.29	0.47
Vortex velocities				
$Ro_x \times 10^2$ [b]	-10.57 ± 0.58	-18.78 ± 1.11	-19.13 ± 1.23	-12.78 ± 2.13
Shear				
$\sigma \times 10^4$ (s^{-1})	1.50[c]	1.54[d]	1.57[e]	1.57[e]
$\sigma/f \times 10^2$	-11.11	-8.02	-8.18	-8.18
Computed dimensions				
β_{calc}	0.57 ± 0.04	0.35 ± 0.04	0.35 ± 0.03	0.47 ± 0.05
$(a/b)_{\text{calc}}$	**1.92** ± 0.10	**1.44** ± 0.10	**1.44** ± 0.09	**1.67** ± 0.13
$(c/a)_{\text{calc}} \cdot 10^3$	7.4 ∈ [6.0,10.7]	9.9 ∈ [7.7,15.5]	9.9 ∈ [7.3,15.7]	8.4 ∈ [6.3,14.8]
c_{calc} (km)	**67** ∈ [54,96]	**33** ∈ [28,51]	**29** ∈ [22,48]	**41** ∈ [30,72]
$(c/a)'_{\text{calc}} \cdot 10^3$	7.7 ∈ [5.9,10.4]	10.8 ∈ [8.7,17.2]	10.4 ∈ [7.4,15.9]	8.4 ∈ [6.3,14.6]
c'_{calc} (km)	**70** ∈ [53,94]	**36** ∈ [27,52]	**31** ∈ [22,47]	**41** ∈ [30,71]

[a] see §2.5.1.2 for these values and uncertainties.
[b] longitudinal Rossby number. When meridional velocity profiles inside the vortices are available (GRS, Oval BA and Oval DE), it is determined by a linear fit in the vortex core. Otherwise (Oval BC), we divide the peak North-South velocities by the vortex semi-major axis a. The velocity profiles used are taken from Choi et al. (2007) for the GRS and Choi et al. (2010) for the Oval BA and DE.
[c] estimated by a linear fit on the wind profile at the GRS latitude, given in Shetty et al. (2007).
[d] estimated from zonal winds data in 2009 provided in Tollefson et al. (2017).
[e] estimated from zonal winds data obtained from Voyager 1 and 2 images (Limaye 1986).

Table 2.3. – Parameters and references used to compute the GRS aspect ratios as a function of time since 1979 (Fig.2.10). The Coriolis parameter f, the stratification difference $N^2 - N_c^2$ and the shear rate σ are not indicated because they are taken equal to the values given in Table 2.2.

	1979	**1996**	**2000**	**2006**
	Voyager 1[b]	*Galileo*[c]	*Galileo*[c]	*HST*[d]
a (km)	9200 ± 400	8927 ± 400	8377 ± 400	8376 ± 400
a_c (km)	5195 ± 400	4233 ± 400	4417 ± 400	4051 ± 400
a/a_c	1.77 ± 0.21	2.11 ± 0.29	1.90 ± 0.26	2.07 ± 0.30
$Ro_x^a \cdot 10^2$	15.41 ± 2.59	21.54 ± 3.75	22.08 ± 3.79	23.09 ± 4.00
	2012	**2015**	**2016**	**2017**
	HST[e]	*HST*[e]	*HST*[e]	*HST*[e]
a (km)	4527 ± 400	4939 ± 400	4650 ± 400	4321 ± 400
a_c (km)	3292 ± 400	3704 ± 400	3704 ± 400	3704 ± 400
a/a_c	1.38 ± 0.29	1.33 ± 0.25	1.26 ± 0.24	1.17 ± 0.23
$Ro_x^a \cdot 10^2$	22.11 ± 4.90	19.65 ± 4.09	20.63 ± 4.19	19.65 ± 4.09

[a] For the GRS in 1996, 2000 and 2006, the longitudinal Rossby number is computed by a linear fit on the meridional velocity profiles (Choi et al. 2007; Asay-Davis et al. 2009) inside the anticyclonic collar. For the other dates, we use $Ro_x \approx \frac{V_{\max}}{a_c f}$ where $V_{\max}$ is the mean peak meridional velocity along an East-West profile and $f = 1.374$ rad s^{-1}.
[b] Mitchell et al. (1981)
[c] Fig.5 in Choi et al. (2007)
[d] Asay-Davis et al. (2009)
[e] Simon et al. (2018)

2.5.2. Three-dimensional instantaneous shape of the GRS (1979) and the Ovals DE, BC (1997) and BA (2007)

With the previously detailed parameters estimates, we can apply our model (equations (2.13) and (2.14)) to predict the ellipticity and the thickness of those Jovian anticyclones. In Table 2.2 we report:

— the predicted horizontal ellipticity (β_{calc}) or aspect ratio ($(a/b)_{\text{calc}}$) of the vortex deduced from equation (2.13);

— the predicted half-thickness c_{calc} of the vortex deduced from equation (2.14). Note that c_{calc} is computed using the *estimated* value of β in equation (2.14), whereas for c'_{calc} we use the *measured* value of β.

The predicted values for the horizontal aspect ratios for the GRS in 1979 (1.92 ± 0.10), the Oval BA in 2006 (1.44 ± 0.09) and the Oval DE and BC in 1997 (1.44 ± 0.10 and 1.67 ± 0.13) are of good order of magnitude and close to the measured ones (respectively 1.93, 1.22, 1.34 and 1.67), hence validating our approach and assumptions. These results are represented in Fig.2.9 as ellipses superimposed to the vortices images and velocity fields.

Contrary to their horizontal shape, the vertical aspect ratio and hence the thicknesses of Jupiter's vortices are currently unknown. Some constraints are given by multi-layer quasi-geostrophic numerical simulations which show that geostrophically balanced vortices tend to be baroclinically unstable if their thickness exceeds their width by a factor greater than $\sim f/N$ (see Vasavada et al. 2005, and references therein). This leads to a maximum depth of ~ 500 km below the clouds for the GRS or the Oval BA. Later, it has been assessed that the large Jovians anticyclones should extend vertically down to the water cloud level (Wong et al. 2011) which is consistent with a half-height of ~ 60 km that emerged from de Pater et al. (2010) observations and scaling analysis and with the range of heights explored in numerical simulations (Legarreta et al. 2008). Our model predicts a thickness of ~ 140 km for the GRS (106 to 188 km with the

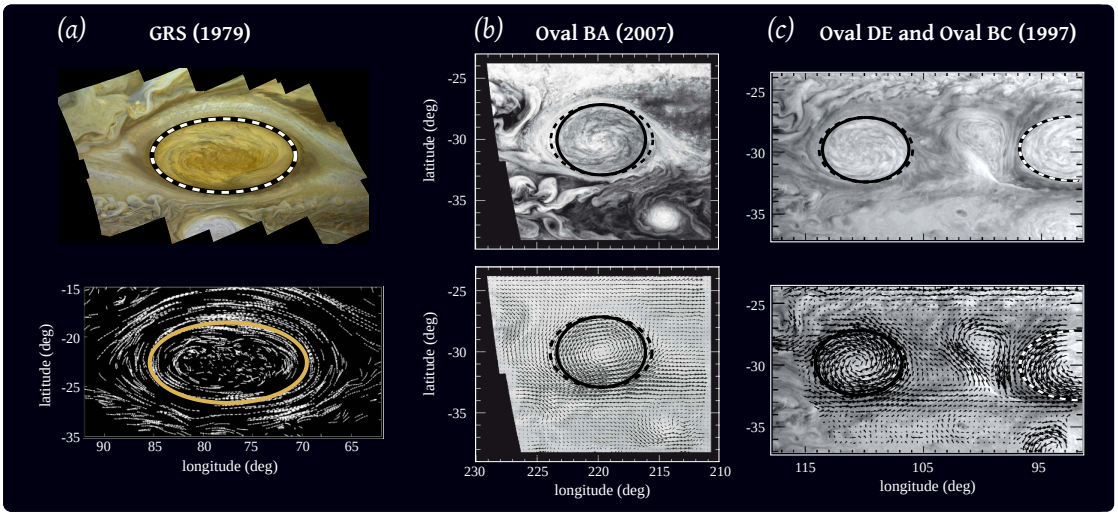

Figure 2.9. – Images and velocity fields of three Jovian vortices to which we superimposed ellipses with the measured aspect ratio (continuous lines) and the calculated one (dashed lines) using law (2.13). The parameters used to compute these aspect ratios are reported in Table 2.3. *(a)* Top: Mosaic of GRS images taken by *Voyager 2* (NASA/JPL) on July 8, 1979. The processing and mosaic was performed by Bjorn Jonsonn and is available online (https://bjj.mmedia.is/images/). Bottom: Velocity vectors of the GRS as determined from *Voyager 1* images (taken from Shetty et al. (2007)). *(b)* Oval BA as imaged by *New Horizons* in February 2007 and associated wind vectors (taken from Choi et al. (2010)). *(c)* Oval DE as imaged by *Galileo* in February 1997 and associated wind velocity vectors (taken from Choi et al. (2010)).

uncertainties). For the Oval BA, we find a vertical extent of 72 km (54 to 104 km), 62 (44 to 94) km for the Oval DE and 82 (60 to 142) km for the Oval BC. These values are coherent with the estimated ones mentioned above and confirm the idea of shallow vortices which do not extend deeply into Jupiter's interior.

2.5.3. Shape evolution of the GRS since 1979

We now focus on the changes that occur in the GRS dynamics over the past 40 years. In Table 2.3, we report the parameters and references used to compute the GRS aspect ratios as a function of time since 1979. The GRS is shrinking in the longitudinal direction (Fig.2.10*(a)*), decreasing from almost 35° extent in the late 1880s to less than 14° today (Simon et al. 2018). The latitudinal extent of the GRS is also decreasing, but less rapidly, leading to a decrease in the horizontal aspect ratio of ~ 0.011 yr^{-1} (Simon et al. 2018) represented by the dashed line in Fig.2.10*(b)*. The velocity field of the GRS has been measured punctually during this evolution showing an increase (in absolute value) in its longitudinal Rossby number. At the same time, the zonal winds velocities remained constant at the GRS latitude (Simon et al. 2018). Using the parameters reported in Table 2.3, we predict the evolution of the horizontal aspect ratio according to our model (blue dots in Fig.2.10*(b)*). The theoretical aspect ratio agrees well with the measurements for the whole GRS evolution, meaning that for a given change in the longitudinal Rossby number, we predict the correct evolution of the horizontal shape, or conversely for a given shape evolution, we predict the correct evolution of the Rossby number. Note that if our quasi-equilibrium model is consistent with the recent evolution of the GRS it does not give, of course, the physical mechanism responsible for this evolution. Finally, our model provides a remote access to the evolution of the GRS thickness for the past 40 years, which is not accessible with the available data. Surprisingly, as shown in Fig.2.10*(c)*, we find that the increase in absolute value of the longitudinal Rossby number compensates the decrease of the horizontal aspect ratio such that (c/b) remained constant through time. Considering that

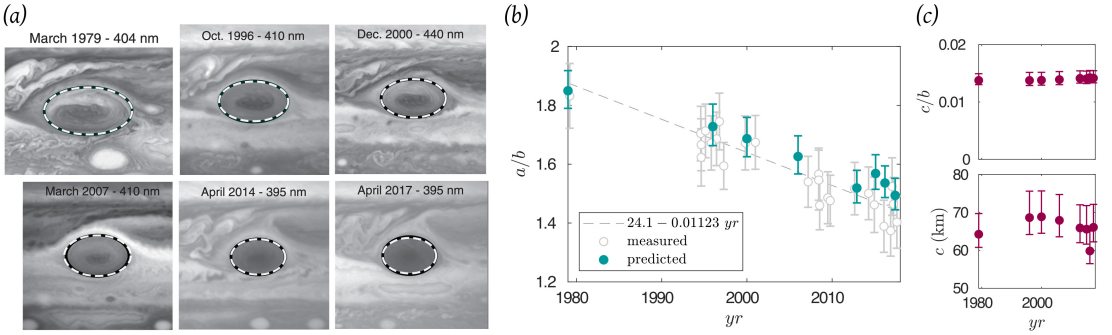

Figure 2.10. – *(a)* GRS appearance at blue/violet wavelengths taken from Fig.1 of Simon et al. (2018). We superimpose to it ellipses with the measured aspect ratio (black line) and the calculated one (white dashed line). *(b)* Evolution of the GRS horizontal aspect ratio over the last 40 years. Measurements of the GRS aspect ratio from spacecrafts data and *Hubble Space Telescope* imagery are represented by the white dots. These data are directly taken from Simon et al. (2018). Errors are calculated based on the largest uncertainties given in Simon et al. (2018) (0.5° in latitude or longitude for each dimension). The dashed line is the decreasing trend of the aspect ratio deduced from the measurements. The blue dots are the aspect ratio computed using our model (equation (2.13)). Error bars account for uncertainties of $\pm$ 10 $\mathrm{m\,s^{-1}}$ in velocities. *(c)* Vertical aspect ratio as a function of time deduced from relation (2.14) using the calculated horizontal aspect ratio plotted in *(b)* and the stratification difference reported in Table 2.2. To convert c in kilometres, we use the measurements of b given in Table 1 of Simon et al. (2018). Error bars account for uncertainties in both velocities and measured aspect ratio.

the latitudinal extent b of the GRS remained almost constant (Simon et al. 2018), this implies that the GRS has kept a thickness of roughly 140 km during its whole shrinkage.

2.5.4. Roots of the vortex

In December 2017, preliminary results of the microwave radiometer (MWR) instrument onboard NASA's Juno spacecraft suggested that the GRS extends at least as deep as the instrument can observe, that is ~ 300 km below the cloud level (Greicius 2017, and Fig.2.11). However, this instrument measures thermal radiation, and the variations in brightness temperature can be interpreted as variations of opacity due to the abundance of chemical components such as ammonia, as well as variations in physical temperature (Janssen et al. 2017). Converting the MWR data into a signature of the density anomaly of the GRS is in our opinion a big interpretation step that requires further investigation. Since no scientific paper is for now published regarding these data, we leave this problem on standby. Nevertheless, if one assumes that the brightness temperature is entirely due to physical temperature variations, then what is measured is the extent of the density anomaly associated with the GRS. We argue that this density anomaly may have a vertical extent significantly bigger than the dynamical vertical extent of the vortex, that is the extent of the flow. We show in the present section that if one uses the density anomaly to measure the vertical extent of the vortex, the latter could easily be ~1.7 times what is measured using the winds. An observed density vertical extent of 300 km would thus give a dynamical vertical extent of 176 km consistent with our predicted range. Note that Juno flybys above the GRS allow gravity measurements among which the GRS signature will be detectable if the winds are deeper than ~ 300 km (Galanti et al. 2019b). Upcoming measurements will thus challenge our model.

Let us illustrate the potential difference between the dynamical thickness of the vortex and the thickness of the density anomaly associated with it. We expect the extent of the density anomaly to be larger than the extent of the wind because, starting from the vortex midplane at $z = 0$, the winds decay when going deeper within the vortex. On the contrary, the density anomaly increases from the centre of the vortex down to its bottom because the vortex is understratified relative to the ambient, with no anomaly at the centre. At the bottom of the vortex,

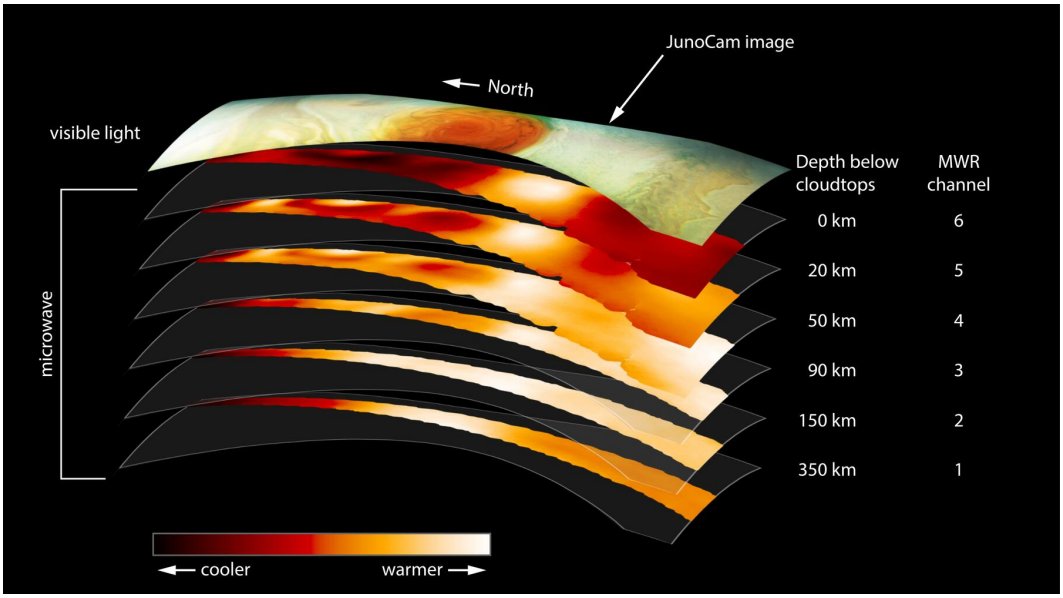

Figure 2.11. – Measurements from the microwave radiometer onboard Juno spacecraft for perijove 7, during which Juno flew over the GRS. Each channel of the radiometer collects data at different wavelengths (1.3 to 50 cm), allowing to probe different depths up to about 550 km below the cloud tops. Qualitative maps of the measured brightness temperature are represented for each channel. Credits: NASA/JPL-Caltech/SwRI (Greicius 2017).

there is no more winds (by definition), but at that location the density anomaly is the highest, and will just begin to reconnect with the ambient stratification. To make it more quantitative, one can start with equations (2.16) and (2.17) in the case of an axisymmetric gaussian vortex:

$$u_\theta(r,z) = Ro\ r\ \exp\left(-\left[\frac{r}{a_0}\right]^2 - \left[\frac{z}{c_0}\right]^2\right), \tag{2.25}$$

$$\delta\rho(r,z) = (N^{*2} - N_c^{*2})\ z\ \exp\left(-\left[\frac{r}{a_0}\right]^2 - \left[\frac{z}{c_0}\right]^2\right). \tag{2.26}$$

At any radius, the ratio of the velocity and density anomalies relative to their maximum are

$$\frac{u_\theta}{u_{\theta,\max}} = \exp\left(-\left[\frac{z}{c_0}\right]^2\right), \tag{2.27}$$

$$\frac{\delta\rho}{\delta\rho_{\max}} = \sqrt{2}\frac{z}{c_0}\exp\left(-\left[\frac{z}{c_0}\right]^2 + \frac{1}{2}\right). \tag{2.28}$$

The density anomaly only starts to decay at $z = c_0/\sqrt{2}$ whereas the velocities decrease from $z = 0$. In both cases, the inflection point in the decreasing part of the profiles corresponds to a decrease of $\sim 40\%$ from the maximum value. But for the velocities the inflection point is located at $z = \frac{c_0}{\sqrt{2}}$ whereas it is reached at $z = \sqrt{3/2}c_0$ for the density anomaly, that is at a distance $\sqrt{3} \sim 1.7$ times larger. This is illustrated in Fig.2.12 where we represent the cross-stream velocity v and the density anomaly $\delta\rho$ on several horizontal slices along z for the reference numerical simulation. The density anomaly clearly spreads more vertically than the cross-stream velocity, even if we stand in a regime where it diffuses less (i.e. $Sc \gg 1$). For instance, a decay of 95% relatively to the max value is reached at $|z| \approx 0.9$ in terms of density and at $|z| \approx 0.5$ in terms of velocity. This justifies that our results (GRS thickness of ~ 148 km) are not incompatible with the latest (unpublished) Juno imaging (Fig.2.11) which seems to indicate a 300 km thickness for the GRS roots.

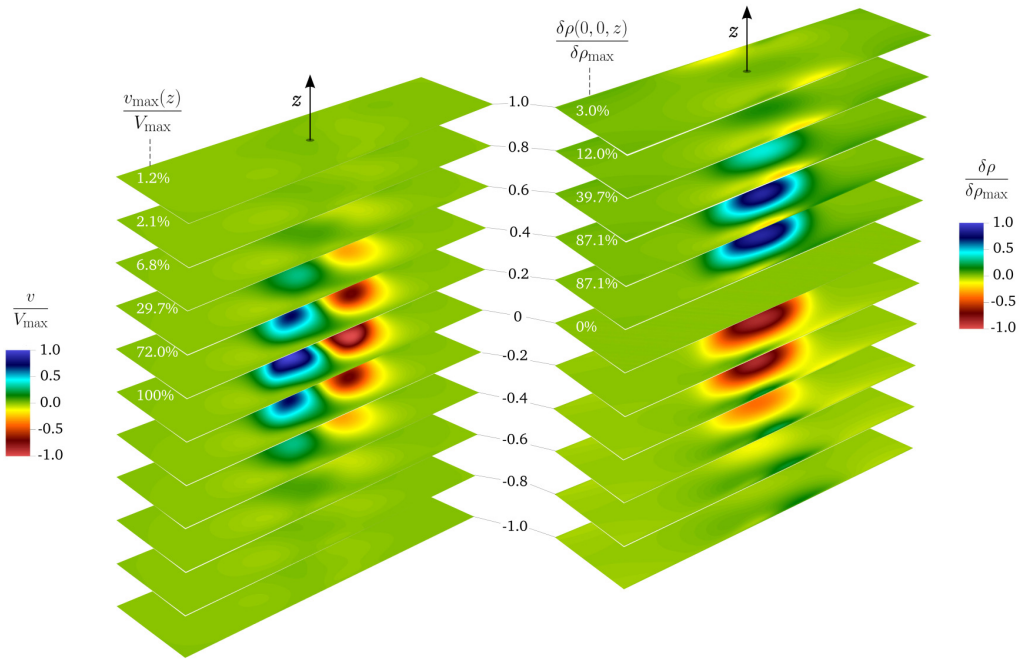

Figure 2.12. – Vertical structure of the vortex for the reference simulation (Table 2.1) at time $t \approx 10$. The cross-stream velocity v (left) and the density perturbation $\delta\rho$ (right) are represented on 11 horizontal slices for $z \in [-1,1]$. The percentages are the ratio of the maximum velocity or density anomaly for a given slice relatively to the maximum velocity or density anomaly in the whole 3D-box.

2.6. Long-term evolution of the vortex

So far, we have focused on describing the quasi-static, inviscid and diffusion-less problem, which allowed us to characterize the equilibrium shape of Jovian vortices embedded in a rotating, stratified and shearing flow. We showed and used the fact that the time derivatives are negligible compared to the dominant balance. This observation fully supports our hypothesis of a quasi-static equilibrium for the vortex, i.e. a time decoupling between the fast effects that control the equilibrium shape (pressure and azimuthal motion) and the slow dissipative processes that control the time evolution. This assumption is also valid in the Jovian atmosphere where vortices are long-lived. As a result, the equilibrium shape of vortices does not depend on the relevant dissipation mechanism (viscosity in the lab compared to radiative cooling on Jupiter). This is further justified by the work of Hassanzadeh et al. (2012) which showed numerically that the laws for the vortex shape in the absence of shear are valid regardless of the dominant dissipation process.

Equations (2.8a)–(2.8c) show that, aside from this quasi-equilibrium, the slow decay of the vortices is characterized by a diffusion of the momentum and density anomaly which accompany the vortex. In this section and for completeness of our experimental and numerical study, we briefly discuss the decay of the vortex through time. Note however that contrary to the quasi-static equilibrium shape, the following results only apply to our laboratory and numerical vortices, not to Jovian ones. Indeed, the Reynolds number of our laboratory vortices is too small, the background flow is not turbulent, and the density dissipation is related to salt diffusion, not thermal radiation. To discuss the vortex evolution, two additional non-dimensional parameters are relevant in addition to the previous ones and will be used in the following of this section: the Reynolds number $Re = d^2 f/\nu$ and the Schmidt number $Sc = \nu/\kappa$.

2.6.1. Advection-diffusion of the density anomaly

In section 2.4.1, we analysed the dominant balances thanks to our reference DNS. In particular, Fig.2.6*(d)* shows the dominant terms in the advection-diffusion equation for the density anomaly, equation (2.8c). Similarly to Facchini et al. (2016), we find that the evolution of the density anomaly of the vortex is due to the vertical advection of the background density field, as demonstrated by the dominant balance $\partial_t \delta\rho \approx N^{*2} w$. This result is important since it can explain the discrepancy between the theory and numerics versus the experimental measurements for the vertical aspect ratio (Fig.2.8). Indeed, to compute $(c/a)_{\text{theo}}$ for the experiments, we assume that the vortex is well-mixed i.e. $N_c = 0$. This is true at $t = 0$, and would remain true at larger times if the stratifying agent was diffusing only since diffusion acts on very long timescales given the high Schmidt number of our experiments ($Sc \approx 700$). But we just showed that advection of the background density field dominates over diffusion. This advection is sufficient to lead to significant variations of the stratification of the vortex, N_c, during its lifetime as shown numerically by Fig.2.13. Even if we work at smaller Sc in our simulations ($Sc = 35$ compared to $Sc \sim 700$), Fig.2.13*(a-d)* shows that no diffusion occurs in the vertical direction, yet the stratification difference between the vortex and the ambient vanishes (Fig.2.13*(e)*). As a consequence, if we were able to measure N_c experimentally, it would likely increase, leading to a higher value for $(c/a)_{\text{theo}}$ for a given $(c/a)_{\text{mes}}$. It could thus explain the discrepancy in Fig.2.8 between our experimental measurements and the theoretical and numerical results.

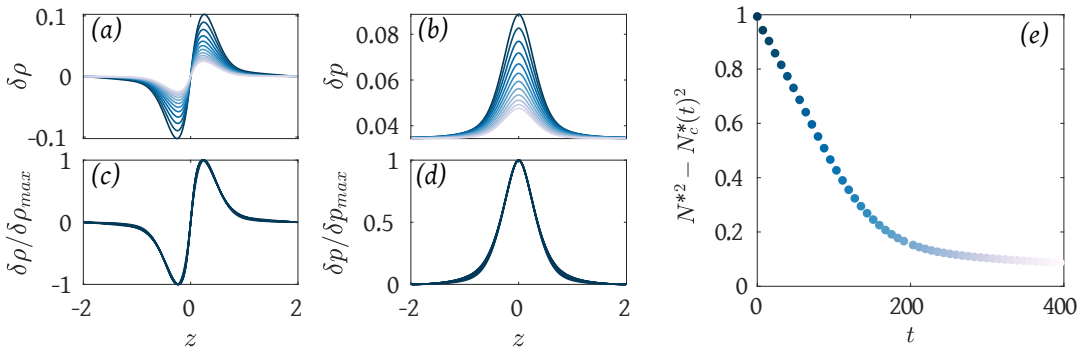

Figure 2.13. – *(a,b)* Evolution through time of the density perturbation $\delta\rho$ and the pressure perturbation δp along the vertical direction. *(c,d)* The same vertical profiles normalized at each time by their maximum. Once rescaled, all the profiles collapse on the same curve showing that approximately no diffusion occurs in the vertical direction. *(e)* Temporal evolution of the stratification difference between the core of the vortex and the ambient. $N^{*2} - N_c^*(t)^2$ is computed as the slope of $\delta\rho(0,0,z,t)$ at $z = 0$.

2.6.2. Decay of the vortex

Besides the advection of the density anomaly, the vortex evolution is accompanied by a decay of its strength, i.e. a decay, in absolute value, of its Rossby number $|Ro|$ visible by the flattening of the slopes of the velocity profiles at $x = 0$ in Fig.2.4. The first row of Fig.2.14 represents the decay of the normalized Rossby number of the vortex as a function of time for different numerical simulations and experiments. The longevity of the experimental vortices is of the order of 30 rotations of the turntable, that is $t \sim 30 \times 4\pi \sim 400$ in our dimensionless units.

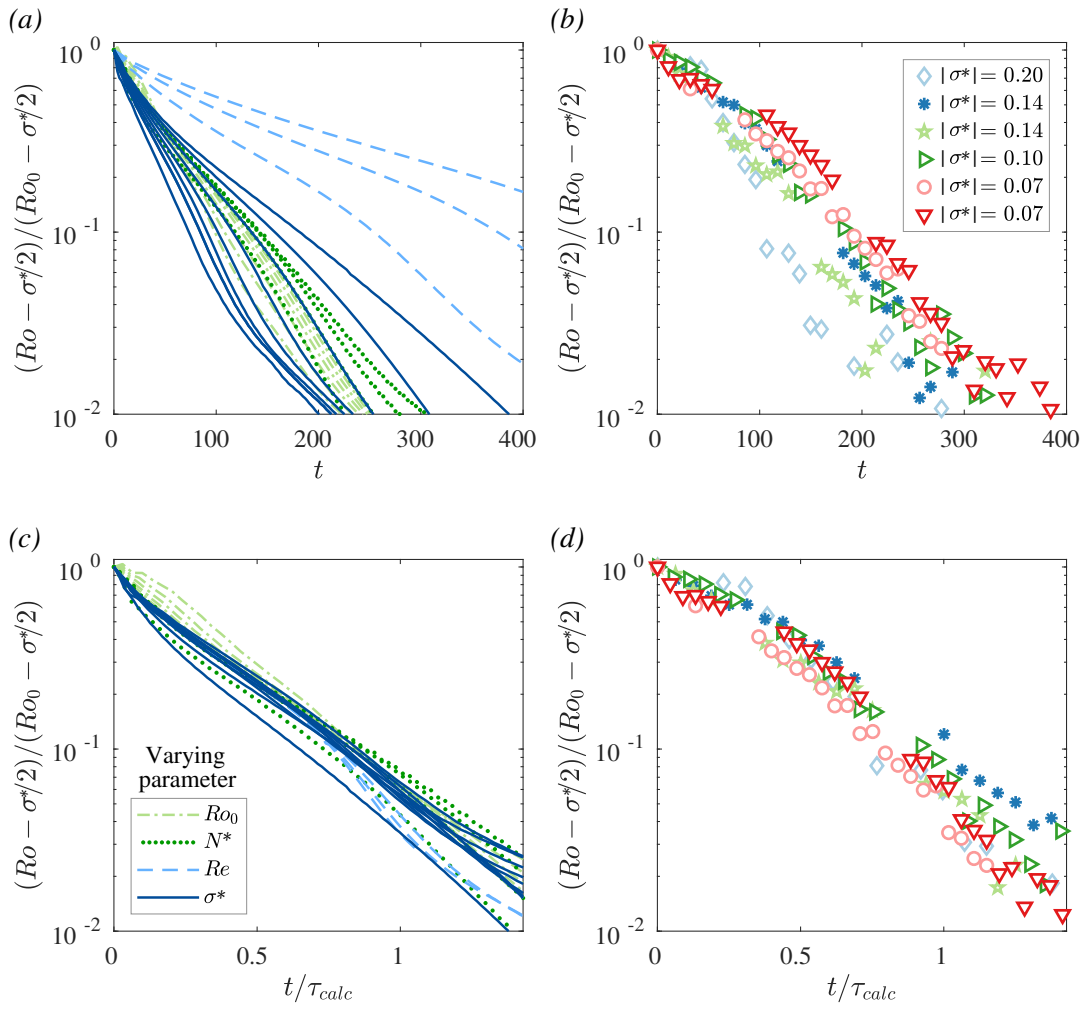

Figure 2.14. – Vorticity decay inside the vortex as a function of *(a,b)* the non-dimensional time and *(c,d)* the time normalized by the theoretical decay time given by equation (2.30). *(a,c)* Numerical simulations with different shear rates, σ^* (dark blue, —), Reynolds number Re (light blue, - - -), initial Rossby number Ro_0 (light green, – · –) and background stratification N^* (dark green, ···) compared to the reference case (see Table 2.1). *(b,d)* Experiments with different shear rates.

In the absence of shear and confinement, Facchini et al. (2016) showed that in the limit of a large Schmidt number, $Sc \gg 1$, a vanishing Ekman number $E = \nu/(2\Omega L^2) \ll 1$, a small Rossby number $Ro \ll 1$ and $N^* = 1$, then the pressure field verifies a radial diffusion equation. As long as the density diffusion does not play an important role, the dynamical evolution of the vortex is thus expected to occur mainly in horizontal directions. This result is fundamental since it is one of the keys to understand the longevity of such systems: even for a very flat vortex, the relevant scale L to estimate its longevity ($T = L^2/\nu$) is the horizontal extent of the vortex (i.e. the largest) rather than the vertical one (i.e. the shortest). In Fig.2.13*(a-d)* and as previously discussed, we verify with our reference DNS that this result still holds in our configuration. We plot successive profiles of the density and pressure perturbations along the vertical axis $(0,0,z)$. These plots show their decay through time with no diffusion in the vertical direction since all the profiles collapse when normalizing them at each time with their maximum.

However, in our case, when no shear is present, confinement prevents spreading in the cross-stream direction as seen in Fig.2.4. The decaying law for $Ro(t)$ should thus be different.

We indeed verified that $(Ro_0/Ro-1)^{1/2}$ is not linear in time contrary to what is expected for a radial diffusion of pressure. Similarly to Facchini et al. (2016), we find that the evolution of the density anomaly of the vortex is due to the vertical advection of the background density field, as demonstrated by the dominant balance $\partial_t \delta\rho \approx N^{*2} w$ shown in Figure 2.6*(d)*. However, the balances in the momentum equation significantly differ at order 1 (order 0 being the cyclo-geostrophic equilibrium): we verified that the diffusive viscous term is not mainly balanced by the Coriolis term. Physically, this means that in our case viscosity does not mainly generate a radial secondary circulation but rather directly acts on the vortex temporal evolution through the viscous coupling with the shearing boundaries. This result further justifies that besides the pure effect of confinement, the physical process at play governing the vortex evolution differs from the case where no shear is applied. We hence expect the decay time to vary significantly with the shear rate.

We performed a numerical systematic study to understand how the decay time varies with key parameters. For each simulation and experiment, we measure a characteristic decay time τ_{mes} corresponding to the time for which the vortex has lost 95% of its initial vorticity, that is $(Ro(\tau_{\text{ mes}}) - \sigma^*/2)/(Ro_0 - \sigma^*/2) = 0.05$. We measure τ_{mes} as a function of the Reynolds number, the Schmidt number, the initial Rossby number, and the shear rate. The results are represented in Fig.2.15 along with their best fits. First, the decay time is proportional to the Reynolds number *Re*, which confirms that the main dissipation mechanism at play is a viscous one. One also notices that the decay rate is independent of the Schmidt number (hence on salt diffusion) once $Sc \geq 35$.

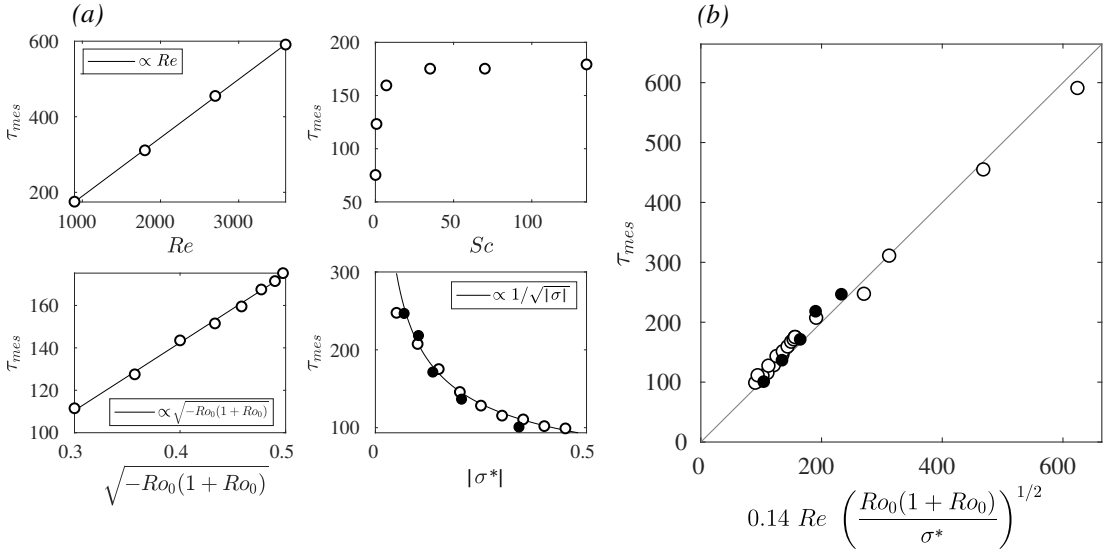

Figure 2.15. – *(a)* Evolution of the characteristic decay time as a function of the Reynolds number *Re*, the Schmidt number *Sc*, $(-Ro_0(1+Ro_0))^{1/2}$ and the absolute value of the shear rate $|\sigma|$. The decay time is defined as the time for which the vortex has lost 95% of its initial vorticity, that is $(Ro(\tau) - \sigma/2)/(Ro_0 - \sigma/2) = 0.05$. *(b)* Measured decay time as a function of the theoretical decay time inferred from the systematic. Numerical simulations are represented by open circles while the black dots represent five experiments with different shear rates σ.

Then, since the dominant balance for the evolution of the density anomaly associated with the vortex is $\partial_t \delta\rho \approx N^{*2} w$, one would expect the characteristic time to be of the form $\tau \sim \delta\rho/(N^{*2}\ W)$ where W is the characteristic vertical velocity. Since the vortex is well-mixed at the beginning of an experiment, the density anomaly scales as $\delta\rho \sim N^{*2} c_0$ (see section 2.3.2.2), leading to $\tau \sim c_0/W$: it is quite intuitive that for a given vertical advection of the background density field, it takes more time to destroy the density anomaly of the vortex if it

extends more vertically. Now, considering $a_0 \sim 1$, the vertical aspect ratio law (2.14) leads to $c_0 \sim (-Ro_0(1+Ro_0))^{1/2}/N^*$, and consequently

$$\tau \sim \frac{(-Ro_0(1+Ro_0))^{1/2}}{N^*\ W}. \tag{2.29}$$

We verified numerically this scaling by varying the initial Rossby number of the vortex while keeping the other parameters constant. Figure 2.15*(a)* shows indeed that the measured decay time τ_{mes} is proportional to $(-Ro_0(1+Ro_0))^{1/2}$.

Relation (2.29) suggests a dependence of the decay time on the background stratification. In the absence of shear, Facchini et al. (2016) showed that the decaying solution of their full linear model is bounded by two self-similar solutions corresponding to a radial diffusion of pressure of characteristic times $\tau_1 = 2/E$ and $\tau_2 = 2/(E\ N^{*2})$. When the background stratification is stronger, the vortex decays faster, and conversely for a weaker stratification. However, we do not observe here any quantitative tendency of how the decay rate varies with N^*. Numerically, we ran several simulations with N^* ranging from 0.5 to 2. As explained in section 2.3.2.3, the cases with $N^* > 1$ were unstable. For $N^* < 1$, no instability occurs and the changes in the vortex decay rate are too small to be significant or to deliver a clear tendency. From the previous estimate (2.29), it is not surprising that a clear scaling is not obtainable. Indeed, we expect the vertical velocity W to decrease as the stratification is stronger (higher N^*), and increase as it is weaker (lower N^*). Consequently, when increasing (or decreasing) N^*, there can be a compensation ($N^*W \sim$ cst) leading to a non-significant variation of the decay time.

Finally, we explored the influence of the non-dimensional shear rate σ^*. Both the experiments and the DNS show that $\tau_{\text{mes}} \propto {\sigma^*}^{-1/2}$ (Fig.2.15*(a)*). Besides, we verified that this scaling still holds when we remove both rotation and stratification of the background flow (i.e. when we simulate sheared columnar vortices). The scaling law of the decay rate with shear is thus independent of the two other physical ingredients of our study and solely depends on how the vortex reconnects with the no-slip shearing boundaries. Note that if the vortex core was passively advected and tear apart by the shear, we would expect the vortex lifetime to decay as ${\sigma^*}^{-1}$ instead of the measured ${\sigma^*}^{-1/2}$ scaling. There may thus be two opposite effects of the shear, one which consists in tearing apart the vortex as if it was a passive scalar, and the other in sustaining its circulation by injecting anticyclonic vorticity in the system.

In figure 2.15*(b)*, the measured decay time is plotted against the phenomenological one. A rather convincing linear 1:1 relationship is found when a prefactor of ~ 0.14 is added to the calculated τ, thus giving the final relation

$$\tau_{\text{calc}} \approx 0.14\ Re \left(\frac{Ro_0(1+Ro_0)}{\sigma^*}\right)^{1/2}. \tag{2.30}$$

In figure 2.14, we show that the decay curves indeed collapse when rescaling the time by τ_{calc} for both the simulations and the experiments.

Note again that this scaling law for the time evolution is relevant for our laboratory vortices only, which have a Reynolds number much smaller that Jovian ones. Nevertheless, the zeroth order equilibrium describing the shape of vortices does not depend on their time evolution.

2.7. Conclusions

In this chapter, we have studied the quasi-static equilibrium and the evolution of lenticular anticyclones embedded in a rotating, stratified and shear flow, three physical ingredients also present in the Jovian troposphere. The main purpose was to study the quasi-static equilibrium shape of such vortices, by combining experimental, numerical, and theoretical approaches,

and to extend our results to Jovian anticyclones. The underlying hypothesis is that despite the fact that our laboratory vortices are not in the regime relevant for Jupiter (essentially in terms of turbulence and dissipation), the quasi-static shape of those vortices does not depend on the dissipation process and should be the same in both cases. This quasi-static equilibrium is cyclo-geostrophic in the horizontal, and hydrostatic in the vertical, and the resulting vortex shape depends on how the pressure field associated with the vortices reconnects with the ambient pressure field of the rotating stratified shear flow. By estimating the relevant parameters for Jovian vortices, we are able to valid our model from the measured horizontal ellipticity of four anticyclones, and then to predict their thicknesses which is inaccessible to direct observations. We show that these anticyclones have thickness of about 60 to 150 km, whereas they extend horizontally over thousands of kilometres, thus confirming the idea that mid-latitude vortices in the Jupiter's troposphere are very shallow structures. Finally, by applying our laws to the recent observed evolution of the GRS, our model predicts that its depth has surprisingly remained constant despite the observed horizontal shrinking. That being said, a critical aspect of our predictions for Jovian vortices is that they depend on how accurate we can estimate the stratification difference between the core of the vortices and the ambient atmosphere. As discussed in section 2.5, the stratification estimates that we use may change if the thermal measurements are performed at deeper levels in the atmosphere; our predictions are thus to be taken as lower bounds for the vortices thickness rather than absolute values.

We ended this chapter by briefly discussing the temporal evolution of our laboratory vortices, which, this time, cannot be extrapolated to Jovian conditions given that the dissipative mechanisms at play are not the relevant ones. The slow radial pressure diffusion mechanism unravelled by Facchini et al. (2016) for a lenticular vortex in a rotating and stratified flow does not hold when applying a viscous shear to the vortex. The vertical advection of the density anomaly associated with the vortex is still dominant compared to vertical diffusion of both salt or momentum, however, this mechanism is strongly influenced by confinement and by the viscous reconnection between the vortex and the shearing boundary. To suppress these confinements and viscous effects and better model the effect of the zonal jets on the vortices, it would be possible numerically to implement a shearing box where the shear is applied in the bulk. This method is however beyond the scope of the present work since the DNS are used to mimic the experiments in which shear is applied viscously.

We conclude this study by pointing towards other limits and possible improvements. First, Jovian vortices exhibit a slight North-South asymmetry, barely visible in their shape, but apparent in their velocities (Choi et al. 2007; Choi et al. 2010; Shetty et al. 2010). Including sources of asymmetry such as the β-effect and parametrizing deviation from ellipticity would improve the model's accuracy. Such effects could be tackled experimentally, with a sloping bottom to induce a topographic β-effect. However, we expect the influence on the vertical extent of those vortices to be negligible, and the β-effect would also induce a translation of the vortices which could make the experiment complicated. Then, more evolved compressible models might lead to some changes of relevance for Jupiter's atmospheric dynamics. For instance, one could expect a vertical asymmetry of the density perturbation associated with the vortex. Additionally, small-scale time-dependent turbulence is present inside and outside Jovian vortices, but not in our laboratory model. The effects of such turbulence should also be tackled, even if we expect that it should generate only small perturbations of the potential vorticity anomaly associated with the vortex. Finally, as underlined by our long-term evolution discussion, it would be interesting in the lab to set up a bulk shear rather than a boundary-driven one, which may lead to a more realistic interplay between the background and the vortex. We nevertheless argue that the results presented here, based on basic physics and first order balances, remain relevant and should be confirmed by up-coming Juno data.

Note finally that the superficial structure of large-scale Jovian vortices contrasts with the deep extension of the zonal winds into which they are embedded. How the deep convective dynamics reconnects with the stratified weather layer is one of the very long-standing questions regarding Jupiter. This coupling may for instance be necessary to understand the emergence and very long lifetime of Jovian anticyclones. In the next chapter, we dive deeper in Jupiter, and focus on the emergence and dynamics of deep, purely barotropic zonal jets, neglecting stratification altogether.

Chapter 3.

Zonal jets in the laboratory: a bistability due to Rossby waves resonance

Chapter 3.

The dynamics, structure and stability of zonal jets in planetary flows are still poorly understood, especially in terms of coupling with the small-scale turbulent flow. In this chapter, we address the questions of zonal jets formation and nonlinear equilibration.

Chapter aims

1. Build up a *Jacuzzi* experimental setup expanding upon Cabanes et al. (2017) to reach gas giants regimes of zonal flows (vanishing Ekman, large Reynolds and large zonostrophy index), with a uniform β-effect and a smaller-scale forcing.
2. Explain zonal jets formation in this setup in light of existing theories.

Highlights

- The *Jacuzzi* setup consists in a water-filled rotating tank, where a strong and uniform topographic β-effect is obtained thanks to the paraboloidal shape of the free surface combined with a specifically designed bottom plate. A small-scale turbulent forcing is performed by circulating water through the base of the tank.
- The flow self-organizes into multiple zonal jets with strong instantaneous signature. Two regimes of jets are observed depending on the forcing intensity. In regime I, the jets are steady, weak in amplitude, and locally accelerated by our forcing through the radiation of Rossby waves. In regime II, we observe highly energetic jets equilibrated at a global scale.
- The transition between the two regimes is of subcritical nature, and accompanied by bistability. We build an experimental hysteresis curve.
- A quasi-geostrophic (QG) theoretical model of the experiment reveals that the transition can be quantitatively explained by the linear resonance between the directly forced Rossby waves and the background zonal flow.
- QG numerical simulations show that the two regimes are retrieved when the forcing scale is reduced or changed from a polar to a cartesian pattern.
- We expect the oceanic jets to be sub-resonant (except the fast Antarctic Circumpolar Current), whereas gas giants jets would be super-resonant.

D. Lemasquerier et al. (2020b). "Gas Giant–like Zonal Jets in the Laboratory". *Physical Review Fluids* **5**: (11), 110506. DOI: 10.1103/PhysRevFluids.5.110506. Paper associated with a *Milton Van Dyke* award for a poster at the Gallery of Fluid Motion (2019 APS/DFD conference).

D. Lemasquerier et al. (2021). "Zonal Jets at the Laboratory Scale: Hysteresis and Rossby Waves Resonance". *Journal of Fluid Mechanics* **910**: A18. DOI: 10.1017/jfm.2020.1000

3.1. Introduction

A recurrent feature of planetary fluid envelopes is the presence of east-west flows of alternating direction, so-called zonal jets. Zonal flows are particularly striking in the gas giants' atmospheres such as on Jupiter, where the zonation of clouds of ammonia and water ice reveals the presence of several jet streams (Ingersoll et al. 2007; Vasavada et al. 2005). On these gas giants, it has been suggested that at the top of the clouds, the jets may contain more than 90% of the total kinetic energy (Galperin et al. 2014b) and penetrate deep into the planet's interior (Kaspi et al. 2018; Kaspi et al. 2020). Apart from their strength, jets on gas giants are also puzzling by their stability since the pattern has barely varied over decades (Porco et al. 2003; Tollefson et al. 2017). On Earth, at least one zonal jet lies in each hemisphere of the atmosphere (Schneider 2006). Perhaps surprisingly, the observation of zonal flows on the gas giants significantly predates that of the zonal flows in the Earth's oceans. This might be explained by the fact that oceanic jets only appear after a careful time averaging (Maximenko et al. 2005). Despite their latent nature, these jets seem to penetrate deep into the ocean (e.g. Cravatte et al. 2012).

There is not yet a commonly accepted mechanism to explain the formation of zonal jets in planetary flows. The only consensus is that the β-effect, arising from the variation of the Coriolis force with latitude (section 1.2.4), is responsible for the anisotropisation of the turbulent flow. In his seminal paper, Rhines (1975) predicted that the β-effect would alter the inverse energy cascade expected in geostrophic turbulence, and redirect energy towards zonal modes at low wavenumbers (see chapter 1, section 1.4.2.2). This work was however mainly heuristic, and since then, the dynamical process of jet formation has been the subject of intensive study. In a recent book, Galperin et al. (2019a) provide a survey of the latest theoretical, numerical and experimental advancements focusing on zonal jets dynamics and their interactions with turbulence, waves, and vortices. As detailed in the introductory chapter 1, several processes can lead to zonal flows formation, such as anisotropic turbulent cascades (Sukoriansky et al. 2002; Galperin et al. 2006; Sukoriansky et al. 2007; Galperin et al. 2019b), modulational instability (Quinn et al. 2019, and references therein) and mixing of potential vorticity (Dritschel et al. 2008; Scott et al. 2012b, 2019). Zonal flows also emerge as statistical equilibria from complex turbulent flows (Galperin et al. 2019a, part VI and references therein). It is not clear yet which mechanism(s) is (are) the most relevant for planetary applications, and for which planetary flow (terrestrial ocean and atmosphere, gas giant atmospheres). For instance, the inverse energy cascade from a small-scale forcing and its anisotropisation by the β-effect implies spectrally local interactions which are not observed in the Earth atmosphere, or at least not at low latitudes where nonlocal eddy-mean flow interactions are expected to prevail (Chemke et al. 2016). Non-local energy transfers towards the mean flow have also been demonstrated in the heated rotating annulus experiments (Wordsworth et al. 2008). On Jupiter on the contrary, the large-scale circulation seems indeed to be powered by a well defined inverse cascade emanating from the scale of baroclinic instabilities at ~2000 km (Young et al. 2017). Then, as a second example, robust zonal jets can form thanks to eddies even when the mixing is not sufficient to turn the initial potential vorticity profile into a staircase profile (Scott et al. 2012b). Finally, the relevance of statistical theories (Bouchet et al. 2012, 2019c), where both the forcing and the dissipation are vanishing, remains to be addressed for planetary flows.

In the present chapter, we wish to better understand zonal jets formation thanks to an experimental setup which allows for the self-organization of the flow into a dominant and instantaneous zonal flow made of multiple jets. In the past, numerous studies focused on the characteristics of *directly* forced zonal flows, either through an imposed zonal acceleration (e.g. Niino et al. 1984; Früh et al. 1999; Barbosa Aguiar et al. 2010) or a radial one which converts

into a zonal acceleration following the action of the Coriolis force (Hide 1968; Sommeria et al. 1989; Solomon et al. 1993). Such a situation is relevant for some terrestrial circulations such as the oceanic zonal currents forced by the wind, or the subtropical jet driven by the poleward motion in the Hadley cell (Read 2019). Here, in the context of self-organized large scale jets, we are interested in the formation of jets through the *indirect* effect of the Reynolds stresses, as a result of systematic correlations in the small-scale turbulent flow. Reproducing zonal jets without directly forcing them is experimentally challenging, namely because of the large boundary dissipation and moderate β-effect typically obtained in laboratory setups, and the difficulties associated with controlling the forcing. Generating significant zonal motions in a rotating flow in a regime relevant to planetary flows requires:

1. a process by which eddying turbulent motions are constantly generated;
2. a small Ekman number $E = \dfrac{\nu}{\Omega h_0^2}$ for the viscous dissipation to be as small as possible (ν being the kinematic viscosity, Ω the rotation rate and h_0 the typical fluid height). This can be achieved thanks to fast rotation and/or large containers;
3. a large Reynolds number $Re = \dfrac{u_{\rm rms} h_0}{\nu}$ for the flow to be turbulent ($u_{\rm rms}$ being the typical root-mean-squared velocity). This can be achieved thanks to a strong forcing;
4. a small Rossby number $Ro = Re \times E$ for the flow to be rotationally-constrained;
5. a large zonostrophy index R_β (equation (1.70)) for the β-effect to be significant compared to friction. This index is basically the ratio between the largest scale of the dynamics, set by the large scale drag, and the scale at which the eddies start to feel the β-effect.

In Fig.3.1, we represent planetary flows as well as experimental studies of zonal jets as a function of the aforementioned non-dimensional parameters. The Table containing the data used to plot this figure is provided in Appendix A.

Point #1, the forcing of the flow, can be achieved thanks to natural instabilities such as barotropic (Condie et al. 1994; Gillet et al. 2007; Read et al. 2015) or baroclinic thermal convection, in the differentially heated rotating annulus configuration (Hide et al. 1975; Bastin et al. 1998; Wordsworth et al. 2008; Smith et al. 2014). Read et al. (2004) and Read et al. (2007) alternatively used a specific convective forcing by spraying dense (salt) water at the free surface of a fresh water layer, and in a similar fashion, Afanasyev et al. (2012) and Slavin et al. (2012) performed a localized forcing involving sources of buoyancy. Another method, which has the advantage of allowing a close control of the location, scale and intensity of the forcing, consists in applying a mechanical forcing, provided that, again, it does not directly force the mean flow. In that purpose, Whitehead (1975) used a vertically oscillating disk, Afanasyev et al. (2005), Espa et al. (2012), Di Nitto et al. (2013), Zhang et al. (2014), and Galperin et al. (2014a) employed an electromagnetic forcing, and several studies performed an eddy-forcing using sinks and sources of fluid (De Verdiere 1979; Aubert et al. 2002; Cabanes et al. 2017; Burin et al. 2019).

Regarding point #5, the β-effect is usually achieved topographically, i.e. through the variation of the fluid height. Two principal approaches have been tested: using a sloping bottom, associated or not with a top-lid, or using the natural paraboloidal shape adopted by a fluid with a free surface in solid-body rotation. But as mentioned above, a β-effect alone is not sufficient for the development of large scale zonal flows. As shown by Fig.3.1*(c)*, reaching a large zonostrophy index is particularly relevant to simulate gas giants zonal flows. Indeed, R_β has been introduced to distinguish friction-dominated regimes ($R_\beta \sim 1.5$, Earth's ocean and atmosphere) and zonostrophic regimes, i.e. regimes of strong jets ($R_\beta > 2.5$, Jupiter and Saturn) (Galperin et al. 2006; Sukoriansky et al. 2007; Galperin et al. 2019b, Table 13.1). As shown in Fig.3.1*(f)*, previous experimental studies lied in the range $R_\beta \in [0.5, 2.5]$ and the observed flows were not in the zonostrophic regime, but recently, Cabanes et al. (2017) were able to reach

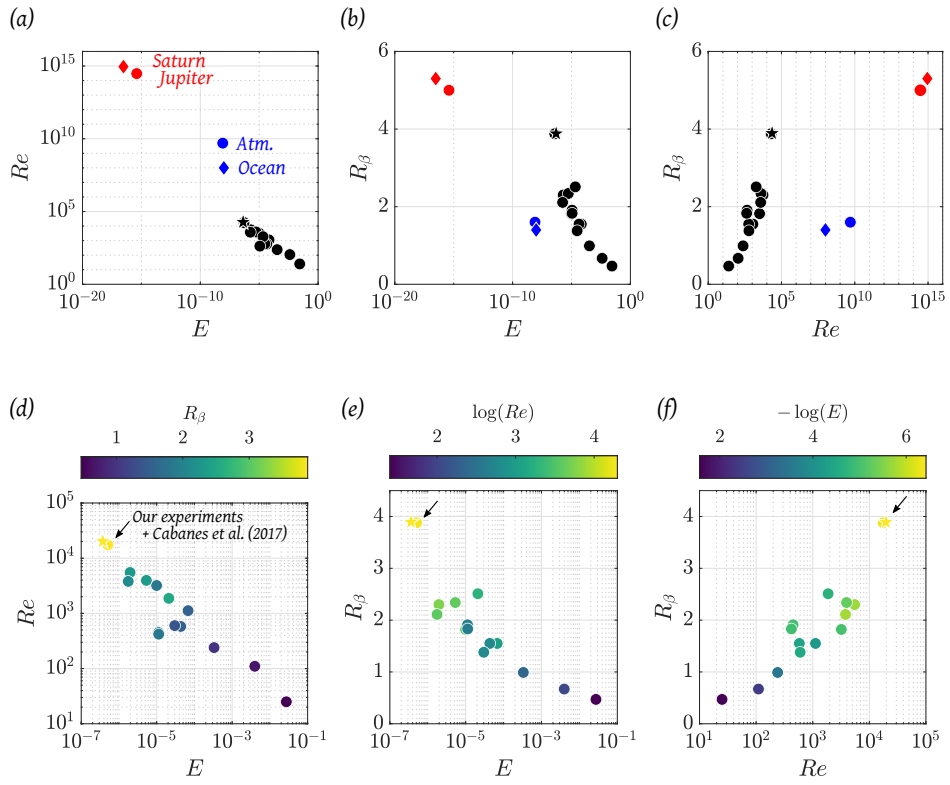

Figure 3.1. – Location of planetary flows and zonal jets laboratory experiments in the non-dimensional parameter space (Re, E, R_β) (Reynolds number, Ekman number, and zonostrophy index). *(a–c)* Black markers: experiments. The star corresponds to the most extreme regime reached in this thesis. Red markers: gas giants. Blue markers: terrestrial flows. *(d–f)* Zoom on the experimental studies. For the sake of comparison, we used similar definitions for all the experimental studies: $Re = u_{\mathrm{rms}} H/\nu$, $E = \nu/(\Omega H^2)$, and $R_\beta = (4 u_{\mathrm{rms}} \beta H^2/(\nu\Omega))^{1/10}$ (see chapter 4 and Table 4.1). The Table containing the data used to plot this figure is provided in Appendix A.

$R_\beta \approx 3.7$ thanks to the fast rotation (75 RPM) of a 1m-diameter tank. In addition to the larger zonostrophy index, this setup allows to reach smaller E (point #2) and larger Re (point #3) while remaining rotationally-constrained (point #4), thus getting closer to the regime observed on gas giants. The present work follows that of Cabanes et al. (2017): we built a close but significantly improved experimental setup, the principal modifications will be mentioned in the following of the chapter.

The layout of the chapter is as follows. In §3.2, we present the *Jacuzzi* experimental setup, for which additional details are provided in appendix B. In §3.3, we describe the main experimental results: we observe a subcritical bifurcation between two regimes of zonal flows depending on the forcing intensity. In §3.4, we develop a theoretical bidimensional model based on the quasi-geostrophic approximation to explain the experimental results. In §3.5, we point towards experimental improvements, we verify the robustness of the two regimes thanks to quasi-geostrophic numerical simulations, and we discuss implications for planetary flows .

3.2. Experimental methods

The experimental setup is an improved version of the setup of Cabanes et al. (2017). Three main modifications were made for this new setup compared to the previous one. First, the vast majority of theories and numerical simulations is performed in the context of the so-called β-plane, where the Coriolis parameter is assumed to vary linearly in the meridional direction,

with β its (constant) derivative (see chapter 1, section 1.2.4). For that reason, we designed the present setup to have a uniform topographic β-effect over the whole tank, rather than a strongly varying one due to the paraboloidal free-surface. Second, in the present experiment, we are able to control the forcing amplitude with radius and we decreased the forcing scale by a factor two (number of inlets/outlets increased from 64 to 128). Finally, and most importantly, the tank is transparent which allows for time-resolving particle image velocimetry (PIV) measurements over long time scales.

Following Cabanes et al. (2017), our experiment consists of a rapidly rotating cylindrical tank filled with water with a free upper surface and a topographic β-effect induced by the parabolic increase of the fluid height with radius due to the centrifugally induced pressure. The tank, made of Plexiglas, has an external diameter of 1m, is 1 cm thick and 1.6 m high. It is covered with a top-lid also made of Plexiglas to bring the underlying air in solid body rotation, thus reducing as much as possible perturbations of the free-surface. The experimental setup is sketched in Fig.3.2.

The topographic β-effect is a source or sink of vorticity induced by radial motions, and is a consequence of the local conservation of angular momentum in a rapidly rotating fluid. Here, the β parameter can be written as

$$\beta = -\frac{f}{h}\frac{\mathrm{d}h}{\mathrm{d}\rho}, \tag{3.1}$$

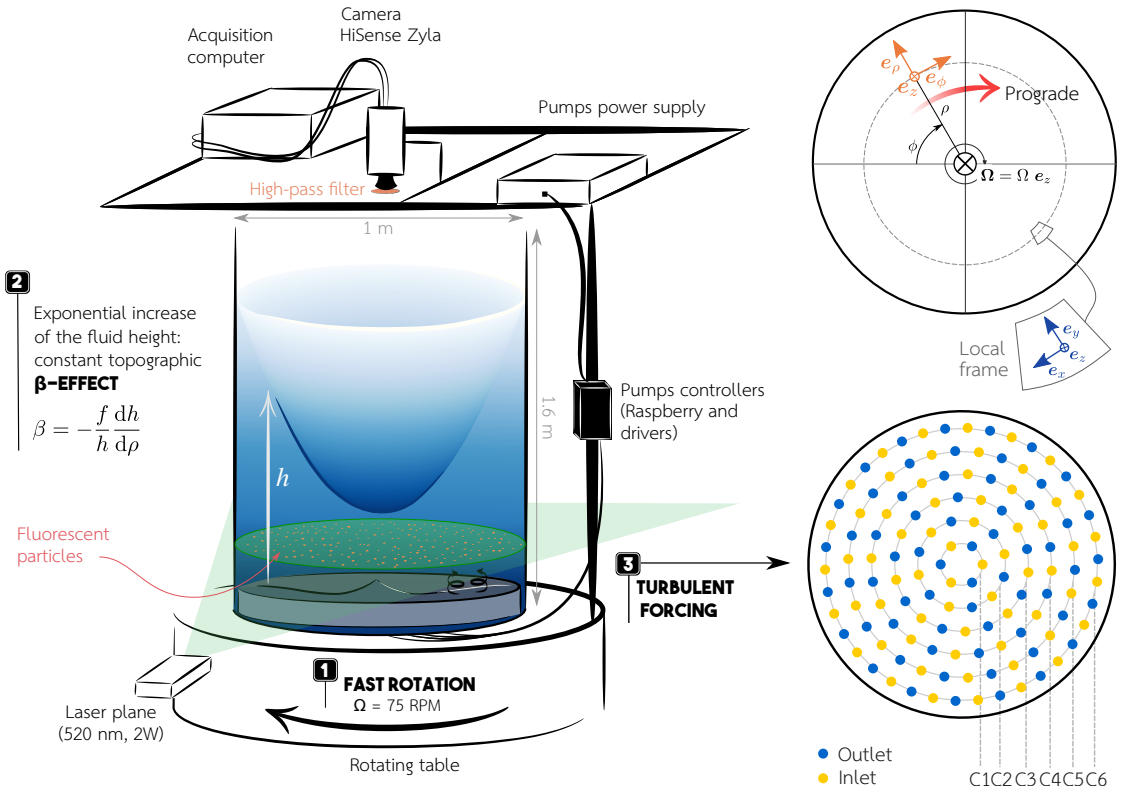

Figure 3.2. – Schematic of the experimental setup. A cylindrical tank of 1m in diameter and 1.6m in height, filled with 600 litres of water, is fixed on a table rotating at 75 RPM. The fluid free-surface takes a paraboloidal shape due to the centrifugally-induced pressure. The bottom plate is designed to achieve a uniform topographic β-effect. A small-scale turbulent forcing is performed by circulating water through 128 holes at the base of the tank. The forcing pattern is sketched on the right: each ring C1–C6 is controlled by an independent pump. Details on the forcing are provided in Appendix B. Time-resolving PIV measurements are performed on a horizontal plane using a side green laser and a top-view camera.

where ρ is the cylindrical radius, $h(\rho)$ is the total fluid height and $f = 2\Omega$ is the Coriolis parameter with Ω the rotation rate. Section 1.2.4.3 in the introductory chapter provides details about the origin of this expression. Equation (3.1) shows that for the topographic β-effect to be uniform over the whole domain, the fluid height should vary exponentially with radius. To achieve this, we choose to compensate the unalterable paraboloidal shape of the free surface using a non-flat bottom plate placed inside of the tank (Fig.3.2 and 3.3). The total fluid height h above the bottom plate is the difference between the free-surface altitude h_p and the bottom topography h_b. In solid body rotation at a rate Ω, the water free-surface height as a function of the cylindrical radius ρ is

$$h_p(\rho) = h_{\min} + \frac{\Omega^2}{2g}\rho^2 = h_0 + \frac{\Omega^2}{2g}\left(\rho^2 - \frac{R^2}{2}\right), \tag{3.2}$$

where g is the gravitational acceleration, R is the tank radius, $h_{\min}$ the minimum fluid height in rotation and h_0 the fluid height at rest. We want the fluid height h to have an exponential increase with ρ such that the β parameter (equation (3.1)) is constant, that is

$$h(\rho) = h_{\min} \exp\left(-\frac{\beta}{2\Omega}\rho\right). \tag{3.3}$$

The topography of the bottom of the tank is thus designed such that $h_b = h_p - h$. In addition, we optimized the choice of the physical parameters for h_b to be the less steep possible in order to minimize the cost of production and corrections to the classical Ekman pumping above a flat surface. Two additional constraints are given by the maximum rotation rate of the turntable (90 RPM) and its maximum load (1500 kg). This process led us to choose

$$h_{\min} = 0.20 \text{ m}; \tag{3.4}$$
$$h_0 = 0.58 \text{ m}; \tag{3.5}$$
$$\Omega = 75 \text{ RPM} \approx 7.85 \text{ rad}\,\text{s}^{-1}; \tag{3.6}$$
$$\beta \approx -50.1 \text{ m}^{-1}\,\text{s}^{-1}. \tag{3.7}$$

With these parameters, the bottom plate has the shape of a curly bracket (Fig.3.3(*c*)) with a maximum height difference of 5.36 cm and a mean absolute slope of 22%. The effective fluid height is minimum at the centre, $h_{\min} = 0.2$ m, and increases up to $h_{\max} = 0.96$ m (Fig.3.3(*b*)). The total volume of water, including the water located below the bottom plate is of about 600 litres. Fig.B.10 shows a comparison between the topographic β-effect obtained with the curved bottom plate and a flat bottom, for various rotation rates. Finally, the chosen rotation rate leads to an Ekman number

$$E = \frac{\nu}{\Omega h_0^2} \approx 3.78 \times 10^{-7}, \tag{3.8}$$

where ν is the kinematic viscosity of water ($\nu = 10^{-6}$ m^2 s^{-1}). Note that we assume ν to be constant, but the experiments discussed in the following were performed at room temperatures varying between 20 and 27°C, leading to $\nu \in [0.8539, 1.0034] \times 10^{-6}$ m^2 s^{-1} and $E \in [3.23, 3.80] \times 10^{-7}$.

We force small-scale fluid motions using an hydraulic system located at the base of the tank (Fig.3.3(*c,d*)). This system is inspired from previous setups designed to study turbulence (Bellani et al. 2013; Yarom et al. 2014) and zonal flows (De Verdiere 1979; Aubert et al. 2002; Cabanes et al. 2017; Burin et al. 2019). The curved bottom plate is drilled with 128 holes (64 inlets and 64 outlets) with a diameter of 4 mm. The forcing pattern is arranged on a polar lattice with 6 rings C_{1-6} located at radii $R_i \in \{0.067, 0.140, 0.214, 0.287, 0.361, 0.434\}$ m as represented in Fig.3.2. Each ring counts respectively 6, 12, 18, 24, 30 and 38 holes, half of

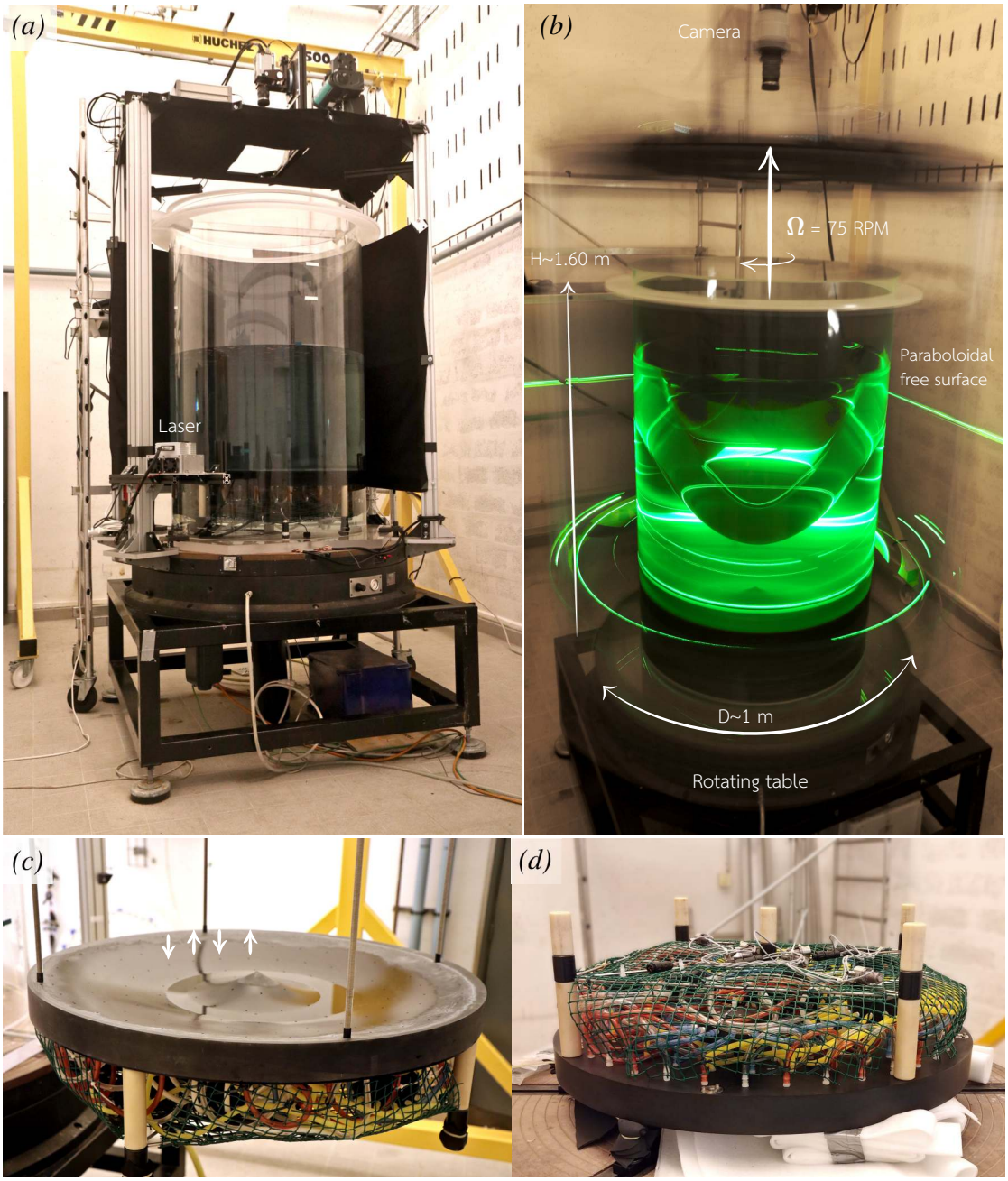

Figure 3.3. – (*a*) Experimental setup at rest. The tank is mounted on a rotating table operated using an air cushion. It is filled with ~600 litres of tap water so that the fluid height at rest above the bottom plate is of ~58 cm. It is closed by a Plexiglas top-lid. (*b*) Experimental setup in solid body rotation at 75 RPM, with the side green laser turned on. The difference in fluid height between the centre of the tank and its border is of ~76 cm and the fluid height at the centre is $h_{\min} = 20$ cm. (*c*) View of the bottom plate through which the forcing is performed. The plate has the shape of a curly bracket for the fluid height to increase exponentially with the radius, see equation (3.3). It is drilled with 128 holes corresponding to 64 inlets and 64 outlets connected to 6 submersible pumps. (*d*) View of the 6 pumps and 128 hoses placed beneath the bottom plate.

them being inlets (sucking water from the tank and generating cyclones) and the other half outlets (generating anticyclones) as represented in Fig.3.2. The holes are uniformly distributed along each ring, leading to a minimum separating distance of 7.0 cm (ring C_1) and a maximum separating distance of 7.6 cm (ring C_5). Note that there is also a spatial phase shift between each consecutive rings in order to minimize the variance in the distance between two neighbouring inlets or outlets (Fig.3.2). All the holes of a given ring are connected to a submersible pump (TCS Micropump, M510S-V) via a network of flexible tubes (Fig.3.3). Six submersible pumps are thus located beneath the bottom plate, and circulate water through the six rings. The resulting circulation induces no net mass flux, since the water is directly sucked from the working fluid and released in it. At this point, it is important to stress that the system was designed to minimize the direct forcing of the zonal mean zonal flow and that only the eddy momentum fluxes should be responsible for its eastward or westward acceleration. Finally, each ring is controlled by one pump independently of the others which allows us to control the forcing intensity with the radius. The pumps are controlled remotely by linking them to their drivers (TCS EQi Controllers) through the base of the tank. The drivers are controlled by a Raspberry Pi connected to a local network. We can chose the power of a given pump to be stationary, or to fluctuate randomly within a prescribed power range every 3 seconds. Additional details, pictures and schematics of the forcing are provided in Appendix B.

To measure velocity fields, time-resolving particle image velocimetry (PIV) measurements are performed on a horizontal plane. A green laser beam (LASER QUANTUUM 532nm CW Laser 2 Watts) associated with a Powell lens is used to create a horizontal laser plane located 11 cm above the edge of the bottom plate (9 cm below the centre of the paraboloid). The water is seeded with fluorescent red polyethylene particles of density 0.995 and 40–47 micrometers in diameter (Cospheric, UVPMS-BR-0.995). Their motion is tracked using a top-view camera (DANTEC HiSense Zyla) placed above the tank (Fig.3.2 and 3.3). A 28 mm lens is mounted on the camera (ZEISS Distagon T* 2/28). The particles emit an orange light (607 nm) so that using a high-pass filter on the lens allows to filter out the green laser reflections on the free-surface and tank sides, leading to a better image quality and hence better PIV measurements. The images are acquired using DANTEC's software DynamicStudio. We reduced the sensor region of interest to fit the tank borders, leading to 1900 × 1900 pixels images. Optical distortion induced by the paraboloidal free-surface is corrected on DynamicStudio using a preliminary calibration performed by imaging a home-made calibration target with a precise dot pattern (see Appendix B, §B.4). An illustrative movie of the particles motion during an experiment is available as supplementary movie 1 in Lemasquerier et al. (2021). The velocity fields are deduced from these images using the MATLAB program DPIVSoft developed by Meunier et al. (2003). We consider 32×32 pixels boxes on 1900×1900 pixels images and obtain 100×100 velocity vector fields (40% overlap between the boxes). Note that due to the refraction of the laser plane by the tank sides, there are two shadow zones where measurements are not possible (see the grey areas in Fig.3.4). As represented in Fig.3.2, all the devices (acquisition computer, camera, synchronizer, laser, pumps power supply, drivers and Raspberry) are attached to the rotating frame. The rotary table operates thanks to an air cushion, allowing us to reach high rotation rates even with a large non-equilibrated load (~1000 kg).

A typical experimental run is as follows. We gradually increase the rotary table rotation rate from rest up to 75 RPM (~30 min). We then wait for the water to be in solid-body rotation which takes approximately 45 min, i.e. $\sim 13\,\tau_E$ where $\tau_E = \Omega^{-1}E^{-1/2}$ is the Ekman spin-up timescale. Note that inertial oscillations are observed even after spin-up, due to the tank's misalignment and the slight non-circularity of its cross-section. These oscillations generate typical radial root-mean-square velocities of $\sim 4\times10^{-4}\,\mathrm{m\,s^{-1}}$. These small amplitudes and large-scale oscillations do not significantly perturb the small-scale forced geostrophic motions. We then turn on

the forcing of the 6 rings simultaneously, potentially with different powers, in a stationary or random state. For a typical run, we record images for 60 minutes, corresponding to 4500 t_R where $t_R = 2\pi/\Omega = 0.8$ s is the rotation period. We record images with framerates between 10 and 30 frames per second to resolve the fluid motions which have typical velocities between 0.1 and 10 $\mathrm{cm\,s^{-1}}$ depending on the forcing amplitude.

The forcing was calibrated in the rotating system by measuring the root-mean-squared (rms) velocity induced on the horizontal PIV plane by the forcing. This measurement was realized for each ring separately and several pump powers just after the forcing was turned on, i.e. before the jets develop. We then performed a linear fit of the induced rms velocity as a function of power to obtain a calibration law for each pump. Details about the forcing calibration are given in Appendix B.2. In the following, we denote the forcing amplitude U_f, which corresponds to the mean of the rms velocities of the six pumps deduced from our calibration.

3.3. Experimental results

For all the experiments performed in our setup, we observe instantaneous zonal flows independently of the number of forcing rings turned on, their power, and their state (stationary or random). However, depending on the forcing amplitude, we observe two different regimes of zonal flows described in the next sections. The results are presented on the horizontal laser plane using the polar coordinates represented in Fig.3.2, with (u_ρ, u_ϕ) the radial and azimuthal velocities and $\zeta = (\boldsymbol{\nabla} \wedge \boldsymbol{u}) \cdot \boldsymbol{e}_z = (\partial_\rho(\rho u_\phi) - \partial_\phi u_\rho)/\rho$ the vertical component of the vorticity.

3.3.1. Regime I: Low-amplitude, locally forced jets

At low, stationary forcing amplitude, we observe the fast development of 5 prograde jets and 6 retrograde ones. A jet is said prograde when the azimuthal flow is in the same direction as the tank's rotation, $u_\phi > 0$ (Fig.3.2). We will refer to this regime as **Regime I**.

To describe this regime, we chose a typical experiment where the pumps power are respectively $P_i = \{7, 10, 20, 30, 45, 90\}$% of their nominal power, corresponding to a forcing amplitude $U_f = 2.4 \times 10^{-3}$ $\mathrm{m\,s^{-1}}$ (see appendix B.2). Figure 3.5(*a*) represents the temporal evolution (Hovmöller diagram) of the instantaneous azimuthal mean of the azimuthal component of the velocity $\langle u_\phi \rangle_\phi(\rho, t)$ – called *zonal flow* in the following of the paper, whereas *mean flow* refers to the time-averaged velocity field. The jets develop almost instantaneously (~ 10 t_R), and reach their saturating amplitude in about 100 t_R (another example is shown in Fig.3.7 for $t < 360$ t_R). Supplementary movie 3 from Lemasquerier et al. (2021) illustrates the development of the vorticity field in regime I.

The velocity and vorticity fields obtained after saturation are represented in Fig.3.4(*a*) and 3.6(*a-c*). The retrograde jets are uniform and quasi-axisymmetric, whereas the prograde jets are associated with clear non-axisymmetric perturbations. Consistently with the direction of the zonal flow, the anticyclones – negative relative vorticity ζ – are located on the outer radius flank of the prograde jets, whereas cyclones are located on their inner radius side. In addition, the prograde jets are thinner than the retrograde ones. These observations highlight the asymmetry between prograde and retrograde jets, generically observed in this type of systems (e.g. Scott et al. 2012b).

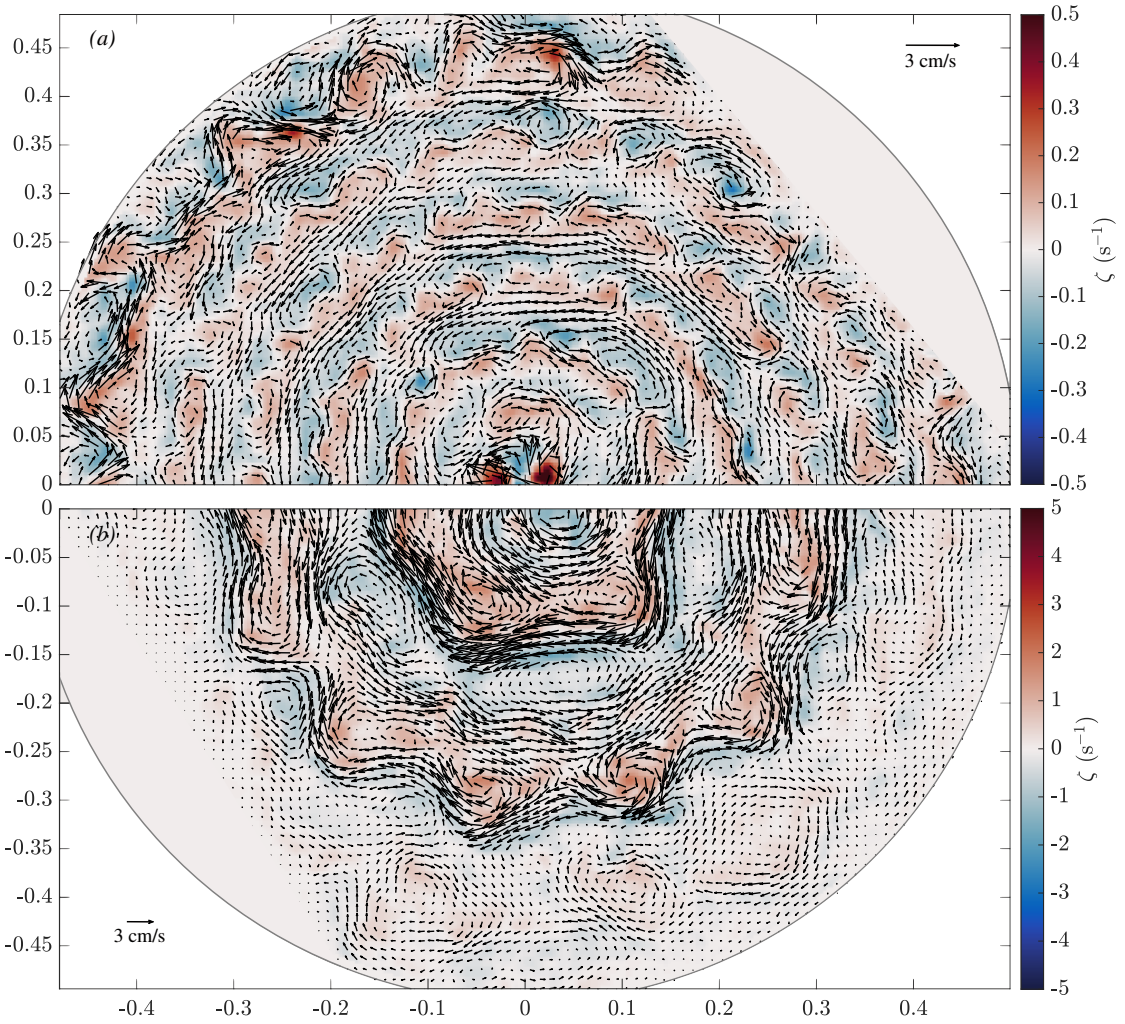

Figure 3.4. – Instantaneous velocity fields computed from PIV measurements in the statistically stationary state reached in the two experimental regimes. The shaded areas in the top-right and bottom-left corners are shadow areas due to the laser refraction: no measurements are performed in these areas. The colours represent the vertical component of the vorticity ζ. Note that there is a factor ten between the colour scales in the two panels. (*a*) Regime I. Velocity field obtained at time t =24 min = 1800 t_R and averaged over 1s. (*b*) Regime II. Velocity field obtained at time t = 19 min = 1425 t_R and averaged over 1s.

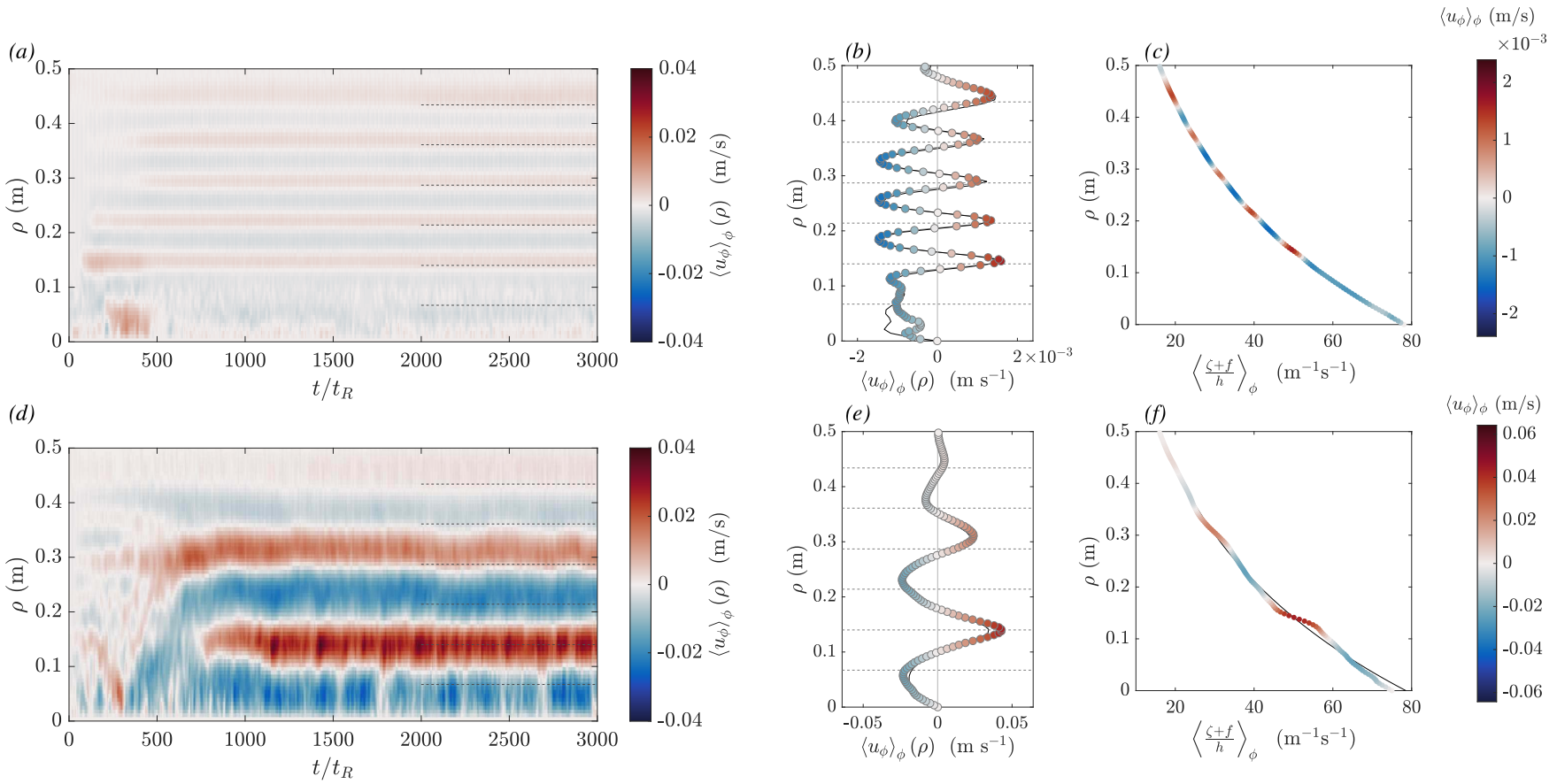

Figure 3.5. – Zonal flow and zonal mean potential vorticity in the two experimental regimes. (*a–c*) Regime I. (*a*) Space-time diagram showing the evolution of the instantaneous zonal flow radial profile $\langle u_\phi \rangle_\phi(\rho, t)$ during the experiment. Dotted lines: location of the forcing rings. (*b*) Symbols: Instantaneous zonal flow at time $t = 2500\, t_R$. Black line: Time-averaged zonal flow $\overline{\langle u_\phi \rangle_\phi}(\rho)$ from t =1500 to 3000 t_R. Dotted lines: location of the forcing rings. (*c*) Symbols: Potential vorticity instantaneous profile at time $t = 2500\ t_R$. Grey line: Initial potential vorticity profile (hidden behind the symbols). (*d–f*) Regime II (the same quantities are plotted).

Regime	$u_{\rm rms}$ ($\mathrm{mm\,s^{-1}}$)	$Ro = \frac{u_{\rm rms}}{fR}$	$Ro_\ell = \frac{u_{\rm rms}}{f\ell}$	$Ro_\zeta = \frac{\zeta_{\max}}{f}$	$Re = \frac{u_{\rm rms}R}{\nu}$	$Re_\ell = \frac{u_{\rm rms}\ell}{\nu}$
I	1.59	1.78×10^{-4}	1.20×10^{-3}	1.91×10^{-2}	671	100
II	16.0	2.07×10^{-3}	1.39×10^{-2}	8.91×10^{-2}	7830	1170

Table 3.1. – Typical instantaneous rms velocity (equation (3.9)), Rossby and Reynolds global and local numbers. R is the tank's inner radius $R = 0.49$ m, and $f = 2\Omega = 15.7$ rad/s. For the local Rossby and Reynolds numbers, we use the distance between two forcing rings as a length scale, $\ell = 7.3$ cm. Note that these values correspond to two typical experiments, but may vary in each regime depending on the forcing amplitude.

The saturated zonal flow profile is plotted in Fig.3.5(b) along with its time-average, and Fig.3.5(c) shows the zonal mean of the potential vorticity $\langle(\zeta+f)/h\rangle_\phi$. In the absence of dissipation, we expect the material conservation of potential vorticity (PV) (see chapter 1, §1.2.4.4). In this limit, zonal flows formation can be viewed as a process of mixing of the initial potential vorticity profile $f/h(\rho)$. Dritschel et al. (2008) showed that this profile should be turned into a staircase where the prograde jets correspond to steep gradients, and the retrograde jets correspond to weak gradients, i.e. zones of strong mixing. Here, despite the visible segregation of vorticity (Fig.3.6(c)), the initial vorticity profile is almost not perturbed, showing that zonal jets can exist instantaneously even without this process of potential vorticity mixing. Said differently, this regime is characterized by a local Rossby number $Ro_\zeta = \zeta/f \ll 1$ (see Table 3.1), hence the initial PV profile is not expected to be strongly modified. The instantaneous root-mean-squared (rms) velocity defined as

$$u_{\rm rms} = \left[\frac{1}{N}\sum_{i=1}^{N}|\boldsymbol{u}_i|^2\right]^{1/2}, \tag{3.9}$$

where N is the number of PIV velocity vectors, is provided in Table 3.1 along with the global and local Rossby and Reynolds numbers of the flow. Here, $u_{\rm rms}$ is computed from the velocity fields of Fig.3.4. It is considered "instantaneous" in opposition to the same quantity computed after a very long time average $\overline{u}_{\rm rms}$ which will be used later in the paper. Table 3.1 shows that the flow is barely turbulent in regime I (the local Reynolds number being approximately 100), and highly constrained by rotation given the very small Rossby numbers. Finally, the zonal flow contains $23\pm5\%$ of the total kinetic energy.

In this regime, each prograde jet stands right above a forcing ring (see the dashed lines in Fig.3.5 and 3.6). The only exception is the inner ring (ring C1), which is geometrically constrained due to its small radius and significantly perturbed by the peak at the centre of the bottom plate (Fig.3.3(c)). Despite this anomaly, the 5 other forcing rings are clearly associated with a prograde jet. This leads us to hypothesize that the prograde jets are forced locally by prograde momentum convergence towards the forcing radii. The local Reynolds stresses generated by our forcing are then balanced by viscous effects. This mechanism of zonal flow formation is reminiscent of the pioneering experiments of Whitehead (1975) and De Verdiere (1979). Whitehead (1975) demonstrated that the generation of a train of Rossby waves in a rotating tank with paraboloidal free surface induces a prograde flow at the radius of the forcing, with two weak retrograde flows on both sides of the forcing. De Verdiere (1979) did the same observation with a forcing consisting in a ring of sink and sources able to be azimuthally translated. Corresponding theoretical studies of Thompson (1980) and McEwan et al. (1980) then followed and accounted for the mechanism of momentum convergence due to eddy-forcing. It is now believed to be the primary mechanism of westerlies formation in the midlatitude atmosphere (Vallis 2017, chapter 12). This mechanism will be further explored in

§3.4. Finally, let us mention that the relaxation dynamics of this regime is consistent with the observation of De Verdiere (1979): when the forcing is stopped, the fluctuating velocities are dissipated more rapidly than the mean flow.

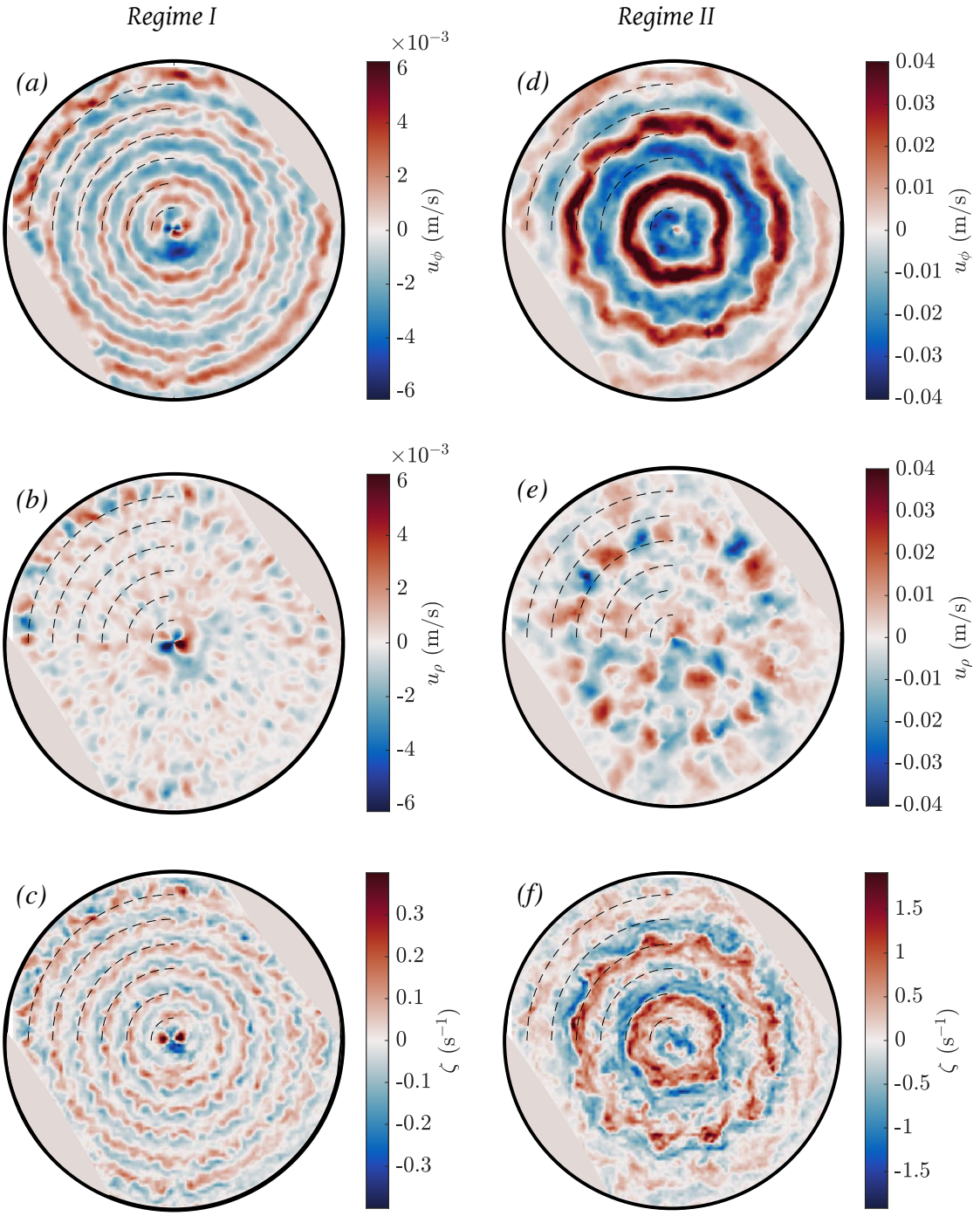

Figure 3.6. – Instantaneous maps in regime I (*a–c*) and II (*d–f*). The black circle marks the tank boundary, and the shaded areas are the shadows where no measurements can be performed. The dashed curves in the top-left quadrant of each subplot represent the forcing rings location. (*a–c*) Regime I at time t = 24 min = 1800 t_R and averaged over 1s. (*a*) Azimuthal component of the velocity u_ϕ. (*b*) Radial component of the velocity u_ρ. (*c*) Vertical component of the vorticity ζ. (*d–f*) Regime II at time t = 19 min = 1425 t_R and averaged over 1s. (*d*) u_ϕ. (*e*) u_ρ. (*f*) ζ. Note the different colour scales for the two regimes.

3.3.2. Regime II: High-amplitude large scale jets

At high, stationary forcing amplitude, regime I develops as a transient before the system reaches a new statistically stationary state with stronger and broader zonal jets, hereafter called **Regime II**.

To describe this regime, we chose a typical experiment where the pumps power are respectively $P_i = \{26, 33, 60, 80, 100, 100\}$% of their nominal power, corresponding to a forcing amplitude $U_f = 4.0 \times 10^{-3}$ m s^{-1} (see appendix B.2). The Hovmöller diagram of this experiment is represented in Fig.3.5(*d*). The steady jets of the first regime reorganize into 3 prograde and 3 retrograde jets. Note that in other experiments, the saturated flow can count 4 prograde jets instead of 3. This spontaneous transition from regime I to regime II is slow, and the statistically steady state is obtained after a transient of about 800 t_R. Furthermore, it involves jet merging events visible in the Hovmöller plots of Fig.3.5(*d*) and 3.7. The reorganization of the jets during this transition also shows that they become more independent of the forcing pattern: in the final steady state of regime II, the jets have a typical width which is twice that of the jets in regime I, and their radial position can be shifted compared to the position of the forcing rings. A retrograde flow is even observed above some forcing rings, for instance above C1 and C3. Thus, in this regime, the system self-organizes at a global scale, and the idea of a direct local forcing is not relevant anymore. Supplementary movie 4 in Lemasquerier et al. (2021) illustrates the development of regime II, and movie 1 shows the particles motion when the system is in steady state.

The velocity field obtained after saturation is represented in Fig.3.4(*b*), and the corresponding maps of velocity and vorticity are plotted in Fig.3.6(*d-f*). The prograde jets are still meandering between cyclones on their right and anticyclones on their left, but these vortices are now large-scale ones. As can be seen in Fig.3.4(*a*), the vortices forced above the inlets and outlets have a typical diameter of ~3 cm in regime I, whereas in regime II (panel (*b*)), we observe fewer vortices, with a typical diameter of ~8 cm. The instantaneous rms velocity (Table 3.1) is about 10 times higher than in the experiment described for regime I. The global and local Rossby numbers are still very small, i.e. the flow is still highly constrained by rotation, but the Reynolds number is multiplied by 10 hence the flow can now be considered fully turbulent. The fraction of kinetic energy contained in the zonal flow in this experiment reaches 58 ± 8%. Figure 3.5(*f*) shows that the PV mixing is increased in this second regime and consistently with Dritschel et al. (2008), the prograde jets correspond to steepening of the PV profile. But again, the small vorticity of our experiment does not allow an efficient mixing process, though the jets are strong and contains most of the kinetic energy.

3.3.3. Nature of the transition: a first-order subcritical bifurcation

In this section, we investigate the nature of the transition between the two previously described experimental regimes.

Figure 3.7 shows a Hovmöller diagram representing the evolution of the zonal flow profile $\langle u_\phi \rangle_\phi(\rho, t)$ during a single experiment as well as the corresponding evolution of the total, zonal, and residual kinetic energy defined respectively as

$$\mathcal{K} = \frac{1}{N} \sum_{i=1}^{N} |\boldsymbol{u}_i|^2, \tag{3.10}$$

$$\mathcal{K}_z = \frac{1}{N} \sum_{i=1}^{N} \langle u_\phi \rangle_{\phi,i}^2, \tag{3.11}$$

$$\mathcal{K}_f = \mathcal{K} - \mathcal{K}_z, \tag{3.12}$$

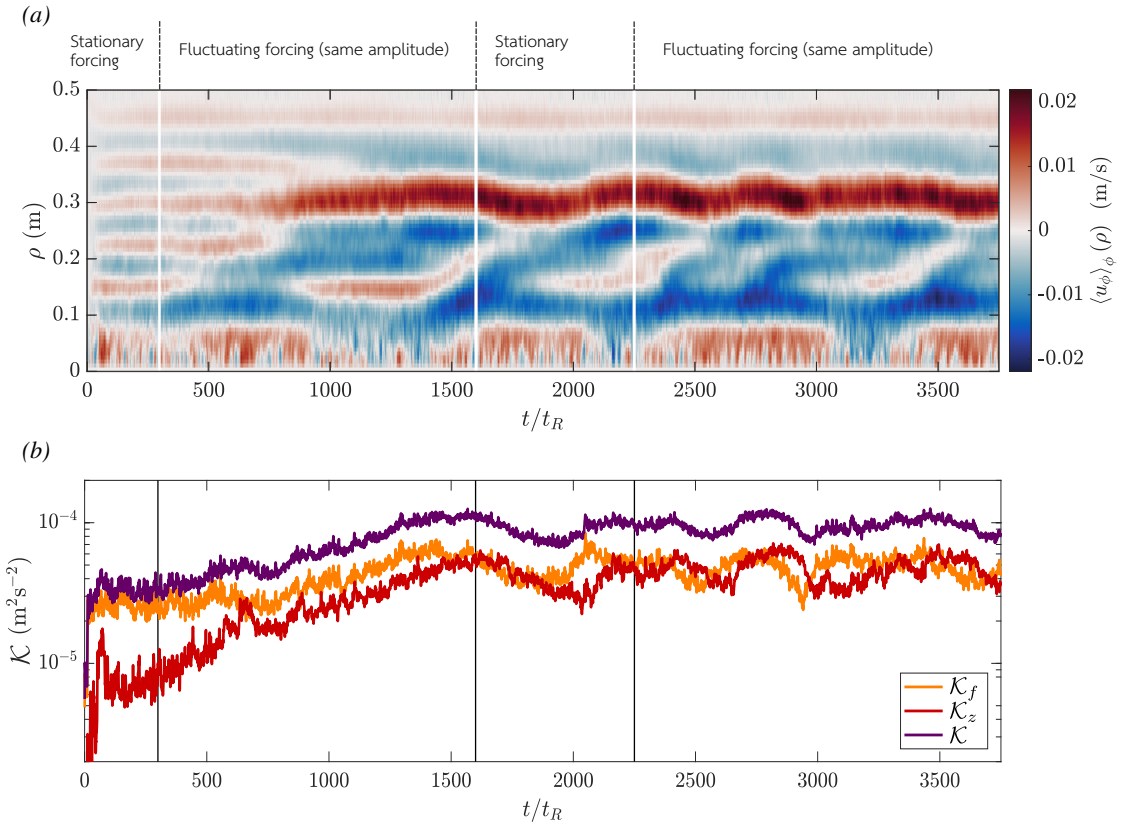

Figure 3.7. – Experiment illustrating the bistability between regimes I and II: the forcing is initially of low-amplitude and stationary, so that we start in regime I ($P_i = \{14,20,46,72,100,100\}$%, $U_f = 3.3\times10^{-3}$ m s^{-1}). At $t = 360\ t_R$, a finite perturbation is created by varying the third forcing ring power randomly around its initial value, leading to the transition to regime II ($P_i = \{14,20,46\pm20,72,100,100\}$%). At $t = 1600\ t_R$, the forcing is set back to its initial state but the flow remains in regime II. At time $t = 2250\ t_R$ a second finite amplitude perturbation is performed ($P_i = \{14,20,46,72\pm20,100,100\}$%) (*a*). Hovmöller plot: zonal flow profile as a function of time. (*b*) Total ($\mathcal{K}$), zonal ($\mathcal{K}_z$) and fluctuating ($\mathcal{K}_f$) kinetic energy as a function of time.

where N is the number of PIV velocity vectors. The experiment plotted in Fig.3.7 is initialized with a stationary forcing ($U_f = 3.3\times10^{-3}$m s^{-1}), leading to a steady state in regime I. After 360 t_R, this forcing is perturbed at finite amplitude by turning the third ring into a random state. Here, it consists in changing the power of the corresponding pump every 3 seconds to random values uniformly distributed in a range centred around ±20% of its initial power. After such a perturbation, Fig.3.7(*a*) shows that the system bifurcates towards the second regime through merging events and increasing zonal flow amplitude. Note that without this perturbation, the system would be locked in regime I, as shown by a separate experiment performed with the exact same forcing, at least up to $t = 1875\ t_R$. During the transition, the fraction of kinetic energy contained in the zonal flow increases from 21±7% to 48±9% (Fig.3.7(*b*)). This second value is significantly lower than the one mentioned previously for regime II since the forcing of this experiment is weaker. After the transition, the system remains attached to this new steady state even when the forcing is set back to its initial stationary state at time $t = 1600\ t_R$. These observations demonstrate that two stable states coexist for this particular forcing and suggest that the transition between the two regimes is of subcritical nature.

To further investigate this bistability, we performed series of experiments where we increase or decrease the forcing step by step. We wait significantly between each step for the system to relax towards a new steady state (typically 20 minutes, i.e. 1500 t_R). We then measure the corresponding mean flow amplitude defined as the rms velocity computed on a time-averaged

velocity field:

$$\overline{u}_{\mathrm{rms}} = \left[\frac{1}{N} \sum_{i=1}^{N} |\overline{\boldsymbol{u}_i}|^2 \right]^{1/2}, \tag{3.13}$$

where $\overline{\cdot}$ denotes the time average over the whole duration of the record once the flow has reached the statistically steady state. Typically, the time average is performed over 200 to 1000 t_R depending on the duration of the record. Figure 3.8 represents the mean flow amplitude (equation (3.13)) as a function of the forcing amplitude U_f as defined in appendix B.2. Typical maps of the time-averaged zonal velocity are also represented. For low values of the forcing amplitude, regime I is observed with the 6 prograde jets structure and $\overline{u}_{\mathrm{rms}} \sim 2.5 \times 10^{-3} \mathrm{m\,s^{-1}}$. As the forcing amplitude increases, the jets structure does not change but their amplitude increases smoothly. When the forcing further increases, a sharp transition occurs around $U_f \approx 3.32 \times 10^{-3} \mathrm{m\,s^{-1}}$ corresponding to a bifurcation from regime I to regime II: both the jets size and amplitude increase abruptly ($\overline{u}_{\mathrm{rms}} \sim 7.5 \times 10^{-3} \mathrm{m\,s^{-1}}$). Once in regime II, the amplitude of the jets continues to increase with the forcing amplitude. When the forcing amplitude is gradually decreased, the bifurcation from regime II to regime I is again abrupt, but obtained at a lower forcing $U_f \approx 3.11 \times 10^{-3} \mathrm{m\,s^{-1}}$. These hysteresis experiments confirm that the two regimes coexist in a given forcing range $U_f \in [3.11, 3.32] \times 10^{-3} \mathrm{m\,s^{-1}}$. The particular forcing of the experiment represented in Fig.3.7 ($U_f = 3.3 \times 10^{-3} \mathrm{m\,s^{-1}}$) belongs to the bistable range in which the first regime is metastable. In §3.4, we propose a model to explain this hysteresis phenomenon.

Finally, we note a significant variability in the mean flow amplitude in regime II. The grey points in Fig.3.8(*a*), located at $U_f = 4 \times 10^{-3} \mathrm{m\,s^{-1}}$, correspond to nine experiments where we apply the exact same forcing ($P_i = \{26, 33, 60, 80, 100, 100\}\%$), starting from solid-body rotation. Despite the similarity of the forcing, the flow may evolve towards different statistically steady states where the mean flow amplitude and scale are roughly the same, but the position of the jets differ. This multistability will be described in chapter 5. Note that the last point of the yellow curve in Fig.3.8 is located below the others probably because it had not reached its steady state when the measurements were performed (500 t_R after the forcing change in contrast to 1500 t_R for the grey points).

It is of interest to compute the transition rates between the two regimes. On Fig.3.9, we plot the evolution of the total kinetic energy for transitions from regime I to regime II and vice versa in order to compute the corresponding timescales. Transitions in the direction II→I (decreasing power) are accompanied by an exponential decay of the total kinetic energy

$$\mathcal{K} = \mathcal{K}_\infty + (\mathcal{K}_0 - \mathcal{K}_\infty) e^{-t/\tau}, \tag{3.14}$$

where $\mathcal{K}_0$ is the kinetic energy in the initial steady state, and $\mathcal{K}_\infty$ the kinetic energy reached in the final steady state after the transition. We plot in Fig.3.9(*b*) the time evolution of the normalized kinetic energy for three transitions with different initial and/or final steady states. Despite these differences, it is clear that the three transitions have the same characteristic time $\tau_{II \to I} \approx 150\ t_R$. The picture is different for transitions in the direction I→II (Fig.3.9(*c*)). The kinetic energy increases in a non-trivial way before saturating in a new steady state. We compare this evolution for three transitions starting from the same initial state in the first regime (red dot I in Fig.3.9(*a*)), but evolving towards three different steady states in regime II ($\mathrm{II}_{1,2,3}$ in Fig.3.9(*a*)). Note that I→II_1 corresponds to a finite amplitude perturbation of a steady state in regime I inside of the bistable range. We plot in Fig.3.9(*c*) the kinetic energy normalized the same way as for II→I transitions. This time, the curves do not collapse. We observe that the closer (in terms of forcing amplitude) the second steady state, the longer the transition. The transition I→II_3 is for instance about 3 times faster than the transition I→II_1.

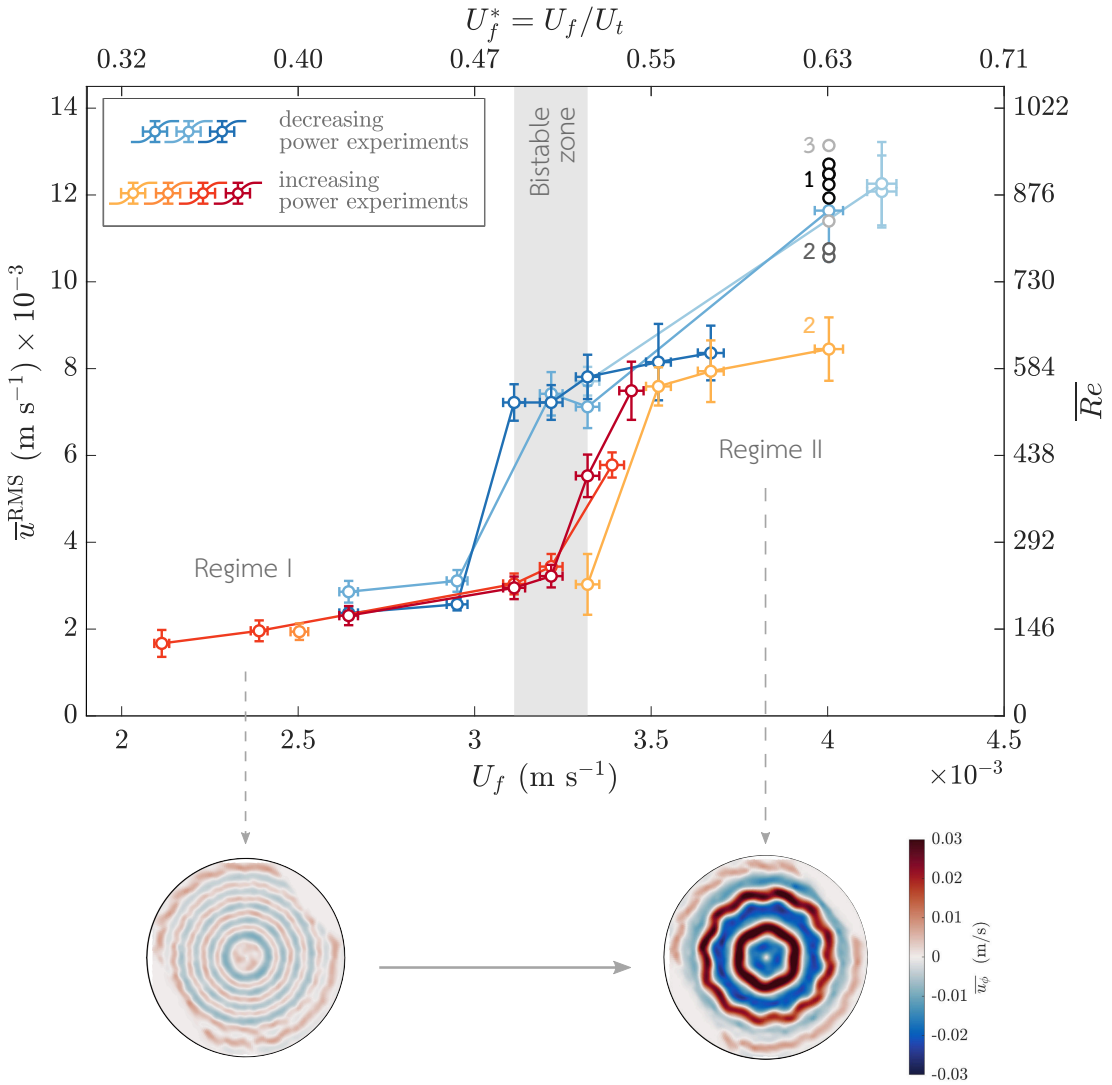

Figure 3.8. – Experimental hysteresis loop. The time-averaged rms velocity of the flow $\overline{u}_{\mathrm{rms}}$ (equation (3.13)) is plotted as a function of the forcing amplitude U_f (see appendix B.2). The top and right axes correspond to associated non-dimensional quantities. On the right-axis, we use the local Reynolds number based on the mean flow rms velocity, $\overline{Re} = \overline{u}_{\mathrm{rms}}\ell/\nu$ (ℓ=7.3 cm is the distance between two forcing rings). For the top-axis, we use the typical velocity expected at the transition U_t (see section 3.4.4 and equation (3.48)). For each curve, the forcing is either increased (reddish) or decreased (bluish) step by step. The different colours correspond to different experiments. The shaded area is the bistable zone. The grey points in regime II correspond to experiments initialized with the exact same forcing and for which saturation leads to three possible jets configurations, as described in chapter 5. The last point of the yellow curve is in configuration 2, but may not have reach its stationary state. Time-averaged zonal velocity maps in regime I and II are represented at the bottom.

These differences highlight an asymmetry in the transition mechanism depending on its direction. We propose the following interpretation. In the case II→I, the transition resembles a classical relaxation following a linear dissipation process. If the Reynolds stresses sustaining the strong jets abruptly decrease when the forcing decreases, the linear friction dominates the zonal flow evolution equation $\partial_t \langle u_\phi \rangle_\phi = -\alpha \langle u_\phi \rangle_\phi$, where α is a linear friction, and the zonal flow decreases exponentially. We then expect the timescale of this transition to be of the order of the Ekman friction timescale $\tau_E = \alpha^{-1} = \Omega^{-1} E^{-1/2}$. In our case, $\tau_E \approx 206$ rotation periods, which is consistent with $\tau_{II \to I} \approx 150\ t_R$ determined previously. On the contrary, in the case I→II, we expect a nonlinear mechanism leading to a non-trivial increase of the zonal flow amplitude. Contrary to the linear friction, this mechanism depends on the forcing amplitude – as may be intuited from the theoretical model developed in §3.4. The higher the forcing, the faster we expect the transition to occur.

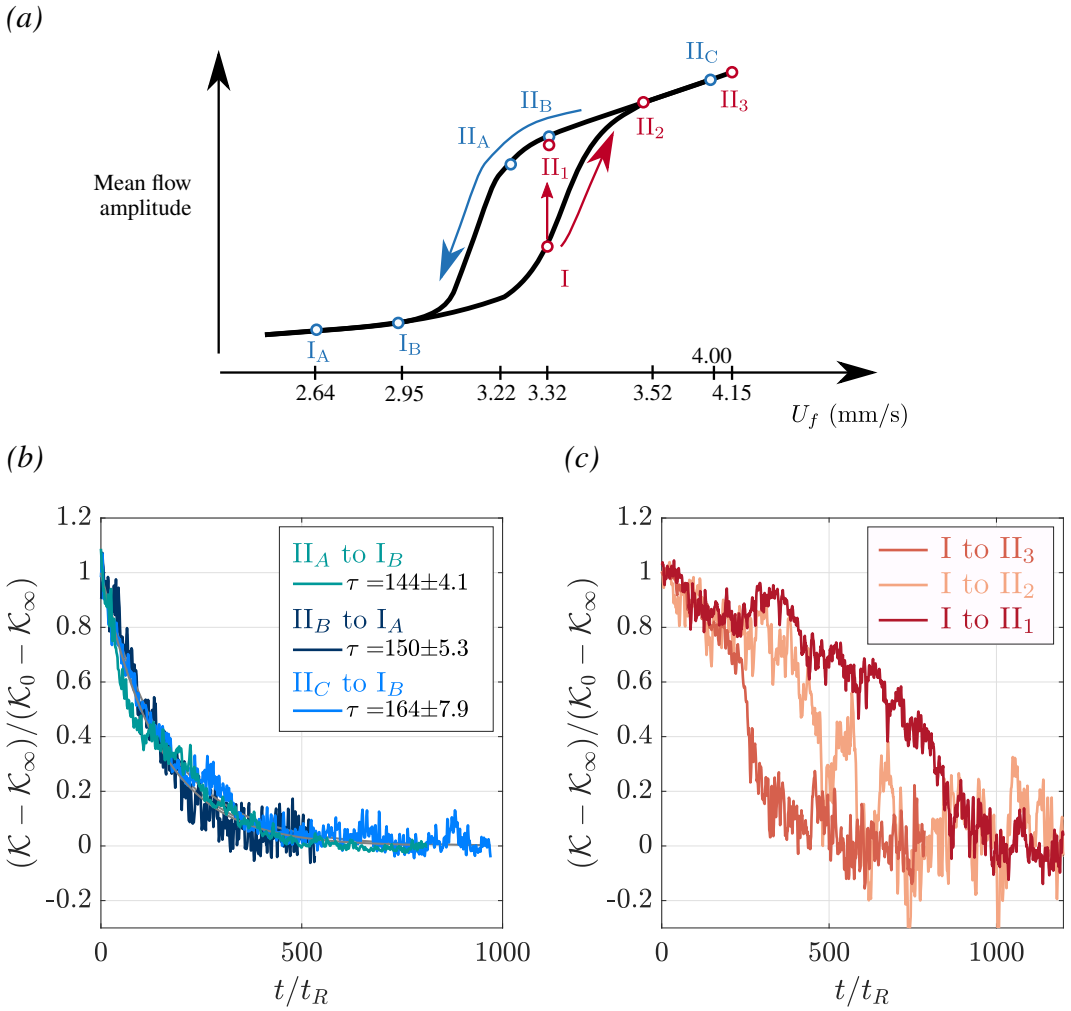

Figure 3.9. – Evolution of the total kinetic energy $\mathscr{K}$ during transitions from regime I → II (red curves) and II → I (blue curves). The normalized total kinetic energy is plotted as a function of time in units of rotation period. (*a*) Qualitative location of the transitions on the hysteresis loop. (*b*) Transitions from II→I. The time is initialized at the moment when the forcing was changed from a super-critical one to a sub-critical one. The normalized kinetic energy decays on a timescale τ obtained from an exponential fit (lines). (*c*) Transitions from I→II, starting from the same initial state.

3.4. Theoretical model for the transition: a Rossby waves resonance

The goal of this section is to derive a simple model to explain the transition observed in the experiment, and the associated bistability. To do so, we use the classical quasi-geostrophic (QG) approximation to reduce the experiment to its 2D β-plane analogue (section 1.2.4.3). Because of the fast background rotation, or equivalently the small Rossby number of the system, the geostrophic balance dominates the experimental flow. As a consequence, the flow is quasi two-dimensional. The curvature of the free-surface as well as the friction over the bottom (Ekman pumping) induce three-dimensional effects. Nevertheless, the weakness of these effects allows their incorporation into quasi-two-dimensional physical models. We derive the conventional QG model corresponding to our experimental setup in appendix C, §C.2 and §C.3, "conventional" meaning that we retain only the linear contributions from these 3D effects. Note that in addition to this QG approximation, we make the rigid lid approximation and neglect the temporal fluctuations of the free surface, i.e. we do not take into account gravitational effects at the interface.

We use the cylindrical coordinates (ρ,ϕ,z) with z oriented downward, and $(\boldsymbol{e}_\rho,\boldsymbol{e}_\phi,\boldsymbol{e}_z)$ the corresponding unit vectors (Fig.3.2). We consider the flow of an incompressible fluid of constant kinematic viscosity ν and density ρ_f, rotating around the vertical axis at a constant rate $\boldsymbol{\Omega}=\Omega\,\boldsymbol{e}_z$, with $\Omega>0$ (the turntable rotates in the clockwise direction). The fluid is enclosed inside a cylinder of radius R, and the total fluid height is $h(\rho)$. We denote the velocity field as $\boldsymbol{u}=(u_\rho,u_\phi,u_z)_{\boldsymbol{e}_\rho,\boldsymbol{e}_\phi,\boldsymbol{e}_z}$, and the vertical component of the vorticity is $\zeta=(\boldsymbol{\nabla}\wedge\boldsymbol{u})\cdot\boldsymbol{e}_z=(\partial_\rho(\rho u_\phi)-\partial_\phi u_\rho)/\rho$. As shown in Appendix C.3, under the QG approximation, the experimental flow can be described by the classical 2D barotropic vorticity equation on the β-plane:

$$\underbrace{\frac{\partial\zeta}{\partial t}+u_\rho\frac{\partial\zeta}{\partial\rho}+\frac{u_\phi}{\rho}\frac{\partial\zeta}{\partial\varphi}}_{\text{Advection}}+\underbrace{\beta\,u_\rho}_{\beta-\text{effect}}=\underbrace{-\alpha\zeta}_{\text{Ekman friction}}+\underbrace{\nu\nabla^2\zeta}_{\text{Bulk dissipation}}\quad, \tag{3.15}$$

with β the topographic β parameter resulting from the radial variations of the fluid height and α the linear Ekman friction parameter:

$$\beta = -\frac{f}{h}\frac{\mathrm{d}h}{\mathrm{d}\rho}, \tag{3.16}$$

$$\alpha = \frac{E^{1/2}fh_0}{2h}. \tag{3.17}$$

In this 2D framework, we decompose the velocity into a zonally averaged flow plus fluctuations using the standard Reynolds decomposition:

$$u_\phi=\langle u_\phi\rangle_\phi(\rho,t)+u'_\phi(\rho,\phi,t) = U+u'_\phi, \tag{3.18}$$

$$u_\rho=\langle u_\rho\rangle_\phi(\rho,t)+u'_\rho(\rho,\phi,t) = u'_\rho, \tag{3.19}$$

$$\zeta=\langle\zeta\rangle_\phi(\rho,t)+\zeta'(\rho,\phi,t) = \frac{1}{\rho}\frac{\partial(\rho U)}{\partial\rho}+\zeta'. \tag{3.20}$$

where $\langle\cdot\rangle_\phi=\frac{1}{2\pi}\int_0^{2\pi}\cdot\,\mathrm{d}\phi$ is the zonal mean. Here, we neglect the $O(E^{1/2})$ mean radial velocity associated with the Ekman pumping, consistently with the choice of keeping only the linear Ekman friction term (see for example the discussion in Sansón et al. 2000, and compare with the full equation derived in Appendix C.4.4). The zonal average of the azimuthal component of the Navier-Stokes equation (equation (C.2)) leads to the zonal mean zonal flow evolution

equation

$$\frac{\partial U}{\partial t} = \underbrace{-\left\langle u'_\rho \frac{\partial u'_\phi}{\partial \rho} + \frac{u'_\rho u'_\theta}{\rho} \right\rangle_\phi}_{\mathscr{R}(\rho,t)} + \mathscr{D}(\rho,t), \tag{3.21}$$

where $\mathscr{D}$ contains both the frictional and bulk dissipation of the zonal flow. Using the zero-divergence of the horizontal velocity, the source term $\mathscr{R}$ can be expressed as the divergence of the Reynolds stresses, or equivalently as an average vorticity flux

$$\mathscr{R}(\rho,t) = -\frac{1}{\rho^2}\frac{\partial \langle \rho^2 u'_\rho u'_\phi \rangle_\phi}{\partial \rho} = -\langle u'_\rho \zeta' \rangle_\phi. \tag{3.22}$$

Hence, the zonal flow evolution equation

$$\frac{\partial U}{\partial t} = \mathscr{R}(\rho,t;U) + \mathscr{D}(\rho,t;U), \tag{3.23}$$

shows that in the absence of direct forcing, the zonal flow requires a source term which is provided through the Reynolds stresses divergence, alternatively called the eddy momentum flux. To explain the generation of the zonal flow in our experiment, this momentum flux $\mathscr{R}$ needs to be modelled. The Reynolds stresses are likely to be influenced by the zonal flow U that they generate through a feedback mechanism. Determining whether the feedback of the zonal flow on the source term $\mathscr{R}$ is positive or negative would allow us to investigate the possibility of bistability. This is the goal of the present section.

We follow the same approach as in Herbert et al. (2020) which focuses on transition to super-rotation based on the mechanism described by Charney et al. (1979) in the framework of topographically forced zonal flows in the midlatitude atmosphere (see also Pedlosky 1981; Held 1983; Weeks et al. 1997; Tian et al. 2001). We determine the Reynolds stresses divergence $\mathscr{R}$ by computing the linear response to a stationary forcing on a β-plane with a background zonal flow. We show that the resulting Reynolds stresses exhibit a resonant amplification leading to a possible bistability. We finally compare this mechanism with the experimental observations.

3.4.1. Linear model for the Reynolds stresses

In this section, we determine the Reynolds stresses divergence $\mathscr{R}$ and the feedback of the zonal flow onto them. To do so, we compute the linear response to a stationary forcing on the β- plane, in the presence of a background zonal flow U. Besides, we adopt a local approach by assuming a length scale separation between the wavelength of the forcing and the spatial variations of the zonal flow. We also assume homogeneity by considering an infinite fluid domain in both directions. This approach allows us to

- forget about the geometrical effects inherent to the cylindrical geometry and work in equivalent 2D local cartesian coordinates (x,y), as represented in Fig.3.2;
- assume that the background flow U is constant in (x,y), which is only true locally, inside of a single jet.

For the basis $(\boldsymbol{e}_x, \boldsymbol{e}_y, \boldsymbol{e}_z)$ to be direct, with $\boldsymbol{e}_z$ downward and $\boldsymbol{e}_x$ zonal, in the same direction as $\boldsymbol{e}_\phi$, $\boldsymbol{e}_y$ has to be oriented towards the axis of rotation (Fig.3.2). We denote $\boldsymbol{u} = (u,v)_{\boldsymbol{e}_x,\boldsymbol{e}_y}$ the 2D cartesian velocity components, and $\zeta = \partial_x v - \partial_y u$ the associated vorticity. The β-plane

barotropic vorticity equation (3.15) reduces to

$$\frac{\partial \zeta}{\partial t} + u\frac{\partial \zeta}{\partial x} + v\frac{\partial \zeta}{\partial y} + \beta v + \alpha\zeta = \nu\nabla^2\zeta + q(x,y), \tag{3.24}$$

with $\alpha = E^{1/2} f/2$ locally constant and

$$\beta = -\frac{f}{h}\frac{\mathrm{d}h}{\mathrm{d}y}. \tag{3.25}$$

Note that in this cartesian framework β is now positive ($\mathrm{d}_y h < 0$). We have added an arbitrary stationary forcing $q(x,y)$ representing a vorticity source. We linearise this equation around a uniform background zonal flow $\boldsymbol{U} = U\,\boldsymbol{e}_x$ by setting $\boldsymbol{u} = \boldsymbol{U} + \boldsymbol{u'}$ with $\|\boldsymbol{u'}\| \ll \|\boldsymbol{U}\|$. Keeping only first order terms, we obtain

$$\frac{\partial \zeta'}{\partial t} + U\frac{\partial \zeta'}{\partial x} + \beta v' + \alpha\zeta' = \nu\nabla^2\zeta' + q(x,y). \tag{3.26}$$

We drop the primes in the following and define the streamfunction ψ ($u = -\partial_y\psi$, $v = \partial_x\psi$ and $\zeta = \nabla^2\psi$) such that

$$\frac{\partial}{\partial t}\nabla^2\psi + U\frac{\partial}{\partial x}\nabla^2\psi + \beta\frac{\partial \psi}{\partial x} + \alpha\nabla^2\psi - \nu\nabla^2\nabla^2\psi = q(x,y). \tag{3.27}$$

We perform a spatial Fourier transform of this equation in both x and y leading to

$$\frac{\partial \hat{\psi}}{\partial t} + [\,\mathrm{i}\,\omega(k,l) + \omega_E(k,l)\,]\,\hat{\psi} = -\frac{\hat{q}(k,l)}{k^2+l^2}, \tag{3.28}$$

where $\hat{\psi}$ and $\hat{q}$ are the Fourier coefficients associated with ψ and q, and $\boldsymbol{k} = (k,l)_{\boldsymbol{e}_x,\boldsymbol{e}_y}$ the wave vector. We denote ω the Rossby waves angular frequency, Doppler-shifted by the advection by the zonal flow

$$\omega(k,l) = kU - \frac{k\beta}{k^2+l^2}, \tag{3.29}$$

(see section 1.2.4.5) and ω_E the damping rate due to the viscous dissipation in the bulk and the bottom friction

$$\omega_E(k,l) = \alpha + \nu(k^2+l^2). \tag{3.30}$$

Note that there is no gravity effects (or deformation radius) in the Rossby waves dispersion relation because we make the rigid lid approximation. The solution to equation (3.28) with the initial condition $\hat{\psi}(k,l,t=0) = 0$ is

$$\hat{\psi}(k,l,t) = \frac{-\hat{q}(k,l)}{(k^2+l^2)(\mathrm{i}\omega(k,l) + \omega_E)}\left[1 - e^{-(\mathrm{i}\omega+\omega_E)t}\right]. \tag{3.31}$$

The inverse Fourier transform $\mathscr{F}^{-1}$ of ψ can be computed numerically to retrieve the physical streamfunction ψ at a time t for a given forcing. Similarly, the vorticity and velocity components can be computed using

$$\begin{cases} \zeta(x,y,t) = \mathscr{F}^{-1}\left(-(k^2+l^2)\,\hat{\psi}(k,l,t)\right), \\ u(x,y,t) = \mathscr{F}^{-1}\left(-\mathrm{i}l\,\hat{\psi}(k,l,t)\right), \\ v(x,y,t) = \mathscr{F}^{-1}\left(\mathrm{i}k\,\hat{\psi}(k,l,t)\right). \end{cases} \tag{3.32}$$

The Reynolds stresses term $\mathscr{R}(y,t;U)$ is then easily computed as

$$\mathscr{R}(y,t;U) = -\frac{\partial}{\partial y}\langle uv\rangle_x = \langle v\zeta\rangle_x. \tag{3.33}$$

The sign difference in the second equality compared to expression (3.22) in cylindrical coordinates comes from $\boldsymbol{e}_y$ pointing inward whereas $\boldsymbol{e}_\rho$ is pointing outward.

3.4.2. Comparison of the linear model with experimental results

To confirm that the reduced QG approximation is an appropriate model for the experiment, we compare the linear solution that we just derived with the very beginning of experiments where only one forcing ring is turned on. Note that a good agreement is expected since in our experiments, the local Rossby number is very small, $Ro_\zeta = \zeta/f \ll 1$ (Table 3.1), which is the main assumption of the QG approximation. To carry this comparison, we first set all the model parameters to the experimental ones, that is

$$\begin{cases} \beta = -\dfrac{f}{h}\dfrac{\mathrm{d}h}{\mathrm{d}y} \sim 50\ \mathrm{m\,s^{-1}}, \\ \alpha = \frac{1}{2} f E^{1/2} \sim 5.6\times 10^{-3}\ \mathrm{s^{-1}}, \\ U = 0\ \mathrm{m\,s^{-1}}. \end{cases} \tag{3.34}$$

When the pump is activated, the fluid is at rest in the rotating frame (solid body rotation). In addition, we design the forcing term to mimic the experimental forcing on the chosen ring: for the third ring, it corresponds to a line of 18 vortices (9 cyclones and 9 anticyclones) regularly spaced onto a perimeter of $2\pi R_3 \approx 0.688$ m. We chose to represent each vortex by a Gaussian source of vorticity:

$$q(x,y) = q_m \sum_{i=1}^{18} (-1)^i \exp\left(-\frac{(x-x_i)^2+(y-y_i)^2}{r_v^2}\right), \tag{3.35}$$

with q_m the forcing amplitude, r_v the radius of the vortices and (x_i, y_i) the centre location of each vortex. The vortices' radius is set to 2/5 times the spacing between two vortices based on the experimental measurements. To estimate the forcing amplitude q_m that we should use to better represent the experimental regime, we measure the vorticity linear growth rate above the forcing injection points and adjust q_m so that the growth rate obtained with the linear model is comparable to the experimental one. This method leads us to use $q_m = 0.5\ \mathrm{s^{-2}}$.

Fig.3.10 shows a comparison between an experiment and the linear model, two seconds after the third forcing ring was turned on at its maximum power. The experimental flow and the linear solution are qualitatively and quantitatively very close. They both exhibit a westward stretching of each vortex, westward meaning in the retrograde direction compared to the background rotation (decreasing ϕ in the experiment, decreasing x in the cartesian model). The dispersive nature of the Rossby waves emitted by the vortex are responsible for this chevron pattern pointing eastward, as explained by Firing et al. (1976) and Chan et al. (1987) in the case of isolated vortices. In particular, the long Rossby waves which propagate westward faster than short waves are responsible for the westward stretching. This response can also be understood as the deformation of each vortex into a so-called β-plume. Stommel (1982) first described β-plumes when trying to understand the circulation induced by rising water from hydrothermal vents in the Pacific, and his theory was further developed by Davey et al. (1989) who considered the evolution of buoyancy sources on a β-plane. In both cases, the convergence or divergence of fluid around the perturbation generates cyclonic or anticyclonic motions which are subsequently elongated westward due to the emission of Rossby waves

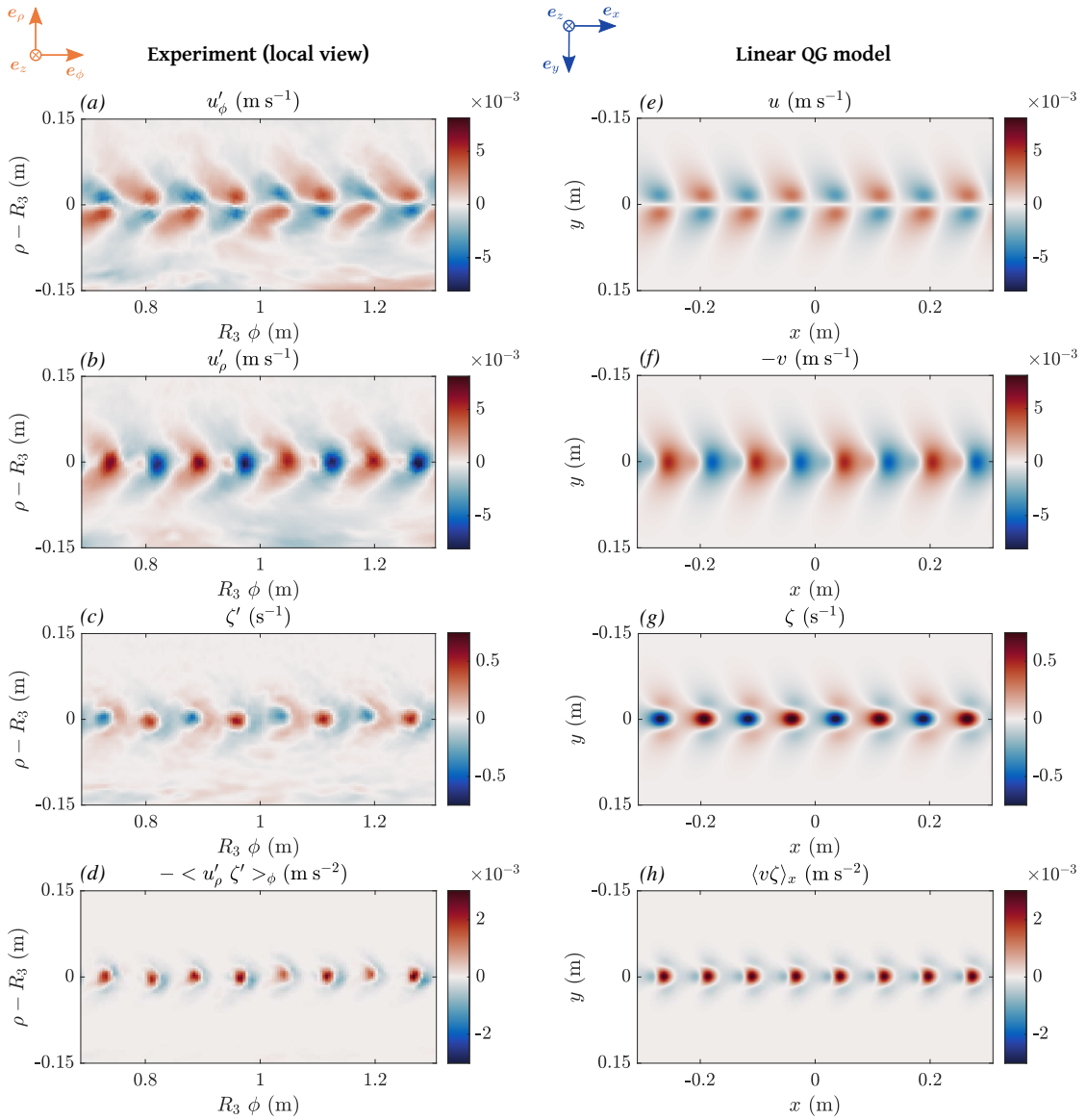

Figure 3.10. – Comparison between the experimental flow and the linear QG model. (*a–d*) Experimental flow measured 2 seconds after the third forcing was turned on. The experimental data, originally obtained in a cylindrical geometry, is remapped for the sake of comparison with our cartesian model. R_3 is the radius of the third forcing ring. Only 8 vortices are visualized, but the third ring contains 18 vortices. (*e–h*) Solution of the linear model (equation (3.31)) at time $t = 2$ s. The model parameters (α, β, q_m, k_f and U) are estimated from the experimental parameters. (*a,e*) Zonal velocity perturbation. (*b,f*) Radial velocity perturbation (note that u_ρ should be compared with $-v$). (*c,g*) Vorticity. (*d,h*) Reynolds stresses divergence (zonal flow acceleration).

(see the review and experiments by Afanasyev et al. (2019)). As a consequence, an east-west asymmetry in the radial component develops, which is clear in Fig.3.10(*b,f*): the advection of the background potential vorticity leads to a weakening of the flow on the west (left) side of each vortex, and a strengthening on their east (right) side, for both cyclones and anticyclones. More interesting for us is the fact that the emission of Rossby waves leads to a prograde momentum convergence towards the region of generation of the vortices as demonstrated by Fig.3.10(*d,h*). Fig.3.11 directly compares the Reynolds stresses divergence profile in the experiment and in the linear solution: the agreement is quantitative. There is indeed an eastward acceleration of the zonal flow in the forcing region, located between two westward acceleration regions. This mechanism thus explains the experimental regime I, i.e. the formation of prograde jets flanked by two retrograde jets above each forcing ring. Vallis (2017, chapter 12) provides an overview of the mechanism of zonal flow acceleration by Rossby waves radiation in the framework of barotropically forced surface westerlies in the atmosphere. Our experiment shows that this mechanism is robust since the generated prograde jets persist at later times, even in the non-linearly saturated regime.

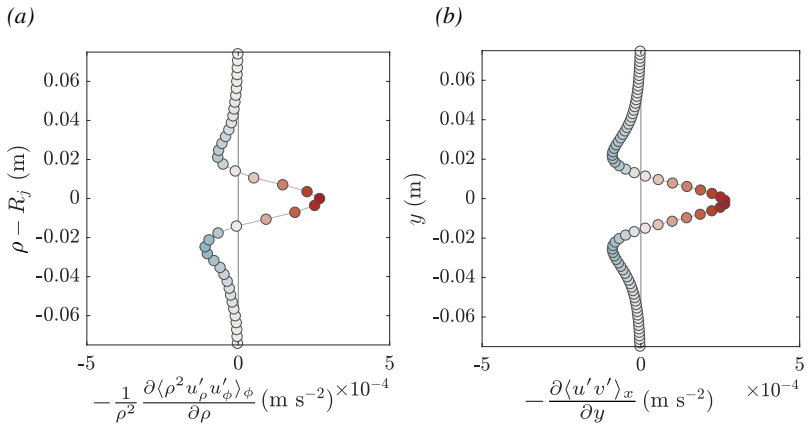

Figure 3.11. – Comparison of the Reynolds stresses divergence between the experiment and the linear model solution. (*a*) Experimental Reynolds stresses divergence (equation (3.22)). (*b*) Reynolds stresses divergence computed from the linear model (equation (3.33)). Both the experiment and the linear model show the generation of a prograde jet at the forcing location, flanked with two retrograde jets.

3.4.3. Resonance of the Reynolds stresses and associated feedback

The previous section shows that our experiment can be successfully described by a linear 2D QG model incorporating only the β-effect and the bottom friction, at least in regime I. We can thus use this model to investigate the feedback that the zonal flow can have on the Reynolds stresses divergence $\mathscr{R}$ and study the possibility of bistability. This is the goal of the present section.

For simplicity, we now forget about the specific geometry of the experimental forcing, and use a generic forcing consisting of a doubly-periodic array of vortices with a wavelength comparable to the experimental one:

$$q(x,y) = q_m \cos(k_f x)\cos(l_f y), \tag{3.36}$$

with $q_m = 0.5$ s^{-2} the forcing amplitude and $k_f = l_f$ the forcing wavenumber. In the following, we work with $k_f = 63$ rad m^{-1} corresponding to a typical forcing wavelength of 10 cm. We show later that the forcing scale has only a small influence on the physical mechanism presented (Fig.3.15). The linear response obtained with this forcing is the superposition of the response to each forcing line, with a prograde acceleration above each forcing horizontal line, and

retrograde accelerations in between.

To study the feedback of the zonal flow, we solve for the stationary linear response to this forcing (equation (3.31) with $t \to +\infty$) for various amplitudes of the background zonal flow U. We recall the local nature of our analysis: the background zonal flow U should be seen as the – uniform – zonal flow at the core of a jet. For each solution, we extract the streamfunction amplitude $|\hat{\psi}|$ and the Reynolds stresses divergence at $y = 0$, and represent them in Fig.3.12 as a function of the zonal flow U. Given the amplitude of the streamfunction

$$|\hat{\psi}| = \frac{q_m}{k_f^2 + l_f^2} \left(\omega(k_f, l_f)^2 + \omega_E(k_f, l_f)^2\right)^{-1/2}, \tag{3.37}$$

we expect a resonance of the linear response when $\omega = 0$, or, in other words, when the directly forced Rossby waves are stationary because the zonal flow velocity exactly cancels their phase speed:

$$U = \frac{\beta}{k_f^2 + l_f^2} = -c \tag{3.38}$$

where c is the directly forced Rossby waves phase speed in the absence of zonal flow (see section 1.2.4.5). The resonant amplification of the response amplitude is illustrated in Fig.3.12(a). Then, the amplitude of the Reynolds stresses is expected to be proportional to the squared amplitude of the streamfunction (equations (3.32) and (3.33)), leading to

$$|\mathscr{R}|(U) \propto |\hat{\psi}|^2 \propto \frac{1}{\omega^2 + \omega_E^2} \propto \frac{1}{\left(1 + \frac{U}{c}\right)^2 + \gamma^2}, \tag{3.39}$$

where γ is a nondimensional parameter characterizing the Rossby waves damping

$$\gamma^2 = \left(\frac{\omega_E}{k_f c}\right)^2. \tag{3.40}$$

For the problem to be analytically tractable, we chose to model the resonant curve $\mathscr{R}(U)$ plotted in Fig.3.12(b) with a parametrized Lorentzian. We thus forget about the spatial structure of the momentum flux convergence, and only focus on the global amplitude by setting

$$\mathscr{R}(U) = \mathscr{R}_m \frac{1}{\gamma^2 + \left(1 + \frac{U}{c}\right)^2}. \tag{3.41}$$

Doing so, we focus on the amplitude of the response rather than on the details due to our particular choice of forcing. The important physical effects of the zonal flow, the β-effect and the friction, are contained in the Lorentzian and influence the position and flatness of the resonant peak. Figure 3.12(b) shows that the amplitude of the Reynolds stresses is indeed largely dominated by this resonant amplification. Hence, we do not loose any important feature by modelling $\mathscr{R}$ with equation (3.41) which has the advantage of making the problem analytically simple.

It is now clear that the momentum flux can lead to abrupt transitions: on the left side of the resonant peak, any increase of a zonal flow U leads to an increased prograde momentum convergence, and an increased acceleration of this zonal flow. We have thus identified a potential positive feedback mechanism, provided that it is not cancelled by the negative feedback of the viscous dissipation. Note that since the Rossby waves propagate in the westward direction, this resonance can only occur in an eastward jet ($U > 0$).

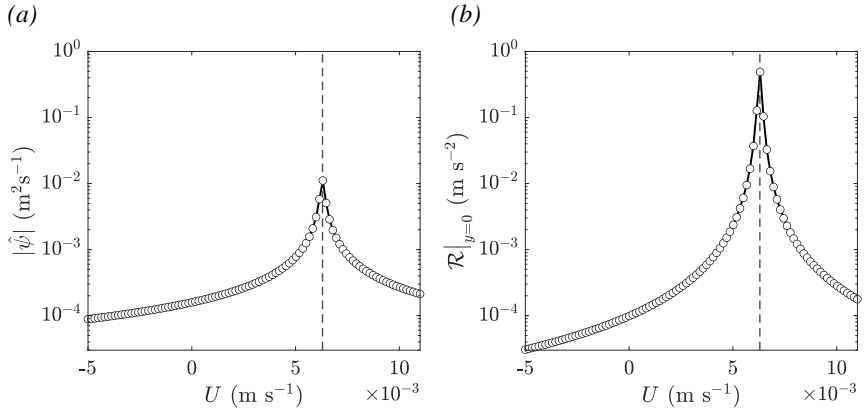

Figure 3.12. – (*a*) Stream-function amplitude as a function of the background zonal flow U. Each symbol is a solution of the linear model with a different background zonal flow. The black line is the corresponding analytical amplitude in the case of a doubly-periodic forcing (equation (3.37)). (*b*) Reynolds stresses at $y = 0$ as a function of the background zonal flow U. Each symbol is a solution of the linear model with a different background zonal flow. The black line represents the best fit of the Lorentzian given by equation (3.41) where the amplitude $\mathscr{R}_m$ is a free parameter. In both panels, the vertical dashed black line shows the location of $U = -c$ where c is the forced Rossby wave phase speed (equation (3.38)).

3.4.4. Stationary solutions and linear stability

The linear QG model showed the resonant amplification of the wave-induced Reynolds stresses when the zonal flow is such that the directly forced Rossby waves are stationary. Our goal is now to verify whether this feedback of the zonal flow can explain the transition and bistability observed in our experiment.

Consistently with our local approach, we consider a minimal model where the zonal flow $U(t)$ is assumed to be only time-dependent, with no spatial modulation. Such a uniform zonal flow is sustained by the Reynolds stresses divergence $\mathscr{R}$ and dissipated by the linear friction due to the Ekman pumping:

$$\frac{\partial U}{\partial t} = \mathscr{R}(U) - \alpha U, \tag{3.42}$$

with $\mathscr{R}(U)$ the Lorentzian given by equation (3.41). The stationary solutions of this equation are the roots of the third-order polynomial

$$P(U) = U^3 + 2c\,U^2 + (1+\gamma^2)c^2\,U - \frac{\mathscr{R}_m c^2}{\alpha}. \tag{3.43}$$

Depending on the sign of the discriminant of P, one or three stationary solutions can exist, as represented in Fig.3.13. We denote U_1, U_2 and U_3 those three solutions such that $U_1 < U_2 < U_3$. For three stationary solutions to exist, i.e. bistability to be possible, a necessary but not sufficient condition is

$$\gamma^2 < \frac{1}{3}. \tag{3.44}$$

When this condition is satisfied, the sufficient condition for three solutions to exist is that

$$\mathscr{R}_m \in [\mathscr{R}_1, \mathscr{R}_2] = -\frac{2}{27}\alpha c\left[9\gamma^2 + 1 - \sqrt{\Gamma},\ 9\gamma^2 + 1 + \sqrt{\Gamma}\right], \tag{3.45}$$

with $\Gamma = \left(1 - 3\gamma^2\right)^3$. Physically, the first condition (3.44) means that bistability can never exist if the Rossby waves are too strongly damped. The second condition shows that even when the friction is not too high, three stationary solutions exist only for a given range of the forcing amplitude $\mathscr{R}_m$. As represented in Fig.3.13, if the forcing is too high, only the super-resonant

solution U_3 exists. Conversely, if the forcing is too weak, only the low-amplitude sub-resonant solution U_1 can exist.

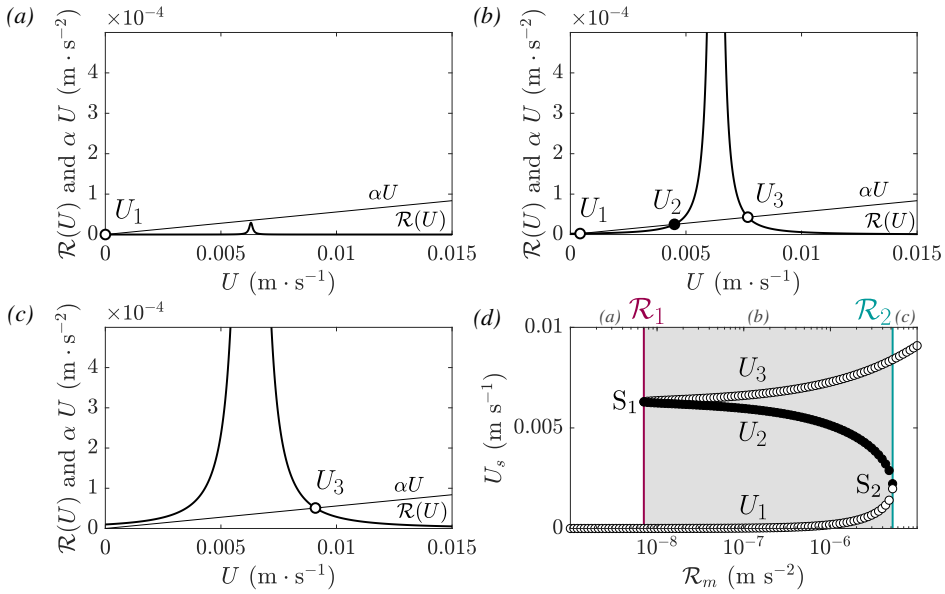

Figure 3.13. – Visualization of the stationary solutions (U_1, U_2, U_3) of the zonal flow evolution equation (3.42). Except the forcing amplitude, all the parameters are fixed and equal to the experimental parameters ($\alpha = 5.6 \times 10^{-3}$ s^{-1}, $k_f = l_f = 63$ rad m^{-1}, $c = 6.3 \times 10^{-3}$ m s^{-1}, $\gamma^2 = 1.99 \times 10^{-4}$). (*a*) Illustrative case of a small forcing amplitude $\mathscr{R}_m < \mathscr{R}_1$ and a small friction *or* a too high friction. Note that U_1 is very small, but not zero. (*b*) Illustrative case of a forcing in the range $\mathscr{R}_m \in [\mathscr{R}_1, \mathscr{R}_2]$ *and* a small friction. (*c*) Illustrative case of a high forcing amplitude $\mathscr{R}_m > \mathscr{R}_2$ *and* a small friction. (*d*) Amplitude of the three stationary solution as a function of the forcing amplitude $\mathscr{R}_m$. The black dots represent the unstable solution whereas the white ones are stable. The shaded area is the bistable range, bounded by $\mathscr{R}_1$ and $\mathscr{R}_2$ (equation 3.45).

To investigate the linear stability of the stationary solutions, we go back to the zonal flow evolution equation (3.42). We linearise the nonlinear operator $\mathscr{R}$ around the stationary state U_s and denote $U'(t) = U(t) - U_s$ the perturbed zonal flow, to obtain the perturbations evolution equation

$$\frac{\partial U'}{\partial t} = \frac{\mathrm{d}\mathscr{R}}{\mathrm{d}U}\Big|_{U_s} U' - \alpha U'. \tag{3.46}$$

We seek U' under the form $U' = U'_0\, e^{\sigma t}$ where σ is the growth rate of the perturbation. Substituting into equation (3.46) leads to

$$\sigma = \frac{\mathrm{d}\mathscr{R}}{\mathrm{d}U}\Big|_{U_s} - \alpha. \tag{3.47}$$

The stationary solution U_s is unstable if and only if the growth rate $\sigma > 0$. This condition is always verified for the second stationary solution U_2 (the sub-resonant one), whereas U_1 and U_3 are stable stationary solutions.

We plot in Fig.3.13(*d*) the amplitude of the stationary solutions obtained for varying forcing amplitudes $\mathscr{R}_m$, all the other parameters being fixed and equal to the experimental parameters ($\alpha = 5.6 \times 10^{-3}$ s^{-1}, $k_f = l_f = 63$ rad m^{-1}, $c = 6.3 \times 10^{-3}$ m s^{-1}, $\gamma^2 = 1.99 \times 10^{-4}$). The three stationary solutions branches are visible, and coexist only in a given range of forcing amplitude bounded by $\mathscr{R}_1$ (purple line) and $\mathscr{R}_2$ (blue line) given by equation (3.45). This figure also demonstrates the bistability and possibility of an hysteresis: for an experiment with increasing forcing, the transition $U_1 \to U_3$ happens for $\mathscr{R}_m = \mathscr{R}_2$. At this forcing, there is a saddle-node bifurcation (S$_2$) through which U_1 loses its stability. But if the forcing amplitude is then decreased, the observed solution will remain U_3 until the forcing reaches $\mathscr{R}_1 < \mathscr{R}_2$ where there is another saddle-node

bifurcation (S_1), and the system goes back to the lower branch solution U_1. Our model predicts that with the experimental parameters and close to the transition, the amplitude of the zonal flow on the lower branch is of $U \approx 2$ mm s^{-1}, and $U \approx -c = 6.3$ mm s^{-1} for the upper branch. Finally, this model allows us to define a typical velocity expected at the transition, to compare with the forcing rms velocity U_f used to characterize the experimental hysteresis, on Fig.3.8. From equation (3.45), the Reynolds stresses at the transition are typically of $\mathscr{R}_{m,t} \sim \alpha|c|(1+9\gamma^2)$. A typical transition velocity can be obtained supposing that the forcing is balanced by friction $U_t \sim \mathscr{R}_{m,t}/\alpha$, leading to

$$U_t \sim |c|(1+9\gamma^2). \tag{3.48}$$

If we use $U_f^* = U_f/U_t$ as a non-dimensional forcing, then the transition should always occur at U_f^* of order unity. The dependence on the β-effect, the friction, and the forcing scale are incorporated in c and γ. Note that the width of the bistable zone will however vary depending on γ.

3.4.5. Comparison of the experimental to theoretical transition

In this section, we report additional experimental observations that support the mechanism of Rossby waves resonance to account for the transition between regimes I and II.

First, the amplitudes of the zonal flow expected in the two steady states, $U_1 \approx 2$ mm s^{-1}, and $U_3 \approx -c = 6.3$ mm s^{-1}, are very close to the experimental ones, where U_1 represents regime I and U_3 regime II, as can be seen in Fig.3.8. Another way to see it is by comparing the zonal flow amplitude with the phase speed of the – non-advected – directly forced Rossby waves: if the zonal jet is faster than $-c$, the system is in the super-resonant steady state, whereas if it is lower than $-c$, the system is sub-resonant. In the experimental setup, with $k_f \approx 63$ rad m^{-1} and $\beta \approx 50$ m^{-1} s^{-1}, the phase speed of the directly forced Rossby waves is $c \approx -6.3$ m s^{-1}, without advection. First, Fig.3.14 demonstrates that the forcing indeed excites Rossby waves. The radial component of the velocity at a given radius exhibits patterns that move in the retrograde direction (i.e. decreasing ϕ), with the same wavelength as the forcing and at the Doppler-shifted speed $\langle u_\phi \rangle_\phi + c$. Then, given this typical phase speed c, Fig.3.8 shows that in regime I the experimental zonal flow is sub-resonant ($\overline{u}_{\rm rms} < -c$), and super-resonant in regime II ($\overline{u}_{\rm rms} > -c$), which is consistent with our model. Furthermore, the model predicts that when the forcing is decreased and U_3 (regime II) loses its stability (S_2 in Fig.3.13(d)), the zonal flow is quasi-resonant ($\langle u_\phi \rangle_\phi \approx -c$) which is again compatible with the measured velocity at the transition II→I in Fig.3.8. Note that if this equilibrium close to resonance can exist (U_3), our analysis only gives an explanation for its origin, ultimately, the non-linearities are responsible for locking the system into a near-resonant state. Note finally that the bistability range and zonal flow amplitudes are only slightly varying with the range of possible forcing wavenumbers for our experiment (Fig.3.15(b)). For a closer match between the predicted zonal flow amplitudes and the measured ones, we would choose $k_f = 57$ rad m^{-1}, which is reasonable given the uncertainty in the relevant forcing scale in our setup.

Second, we have not yet discussed the inherent asymmetry between the prograde and the retrograde jets in our model. Since the Rossby waves propagate in the retrograde direction, their only way to become stationary and resonate with the fixed forcing is within a prograde jet. This implies that the transition only occurs in the prograde jets which is again consistent with our experimental observations. Indeed, the prograde jets govern the dynamics, by increasing in amplitude and merging, whereas the retrograde flow seems to adjust passively to the transition (see e.g. Fig.3.7). If we suppose that the forcing imparts no net angular momentum to the fluid, then the integral of the angular momentum per unit mass, $\rho(u_\phi + \Omega\rho)$, over the domain should be constant. If an eastward acceleration is produced by the transition, then this convergence of

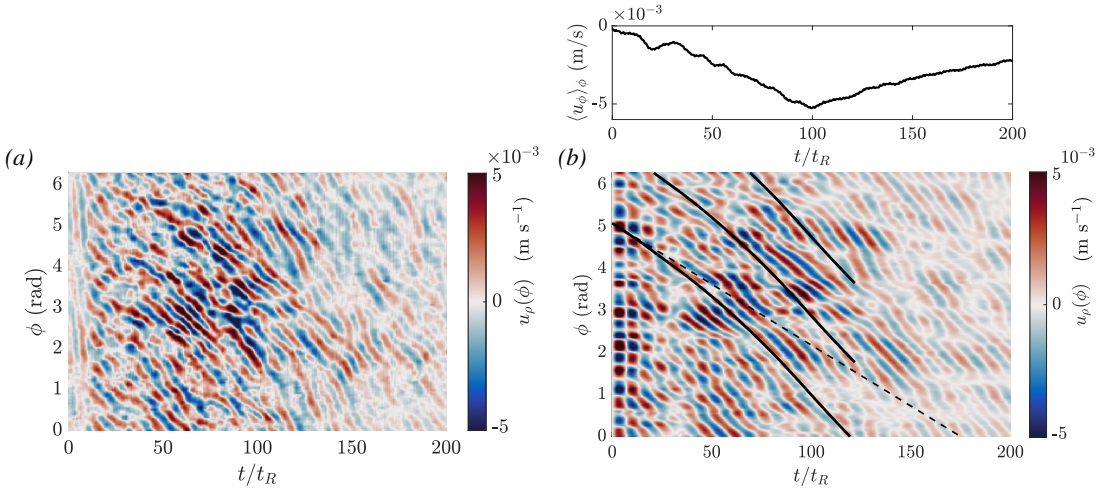

Figure 3.14. – Rossby waves excited by the forcing. The third forcing ring ($R_3 = 0.214$ m) is turned on at its maximum power from time $t = 0$ to 75 t_R. (*a*) Time evolution of the radial component of the velocity at a fixed radius $\rho = 0.17$ m. (*b*) Same data band-passed filtered between 0.06 and 0.12 Hz. The slope of the dashed line is the non Doppler shifted phase speed of the Rossby waves excited by the forcing (equation 3.38) $c \approx -6.3$ mm s^{-1}. The slope of the continuous line is the Doppler shifted phase speed $\langle u_\phi \rangle_\phi + c$. It increases in absolute value since the zonal flow increases when the forcing is turned on, and at the chosen radius the flow is retrograde, as represented on the top panel.

prograde angular momentum should be balanced by negative angular momentum elsewhere (see the Reynolds stresses profile in Fig.3.11). The retrograde flows in our experiment seem to arise as such, which is consistent with the fact that the retrograde flow is smooth whereas the prograde one strongly interacts with vortices (Fig.3.4).

Third, our model implies that the faster the Rossby waves, the stronger the forcing will have to be to reach the transition (increasing U_t), and conversely for slower Rossby waves. Changing the β-effect is thus a good way of challenging our model. We performed experiments at 80 RPM and 60 RPM (not shown) instead of the 75 RPM for which the bottom plate was designed. In these experiments, β is no longer uniform, but slightly varying with radius (see Fig.B.10). It is higher at 80 RPM due to the increased curvature of the free-surface ($\beta_{80} \in [57, 73]$ m^{-1} s^{-1} with a mean at 65.5 m^{-1} s^{-1}) and weaker at 60 RPM ($\beta_{60} \in [20, 30]$ m^{-1} s^{-1} with a mean at 22.8 m^{-1} s^{-1}). As a consequence, the forced Rossby waves are respectively faster and slower ($|c| = 8.3$ and 2.9 m s^{-1}). Consistently with our model, we observed that for a similar forcing ($U_f = 4.0$ mm s^{-1}), regime II is obtained at 75 RPM whereas regime I is observed at 80 RPM. Conversely, for a forcing at which regime I is observed at 75 RPM ($U_f = 2.9$ mm s^{-1}), regime II is obtained at 60 RPM. The transition thus occurs at larger forcing amplitudes for an increased β-effect. Fig.3.15*(c)* illustrates more quantitatively the sensitivity to the β-effect.

Finally, we wish to discuss the local aspect of our model relatively to the experiment. Our model only explains the local feedback mechanism inside of a given prograde jet. How the global system responds is a different question. Based on the Rhines scale $L_R \sim (u_{\text{rms}}/\beta)^{1/2}$ (Rhines 1975), where we recall that u_{rms} takes into account all the components of the flow (equation (3.9)), we do expect an increase of the jets width during the transition, since the rms eddy velocity increases. However, our model does not explain why the jets merge during the transition. In the conclusion chapter 7, we propose a possible line of work to build a global scale model incorporating the radial structure of the zonal flow and its feedback on the Rossby waves. In addition, we note that our model does not rule out the possibility of the coexistence of regime I and regime II flows side by side. For instance, the most external forcing ring in our experiment (above C6) has a greater pressure loss because of the number of hoses (38) and it is possible that on this ring, the forcing is never super-resonant. This suggests that *regional*

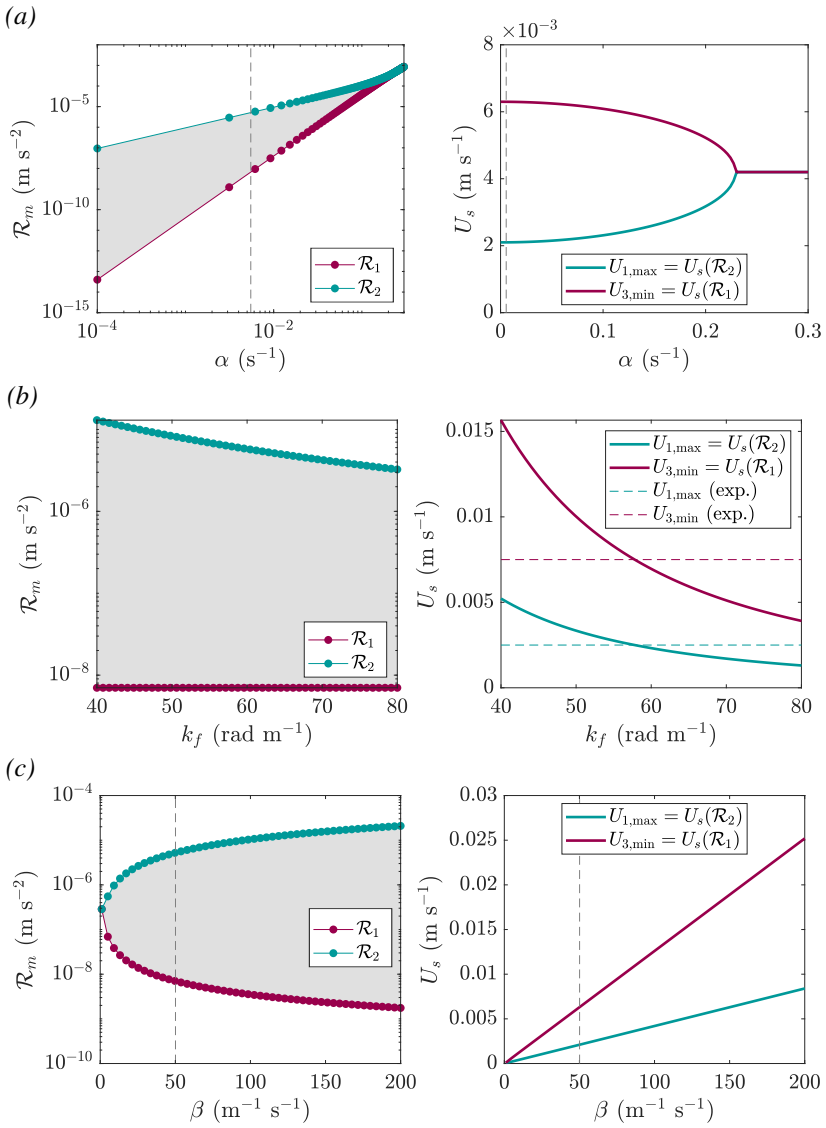

Figure 3.15. – Sensitivity of the width of the bistable zone (left) and the mean flow amplitude at the transition (right) to the model parameters. $\mathscr{R}_1$ and $\mathscr{R}_2$ are respectively the lower and upper limits of the bistable zone, in terms of forcing amplitude (see Fig.3.13). $U_{1,\max}$ and $U_{3,\min}$ are the mean flow amplitude at the saddle-node bifurcation S_2 and S_1 respectively (Fig.3.13).(*a*) Varying friction coefficient α. The vertical dashed line shows the experimental friction. (*b*) Varying forcing wavenumber k_f. The horizontal dashed lines show the mean flow amplitude at the transitions measured experimentally. (*c*) Varying β parameter. The vertical dashed line shows the experimental β.

stable equilibria, where both regimes can be locally sustained in distinct regions of space, may exist. Finally, we observe that the merger events during the transition are associated with a radial shift of the jets leading to an uncorrelation between the jets position and the forcing rings. This further suggest that a local approach will not be sufficient to explain the saturation in regime II. Instead, it may be relevant to adopt a global approach based, for instance, on the turbulent properties and energy transfer of anisotropic turbulence on a β-plane. This type of approach has led to the development of the theory of zonostrophic turbulence (Galperin et al. 2019b, and references therein). Due to its fast rotation and owing to the Taylor-Proudman theorem, the flow is quasi two-dimensional and may bear an inverse turbulent energy cascade. Because of the β-effect and associated Rossby waves, the energy transfer becomes anisotropic and redirected towards zonal currents. Ultimately, the large scale drag halts the expansion of the inverse cascade (Sukoriansky et al. 2002, 2007). Determining whether such a theory is valid to explain the non-linear saturation in regime II is the focus of chapter 4. To conclude, we wish to underline that Cabanes et al. (2017) probably only observed regime II in their experimental setup because their forcing was of larger amplitude than in the present study, thus probably always super-resonant.

3.5. Conclusions and discussion

3.5.1. Robustness of the transition with the forcing pattern: insights from quasi-geostrophic numerical simulations

We previously underlined the local aspect of our model for the transition. As such, it is supposed to only describe what is happening inside of a single jet. In our experiment, the forcing rings are rather decoupled from each other since they are separated by a distance of the same order as the jets spacing. It is not trivial, a priori, to determine if the transition should hold when the forcing is performed at a smaller scale, i.e. significantly smaller than the final scale of the jets. Similarly, does the transition persists when the forcing pattern is cartesian instead of polar? Indeed, with a polar array, all the vortices of a given ring contribute to accelerating a prograde flow at the same radius. With a cartesian pattern, there is no zonal alignment of the forcing sources anymore, and the first regime could be lost, along with the transition. Finally, it would be necessary to explore the effect of the stationarity of the forcing, both in space and time. Addressing these questions is important for planetary relevance where the forcing is presumably at small scale, randomly distributed, fluctuating in time, and probably propagating.

In this subsection, we restrict ourselves to investigating if the transition observed experimentally is due to the fact that our forcing pattern is a polar array, and if it holds at smaller forcing scales. Given the cost of building several bottom plates for the experiment, and the fact that the number of forcing inlets and outlets is already at the edge of what we can be reasonably done manually, we chose to investigate this aspect numerically. In that purpose, we use a quasi-geostrophic numerical code which relies on the exact same hypotheses as described previously for the theoretical QG model, except that we keep higher order terms to account for the parametrized three-dimensional effects (β-effect and Ekman friction). This numerical model is fully described in Appendix C.4. The significant advantage of such a 2D QG numerical model is that it allows us to exactly match the experimental conditions in terms of Reynolds, Rossby and Ekman numbers at a moderate computational cost, such that we can run several simulations over time scales comparable with that of the experiments (thousands of rotation times). This would have been inconceivable using 3D direct numerical simulations.

In a nutshell (see details in Appendix C.4), our QG numerical model solves for the classical

2D barotropic vorticity equation and associated Poisson equation for the streamfunction:

$$\frac{\partial \zeta'}{\partial t'} + \mathscr{J}(q', \psi') - \frac{E_R^{1/2}}{2h'} \boldsymbol{\nabla}' \psi' \cdot \boldsymbol{\nabla}' q' = \frac{E_R}{2} \nabla'^2 \zeta - \frac{E_R^{1/2}}{2h'} \zeta' (\zeta' + 1) + F', \tag{3.49}$$

$$\zeta' = -\frac{1}{h'} \nabla'^2 \psi' + \frac{1}{h'^2} \boldsymbol{\nabla}' h' \cdot \boldsymbol{\nabla}' \psi' + \frac{E_R^{1/2}}{h'^2} \mathscr{J}(h', \psi'). \tag{3.50}$$

All the variables denoted with a prime are non-dimensional using $1/f$ as the time-scale, and R as the length-scale. $\mathscr{J}$ is the non-dimensional Jacobian operator in cylindrical coordinates

$$\mathscr{J}(a, b) = \frac{1}{\rho'} \left(\frac{\partial a}{\partial \rho'} \frac{\partial b}{\partial \varphi} - \frac{\partial b}{\partial \rho'} \frac{\partial a}{\partial \varphi} \right),$$

and we introduced the potential vorticity

$$q' = \frac{\zeta' + 1}{h'}.$$

With our choice of length and time scales, the Ekman number appearing in the vorticity equation is based on the radius instead of the fluid height: $E_R = \nu/(\Omega R^2) = (h_0/R)^2 E$. Equations (3.49)-(3.50) are solved on a polar domain with a no-slip boundary condition for the outer boundary, and a stress-free one for the inner boundary located at an inner radius of 0.05. Details on the numerical method can be found in Appendix C.4. The simulations are performed with the same fluid height profile as in the experiment, $h'(\rho') = h'_{\min} \exp((\beta R/f)\rho')$, and an Ekman number $E_R = 1.25 \times 10^{-7}$. To best reproduce the experimental forcing, the forcing term F' in equation (3.49) consists in Gaussian sources of vorticity of amplitude F'_0 and alternative sign (cyclonic and anticyclonic), distributed on a prescribed and stationary array (see Appendix C.4.3). We tested three different forcing patterns:

— The first one is designed to match the experimental forcing pattern, with 128 inlets and outlets arranged on a polar lattice made of 6 concentric rings ($k'_f = k_f R \approx 42$). The vorticity sources have a radius of 2.23×10^{-2}, corresponding to 1.1 cm in dimensional units.

— The second one is a forcing pattern having a typical scale about half the experimental one ($k'_f = k_f R \approx 90$), but still distributed on a polar lattice (540 inlets and outlets arranged on 12 forcing rings). The vorticity sources have a radius of 1.11×10^{-2}, corresponding to 5.5 mm in dimensional units.

— The third one is similar to the second one, but with vorticity sources arranged on a cartesian pattern instead of a polar one ($k'_f \approx 79$).

Fig.3.16 shows the results of two simulations performed with the forcing aiming at mimicking the experimental one. The two simulations are performed with a low and high forcing amplitudes, $F'_0 = 1 \times 10^{-3}$ and $F'_0 = 6 \times 10^{-3}$, corresponding to 0.25 s^{-2} and 1.48 s^{-2} respectively in dimensional units. The two experimental regimes are retrieved, with a transition between locally and globally forced zonal jets. The first simulation is in regime I, since a prograde jet develops above each forcing ring, and the radial velocity field clearly shows the previously described Rossby waves pattern with an elbow shape directed westward (note that in the QG simulation, the background rotation is anti-clockwise such that the west direction is clockwise, contrary to the experiment). For the second simulation, the observed flow is drastically different, and instead of 6 prograde jets, the final state consists in two intense prograde jets equilibrated at a larger scale. This simulation is thus consistent with regime II. In each case, we note that the vorticity, radial velocity and azimuthal velocity maps match remarkably well the

experimental measurements (compare with Fig.3.6). The different number of jets in regime II might come from the fact that the QG forcing is spatially uniform, whereas in the experiment, the most external rings are less forced because of the increasing pressure drop due to the increasing number of inlets/outlets per ring (see Appendix B).

Fig.3.17 shows the results of two simulations performed with the second forcing pattern, which is again polar but of typical length scale twice smaller than the experimental one. Note that when reducing the forcing scale, we expect that the transition will occur at lower forcing amplitudes, because the forced Rossby waves are propagating slower for decreasing wavelength (equation (3.38)). The first simulation ($F_0' = 5 \times 10^{-4}$) is again in regime I, whereas the second simulation ($F_0' = 5 \times 10^{-3}$) is in regime II, with a final state consisting in three intense prograde jets instead of 12. Finally, Fig.3.18 shows the results of two simulations performed with the third, cartesian forcing pattern, of approximately same length scale as in the polar case discussed previously. Fig.3.18*(a–d)* shows that regime I is indeed recovered with a cartesian forcing pattern: the narrow jets are slightly perturbed by the fact that the forcing inlets and outlets are not aligned anymore, but nevertheless persist and are completely steady. The same simulation performed with a forcing amplitude ten times higher shows the flow organization in regime II (Fig.3.18*(e–h)*). The resulting statistically steady state is similar to what is obtained with a polar array. Interestingly, we note that the cartesian forcing seems to allow for a slow radial drift of the prograde jets, probably because the forcing cannot be strictly equal on both sides of each jet given its cartesian distribution.

These three pairs of simulations show that the existence of two regimes of zonal jets is not sensitive to the detail of the forcing pattern in terms of length scale and distribution. The question of the effect of the stationarity would require further investigation: additional simulations show that a fixed forcing with fluctuating amplitude does not affect the transition. The next step would be to implement a propagating forcing, with a control parameter representing how the forcing is decoupled from the zonal flow, and progressively switch from a fixed forcing to a forcing passively advected by the generated zonal flow. Note that apart from the forcing details, the fact that the transition is fully recovered in these quasi-geostrophic numerical simulations is also a result by itself. First, it provides further justification for basing our theoretical modelling of the transition on a purely quasi-geostrophic framework. Second, we note that the characteristics of the flow in regime II are remarkably close to the experimental ones, in terms of number, position, size and intensity of the jets. Hence, explaining the saturation at a global scale in regime II should again be feasible in a quasi-geostrophic framework where the details of the forcing and three-dimensional dynamics are negligible.

3.5.2. Conclusions and future work

We have described an experimental setup capable of generating robust zonal jets even in the presence of boundary dissipation. In this setup, we observed a subcritical transition between two different steady states with instantaneous zonal flows. In the first regime, obtained for a weak forcing and a moderate local Reynolds number, the jets are steadily forced by prograde momentum convergence towards the eddy-forcing regions, through the indirect action of Reynolds stresses. In the second regime, obtained for a strong forcing and larger Reynolds numbers, the jets merge into higher amplitude zonal flows at a larger scale. While the two regimes are obtained at different Reynolds numbers, they both correspond to low Rossby number QG dynamics. The two regimes coexist in a small forcing range, leading to bistability, and we are able to follow the corresponding hysteresis cycle. The transition is found to arise from the resonance occurring when the forced Rossby waves become stationary because of their advection by the zonal flow. Note that, in the present work, we explain the bistability with the linear resonance mechanism originally explored by Charney et al. (1979), which predicts

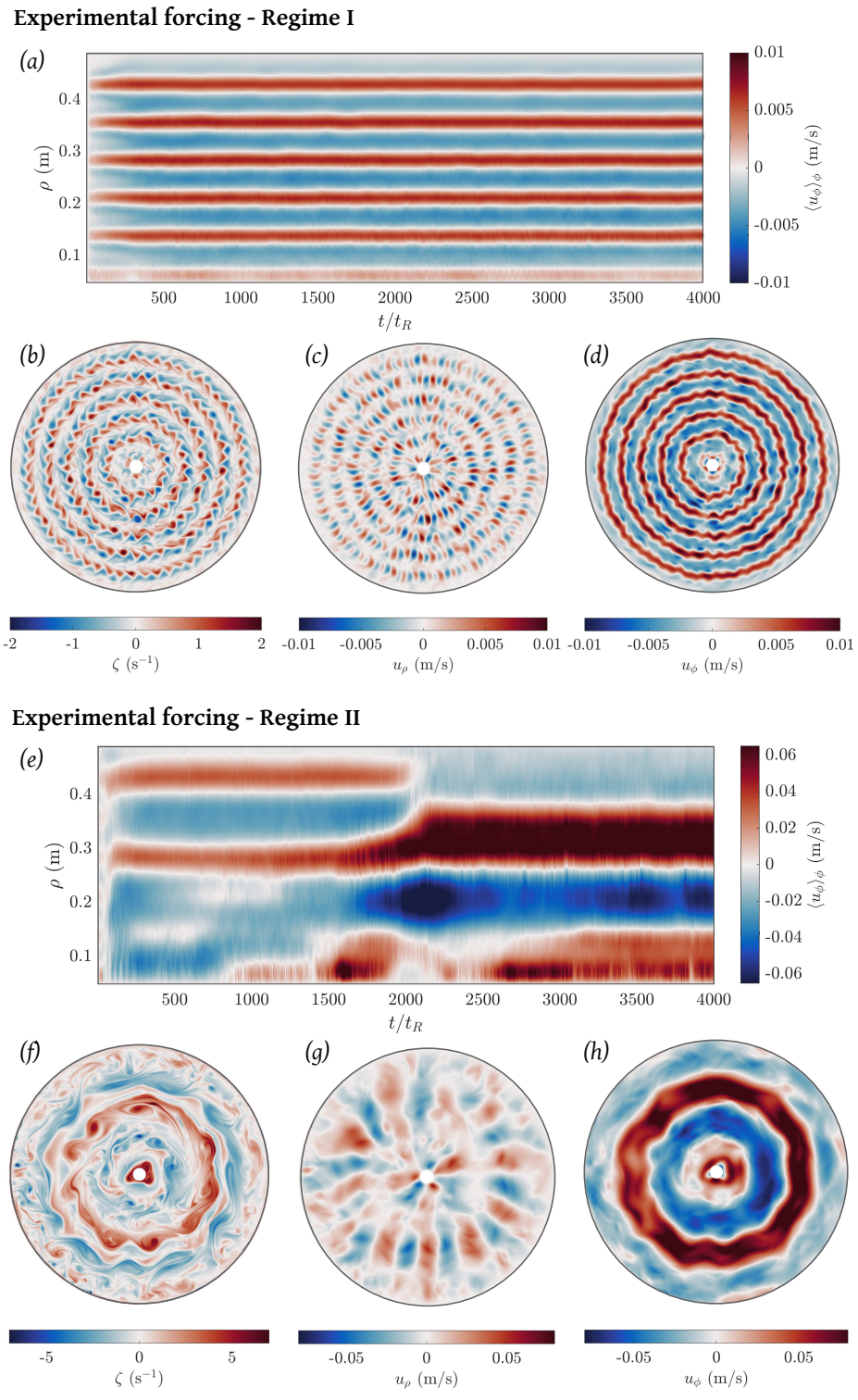

Figure 3.16. – Quasi-geostrophic numerical simulations forced on a polar array similar to the experimental one. *(a)* Non-dimensional forcing amplitude $F_0' = 1 \times 10^{-3}$ ($F_0 = 0.25$ s^{-2}) (Appendix C.4.3), leading to regime I. *(b,c,d)* Vorticity, radial velocity and azimuthal velocity at time $t = 4{,}000\ t_R$ in regime I. *(e)* Forcing amplitude $F_0' = 6 \times 10^{-3}$ ($F_0 = 1.48$ s^{-2}), leading to regime II. *(f,g,h)* Vorticity, radial velocity and azimuthal velocity at time $t = 4{,}000\ t_R$ in regime II.

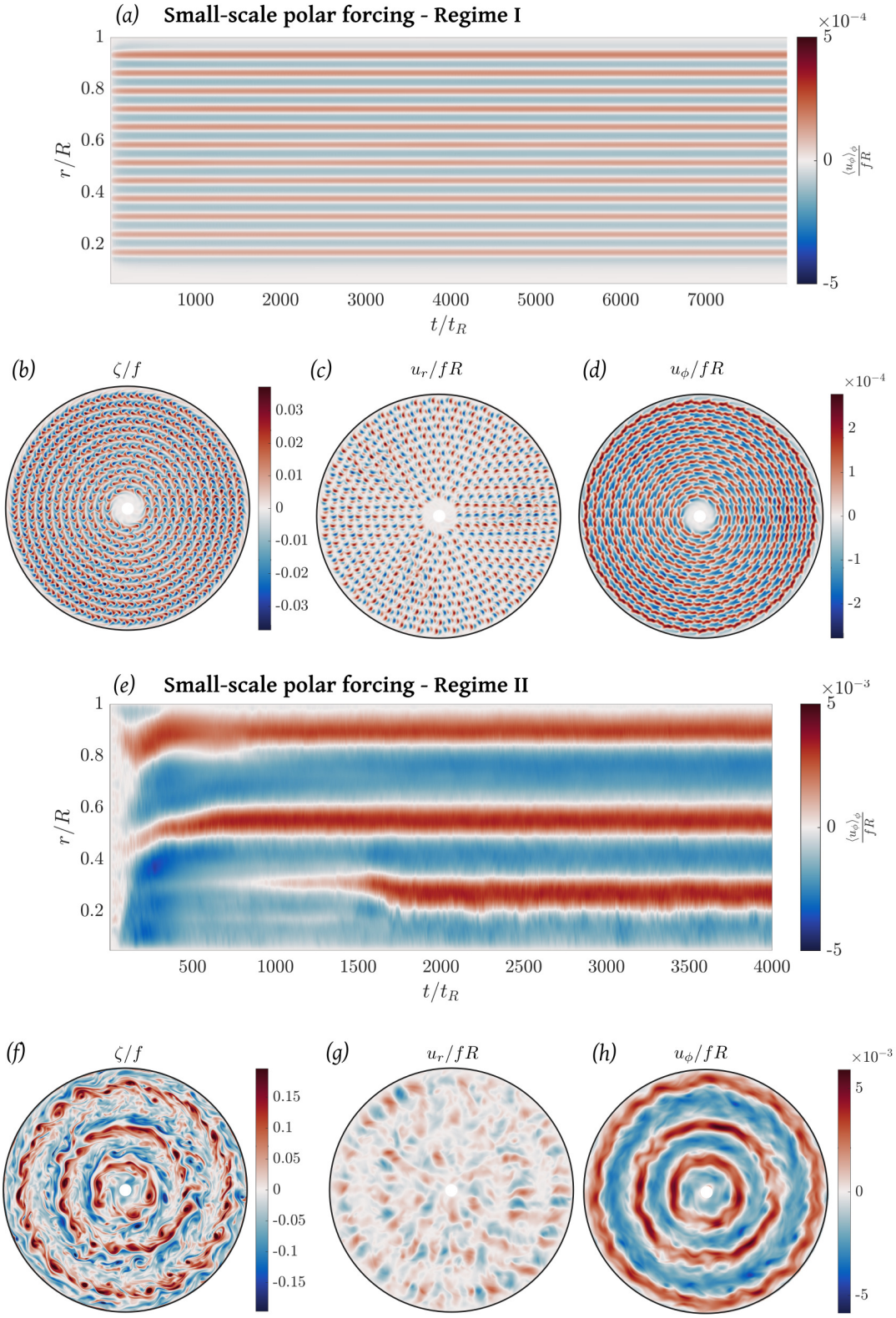

Figure 3.17. – Quasi-geostrophic numerical simulations forced on a polar array of typical wavelength $L_f/R \approx 0.07$ ($k_f R \approx 90$). *(a–d)* Hovmöller diagram, vorticity and velocity fields for a simulation in regime I with a forcing amplitude $F_0' = 5 \times 10^{-4}$ (see Appendix C.4.3). *(e–h)* Hovmöller diagram, vorticity and velocity fields for a simulation in regime II with $F_0' = 5 \times 10^{-3}$.

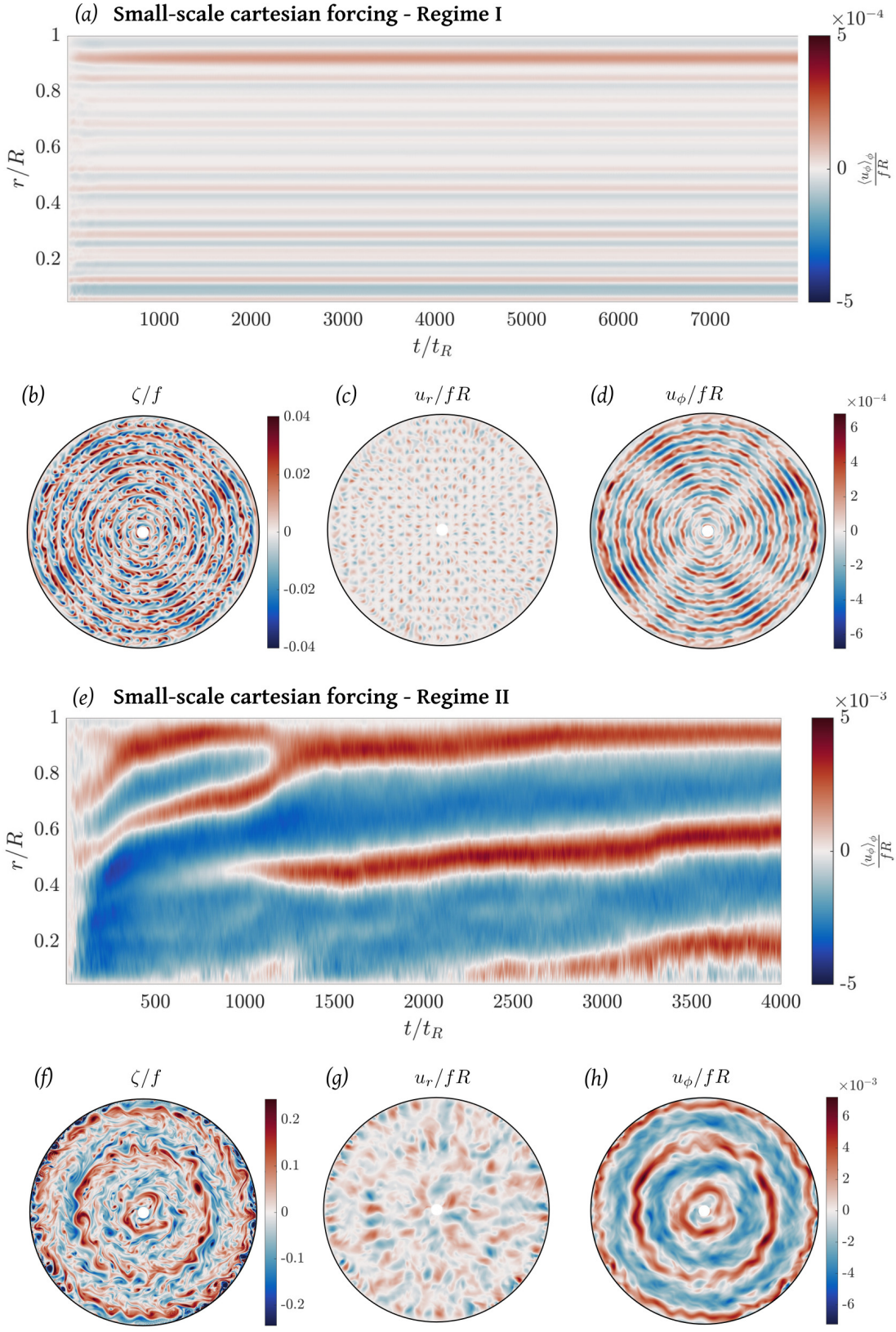

Figure 3.18. – Quasi-geostrophic numerical simulations forced on a cartesian array of typical wavelength $L_f/R \approx 0.08$ ($k_f R \approx 79$). *(a–d)* Hovmöller diagram, vorticity and velocity fields for a simulation in regime I ($F_0' = 5 \times 10^{-4}$). *(e–h)* Hovmöller diagram, vorticity and velocity fields for a simulation in regime II ($F_0' = 5 \times 10^{-3}$).

two stable states with different waves and zonal flow amplitudes. The bending of the same resonance due to weakly non-linear effects (Malguzzi et al. 1996, 1997) is also a potential candidate to account for the observed bistability. However, the two regimes would then be expected to have similar zonal flow velocities, which is in contradiction with our observations.

In laboratory experiments, bifurcations involving multiple zonal flows steady states have been observed only a few times. Weeks et al. (1997) and Tian et al. (2001) observed bistability in the context of mid-latitude atmospheric jets, following the same resonance but with topography. However, in these experiments, the zonal flow is *directly* forced by pumping fluid in at a larger radius than where it is pumped out. Bifurcations over *indirectly* forced zonal flows were observed by Semin et al. (2018) in their experimental model of the quasi-biennial oscillation, but in that case, the flow is laminar, and the low forcing amplitude state has no mean flow. In the present study, we describe bistability between two steady states sustaining indirectly forced and multiple zonal jets. Let us mention here that bistability has also been observed numerically in the context of rotating thermal convection where zonal flows emerge due to the spherical domain. At intermediate Ekman numbers, the saturation of the convective instability can lead to either a weak branch or a strong branch, both supporting zonal flows but which are much more vigorous on the strong branch (Guervilly et al. 2016; Kaplan et al. 2017). The question whether this bistability may be linked to a somewhat similar resonance involving thermal Rossby waves is however far from trivial. For instance, there is no obvious reason for the convective eddies that force the zonal flow to be stationary, and to what extent they are decoupled from the zonal flow remains to be determined.

The results presented in this chapter raise several questions, some of which will be investigated in the following of the manuscript. First, it is important to question the specificity of the observed transition to our forcing pattern. In the previous section, we partially investigated this aspect numerically, by showing that the transition holds at a smaller forcing scale whether the forcing pattern is polar or cartesian. The next step is to investigate the effects of spatial non-stationarity. Then, explaining the transition's origin does not explain the non-linear saturation in the second regime, and its evolution as a global system. The description of the final equilibrated state in regime II, which is closer to the planetary ones, is the subject of chapter 4. Future work is also needed to investigate the long-term dynamics (or stability) of the zonal flows. Such a task is difficult given the time-scale separation between the turbulence and the slowly varying zonal flow. In this regard, laboratory experiments have a major role to play since they allow for measurements at high-resolution over long times. In chapter 5, we discuss the long-term stability of the system by characterizing the multistability of regime II observed in both experiments and QG numerical simulations.

3.5.3. Modelling and relevance for planetary systems

Finding an explicit expression for the Reynolds stresses is the basis of the out-of-equilibrium statistical theories aiming at explaining zonal jets formation from an homogeneous turbulent flow (see e.g. Constantinou et al. 2014). Indeed, it yields to a closed system for the zonal flow dynamics. Here, a very simple framework based on the QG approximation is sufficient to explain our experimental observations but more sophisticated models where, for instance, the spatial modulations of the zonal flow are taken into account are necessary to help understand observations at a global scale.

In the present study, the key mechanism is the local resonant amplification of the Reynolds stresses by the zonal flow. It has been applied previously in two main geophysical frameworks: mid-latitude atmospheric jets and equatorial super-rotation, which refers to the presence of a prograde jet at the equator. For the Earth's atmosphere, the Rossby waves resonance has been employed to explain abrupt transitions of the jet stream between blocked and zonal

flows (Charney et al. 1979), and it is now considered as a valuable candidate to explain extreme weather events in the past 20 years (Petoukhov et al. 2013; Coumou et al. 2014). Then, in the case of equatorial jets, abrupt transitions to super-rotation and bistability have been observed in global climate models and numerical simulations. The same wave-jet resonance feedback as for mid-latitude jets, which arises in response to a stationary equatorial heating, has been recently considered as a robust mechanism for this transition (Arnold et al. 2011; Herbert et al. 2020). The fact that in those two frameworks, the resonance successfully explains observations at a global scale is encouraging. However, to the best of our knowledge, such a mechanism has never been studied for its potentiality to generate strong zonal jets in the broader context of an eddy-forcing, neither for its applicability to extra-equatorial jets on the gas giants or in the Earth's oceans.

First, we can briefly compare the zonal flow amplitudes relatively to the Rossby waves intrinsic phase speed (equation (3.38)):

— If $U > -c$, then the Rossby waves propagate eastward and the zonal flow is super-resonant (regime II);

— If $U < -c$, then the Rossby waves propagate westward and the zonal flow is sub-resonant (regime I).

With topographically forced waves phase speed of typically $-16\,\mathrm{m\,s^{-1}}$, the Earth mid-latitude jet stream may fall in the bistable range, with a zonal flow either sub-resonant or super-resonant as proposed by Charney et al. (1981). In the Earth's oceans, the zonal propagation of eddies can be associated with long Rossby waves, and compared with the depth-mean velocity. Using eddy-tracking, Klocker et al. (2014) show that eddies are propagating westward except in the Southern Ocean, where eddies are advected eastward in the core of the Antarctic Circumpolar Current, ACC (see Fig.3.19*(a)*). The zonal jet associated with the strong ACC could thus be super-resonant, whereas the majority of other oceanic jets would be sub-resonant. For the gas giants, we can use the measurements of propagation speed of features interpreted as Rossby waves. For instance, on Jupiter, the dark projections located at 7°N are interpreted as Rossby waves of intrinsic phase speed of about $-50\,\mathrm{m\,s^{-1}}$ relatively to the eastward jet of zonal speed of $150\,\mathrm{m\,s^{-1}}$ at that latitude (Fig.3.19*(b,c)*). The associated zonal jet would thus be super-resonant (regime II). The conclusion is the same for Saturn, if we take the example of the jet located at 42°N. The North ribbon, at that latitude, is compatible with Rossby waves propagating at a Doppler-shifted phase speed represented by the blue dots in Fig.3.19*(e)*. These waves are advected eastward by the zonal flow, which would thus be super-resonant (regime II).

Let us stress out that for the present mechanism to hold in planetary systems, there is the need for a partial decoupling between the forcing source and the jets, such that the forced waves advected by the zonal flow can become resonant with the forcing. For the Earth jet stream, this decoupling comes from the fact that the topography exciting the waves is fixed, just like in our experiment. For Jupiter, the forcing origin is not clear. It can take place in the weather layer due to moist convection or band-to-band horizontal contrasts in heating, but it can also arise from the deep molecular convective interior of the gas giant (Vasavada et al. 2005). At which speed the convective structures propagate relatively to the zonal flow is certainly not clear. All these questions require dedicated studies, but the important point is that even with an unsteady forcing, propagating azimuthally, the resonance mechanism should still hold provided that the forcing is not passively advected by the zonal flow it generates, the only consequence would be that the zonal flow speed at the transition will change.

In addition to the previous simple velocities comparison, the important parameter of the model is $\gamma^2 = \left(\alpha/(k_f c)\right)^2$. This parameter compares the Rossby waves period $1/(k_f c)$ to the friction timescale $1/\alpha$, and we have shown that it should be small (equation (3.44)) for the super-resonant solution or bistability to exist. The question whether such a mechanism is

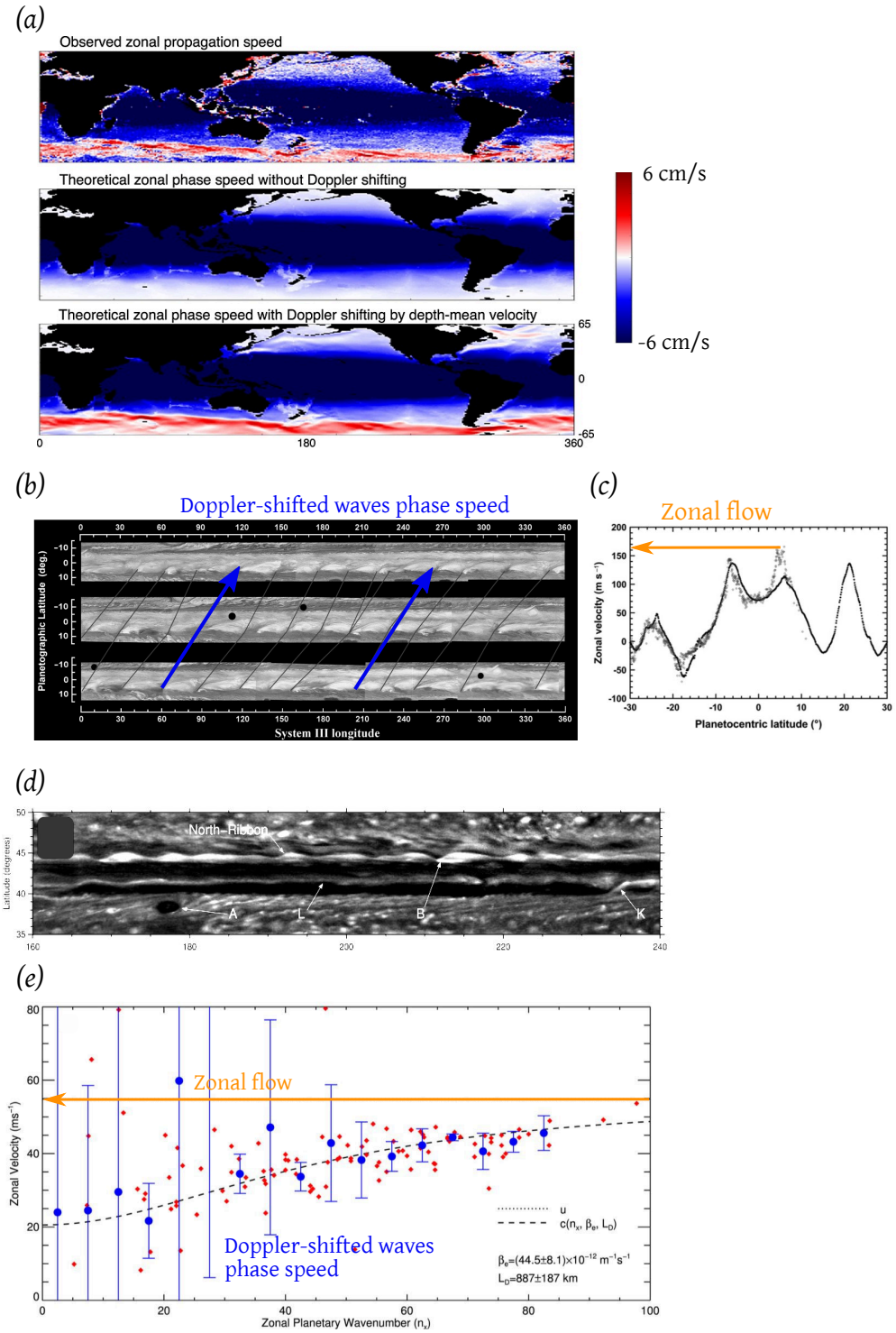

Figure 3.19. – Estimates of zonal flow velocities and Rossby waves phase speed for different planetary flows. If the prograde zonal jets are sufficiently fast that the Rossby waves propagate eastward, then the zonal flow is presumably super-resonant (regime II). *(a)* Observed zonal propagation speeds of oceanic eddies and comparison with the theoretical zonal phase speed of Rossby waves Doppler-shifted by zonal currents (Klocker et al. 2014). *(b)* Long-term tracking of the so-called "hot spots" located at 7°N on Jupiter, interpreted as Rossby waves propagating eastward at $\sim 100\,\mathrm{m\,s^{-1}}$ (Arregi et al. 2006) *(c)* At the latitude of the hot spots is located a prograde jet of $\sim 150\mathrm{m\,s^{-1}}$ (García-Melendo et al. 2011b). *(d)* Saturn's North ribbon (42°N) has been interpreted as a superposition of Rossby waves of (Doppler-shifted) phase speed represented by the blue dots on panel *(e)*. The orange line is the zonal flow velocity at the latitude of the North-ribbon, which would then be super-resonant (figures adapted from Gunnarson et al. 2018).

expected for extra-tropical jets in planetary flows is beyond the scope of the present study and would require an extensive systematic study. Besides, one should properly define the bounds of the physical parameters for the model to still be self-consistent. We recall for instance that the model is based on the *linear* response to a stationary forcing. Finally, determining the relevant dissipation parameter for the Rossby waves is not trivial either, and it cannot be reduced to a simple Ekman friction like in our experiment. That being said, for completeness, Fig.3.15(*a*) illustrates the sensitivity of the bistability to the model parameters (α, β, k_f). Interestingly, the bistable range is shifted towards lower values of the forcing amplitude as $\alpha \to 0$, meaning that for infinitely small Rossby waves dissipation, the super-resonant solution U_3 (regime II) would be obtained even at a very small forcing amplitude, while the sub-resonant solution U_1 (regime I) would never be observed. Regime II is thus expected in most planetary applications.

Chapter 4.

Non-linear saturation into the zonostrophic regime of zonal jets: turbulence statistics and transport properties

Chapter 4.

In chapter 3, we have described the transition between regimes I and II of zonal flows. We now focus on the turbulent properties of the more planetary-relevant regime II, far from the transition.

Chapter aims

1. Modify the forcing of the *Jacuzzi* setup to reach more extreme regimes and describe the saturated turbulent state obtained in regime II, far from the transition.
2. Compare our experimental results with the theory of zonostrophic turbulence. Compute kinetic energy spectra and address their consistency with the scalings expected in the zonostrophic regime, relevant for gas giants.
3. Evaluate the degree of potential vorticity (PV) mixing.
4. Evaluate the turbulent transport properties in terms of effective diffusivity. Investigate the effect of the zonal flow on the isotropy and homogeneity of the turbulent transport.

Highlights

- In our most extreme experiments, we reach regimes characterized by $Re \sim 2 \times 10^4$, $E \sim 3.8 \times 10^{-7}$, $Ro \sim 7 \times 10^{-3}$. These regimes are closer to planetary regimes than previous experimental setups.
- From the kinetic energy spectral analysis, we retrieve scalings and amplitudes expected in the zonostrophic regime of β-plane turbulence, relevant for gas giants. With Cabanes et al. (2017), these are the first experiments able to reach the zonostrophic regime.
- Despite the intense turbulence and the strength of the zonal flows, we do not observe a strong PV mixing, and the modification of the background PV profile into a staircase is only moderate.
- We show that kinetic energy transfer rates can be computed by three independent methods (spectral analysis, local PV mixing and estimates of eddy diffusivities) which agree relatively well with each other. These methods may be applied for measurements in natural flows, depending on the precision and coverage of the available data.
- A Lagrangian analysis shows that the zonal flows introduce a strong anisotropy and inhomogeneity in the turbulent transport. Regarding inhomogeneity, we confirm the so-called suppression effect of zonal flows on eddy-diffusivity, which may hence be important to take into account in models parametrizing small-scale processes.

4.1. Introduction

In the previous chapter, we have studied a transition between two regimes of multiple zonal jets. We showed that the first regime, where the jets are individual and locally forced, may be relevant for jets in the terrestrial oceans. However, the second regime, which is accompanied by a coarsening and an intensification of the zonal jets, is closer to the planetary ones, and particularly to the one relevant for the gas giants. We physically described the origin of the transition, and we are now ready to describe the saturated turbulent and statistically steady state obtained in regime II, far from the transition.

Contrary to regime I, a local approach is not sufficient to explain the non-linear saturation in regime II. Indeed, the jets interact and merge to equilibrate in a new configuration where, qualitatively, the energy initially injected at the forcing scale feeds larger scales. We thus leave the local QG approach developed in chapter 3, and instead, we compare our experimental results with different theories which aim at explaining zonal jets properties at a global scale. The first theory on which we focus relies on the turbulent properties and energy transfer of anisotropic turbulence on a β-plane, the so-called theory of zonostrophic turbulence (see Galperin et al. (2019b) and section 1.4.2.2). Since the flow is quasi two-dimensional, it may bear an inverse turbulent energy cascade. But because of the β-effect and associated Rossby waves, the energy transfer to large scales becomes anisotropic and redirected towards zonal currents. Ultimately, the large scale drag halts the expansion of the inverse cascade (Sukoriansky et al. 2002, 2007). The advantage of this theory is that it allows to compare experiments and numerical simulations of zonal jets with a single non-dimensional parameter, the zonostrophy index R_β (see Fig.3.1 in the previous chapter). This index is basically the ratio between the largest scale of the dynamics set by the large scale drag, and the scale at which the eddies start to feel the β-effect. Friction-dominated regimes (Earth's oceans and atmosphere) have a small ($R_\beta \sim 1.5$), whereas zonostrophic regimes, i.e. regimes of strong jets, are characterized by $R_\beta > 2.5$, with $R_\beta \sim 5$ for Jupiter and Saturn (Galperin et al. 2006; Sukoriansky et al. 2007; Galperin et al. 2019b, table 13.1). As discussed previously, our experimental setup was designed to favour the emergence of strong jets, and thus large R_β, thanks to a strong β-effect, strong flows ($Re \gg 1$), but still dominated by rotation ($Ro \ll 1$), and small viscous dissipation using the fast rotation of a large tank ($E \ll 1$). The analysis performed in Cabanes et al. (2017) for the previous version of the experiment and corresponding DNS supports the idea that the second regime is close to zonostrophic turbulence. But the particle tracking method allowed computation of kinetic energy spectra for the zonal flow only, not the fluctuations. With the new setup, the temporal and spatial resolution of our PIV measurements allows us to quantify turbulence statistics for both the zonal and fluctuating components of the flow, and to complete the analysis in the framework of zonostrophic turbulence.

The second theoretical framework to which we compare our experimental results is the one of potential vorticity (PV) mixing (Dunkerton et al. 2008; McIntyre 2008; Dritschel et al. 2008; Scott et al. 2012a). In our case of a barotropic fluid with varying height, the PV is $q = (\zeta + f)/h$, where ζ is the relative vorticity, $f = 2\Omega$ is the "planetary" vorticity, and h the fluid height (see chapter 1, §1.2.4.4). In the framework of PV mixing, zonal jets are described as emerging from the mixing of this scalar field, which is materially conserved in the absence of viscous dissipation. Retrograde jets correspond to well-mixed regions of PV, whereas prograde jets would correspond to steep gradients of PV, thus defining a staircase-like profile in the radial direction if multiple jets are present (see Fig.1.15). The mechanism of staircase formation was described in Dritschel et al. (2008) by analogy with what happens when a stratified fluid is mixed, the so-called "Phillips-effect" (Phillips 1972). The idea is that of a feedback mechanism: stratification is reduced in the mixed regions, the restoring force at the origin of gravity waves

(buoyancy) is thus weakened, which allows for further mixing. Instead, where interfaces are forming, steeper stratifications locally develop, and the gravity waves elasticity is enhanced, thus inhibiting mixing across the interface. For a PV gradient instead of a density gradient, the mechanism is analogous but invokes Rossby waves whose propagation depends on how steep is the local PV gradient. That being said, subtleties arise from the fact that PV is different from density since there is a direct relationship between the flow dynamics and PV through the vorticity. One possible application is that, according to this theory, there is a relation between the jets spacing (the staircase width) and the jets intensity (the PV jump at the interfaces). This could be readily tested in our experiments, but we are confronted with the fact that our experiments are spatially confined, and that only a small number of jets develops: the measure of the jets spacing is then compromised by finite-size effects. Galperin et al. (2014a) proposed to use the analogy between PV and density staircases to quantify PV mixing, through the method of PV monotonizing. The idea is to use local and instantaneous PV (or density) profiles to quantify the turbulent overturn by measuring the equivalent of a Thorpe scale (Thorpe 2005; Gargett et al. 2008). The initial PV (density) profile, due to background rotation and β-effect, is monotonous and decreasing with radius. Locally, turbulent eddies can cause overturns and bring fluid parcels with higher PV (higher density) outward (above) compared to a fluid parcel with smaller PV (smaller density); an unstable configuration. By sorting the non-monotonous PV profile into a monotonous one, one can define a Thorpe scale L_T, which is the root-mean-squared displacement of the fluid parcels needed to bring them back to a stable position. Galperin et al. (2014a) shows experimentally that similarly to stratified flows where L_T is close to the Ozmidov scale, which is the scale at which turbulent eddies feel the stratification, L_T is commensurate with the transitional scale, L_β, at which turbulent eddies feel the β-effect. If a robust relationship exists between the Thorpe and transitional scales, then sorting PV would constitutes a powerful tool to estimate L_β and indirectly, the turbulent dissipation rate. The only requirement would then be to measure instantaneous profiles of potential vorticity of the flow (see for instance Cabanes et al. 2020a, for an application to Jupiter and Saturn). However, the three experiments used in Galperin et al. (2014a) are far from the zonostrophic regime: the forcing, which is performed using magnets and a saline solution, accelerates a westward zonal flow locally but also directly (all the magnets are aligned and have the same polarity). To what extent the scaling between the Thorpe and the transitional scale holds in our experiments in regime II, where the jets are strongly turbulent and self-developed from a fluctuating forcing with no azimuthal mean, thus remains to be addressed.

Finally, better understanding the transport properties of zonal flows is important given their omnipresence in natural flows, including Earth's oceans. Transport of heat, momentum or passive scalars in the oceans is the key to numerous scientific questions regarding energy and heat budgets, carbone dioxyde uptake, dispersion of pollutants, or oxygen and phytoplankton distributions (van Sebille et al. 2018). In addition, progress is needed to better parametrize the effective diffusion of subgrid-scale processes in global circulation models (Fox-Kemper et al. 2019). The two theoretical frameworks mentioned give clues and predictions in terms of the turbulent transport properties of the considered flow. First, the framework of zonostrophic turbulence provides kinetic energy spectra for the flow. Using mixing-length theory, Sukoriansky et al. (2009) derive from these spectra an expected effective diffusivity. In particular, in the zonostrophic regime, they argue that only the scales smaller than the transitional scale can contribute to the mixing. This leads to the prediction that the effective diffusivity is independent of scale (like in a standard diffusive process at the molecular scale) and can be estimated knowing the energy transfer rate and the transitional scale only. Second, the framework of PV mixing has led to the idea that zonal jets are barriers to meridional (radial) transport (Dritschel et al. 2008; Beron-Vera et al. 2008; Thompson 2010). We propose preliminary tests of these hypotheses

with three of our experimental records for which we have high frequency acquisitions and can quantify diffusivity via Lagrangian particles dispersion. To do so, we numerically seed our experimental flows with passive particles and compute their Lagrangian trajectories from the Eulerian PIV velocity fields. We measure associated effective diffusivities, and discuss the influence of zonal flows and possible clustering.

The chapter is organized as follows. In §4.2, we describe the set of experiments in regime II selected for the present chapter in terms of typical length scales and non-dimensional parameters. In §4.3, we compute kinetic energy spectra to discuss the relevance of the zonostrophic turbulence theory in our experiments, and measure a turbulent energy dissipation rate from them. In §4.4, we quantify the PV mixing and compute the associated Thorpe scale which allows to measure a second upscale energy transfer rate. In §4.5, we characterize the Lagrangian transport properties of our flow and measure an effective diffusivity which allows to define a third upscale energy transfer rate. We additionally discuss the influence of the zonal flow on the diffusivity. In §4.6, we provide conclusions about the different methods that are available to measure the upscale energy transfer rate. We finally discuss possible implications of the impact of zonal flows on transport properties for large scale ocean, atmosphere and climate models.

4.2. List of experiments and non-dimensional parameters

The experimental set-up used in this chapter is the same as the one described in chapter 3, except that we now focus on experiments in regime II. However, for some experiments, we changed some of the submersible pumps used for the forcing to newly released models with higher flow rates. This substitution was applied for the three most external rings, $C_{4,5,6}$, since these rings are the ones with the most important pressure drop due to an increasing number of inlets and outlets per ring (Fig.3.2). The TCS pumps M510S (max flow rate of 8 $\mathrm{L\,min^{-1}}$) were replaced by the TCS M3000 model (max flow rate of 50 $\mathrm{L\,min^{-1}}$). This modification allows us to reach significantly larger Reynolds numbers, while keeping the forcing homogeneous across the tank. In Table 4.2 where the experiments are listed, "Set 1" corresponds to the first configuration (that of chapter 3), and "Set 2" to the new one. Details and pictures of the two sets of pumps, with the associated forcing calibrations, can be found in Appendix B.

4.2.1. Characteristic length scales

Before introducing the experiments and associated non-dimensional parameters, we recall the three typical length scales that were introduced in chapter 1 (section 1.4.2.2) and that will be used in the chapter, as well as their link with the zonostrophy parameter. Neglecting molecular diffusion effects, we characterize the flow by

— its root-mean-squared (rms) velocity $u_{\mathrm{rms}} = (2\mathcal{K})^{1/2}$, where $\mathcal{K}$ is the total kinetic energy of the flow;

— its rate of upscale energy transfer within the turbulent energy cascade, ϵ;

— its gradient of potential vorticity, β.

Alternatively to ϵ, the friction rate α can be used by assuming that dissipation mainly occurs in the Ekman boundary layers in rapidly rotating flows. The friction rate can be expressed as $\alpha \sim \Omega E^{1/2} = 1/\tau_E$, where E is the Ekman number and τ_E is the Ekman spin-down time scale. If one assumes that the upscale energy transfer ϵ is due to this dissipation process, then

$$\epsilon \sim \frac{u_{\mathrm{rms}}^2}{2\tau_E} = \frac{u_{\mathrm{rms}}^2 \Omega E^{1/2}}{2} = \frac{u_{\mathrm{rms}}^2 \alpha}{2}, \tag{4.1}$$

With the parameters $(u_{\rm rms}, \alpha, \beta)$ or alternatively $(u_{\rm rms}, \epsilon, \beta)$, we can define three length scales L or associated wavenumbers k:

— A large frictional length scale ($L_\alpha = 2\pi/k_\alpha$), based on the equilibrium between the available kinetic energy and the Ekman friction:

$$k_\alpha = \frac{\alpha}{2u_{\rm rms}} = \frac{\epsilon}{u_{\rm rms}^3}; \tag{4.2}$$

— A transitional scale ($L_\beta = 2\pi/k_\beta$), which is the scale at which a turbulent eddy turnover time ($(k^2\epsilon)^{-1/3}$) equates a Rossby wave period (k/β), i.e. the scale at which the turbulence becomes anisotropic:

$$k_\beta = \left(\frac{\beta^3}{\epsilon}\right)^{1/5}; \tag{4.3}$$

— A Rhines scale ($L_R = 2\pi/k_R$), which has been found to describe the large scale of the jets in the regime where the β-effect dominates the flow, and corresponds to the scale at which the inertial term equates the β term:

$$k_R = \left(\frac{\beta}{u_{\rm rms}}\right)^{1/2}. \tag{4.4}$$

Traditionally, the zonostrophy parameter R_β is expressed as the ratio of the Rhines scale L_R to the transitional scale L_β. As we saw in chapter 1, §1.4.2.2, this non-dimensional parameter aims at describing the regime of β-plane turbulence of a given flow, and in particular the strength of the jets and the quality of their delineation (Galperin et al. 2006; Sukoriansky et al. 2007). The zonostrophy parameter can be alternatively expressed using the frictional length scale, L_α:

$$R_\beta = \frac{L_R}{L_\beta} = \left(\frac{L_\alpha}{L_R}\right)^{1/5} = \left(\frac{L_\alpha}{L_\beta}\right)^{1/6} = \left(\frac{u_{\rm rms}^5\beta}{\epsilon^2}\right)^{1/10} = \left(\frac{4u_{\rm rms}\beta}{\alpha^2}\right)^{1/10}. \tag{4.5}$$

These expressions show that R_β simultaneously compares the three scales. It is quite intuitive to use the ratio L_β/L_α as an indicator of how strongly zonal the turbulent regime investigated is, since it compares large scale friction with the β-effect (this is what is used by Danilov et al. (2004a) and Danilov et al. (2004b)). On the contrary, it is more difficult to physically differentiate L_R and L_β. The Rhines scale is nevertheless commonly employed in studies of eddy-driven zonal jets, because it is more easily estimated for a given flow that the dissipation scale. Expression 4.5 helps to interpret physically the zonostrophy parameter:

— if $R_\beta < 1$ ($L_\alpha < L_R < L_\beta$), then the β-effect is weak and the scale of the flow is defined by L_α which is then smaller than L_R and L_β. Since the frictional scale is smaller than the transitional scale, the energy is dissipated before that the flow feels the β-effect. In that case, one would expect the flow to remain nearly isotropic and show features of the classical KBK turbulence described in chapter 1 (§1.2.5.2).

— if $R_\beta > 1$ ($L_\beta < L_R < L_\alpha$), then the β-effect is strong, and the turbulence is anisotropic since its equilibrium scale is larger than the transitional scale . The large scales are then limited at a value less than L_α.

The regime of strong and rectilinear jets – so-called *zonostrophic regime* – is obtained when the scale at which the eddies start being deformed by the Rossby waves is well separated from the scale of the final jets, i.e. for large zonostrophy index. From 2D simulations on the sphere, Galperin et al. (2010) show that the zonostrophic regime is observed when $R_\beta \gtrsim 2.5$ whereas the

regime is friction-dominated when $R_\beta \lesssim 1.5$, as seen in Fig.1.15*(a)*. Jovian mid-latitude jets have $R_\beta \approx 5$ and are expected to be in this regime of zonostrophic turbulence (Galperin et al. 2014b). On the contrary, Earth's oceans are under the threshold with $R_\beta \approx 1.5$ (Galperin et al. 2019b).

4.2.2. Non-dimensional parameters

The experimental flows we consider are defined by five dimensional parameters, the rms velocity, $u_{\rm rms}$, the rotation rate, Ω, the mean fluid height, h_0, the molecular viscosity, ν, and the gradient of potential vorticity β. With two dimensions (length and time), our experiments can be characterized by three independent non-dimensional parameters, which we chose to be the Ekman number, E, the Reynolds number, Re and the zonostrophy index R_β. The Ekman number compares the viscous to Coriolis forces, the Reynolds number compares the inertial to viscous forces, and the zonostrophy index compares the restoring force arising from the gradient of the potential vorticity (the β-effect) to the large scale frictional force. The expression of these parameters using $(u_{\rm rms}, h_0, \Omega, \nu, \beta)$ are given in Table 4.1. Alternatively to the fluid height h_0, and as previously discussed, we can express these parameters as a function of turbulent energy dissipation rate ϵ by assuming that dissipation mainly occurs in the Ekman boundary layers (equation (4.1)): $\epsilon \sim u_{\rm rms}^2 (\nu\Omega)^{1/2}/(2h_0)$. We use this assumption because it allows us to estimate ϵ *a priori*, and hence have an idea of the zonostrophy parameter of our experiments beforehand. We will see later that ϵ can actually be measured, and agree relatively well with this estimate. In the remaining of the chapter, we make the difference between the *estimated* energy transfer rate, ϵ^E and the *measured* one ϵ^S. The three non-dimensional parameters expressed using $(u_{\rm rms}, \epsilon, \Omega, \nu, \beta)$ are also given in Table 4.1. We add the Rossby number Ro for completeness, which compares the inertial to Coriolis forces, even if it is not independent of the others ($Ro = Re \times E$).

Several important dynamical constraints arise from the nature of the flow that we wish to model. The atmospheric flows of Jupiter are fully turbulent and rotation-dominated, as characterized by their large Reynolds number $Re \sim 10^{13}$ and very small Ekman number $E \sim 10^{-15}$ ($Ro \sim 0.01$), and this turbulence is highly anisotropic and dominated by the β-effect, leading to a large zonostrophy index of approximately 5 (Young et al. 2017; Galperin et al. 2014b). Experimentally, such a regime can only be achieved by using the biggest possible experimental devices, rotating as fast as possible, and forced as strongly as possible. However, a big limitation is that it is not sufficient that the Ekman number is small and the Reynolds is high, since the product of the two (the Rossby number) should remain well below one to be in a turbulence dominated by rotation. Hence, for a given rotation rate, the flow cannot be forced too strongly. In our experiment, these constraints are fulfilled, as indicated by the values reported in Table 4.1. Note that our Ekman number is much higher than that of Jupiter, and our Reynolds is much smaller, but these discrepancies compensate in the Rossby number which has the good order of magnitude. Physically, this means that we have the good ratio of inertial to Coriolis forces, but our experimental flow is overly damped by viscous effects which are vanishingly small on Jupiter. We are nevertheless in the relevant regime, turbulent and dominated by rotation ($Re \gg 1$, $E \ll 1$), and we showed in the previous chapter that following on from Cabanes et al. (2017) we explore more extreme regimes compared to previous experimental studies (Fig.3.1).

4.2.3. List of experiments

In Table 4.2, we report the physical and non-dimensional parameters of the experiments in regime II that are used in the following. Note that our experimental set-up was designed to work at a single rotation rate of 75 RPM at which the β-effect is then uniform across the tank. However, we performed few experiments at rotation rates of 60 and 80 RPM to investigate the

	$(u_{\rm rms}, h_0, \Omega, \nu, \beta)$	$(u_{\rm rms}, \epsilon, \Omega, \nu, \beta)$	Constraints	Typical values
E	$\dfrac{\nu}{\Omega h_0^2}$	$\dfrac{4\epsilon^2}{\Omega^2 u_{\rm rms}^4}$	$\ll 1$	3×10^{-7}
Re	$\dfrac{u_{\rm rms} h_0}{\nu}$	$\dfrac{u_{\rm rms}^3 \Omega^{1/2}}{2\epsilon\nu^{1/2}}$	$\gg 1$	1×10^{4}
$Ro = Re\times E$	$\dfrac{u_{\rm rms}}{\Omega h_0}$	$\dfrac{2\epsilon}{\Omega^{3/2}\nu^{1/2}u_{\rm rms}}$	$\ll 1$	3×10^{-3}
R_β	$\left(\dfrac{4\beta u_{\rm rms} h_0^2}{\nu\Omega}\right)^{1/10}$	$\left(\dfrac{u_{\rm rms}^5\beta}{\epsilon^2}\right)^{1/10}$	>2.5	>3

Table 4.1. – Non-dimensional parameters used to describe the experimental flow. The Ekman number, E, Reynolds number Re and zonostrophy parameter R_β are independent, the Rossby number Ro is indicated for completeness but can be expressed as $Ro = Re\times E$. These parameters can be expressed using h_0, the fluid height, or alternatively, the estimated upscale energy transfer rate $\epsilon \sim u_{\rm rms}^2(\nu\Omega)^{1/2}/(2h_0)$ (equation (4.1)).

Label	Date (AA/MM/DD)	Set	β ($\mathrm{m^{-1}\,s^{-1}}$)	$\mathscr{K}$ ($\mathrm{m^2\,s^{-2}}$)	ϵ^E ($\mathrm{m^2\,s^{-3}}$)	L_T (cm)	$E\times10^7$	$Re\times10^{-3}$	R_β
A	20/11/18	2	50.1	5.74×10^{-4}	27.8×10^{-7}	1.67	3.78	19.7	3.52
B	20/11/18	2	50.1	3.64×10^{-4}	17.6×10^{-7}	1.40	3.78	15.7	3.44
C	20/11/17	2	65.5	5.02×10^{-4}	25.0×10^{-7}	0.87	3.55	18.4	3.57
D	20/11/16	2	22.8	5.92×10^{-4}	25.6×10^{-7}	2.28	4.73	20.0	3.33
E	20/10/06	2	50.1	4.38×10^{-4}	21.2×10^{-7}	1.13	3.78	17.1	3.47
F	20/10/01	2	50.1	5.44×10^{-4}	26.3×10^{-7}	1.42	3.78	19.1	3.51
G	20/09/25	2	50.1	5.37×10^{-4}	26.0×10^{-7}	1.45	3.78	19.0	3.51
H	20/01/22	1	50.1	1.31×10^{-4}	6.34×10^{-7}	0.81	3.78	9.40	3.27
I	19/12/12	1	50.1	1.69×10^{-4}	8.18×10^{-7}	1.19	3.78	10.7	3.31
J	19/11/12	1	50.1	1.74×10^{-4}	8.45×10^{-7}	1.09	3.78	10.8	3.32
K	19/11/04	1	22.8	1.28×10^{-4}	5.53×10^{-7}	1.72	4.73	9.28	3.08
L	19/06/27	1	50.1	0.69×10^{-4}	3.36×10^{-7}	0.75	3.78	6.84	3.17
M	19/07/26	1	50.1	0.77×10^{-4}	3.72×10^{-7}	0.64	3.78	7.19	3.18
N	19/10/30	1	50.1	0.42×10^{-4}	2.04×10^{-7}	0.58	3.78	5.34	3.09

Table 4.2. – Parameters of the experiments in regime II used in the present chapter. The "Set" entry corresponds to the set of pumps used in the experiment. For the set #2, pumps with higher flow rates were employed, allowing us to reach larger Reynolds numbers (see Appendix B for more details). $\mathscr{K} = u_{\rm rms}^2/2$ is the total kinetic energy averaged over 500 rotation times. ϵ^E is an estimate of the upscale energy transfer rate based on dissipation in the Ekman boundary layers (equation (4.1)). L_T is the Thorpe scale measured experimentally and discussed in section 4.4. The Ekman number, E, the Reynolds number Re and the zonostrophy parameter R_β are defined in Table 4.1.

consequences of a modified β-effect. At these rotation rates, as shown in Appendix B.5, the β-effect is no more uniform but nevertheless varies in a limited range ($\beta_{80} \in [57,73]$ $\mathrm{m^{-1}\,s^{-1}}$ with a mean at 65.5 $\mathrm{m^{-1}\,s^{-1}}$ and $\beta_{60} \in [20,30]$ $\mathrm{m^{-1}\,s^{-1}}$ with a mean at 22.8 $\mathrm{m^{-1}\,s^{-1}}$). Fig.4.1 represents the experiments listed in Table 4.2 in the non-dimensional parameters space (E, Re, R_β). The apparent correlation between the non-dimensional parameters reflects the experimental constraints. Experimentally, the essential control parameter that we have is the forcing intensity (i.e. indirectly $u_{\rm rms}$). This allows us to explore significantly different Reynolds numbers, however, increasing $u_{\rm rms}$ also increases R_β by decreasing the relative importance of large-scale drag (Fig.4.1 *(c)*). Finally, we cannot explore a large range of Ekman numbers because the rotation rate of the experiment is fixed, as mentioned above. For the three experiments performed at a different rotation rate, both E and R_β are modified since changing the rotation rate also modifies the β-effect by changing the fluid height.

Fig.4.2 shows two instantaneous velocity fields as measured by PIV once the statistically steady state is achieved. Both experiments are in regime II but correspond to different sets

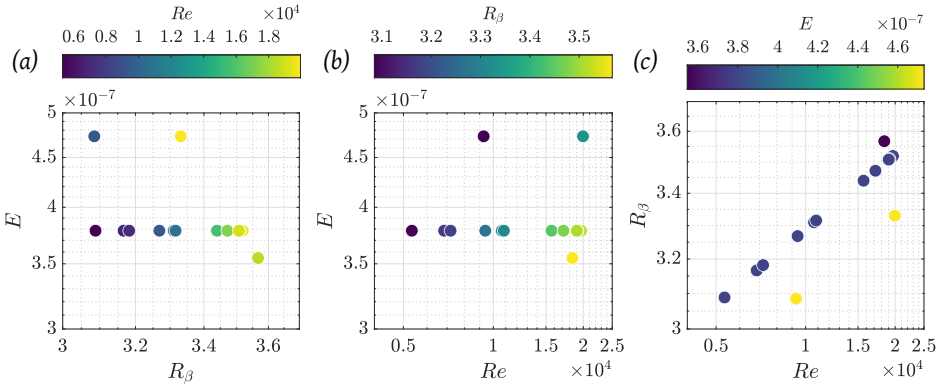

Figure 4.1. – Location of the experiments listed in Table 4.2 in the non-dimensional parameters space (E, Re, R_β). These parameters are defined in Table 4.1.

of pumps, leading to $Re = 10.8 \times 10^3$ and 19.7×10^3 respectively (experiments J and A of Table 4.2). Qualitatively, our experiments performed at higher Reynolds number lead to broader and intensified zonal jets, as can be seen in Fig.4.3 which shows the zonal flow profile for experiments N, J and A. The broadening of the prograde jets also leads to the fact that for our most extreme experiments, only one prograde jet can fit in the experimental domain, whereas two to three prograde jets can be obtained for the smallest Re. As the forcing is increased, we also notice that the prograde jets become less "wavy". Our hypothesis is that for moderate Re, the flow is close to the transition threshold and thus quasi-resonant, as described in chapter 3. Farther from the transition threshold, the resonant Rossby waves are less prone to develop and interact with the jet.

4.3. Spectral analysis of experimental measurements: signature of the zonostrophic regime

4.3.1. Zonal and residual kinetic energy spectra

As detailed in chapter 1 (§1.4.2.2), in the inertial range of the zonostrophic regime, i.e. between k_β and k_α, the kinetic energy spectra computed from the axisymmetric (zonal) component of the flow E_Z and from the residual non-axisymmetric component E_R follow different scalings similar to those in β-plane turbulence (Huang et al. 2000; Sukoriansky et al. 2002; Galperin et al. 2006; Sukoriansky et al. 2007). Since high wave number modes are nearly isotropic, the residual spectra is expected to be the classical one of KBK theory of 2D turbulence:

$$E_R^{\text{theo}}(k) \sim C_K \epsilon^{2/3} k^{-5/3}, \tag{4.6}$$

where k is the total wavenumber, and $C_K \approx 6$ (Boffetta et al. 2012) is the universal Kolmogorov-Kraichnan constant. On the contrary, the zonal spectrum follows a steeper slope:

$$E_Z^{\text{theo}}(k_r) \sim C_Z \beta^2 k_r^{-5}, \tag{4.7}$$

with k_r the wavenumber in the direction orthogonal to the zonal flow, i.e. the radial wavenumber in our case. C_Z is a constant of order unity (Rhines 1975; Chekhlov et al. 1996; Huang et al. 2000), which value was shown to lie around 0.5 by numerical simulations (Sukoriansky et al. 2002), and around 2 for Jupiter (Galperin et al. 2014b) and from 1.7 to 3.7 in the experiments of Cabanes et al. (2017). The theory of zonostrophic turbulence shows that the kinetic

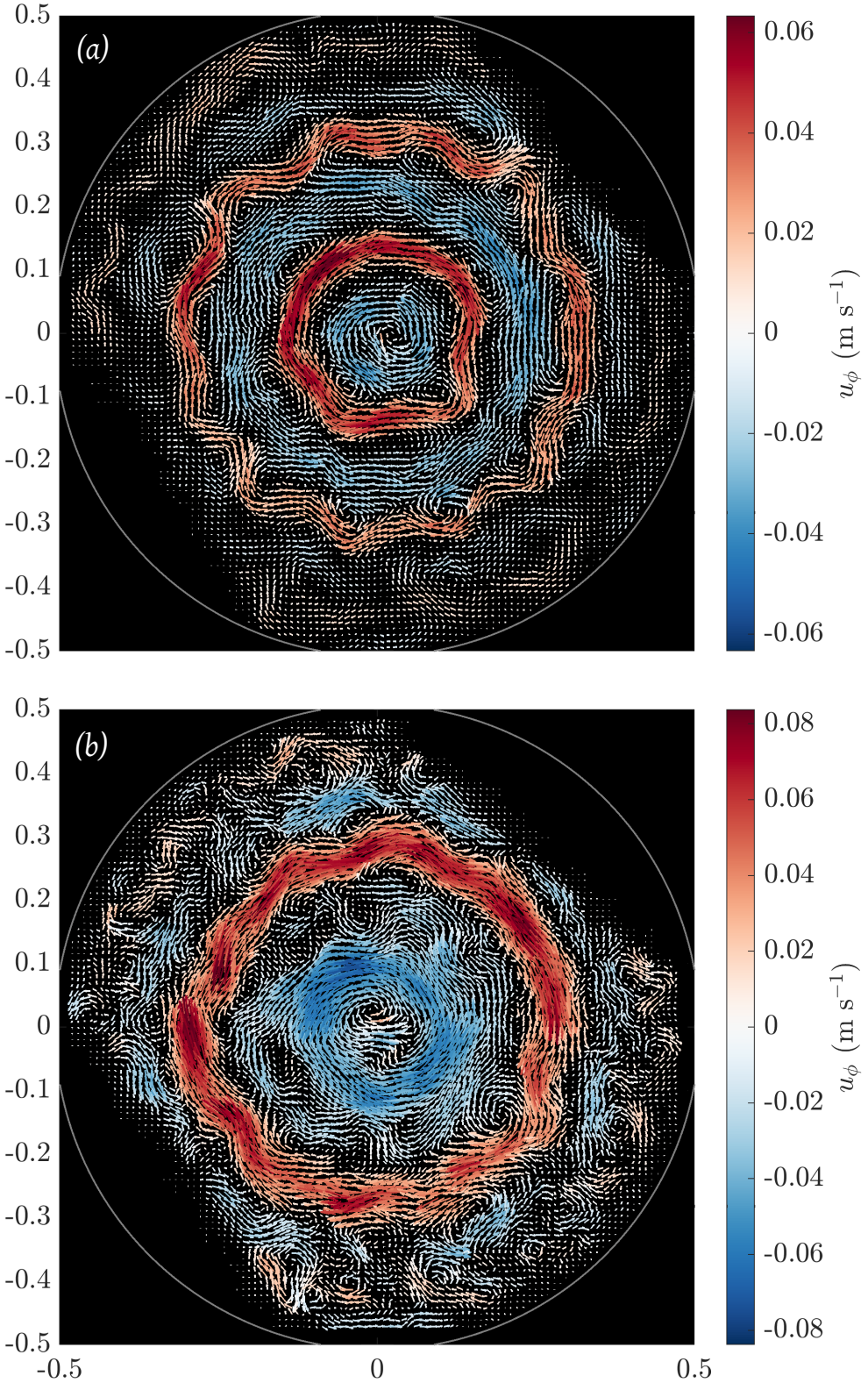

Figure 4.2. – Instantaneous velocity fields measured from PIV in the statistically steady state of *(a)* experiment J and *(b)* experiment A of Table 4.2. The vectors magnitude scale is the same for the two plots.

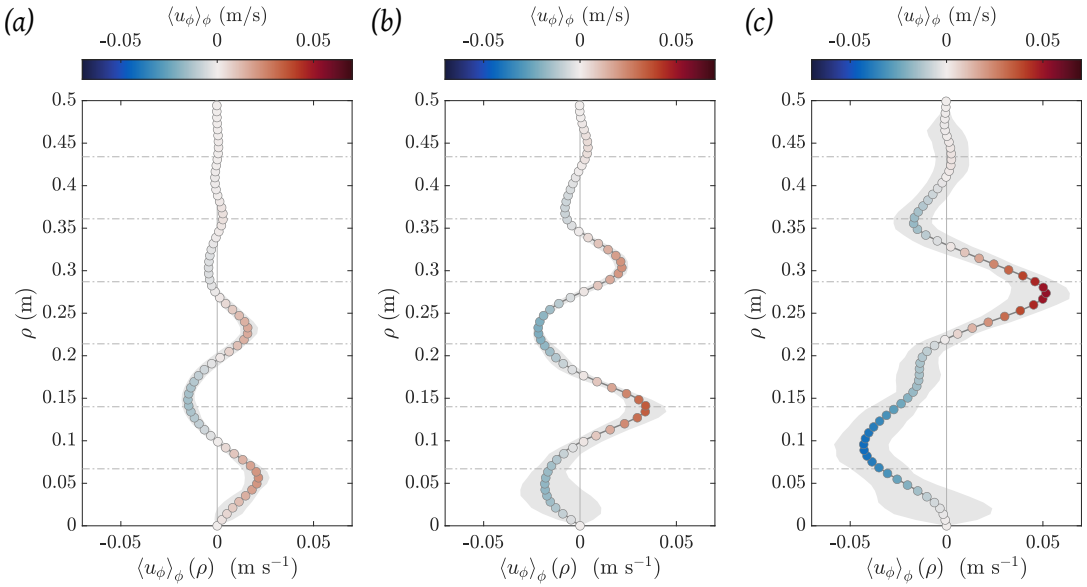

Figure 4.3. – Time-averaged zonal flow in *(a)* experiment N, *(b)* experiment J and *(c)* experiment A of Table 4.2. The shaded area represents the envelope of all the instantaneous profiles. Dashed lines represent the location of the forcing rings.

energy spectra can provide a useful insight on the exchange of energy between scales as well as a diagnostic tool to determine to what extent a given flow is in the regime of zonostrophic turbulence. In this section, we compare the predictions of this theory with our experimental measurements.

Given the rotational symmetry of the experimental 2D velocity fields obtained from PIV, we perform a Bessel-Fourier decomposition relevant to the polar system of coordinates (ρ, ϕ), for which details can be found in Appendix D. Owing to the periodicity in ϕ, the finite domain in radius, $\rho \leq R$, and the zero-value boundary condition at $\rho = R$, the relevant basis functions Ψ_{nm} to decompose our fields are separable in polar coordinates and consist in a complex exponential for the angular part, and normalized Bessel functions for the radial part:

$$\Psi_{nm}(\rho,\phi) = \frac{1}{\sqrt{2\pi N_{nm}}} J_m(k_{nm}\rho) e^{im\phi}, \tag{4.8}$$

$$\text{with } N_{nm} = \frac{R^2}{2} J^2_{m+1}(\alpha_{nm}). \tag{4.9}$$

J_m is the Bessel function of the first kind of order m, α_{nm} is the n^{th} positive zero of J_m, and the radial wavenumber $k_{nm} = \alpha_{nm}/R$ takes discrete values since the domain is bounded. For each Ψ_{nm}, m is the number of periods in the angular direction, and $n-1$ corresponds to the number of zero crossings in the radial direction. The value of k_{nm} is thus an indication of the scale of the basic patterns, similarly to the normal Fourier transform (see Fig.D.1 in Appendix D). Any function, including our velocity fields $\boldsymbol{u} = (u_\rho, u_\phi)$ can be decomposed on this basis such that

$$\boldsymbol{u}(\rho,\phi) = \sum_{n=1}^{\infty} \sum_{m=-\infty}^{+\infty} \hat{\hat{\boldsymbol{u}}}_{nm} \Psi_{nm}(\rho,\phi), \tag{4.10}$$

where the double hat indicates the double transform. The Bessel-Fourier transform coefficients are

$$\hat{\hat{\boldsymbol{u}}}_{nm} = \int_0^R \int_0^{2\pi} \boldsymbol{u}(\rho,\phi) \Psi^*_{nm}(\rho,\phi) \rho \, d\rho \, d\phi. \tag{4.11}$$

For our experimental results, the PIV fields are obtained on a regular Cartesian grid. To evaluate the coefficients $\hat{\boldsymbol{u}}_{nm} = (\hat{u}_{\rho,nm}, \hat{u}_{\phi,nm})$, the velocity field is interpolated on a polar grid where the radial and azimuthal parts of the transform are separable. Since the velocity field is discrete, the coefficients (4.11) are computed using fast Fourier transform and discrete Hankel transform algorithms. The angular part is done using the Matlab *fft* function, and the radial part is performed using the Matlab algorithm provided by Guizar-Sicairos et al. (2004). Using the Parseval relation which arises from the orthogonality of the basis functions, kinetic energy spectra can be computed directly in the spectral space, and are proportional to $\hat{\boldsymbol{u}}_{nm}\hat{\boldsymbol{u}}^*_{nm}$ (see Appendix D). We denote E_{nm} the kinetic energy contained at the wavenumber k_{nm}. We distinguish the kinetic energy contained in the zonal mode, $m = 0$, denoted E_Z and the residual kinetic energy spectra E_R, which is the sum of the contribution of all the non-zonal modes, $m \neq 0$.

Fig.4.4 shows the zonal and residual kinetic energy spectra for three experiments, computed once the statistically steady state is achieved and averaged over 50 spectra spanning 600 rotation times. The spectra are plotted for the experiments M and B of Table 4.2, as well as an experiment in Regime I for the sake of comparison. Experiments M and B are both in Regime II, but experiment M was perform with the first set of pumps, and B with the second one and has a Reynolds number about twice higher (15700 versus 7200). Compensated spectra, i.e. spectra divided by the theoretical predictions, are also represented.

The energy spectra provide different information if we are looking at scales smaller or larger than the forcing scale. Experimentally, the forcing scale is assumed to be approximately the mean distance between two injections on the bottom plate, i.e. $L_f \approx 7.4$ cm and $k_f \approx 84.9\,\mathrm{rad\,m^{-1}}$. First, at scales smaller than the forcing scale, $k > k_f$, we observe a slope close to k^{-4}. This slope is steeper than the -3 slope expected from the direct cascade of enstrophy, but this behaviour is commonly observed in both numerical simulations and experiments of 2D turbulence, and may be due to a lacking logarithmic correction, or to friction effects (Boffetta et al. 2012). For the remaining of the chapter, we thus focus scales larger than the forcing scale ($k < k_f$), corresponding to the shaded area on the compensated spectra (Fig.4.4*(b,d,f)*). We observe that the residual energy spectra follow a $-5/3$ slope consistent with the presence of an inverse cascade of energy. This slope proceeds farther than k_β, meaning that the inverse cascade continue past the anisotropisation threshold, consistently with the numerical spectra of Sukoriansky et al. (2007). For the zonal energy spectra, in Regime I (Fig.4.4*(a,b)*), the zonal energy is peaked at $k = k_f$, meaning that the zonal flow develops at the forcing scale and is locally forced. This is consistent with the mechanism described in the chapter 3 for zonal jets formation in Regime I. In addition, the $m = 0$ mode contains less energy than the residual ones at all scales except the forcing one. More precisely, the time-averaged total kinetic energy in the flow is of $8.12 \times 10^{-6}\mathrm{m^2\,s^{-2}}$, with a zonal part of $1.63 \times 10^{-6}\mathrm{m^2\,s^{-2}}$, such that the $m = 0$ mode contains $\sim 20\%$ of the total kinetic energy. In Regime II, for both experiments B and M, the zonal energy spectra are not peaked at the forcing scale anymore, and instead the spectrum follows a steep k^{-5} slope up meaning that there is an energy transfer towards scales larger than the forcing one. Fig.4.5*(b)* shows the superposition of the zonal spectra for the three experiments. For experiments M and B, the zonal energy peaks at $k \sim 30$ and 24 respectively, corresponding to wavelengths of 21 cm and 26 cm which represent the large radial wavelength of the zonal jets seen in Fig.4.5*(a)*. At the largest scales, the zonal mode now contains more energy than all the residual modes. Note that the energy progressively flows towards these large scales, since this steep slope is not developed yet during the transient of the same experiments (dashed line in Fig.4.4*(e)*). For experiment M, the total kinetic energy is of $7.75 \times 10^{-5}\mathrm{m^2\,s^{-2}}$ and the zonal mode contains 58% of it, whereas for experiment B, the total kinetic energy is of $3.66 \times 10^{-4}\mathrm{m^2\,s^{-2}}$ and the zonal mode contains 68% of it.

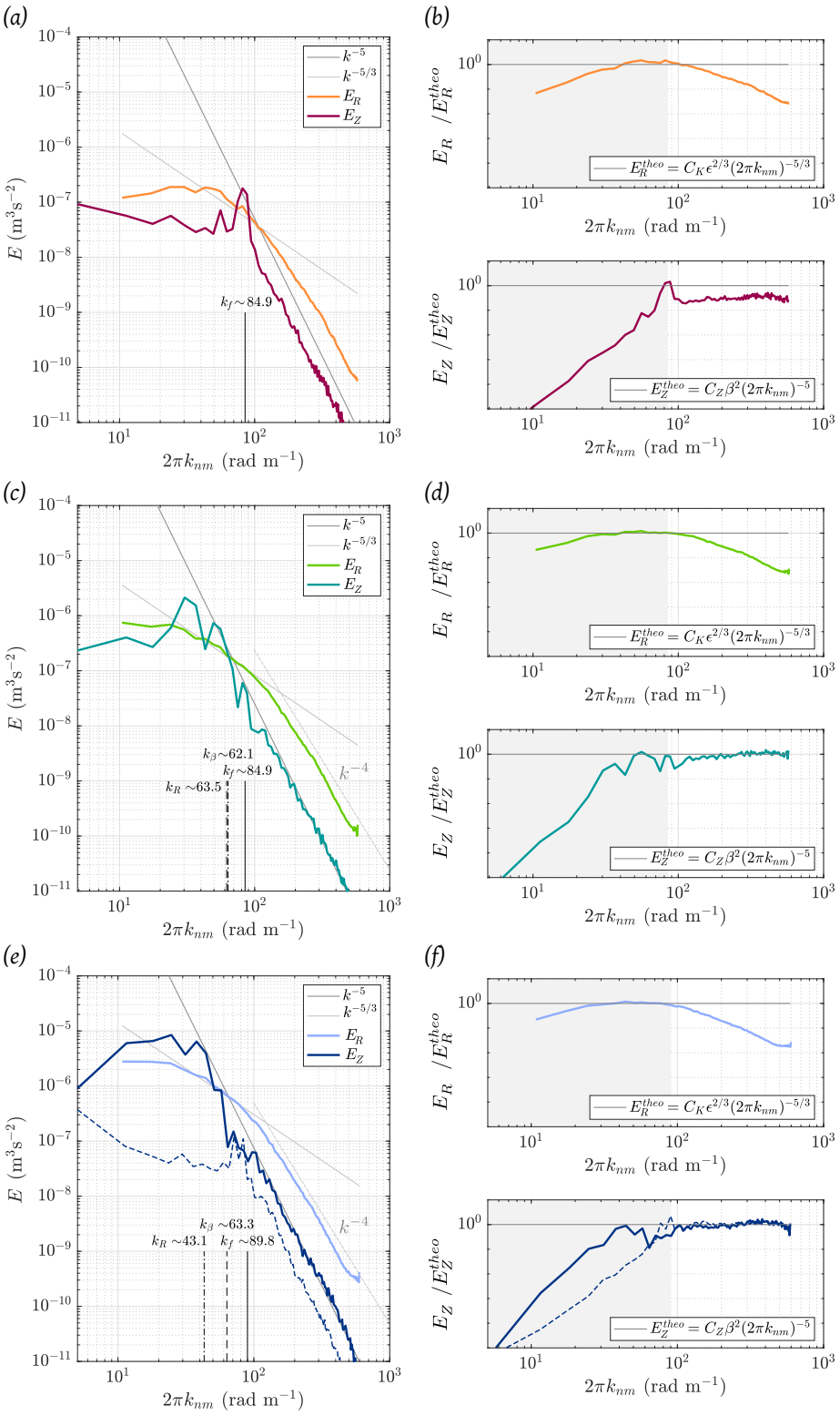

Figure 4.4. – Kinetic energy spectra for three different experiments. We separate the zonal (E_Z) and residual (E_R) contributions. The grey lines correspond to the theoretical predictions given by equations (4.6) and (4.7). On the right side, the spectra are normalized by these theoretical predictions, and the shaded area corresponds to $k < k_f$. For E_R^{theo}, we take $C_K = 6$ and find ϵ that best fits the experimental spectra. For E_Z^{theo}, since β is known, we find C_Z that best fits the data. *(a,b)* Experiment in Regime I. *(c,d)* Experiment M of Table 4.2. *(e,f)* Experiment B of Table 4.2. The dashed lines correspond to E_Z computed during the transient of the experiment.

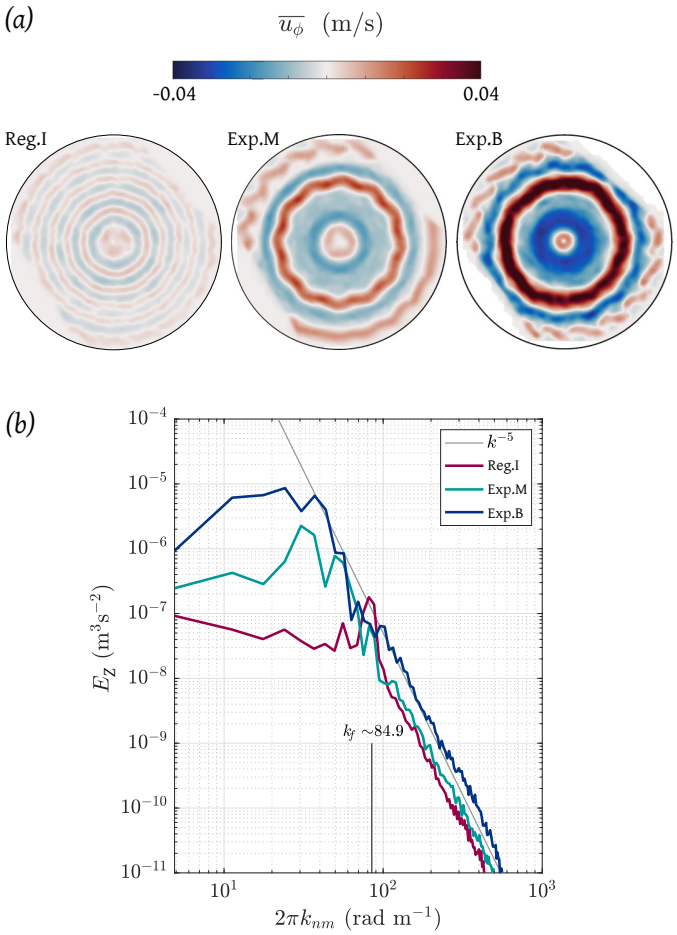

Figure 4.5. – *(a)* Time-averaged azimuthal component of the velocity $\overline{u_\phi}$. The time average is performed over 600 rotation times, similarly to the spectra. *(b)* Superposition of the zonal kinetic energy spectra of the three experiments of Fig.4.4.

4.3.2. Rate of upscale energy transfer

Previously, we estimated the upscale energy transfer of the inverse cascade, ϵ^E, by assuming that dissipation consists in Ekman friction. The amplitude of the theoretical spectra can be used to actually measure ϵ (equation (4.6)) which is otherwise difficult to do experimentally. To do so, we take the commonly accepted value $C_K \approx 6$ for the Kolmogorov-Kraichnan constant (Boffetta et al. 2012) and deduce ϵ^S from the fit of the $-5/3$ slope on the spectra. The deduced values are reported in Table 4.3, and lie between 5×10^{-8} and $3\times10^{-6}\mathrm{m}^2\,\mathrm{s}^{-3}$ for the selected experiments. We see from Table 4.2 that the estimated ϵ^E has the correct order of magnitude compared to the measured one ϵ^S, but the precise comparison between the two, visible in Fig.4.6*(a)*, shows a small deviation from a pure proportionality relationship. For the zonal spectra, since β is known, we report the values of C_Z corresponding to our fits (equation (4.7)). C_Z is supposedly universal in the zonostrophic regime. According to the numerical simulations reported in Sukoriansky et al. (2002), Galperin et al. (2006), and Sukoriansky et al. (2007), it should lie around 0.5. Our experimental measurements show that $C_Z \sim 0.2-0.3$ and remains almost the same for all of our experiments despite very different upscale energy transfer rate, which comforts the idea of a universal constant. Its value is smaller for our weakest experiments (M,N), but these experiments are only slightly super-critical with respect to the transition from Regime I to II, and they are probably only marginally zonostrophic. We also note that our value for C_Z is smaller than that of Cabanes et al. (2017) who found $C_Z \sim 1.7-3.7$. This difference may come from the fact that the experiments of Cabanes et al. (2017) are not in the β-plane framework since β is strongly varying with radius (see Fig.B.10*(b)*). The β parameter to use in equation 4.7 is thus uncertain, whereas in our case β is uniform and uniquely defined. In addition, the forcing scale in Cabanes et al. (2017) is twice larger than the present one, and close to the transitional scale as we discuss later. Galperin et al. (2006) report that in that case, the spectra exhibit non-universal behaviours.

The intersection of the theoretical $-5/3$ (equation (4.6)) and -5 (equation (4.7)) slopes defines a spectral transitional wavenumber k_β^S, which can be expressed as

$$k_\beta^S = \left(\frac{C_Z}{C_K}\right)^{3/10}\left(\frac{\beta^3}{\epsilon}\right)^{1/5}. \tag{4.12}$$

This scale thus defines the scale above which the zonal mode contains more kinetic energy than all the residual modes considered together. In our case, since $C_K = 6$ and $C_Z \sim 0.2-0.3$, the prefactor $(C_Z/C_K)^{3/10}$ is of about $0.36-0.4$. The spectral transitional wavenumber, k_β^S is thus less than half that based on the values of ϵ and β only, k_β^ϵ (equation (4.3)). Both values are reported in Table 4.3 for our selected experiments. We additionally report the values of the Rhines wavenumber k_R, based on the total rms velocity. The Rhines and transitional scales are also indicated on the spectra, in Fig.4.4. Finally, the last two columns of Table 4.3 report the zonostrophy parameter with or without using the prefactor on the transitional wavenumber: $R_\beta^S = k_\beta^S/k_R$ and $R_\beta^\epsilon = k_\beta^\epsilon/k_R$. The spectral zonostrophy index of our experiments lies between 0.95 and 1.6, whereas without the prefactor on k_β, we obtain values between 3 and 4.

4.3.3. Discussion on the zonostrophic theory

The measured values of R_β^S question the extent to which our experiments are in the zonostrophic regime. Using 2D barotropic simulations on the sphere, Galperin et al. (2006) and Sukoriansky et al. (2007) found $C_Z \sim 0.5$ and $C_K \sim 6$ (prefactor $(C_Z/C_K)^{3/10} \sim 0.5$), and a lower bound for the zonostrophic regime $R_\beta^S \gtrsim 2.5$. We would then be in the transitional regime between the dissipation-dominated regime and the zonostrophic turbulence. But since we

Label	u_{rms} ($\mathrm{cm\,s^{-1}}$)	$\epsilon^S \times 10^7 (\mathrm{m^2\,s^{-3}})$	C_Z	$k_\beta^S (\mathrm{rad\,m^{-1}})$	$k_\beta^\epsilon (\mathrm{rad\,m^{-1}})$	$k_R (\mathrm{rad\,m^{-1}})$	R_β^S	R_β^ϵ
A	3.39	$27.6 \in [24.7, 30.8]$	0.3	58.0	135.4	38.1	1.43	3.52
B	2.70	$11.4 \in [10.2, 12.8]$	0.3	63.3	161.6	43.1	1.52	3.75
C	3.17	$22.0 \in [18.5, 26.2]$	0.2	61.4	166.4	45.0	1.32	3.66
D	3.44	$37.1 \in [33.6, 40.8]$	0.2	33.7	79.6	25.7	1.11	3.09
E	2.96	$15.4 \in [12.4, 18.9]$	0.2	54.0	152.2	41.0	1.33	3.70
F	3.30	$29.1 \in [24.7, 3.08]$	0.3	58.6	134.0	38.9	1.40	3.44
G	3.28	$20.7 \in [16.8, 25.4]$	0.3	58.8	143.5	39.1	1.49	3.67
H	1.62	$3.78 \in [3.01, 4.76]$	0.3	76.9	201.6	55.5	1.47	3.62
I	1.84	$3.69 \in [2.70, 5.05]$	0.3	73.3	202.6	52.1	1.58	3.88
J	1.87	$3.62 \in [2.75, 4.76]$	0.3	72.9	203.3	51.8	1.60	3.92
K	1.60	$2.70 \in [2.18, 3.32]$	0.3	50.2	134.4	37.7	1.45	3.56
L	1.18	$1.80 \in [1.59, 2.03]$	0.2	77.4	233.8	65.2	1.29	3.59
M	1.24	$1.63 \in [1.40, 1.91]$	0.1	62.1	238.5	63.5	1.09	3.75
N	0.92	$0.56 \in [0.45, 0.69]$	0.05	57.0	295.3	73.7	0.95	4.00

Table 4.3. – Parameters deduced from the spectral analysis. We use $C_K = 6$ and deduce ϵ^S from equation (4.6) and a fit of the $-5/3$ slope the residual spectra. The constant C_Z is determined by a fit on the -5 slope of the zonal spectra, since β is known (Table 4.2). The transitional wavenumber based on the spectral slopes intersection is denoted k_β^S (equation (4.12)), whereas the transitional wavenumber based on ϵ only is denoted k_β^ϵ (equation (4.3)). k_R is the Rhines wavenumber (equation (4.4)), $R_\beta^S = k_\beta^S / k_R$ and $R_\beta^\epsilon = k_\beta^\epsilon / k_R$.

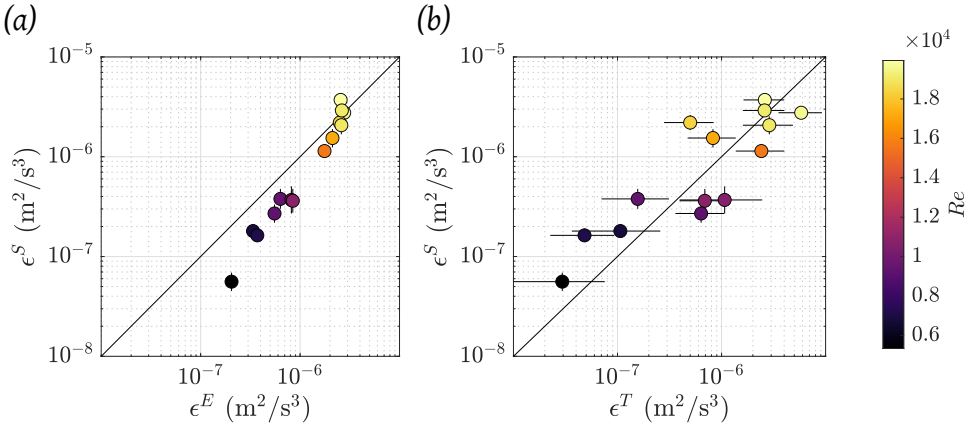

Figure 4.6. – Upscale energy transfer rate measured on the spectra, ϵ^S, versus *(a)* the estimated one based on dissipation by Ekman friction (4.1), ϵ^E, and *(b)* the deduced one from the Thorpe scale, ϵ^T, assuming that $L_\beta^T = L_T / 0.031$ (Fig.4.9*(b)*) and $\epsilon^T = (L_\beta^T / 2\pi)^5 \beta^3$. Vertical error bars account for the uncertainty in ϵ^S due to the uncertainty in the slope measured on the spectra. Horizontal error bars account for the standard deviation when measuring the Thorpe scale.

measure $C_Z \sim 0.2-0.3$, the prefactor is reduced, and the threshold should be rescaled as $R_\beta^S \gtrsim 1.8$. In addition, as seen in Fig.1.15*(a)*, the 2.5 threshold is only indicative (the boundary between the regimes is not a strict proportionality relationship, and implies an offset). That being said, in Galperin et al. (2006) and Sukoriansky et al. (2007), the authors in fact use the spectra as a diagnostic tool to determine the flow regime. In other words, the simulations considered in the zonostrophic regime are those where the predicted spectra are recovered, with a *universal* behaviour and a $C_Z \sim 0.5$ constant. Consistently, we argue that one should rather look at the spectra to determine in which regime we stand, and not the absolute value of the zonostrophy index alone. The important differences between our 3D experiments and their 2D simulations on the sphere is very likely to induce significant differences in the threshold of the zonostrophic regime. The fact that we recover a -5 steep slope for the zonal spectrum, and that the zonal flow contains more energy than the fluctuations at large scales is somewhat more robust and physically meaningful that the absolute value of R_β alone. The zonostrophy parameter is nevertheless useful to compare the degree of zonostrophy of different experiments, as soon as it is computed the same way for each experiment. This is what was done to plot Fig.3.1, where we compare various experiments on zonal jets.

A second point that we want to discuss is the importance of the forcing scale. In the theory of zonostrophic turbulence, the zonostrophic regime is not defined by a single inequality on R_β, but rather a series of inequalities: $30/R \leq 8k_\alpha \leq 2k_\beta \leq k_f$, where R is the radius of the sphere, and we recall that k_f is the forcing wavenumber (Galperin et al. 2006). The forcing should thus act at a scale smaller than the scale at which the eddies start to feel the β-effect for a significant Kolmogorov-Kraichnan inertial range to exist and an isotropic inverse cascade to develop. Practically, when the forcing scale is too large, Galperin et al. (2006) report that non-universal behaviours are observed on the spectra, without giving much additional details. In environmental flows (oceans and planetary atmospheres), typically, the forcing acts at a scale smaller than the scale of turbulence anisotropisation L_β by a factor 2 to 3 (Galperin et al. 2019b, table 13.1). In our experiment, and as discussed previously, we can estimate that the forcing scale is in fact about one to twice L_β^ϵ. The forcing is thus already directly influenced by the β-effect, which is quite clear on the fluid response at the earliest times of our experiments (see Fig.3.10 of the previous chapter). The variability in the forcing scale compared to L_β may explain the rather non-universal estimates of C_Z in simulations on the sphere compared to Jupiter's zonal flows and experiments. Second, it is probable that we prevent the initial *isotropic* inverse energy cascade – an anisotropic cascade is present since the jets scale remains larger than the forcing scale. Since we do obtain the scalings expected in the zonostrophic regime, our experiments hence seem to demonstrate that the scale of the forcing is not such an important parameter for the zonal flow to develop at large scales, and that a steep zonal spectra may develop even if $k_f \sim k_\beta$. Again, it is not extremely surprising that the condition on the forcing scale might be relaxed in an experimental, 3D flow, compared to numerical simulations of a purely 2D flow. These considerations on the forcing scale are consistent with the work of Scott et al. (2019), who demonstrated in the framework of potential vorticity mixing that the late-time resulting zonal jets profile is the same whether the forcing is performed at large scale or at small scale, the important parameter being the zonostrophy index R_β only. Here, despite forcing the flow at a relatively large scale, the observed jets are highly energetic and instantaneous. If nevertheless one wishes to reach the regime of a well-developed inverse turbulent cascade, the goal should be to decrease the forcing scale, which is then a further experimental challenge.

4.4. Potential vorticity mixing

We now turn to the second theoretical framework thanks to which we can better understand the saturation in regime II, and use it to quantify turbulent dissipation rates independently of the spectral analysis presented in the previous section.

In the inviscid limit, the quasi-geostrophic model of the experimental flow reduces to the material conservation of the potential vorticity (PV) q defined as

$$q(\rho,\phi,t) = \frac{\zeta(\rho,\phi,t)+f}{h(\rho)} \tag{4.13}$$

(see equation (C.29) in Appendix C). An mentioned in the introduction, in the framework of PV mixing, narrow prograde jets correspond to strong gradients of PV whereas large retrograde jets coincide with regions of weak gradients, leading to the establishment of a PV staircase, as illustrated in Fig.1.15*(d)*.

In Fig.4.7, we plot instantaneous PV contours and associated PV maps for the experiments J and A (Table 4.2), which correspond to increasing Reynolds numbers. Because the fluid height h increases exponentially with radius, the background PV profile, f/h, obtained when the flow is at rest in the rotating frame, is maximum at the centre and decreases smoothly towards the edge of the tank. When zonal jets develop, the PV maps show that the PV does not decrease smoothly radially, but instead thin areas of sharp gradients develop. In Fig.4.8*(a,b)*, we represent the associated azimuthally-averaged PV profiles, $\langle q\rangle_\phi(\rho)$ (referred to as "zonal PV"). The steps are more readily visible on these profiles, and each of them corresponds to the presence of a prograde jet, whereas the regions in between are supporting a retrograde flow. As underlined in chapter 3, despite significantly increasing *Re*, and thus increasing degree of mixing, the "staircasing" remains moderate even for our most extreme experiments.

To obtain quantitative information from this framework of potential vorticity mixing, we follow the idea developed in Galperin et al. (2014a) which takes advantage of the analogy that exists between the salinity staircases that develop in stratified turbulence (observed in the oceans), and the PV staircases that develop in β-plane turbulence (observed on the gas giants). A common analysis performed in stratified turbulence is to quantify the efficiency of the turbulent mixing by computing how far is an instantaneous density profile from a monotonous density profile, where density would increase monotonously with depth. This is quantified using Thorpe's sorting algorithm, where each profile of density with depth is sorted in ascending order, and the corresponding rms displacement of the fluid parcels from their initial position is deduced. This rms displacement is called the Thorpe scale, L_T, and gives an estimate of the size of the overturns due to turbulent eddies (Thorpe 2005). We apply this procedure to instantaneous PV profiles along the radius, for all the possible angles ϕ. Examples of such profiles before and after sorting are shown in Fig.4.8*(b,e)*, and the resulting Thorpe scale estimated on several profiles at different angles are represented in Fig.4.8*(c,f)*. The increase in the Thorpe scale and thus in the turbulent mixing is clear when the Reynolds number of the experiment is increased: experiment J shows almost no deviation from a monotonous PV profile, meaning that overturns are not frequent and the PV is not efficiently mixed, whereas strong deviations are observed for experiment A.

The advantage of the Thorpe scale is that it is very easily measured a posteriori, for a given flow, and that it is an indirect measure of turbulence intensity (Thorpe 2005). For stratified turbulence, the Thorpe scale can be used to estimate the so-called Ozmidov scale, L_O which corresponds to the scale at which the turbulent turnover time is equal to the internal waves period, i.e. the scale at which turbulence starts to feel the stratification of buoyancy frequency

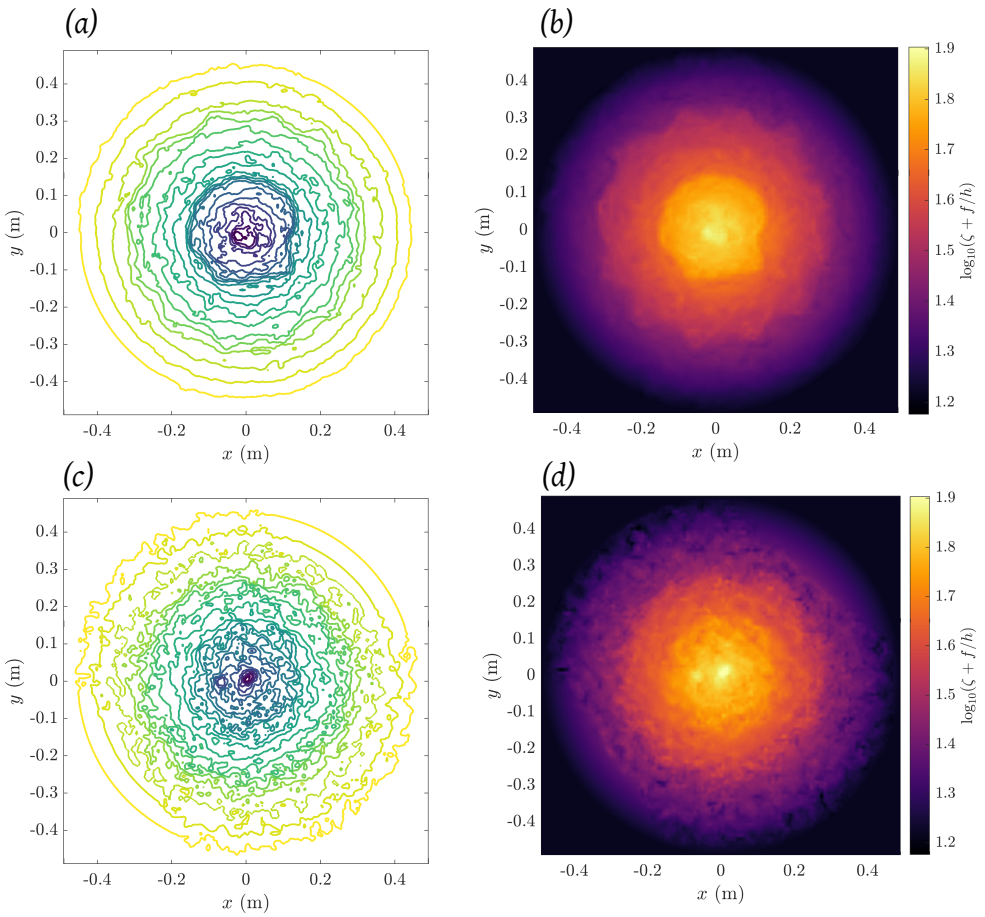

Figure 4.7. – Instantaneous potential vorticity contours and maps. The contours are plotted from q =15 to 85 $\mathrm{m^{-1}\,s^{-1}}$ with a step of 3.5 $\mathrm{m^{-1}\,s^{-1}}$. *(a,b)* Experiment J. *(c,d)* Experiment A.

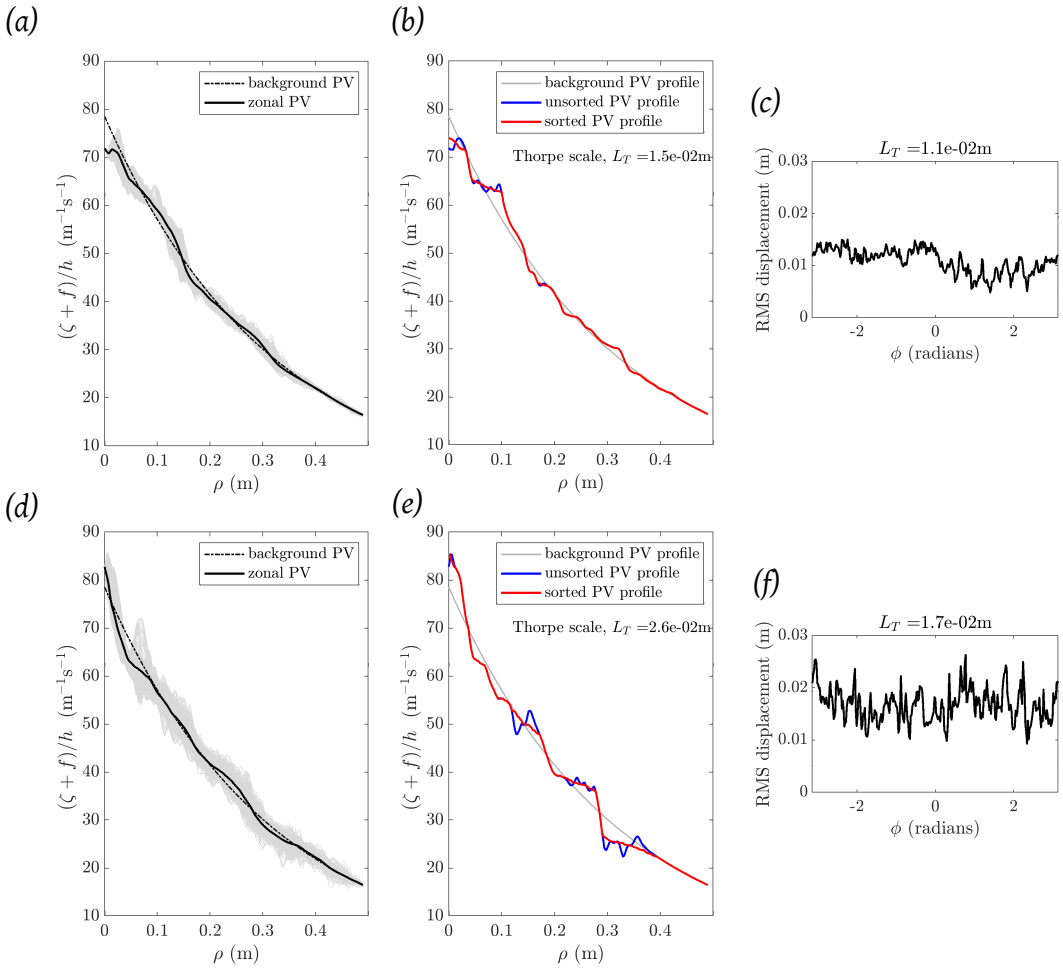

Figure 4.8. – *(a,d)* Instantaneous zonally-averaged potential vorticity profiles $\langle q \rangle_\phi(\rho)$ (black line). The grey lines show the variability of the PV profiles before performing the zonal average. *(b,e)* Instantaneous PV profile at a fixed angular position $q(\rho,\phi_0)$. Blue line: before sorting, red line: after sorting. *(c,f)* Thorpe scale computed by the sorting processing for all the possible angular positions $\phi_0 \in [-\pi,\pi]$. The indicated value, L_T, corresponds to the averaged value for all angles. Top row: experiment J. Bottom row: experiment A.

N:

$$L_O = \left(\frac{\epsilon}{N^3}\right)^{1/2}. \tag{4.14}$$

L_O is thus the largest isotropic scale of the system, and is analogous to the transitional scale, L_β. Hence, if L_T allows to estimate L_O in stratified turbulence, it may allow to estimate L_β in β-plane turbulence. This is of interest because ϵ can then be estimated from L_β (equation (4.3)). Here, we wish to confront this hypothesis to our experimental measurements, where we have measured ϵ and thus L_β^ϵ in a completely independent way using the spectral analysis. Fig.4.9 compares the Thorpe scale measured in our experiments with the Rhines scale L_R and the transitional scales L_β^ϵ and L_β^S. These figures show that there is a very good correlation between L_T and both L_R and L_β. The fact that the correlation works equally well for those two scales arises from the fact that in our experiments, we always have $L_R \sim 3L_\beta^\epsilon$, i.e. the zonostrophy parameter does not vary sufficiently for the two scales to behave independently. This is however a demonstration that L_T can be used as a proxy of the typical length scales of the flow. If one assumes $L_T \sim 0.031 L_\beta^\epsilon$ as determined from Fig.4.9*(b)*, then we can defined a Thorpe estimate of the turbulent dissipation rate ϵ^T computed from the relation between L_β and ϵ (equation (4.3)). The comparison between the measured ϵ^S and ϵ^T is represented in Fig.4.6*(b)*. There is a non-negligible dispersion around the 1:1 relationship, but the overall tendency is good, suggesting that PV sorting can effectively be used to estimate turbulent energy transfers. Note that to properly address the correspondence between L_T and L_β, it would be necessary to explore the parameter space (E, Re, R_β) more extensively. This is beyond what is reachable with our experiments, because we cannot explore *independently* a sufficient range of Ekman, Reynolds and zonostrophy parameters. In that prospect, performing numerical simulations where each of the non-dimensional parameters can be varied while keeping the two other fixed would be relevant. That being said, the scaling that we found holds for the whole range of Re explored.

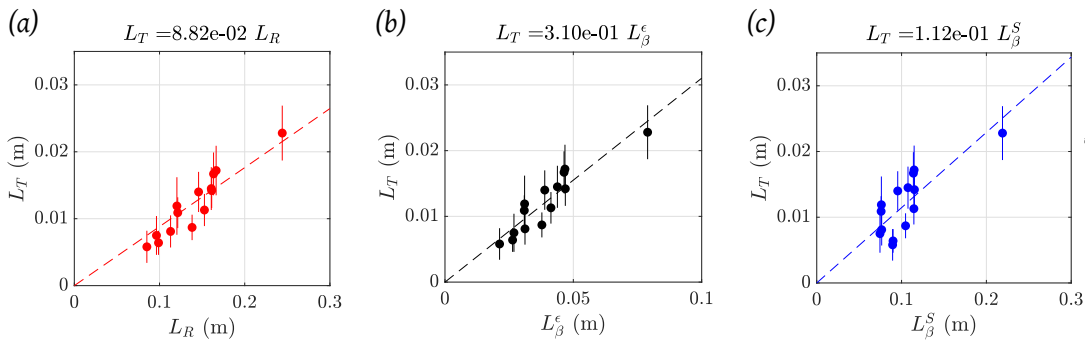

Figure 4.9. – Comparison between the Thorpe scale L_T and *(a)* the Rhines scale (4.4), *(b)* the transitional scale based on the upscale energy transfer (4.3), and *(c)* the spectral transitional scale (4.12). The equation at the top of each panel is the best linear fit plotted in dashed line.

We mentioned in the chapter's introduction that PV mixing is associated with the idea that prograde zonal jets act as meridional (radial) transport barriers owing to the Rossby waves elasticity. As will be discussed further in section 4.6, the transport properties of zonal flows have important implications for oceans, atmospheres but also liquid cores dynamics and budgets of heat and energy. In the next section, we present preliminary results on the turbulent transport properties of our experimental zonal flows.

4.5. Effective turbulent diffusivities and zonal jets as transport barriers

A problematic closely related to the turbulent saturation in Regime II is the characterisation of the transport properties of the associated flow. Indeed, the flow being both turbulent and anisotropic, we expect that the dispersion properties of a passive scalar can provide information on both the turbulent intensity and the degree of anisotropy of the flow. For geophysical applications, the interest is twofold:

— Measuring Lagrangian transport properties in a natural flow can provide a third way of estimating ϵ. This is particularly relevant for the terrestrial oceans, for which we have dispersion data from floats (van Sebille et al. 2018);

— Since the anisotropy of natural flows can be estimated from velocity fields, one could deduce from it the influence on both the magnitude and the anisotropy of the turbulent diffusivity. Understanding such effects is important for improving global circulation models of oceans or atmospheres since the effective turbulent diffusivities are parametrized and do not results from the actual dynamics of resolved scales (Fox-Kemper et al. 2019).

These points will be further developed in the discussion section, §4.6. To quantify turbulent transport, we perform two distinct analyses described in the next two sections: first, we compute the finite-scale Lyapunov exponent of our flows to quantify anisotropy and identify different dispersion regimes. Second, we estimate more directly an effective diffusivity as a function of radius to evaluate how the zonal flow affects the transport. Both analyses rely on the post-processing of numerically integrated Lagrangian trajectories computed from PIV velocity fields.

4.5.1. Finite scale Lyapunov exponent (FSLE) analysis

4.5.1.1. Method

Using Finite Scale Lyapunov Exponents (FSLE) to characterize transport properties is useful because it provides a scale-dependent quantification of transport (LaCasce 2008). In our flows, the presence of a transitional scale separated from the scale of the jets let us think, a priori, that dispersion will indeed be dependent on the considered scale, as concluded by Ollitrault et al. (2005) from oceanographic data, and Lacorata et al. (2012) from laboratory experiments. In addition, the scaling law between the FSLE and the scale tells about the nature of the dispersion regime, and has been used in regional oceanic flows to quantify the contribution of different scales to oceanic mixing (e.g. Corrado et al. 2017).

From mixing length theory, the effective diffusivity at a scale δ is

$$D(\delta) = E_{\mathrm{cml}}(\delta)^{1/2}\delta, \tag{4.15}$$

where $E_{\mathrm{cml}}(\delta)$ is the turbulent energy cumulated up to scale δ. The underlying assumption is that all scales smaller than δ contribute to dispersion at this scale. If the flow is isotropic, then

E_{cml} can be estimated by integrating the kinetic energy spectra up to scale δ:

$$\begin{aligned} E_{\text{cml}}(\delta) &= \int_{k_\delta}^{+\infty} E(k)dk && (4.16)\\ &= C_K\epsilon^{2/3}\int_{k_\delta}^{+\infty} k^{-5/3}dk && (4.17)\\ &= \frac{3}{2}C_K\epsilon^{2/3}k_\delta^{-2/3} && (4.18)\\ &= \frac{3C_K}{2(2\pi)^{2/3}}\,\epsilon^{2/3}\delta^{2/3} && (4.19) \end{aligned}$$

where we used the theoretical kinetic energy spectrum expected from an inverse cascade of energy (equation 1.58). The associated effective diffusivity then reads

$$D(\delta) = \frac{(3/2C_K)^{1/2}}{(2\pi)^{1/3}}\,\epsilon^{1/3}\delta^{4/3}. \tag{4.20}$$

This is the so-called Richardson diffusion law, where diffusivity depends on the scale at the power $4/3$.

Now, for a strongly anisotropic turbulence, it has been argued that different regimes of turbulent dispersion should be observed at different scales. For β-plane turbulence, the idea is based on the same assumptions as those of zonostrophic turbulence:

— At small scales, $\delta \leq L_\beta$, isotropic KBK turbulence exists and we expect to be in a Richardson regime (equation (4.20)). In addition, we expect no difference between the radial and azimuthal dispersion since the flow is supposed to behave in an isotropic way below the transitional scale. Hence,

$$D_{\text{rad}}(\delta \leq L_\beta) = D_{\text{zon}}(\delta \leq L_\beta) \propto \epsilon^{1/3}\delta^{4/3}. \tag{4.21}$$

— At large scales, $\delta \geq L_\beta$, the turbulence becomes strongly anisotropic. The inverse cascade can still proceed in the azimuthal direction, hence we expect that the Richardson regime should hold for the azimuthal dispersion. On the contrary, the inverse cascade is blocked in the radial direction, and the radial diffusivity should be strongly affected by the presence of zonal jets. Sukoriansky et al. (2009) argues that the radial dispersion becomes independent of the length scale, and that we should reach a Taylor regime of constant diffusivity where all the scales smaller than L_β contribute to the diffusion, but scales larger do not, i.e.

$$D_{\text{rad}}(\delta > L_\beta) \propto \epsilon^{1/3}L_\beta^{4/3} \propto \epsilon^{3/5}\beta^{-4/5}. \tag{4.22}$$

To retrieve these scalings, it is necessary to quantify the Lagrangian dispersion in a scale-dependent way. One method consists in computing the finite-scale Lyapunov exponent (FSLE). If two passive particles initially separated by a distance δ takes the time $\tau(\delta)$ to become separated by a distance $\mu\delta$, then the FSLE is defined as

$$\lambda(\delta) = \frac{\ln(\mu)}{\langle\tau(\delta)\rangle} \tag{4.23}$$

where the brackets denote an ensemble average over a large number of particles pairs, and μ is a growth factor. λ thus physically represents a dispersion rate. The computation of the FSLE is valid only in the limit where the separation between two trajectories is only slightly perturbed, i.e. the growth factor should be of order 1. In addition, keeping $\mu = O(1)$ ensures that

contributions from different scales are not cumulated. In the Richardson regime, the ensemble average of the squared distance between two particles evolves as $\langle \|\delta \boldsymbol{x}(t)\|^2 \rangle = C_R \epsilon t^3$, where C_R is a constant. We can deduce from it the expected FSLE:

$$\langle \tau(\delta) \rangle = \left(\frac{(\mu\delta)^2}{C_R\epsilon} \right)^{1/3} - \left(\frac{\delta^2}{C_R\epsilon} \right)^{1/3} \tag{4.24}$$

$$= (C_R\epsilon)^{-1/3} (\mu^{2/3} - 1)\delta^{2/3} \tag{4.25}$$

$$\implies \lambda_{\mathrm{Ri}}(\delta) = \frac{C_R^{1/3} \ln(\mu)}{\mu^{2/3} - 1} \epsilon^{1/3} \delta^{-2/3}. \tag{4.26}$$

In the Taylor regime, $\langle \|\delta \boldsymbol{x}(t)\|^2 \rangle = 4Dt$ where D is the scale-independent diffusivity. Similarly, we can deduce that the FSLE in this regime should scale as

$$\lambda_{\mathrm{Ta}}(\delta) = \frac{4\ln(\mu)}{\mu^2 - 1} D\delta^{-2}. \tag{4.27}$$

The FSLE should thus allow us to make the distinction between Richardson ($\lambda \sim \delta^{-2/3}$) and Taylor regimes ($\lambda \sim \delta^{-2}$).

The FSLE is measured the following way in our experiments. We work with experiments A, B and N of Table 4.2 for which we have PIV Eulerian velocity fields separated by a time step of 0.05s, for a total duration of 300s (6000 velocity fields). These Eulerian velocity fields allow to compute Lagrangian trajectories for passive and punctual particles by integrating the equation

$$\frac{d\boldsymbol{x}}{dt} = \boldsymbol{u}(\boldsymbol{x}, t), \tag{4.28}$$

where $\boldsymbol{x}$ is the position vector of a particle. Integrating this equation requires to know the Eulerian velocity at the particle position, which in general does not coincide with a node of our velocity field grid. We thus employ a fourth-order Lagrange interpolation of the velocity field in both directions. The time integration is performed using a third-order Adams-Bashforth scheme. The particles initial positions are randomly distributed in the experimental domain. Once the trajectories have been computed, we eliminate the trajectories that went out of the domain due to experimental noise, or that went in the two shadow regions where no PIV measurement is available. For the results presented here, we computed 10,000 trajectories per experiment. Two examples of the resulting trajectories are represented in Fig.4.10. For each pair of particles, we then compute its initial separation distance δ and the time necessary for the two trajectories to become separated by a distance $\mu\delta$, where we use $\mu = 1.1$. We chose μ as close as possible to 1, but such that the measure of τ is not dominated by experimental noise. We use a linear interpolation to determine the separation time with a sub-timestep accuracy. To make the distinction between radial and azimuthal dispersion processes, in addition to the total FSLE, λ, based on the total distance between particles, we compute separately a radial FSLE, λ_r and a zonal FSLE, λ_ϕ. For λ_r, the time τ is based on the radial separation distance $\delta_r(t) = |\rho_2(t) - \rho_1(t)|$. For λ_ϕ, the time τ is computed based on the azimuthal separation distance, $\delta_\phi(t) = |\rho_2(t)\phi_2(t) - \rho_1(t)\phi_1(t)|$. Note that to avoid considering pairs of particles that are initially close radially, but far azimuthally, or vice versa, we only keep pairs of particles for which the total initial distance $\delta = \|\boldsymbol{x}_2 - \boldsymbol{x}_1\|$ is smaller than $1.2\delta_r$ and $1.2\delta_\phi$ when computing the FSLE. After this selection process, for each separation distance δ_i, 1000 and 5000 pairs are typically taken into account when computing the radial and zonal FSLE respectively. Note that for all the results presented here, the trajectories are computed from the raw PIV velocity fields. We verified that if we filter the experimental data with a Gaussian kernel before computing the trajectories, the same statistical results are obtained. The results are hence unrelated to the experimental noise,

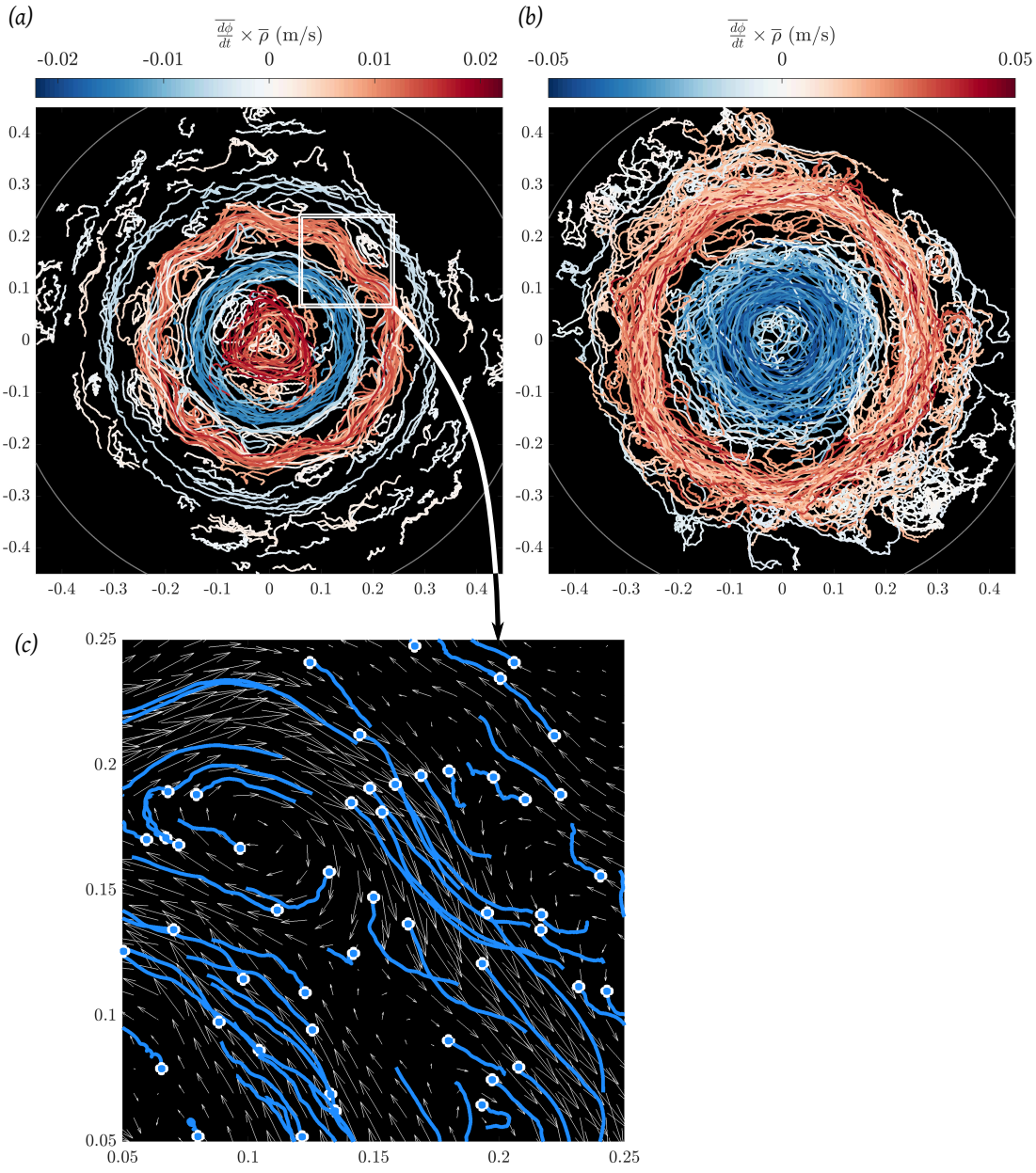

Figure 4.10. – Typical Lagrangian trajectories computed by numerically integrating equation (4.28) using the measured Eulerian velocity fields from PIV. *(a)* Experiment N. 310 trajectories out of 10,000 are represented, for a duration of 50s. *(b)* Experiment A. 165 trajectories out of 10,000 are represented, for a duration of 50s. The colour of each trajectory represents the mean angular velocity of the particle times its mean radial position (negative for a retrograde, anti-clockwise motion, and positive for a prograde motion). *(c)* Zoom showing the superposition of the Eulerian velocity field to some computed Lagrangian trajectories. Each trajectory corresponds to 100 time steps, i.e. a duration of 5 seconds. Note that the displayed velocity field corresponds to the first time step, hence the trajectories are expected to be tangential to the velocity vectors at the very beginning only.

even if it can lead to individual unphysical trajectories (e.g. trajectories leaving the domain). Note however that the PIV resolution intrinsically filters small-scale fluctuations which might contribute to the dispersion, but are discarded by the current approach.

4.5.1.2. Results

The results of FSLE computations are represented in Fig.4.11 for the statistically steady state of experiments A, B and N, as well as for the transient of experiment N, before any zonal jet develops. The typical separation times measured range between 2s and 20s. For the transient of experiment N, the flow does not show a profound anisotropy yet since the zonal jets are not developed. Accordingly, Fig.4.11*(a)* shows that $\lambda_r \approx \lambda_\phi$ at all scales. The picture is significantly different for the saturated flows (Fig.4.11*(b,c,d)*). The total FSLE, λ (black markers), shows that a $-2/3$ slope indicative of a Richardson regime is only recovered for the most turbulent experiments, A and B. For these two experiments, when the total scale approaches the Rhines scale, which is approximately the scale of the jets, λ starts to follow a steeper slope, but it seems that our experimental domain may be too small to see the Taylor diffusion regime at large scales.

The distinction between radial (red markers) and azimuthal (blue markers) dispersion should, in principle, allow to better visualize Richardson and Taylor regimes, since the Taylor regime is expected for the radial dispersion only. At a scale $\delta \sim L_\beta^\epsilon$, λ_r and λ_ϕ starts to follow different trends, with a systematically more efficient azimuthal dispersion. The radial slope (red markers) is steeper, but we see that it does not properly follow a -2 scaling. In addition, a plateau (labelled $p1$ in Fig.4.11) is present in λ_r at scales slightly smaller than the jets scale. It seems to be also present in the measurements of Lacorata et al. (2012) and Galperin et al. (2016), but with a reduced extent, similar to what we obtain for the less turbulent experiment N. A constant λ corresponds to an exponential separation, which may indicate a chaotic and non-local advection of the particles by structures of scale larger than the particles separation (LaCasce 2008). The observed plateau may thus be indicative of a coherent structure into which the particles are trapped, and it is tempting to associate it with the core of the jets. This would be compatible with the fact that the plateau is larger as Re increases (compare Exp.B and A in Fig.4.11), since the jets becomes more coherent, less wavy, and broader. After this plateau, λ_r continues to follow a steep slope, possibly close to -2. But overall, it is difficult to argue for a clear Taylor regime, we can only say that the FSLE scaling is steeper than what would be obtained with a Richardson regime. Similarly, we do not recover a clear Richardson regime for the zonal FSLE (blue markers). Another plateau (labelled $p2$) is observed for λ_ϕ for experiment N on panel *(b)*. Such a plateau in the zonal dispersion is also recovered by Galperin et al. (2016), and can be associated with particles being trapped in the coherent vortices or Rossby waves that interact with the jet. As visible in Fig.4.10*(a)*, 9 large-scale vortices strongly deflect the jet in experiment N. The distance between two vortices is of $\sim$ 14 cm, compatible with the scale at which the plateau $p2$ is observed for λ_ϕ. Fig.4.10*(b)* shows that these vortices are not present anymore in experiments A and B, and consistently, the plateau completely disappears from the zonal FSLE of these experiments (Fig.4.11*(c,d)*).

As underlined previously, Galperin et al. (2016) used experiments where a unique westward jet is directly and locally accelerated. It is thus not surprising that we do not recover the same results. The difference with Lacorata et al. (2012) is more surprising, given that their forcing (described in Espa et al. (2010)) consists this time in an electromagnetic array from which both westward and eastward jets indirectly develop. The difference between our experiments lie essentially in the regime, where $R_\beta^\epsilon \sim 1$ in their setup whereas $R_\beta^\epsilon \sim 3$ here. In addition, their local Reynolds number is of about 240, which is an order of magnitude smaller than experiment A. As a consequence, their jets are less strong but also thinner, and two to three jets are present in

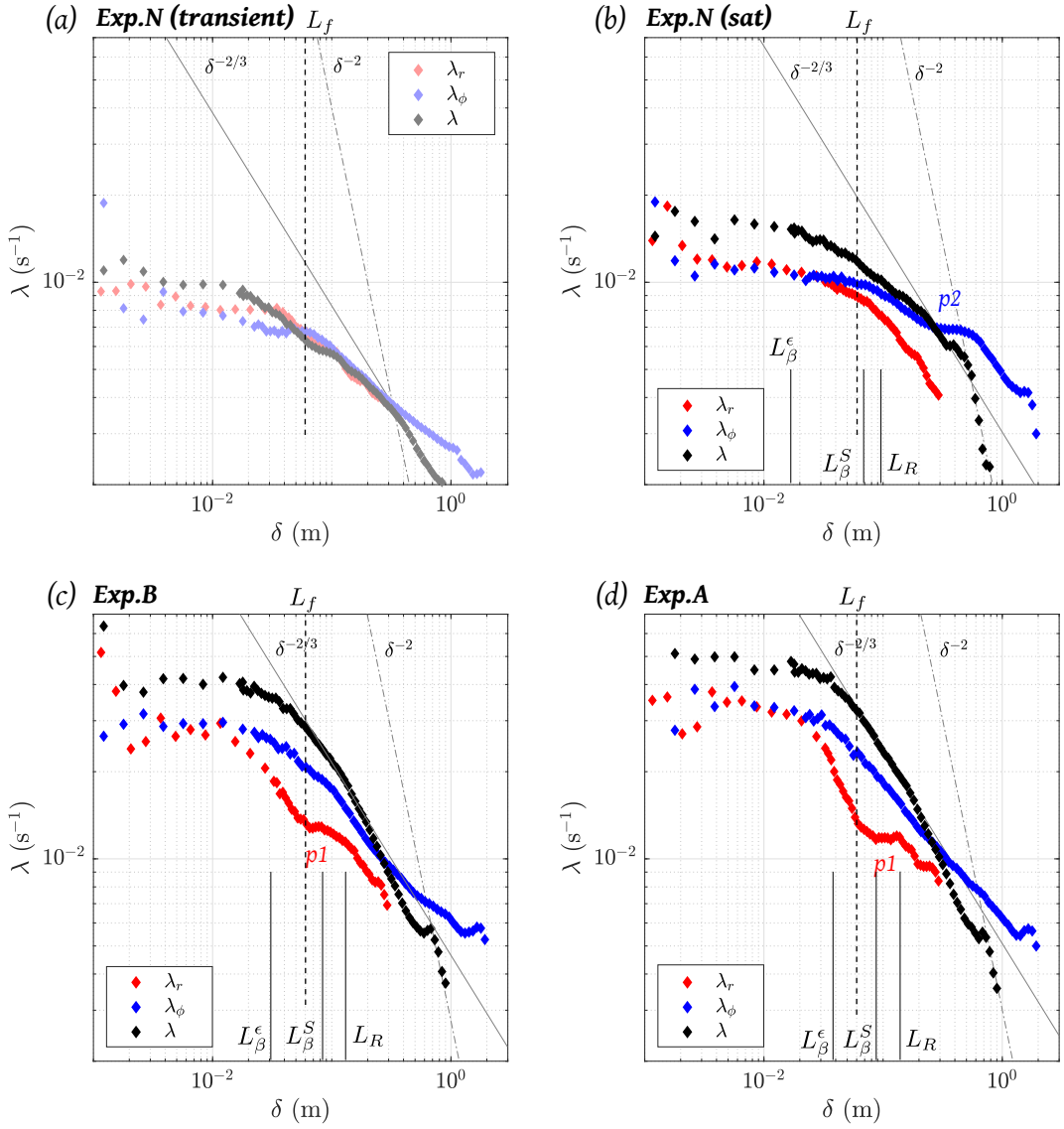

Figure 4.11. – Total (λ, black), radial (λ_r, red) and azimuthal (λ_ϕ, blue) finite-scale Lyapunov exponents. *(a)* Transient of experiment N. *(b)* Experiment N. *(c)* Experiment B. *(d)* Experiment A. The forcing scale L_f, Rhines scale L_R (4.4) and transitional scales L_β (equations (4.3) and (4.12)) are superposed for indication. The δ^{-2} scaling is indicative of a Taylor diffusion regime, the $\delta^{-2/3}$ of a Richardson regime and a constant λ corresponds to exponential separation. $p1$ and $p2$ refer to the two plateaus discussed in the text.

the domain, leading to a better scale separation between the experimental domain and the jets scale, allowing to explore further dispersion at large scale.

4.5.2. Direct measure of effective diffusivity and its anisotropy

To better characterize the link between the Lagrangian diffusivity and the zonal flow, we adopt a different and perhaps more intuitive method compared to the FSLE for which a clear physical interpretation of the results is difficult. Here, we instead propose to directly measure effective radial and zonal diffusivities as a function of radius in our experimental flow. To do so, we release 2000 particles at a given radius, ρ_0, and random angular positions, and we compute their Lagrangian trajectories to follow the dispersion of the particles through time. Two examples of the evolution of the zonally-averaged concentration in particles as a function of radius are represented in Fig.4.12. We note that there can be an important anisotropy between diffusion towards the centre or the exterior of the tank. This is readily visible in Fig.4.12 where the release at $\rho_0 = 0.15$ cm disperses in a symmetric way, whereas the release at $\rho_0 = 0.25$ cm disperses in an asymmetric way. To quantify the dispersion, we fit the radial concentration profiles separately for $\rho \geq \rho_0$ or $\rho \leq \rho_0$ with a Gaussian profile, which is expected in case of a diffusive process:

$$N(\rho \geq \rho_0, t) = N_m \exp\left(-\frac{(\rho-\rho_0)^2}{4D^+_{\text{rad}}\, t}\right), \tag{4.29}$$

$$N(\rho \leq \rho_0, t) = N_m \exp\left(-\frac{(\rho-\rho_0)^2}{4D^-_{\text{rad}}\, t}\right). \tag{4.30}$$

D^+_{rad} is thus the effective diffusivity towards the exterior of the tank, and D^-_{rad} towards the centre. For the zonal diffusivities, in addition to being localized radially, the releases are confined azimuthally in a given $\Delta\phi = 2\pi/50$ centred on ϕ_0. We compute a zonal diffusivity again by fitting a Gaussian function to the dispersed profiles in the azimuthal direction:

$$N(\rho_0\phi, t) = N_m \exp\left(-\frac{(\rho_0\phi-\rho_0\phi_0)^2}{4D_{\text{zon}}\, t}\right). \tag{4.31}$$

In Fig.4.13, we plot zonally-averaged radial concentration profiles for a release located at $\rho_0 = 0.25$ cm, on the inward flank of the prograde jet. These profiles are averaged over seven realisations, and plotted at six different times. We again see that the radial dispersion of the particles is asymmetric and more efficient towards the exterior of the tank, i.e. towards the peak of the jet. For a single realisation (not shown) peaks would appear in the radial distributions, corresponding to clusterings of particles along preferred paths, as seen in the 2D views of Fig.4.12. Averaging over several realisations smooth the distributions, which are statistically close to Gaussian profiles.

Fig.4.14 shows the resulting radial and zonal effective diffusivities as a function of radius. The radial diffusivity profiles for experiment A (panel *(b)*) confirm the asymmetry that we just mentioned. D^+_{rad} peaks at the inward flank of the prograde jet, whereas D^-_{rad} peaks at the outward flank of the jet, even if the difference is less pronounced. This means that the prograde jet tends to trap particles in its core as a result of this asymmetric diffusive-like behaviour. Note that at the core of the jet, the diffusivity is instead reduced compared to its flanks. This behaviour is consistent with the presence of a plateau previously mentioned in the radial FSLE (Fig.4.11*(c,d)*), which we interpreted as particles trapped in the jets. The same behaviour seems to hold for the less turbulent Experiment N (panel *(a)*), where the jet has a different position. Note also the big difference in the magnitude of the radial diffusivity between the

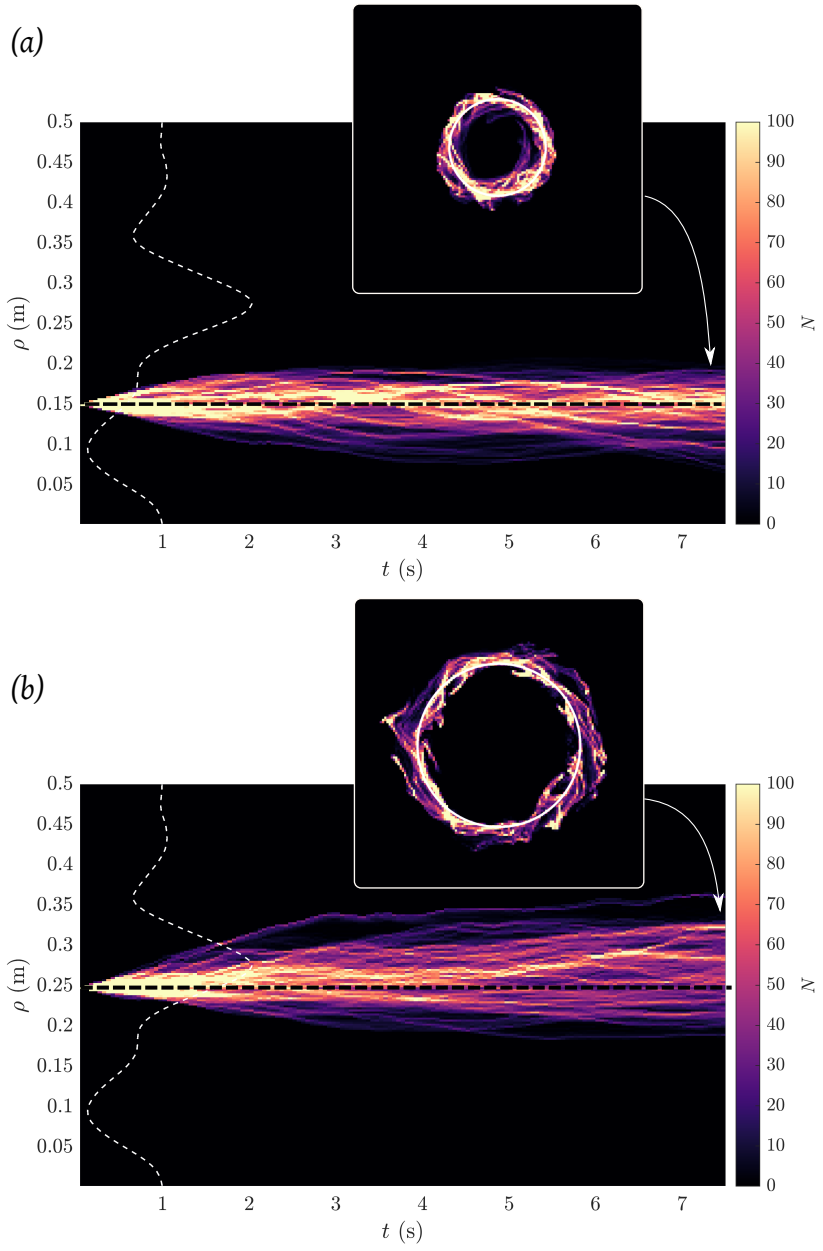

Figure 4.12. – Evolution of the radial distribution of 2000 passive particles released at an initial radius ρ_0 (horizontal dashed line) for a single realisation. The vertical sinuous white dashed line is the mean zonal flow of Experiment A, in arbitrary units. The colour scale represents the number of particles per unit area and is equivalent to a concentration. The squared panels show the particles concentration after a time t=7.5s, where the white circle shows the initial position of the particles. *(a)* $\rho_0 = 0.15$ m. *(b)* $\rho_0 = 0.25$ m.

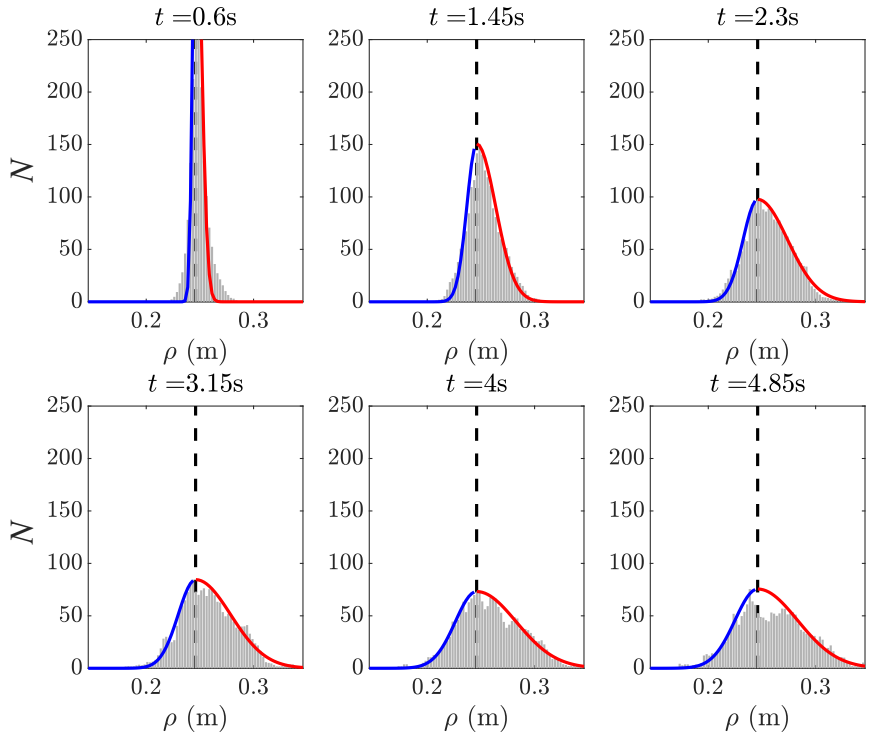

Figure 4.13. – Radial dispersion of Lagrangian particles initially released at a radius $\rho_0 = 0.25$ cm (vertical dashed line) in Experiment A. The histograms show the number of particles per unit area, as a function or radius. They are averaged over 7 realisations at different times. The asymmetry of the dispersion towards larger or smaller radii than the initial one is clearly visible. The red and blue curves correspond to best fits of the data with half Gaussian profiles (equations (4.30))

two experiments. For the zonal diffusivity (panel *(c)*), we again see a correlation with the mean zonal flow: the zonal diffusivity peaks at both edges of the prograde jet. This result is less surprising than the radial diffusivity: the shear is maximum at the jets edges. Close to the jet, some particles will be advected in the prograde direction whereas others in the retrograde direction, leading to an enhanced zonal dispersion. The positive correlation between the zonal diffusivity and the shear (dashed line) is clear on Fig.4.14*(c)*.

In terms of magnitude, by averaging D^+ and D^- over the whole domain, we measure a mean radial diffusivity of $D_{\text{rad}} = 8.78 \times 10^{-6} \text{m}^2\,\text{s}^{-1}$ for experiment N, $D_{\text{rad}} = 5.07 \times 10^{-5} \text{m}^2\,\text{s}^{-1}$ for experiment A, and $D_{\text{rad}} = 2.54 \times 10^{-5} \text{m}^2\,\text{s}^{-1}$ for experiment B (not shown). The diffusivity can also be separately predicted following equation (4.22), which assumes that only scales smaller than L_β contributes to the mixing: $D_{\text{rad}}^{\text{theo}} \propto \epsilon^{1/3} k_\beta^{-4/3}$. Fig.4.15 shows that our three estimates are in quantitative agreement with the theoretical predictions, with $D_{\text{rad}} \approx 0.7 D_{\text{rad}}^{\text{theo}}$. The prefactor falls in the range observed in numerical simulations by Sukoriansky et al. (2009), who found a prefactor between 0.3 and 2 for the zonostrophic and frictional regimes respectively. Of course, more than three measurements would be needed to confirm the adequacy between the experimental diffusivities and the theoretical prediction. Due to memory constraints, it is impossible for us to record both at high acquisition rates and over long times (several thousands rotation times). Since the other experiments of Table 4.2 were performed to study long-term dynamics, velocity fields were computed every second, which is not sufficient to conduct the same Lagrangian post-processing.

Given the results on the radial diffusivity, we expect that the zonal flow may lead to clustering

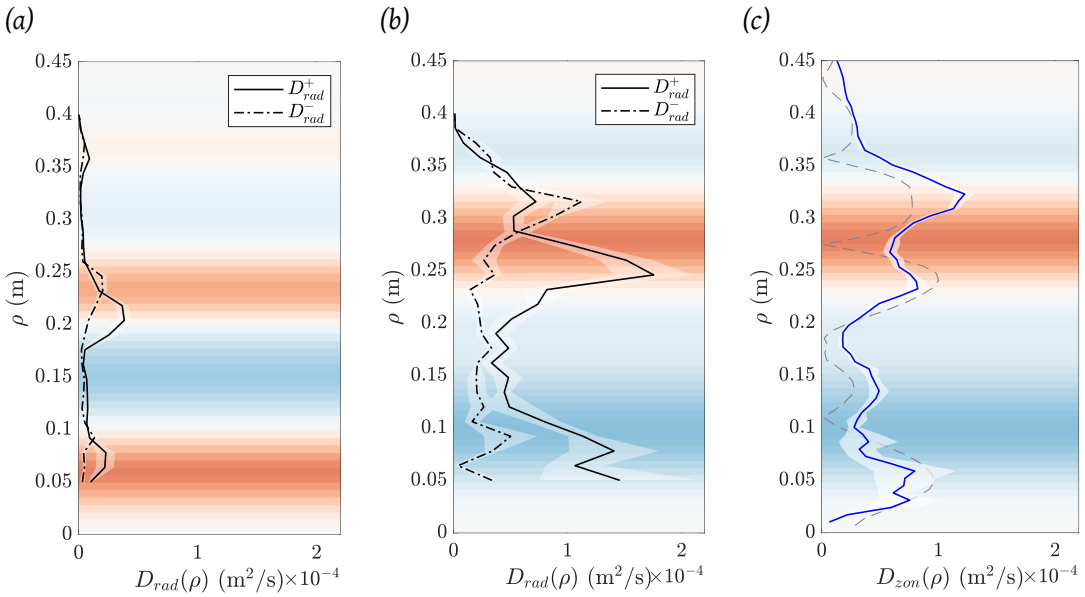

Figure 4.14. – Profiles of diffusivity as a function of radius. *(a,b)* Radial diffusivity towards increasing radius (D^+_{rad}) (black continuous line) and radial diffusivity towards decreasing radius (D^-_{rad}) (black dashed line) for experiments N and A, respectively. (c) Zonal diffusivity (D_{zon}) (blue line) and absolute value of the radial derivative of the mean zonal flow (grey dashed line) for experiment A. In all panels, the background colours represent the mean zonal flow (red: prograde, blue: retrograde) and the transparent envelope represents the variability when applying the same measurement at seven different initial times.

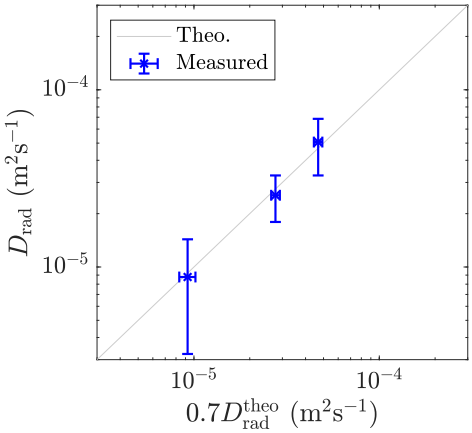

Figure 4.15. – Measured radial diffusivity in experiments A, B and N, as a function of the theoretical prediction. The vertical error bars account for the standard deviation when performing the mean along the radial profile, and the horizontal error bars account for the uncertainty in the measurement of ϵ^S, and thus in $D^{\text{theo}}_{\text{rad}} = (\epsilon^S)^{1/3}(k^S_\beta)^{-4/3}$.

of Lagrangian particles in preferred areas of the flow. This clustering is not that clear in our Lagrangian trajectories experiments, probably because the duration of available experimental data ($375 t_R$) is not long enough. For instance, according to the estimated radial diffusivity for experiment A, the timescale to diffuse over a distance $R/2$ is $R^2/4D_{\text{rad}} \sim 1480\ t_R$. Some tendencies are nevertheless visible with the available data. Fig.4.16 shows the evolution of the zonally-averaged concentration profiles as a function of time for the end of the integration. Whereas the particles are initially distributed homogeneously, one can see that on average, their concentration seems to increase inside of the prograde jet. This average behaviour however corresponds to the displacement of particle "trains", i.e. regions highly concentrated which move radially while oscillating at the same time. This observation is consistent with the previous one of particles trapped along preferred path while dispersing. Fig.4.16*(b,c)* show the time-averaged probability of finding a particle at a given radius (which is equivalent to a normalized concentration). The initial probability density, $p_i(\rho)$ is almost homogeneous (the inhomogeneities comes from the fact that we eliminate trajectories that exit the experimental domain). On the contrary, the final probability density, averaged over 5s, exhibits preferred locations for the particles. The difference, $p_f - p_i$, is plotted in Fig.4.16*(d)* and shows that the areas which have gained particles coincide with the presence of a prograde jet. On the contrary, the areas of retrograde flow lost particles. The correlation between $p_f - p_i$ and the amplitude of the zonal flow is represented in Fig.4.16*(e)* and confirms this tendency.

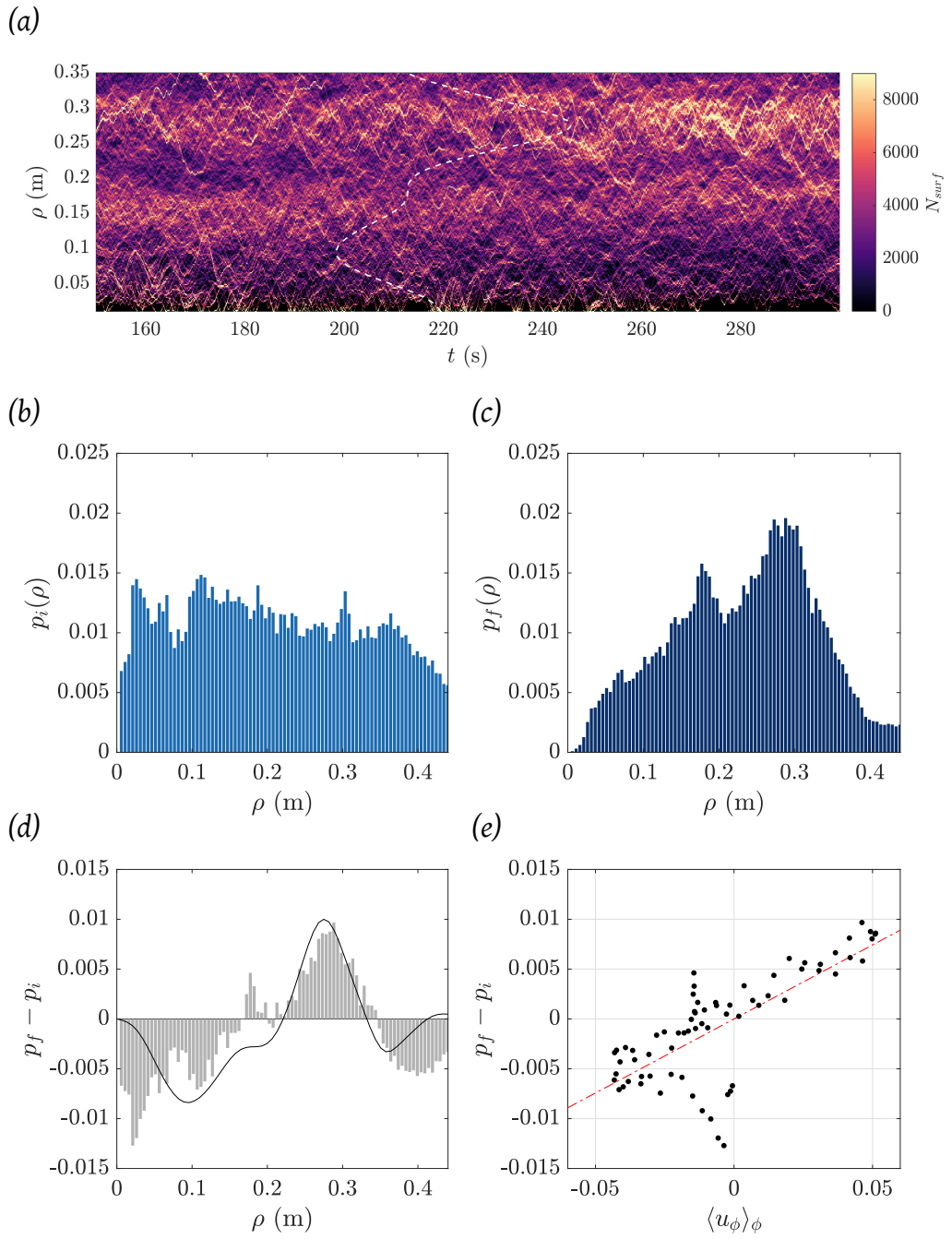

Figure 4.16. – Evolution of the radial distribution of the Lagrangian particles after integrating the trajectories over 300s, i.e. $375 t_R$ for Experiment A. *(a)* Radial profile of the number of particles per unit area as a function of time. The white dashed line shows the mean zonal flow in arbitrary units. *(b)* Probability of finding a particle at a given radius averaged over the 5 first seconds of the integration (100 time steps). *(c)* Probability of finding a particle at a given radius averaged over the last 25 seconds of the integration (500 time steps). *(d)* Difference between panels *c* and *b*. The black line is the mean zonal flow in arbitrary units. *(e)* Difference of the probability density function at the end and at the beginning of the integration as a function of the amplitude of zonal flow (in $\mathrm{m s^{-1}}$).

4.6. Conclusions and discussion

4.6.1. Advantages and drawbacks of different methods for estimating the turbulent energy transfer rate

Apart from the adequacy of the frameworks of zonostrophic turbulence and potential vorticity mixing, our experiments allow to address their efficiency in the prospect of using them as tools to quantify the upscale energy transfer rate of a given turbulent flow with a β-effect. ϵ can indeed be estimated independently from kinetic energy spectra, PV mixing, and dispersion measurements. Our experiments can shed light on the most efficient method depending on the studied geophysical flow.

1. The first and simplest estimate that can be made is based on the assumption that the energy is dissipated by Ekman friction at a rate $\alpha = \Omega E^{1/2}$, and hence ϵ can be estimated simply by measuring the total kinetic energy of the flow: $\epsilon^E \sim \mathcal{K}\,\alpha$.
2. The second method, and perhaps the most rigorous one, consists in computing the residual kinetic energy spectra and fitting the $-5/3$ slope, s, which is proportional to $\epsilon^{2/3}$: $\epsilon^S \sim (s/C_K)^{3/2}$.
3. The third method consists in measuring a Thorpe scale by sorting local and instantaneous PV profiles. The deduced scale, assuming that it is correlated with L_β, allows to retrieve ϵ thanks to the relation $\epsilon^T \sim \beta^3 (L_\beta^T)^5$.
4. The fourth method consists in measuring an effective turbulent diffusivity, by computing finite-scale Lyapunov exponents or by following the dispersion of a passive scalar. Indeed, the diffusivity can be expressed in terms of ϵ and L_β by assuming that only scales below L_β contributes to it: $D \sim \epsilon^{1/3} k_\beta^{-4/3}$.

In this chapter, we consider the results of method 2 to be the reference ones, and compare the results of other methods to it.

— Method 1 gives a good order of magnitude for ϵ, but we did not found an exactly linear relationship between the two (Fig.4.6*(a)*), probably because bulk viscous dissipation and side friction are not completely negligible in our experiment. In addition, the main dissipation mechanism in natural flows is far from being a simple Ekman friction, and this is rather a practical scaling for idealized experimental or numerical model than a true method. While this first method supposes that dissipation is due to viscous boundary layers only, the three other methods do not make any hypothesis on the nature of the dissipation process.

— Method 2, which we consider as the reference one, is probably the most robust but requires to have high resolution spatial and temporal observations to be able to compute energy spectra.

— For method 3, we show that the Thorpe scale is strongly correlated with the transitional scale, suggesting that the turbulent transfer rate could be efficiently retrieved in natural flows using simple measurements of instantaneous potential vorticity profiles. The success of this method however requires a precise estimate of the scaling law between L_T and L_β. Here, we found $L_\beta \sim 3.2 L_T$, but this factor may potentially vary. We show nevertheless that this scaling holds for the whole range of Reynolds numbers explored. A complete systematic study, where E and R_β are varied independently would allow to determine the validity of this scaling depending on the flow regime. Note that the Thorpe scale is routinely used in oceanography on the vertical direction, to measure the vertical mixing of stratified turbulence. Our results support the analogy raised by Galperin et al.

(2014a), i.e. that an equivalent method can be used on horizontal directions to measure the lateral mixing due to β-plane turbulence.

— Finally, for method 4, we first show that our experiments poorly support the finite scale Lyapunov exponent estimates of diffusivity in the zonostrophic regime. If FSLE are largely employed for oceanographic data (van Sebille et al. 2018), it hence remains to be seen if such a method could be applied to gas giants flows. For instance, it would be interesting to perform similar Lagrangian dispersion experiments in the Jovian atmosphere based on velocity fields derived from cloud-tracking. Apart from the FSLE, we nevertheless show that the estimated radial diffusivity in our experiments indeed scales as predicted, $D \propto \epsilon^{1/3} k_\beta^{-4/3}$, and could be used to estimate ϵ provided that the transitional scale is known.

Note that an alternative use of method 4 is that, if one knows the upscale energy transfer rate, it is possible to deduce an effective diffusivity, which can be useful to better constrain or model the transport of momentum, heat or passive scalars in natural flows, namely in global scale simulations of oceanic and atmospheric circulations. However, this method would only provide an average estimate of the global diffusivity. Our results on transport properties show that it may be important to take into account the inhomogeneity of the diffusivity due to the zonal flow, for which ϵ gives no information. This point is discussed below.

4.6.2. A zonal-flow dependent diffusivity for planetary transport and modelling

Analysing Lagrangian transport is important when it comes to modelling global circulation for any planetary flow, and in particular for Earth's oceans. Indeed, for now, performing direct Navier-Stokes simulations of the global oceanic circulation is far beyond reach. Global oceanic and climate simulations thus have temporal and spatial resolutions which are too coarse to resolve all the dynamics, however, the unresolved small-scale dynamics is crucial for the long-term evolution of the system. An important contribution of mesoscale eddies is that they transport tracers, momentum, and energy (Fox-Kemper et al. 2013), and affect large scale properties of the ocean such as heat uptake or carbone storage (Fox-Kemper et al. 2019). In place of being resolved, mesoscale and sub-mesoscale motions are routinely parametrized which can limit the predictability of global-scale models given their sensitivity to these parametrizations (Fox-Kemper et al. 2019). The parametrizations consist in explicitly specifying a sub-grid scale term in the momentum and tracer concentration evolution equations, by employing diffusion-based description. Generally, it is assumed that any tracer flux due to mesoscale eddies is related to the mean tracer gradient through an eddy diffusivity (Ferrari et al. 2010). This type of parametrization arises from the fact that the effects of small-scale motions must be represented entirely in terms of large-scale features to close the equations. The specification of the associated eddy-diffusivity coefficients remains the problematic point as there is no consensual formulation of these coefficients as a function of large-scale features only.

The point that we want to raise is that, a priori, the diffusivity is expected to be temporally variable, inhomogeneous and anisotropic. Indeed, unlike molecular diffusivity, eddy-diffusivity is likely to be modulated by the large scale circulation. Most oceanic models ignore these modulations, which could however be crucial to take into account. Evidence that mean flows affect eddy diffusivity exists for a long time, but it is only recently that a modelling effort has been made to quantify this effect of "mean flow-suppression" of mixing (Ferrari et al. 2010; Klocker et al. 2012; Groeskamp et al. 2020). Assuming that eddy mixing can be represented as a stochastically forced wave equation, these studies show that the eddy-diffusivity taking into

account mean-flow suppression expresses as

$$\tilde{K} = K \frac{1}{1 + k^2 \alpha^{-2} (c_w - U)^2}, \tag{4.32}$$

where k is the Rossby (eddy) wave number, c_w is their Doppler-shifted phase speed, and α is a decorrelation rate (taken to be a frictional rate). The reduction in diffusivity is proportional to the ratio of the decorrelation time scale α^{-1} to the advection time scale $1/k(c_w - U)$. K is the non-corrected eddy-diffusivity estimated from mixing-length theory, in the case where eddies do not propagate relatively to the mean flow (passive advection): $K = (k/k_t)^2 \mathrm{EKE} \alpha^{-1}$ (EKE is the eddy kinetic energy, and k_t the total wavenumber). Suppression in then expected to be strong at the core of strong currents where $c_w - U$ is large, to vanish at the critical levels where $c_w - U = 0$, and to be weak where there is no mean flow. Physically, Ferrari et al. (2010) explains that when there is a high velocity difference between the eddies propagation and the zonal flow, the zonal flow advects tracer out of the eddy before much filamentation has occurred, leading to a reduced mixing length, and thus a reduced diffusivity based on mixing-length theory. On Fig.4.17, we plot the effective diffusivities measured by Klocker et al. (2012) in the Southern Ocean using numerical advection of tracers from a proxy velocity field. If the zonal flow is artificially suppressed from the velocity field, the diffusivity peaks in the core of the jet where the EKE is also the largest, consistently with mixing-length theory. But when the whole velocity field is used, it is clear that the suppression effect is the most effective in the core of the Antarctic Circumpolar Current (ACC) where diffusivity is reduced because the eddies have a greater zonal speed difference with the zonal flow. Fig.4.17 also shows that the diffusivity is then greater at the flanks of the ACC, consistently with the idea of critical layers where the eddies do not propagate relatively to the zonal flow. Note that the aforementioned theories rely on a scale separation between the eddies and the zonal flow. Its applicability to systems where the zonal jets have width comparable to the eddies size remains to be addressed, even if the fact that it works well for the ACC is encouraging.

Our experimental diagnosis corroborates well these results. Similarly to Ferrari et al. (2010), we find that cross-stream diffusivity is increased at the flanks of the zonal jet, and decreased at the core of the jet, as can been seen by comparing Fig.4.14*(b)* and Fig.4.17. Our results constitute an additional suggestion that their theoretical model may hold even when the eddies diameter is comparable to the jet width. Of course, the present work does not constitute a full quantitative comparison with their theoretical model, which would need precise estimates of eddies/Rossby waves propagation speed as a function of radius as well as estimates of the decorrelation time. This comparison could be the scope of future work since all the needed experimental data are available. Then, the zonal diffusivity is not discussed in these studies since, from the parametrization point of view, studying transport along zonal direction is less interesting because it is dominated by mean flow advection rather than by the effects of small-scale eddies. Finally, we also want to mention that here, we use a Lagrangian method to estimate the diffusivity in our experimental flows by following dispersion of passive particles. An alternative method to compute the radial diffusivity, and which would be closer to what is usually done in oceanographic Lagrangian analysis, would be to solve for the advection (or advection-diffusion) equation of a passive tracer of concentration c, measure the radial eddy flux $\langle u_\rho c \rangle_\phi$ and define the diffusivity as the ratio between the flux and the mean tracer gradient $\partial_\rho \langle c \rangle_\phi$.

Apart from diffusivity, clustering into jets has been less discussed in the literature of ocean dynamics. For instance, the aforementioned works do not mention if the enhanced diffusion at the flanks of the jets is symmetric or not, whereas our experiments clearly exhibit an asymmetry. To find discussion about clustering, one should turn to the literature on Lagrangian transport

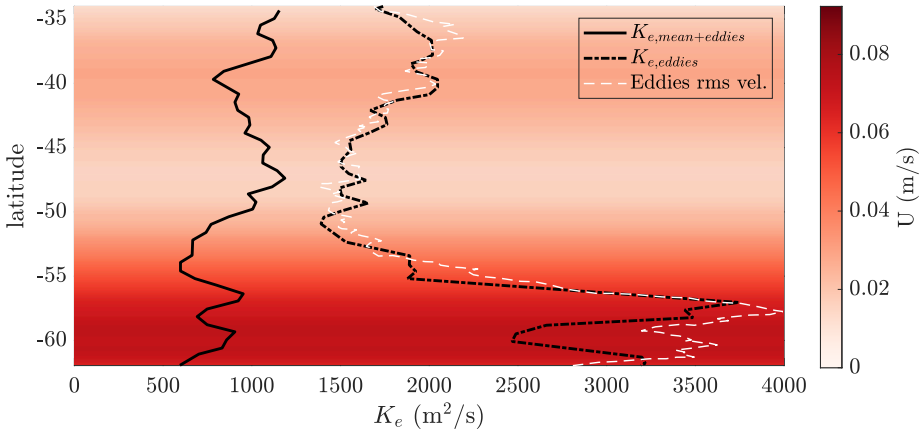

Figure 4.17. – Diffusivities estimates in the Southern Ocean from Klocker et al. (2012). The continuous line is the effective diffusivity measured by tracer advection numerical experiments in the Southern Ocean. The dashed black line is the same quantity, but measured after removing the zonal flow from the velocity field. The white dashed line is the measured eddies rms velocity in arbitrary units. The colours indicate the intensity of the zonal flow as a function of latitude. The largest amplitudes correspond to the Antarctic Circumpolar Current. The represented data have been digitized from Figures 1 and 3 in Klocker et al. (2012).

barriers. As discussed in the introduction about PV mixing, zonal jets have been associated to transport barriers. Initially, this idea emerged from the argument of Rossby wave "elasticity": large PV gradients are associated with a large restoring force for Rossby waves that inhibits meridional (radial) exchange of fluid (Dritschel et al. 2008). This argument would mean that only prograde jets are transport barriers, since retrograde jets are well-mixed regions of small PV gradient. An alternative mechanism shows that in fact, the meridional shear (i.e. the radial derivative of the zonal flow) is instead responsible for an increased meridional exchange, leading to enhanced exchange at the edges of the jets where the shear is maximum, and minimum exchange at the core of both westward and eastward jets (Rypina et al. 2007; Beron-Vera et al. 2008). From numerical simulations, Thompson (2010) show that strong mixing regions are found on the flanks of the eastward jets, and that cores of the eastward jets are strong barriers to transport, while cores of the westward jets are weaker barriers to transport. For Jupiter, Beron-Vera et al. (2008) argue that the idea of transport barrier is consistent with observations of Jupiter's clouds, where the limits between belts and zones (of different chemical composition) coincide with local extrema of the zonal flow, i.e. peaks of both prograde and retrograde jets. In the oceans, transport barriers have often been associated with fronts of advected tracers, for instance sea-surface temperature, chlorophyll, oxygen or oil spills (van Sebille et al. 2018, and references therein). But to the best of our knowledge, there is no particular emphasis of fronts formation in zonal jets, maybe because of the moderate intensity and coherence of jets in the oceans compared to gas giants. Finally, besides transport properties of oceanic or atmospheric circulations, the problematic of how zonal jets modify turbulent transport is also of importance when studying the heat budget of rapidly-rotating thermal convection in liquid outer cores. In these planetary envelopes, convection is indeed the main heat transport mechanism. But the spherical geometry of the system and the fast-rotation leads to development of intense zonal flows (e.g. Guervilly et al. 2017). Just like mean currents in the ocean, zonal and shear flow indirectly modifies heat transport by modulating convection. Guervilly et al. (2017) show that despite radial rms velocities are high in prograde jets, the heat transfer is reduced there consistently with the previous discussion on mean flow suppression effect. The argument provided by the authors is that of Rossby waves elasticity, i.e. that the radial velocities in the core of the jets are mainly associated with Rossby waves, which are not

efficient for transporting heat outward. The prograde jets thus act as a barrier for heat transport. It could be interesting for future work to estimate if the mechanism of mean-flow suppression could be applied to rotating convection and help predict and diagnose heat transport in such systems.

To conclude, our experimental diagnosis confirms the idea that both the effects of the mean flow and anisotropy should be taken into account when modelling transport in geophysical flows, and incorporated in sub-grid-scale eddy closures of coarse resolution models. Of course, both our studies of diffusivity and clustering are preliminary, and we do not pretend that the present results are definitive in either case. The idea was to use available experimental data to pull together some generic points and ideas that are present in the literature, quantify their applicability and relevance depending on available data, and open pathways to deeper dedicated analysis which will be performed in the future. Regarding the improvement of ocean models, the first step would be to introduce spatial variation of an *isotropic* diffusivity based namely on the mean flow, but ultimately one should seek to implement spatial variation of an *anisotropic* diffusivity, since meridional and zonal diffusivities are not expected to be similarly affected by the zonal flows. Implementing mean-flow dependent mixing parametrizations has not yet been done in global models, but it may be soon. Groeskamp et al. (2020) gives for instance a practical method for taking into account the previously presented suppression mechanism of eddy diffusivity using available observations at the surface (salinity, temperature, pressure and EKE).

Chapter 5.

Non-linear saturation into the zonostrophic regime of zonal jets: long-term stability and multistable states

Chapter 5.

Despite an apparent quasi-steady state, turbulent zonal flows can exhibit long-term behaviours such as drift, nucleation or coalescence. Long-time experiments were performed to address this slow dynamics, which is the focus of the present chapter.

Chapter aims

1. Study the long-term dynamics of zonal flows in regime II.
2. Evaluate the uniqueness of the zonal flow profile obtained in the statistically steady state.

Highlights

- Drifting, nucleations and coalescences of jets are only observed during the transient dynamics. Once in statistically steady state, the obtained zonal flow profile is stable, at least for the duration of our experiments ($\sim 40,000$ rotation periods for the longest experiments).
- The zonal jets configuration in regime II is multistable. Based on two sets of fixed external parameters for which we performed multiple realisations, we identify respectively three and two multistable configurations. This multistability is retrieved in QG numerical simulations.
- Spontaneous transitions between multistable states are not observed experimentally, even when stochasticity is introduced in the forcing (fluctuating amplitude and spatial distribution). Nevertheless, it seems possible to trigger transitions by abruptly changing the rotation rate – and consequently the β-effect – to a close value.
- We report that in regime II, close to the transition described in chapter 3, the jets sometimes exhibit a long-term fluctuating behaviour and destabilize into possibly solitary Rossby waves, reminiscent of the so-called zonons (Sukoriansky et al. 2008).

5.1. Introduction

In chapter 4, we described the turbulent statistics and transport properties of regime II. We analysed the properties of the flow obtained after thousands of rotation periods, i.e. once a statistically steady state has been reached. In the present chapter, we discuss the long-term dynamics (or stability) of the zonal flows obtained in regime II. Indeed, despite an apparent quasi-stationary state, the flow can undergo very slow evolution and transitions, as observed in other chaotic natural systems such as the global climate (e.g. Abe-Ouchi et al. 2013) or planetary magnetic fields (e.g. Berhanu et al. 2007; Gissinger 2012). Understanding the long-term chaotic behaviour of non-linear systems is important, for instance regarding their predictability. However, this requires to be able to change the system external parameters to study its response, which cannot be done in natural systems. In this regard, experimental and numerical studies based on idealized models are crucial to provide insights into the behaviour of such systems.

For turbulent zonal flows, capturing the long-term dynamics requires to correctly represent the complex interaction between the small-scale turbulence and the slowly varying zonal flow, which is difficult given the time-scale separation between the two. Laboratory experiments then have a major role to play since they allow for measurements at high-resolution over long times. Studying long-term dynamics using 3D direct numerical simulations is on the contrary out of reach because of computational costs. That being said, recently, some studies showed that it is possible to overcome this obstacle using rare-event algorithms which focus on rare transitions instead of simulating the whole dynamics (Bouchet et al. 2019b). In experiments, the full three-dimensional dynamics is naturally solved, and we can let the experiment run as long as we need, in principle. The long-term dynamics of jets can be divided between two rather different processes described in the literature:

— On one hand, the slow, progressive dynamics of the zonal flow due to accumulated effects of the small-scale turbulence (e.g. drifting);

— On the other hand, critical transitions between attractors of the system (e.g. abrupt nucleations and coalescences leading to a change in the number of jets).

The first type of dynamics – migration of jets – has been described in various numerical models, e.g. in the seminal work of Panetta (1993) using QG baroclinic simulations, but also in more realistic frameworks like rotating thermal convection in planetary cores (Guervilly et al. 2017). However, such long-term dynamics is not that common in natural systems. For instance, as shown in Fig.5.1, jets on Jupiter are remarkably steady since we observe them (Tollefson et al. 2017), even if one Jovian jet seems to have broken apart into vortices in 1939-1940 (Rogers 1995; Youssef et al. 2003). Similarly, in laboratory experiments, meridional jet migration has only been described by Smith et al. (2014), and the authors underline that it may be due to a long-term thermal equilibration, i.e. a transient rather than a long-term drift. In our experiments, the radial migration of the jets is always associated with transients, or with merging events, and is not a robust long-term behaviour. Using QG simulations, we can show that the stability of the jet's position is not due to the fact that we work with a uniform β-effect. Our simulations suggest that it could arise from the particular forcing pattern on concentric rings. We can also reasonably assume that the spatial confinement of the experiment, and the fact that there is not a huge scale separation between the jets and the tank size may impede drifting.

The second type of dynamics – critical transitions between attractors – has been described in simulations of stochastically forced barotropic jets on the β-plane (Bouchet et al. 2019b; Simonnet et al. 2021). Multistability refers to the coexistence of several stable states for a given set of external parameters. It has been observed for an extremely large class of natural and experimental nonlinear systems, from neurology to solid state physics and climate (Feudel et al. 2018). In particular, multistability and bifurcations over turbulent flows have been

observed experimentally in various setups such as Von Kármán flows (Ravelet et al. 2004, e.g.), quasi-2D turbulence (Michel et al. 2016), turbulent wakes (Cadot et al. 2015), non-rotating (Sugiyama et al. 2010) and rotating (Stevens et al. 2009; Favier et al. 2019) Rayleigh-Bénard convection, as well as a dynamo experiment (Berhanu et al. 2007). Bouchet et al. (2019b) and Simonnet et al. (2021) show that β-plane turbulence is not an exception. For identical external parameters, several turbulent steady states corresponding to different number or position of jets are possible, and similarly to the magnetic field, "reversals" between different jets configurations can occur. Contrary to drifting, we do recover some multistability within our experiments. Even if the turbulent statistics remain the same, we show the coexistence of different large-scale configurations of the zonal flow for identical external parameters.

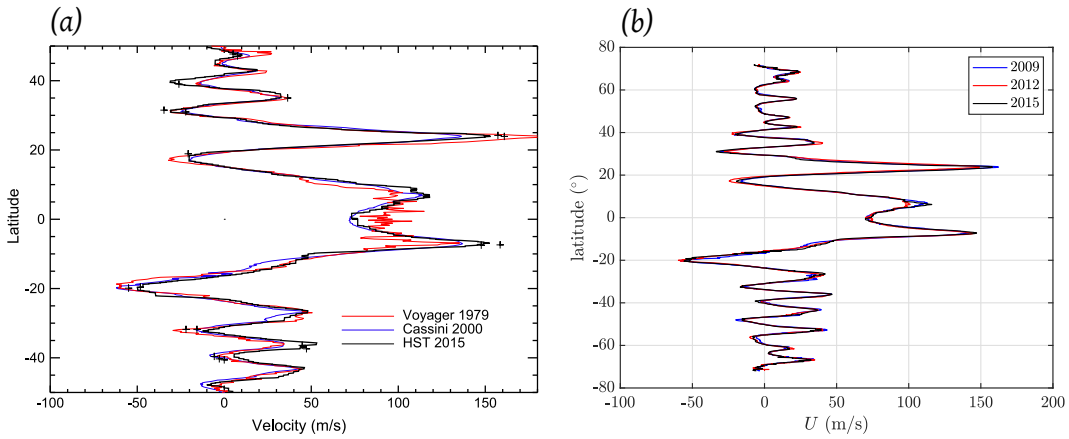

Figure 5.1. – *(a)* Comparison of Jupiter's zonal winds profile in 1979, 2000 and 2015 (figure taken from Simon et al. (2015)). *(b)* Comparison of Jupiter's zonal winds profile in 2009, 2012 and 2015 (figure plotted from data sets provided in Tollefson et al. (2017)).

The chapter is organized as follows. In §5.2, we explain the experimental and numerical approaches that were used to characterize the multistability of the system. In §5.3, we describe the multistable states observed experimentally for two sets of external parameters, and in the quasi-geostrophic (QG) numerical simulations. In §5.4, we report experimental investigations which goal was to trigger transitions between multistable states. In §5.5, we discuss the origin of the observed multistability, and why we have not been able to observe transitions. We finally report another type of long-term dynamics observed in some experiments and consisting in periodic perturbations of the zonal flow which may be associated with the generation of nonlinear Rossby waves, reminiscent of so-called zonons.

5.2. Methods

5.2.1. Experimental approach

To characterize the multistability observed in our experiments, we performed three types of investigations:

— Realisations: we repeated the exact same experiment several times, to see if the final steady state obtained can be different with the same set of external parameters;

— Long time experiments: for external forcings which exhibit multiple possible states, we performed three continuously forced experiments over long times (about 8 hours, corresponding to 40,000 rotation periods) to track possible spontaneous transitions;

— Transition experiments: we performed experiments aiming at triggering a transition between two multistable states, instead of waiting for a spontaneous one.

The associated experiments are listed in Table 5.1. The three types of investigations were conducted with the first or the second set of pumps (see Appendix B). We recall that the second set of pumps was installed in order to reach more turbulent regimes, but also to homogenize the forcing radially. Reaching higher Reynolds number was also motivated by the fact that it increases the background noise and thus the probability of seeing transitions.

In addition to the two sets of pumps, we tested both stationary and fluctuating forcings, again with the idea of increasing noise and transitions probability. More precisely, each forcing ring can fluctuate randomly around a prescribed mean within an imposed interval around this mean, with a period of 3 seconds. This time step is the smallest that we can achieve given the delay of the pumps in responding to a change in the input power. This type of forcing is referred as "Fluct." in Table 5.1. Finally, we also explored more drastically fluctuating forcings where one ring out of two is switched off alternatively every prescribed time interval Δt. This means that during Δt, only the rings C_1, C_3 and C_5 are switched on, and the following Δt, only the rings C_2, C_4 and C_6 are activated. This type of alternating forcing referred as "Alt." in Table 5.1, and we report the associated duration of the time interval.

Note that given the time scales of the experiments, we could not afford to perform tens or hundreds of realisations to obtain statistical results. Instead, for each set of pumps, we have about 10 realisations. In our case, this seems however sufficient to identify the possible states. Similarly, the duration of our long-time experiments is limited by the duration of the day, since letting the rotating table run overnight is not possible, for security reasons.

5.2.2. Numerical approach

To complement our experiments, multistability was also tested using quasi-geostrophic numerical simulations (Appendix C.4). All the simulations presented here were performed with the experimental β-effect, an Ekman number $E_R = 1.25 \times 10^{-7}$ and a small-scale polar forcing similar to the one discussed in chapter 3 (12 forcing rings, and a typical forcing scale $L_f/R \sim 7.1 \times 10^{-2}$). This forcing scale is half the experimental one. We recall that QG numerical simulations performed with the experimental forcing pattern are presented in chapter 3 (Fig.3.16). The goal is again to address the robustness of the experimental results with decreasing forcing scale, with planetary applications in mind. The initial condition of the simulations is a fluid at rest, plus a noise added to the vorticity field (we use the fortran subroutine *ranset*). When different realisations are mentioned, it simply means that the seed of the initial noise was changed.

5.3. Observed multistable jets configurations in experiments and QG simulations

The identified multistable states are represented in Fig.5.2 (2D maps of azimuthal velocity) and 5.3 (zonal flows) for the QG simulations, experiments with set#1 and experiments with set#2. With forcing set#1, based on 11 realisations, we have identified 3 different steady states where the configuration of the jets are different. These states are labelled E1.1, E1.2 and E1.3 in Table 5.1. Fig.5.3*(b)* shows that they correspond to permutations between the location of the jets. In the three configurations, the local extrema of the zonal flow are the same, but they can be prograde or retrograde. For instance, E1.3 can be obtained by shifting E1.1 radially outward over a distance of ~13 cm. E1.2 has the central prograde jet of E1.1, and the most external jet

Label	Date (AA/MM/DD)	Type	Set	U_f (mm s^{-1})	Forcing type	Configuration
1A	19/11/12	Realisation1	1	6.8	Stat.	E1.1
1B	19/11/12	Realisation2	1	6.8	Stat.	E1.2
1C	19/11/12	Realisation3	1	6.8	Stat.	E1.3
1D	19/12/12	Realisation4	1	6.8	Stat.	E1.1
1E	19/12/12	Realisation5	1	6.8	Stat.	E1.2
1F	19/12/12	Realisation6	1	6.8	Stat.	E1.3
1G	19/12/12	Realisation7	1	6.8	Stat.	E1.1
1H	19/12/12	Realisation8	1	6.8	Stat.	E1.3
1I	19/12/12	Realisation9	1	6.8	Stat.	E1.1
1J	19/12/12	Realisation10	1	6.8	Stat.	E1.1
1K	20/01/22	Realisation11	1	6.7	Fluct. $\Delta t = 3$s	E1.3
1L	19/12/05	Long time	1	6.8	Stat.	E1.1
1M	20/01/23	Long time	1	6.7	Fluct. $\Delta t = 3$s	E1.3
1N	19/10/28	Transition	1	6.8	Stat.	E1.1&2
2A	20/10/06	Realisation1	2	25	Stat.	E2.1
2B	20/10/06	Realisation2	2	24	Stat.	E2.1
2C	20/10/06	Realisation3	2	24	Stat.	E2.1
2D	20/10/06	Realisation4	2	24	Stat.	E2.2
2E	20/10/06	Realisation5	2	24	Stat.	E2.1
2F	20/10/06	Realisation6	2	24	Stat.	E2.2
2G	20/10/06	Realisation7	2	24	Stat.	E2.2
2H	20/10/06	Realisation8	2	24	Stat.	E2.2
2I	20/11/05	Realisation9	2	24	Stat.	E2.2
2J	20/11/18	Realisation10	2	24	Stat.	E2.2
2K	20/10/01	Long time	2	24	Fluct. $\Delta t = 3$s	E2.1
2L	20/11/09	Transition	2	24	Alt.$\Delta t = 7$s	E2.2
2M	20/11/10	Transition	2	24	Alt.$\Delta t = 35$s	E2.2
2N	20/11/12	Transition	2	24	Alt.$\Delta t = 117$s	E2.2
2O	20/11/13	Transition	2	24	Alt.$\Delta t = 76$s	E2.2

Table 5.1. – Parameters of selected experiments performed to evaluate the long-term stability of regime II. The "Set" column refers to the type of pumps used to perform the forcing (see Appendix B). The forcing is indicated as a mean rms velocity (see appendix B.2 and B.3 for details on the forcing calibration). The forcing can be stationary ("Stat."), fluctuating around a given mean with a period of 3 seconds ("Fluct."), or alternating between rings $C_{1,3,5}$ and $C_{2,4,6}$ ("Alt."). The observed jets configurations (last column) are represented in Fig.5.2 and 5.3.

of E1.3. In terms of probability, if we include the long-time experiments, E1.1 was observed 6 times out of 13, E1.2 was obtained 2 times out of 13 and E1.3 was obtained 5 times.

With forcing set#2, as discussed in the previous chapter, due to increasing rms velocities the jets are more intense but also broader. Instead of having three to four prograde jets in the tank, we obtained only one or two prograde jets for all the experiments with set#2. For the same external forcing, we observed two multistable states represented in Fig.5.2*(c)* and Fig.5.3*(c)*. State E2.1 consists in two prograde jets, with a broader external one. State E2.2 consists in a single broad prograde jet and a strong retrograde flow inside, with a very small prograde flow at the centre of the tank. E2.1 was obtained 5 times and E2.2 was obtained for 6 realisations out of 11.

Finally, we are able to recover this multistability in QG numerical simulations. Fig.5.4*(a–c)* show the space-time diagram of 3 realisations of the same simulations with a different initial noise. For a non-dimensional forcing amplitude $F_0' = 5 \times 10^{-3}$ (equation (C.4.3)), we obtain different final steady states reminiscent of what is obtained experimentally, where the jets positions differ. Despite the reduced forcing scale compared to the experiment, the final jets are comparable to the ones measured, suggesting that these states are intrinsic properties of the system and unrelated to the details of the forcing pattern. We note that in the QG simulations, the difference between realisations is less pronounced compared to the experiments. This is due to the exact stationarity of the forcing in the simulations, whereas fluctuations are naturally present in the experiment due to the three-dimensionality of the flow for instance. Using a numerical stochastic forcing would probably lead to larger spread in the QG, but would also require tuning the correlation time of the forcing.

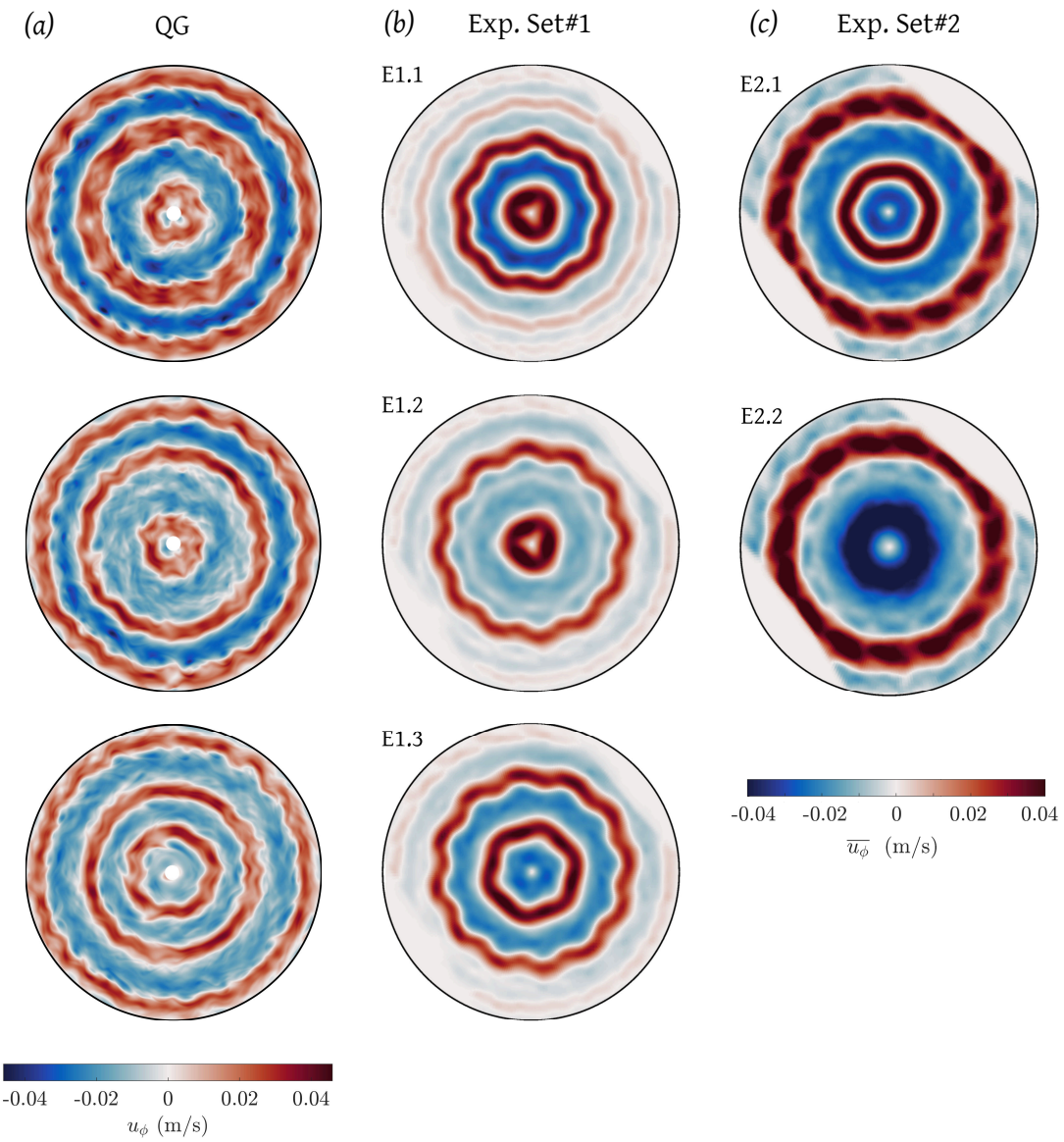

Figure 5.2. – Multistable states. *(a)* QG numerical simulations with $F_0' = 5 \times 10^{-3}$ (see Fig.5.4 for corresponding space-time diagrams). *(b)* Experiments with the first set of pumps. *(c)* Experiments with the second set of pumps. The configurations labels refer to those reported in Table 5.1. The colour scale is the same for all experiments.

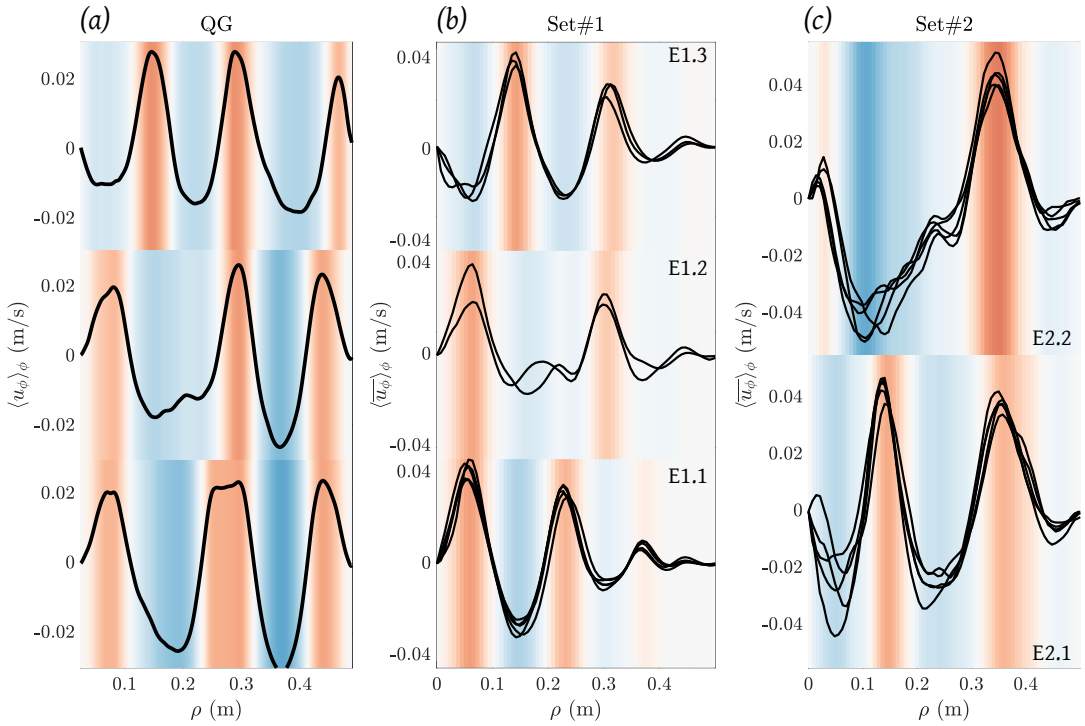

Figure 5.3. – Zonal flow associated with the multistable states represented in Fig.5.2. *(a)* QG numerical simulations, *(b)* experiments with the first set of pumps, *(c)* experiments with the second set of pumps. The multiple lines represent the different realisations reported in Table 5.1.

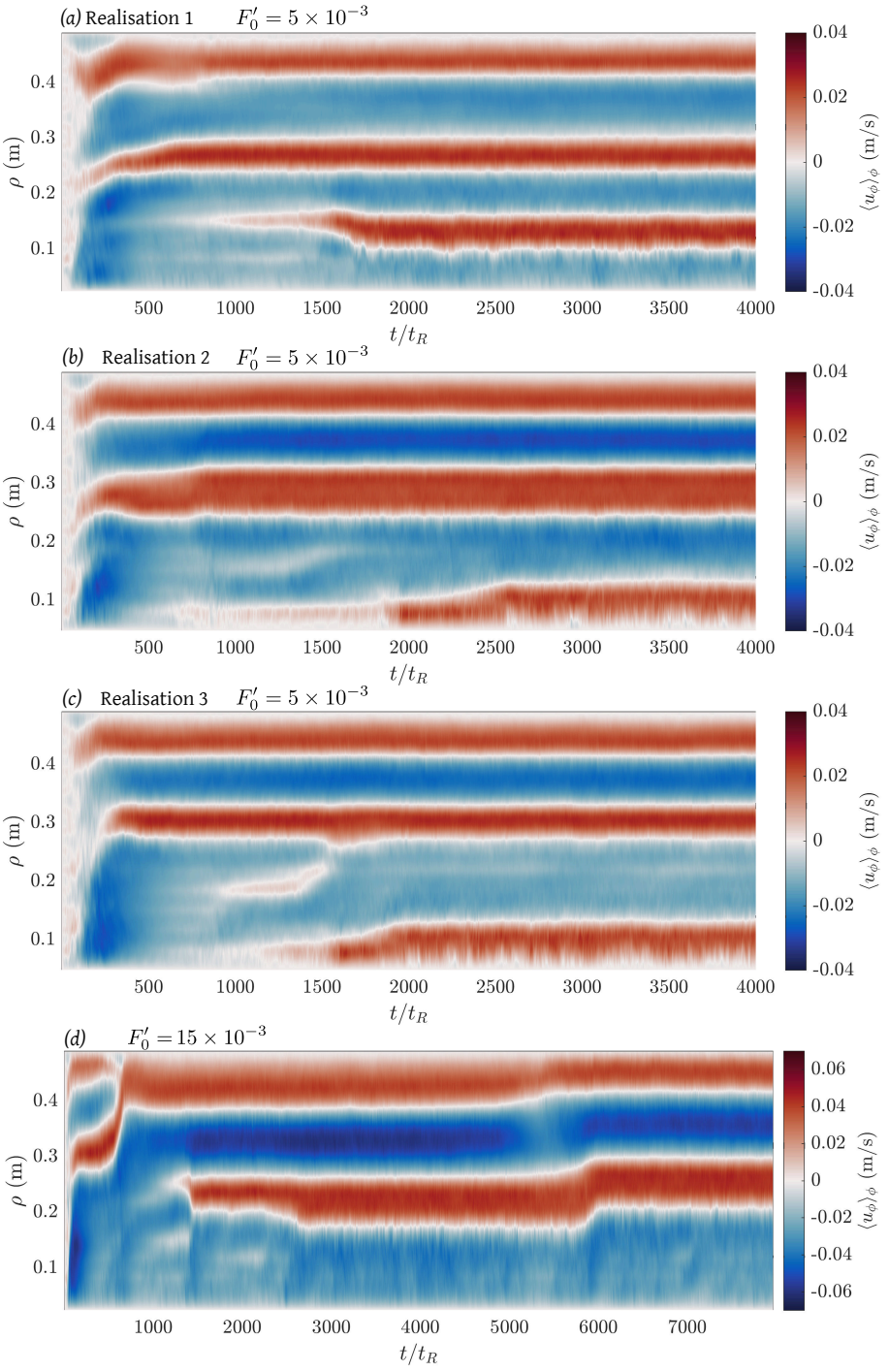

Figure 5.4. – *(a–c)* Space-time diagrams of the zonal flow in three QG numerical simulations corresponding to the exact same forcing, $F_0' = 5 \times 10^{-3}$, but different initial noise. The three statistically steady states obtained are represented in Fig.5.2*(a)* and Fig.5.3*(a)*. *(d)* Space-time diagram for a QG simulation at a forcing $F_0' = 15 \times 10^{-3}$ and over a doubled duration. A spontaneous transition between two multistable states occurs at $t \sim 6000 t_R$.

5.4. Seeking transitions between multistable states

5.4.1. Search for spontaneous transitions

The QG numerical simulations show that at relatively high forcing amplitude, spontaneous transitions between multistable states can occur, even in our experimental regime. An example is plotted in Fig.5.4*(d)*, with a forcing amplitude $F_0' = 15 \times 10^{-3}$. At a time $t \approx 6000\ t_R$, a spontaneous transition between two co-stable states occurs, despite a completely stationary forcing. According to such simulations, it should thus be possible to observe transitions in our experiment, with reasonable waiting times. These observations motivated us to perform long-time experiments to seek such spontaneous transitions, and were also one of the reasons why we changed the forcing pumps from set#1 to set#2.

As reported in Table 5.1, we realised three day-long experiments, thus lasting tens of thousands of rotation times. We performed one experiment with a stationary forcing and set#1, one with a fluctuating forcing and set#1, and one with a fluctuating forcing and set#2. For the fluctuating experiment with set#1, the power of each pump fluctuates around ±10% of its mean value, with a time step of 3 seconds. For the fluctuating experiment with set#2, the fluctuation interval is ±20% of the mean power for each pump. These experiments are labelled 1L, 1M and 2K in Table 5.1. We recorded images of the flow at regular time intervals during these experiments (typically every 30 min). Hovmöller diagrams for experiments 1L and 2K are available in Appendix E. Fig.5.5 shows a condensed view of the evolution of the zonal flow radial profile. Despite the clear identification of multistable states for the two forcings investigated, we have never observed spontaneous transitions in these long-lasting experiments. The steadiness of the zonal flow is striking. Fluctuations are more important for experiment 2K performed with set #2, and a very slight migration of the jets is maybe occurring at the end, but overall, the conclusion is that the obtained jets state is incredibly stable through time.

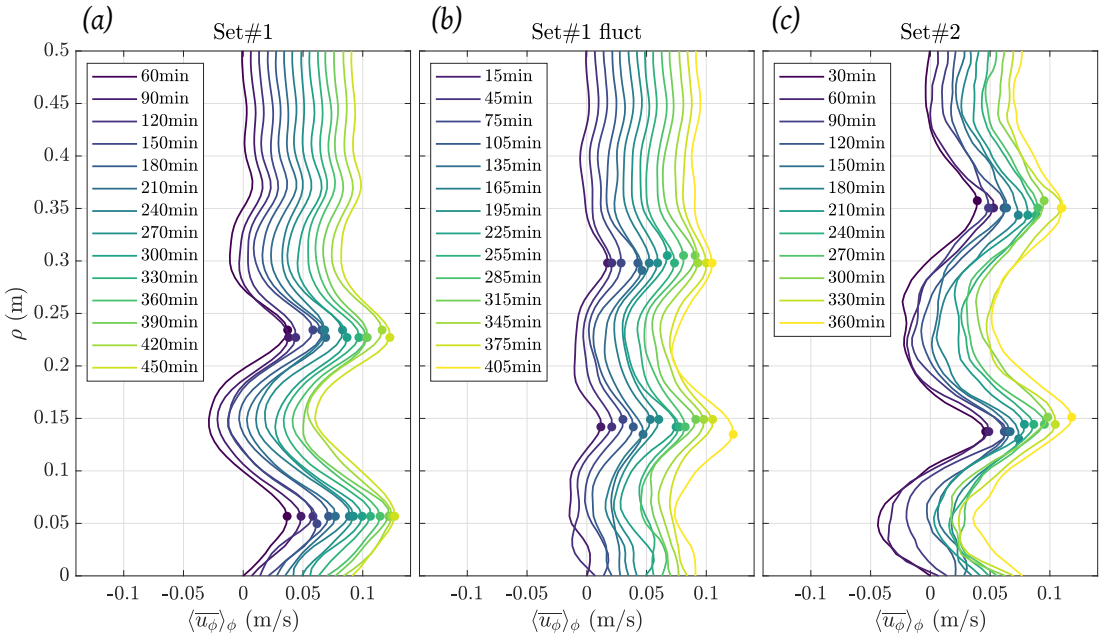

Figure 5.5. – Evolution of the zonal flow profile for the three long-time experiments. *(a)* Experiment 1L. *(b)* Experiment 1M. *(c)* Experiment 2K. The dots localize the maximum prograde velocity. Each curve corresponds to a different time and is shifted horizontally compared to the previous one for a better visualisation. Corresponding Hovmöller diagrams are provided in Appendix E for experiments 1L and 2K.

5.4.2. Experimentally forced transitions

Our last attempt to observe transitions consisted in trying to experimentally trigger them, by introducing finite amplitude perturbations stronger than a simple noise due to a fluctuating forcing.

The first example that we describe is an experiment where we keep the forcing constant, but we slightly increase the β-effect halfway through an experiment. The corresponding Hovmöller diagram is represented in Fig.5.6. More precisely, we started with a rotation rate of 70 RPM and waited for a statistically steady state to be achieved. 15 minutes ($1125\,t_R$) after the beginning of the experiment, the system is in the steady state E1.1. We then increase the rotation rate of the turntable by 1 RPM every 3 minutes until we reach a rotation rate of 75 RPM at time $t = 27\text{min} = 2025\,t_R$. After relaxation, the system is now in the steady state E1.3, different than its initial state. The initial and final zonal flow profiles are represented in Fig.5.6*(c,d)* and compared with the profiles of all the other experiments in states E1.1 and E1.3. The profile obtained before the successive spin-ups is a little bit different in amplitude from the other ones, but this is probably due to the fact that at 70 RPM, the β-effect is slightly different from that at 75 RPM, with a mean value of $38.7\ \text{m}^{-1}\,\text{s}^{-1}$ and maximum and minimum values of 42.9 and $36.5\ \text{m}^{-1}\,\text{s}^{-1}$ respectively (see Fig.B.10).

Of course, changing the rotation rate does not instantaneously change β. The acceleration of the fluid due to the increase of the rotation rate occurs typically over several spin-up time scales, $\tau \sim \Omega^{-1}E^{-1/2} = 3.45$ min $= 258\,t_R$. Since the camera is rigidly fixed in the rotating frame, each acceleration appears as an instantaneous retrograde solid-body rotation of 1 RPM superposed to the actual flow (blue steps in Fig.5.6*(a)*), until the fluid is accelerated towards a new mean solid body-rotation equal to that of the tank. In Fig.5.6*(b)*, we have removed the mean angular velocity induced by the sudden change of frame of reference, which allows to better visualize the intrinsic evolution of the zonal flow. More precisely, we plot $\langle u_\phi\rangle^c_\phi = \langle u_\phi\rangle_\phi - \Omega_f(t)\rho$, where Ω_f is the solid-body rotation rate of the fluid, computed by averaging radially the zonal flow: $\Omega_f = 2/R \times \langle\langle u_\phi\rangle_\phi\rangle_\rho$. This figure shows that despite the strong perturbations induced by accelerating the whole fluid, the zonal flow remains coherent and the jets are not broken. Instead, the successive spin-ups triggered a merging between two jets of state E1.1 to give a new prograde jet at an intermediate radius between the two, leading to state E1.3. We can also see that the additional space due to the new radial position of this jet allows the central jet to broaden and intensify. Of course, we acknowledge that between 70 and 75 RPM, β is increased by about 20%, hence one could question the notion of "perturbation" and the fact that the two observed states correspond to the same set of external parameters.

Finally, a second type of experiments was performed to trigger transitions. Fig.5.7 shows the results of experiments where the forcing alternates as a whole between rings $C_{1,3,5}$ and $C_{2,4,6}$ with a time step Δt. The idea is again to sufficiently perturb the system to trigger transitions between multistable states. The time steps were chosen as natural prominent frequencies of the system. To identify them, we performed temporal Fourier transforms of the flow with a stationary forcing, and selected frequencies corresponding to peaks in the spectrum amplitude. We identified peaks at frequencies of $[0.07, 0.014, 0.0066, 0.0043]$ Hz, corresponding to time steps of $[7, 35, 76, 117]$ seconds, or $[8.75, 43.8, 95, 146]\,t_R$. The two highest frequencies correspond to fast dynamics inside of the prograde jet, whereas the two low frequencies correspond to the slow migrations/nucleations which can be guessed in the retrograde flow in Fig.5.7*(a)*. Fig.5.7*(b,c,d,e)* show that this alternating forcing did not trigger any transition for the duration of our experiments. The low frequency forcing enhances and regularizes the nucleation and merging of jets in the retrograde flow, but overall, the position and intensity of the jets remain extremely stable.

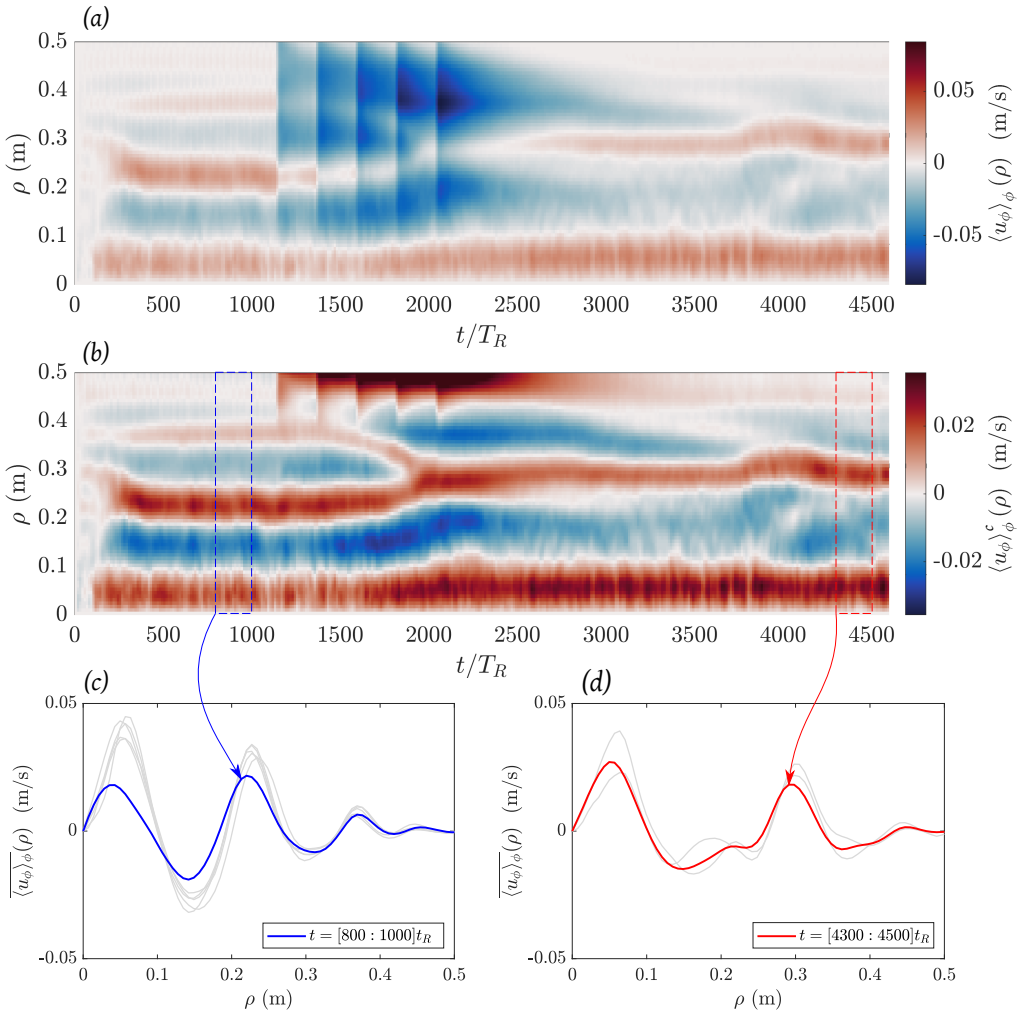

Figure 5.6. – Forced transition between states E1.1 and E1.2 observed in experiment 1N. *(a)* Raw space-time diagram. At times $t = [1125, 1350, 1575, 1800, 2025]$ t_R, the rotation rate of the tank is increased by 1 RPM (initially, $\Omega = 70$ RPM, and at the end, $\Omega = 75$ RPM). *(b)* Space-time diagram where we have removed the angular velocity induced at each RPM increase. *(c)* Zonal flow profile before the spin-ups. The grey lines are the zonal flows observed in other experiments in state E1.1. *(d)* Zonal flow profile after the spin-ups. The grey lines are the zonal flows observed in other experiments in state E1.3.

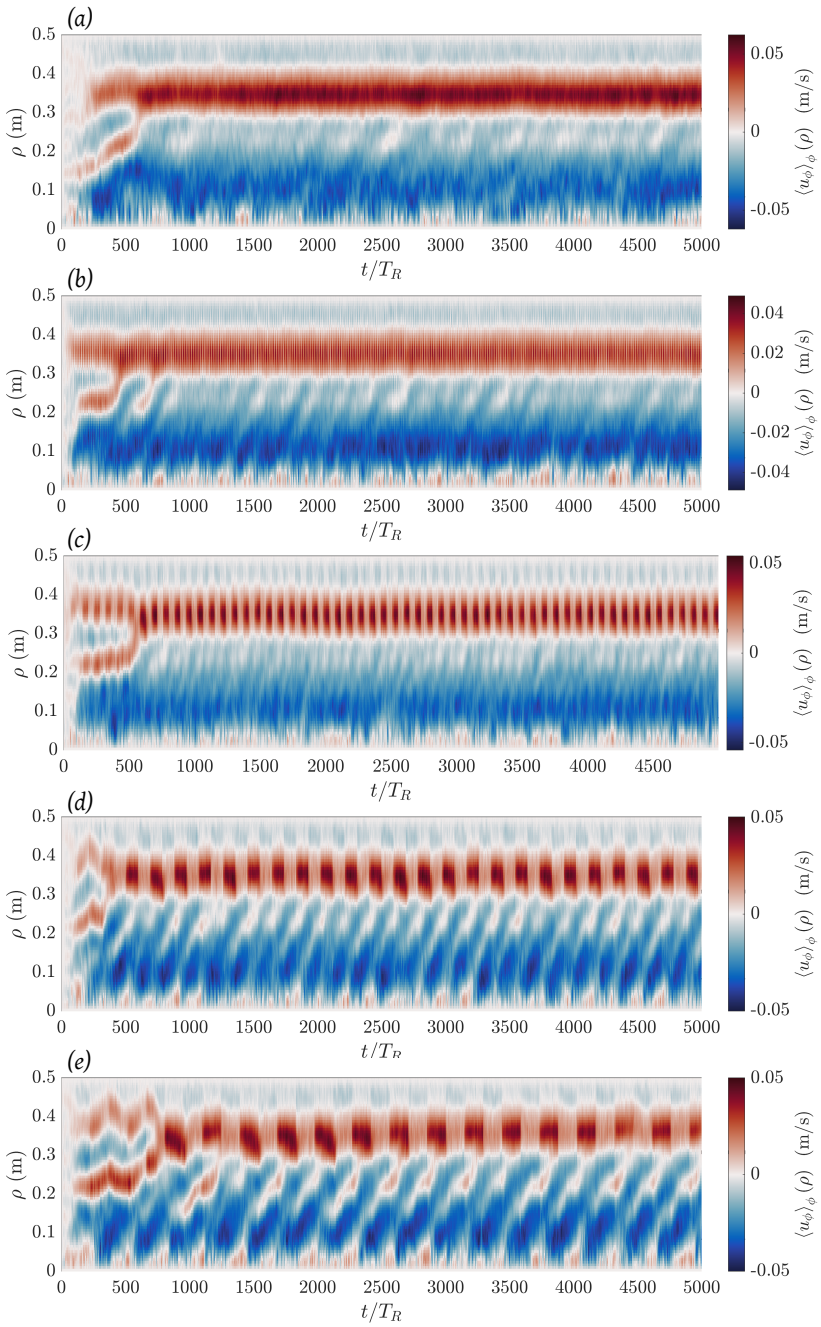

Figure 5.7. – Space-time diagrams of experiments *(a)* 2I, *(b)* 2L ($\Delta t = 7$s), *(c)* 2M ($\Delta t = 35$s), *(d)* 2O ($\Delta t = 76$s) and *(e)* 2N ($\Delta t = 117$s). For each experiment except 2I, the forcing alternates between rings $C_{1,3,5}$ and $C_{2,4,6}$ with a time step Δt. The power of each ring is identical for the five experiments.

5.5. Discussion

5.5.1. Origin of the multistability

To the best of our knowledge, this is the first time that multistability among multiple zonal jets states is described experimentally. In the context of transition to super-rotation for planetary atmospheres, the existence of two bistable states (one super-rotating, and the other not) has been discussed and observed both numerically and experimentally (Charney et al. 1979; Charney et al. 1981; Weeks et al. 1997; Tian et al. 2001; Arnold et al. 2011; Herbert et al. 2020). We have shown in chapter 3 that such bistability holds for out-of-equator dynamics, and is observed at the transition between regimes I and II. However, this bistability describes two possible states for a single jet (sub or super-resonant states). The multistability described in the present chapter is different. It applies to the system at a global scale, and can be described in terms of mutual organisation of the zonal jets. For the exact same set of external parameters, the jets, of fairly similar amplitude and width, can organize differently in space, leading to multiple – but a priori a finite number of – configurations.

Recently, multistability between jets configurations was observed numerically thanks to rare-events algorithms applied to stochastically forced barotropic turbulence (Bouchet et al. 2019a,b; Simonnet et al. 2021). In particular, Simonnet et al. (2021) describe transitions between states with two or three jets, associated with nucleations or merging events. They show that states with 3 jets have 6 possible configurations (3! permutations). Their results hold with either periodic meridional boundary conditions, or in a channel flow with stress-free boundary conditions. This is important for experimental comparisons or planetary applications, where the domain has a finite size, and where confinement may play an important role. In Fig.5.8, we represent qualitatively the 6 states that Simonnet et al. (2021) observe in a channel flow. Our experiments have of course no-slip boundary conditions, which may decrease the number of states allowed, but qualitatively their results are reminiscent of what we observed (compare for instance with Fig.5.3). If we assume that the origin of the multistability is similar in our experiments and in their numerical simulations, then it is not surprising that we could not observe spontaneous transitions in our experiments, or we would have been very lucky! Simonnet et al. (2021) observe transitions over time scales of about 10^5 or even 10^6 turnover times. In our experiments, based on the vorticity field, a turnover time lasts between typically 5 to 15 rotation periods. Our day-long experiments (40,000 rotation periods) would hence represent at best 10^4 turnover times, thus 10 to 1% of the typical duration that one has to wait before a transition! Note that Bouchet et al. (2019b) and Simonnet et al. (2021) explicitly state that these incredibly long transition times are precisely the reason why despite decades of studies, they were not observed before in direct numerical simulations of zonal flows. That being said, it is hard to say to what extent our studies can be compared to each other. For instance, their numerical results stand in a regime where both the friction and the forcing are vanishing, whereas our experiments are both strongly forced and strongly dissipative. With their choice of non-dimensional parameters, the ratio of turnover time to dissipative time is of $\sim 10^{-3}$ in their study, whereas we estimate it between 0.2 and 0.02 for our experiments, depending on the length scale used for the turnover time. Our non-dimensional β is also between 100 and 1000 whereas they consider $\beta \in [4, 12]$. The fact that our experiments are strongly forced will certainly results in strong correlations between the forcing and the jets, and may result in locking them in a given configuration. For planetary applications, the extent to which the forcing resulting from convection or baroclinic instabilities could be considered as "vanishing" is not a trivial question. That being said, multistability is a tempting mechanism to explain, for instance, the asymmetry between the zonal winds profile in the northern and southern hemispheres of the gas giants, which is represented in Fig.5.9. A priori, the two hemispheres are subject to the same forcing, and have the same β-effect, but it

is possible that two different multistable states developed independently in each hemisphere. If one could spin down and spin up again the gas giants, the resulting zonal flows profiles may be different from what we observe today.

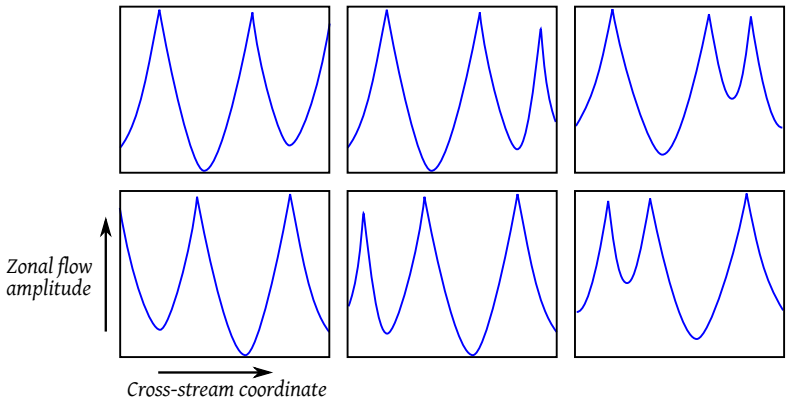

Figure 5.8. – Qualitative illustration of the multistable states with 3 jets obtained by Simonnet et al. (2021) in a barotropic channel flow with free-slip boundary conditions. The horizontal axis represents meridional (radial) position, and the vertical axis is the zonal flow amplitude.

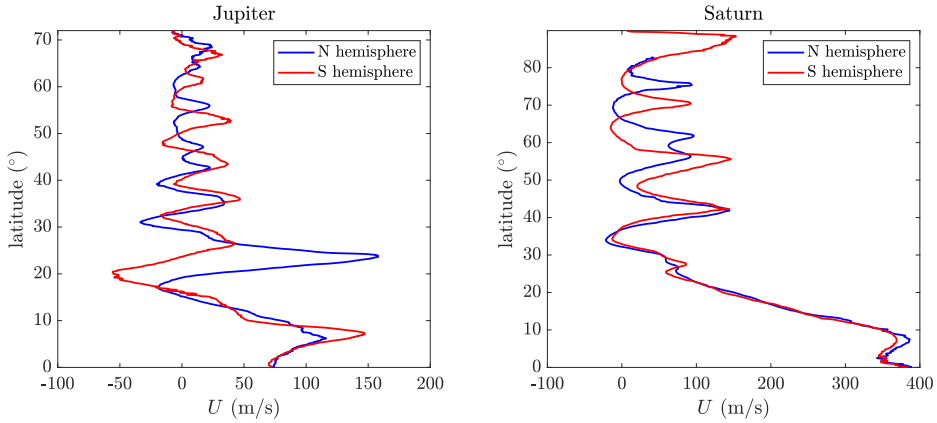

Figure 5.9. – Comparison of zonal winds profile in both hemispheres of Jupiter (in 2016) and Saturn (average from 2004 to 2009). The data are taken from Tollefson et al. (2017) for Jupiter, and García-Melendo et al. (2011a) for Saturn.

5.5.2. Non-zonal features

Despite the apparent long-term stability of the jets in our experiments, we would like to mention that the prograde jets in regime II sometimes have a long-term fluctuating behaviour with the repetition of cycles where the jets destabilize into vortices before recovering their initial state. This phenomenon is illustrated in Fig. 5.10 and supplementary movie 5 in Lemasquerier et al. (2021). More precisely, we observed the growth of zonal perturbations of the zonal flow (figure 5.10(*b*)) followed by episodes of vortices “surfing" along the jet in the prograde direction (figure 5.10(*c-e*)). These zonal packets of vortices may correspond to envelope Rossby solitary waves, and are also reminiscent of non-linear waves called “zonons" which have been described within barotropic jets in numerical simulations (Sukoriansky et al. 2008; Galperin et al. 2010; Sukoriansky et al. 2012; Bakas et al. 2013).

Fig.5.11 shows the example of an experiment in regime II performed with the forcing set#1. The arrows point to moments when the zonal jet slightly intensifies, corresponding to periods

with no propagating vortices, separated by periods when the zonal jet is slightly weaker, and with packets of vortices propagating. Fig.5.11*(b)* shows the radial component of the velocity as a function of ϕ at a fixed radius $\rho = 0.2$ m. The dominant azimuthal mode visible is that of the forcing. This diagram confirms the notion of wave-packets. At a given time, the vortices are confined azimuthally, and they propagate in the prograde direction coherently, as indicated by white stripes going towards the top-right of the figure. Inside each envelope (between two stripes), we see that the vortices propagate in the retrograde direction (see the schematic in Fig.5.11*(c)*). The picture is then that of Rossby wave packets of prograde group velocity and retrograde phase speed, propagating in the vicinity of prograde jets. For the experiment of Fig.5.11, the group velocity is of about 4.5 $\mathrm{cm\,s^{-1}}$ (faster than the jet), and the phase speed can reach -1.5 $\mathrm{cm\,s^{-1}}$. Note that in experiments, meandering jets are frequently observed due to barotropic or baroclinic instabilities, where the most unstable zonal wavenumber can lead to the formation of polygonal jets and vortices (e.g. Barbosa Aguiar et al. 2010, and references therein). The relevance of the barotropic instability to explain the observed vortices drift should be addressed. But given the origin of the transition to regime II, we think that the observed phenomenon is associated with a direct amplification of the quasi-resonant Rossby waves rather than an indirect growth following a shear instability.

Finally, we would like to stress out that all these features are recovered in our QG numerical simulations when a single jet is forced by turning on only one forcing ring. In these simulations, the emission of the wave packets is enhanced, probably because the forcing is much steadier than in real experimental configurations. As a result, a clear succession of events is observed: first, the jet is perturbed zonally at the wavelength of the forcing, then, the amplitude of the wave grows until a modulation appears and packets of vortices detach to propagate along the jet, in the prograde direction. This propagation lasts until the vortices break, and a new cycle with a growing linear wave begins. The cycles repeat regularly and never stop, but for the same simulation, we also observed cases where the state with drifting vortices remains stable for very long times. This long-term dynamics is probably due to the fact that in regime II close to the transition, the jet is locked in a quasi-resonant state where the forced Rossby waves are quasi-stationary. The forcing can thus almost directly force the waves, which may eventually become non-linear because of this amplification. A feedback mechanism between the jet and the excited solitary waves may then be responsible for the observed cycles, since Rossby waves are enhanced by steep potential vorticity gradients associated with prograde jets.

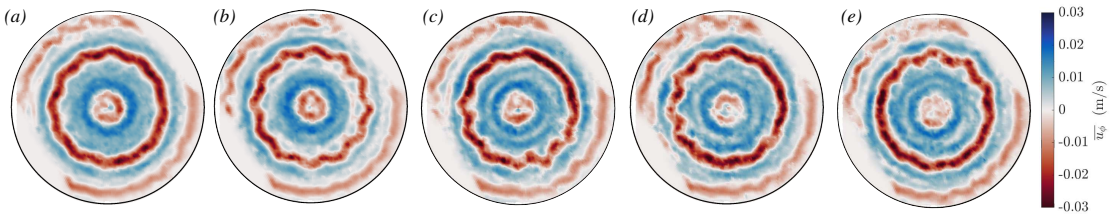

Figure 5.10. – Illustration of the jet's instability for an experiment in regime II, and forcing set#1 (*a*) $t = 2412$ to 2436 t_R. (*b*) $t = 2486$ to 2511 t_R. (*c*) $t = 2568$ to 2580 t_R. (*d*) $t = 2580$ to 2593 t_R. (*e*) $t = 2593$ to 2605 t_R. This sequence is also available as supplementary movie 5 in Lemasquerier et al. (2021).

Even if we have not investigated further the physical origin of these waves yet, it is worth mentioning that analogous phenomena are observed in different natural and idealized systems. Their possible link or difference with the present phenomenon remains, of course, to be addressed. First, in the Earth atmosphere community, there is a substantial literature describing so-called Rossby Wave Packets. Wirth et al. (2018) give for instance a review of Rossby Wave Packets which are observed to propagate in longitude along the midlatitude jet stream, and which are sometimes precursors of extreme weather events. The interpretation of these wave

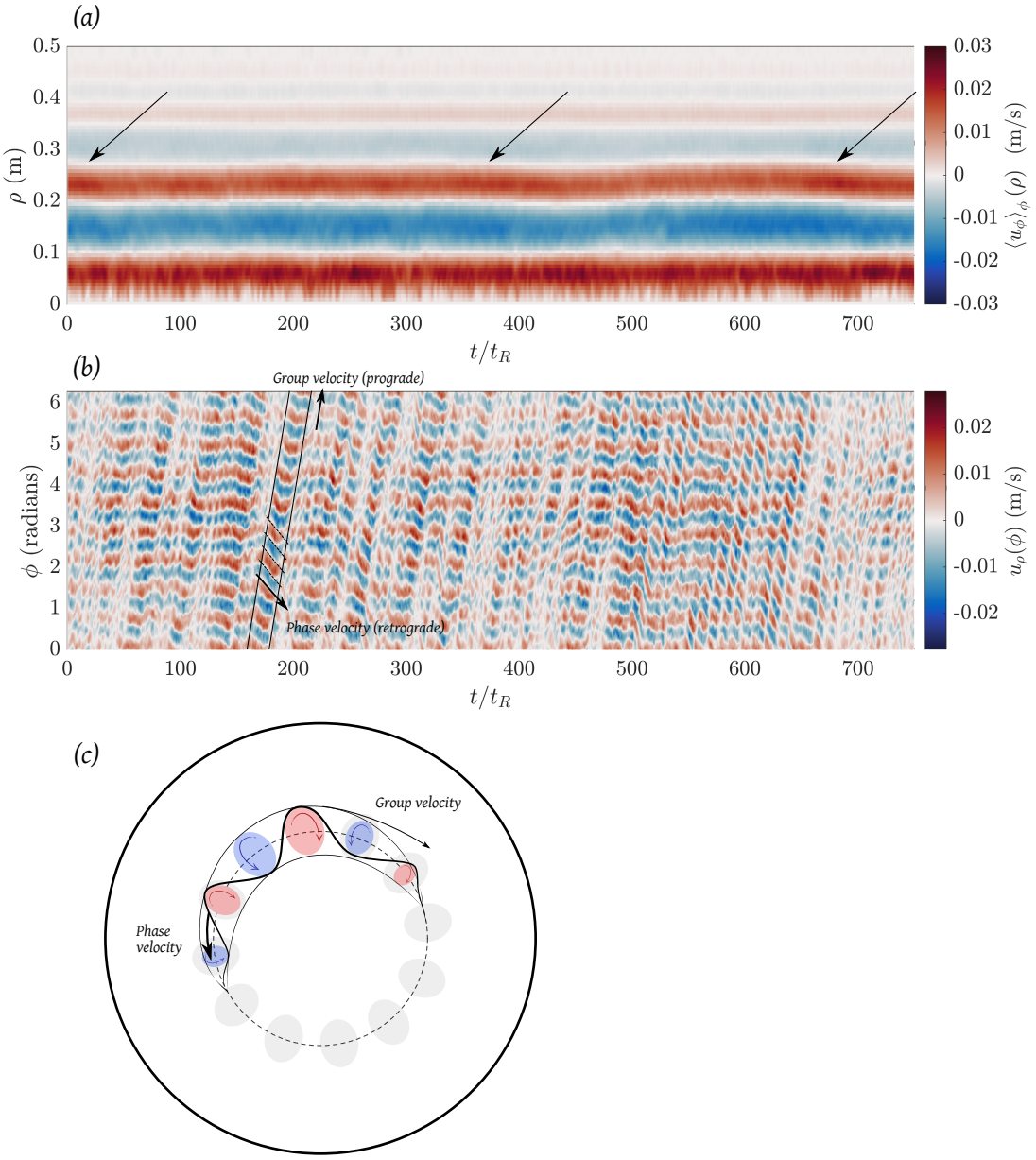

Figure 5.11. – *(a)* Space-time diagram of the zonal flow. The arrows indicate moments of intensification of the zonal flow which precede the release of wave-packets. *(b)* Space-time diagram of the radial velocity as a function of angular position ϕ at a fixed radius of 0.2 m (inward flank of a prograde jet, see panel *a*). The continuous black lines materializes the edges of a wave-packet, which thus propagate in the prograde direction. The dashed lines materializes the retrograde phase speed of each wave crest. *(c)* Qualitative schematic of a Rossby wave packet at a given time, corresponding to a vertical line in panel *b*. The envelope of the wave-packet propagates in the prograde direction (clockwise), whereas each vortex inside of it propagate in the retrograde direction. Not that several packets can be present at the same time, as visible in panel *b*.

packets as envelope solitary Rossby waves arising from a Benjamin-Feir instability is supported by theoretical (e.g. Redekopp 1977; Esler 2004) and two-layer QG numerical models (e.g. Lee et al. 1993). But how the theory of solitons may apply to the real atmosphere remains to be studied. Similarly, Sukoriansky et al. (2012) points towards the analogy between zonons observed in 2D turbulent simulations on the sphere and solitary Rossby waves. However, to date, there has been no quantitative comparison between the Kortevieg-De-Vries or Non-Linear Schrödinger equations derived analytically and observations in more complex systems such as β-plane barotropic or baroclinic turbulence.

Then, we would like to mention that somewhat similar features were observed in recent direct numerical simulations of gas giants' compressible convective flows, where large-scale vortices drift along zonal jets, particularly at high latitudes where the β-effect is smaller. We refer the reader to Fig.4 in Yadav et al. (2020) and their supplementary movie S1. In these simulations, the forcing is not external but comes naturally from small-scale thermal convection. The observed large scale vortices thus emerge from the inverse energy cascade, and persist thanks to stress-free boundary conditions. As suggested by Yadav et al. (2020), the deep large scale vortices and associated wavy aspect of the jets may explain the polygonal aspect of the polar jets on Saturn, such as the hexagonal jet at the North Pole (Sayanagi et al. 2018). At the South Pole, completely polygonal jets are not observed, but a partial $m = 12$ azimuthal mode (confined in longitude) has been described by Vasavada et al. (2006), which is consistent with the idea of propagating azimuthal wave-packets (see Fig.6.1). Meandering jets as well as cyclic "bursts of eddies" have also been described in a Global Circulation Model (GCM) of Saturn recently developed (Spiga et al. 2020). The same phenomenology of large-scale vortices at high latitudes associated with meandering jets also seems to occur in Jupiter's GCM (Young et al. 2019).

We argue that possibly, Rossby wave packets along jet streams in the Earth atmosphere, gas giants convective envelope, or what we observe experimentally, may be described within a unified framework of solitary Rossby waves propagating along potential vorticity fronts. The degree of supercriticality of the zonal flow would then determine the frequency of emission and amplitude of such solitons relatively to the jets. In our experiments, the large-scale vortices associated with meandering jets are somewhat directly forced, even if they certainly grow in size following an inverse cascade since vortices in regime II are larger than those observed in regime I (see for instance Fig.3.4). The azimuthal wavenumber of meandering jets is thus selected by our forcing pattern, but based on the aforementioned studies, we argue that despite different source mechanisms, the resulting dynamics may be relevant to more planetary-like flows and deserves further study.

Chapter 6.

Collective drift of floating cyclones towards the pole and clustering: a preliminary experimental study

Chapter 6.

NASA's Juno spacecraft produced for the first time images of Jupiter's poles. They revealed striking clusters of cyclones around each pole, a picture significantly different from the single giant cyclone that is seen at each pole of Saturn. How these clusters form under Jupiter's conditions remains unclear. In this chapter, we experimentally study the drift of single and multiple cyclones under a polar β-effect.

Chapter aims

1. Build up a setup in which long-lived cyclones can be externally generated in a configuration analogous to the pole, and in particular with a polar β-effect.
2. Compare the drift of isolated cyclones to the β-drift mechanism.
3. Study the collective drift of multiple cyclones generated simultaneously. Determine in particular if cyclones coalesce at the pole, towards which they are attracted, or if they can equilibrate without merging.

Highlights

- We modified the *Jacuzzi* experiment to come up with the *Clusters* setup. We removed the bottom forcing plate, and added a system where six cyclones can be generated by sucking fluid from the top. The polar β-effect comes from the paraboloidal shape of the free surface, and tends towards zero at the pole (centre of the tank).
- Two configurations are employed. The first one is a "deep" configuration in which we use a single homogeneous layer of water, thereby generating barotropic vortices extending vertically down to the bottom of the tank. The second one is a "shallow" configuration where the cyclones are generated in a top, thin layer of fresh water resting on a deep, dense layer of salt water.
- The trajectory of the cyclones is consistent with the β-drift: they translate towards the north-west and end up at the centre of the tank, analogous to the pole. The cyclones are much more long-lived in the shallow configuration, which is used in the cases of multiple cyclones.
- When multiple cyclones are generated, their β-drift is perturbed by adjacent cyclones. We observed both mergers (occurring essentially when the cyclones are close to each other from the start), and repulsive behaviours. The competition between attraction to the pole and repulsion may lead to an equilibrium around the pole without merging.

6.1. Introduction

In the previous chapters, we focused on gas giants dynamics at midlatitudes, where the large variation of the Coriolis force with radius is responsible for a strong β-effect and hence strong zonal flows. The midlatitude deep ($\sim 3{,}000$ km) zonal flows coexist with large-scale shallow (~ 100 km) vortices, mostly anticyclonic. At increasing latitudes, the gradient of the Coriolis forces decreases and tends towards zero at the pole. Consequently, the zonal jets weaken, and the dynamics becomes more isotropic, with a predominance of vortices rather than jets (see Fig.1.12). In addition, the vortices become predominantly cyclonic, contrary to what is observed at midlatitudes. This transition in the dynamics with increasing latitude has been first suggested by Theiss (2004) for Earth's oceans, and later observed in shallow-water turbulence models on the sphere (e.g. Cho et al. 1996; Scott et al. 2007).

In terms of observations, before Juno, we had very little information on the polar dynamics of Jupiter. Our picture of the polar dynamics of gas giants was then that of Saturn, which was much better characterized thanks to the Cassini mission, as shown in Fig.6.1 (Sayanagi et al. 2018). In particular, Saturn exhibits a hexagonal jet stream at its North Pole, surrounding a large-scale cyclone centred at the pole (Fig.6.1*(c)*). At the South Pole, a central cyclone is also observed, but the surrounding jet is not polygonal, even if one high latitude jet exhibit a partial polygonal shape (Fig.6.1*(b)*). Before the observations of Juno, modelling efforts were dedicated to explain how a cyclone could develop at the pole. Again, most of the investigations were performed in the shallow-water framework (see e.g. Scott 2011; O'Neill et al. 2015, 2016).

When Juno spacecraft arrived at Jupiter, visible and infrared observations from above the poles revealed an incredible dynamics consisting in persistent polygonal patterns of large cyclones (Adriani et al. 2018). As represented in Fig.6.2*(a)*, in the north, eight cyclones encircle a polar one, and in the south, five cyclones encircle a central one. Adriani et al. (2020) reported the evolution of these structures two years after their discovery. Their results are reproduced in Fig.6.2*(b,c)*. Both the position and the internal structure of the north circumpolar cyclones remained stable during the observation period. At the South Pole, the pentagonal structure also remained unchanged, even if one intruder changed the pentagon into an hexagon temporarily. This stability is particularly surprising given the highly turbulent nature of the flow, but also given that the cyclones of a given cluster are clearly in contact with each other as demonstrated by well visible spiralling arms (Adriani et al. 2018). Hence, while Saturn guided modelling efforts towards the formation of a single polar cyclone, Jupiter raises a significantly different question: how can several cyclones pack together and form a stable polygonal pattern surrounding the pole without merging?

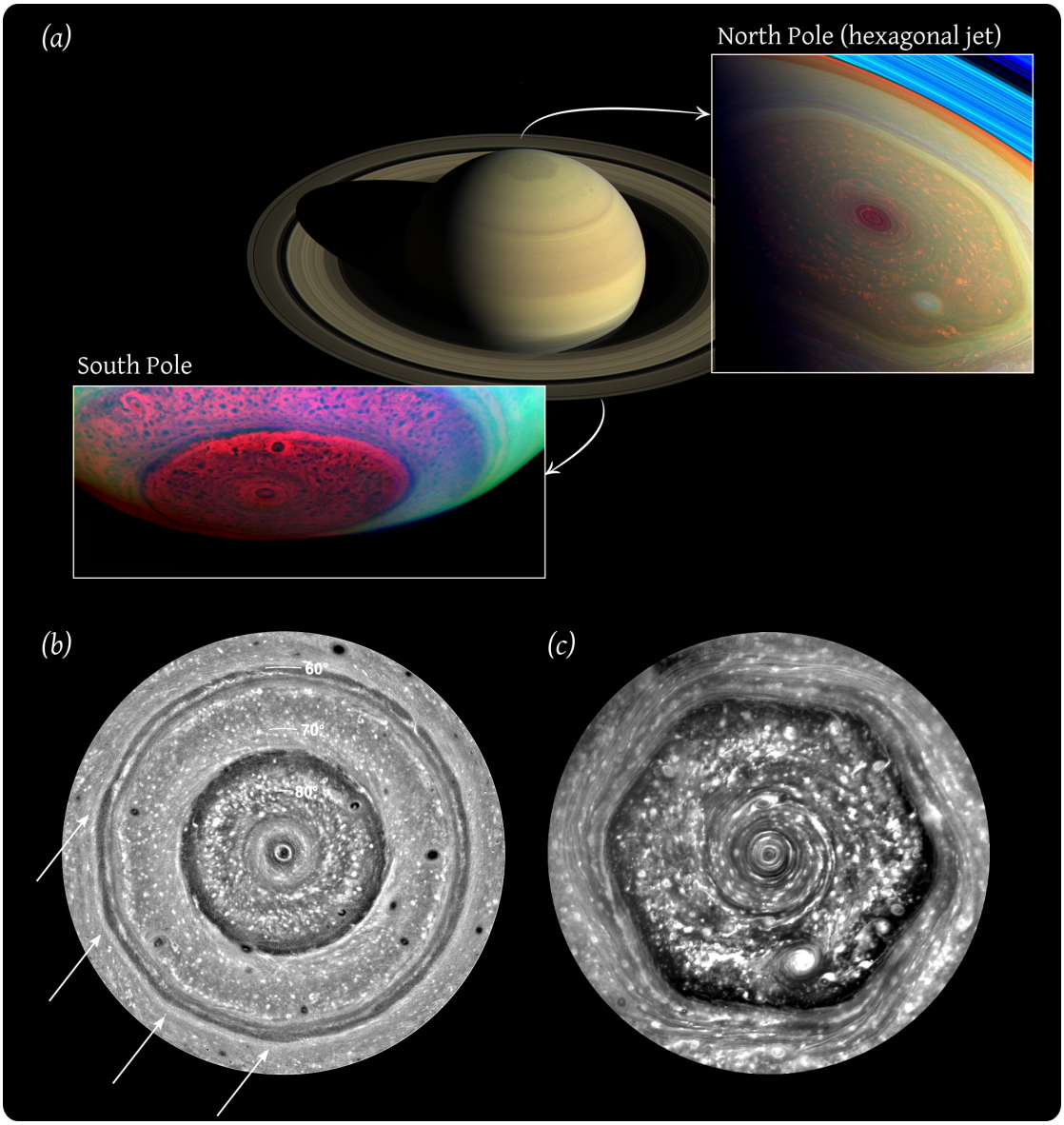

Figure 6.1. – *(a)* Top-right: False-colour image taken in near-infrared by NASA's Cassini mission (Credits: NASA/JPL-Caltech/Space Science Institute). Bottom-left: False-colour image of the South Pole taken in near-infrared by Cassini in 2007 (Credits: NASA/JPL/University of Arizona) *(b)* Polar stereographic projection of Saturn's southern hemisphere on 18 September 2004 (adapted from Fig. 2 in Vasavada et al. (2006)). *(c)* North Pole observation made by Cassini in 2012, taken in wavelengths ranging from ultraviolet to infrared (Credits: NASA/JPL-Caltech/SSI/Hampton University).

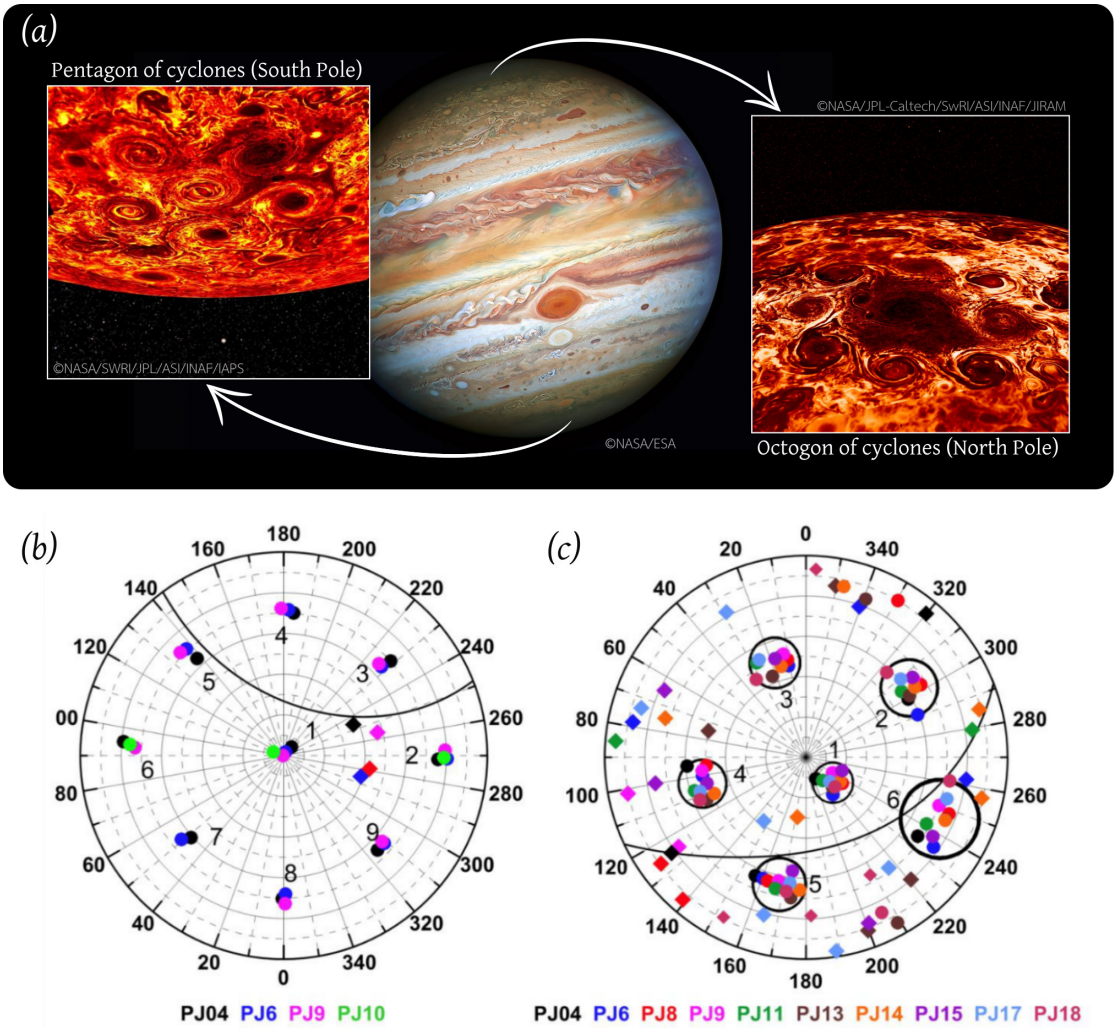

Figure 6.2. – Views and data of Jupiter's poles collected by Juno. *(a)* Images of Jupiter's south and north poles generated from Juno's JIRAM (Jupiter InfraRed Auroral Mapper) measurements (Adriani et al. 2018). *(b)* Positions of the cyclones centre for the North Pole during an observation period of 10 months (perijove 4 to 10). *(c)* Positions of the cyclones centre for the South Pole during an observation period of two years (perijove 4 to 18). Panels (b) and (c) are both taken from Fig. 4 in Adriani et al. (2020).

When the polar observations of Juno arrived, the concept of clusters of vortices (or vortex crystals) was already existing for a long time for two-dimensional Euler flows. It has been shown that polygonal vortex patterns can develop and remain stable on a background of weaker vorticity (Fine et al. 1995; Schecter et al. 1999). But the Euler equations do not represent the fundamental physics of the gas giants dynamics. Among others, rotation but also the variation of rotational effects with latitude, i.e. the β-effect, are missing. Rotation is responsible for the zeroth order geostrophic balance of the vortices, and the β-effect is responsible for the poleward drift of cyclones and southward drift of anticyclones (van Heijst et al. 2009, and references therein). Any consistent model of polar clusters should include these effects, and hence remains to be derived in gas giants context.

Recent studies tackled the problem of polar dynamics and clusters formation and stability. O'Neill et al. (2015, 2016) used a $2-1/2$ shallow-water model on the γ-plane (polar β-effect): two layers are located above a third abyssal and quiescent layer, and the flow is forced with parametrized moist convection in the top layers. They showed that with Saturn-like parameters, a strong single polar cyclone develops at the pole. With Jupiter-like parameters, multiple

vortices persist around the pole, but they are not organized in a polygonal pattern. Still in the shallow-water framework, Brueshaber et al. (2019) showed that if the Rossby radius of deformation is large, a single polar cyclone is favoured whereas a smaller radius of deformation leads to multiple cyclones, but again, they do not form clusters and do not persist over long times. Li et al. (2020) used a somewhat different approach, consisting in studying the stability of an already defined polygonal pattern of vortices, instead of letting the vortices form by convection. They conclude that a key parameter to the stability of clusters is the extent to which the vortices are shielded (or in other words, isolated), i.e. how pronounced is the ring of anticyclonic vorticity that surrounds the cyclonic core of the vortices. In the framework of deep convection, Heimpel et al. (2020) observed a variable pattern of vorticity depending on latitude, with shallow anticyclonic vortices favoured at mid-latitudes and deeply seated cyclones near the poles. The deep-roots of polar cyclones are qualitatively attributed to the alignment of thermal plumes with the rotation axis in the polar regions, as already noted by Aurnou et al. (2008). But in these global scale simulations, no persistent clustering of cyclones emerge at the pole. Finally, Cai et al. (2021) performed large eddy simulations of compressible convection by parametrizing subgrid-scale processes. They show that on the γ-plane small-scale convective eddies can merge up to a saturation scale and organize in polygonal patterns. This last study is impressive because it combines the results of the aforementioned ones: natural vortices emerging from convection, a possible inverse cascade, and stable polygonal patterns. However, the computational cost of these simulations impedes to freely vary the model parameters, and they include lots of different effects, which renders the analysis difficult. The work of Cai et al. (2021) also lacks a description of the transient which lead to the formation of the large scale vortices and their equilibration. Here, we aim at using an idealized experimental setup to study the conditions under which cyclones can self-organize into polygonal patterns, and identify the physical mechanisms at play. Our approach is similar than that employed by Li et al. (2020), except that it is experimental, since we artificially generate cyclones in a fluid with a polar β-effect, and follow their trajectory towards the pole and their interactions. Note that the experiments that we performed up-to-date are preliminary. The goal was to build a setup and perform a first exploration to identify, in a limited time, directions to follow for future work. The results that we present are mostly qualitative, and constitute an avenue for more thorough future work.

The chapter is organized as follows. In §6.2, we list the non-dimensional parameters relevant to describe the dynamics of cyclones in a two-layer, reduced gravity configuration. We provide estimates for these parameters in the Jovian case and in our experimental setup. In §6.3, we present results of experiments in one-layer and two-layer configurations where one, two, three or six cyclones were generated simultaneously. In §6.4.1, we discuss these preliminary experimental observations in light of previous results and experiments on vortices pairing and drift. In §6.4.2, we list ideas of experimental modifications and directions that could be followed in future work.

6.2. Experimental set-up

6.2.1. Non-dimensional parameters

In the experiments that we will present, the cyclones are generated in a shallow upper layer of fresh water on top of a deep layer of salt water. The bottom layer is analogous to the deep, convective region in which the jets extend, whereas the top layer is the layer supporting the vortices, assumed to be shallow. Experimentally, this situation is an advantage since floating cyclones, which do not extend down to the bottom of the tank, are much more long-lived

than their barotropic equivalent. In our setup, the bottom layer is much larger than the upper one (Fig.6.3). We chose to treat it as a quiescent layer in the following, and consider only the thickness h of the top layer as a relevant physical parameter of the problem. This configuration is analogous the the so-called $1-\frac{1}{2}$ shallow-water model, also called the reduced gravity shallow water system, where an active layer lies over a deep, denser, quiescent layer (see section 3.2 in Vallis 2017). The other relevant parameters of the background flow are the gravitational acceleration, g, the density of the top and bottom layers, ρ_t and ρ_b respectively, the rotation rate or the associated Coriolis parameter, $f = 2\Omega$, and the gradient of the background rotation, β. An important scale that quantifies stratification is the internal Rossby radius of deformation, R_d, which corresponds to the length scale at which rotational effects become as important as buoyancy effects:

$$R_d = \frac{(g'h)^{1/2}}{f}, \tag{6.1}$$

where g' is the reduced gravity $g' = g\dfrac{\rho_b - \rho_t}{\rho_b}$.

Contrary to the *Jacuzzi* experiment of chapters 3-5, it is not the whole layer of fluid that is relevant for the β-effect since the vortex is confined in the upper layer. For a thin, shallow layer of fluid, the β-effect arises from the fact that the normal to the free-surface is not aligned with the rotation axis. If we assume that the motion are quasi-2D and constrained in a plane perpendicular to the local normal to the surface, then only the component of the rotation vector aligned with the normal enters in the Coriolis force (see the schematic in Fig.6.3). Just like in the *Jacuzzi* experiments, the free surface is paraboloidal with a height

$$h_{\text{surf}}(\rho) = h_0 - \frac{\Omega^2}{2g}\left(\frac{R^2}{2} - \rho^2\right). \tag{6.2}$$

The angle between the normal and the rotation axis, θ, varies with radius following $\theta(\rho) = \mathrm{d}h_{\text{surf}}/\mathrm{d}\rho = (\Omega^2/g)\rho$. A β-effect thus arises due to the variation of the normal projection of the rotation vector, $\Omega_n(\theta)$:

$$\beta_{\text{shallow}} = 2\frac{\mathrm{d}\Omega_n}{\mathrm{d}\rho} = 2\Omega\frac{\mathrm{d}\cos(\theta(\rho))}{\mathrm{d}\rho} = -\frac{2\Omega^3}{g}\sin\left(\frac{\Omega^2\rho}{g}\right). \tag{6.3}$$

The corresponding curve is plotted in Fig.6.3. For completeness and comparison, we performed an experiment with a single layer of fluid where vortices extend through the whole fluid column. The motions are then quasi-2D in a horizontal plane, and we recover the topographic "deep" β-effect related to the variation of the total fluid height with radius:

$$\beta_{\text{deep}} = -\frac{2\Omega}{h_{\text{surf}}}\frac{\mathrm{d}h_{\text{surf}}}{\mathrm{d}\rho} = -\frac{2\Omega^3}{g}\frac{\rho}{h_{\text{surf}}(\rho)}. \tag{6.4}$$

The corresponding curve is plotted in Fig.6.3. The shallow and deep β-effects vary qualitatively similarly: they are maximum at the border of the tank and tend towards zero at the centre of the tank. This configuration is analogous to the poles of the planets where both the topographic (deep) and Coriolis (shallow) β-effects vanish (see chapter 1, section 1.2.4).

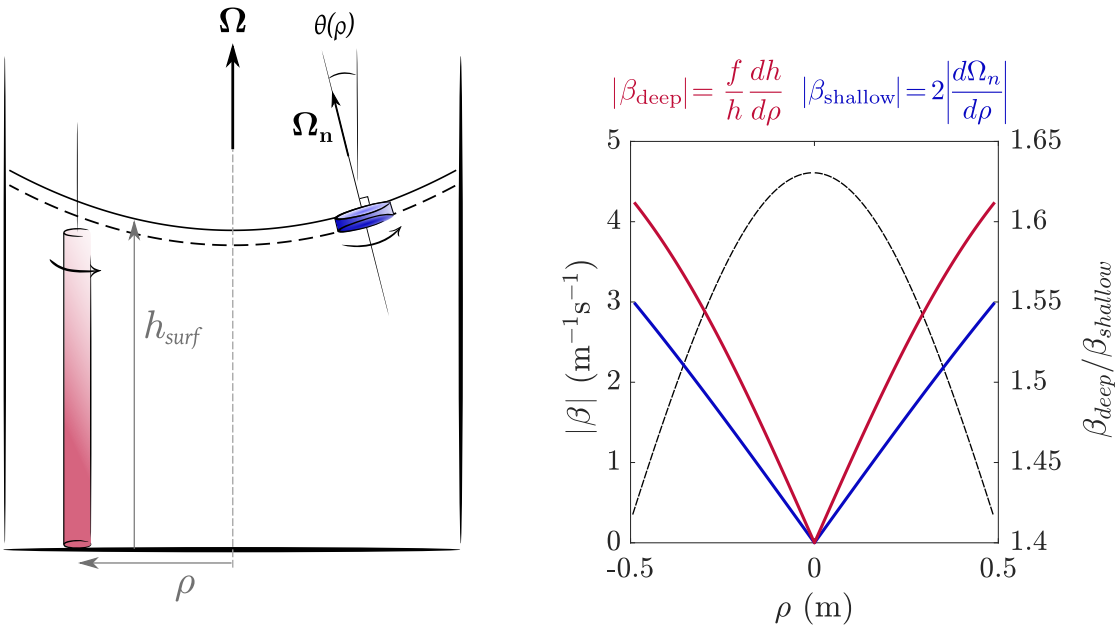

Figure 6.3. – Illustration of the differences between the shallow and deep β-effects. Left: Sketch of the two types of vortices. $\mathbf{\Omega}$ is the global rotation vector, $\mathbf{\Omega_n}$ is its component normal to the free-surface. $f = 2\Omega$ is the Coriolis parameter. h_{surf} is the height of the free-surface. ρ is the distance to the spin axis. Right: β-effect as a function of radius felt by a deep or a shallow vortex (left axis). Dashed line: ratio between the deep and shallow β (right axis).

In addition to the background physical parameters $(f, h, g, \rho_t, \rho_b, \beta)$, the generated vortices introduce two supplementary parameters: their maximal tangential velocity, V and their radius R_v. With 8 parameters and 3 dimensions, we can describe our experimental regime with 5 independent non-dimensional parameters:

1. The relative density difference between the two layers: $\Delta\tilde{\rho} = \dfrac{\rho_b - \rho_t}{\rho_b}$.
2. The Burger number of the vortex, which compares the Rossby radius of deformation (equation (6.1)) to the vortex radius:

$$Bu = \left(\frac{R_d}{R_v}\right)^2 = \frac{g\Delta\tilde{\rho}h}{f^2 R_v^2}.$$

   When $Bu \gg 1$, the vortex is much smaller than the deformation radius, and is inefficient in deflecting the interface between the two layers; gravitational effects are negligible. When $Bu \lesssim 1$, buoyancy effects become important for the vortex dynamics.
3. The Rossby number of the vortex, which compares the vorticity of the vortex to the background vorticity due to rotation:

$$Ro = \frac{V}{fR_v}.$$

   When $Ro \ll 1$, rotation is dominant and the vortex is in geostrophic balance at zero-th order.
4. The vortex aspect ratio R_v/h, which should be $\gtrsim 1$ for the shallow hypothesis to hold.
5. A non-dimensional β-effect, which compares the background gradient of potential vorticity to the dynamical gradient of PV due to the vortex flow:

$$\hat{\beta} = \frac{\beta R_v^2}{V}.$$

According to Li et al. (2020), a last non-dimensional parameter should be introduced to quantify the shielding of the vortices, i.e. how rapidly the tangential velocity of the vortex decreases from its centre. In other words, this parameter should quantify the strength of the anticyclonic vorticity ring that surrounds the cyclonic vortices. In the literature, non-isolated vortices are close to the Rankine model, in which the vorticity is constant in the core of the vortex, and velocity decreases as a potential $1/r$ flow outside (van Heijst et al. 2009). The following functional functions give a good description of non-isolated laboratory vortices:

$$v(r) \propto \frac{1}{r}\left[1-\exp\left(-\frac{r^2}{2R_v^2}\right)\right] \tag{6.5}$$

$$\zeta(r) \propto \exp\left(-\frac{r^2}{2R_v^2}\right), \tag{6.6}$$

where r is the distance to the vortex centre, and ζ is the vorticity $\zeta = \partial_r(rv)/r = \partial_r v + v/r$. These vortices have a net circulation because the surface integral of the vorticity is not zero, and are consequently considered as non-isolated. On the contrary, isolated Gaussian vortices have a zero total circulation, and are commonly described by the functions

$$v(r) \propto r\exp\left(-\frac{r^2}{2R_v^2}\right) \tag{6.7}$$

$$\zeta(r) \propto \left(1-\frac{r^2}{2R_v^2}\right)\exp\left(-\frac{r^2}{2R_v^2}\right). \tag{6.8}$$

This time, the vorticity profile is not single-sided, and there is a region of opposite vorticity surrounding the vortex core. To account for different intensity of shielding, Li et al. (2020) proposes to introduce the single parameter b in the velocity profile as

$$v(r) = v_m \frac{r}{r_m}\exp\left[\frac{1}{b}\left(1-\left(\frac{r}{r_m}\right)^b\right)\right] \tag{6.9}$$

where v_m the maximum velocity, reached at $r = r_m$. Vortices with such velocity profile have again a zero net circulation irrespective of b. Velocity and vorticity profiles with different shielding parameters are represented in Fig.6.4. It is clear that for a vortex with a given Rossby number, an increasing b leads to a stronger anticyclonic ring. The case $b = 2$ corresponds to the classical Gaussian profile of an isolated vortex (equation (6.8)).

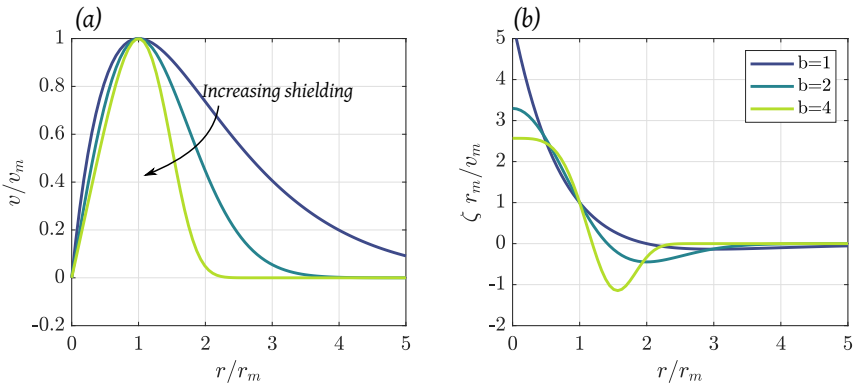

Figure 6.4. – Tangential velocity *(a)* and vorticity *(b)* profiles corresponding to equation (6.9) with different shielding parameters, b.

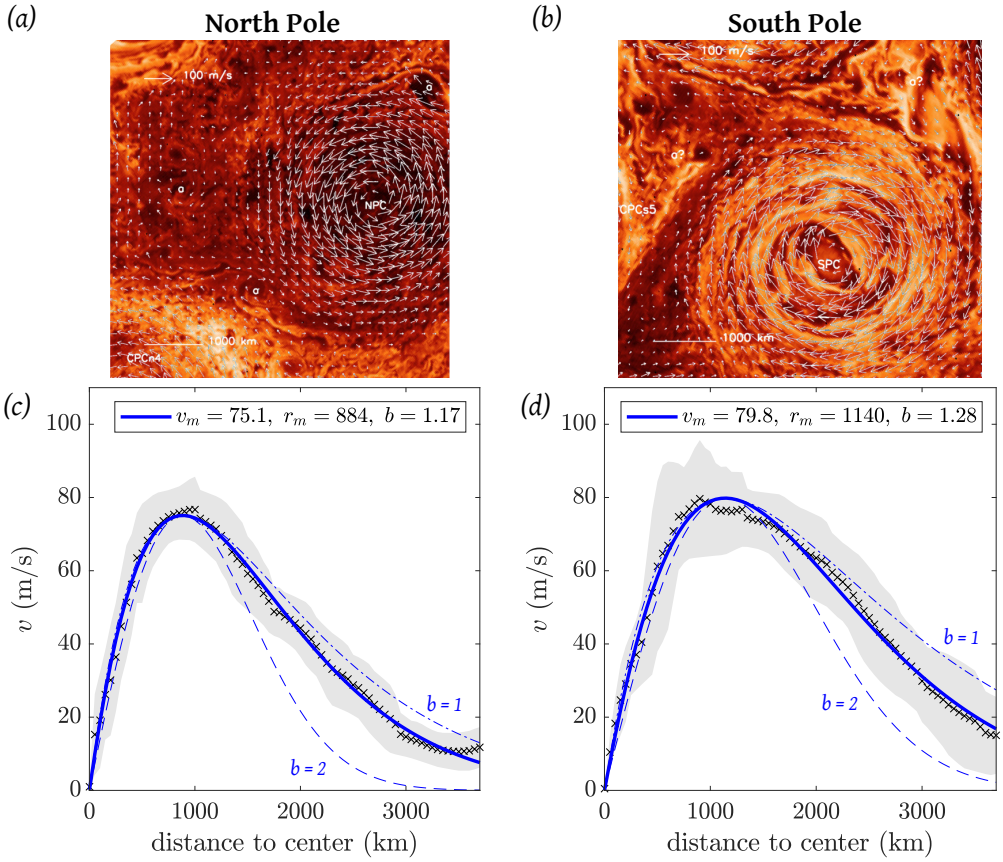

Figure 6.5. – Velocity measured inside Jupiter's polar cyclones. *(a,b)* Velocity field for a single cyclone (adapted from Fig.7 in Grassi et al. (2018)). *(c,d)* Velocity profiles measured for all the polar cyclones. Shaded area: envelope of all the velocity profiles considered together (digitized from Fig.6 in Grassi et al. (2018)). Black crosses: mean value of the measured velocity. Blue line: best fit of the data with equation (6.9) (the deduced values of v_m are in m/s, r_m, in km, and b is non-dimensional). The dashed blue lines show velocity profiles with different shielding parameters for comparison.

Li et al. (2020) provide estimates of the physical parameters of Jovian circumpolar cyclones. We recall the associated non-dimensional parameters below. Grassi et al. (2018) performed the first velocity fields measurements of Jupiter's circumpolar cyclones. In Fig.6.5, we report two examples of velocity fields, as well as the average tangential velocity profiles for the north and south cyclones. A best fit using equation (6.9) gives maximum velocities of v_m =75 and 80 m/s respectively, radii r_m =884 and 1140 km, and shielding parameters b =1.17 and 1.28. Jovian circumpolar cyclones are hence moderately shielded (note that Li et al. (2020) finds $b \sim 1.5$ considering single profiles instead of averages). With $\Omega = 1.76 \times 10^{-4}$ rad s^{-1}, the Rossby number of these circumpolar cyclones is $Ro \in [0.20, 0.24]$. At the latitude of the cyclones, the β-effect is locally $\beta \sim 2\Omega\, \mathrm{d}\cos(\theta)/\mathrm{d}\rho$ where ρ is the distance to the pole, and θ is the colatitude: $\theta \approx \rho/R_J$ (R_J is Jupiter's radius). This gives $\beta \sim 2(\Omega/R_J^2)\rho$. The cyclones are approximately at $\rho \sim 8{,}700$ km from the poles, and Jupiter's polar radius is $R_J \sim 66{,}854$ km, leading to $\beta \sim 6.85 \times 10^{-13}$ m^{-1} s^{-1}. The corresponding non-dimensional β is $\hat{\beta} \in [0.007, 0.011]$. Finally, the most uncertain parameter is the Burger number of the cyclones, which requires an indirect estimate of the stratification through the radius of deformation. Li et al. (2020) proposes a radius of deformation $R_d \in [350, 1300]$ km, leading to $Bu \in [0.09, 2.16]$. These parameters are reported in Table 6.1. For Jupiter, the β-effect is thus very small at the latitude of the circumpolar cyclones, and the vortices have a size comparable to or even larger than the deformation radius, meaning that buoyancy effects are of importance.

	$Bu = (R_d/R_v)^2$	$Ro = V/(fR_v)$	$\hat{\beta} = \beta R_v^2/V$	b
Present. Exp.	0.27	0.03-0.1	0.28	1.5-2.1
Jupiter	0.09-2.16	0.20-0.24	0.007-0.011	1.2-1.5
Li et al. (2020)	1-1000	0.23	0.0074	0.5-4
Flór et al. (2002)	625-6900	0.1-1.2	0.009-0.125	≤ 2
Carnevale et al. (1991)	6-100	~ 1	~ 0.1	1-2
Firing et al. (1976)	∞	0.02-0.15	0.16-1.23	?
Stegner et al. (1998)	0.06-1.56	0.1-0.3	0.2-0.5	isolated

Table 6.1. – Non-dimensional parameters for Jupiter and different studies of cyclones dynamics in a flow with a β-effect. *Bu* is the Burger number of the vortex, *Ro* the Rossby number of the vortex, b the shielding parameter. Details on these parameter estimates are provided in the text.

6.2.2. Description of the setup

The experiments that we performed are preliminary, and consisted in building a setup and performing first tests to identify, in a limited time, directions to follow for future work. For this reason, we focused only on one set of non-dimensional parameters (see Table 6.1), which we describe in the following.

The experimental setup that we built is sketched in Fig.6.6, and pictures are shown in Fig.6.7. We used both the tank and the external structure of the *Jacuzzi* experiment. We recall that the tank is 1m-diameter, and 1.6m-high. The tank is still mounted on the turntable, and for all the experiments that we performed, it rotates at 30 RPM ($f = 2\Omega = 2\pi$ rad s^{-1}). Our choice of rotation rate is a compromise between several effects, discussed in section 6.4.2.

We work with a deep layer of salt water 67 cm-thick and of density $\rho_b = 1030 \pm 6$ kg m^{-3}. It corresponds to adding 25 kg of NaCl in 505 litres of water. The top layer of fresh water is 3 cm-thick, and has a density $\rho_t = 998 \pm 1$ kg m^{-3}. The uncertainties correspond to temperature variations between different experiments, but also to the fact that we do not generate a new bottom layer for each experiment. After the spin-down, the two layers are almost mixed because of centrifugal instabilities. We complete the mixing by pumping the tank's water in closed-circuit, and we add salt to reach the same salinity as before mixing. We finally remove 3 cm of water to go back to a 67 cm height. A new upper layer of fresh water is then added for each experiment. To generate the upper layer, we use a siphon and add a floating foam between the exit of the siphon and the free surface to avoid mixing at the forming interface. Typically, we make up the upper layer in 3 hours.

Before generating the cyclones, the two-layer system needs to be brought to solid body rotation. When spinning up a two-layer system, the bottom layer spins-out faster because of the frictional coupling with the bottom solid surface, whereas it is the velocity difference with the bottom and upper layers that brings the top layer in solid-body rotation (Pedlosky 1967). The Ekman spin-down timescale taking into account the whole fluid height of H =70 cm is $t_E = H/\sqrt{\nu\Omega} = 395$ s. In the first experiments that we performed, the top layer was opaque due to the addition of Kalliroscope, which allowed us to qualitatively visualize its deformation during the spin-up. The Ekman pumping in the bottom layer seems to advect part of the upper layer downward at the centre of the tank. The upper layer finally relaxes upward once the solid-body rotation is reached. Note that due to the circulation during the spin-up, some mixing probably occurs at the interface between the two layers. The two layers are hence separated by a stratification rather than a sharp density jump. To perform a slow spin-up, we increase the rotation rate by 5 RPM every 5 minutes, leading to a 1 hour process to reach 30 RPM. We then wait another 1h15 before starting an experiment to make sure that the two layers are both in solid body rotation. The total duration of a spin-up is then of 20 t_E.

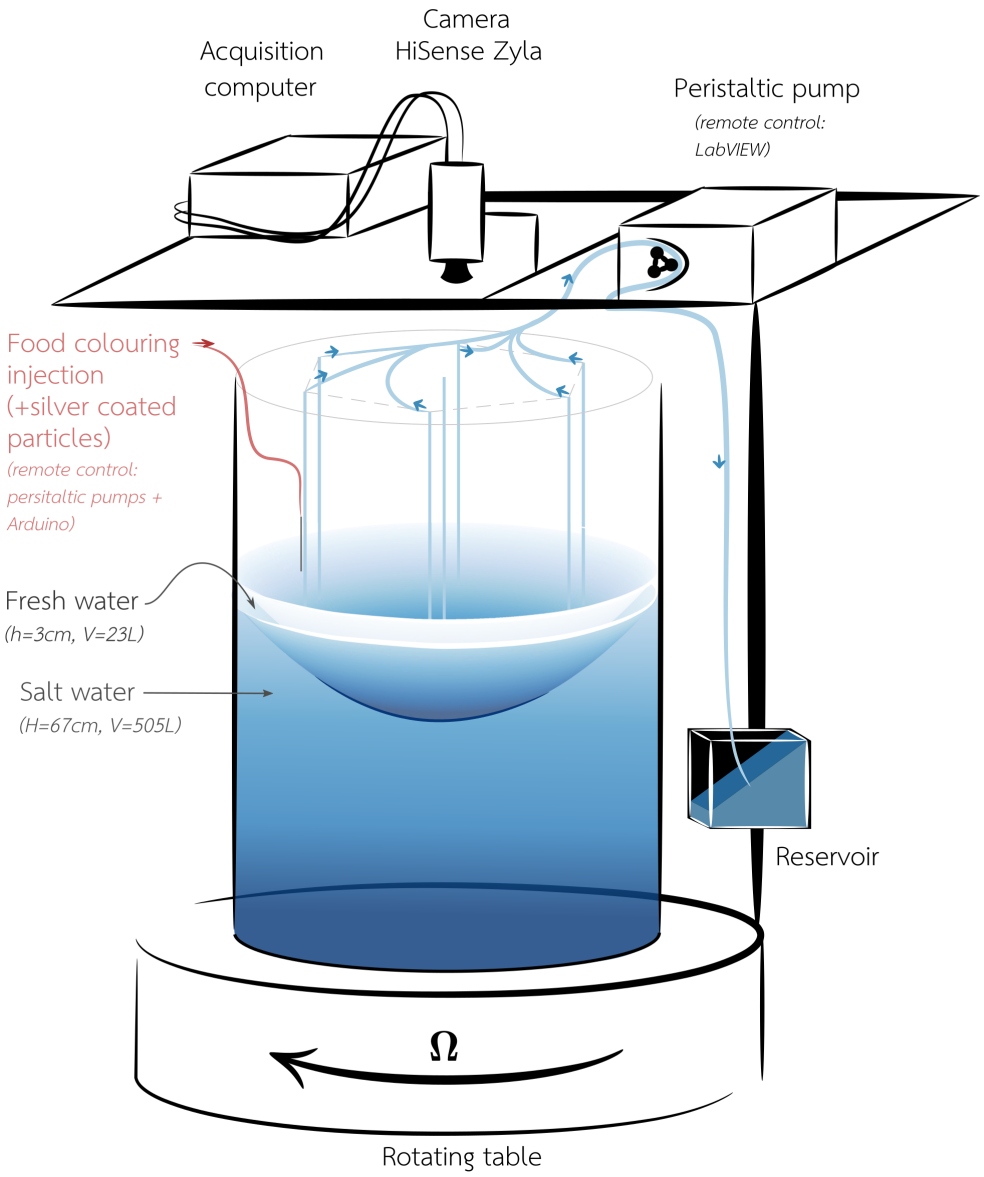

Figure 6.6. – Sketch of the experimental setup. The tank is 1m-diameter and 1.6m-high. Up to six cyclones can be generated simultaneously in the upper layer by sucking water from it using a peristaltic pump. Food colouring is dropped in the core of the cyclones at the end of their formation for visualisation and tracking of their position. Silver coated PIV particles can be added to compute streamlines (see Fig.6.17) and velocity fields (Fig.6.8). Additional details are provided in the text.

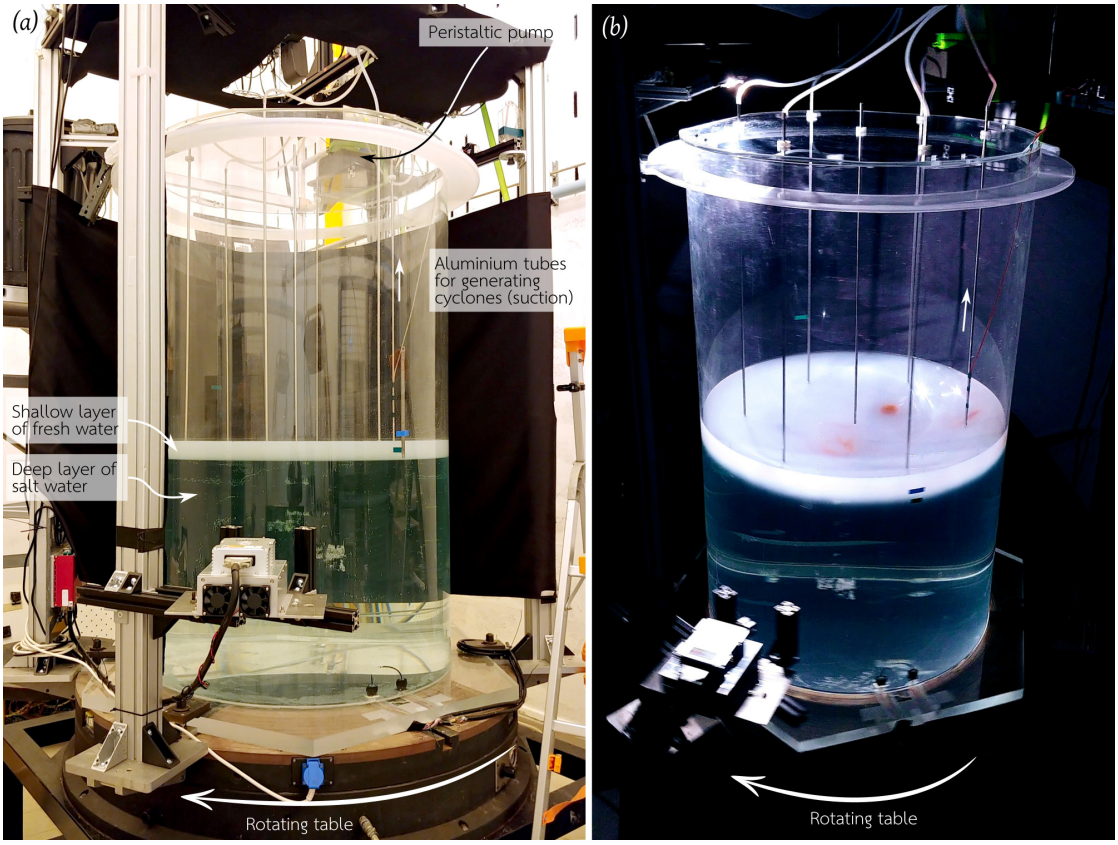

Figure 6.7. – Pictures of the experimental setup. *(a)* At rest. In this picture, the top layer of fresh water is opaque because it contains Kalliroscope. *(b)* Picture after spin-up of the two-layers system at 30 RPM. The slight deformation of the free-surface is visible. At 30 RPM, the altitude difference between the highest and lowest point of the free surface is of 12 cm. The red spot is a cyclone during its drift.

To generate cyclones in the top layer, we use a system to pump water through aluminium tubes and release it in a side reservoir (see Fig.6.6). Each aluminium tube is 1m-long, has an inner diameter of 7 mm, and is held fixed by going through the top plexiglas lid which covers the tank. A small piece fixing each tube on the lid allows them to slide vertically, such that their vertical position can be adjusted. With the present setup, we can generate 6 vortices simultaneously, plus a central one. The six tubes are arranged on a hexagonal pattern, at a distance $\rho_0 = 34.6 \pm 0.5$ cm from the centre of the tank. This position was chosen because it coincides with the position at which the free-surface height is always the same for any rotation rate (see Fig.B.10). This allows to change the rotation rate without having to vary the vertical position of the tubes. The aluminium tubes are linked to a peristaltic pump (Fischer FH100) with a flow rate up to 45 mL/s. We tested different pumping rates, but we observed that the maximum flow rates formed the stronger vortices and gave the best results. All the experiments presented here are thus performed with the maximum flow rate of the pump. In fact as we will see later, even at this maximum flow rate the Rossby number of our cyclones is very small, and we plan to replace the pump with a more powerful one. This peristaltic pump is controlled remotely using the pump's D-shell connector, a National Instruments card (USB-6001) and LabView, installed on the computer fixed in the rotating frame (see Fig.6.6). Typically, the cyclones were generated by pumping fluid from the upper layer for 30 seconds. Indeed, after 30 s of pumping, the cyclone already begins to drift and detach. Continuing the pumping would lead to the formation of a second cyclone following the first one that has departed from below

the aluminium tube.

To visualize the vortices, we tested several techniques. Particle image velocimetry is not easy because the cyclones are confined in a thin paraboloidal layer, whereas the laser plane is strictly planar. In addition, for these preliminary experiments, we wanted to be able to qualitatively follow the cyclones position through time rather than perform precise quantitative measurements. We first tested the addition of Kalliroscope particles in the top layer. Kalliroscope particles are tiny reflective and anisotropic flakes that align with the flow and thus allow a qualitative visualisation, in particular of shear layers. We made our own Kalliroscope-like fluid following the method of Borrero-Echeverry et al. (2018), i.e. by diluting shaving cream in water. However, we suspect that the use of shaving cream modified the surface tension of the top layer water, and perturbed the vortices evolution, since the cyclones are associated with a deflection of the free surface. The use of Kalliroscope was however useful during our first tests to distinguish the two layers and follow their evolution during the spin-up (see Fig.6.7). For all the results presented here, no Kalliroscope was added to the top layer. Instead, we chose to visualize the vortices using food colouring. This technique is commonly used to visualize vortices evolution, but mostly anticyclones. Indeed, to generate anticyclones, one has to inject fluid, and the colouring can thus be mixed to the injection fluid beforehand. For cyclones, one has to suck fluid. The colouring needs to be added at the end of the cyclone generation, by letting a few drops fall into the cyclone's core: a too strong injection would create an overpressure and thus an anticyclone inside of the cyclone. Finally, in our case, we need a remote control for dropping food colouring because we do not have access to the interior of the tank while it is rotating. We ended up with the following system: we use six small peristaltic pumps (Garosa), i.e. one pump for each tube, plugged in parallel to a power supply. We use a power relay, i.e. a programmable electrical switch, that we control with a micro-controller (Arduino Nano), to remotely turn on and off the six pumps simultaneously. We can choose the time during which we inject food colouring using this system. Note that the colouring is injected through thin capillary tubes which are fixed along the aluminium tubes used for generating the cyclones (see Fig.6.6). The drops fall along the aluminium tube, thus gently impacting the free surface, and do not seem to perturb the cyclone much. Images are acquired from a top-view camera, at a frame-rate of 1 Hz. Finally, for some experiments, we added silver-coated PIV particles to the colouring fluid. These particles are slightly less dense than the top fluid layer, and thus float on the free surface. Using a top light, the reflection on the particles allows to follow their displacement at the surface. Since the motions are extremely slow, this allowed us to perform PIV measurements for selected experiments and estimate velocity profiles in the core of the cyclones.

Fig.6.8 shows two examples of velocity fields and profiles measured by surface PIV measurements for an experiment where three cyclones were generated. We estimate that the generated cyclones have typical radii $r_m \sim 3$ cm and maximum tangential velocities of $V \sim 5$ mm. In terms of non-dimensional parameters, we thus have $Ro \sim 0.027$, $Bu \sim 0.27$. Note that for experiments with a single cyclone, we estimate that the initial Rossby number is initially larger (~ 0.1) because all the power of the pump is dedicated to forming only one cyclone. The experimental shallow β-effect has a mean value of $\beta \sim 1.57$ m^{-1} s^{-1} (see Fig.6.3), leading to $\hat{\beta} = 0.28$. Finally, velocity profiles fit show that our sink vortices are shielded, with $1.5 \lesssim b \lesssim 2.1$, i.e. they are close to Gaussian isolated vortices. This point is important to mention given that both Carnevale et al. (1991) and Flór et al. (2002) report that their vortices formed by suction are not isolated. The difference may come from the different diameter of the pipe used for suction. The experimental non-dimensional parameters are reported in Table 6.1. Compared to Jupiter's parameters, our cyclones are weaker, and the β-effect is larger, even if we are in the relevant regime where the vortex induced PV gradient is larger than the ambient one. We also want to underline that with

this setup, we can explore small Bu cases, which may be relevant for Jupiter and which have not been explored experimentally, except by Stegner et al. (1998), for anticyclones only.

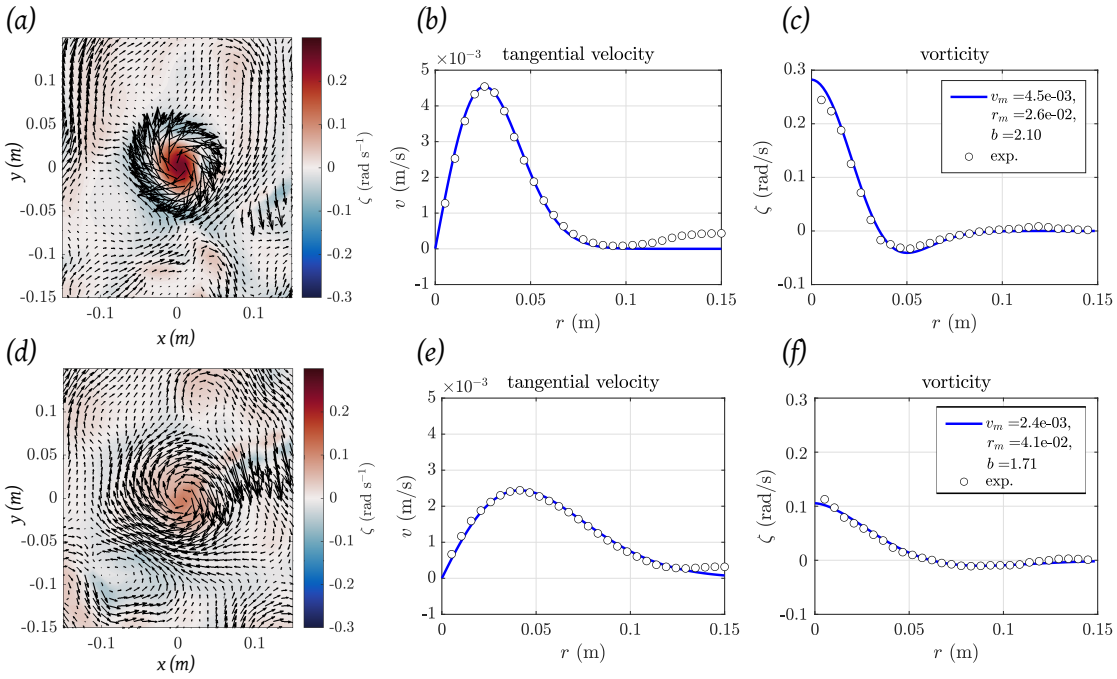

Figure 6.8. – Examples of velocity fields and profiles for the floating cyclones generated by suction. The velocity and vorticity profiles are azimuthally averaged. *(a-c)* Velocity field, tangential velocity profile, and vorticity profile at time $t = 700$ s $= 1.8\ t_E$. Sudden large velocity vectors are spurious ones due to reflections on the free surface. *(d-f)* Same quantities for the same experiment at time $t = 2050$ s $= 5.2\ t_E$. The blue lines, and associated parameters, correspond to the best fit of the data with equation (6.9).

6.3. Results

6.3.1. Single cyclone drift towards the pole

6.3.1.1. Qualitative evolution

Fig.6.8 shows that initially, our vortices are close to Gaussian isolated vortices ($b \approx 2$), and they seem to remain shielded over the whole duration of the experiment. An experiment typically lasts 2,000 s, i.e. 1,000 t_R where t_R is a rotation period or equivalently 5 t_E, where t_E is the Ekman spin-down timescale. The cyclones can merge or split during their evolution, particularly when several vortices interact with each other, but overall, they are extremely long-lived and we generally stop the recording even before that they are completely dissipated.

Fig.6.9 shows the qualitative evolution of a single dyed cyclone. For all our 25 experiments, the cyclones drift northward (towards the centre of the tank, which represents the pole) and westward (anticlockwise). The trajectory followed during the drift is very robust and has been observed for all of our experiments. Note that on the contrary, if an anticyclone is generated, it drifts towards the south, hits the border of the tank, and remains along the border until it dissipates (not shown).

These qualitative observations are consistent with the β-drift of vortices on the beta plane. It has been shown theoretically, numerically, and experimentally that cyclones drift in the north-west direction (e.g. McWilliams et al. 1979; Sutyrin 1988; Carnevale et al. 1991; Reznik 1992; Stegner et al. 1998; Flór et al. 2002). This mechanism is also invoked to explain the

trajectories of tropical cyclones in Earth's atmosphere (Bin et al. 1999). The β-drift is explained by a non-linear advection mechanism due to the development of a secondary circulation called a beta-gyre (Sutyrin et al. 1994). Basically, a cyclone advects fluid particles towards the south to its west side, and towards the north to its east side, leading to the formation of a secondary cyclone to its west and anticyclone to its east, owing to potential vorticity conservation. This secondary circulation results in a global northward flow at the primary vortex location, but with an east-west asymmetry, pushing the vortex globally towards the north-west (see for instance Fig.2 in Bin et al. 1999). On the contrary, anticyclones are expected to drift in the south-west direction.

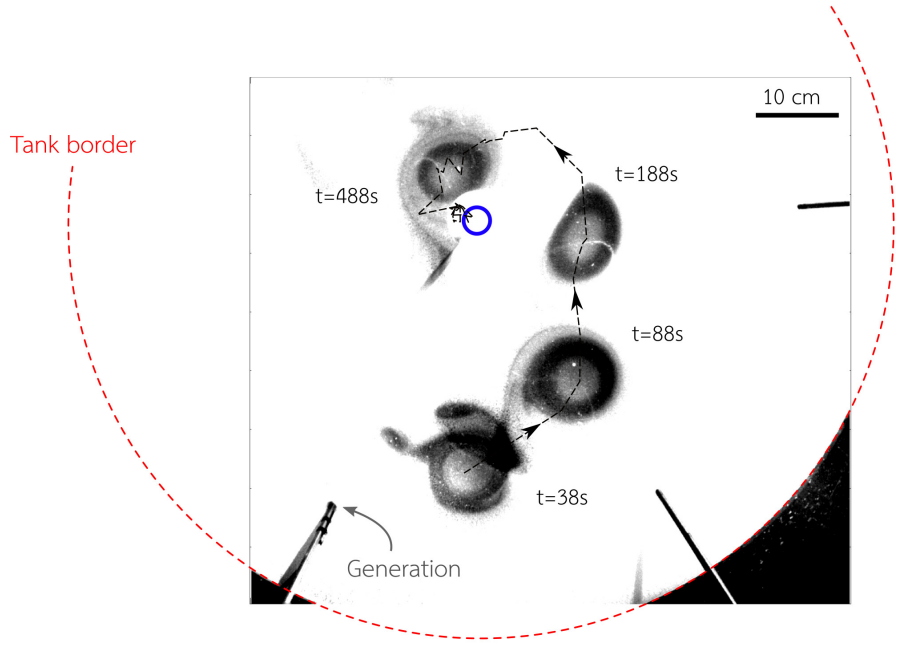

Figure 6.9. – Superposition of visualisations of a single cyclone during its trajectory towards the centre of the tank. The vortex is dyed with food colouring by letting drops fall at the end of its generation. The pole is the centre of the tank (blue circle), and the west direction is anti-clockwise.

6.3.1.2. Comparison between barotropic and baroclinic vortices evolution

All of the experiments presented in this chapter are performed in the two-layer configuration, except one series of experiments performed with a single layer of salt water, 70-cm thick. As underlined before, in this single layer, the cyclones are not floating ones but are barotropic and extend through the whole fluid layer as Taylor columns. They hence feel a different β-effect, but also an increased dissipation due to Ekman friction at the bottom of the tank. This series of barotropic experiments serves as a reference to motivate the use of the two-layer system, and to compare the β-drift of barotropic and floating vortices.

Fig.6.10 shows the trajectories of barotropic (deep) cyclones on the left, and shallow ones on the right. To determine the vortex position we combine a manual pointing of the vortex centre with a detection of the circular shape best fitting the vortex using Matlab *imfindcircles* function. Qualitatively, the trajectories of deep and shallow cyclones are similar. This is expected given the similarity of the β-effect profiles in the deep and shallow cases (see Fig.6.3). Furthermore, this indicates that the drift is not controlled by dissipative mechanisms, which are fairly different in the two cases. This is in agreement with the QG simulations of Carnevale et al. (1991) which show no difference between viscous and inviscid trajectories for barotropic vortices. The major difference between the barotropic and shallow setups rather resides in the

fact that the deep cyclones reach the centre of the tank much more rapidly, but also dissipates much faster. Fig.6.10*(c-f)* shows the evolution of the distance to the centre as well as the translational velocity of the cyclones. We recall that the Ekman spin-down timescale taking into account the whole fluid height is $t_E = 395$ s $= 197\ t_R$. Lateral diffusion of momentum occurs on the contrary on a timescale $t_\nu = R_v^2/\nu = 900$ s $= 450\ t_R$. Deep barotropic cyclones reach the pole in about 3 minutes ($90 t_R = 0.46 t_E$), and have a translational speed about 1.5 times faster than shallow vortices. Shallow vortices initially drift quite fast too, but much slower once they have reached a distance of ~ 20 cm from the pole. Due to this very slow drift, they reach the pole in about 17 minutes ($500 t_R = 2.5 t_E$).

The difference in the translational speed of the deep and shallow vortices constitutes a good opportunity to test the hypotheses of a deep, topographic β-effect in the barotropic case, and a shallow β-effect for the two-layer configuration. If the translational speed due to β-drift is proportional to β, then the difference in magnitude between the shallow and deep β let us indeed expect a factor ~ 1.5 between the two drifts (see Fig.6.3, dashed curve). However, we expect the drift speed to also depend on the size and strength of the cyclones, as well as the radius of deformation (equation (6.1)), due to combined effects of Rossby waves and non-linear advection. The phase speed of Rossby waves of length scale R_v scales as

$$c(\rho) = -\beta(\rho)\frac{1}{R_v^{-2} + R_d^{-2}} \tag{6.10}$$

(Vallis 2017). The term involving the deformation radius R_d is only relevant for the two-layer configuration due to buoyancy effects at the interface. A priori, the Rossby waves phase speed depends on the distance ρ to the pole since β decreases. In a similar fashion, we expect the translational speed to decrease with radius. In Fig.6.11, we plot the translational speed U and the phase speed of Rossby waves c as a function of the distance to the pole. In both the barotropic and two-layer cases, the observed decrease of the drift speed is qualitatively consistent with the decrease of β. Many reasons may explain why we do not perfectly recover the β trend: the initial adjustment of the vortex, the zonal flow induced when we generate the cyclones, the decrease of the vortex strength, finite size effects, etc. When comparing the drift speed with the Rossby waves phase speed, we find that the drift speed is systematically higher, with $U \approx 2.5c = 2.5R_v^2\beta$ for the barotropic case. This is consistent with the experiments of Flór et al. (2002), who found $U \approx 3R_v^2\beta$ for $\hat{\beta} > 0.1$ (see their Fig.10*(a)*). Note that here, we assumed that the Rossby waves excited by the vortex have a wavelength equal to the vortex radius corresponding to the maximum velocity. It is possible that their wavelength is larger and based, for instance, on the vorticity shield radius, which would subsequently reduce the 2.5 factor. In the shallow case, the deformation radius is finite. Based on initial conditions (equation 6.1), we have $R_d = 1.6$ cm. Since our cyclones have a scale similar than the deformation radius, their trajectory should be mainly westward and tend towards the maximum phase speed of the baroclinic Rossby waves, $c_m = R_d^2\beta$ (Sutyrin 1988). We observe $U \approx 15c_m$. Such high scaling is also observed by Flór et al. (2002) for barotropic vortices, but they work with a smaller $\hat{\beta}$. Note that the radius of deformation might be larger than the value we used, due to mixing and thickening of the density interface during spin-up, leading to larger phase speeds.

A precise experimental study of β-drift of baroclinic vortices would be interesting to perform, and is lacking in the literature. However, it is beyond the scope of the present chapter. It would namely require cases where not only the trajectory is known, but also the evolution of the velocity field inside of the vortex during its evolution. Theoretical predictive models for baroclinic vortices indeed require the knowledge of $v(r)$ along the trajectory (e.g. Sutyrin et al. 1997; Reznik et al. 2007). Here, the goal is rather to perform proof-of-concept experiments to investigate if β-drift of multiple vortices in a polar laboratory analogue can lead to interesting

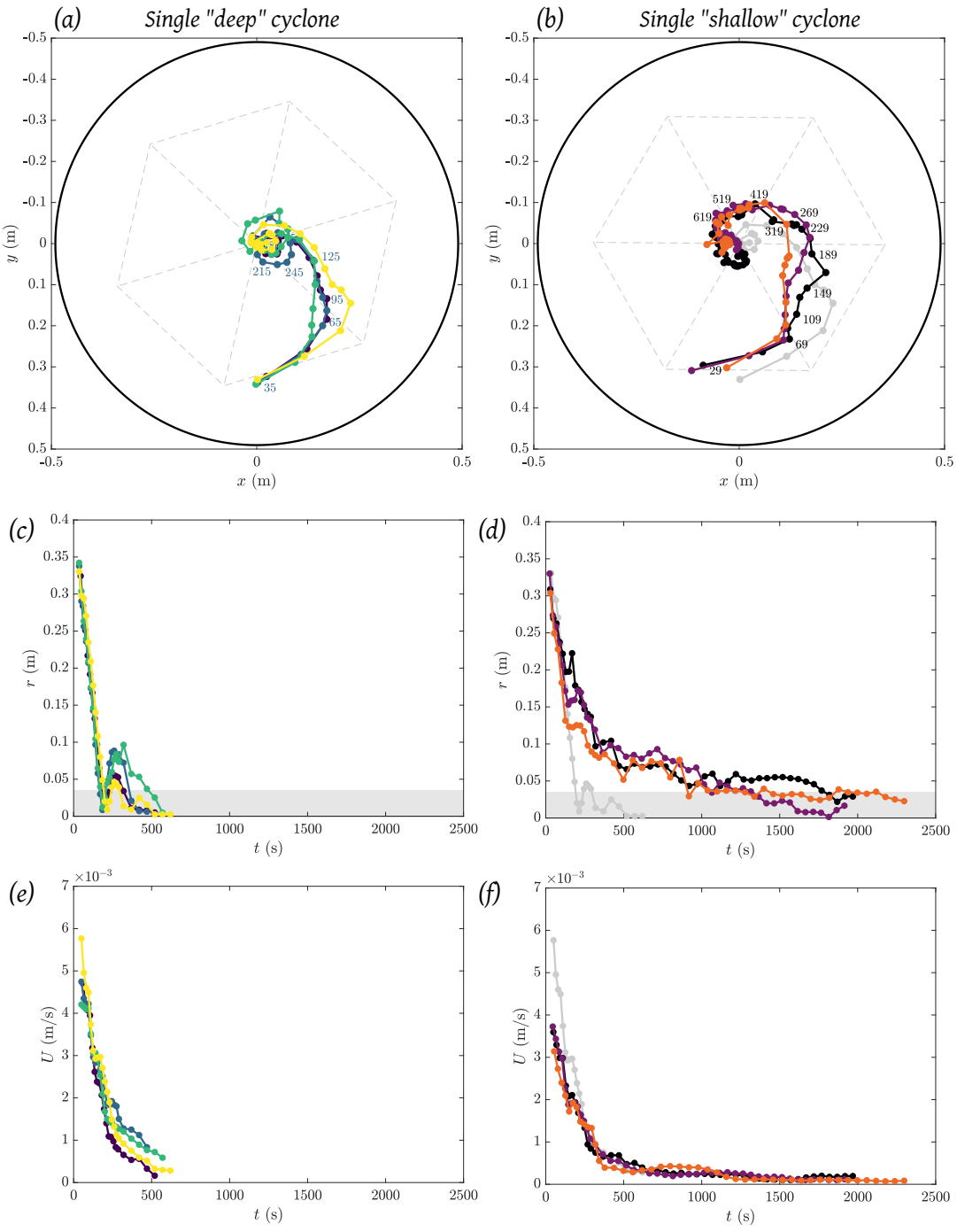

Figure 6.10. – Left: evolution of a single cyclone formed in the deep configuration. Right: shallow configuration. The grey dots and curves are from one deep experiment, for comparison. *(a,b)* Trajectories for three realisations in each case. The numbers correspond to the time, in seconds. *(c,d)* Distance from the pole. The shaded area is the typical radius of the vortex: the vortex begins to overlap the centre of the tank when its position enters the shaded area. *(e,f)* Translational speed.

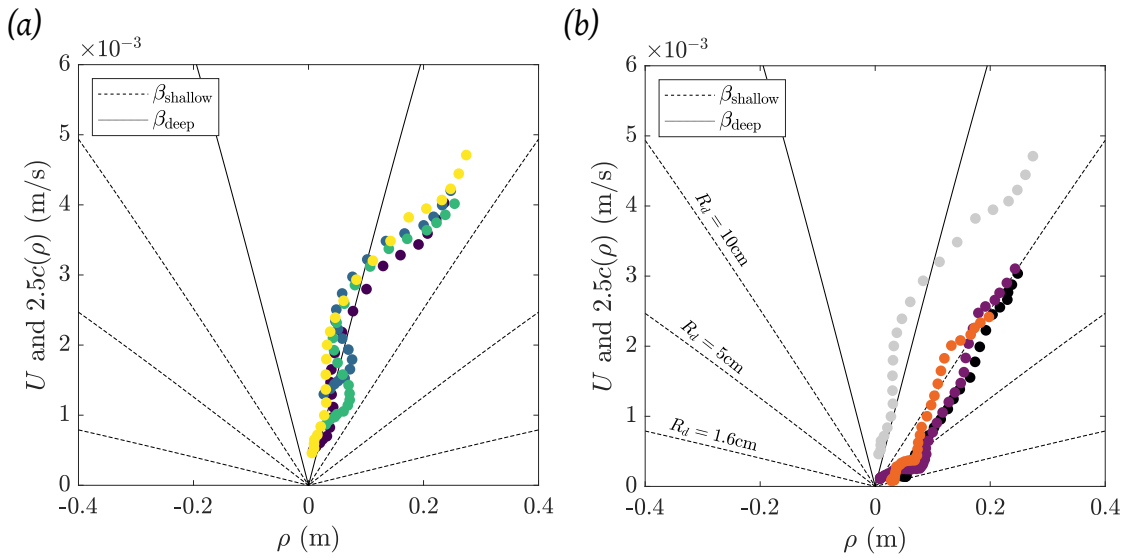

Figure 6.11. – Translational speed of the cyclones compared to the Rossby waves phase speed as a function of their distance to the centre of the tank (the pole). *(a)* Single deep cyclones. The dots correspond to the three realisations represented in Fig.6.10*(a)*. The continuous black line is 2.5 times the Rossby waves phase speed, c, at the scale of the cyclones. In this barotropic case, $c(\rho) = \beta_{\text{deep}}(\rho)R_v^2$. *(b)* Single shallow cyclones. In this baroclinic case, the Rossby waves phase speed is different because of a different β-effect, but also because the radius of deformation R_d becomes non-negligible due to stratification: $c_m(\rho) = \beta_{\text{shallow}}(\rho)R_d^2$. The dashed lines are 2.5 times the phase speed for different values of R_d. The grey dots are from one barotropic experiment, for comparison.

interactions.

6.3.2. Interaction of multiple cyclones generated simultaneously

Given the robustness of the observed trajectories when a single cyclone is formed, and its long-lived behaviour, we chose to explore the effect of generating multiple vortices simultaneously. All the other parameters are equal to the previous ones, and we work with the two-layer system exclusively. We have tested the following initial configurations:

— 2 opposite cyclones;

— 2 adjacent cyclones;

— 3 cyclones at the vertex of an equilateral triangle;

— 6 cyclones at the vertex of an hexagon.

6.3.2.1. Two cyclones

Fig.6.12 shows the cyclones trajectories in three experiments where two cyclones are generated opposite to each other, as well as their radial position and translational speed as a function of time. The two opposite cyclones spiral around each other, each following the same trajectory towards the north-west. One of the two cyclones ends at the pole, and interestingly, the second one does not merge with it at the centre, but instead remains at a radial distance between 15 and 20 cm. Fig.6.13 shows the same quantities for two experiments where the cyclones are generated side by side, i.e. at two adjacent vertex of the hexagon. Contrary to initially opposite cyclones, the two cyclones generated side-by-side always end up merging at the pole.

These experiments seem to indicate that there is a competition between the drift, that tends to attract all the cyclones towards the pole, and a repulsive effect between vortices. In the case where the cyclones are adjacent, they may get too close to each other too soon, i.e. before

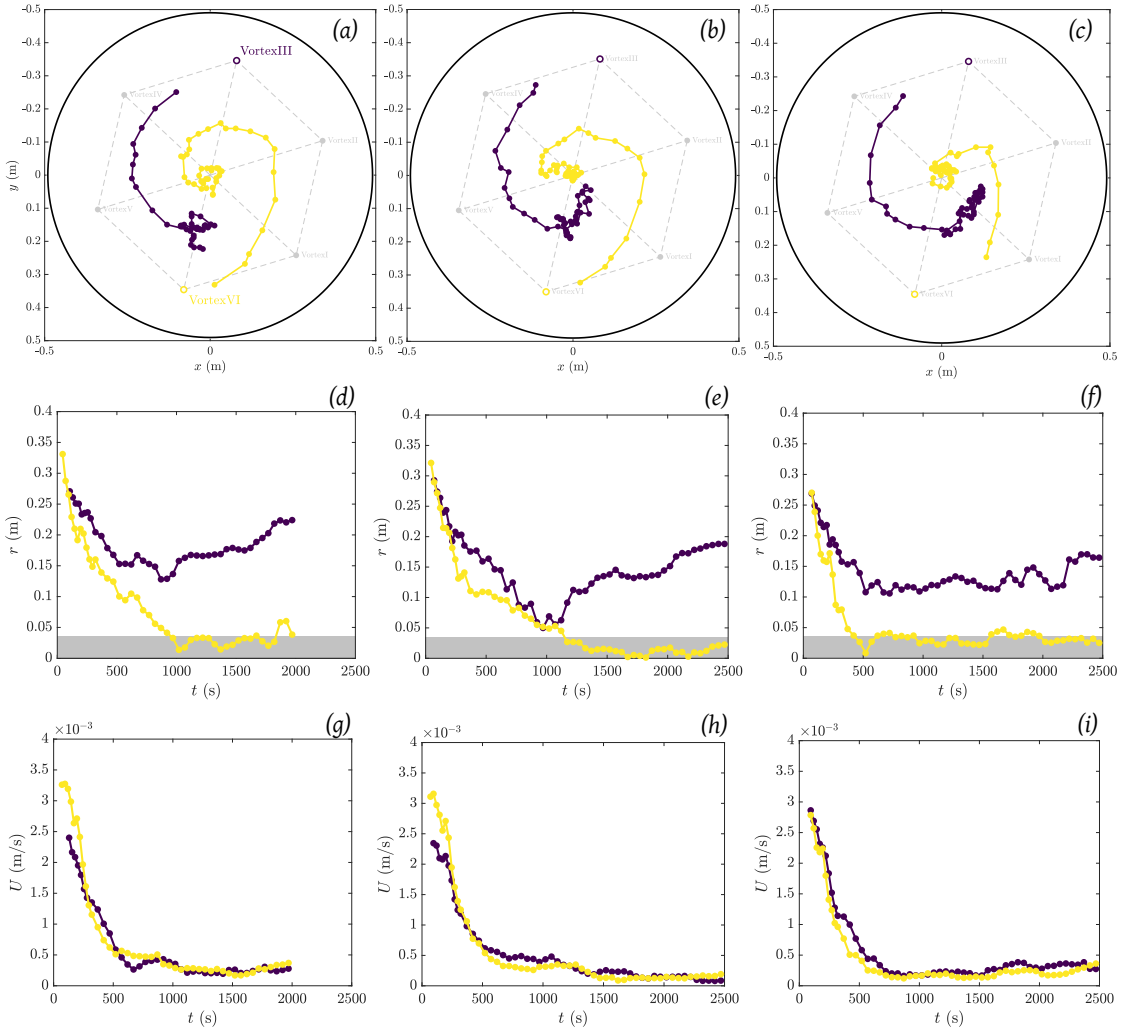

Figure 6.12. – Experimental results for two opposite cyclones (3 realisations). *(a-c)* Trajectories. *(d-f)* Distance to the pole. *(g-i)* Translational speed.

that the repelling effect becomes significant. For instance, we verified that in the case of two opposite cyclones, a separation distance of 15 cm between the two vortices is reached after 700s, i.e. when one of the cyclones is already at approximately 5 cm from the pole. For two adjacent cyclones, the moment when they are at 15 cm from each other is reached sooner, at time t=370s, i.e. when they are both at 15 cm from the pole. The natural assumption is that the repelling effect becomes greater compared to the β-drift when the cyclones get closer to the pole, where β-vanishes. In the experiment with two opposite cyclones, the repelling effect is hence more efficient.

We note that when cyclones do not merge, they remain at a distance between 15 to 22 cm from each other. From Fig.6.8 and other measurements (not shown), we know that the radii of the cyclones is of about 3-4 cm during the second half of our experiments. The minimal distance between two non-merging cyclones thus falls between 3 and 3.75 R_v. This critical distance is reminiscent of the critical initial distance below which barotropic (Leweke et al. 2016) and baroclinic (Griffiths et al. 1987; Estrada et al. 2020) vortices coalesce. This point is discussed further in §6.4.1.

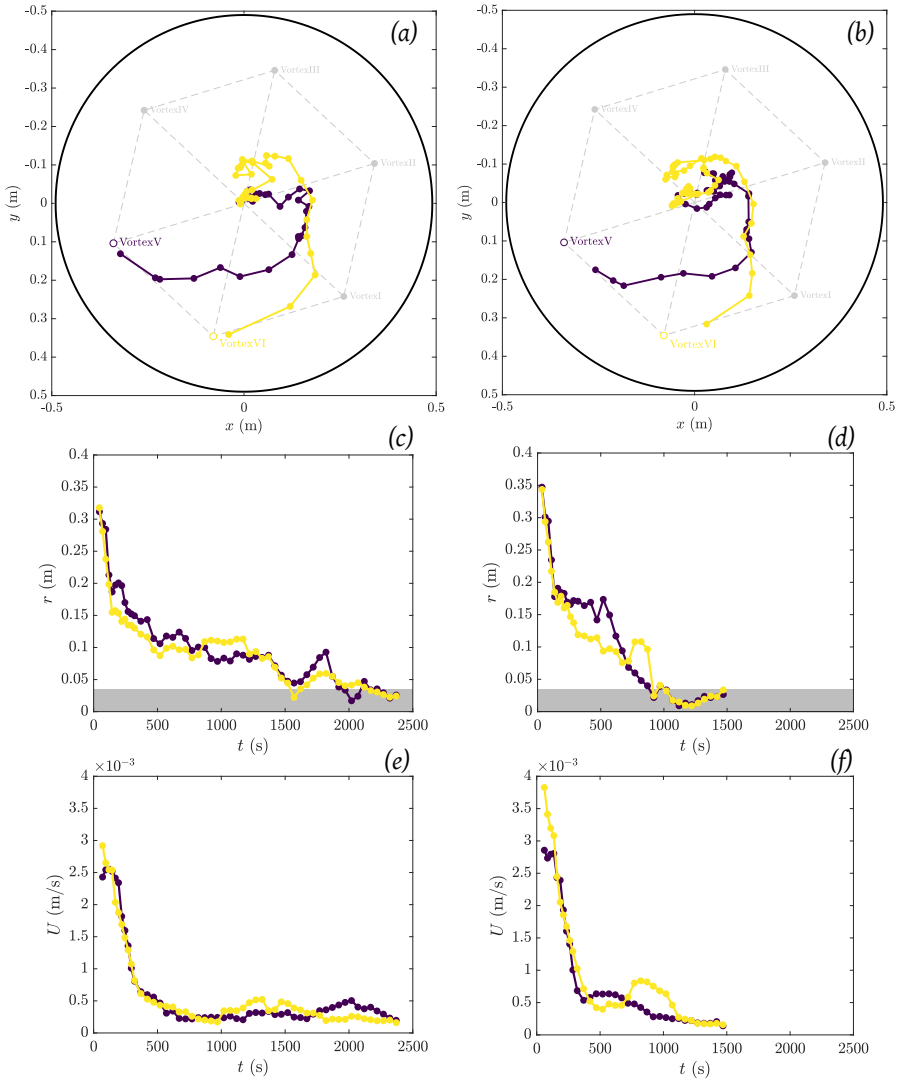

Figure 6.13. – Experimental results for two adjacent cyclones (2 realisations). *(a,b)* Trajectories. *(c,d)* Distance to the pole. *(e,f)* Translation speed.

6.3.2.2. *Three cyclones*

Fig.6.14 shows trajectories in three experiments with three cyclones and the corresponding evolution of the distance to the pole and translational speed. We observe a combination of the aforementioned dynamics: two cyclones end up merging, whereas the third one remains at distance from them. Note that interestingly, there is not necessarily always a cyclone ending up at the pole. This is the case for Fig.6.14*(a,b)*, but in panel *(c)*, the two remaining cyclones are located on either side of the pole. Note that we retrieve in these experiments the critical distance of 15 to 20cm at which non-merging vortices remain from each other.

6.3.2.3. *Six cyclones*

Fig.6.15 show trajectories during three experiments where six cyclones were generated simultaneously. In this case, the dynamics gets more complicated because cyclones begin to interact with each other very soon in the experiment. This leads to early coalescences, and also splitting events. In this figure, two curves may thus correspond to the same initial cyclone

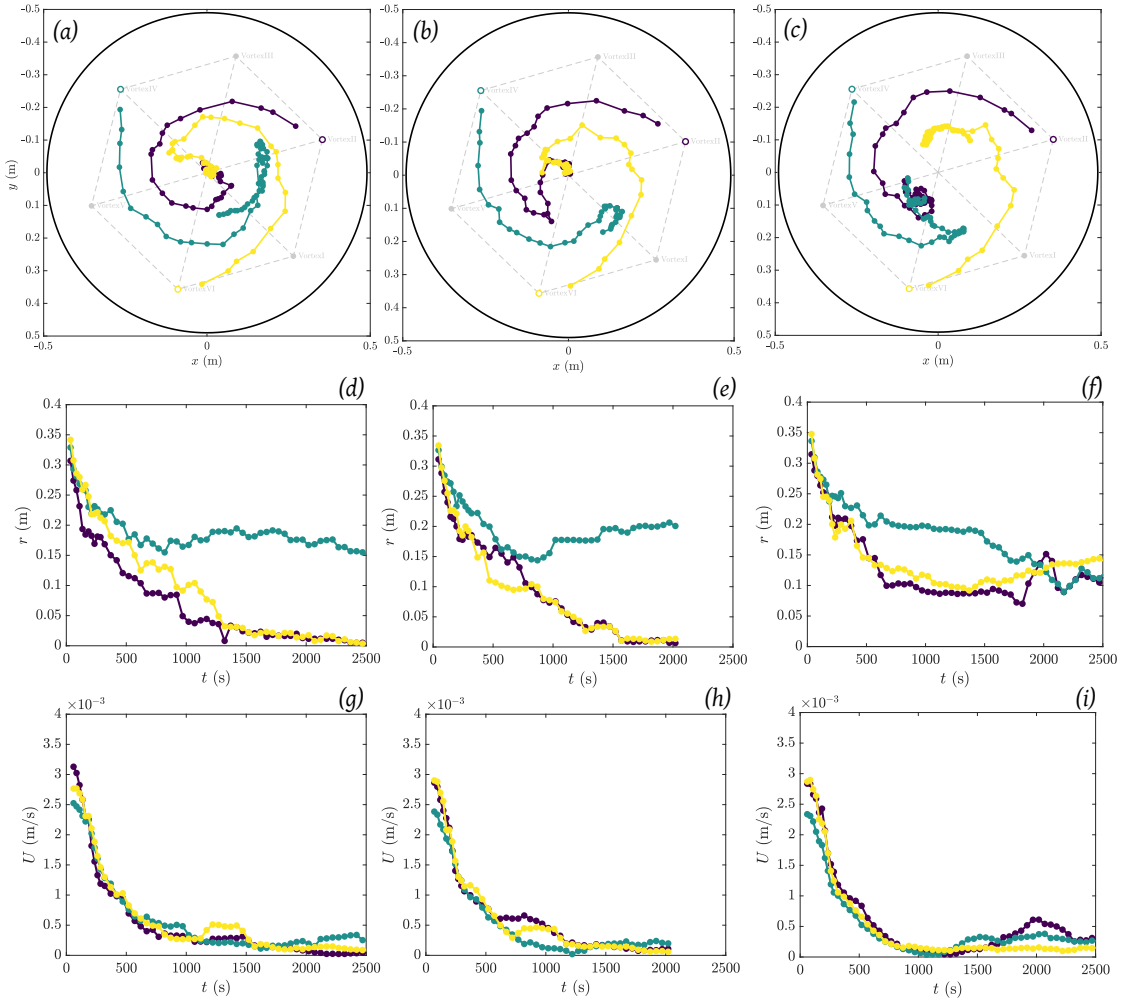

Figure 6.14. – Experimental results when three cyclones are generated simultaneously (3 realisations). *(a-c)* Trajectories. *(d-f)* Distance to the pole. *(g-i)* Translational speed.

which ended up separating into two cyclones. Similarly, two curves are superposed if the corresponding cyclones merged. This is why there are 8 curves in Fig.6.15*(a)* (2 cyclones split), 7 curves in panel *(c)* (1 cyclone split), and 6 in panel *(e)*. Despite this complicated transient dynamics, the final organisation of these multiple cyclones exhibits interesting features. The right column of Fig.6.15 (panel *(b,d,f)*) shows the trajectories at the end of the experiments (600 last rotation times over 1500). In the first experiment, four cyclones surround the pole, with none at the centre. Fig.6.16*(a)* show that once again, they equilibrate at a distance between 15 and 20 cm from the pole. In the second experiment, we again retrieve a quadrupole, but this time with a polar cyclone. Consistently with the presence of a polar cyclone, the four circumpolar cyclones equilibrate at a greater distance from the pole (between 20 and 25 cm, see Fig.6.16*(b)*). In the last experiment, no clear organisation is visible at the end of the experiment, with three cyclones surrounding a more central one and a polar cyclone. It is possible that we may need to run the experiment longer in that case to reach an organised state.

Fig.6.17 shows alternative visualisations of the flow for the final state of the two first experiments. In these experiments, silver-coated particles were added to the colouring. We post-processed the images by removing both the mean background and a median filtering of

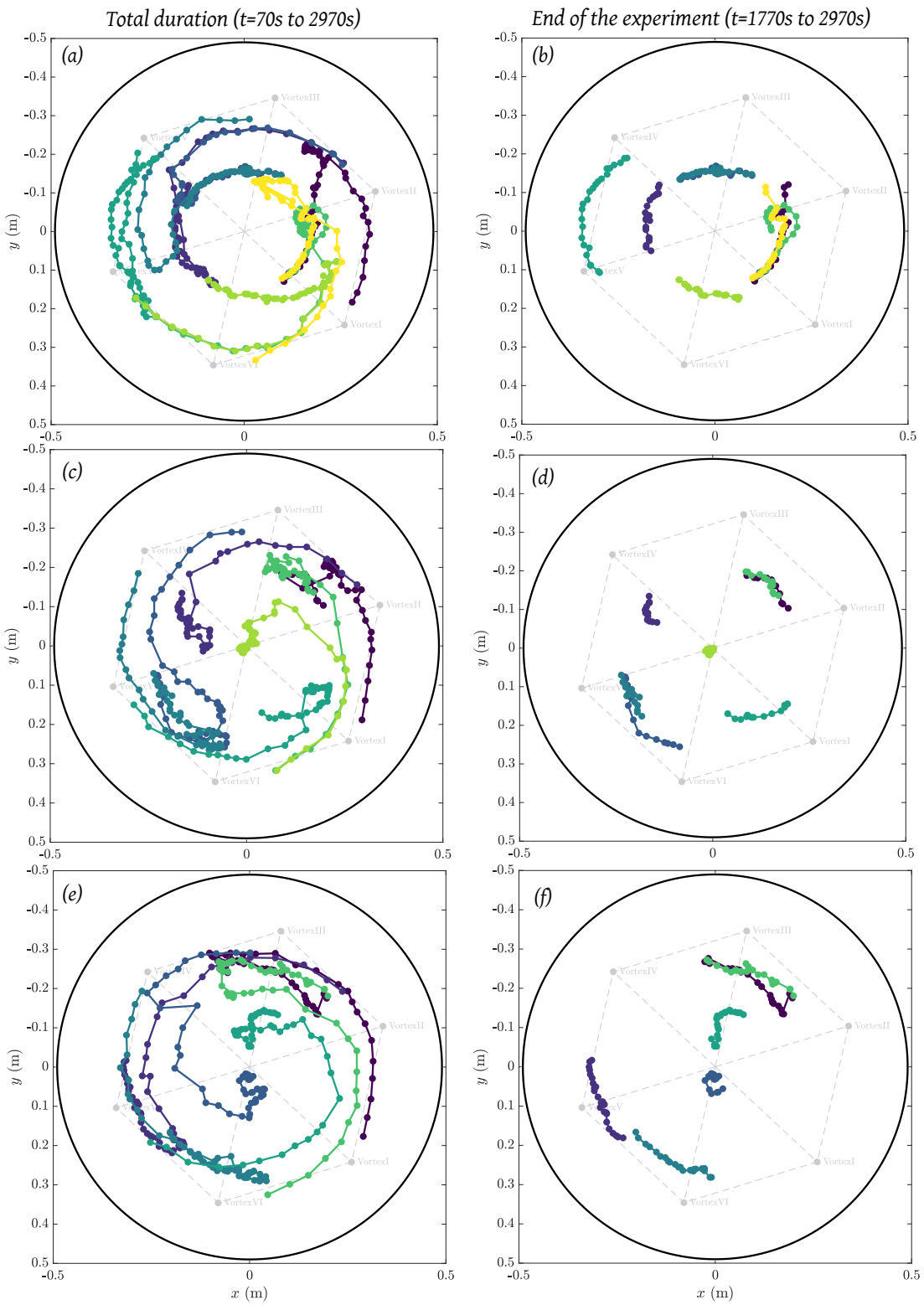

Figure 6.15. – Trajectories obtained when 6 cyclones are generated simultaneously. *(a,c,e)* Full trajectories. *(b,d,f)* Trajectories during the last 1200 seconds of the experiment, to visualize the final configuration.

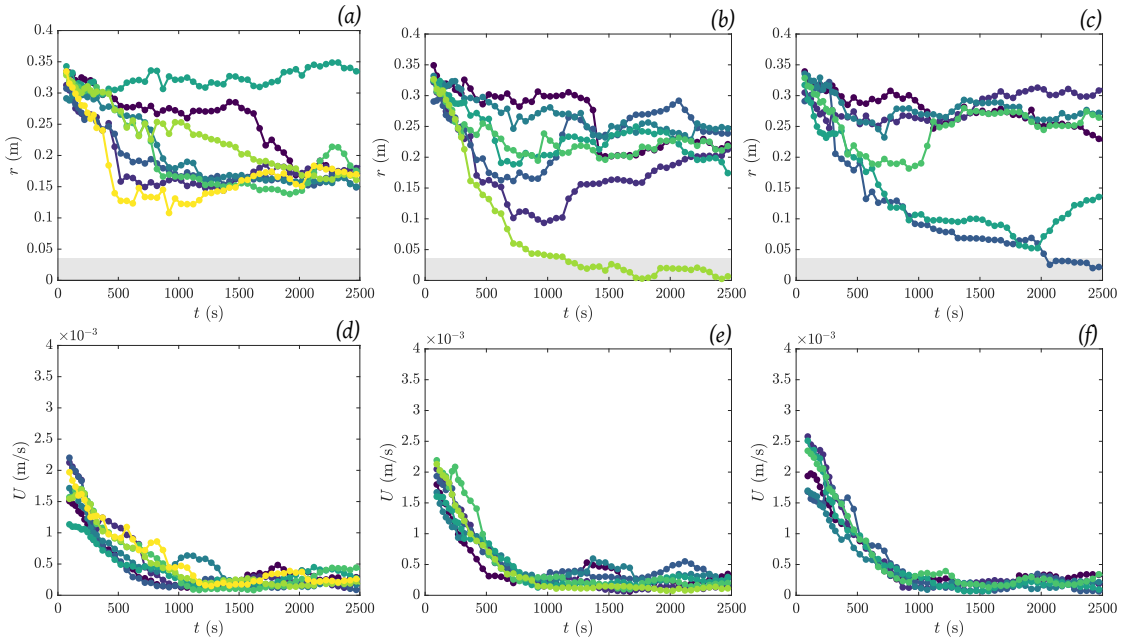

Figure 6.16. – Distance to the pole *(a-c)* and translational speed *(d-f)* for the three experiments where 6 cyclones are generated simultaneously. See Fig.6.15 for corresponding trajectories.

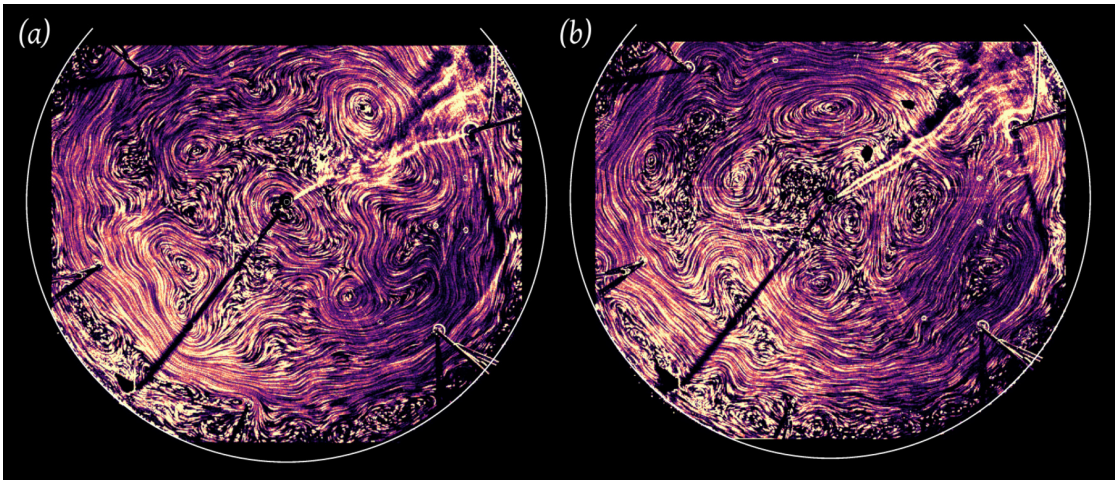

Figure 6.17. – Streamlines of the flow for the final configurations of the 6 cyclones experiments. Images of silver-coated PIV particles were stacked to obtain these streamlines.

the images to have an optimal contrast for the particles. We then stacked images to visualize streamlines of the flow. The tetragons of cyclones are visible, along with quasi-zonal currents surrounding the vortices. These mean currents probably also interact with the vortices. The fact that the cyclones are able to organise despite the complications of the background flow is hence encouraging.

Finally, Fig.6.18 allows to visualize the progression of the self-organisation of the vortices through time, for the experiment corresponding to Fig.6.15*(a)*. We plot, for each pair of vortices, the distance and the angle (seen from the pole) between them. We additionally plot the corresponding histograms, counting distances and angles between times t =2020 and 2970 s. The two peaks in the distances histogram correspond, first, to the mean distance between two adjacent cyclones of the tetragon ($\sim \sqrt{2} \times 18$ cm), and the second peak to the mean distance

between two facing cyclones ($\sim 2 \times 18$ cm). Similarly, both the evolution of the angle between cyclones of a given pair and the histogram show a progressive tendency towards angles of 90 and 180°, which demonstrate a progressive tetragonal organisation.

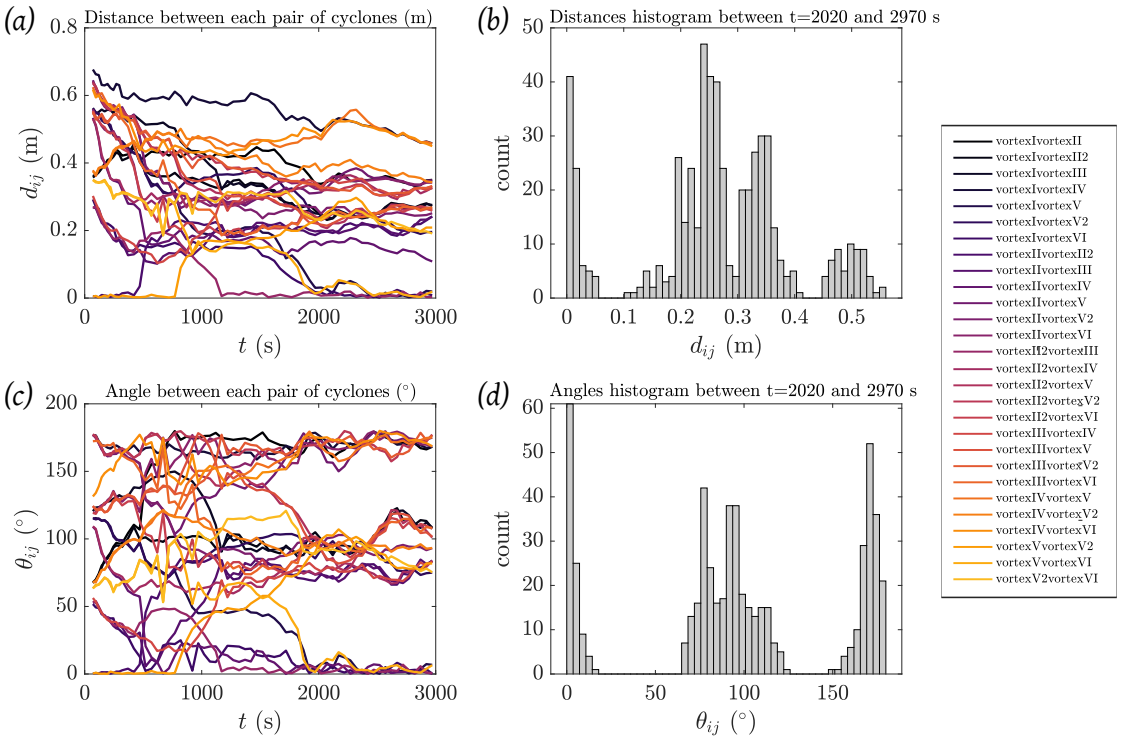

Figure 6.18. – Distances and angles between two cyclones for each pair of vortices in one of the six-cyclones experiments. *(a)* Evolution of the distance between two vortices (the pairs are listed on the right). *(b)* Corresponding histogram of the distances measured from time $t = 2020$ to 2970 seconds. *(c)* Evolution of the angle between the two cyclones of each pair. The angle is measured from the pole. *(d)* Corresponding histogram of the angles measured from time $t = 2020$ to 2970 seconds.

6.4. Discussion and future directions

6.4.1. Conclusions

As underlined before, the experiments presented here are preliminary, and give a first picture of what could be explored in the future for an experimental study of the evolution and mutual organisation of cyclones at the poles of gas giants. That being said, this first attempt with a single set of parameters is very encouraging regarding what can be achieved experimentally, and several points are already unambiguous here.

First, we demonstrate that the β-drift persists in the so-called reduced gravity system, where shallow vortices float on a deep, denser and quiescent layer. To the best of our knowledge, β-drift has never been investigated experimentally in this configuration. From the experimental point of view, the big advantage is that floating cyclones are long-lived compared to their barotropic counterparts (almost a factor 10 between their lifetime based on our experiments), even if complications arise, of course, for spinning-up this two-layer system and for having a precise knowledge of the stratification. The two-layer configuration is particularly relevant for the gas giants, where, contrary to the Earth, there is no solid surface onto which the cyclones dissipate. We observe a systematic and reproducible north-westward trajectory of the

cyclones towards the pole, whereas anticyclones drift towards the south-west. We observed that barotropic vortices, generated in a one-layer system drift and dissipate more rapidly than baroclinic vortices in a two-layer system. We hypothesize that the difference in the drift speed comes from the different origin of the β-effect in each case (deep and topographic, or shallow, due to the curvature of the layer into which the cyclone evolve), in addition to the difference in the Rossby deformation radius.

The motion of vortices on a β-plane has been studied experimentally for barotropic vortices only (Flór et al. 2002; Carnevale et al. 1991; Firing et al. 1976; Masuda et al. 1990; Stegner et al. 1998). The non-dimensional parameters of these experimental works are reported in Table 6.1. They all stand in the regime $Bu \gg 1$, because they work with an homogeneous and relatively deep layer of water, hence surface buoyancy effects are negligible. The only exception is Stegner et al. (1998) who worked with a very thin layer of fluid in a paraboloid vessel. Let us briefly compare our observations with the aforementioned studies. Our trajectories for single cyclones are strikingly similar to those observed by Carnevale et al. (1991) for their case with a flat bottom (see their Fig.9). Note that in their experiments, the vortex is strongly looping around the centre. This behaviour was observed in our barotropic case but in a reduced way, and it disappeared in the two-layer system. The major difference between our experiments is that their β-effect is smaller ($\Omega = 1$ rad s^{-1}), and their vortices have much higher Rossby numbers (of order 1 initially), thus their $\hat{\beta}$ is of about 0.003, much smaller than ours. Then, both Carnevale et al. (1991) and Flór et al. (2002) observe that vortices formed by stirring fluid are shielded, whereas sink vortices are not. In these studies, isolated vortices also have a more important northward drift compared to the westward component. In our experiments, even if our cyclones are formed by suction, we verified that they are well shielded. Second, despite being isolated, it is clear from the trajectories that the westward component of the drift is important or even dominant. This discrepancy could come from the difference in the system used for generating the cyclones, but probably also from the very low Rossby number of our vortices, for which the drift may be dominated by Rossby waves rather than by non-linear advection, even if they are shielded. For baroclinic vortices, the fact that the westward drift dominates is a priori expected from theory, since we are in a regime where the vortices have a scale comparable with the radius of deformation (Sutyrin 1988). This strong westward drift is also consistent with the experimental observations of Stegner et al. (1998) at small Burger number.

Second, it is interesting to compare our results to predictions regarding vortices merger in a stratified fluid. Aside from the question of clusters stability, vortex pairing in a stratified flow in the presence of a β-effect has never been investigated experimentally. In 2D, inviscid flows, vortex pairing occurs when the initial distance between the two vortices is below a critical distance $d_c \approx 3.3\ R_v$ (Leweke et al. 2016). In a 3D, stratified flow, this picture is significantly modified by buoyancy effects. In two-layer experiments, Griffiths et al. (1987) showed that d_c depends on the radius of deformation. Numerical simulations and recent experiments in a linearly stratified fluid then demonstrated that the dependence with the stratification strength is in fact non-monotonous (see Estrada et al. 2020, and references therein). At first, the critical distance increases with stratification from $d_c \sim 3R_v$ to $d_c \sim 7R_v$. This increase occurs up to a radius of deformation of $R_d \sim 2-3R_v$, meaning that first, pairing is enhanced by stratification. But after this maximum, d_c then decreases when further increasing the stratification. In our case, the stratification is very weak ($R_d/R_v \sim 0.5$), and the aforementioned studies predict that we should recover the barotropic critical distance $d_c \approx 3.3R_v$. We observed that when vortices do not coalesce, they equilibrate at a distance always greater than 3 times the cyclones radius, which is consistent with the aforementioned results.

According to numerical studies, the picture should however be significantly different when

vortices are shielded. The non-monotonous behaviour of the critical distance with increasing stratification disappears. Instead, pairing is inhibited compared to the barotropic case with a smaller critical distance $d_c \sim 2.2 - 2.5 R_\nu$ (Valcke et al. 1997; Ciani et al. 2016). Physically, the mechanism invoked is that the vorticity initially in the shielding ring is redistributed to form two lateral poles, making the vortices diverge from one another instead of merging. Note that this behaviour was observed in numerical simulations in the two-layer and $1-1/2$ layer frameworks (Valcke et al. 1997), as well as for linearly stratified fluids (Ciani et al. 2016), but was not recovered in the experiments of Estrada et al. (2020), despite the shielded aspect of their anticyclones, which is puzzling. Finally, all the aforementioned studies are performed without considering a β-effect. Studies including the β-effect for oceanographic applications are always considering midlatitude dynamics, i.e. a β-plane approximation. In this framework, cyclones drift due to β, but in the same direction, whereas with the polar β-effect cyclones are attracted towards each other at the pole. Intuitively, one could think that if all the cyclones are attracted at the pole, they will always at some point be closer to each other than the critical distance d_c and merge. This is not what we observe, hence there seem to be a long-range repelling effect. This effect could have the same origin as the redistribution of PV mentioned by Valcke et al. (1997), or it could be due to a local inversion of the PV gradient in the ring, as proposed by Li et al. (2020). Our experiments show that the relative strength of the anticyclonic vorticity ring compared to the local gradient of PV probably plays an important role, since cyclones meeting at larger distance from the pole tend to coalesce. In any case, we think that the mechanism at play deserves to be further investigated.

Finally, our experiments leading to tetragons are encouraging regarding what could be achieved experimentally. Further exploration of the parameters space, as detailed below, could lead to an experimental regime where clusters formation is robust and may be studied in depth.

6.4.2. Future work

According to me, the main directions that could be followed in the future to explore this topic deeper are the following. First, the Rossby number of our cyclones is very small, and could be increased by one order of magnitude, while still being in a quasi-geostrophic regime. We were limited by the capacity of our peristaltic pump, but in principle, it should be possible to reach higher flow rates with another pump. Vortices with a larger Rossby number will lead to a smaller $\hat{\beta}$, i.e. a stronger PV inversion by the anticyclonic vorticity ring, and a possibly stronger repulsive effect between the vortices, hence less mergers. Regarding the vortices, it also seems necessary to explore the behaviour of non-isolated vortices to investigate the importance of shielding in the observed repelling behaviour.

Exploring different rotation rates is also something that may help to distinguish important physical effects. Our choice of working at 30 RPM is a compromise:

— At higher rotation rates, β is stronger and the parietal friction is reduced, the vortices live longer, and drift more rapidly. However, they also radiate stronger Rossby waves during their formation. If β is too strong, the mechanism of inversion of the local PV gradient by the vortices themselves invoked by Li et al. (2020) would also be impeded (in other words, $\hat{\beta}$ needs to be small). Increasing the rotation rate also complicates the spin-up process of the two-layer system which needs to be performed extremely slowly to avoid mixing the interface. Finally, a larger deformation of the free surface would make the visualisation more difficult.

— At lower rotation rate, the friction is increased. The issue is then that the vortex may drift on a similar timescale than it is viscously dissipated. A too small rotation rate may thus impede the observation of interesting interaction dynamics because vortices

may dissipate before reaching the centre of the tank. This problem could however be overcome if we generate stronger vortices. Investigating smaller Ω might be interesting to explore smaller $\hat{\beta}$, because the balance between attracting-β and repelling-shielding will be increased in favour of shielding. Note however that the duration of the experiments will then also necessarily increase.

Another parameter that could be varied is the Burger number of the cyclones, by changing either the upper layer thickness, or the density difference between the two layers. Here, we worked with a relative density difference of $\Delta\tilde{\rho} \sim 3\%$, but we could achieve up to 17% of density difference by saturating the bottom layer in salt. The height of the top layer can also be increased, but we argue that we should seek to remain in the limit $R_v/h \leq 1$, otherwise the cyclones may not feel anymore the shallow β-effect due to their confinement in a curved thin layer. That being said, the shallow-water results of Li et al. (2020) seem to show that the Burger number has not an important effect on the stability of polygonal patterns of vortices.

To have a better control on the interface thickness between the two layers, it may be necessary for the future to conceive a setup where the two-layer configuration is generated once one of the two layers is already in solid-body rotation. We argue that here, and similarly to previous studies working with rotating two-layers systems (e.g. Linden et al. 1984), the mixing at the interface occurring due to instabilities or Ekman circulation during the spin-up only thickens the interface, which is then diffuse rather than sharp. However, the important point in our experiments is that the upper, shallow vortex is insensitive to friction at the bottom of the tank, rather than the detail of the stratification profile. A compromise would be to first install a system to measure vertical density profiles after spin-up, and thus have a better idea of the sharpness of the interface at the beginning of an experiment. Immiscible fluids may also be employed, but then care should be taken to avoid introducing important surface tension effects.

Finally, here, we adopted an idealized approach consisting in generating almost similar cyclones in a controlled environment. The goal is to determine to what extent do they drift, merge or equilibrate in polygonal configurations, and identify the dominant physical effects at play. The next step, would be to progressively switch to a more Jupiter-like flow. First, instead of generating a finite number of vortices, we could think of generating a large number of cyclones at the same time, or periodically in time, and see how they equilibrate. In a way, our experiments with 6 cyclones almost fall in this category, because the transient of the experiment becomes complicated and characterized by numerous interactions between vortices. The extreme limit of this approach would consist in sustaining a turbulent flow, let the vortices grow in size following the inverse cascade, and self-organize around the pole. We could consider using a similar forcing than the one used for the *Jacuzzi* experiment. If β is small because of a a low rotation rate, no strong jets should develop, but the vortices should nevertheless feel the small background gradient of PV and organize around the pole. The experimental challenge posed by this turbulent approach is twofold. First, experimentally, the rotation rate and the β-effect are not independent. A small β implies a small rotation rate, hence a large Ekman number, and it will be difficult to reach high, turbulent, Reynolds number while keeping the local Rossby number small. The turbulence will necessarily have to be moderate. Second, to avoid the strong friction due to the large Ekman, it would be nice to work in the two-layer system. But then the challenge is to be able to generate turbulence in the thin top layer without mixing it with the bottom one.

Chapter 7.

Conclusions and future prospects

7.1. Main results

The global aim of the present thesis was to develop idealized modelling to better identify the basic physical mechanisms at play on Jupiter. In particular we focused on three aspects of Jupiter's dynamics which are midlatitude floating vortices, zonal jets, and polar vortices. We employed three different experimental setups, complemented by numerical and theoretical analyses when relevant. The principal results of the present work are summarised below.

- Following on from Aubert et al. (2012) and Facchini et al. (2016), we used the pre-existing *Revival* experimental setup, complemented by direct numerical simulations and theoretical modelling to show that the quasi-static equilibrium shape of anticyclones embedded in a rotating and stratified shear flow is predictable based on the ambient parameters. Using estimates of velocity fields, rotation, and stratification difference between Jovian vortices and the surrounding atmosphere, we confirm that they are very shallow structures, extending over thousands of kilometres horizontally but with a thickness of only 50 to 150 km. Our model additionally predicts that despite its recent shrinkage, the Great Red Spot has kept a constant thickness comprised between 100 and 200 km during its evolution. These results are compatible with the recent observations of the Juno mission, which suggest that the density anomaly associated with the GRS could extend up to 300 km, i.e. winds that would extend up to about 180 km deep.

- We designed a new experimental *Jacuzzi* setup, expanding upon that employed by Cabanes et al. (2017), to study extreme regimes of barotropic zonal jets in the deep model scenario. Our experiments, associated with a linear quasi-geostrophic model, show that the jets are forced by a wave-mean flow interaction, but that two different regimes can be reached. In regime I, at low forcing amplitude, the Rossby waves excited by the forcing lead to the development of local, steady prograde jets at the forcing locations. When the forcing is sufficiently strong, the Rossby waves become stationary in the prograde jets because of their eastward advection by the zonal flow. This linear resonance leads to a transition to regime II where the jets merge and become non-local, broader, and of higher amplitude. The transition is characterized by a bistability and a hysteresis, observed experimentally and well explained by a simple low-dimensional model which incorporates the resonance. In previous studies, such resonance was shown to be possibly relevant for Earth's atmospheric jet stream, and may explain extreme weather events as well as super rotation in terrestrial atmospheres. Based on Rossby waves zonal velocity measurements, we propose that it could also explain the difference between Earth oceanic jets, which may be sub-resonant, except the Antarctic Circumpolar Current, and the gas giants jet streams which are presumably super-resonant. Drawing conclusions for planetary flows however require to further investigate the influence of the forcing coupling with the zonal flow, as discussed later.

- We analysed the statistical properties of the intense, experimental β-plane turbulence obtained in regime II by modifying the *Jacuzzi* setup to reach more extreme regimes, far from the transition. We show that the turbulent flow shares the properties of the so-called zonostrophic turbulence, relevant to the gas giants, in which the zonal flow alone contains more kinetic energy than the remaining of the flow. Along with Cabanes et al. (2017), these are the first experiments able to reach such extreme regimes (see Fig.3.1). Despite the strength and rectilinear shape of the zonal jets in our most extreme experiments, they are not accompanied by a strong potential vorticity mixing. However, we show that estimating the potential vorticity mixing via the Thorpe scale allows to retrieve a good order of magnitude of the upscale energy flux measured using spectral

analysis. This result underlines the consistency between the zonostrophic turbulence and potential vorticity mixing theories.

- From a Lagrangian analysis of the turbulent flow in regime II, we show that the transport properties of the flow are anisotropic and inhomogeneous due to the retroaction of the zonal flow: we namely confirm the so-called suppression effect of the zonal flow on the turbulent transport efficiency, which underlines the importance of accounting for the retroaction of zonal flows on turbulent transport in global oceanic or atmospheric circulation models, where small-scale turbulence must be parametrized.

- By performing repeated realisations of experiments with the same set of external parameters, we show that, in regime II, the final zonal flow profile is multistable, thereby supporting recent idealized numerical observations (Simonnet et al. 2021). However, once in a given steady state, the zonal jets are extremely stable; no spontaneous transitions between multistable states have been observed over the duration of our experiments, even when introducing large fluctuations in the forcing amplitude and distribution.

- Finally, we show using the *Clusters* experimental setup that shallow cyclones, floating above a deep denser layer, drift westward and towards the pole when subject to a polar β-effect in agreement with the β-drift mechanism. When multiple cyclones are simultaneously generated, we sometimes observe a repulsion between the vortices, which can eventually lead to their equilibration around the pole without merging. Continuing these preliminary experiments could help to understand the formation of clusters of cyclones at the poles of Jupiter.

7.2. Complementarity of experimental and numerical approaches for studying gas giants' dynamics

Both experiments and numerical simulations have their pros and cons for studying gas giants dynamics. We would like to briefly discuss this point in light of the present work.

7.2.1. Advantages of experimental approaches

For studying zonal jets, the main advantage of the *Jacuzzi* experimental setup is that it allows to model a fully three-dimensional system, without any *a priori* assumption on the bidimensionality of the flow. The fact that jets can emerge spontaneously from a deep, fast rotating, fully-3D turbulent flow, even in the presence of a large bottom drag (relatively to that on Jupiter), supports the deep hypothesis of zonal jets origin.

The regimes reached experimentally ($E \sim 3 \times 10^{-7}$, $Re \sim 10^4$, $Ro \sim 10^{-3}$) are not impossible to reach in direct numerical simulations, but at very large cost. To give an order of magnitude, a single DNS of 1,000 rotation times at a larger Ekman number $E \sim 10^{-6}$ represents 13 minutes of an experiment, but would require 13 days of computation on 2048 CPU cores (650,000 CPU hours). This type of DNS was performed in Cabanes et al. (2017), but it is clear that numerical systematic studies in these regimes are inconceivable. The high cost of these DNS is inherent to 3D simulations of geostrophic turbulent flows, where both large-scale structures and small-scale turbulent eddies and inertial waves are present and need to be resolved simultaneously. On the contrary, one experimental realisation "costs" about 2 days (one for the actual experiment, and one for saving and post-processing the images through the PIV algorithm), which allows for multiple realisations and exploration of the parameter space. In addition, the dynamics of the large-scale jets is slow, and results from cumulative

effects from the underlying turbulence. Studying their long-term dynamics requires to wait for very long times. Experimentally, we can easily reach several thousands of rotation times, and time-resolved particle image velocimetry allows for high-resolution records of the interactions between the turbulent flow and the slowly evolving large-scale jets.

Of course, idealized numerical models allow to circumvent these difficulties. This is the case for instance of reduced bidimensional models, such as shallow-water models and quasi-geostrophic models including the one employed in the present thesis. Statistical simulations and quasilinear models (e.g. Constantinou et al. 2014) where eddy-eddy interactions are neglected can also be used. Recently, rare events algorithm have also been employed to study multistability and spontaneous transitions among zonal jets (Bouchet et al. 2019b). However, the assumptions underlying each of these models and their relevance for gas giants dynamics need to be systematically addressed.

7.2.2. Limitations of experimental approaches

Of course, the advantages of experimental exploration comes along with limitations, which is why combining them with numerical investigations is complementary. The main limitations that we encountered are the following:

— The spatial confinement of the experiment is problematic for studying zonal jets equilibration. For instance, finite-size effects "discretize" the evolution of jets spacing when varying any control parameter. Due to confinement, jets are not free to evolve in space, and this may for instance impede long-term drift or nucleation of jets. One could nevertheless argue that jets on the planets are also confined, but there are still about ten prograde jets on Jupiter, leading to a scale separation between the size of the domain and the jets. We should hence seek to build experiments where the scale of the tank is large compared to the scale of the jets. This is challenging, because when trying to reach more extreme regimes, we increase the turbulence intensity or decrease the Ekman friction, which increases the jets scale. Imposing a fast rotation on larger scale containers is also a technical challenge.

— The high rotation rates of experiments allow to reach regimes with small friction ($E \sim 3 \times 10^{-7}$), but never asymptotically small. We stand in a strongly forced-dissipative regime, and it is difficult to address the relevance of the comparison with idealized models where both the forcing and the dissipation are vanishing.

— The experimental forcing is performed at small-scale, but it is difficult to reach the same scale separation as in numerical simulations. Exploring numerically the effect of the forcing scale and spatio-temporal stationarity is hence required to extrapolate experimental results to more realistic planetary conditions.

— Finally, and as discussed in chapter 4, a last difficulty is that we cannot vary independently the Ekman and Reynolds numbers and the zonostrophy index of the flow. Changing the rotation rate modifies the Ekman number but also the zonostrophy index because it changes the free surface shape. One way of avoiding this is to use a sloping bottom and a rigid lid instead of a free surface for the β-effect, but it introduces a supplementary friction. This remark is also valid for the *Clusters* setup, in which reducing the β-effect requires to reduce the rotation rate and increase Ekman friction.

To conclude, we think that the numerical investigations necessary to complement experimental investigations can be divided into three types. The first type is numerical simulations which reproduce the experimental conditions, and allow to explore one by one some effects artificially introduced by the experimental constraints (forcing nature, spatial confinement,

high viscosity, boundary conditions, etc.). The second type should investigate, in idealized frameworks, the addition of physical effects which will hardly be incorporated in experiments, such as magneto-hydrodynamical dissipation of zonal flows or compressibility effects on zonal jets and vortices. The goal of these idealized experimental and numerical models is then to shed light on fundamental mechanisms governing the dynamics of the system, rather than be quantitatively predictive regarding the specific case of Jupiter. That is why global scale simulations constitute the third type of complementary simulations, by incorporating as accurately as possible planetary processes, in the limit of what can be achieved with available computational resources.

7.3. Future lines of work

We conclude this thesis by pointing towards possible improvements of the methods and results presented here, and by proposing future lines of investigation.

7.3.1. Future work on midlatitude and polar vortices

For midlatitude large-scale anticyclones, a possible improvement of our conclusions on their equilibrium shape would be to numerically include compressibility effects, which will lead to an asymmetry in the vertical extent of Jovian vortices. In addition, those vortices form in a highly turbulent flow, whereas turbulence is absent from the *Revival* experiments. In chapter 2, our assumption is that the large-scale equilibrium is unaffected by the small-scale turbulence, which is not expected to significantly modify the large-scale potential vorticity anomaly associated with the vortex. However, including turbulence and more realistic dissipation processes such as radiative heat transport is likely important to explain the longevity of these structures. Finally, those anticyclones are a priori expected to drift towards the equator because of the β-effect. Quantifying the effect of the shear on the β-drift would be interesting and could be tackled experimentally, with a sloping bottom to induce a topographic β-effect. In that purpose, it may be necessary to set up a bulk shear rather than a boundary-driven one, which would be much more easily incorporated in simulations than in experiments.

Given their very recent discovery, a lot remains to be investigated regarding the dynamics of high latitude cyclones. From the experimental perspective, the work exposed in chapter 6 needs to be completed by experiments with higher vortex Rossby number or lower β-effect, such that the potential vorticity gradients induced by the vortex are dominant compared to the planetary vorticity gradient, which is the case of Jovian polar cyclones. However, similarly to the *Jacuzzi* experiment, reducing the β-effect requires to slow down the rotation rate, which increases viscous dissipation. This may be problematic and impede the cyclones equilibration at the pole before being viscously dissipated. Another possible improvement of the setup would be to use immiscible fluids rather than two miscible aqueous layers, in order to better control the two-layer system properties after the spin-up. In a similar fashion to what was done for the *Revival* and *Jacuzzi* experiments, the *Clusters* setup is also currently under numerical investigation by Djihane Benzzegoutta who uses the quasi-geostrophic numerical model in a configuration close to the experiment. This will allow to guide future experiments, for instance by determining at moderate cost the relative importance of the β-effect, the Ekman number, and the shielding of the vortices, to allow for their equilibration without merging. Given the small Burger number of the experimental vortices, it may be necessary to set-up a two-layer quasi-geostrophic model rather than a barotropic one, where buoyancy effects enter into play. Finally, complementary numerical investigations could also consist in exploring the

spontaneous emergence of vortices from a turbulent flow close to the conditions at the poles of Jupiter, rather than imposing them beforehand as an initial condition.

7.3.2. Jets forcing mechanisms: local or non-local energy transfers?

We show in chapter 3 that the jets developing in the *Jacuzzi* experiment are initially due to wave-mean flow interactions through the transport and deposition of momentum by Rossby waves, i.e. a streaming process. The nature of the transition towards the second regime, a Rossby wave resonance, leads us to the hypothesis that wave-mean flow interactions are probably also of importance in the second regime, even in the highly turbulent cases. The acceleration of the zonal flow by the streaming process is non-local, contrary to what is assumed for a turbulent cascade mechanism. However, we showed that the kinetic energy spectra of our flow are in agreement with that expected in the regime of zonostrophic turbulence. This is not necessarily inconsistent, since both local turbulent cascades and direct transfers between waves and the mean flow can coexist. One possible line of investigation would be to continue the spectral analysis a little bit further to confirm or not the presence of a turbulent inverse cascade of energy, for instance via the computation of structure functions. This would also allow for a direct comparison with the turbulent statistics of Jupiter derived from the Cassini movie (Young et al. 2017). We could for instance verify if we also retrieve a direct energy cascade despite the quasi-bidimensionality of our fast-rotating experimental flows.

7.3.3. Sensitivity of the Rossby waves resonance to a more realistic forcing

The Rossby waves resonance described in chapter 3 explains quantitatively the experimental transition between two regimes of zonal jets. To address the relevance of such a mechanism for planetary flows, further work is required to tend towards more realistic forcing. The experiments are essentially limited by their high viscosity due to the use of water, and the necessary idealized nature of the forcing, which is mechanically prescribed at the bottom of the tank. Given the size and rotation rate of our setup, viscous effects are in fact already small. For instance, we verified thanks to the QG numerical model that the experimental flow obtained in regime II does not significantly change when decreasing the Ekman number by an order of magnitude (see Fig.7.1 below). Furthermore, for vanishing friction, the bistable range described in chapter 3 is expected to increase (Fig.3.15). On the contrary, the nature of the forcing has much more significant effects. In particular, the experimental forcing is spatially stationary because the bottom plate is fixed in the rotating frame. Such stationary forcing is possibly relevant for zonal flows in Earth's atmosphere, where Rossby waves are excited by the stationary topography and equatorial heating. On the gas giants, which are fully fluid, there is a priori no reason for stationary features to develop. An important point is thus to address the robustness of the resonance to a non-stationary forcing, both in space and time. This could again be explored numerically, using the quasi-geostrophic numerical model. For instance, in Fig.7.2, we show the results of simulations where the forcing pattern is rotated azimuthally by a random angle every time interval Δt, for three different values of Δt. These simulations show that despite the addition of stochasticity in the forcing, the distinction between locally and globally forced jets seems to persist. That being said, using a stochastic forcing is not necessarily a better approach than a stationary one to better simulate the planetary forcing. Ideally, one would need to define a single parameter that can be varied to switch progressively from a stationary forcing to a forcing passively advected by the zonal flow that it generates. Regarding the resonance, we expect that as soon as the forcing is not passively advected by the zonal flow, there should always be a prograde jet speed for which the excited Rossby waves will be phase locked with the forcing.

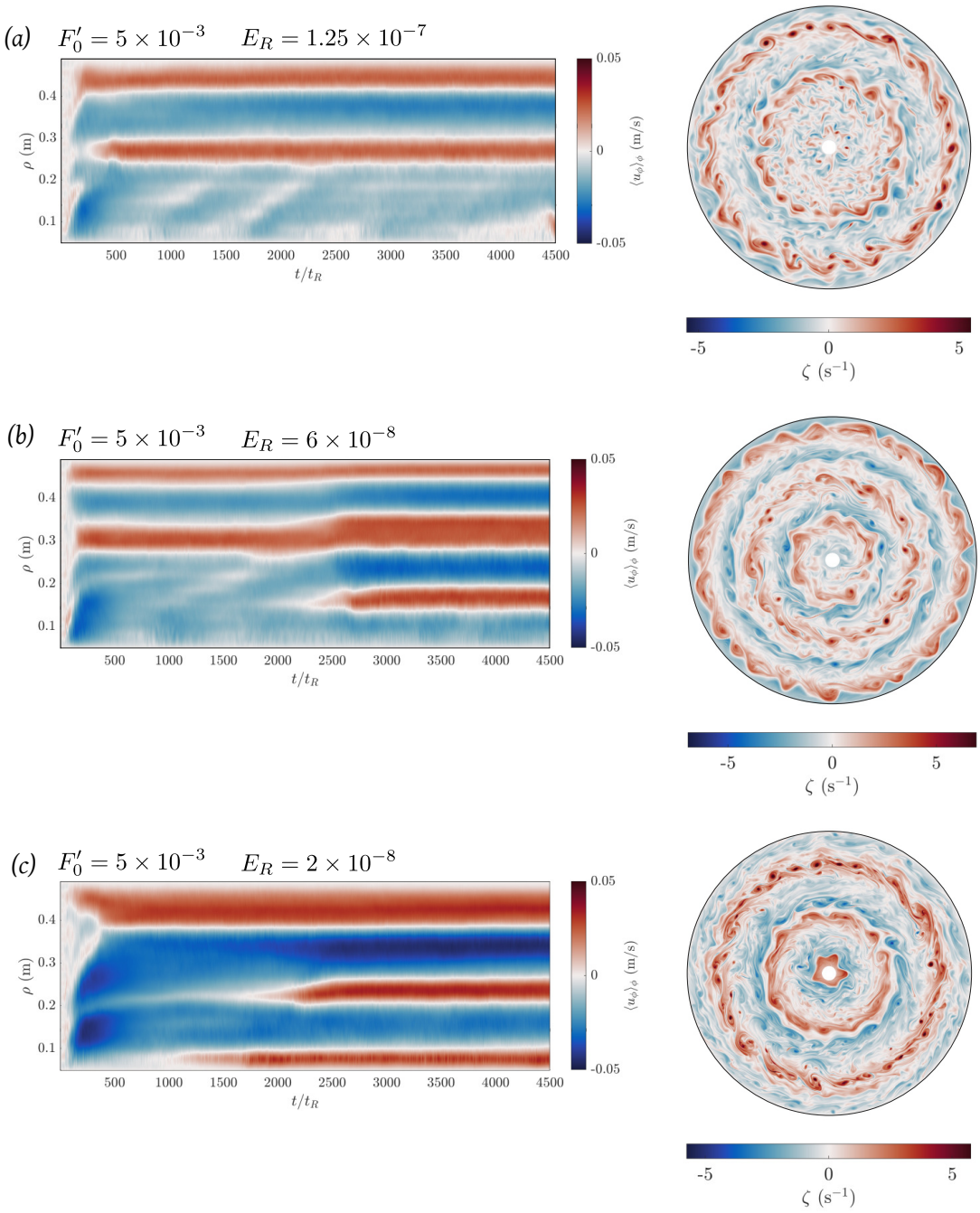

Figure 7.1. – Results of QG numerical simulations with a decreasing Ekman number and a fixed forcing amplitude $F_0' = 5 \times 10^{-3}$. The forcing pattern is the same as in Fig.3.17, i.e. a polar forcing pattern at a scale about half the experimental one ($k_f' \sim 90$). These simulations are performed with a free-slip boundary condition for both the inner and outer boundaries.

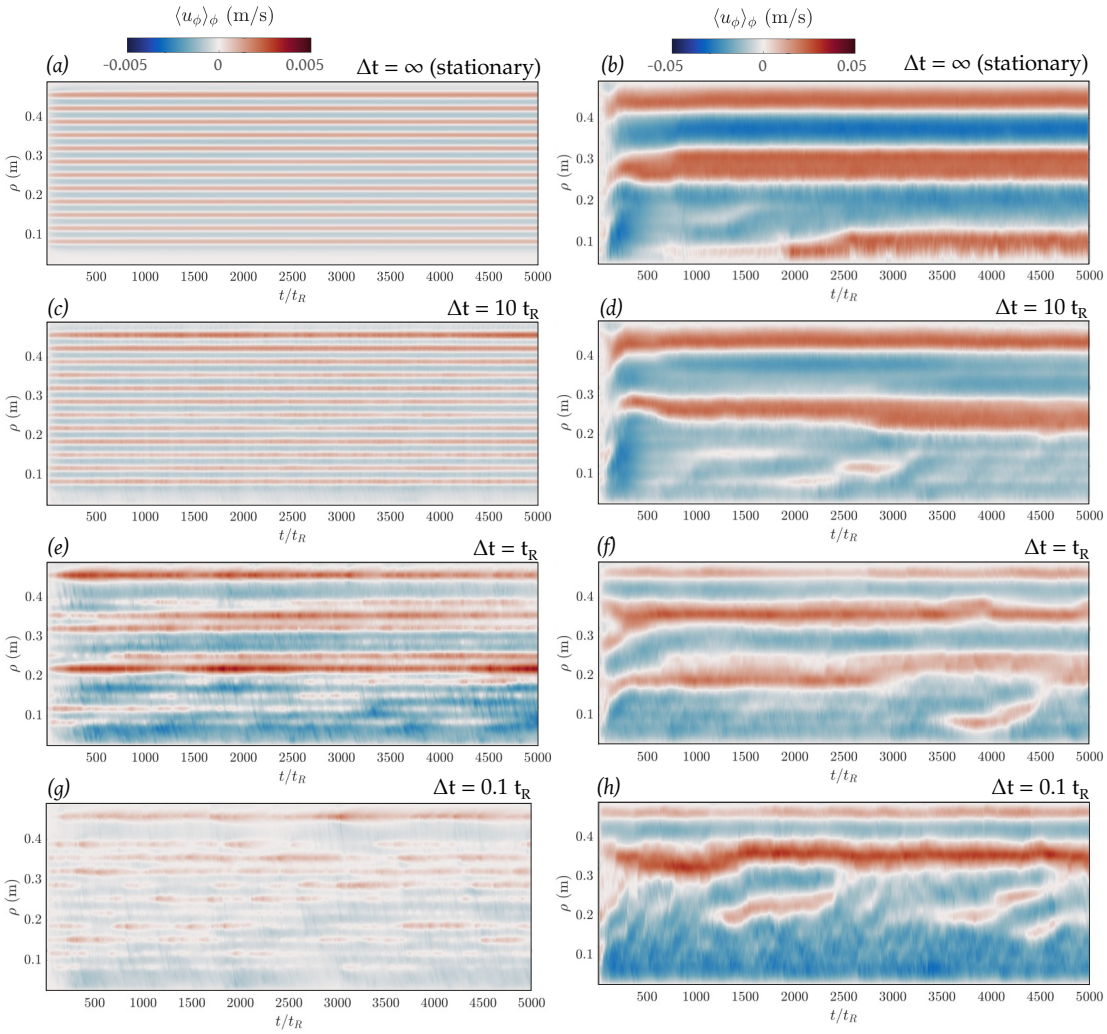

Figure 7.2. – Results of QG numerical simulations with a stationary forcing (top row) or with a forcing pattern rotated azimuthally by a random angle every Δt. The time interval at which the position of the forcing is varied is indicated at the top of each plot. The forcing pattern is the same as in Fig.7.1. *(a,c,e)* Forcing amplitude $F_0' = 5 \times 10^{-4}$ (Regime I). *(b,d,f)* Forcing amplitude $F_0' = 5 \times 10^{-3}$ (Regime II). *(g)* $F_0' = 5 \times 10^{-3}$. *(h)* $F_0' = 5 \times 10^{-2}$

7.3.4. Zonal jets equilibration in regime II: a wave-mean flow WKB model.

For the transition from regime I to regime II, we used a simple low-dimensional model where we assumed the zonal flow U to be uniform in space (chapter 3). By accounting for Rossby waves emitted by the experimental forcing, this model showed that the sudden acceleration of the zonal flow in regime II, and the associated hysteresis, can be explained in terms of a linear resonance of Rossby waves. However, because the zonal flow is assumed uniform, this model cannot explain the changes in the meridional profile of the zonal flow, and in particular the new scale of the jets in regime II. I propose that a similar approach, which focuses only on wave-mean flow interactions, could be employed to explain the saturation in regime II.

To do so, I would like to build again a low-dimensional model of the mean flow evolution, but which incorporates both the meridional structure of the zonal flow $U(y)$, and the retroaction of the meridional curvature of the zonal flow, $\partial_y^2 U$, on the Rossby waves. To derive such a model, it is possible to adopt an approach analogous to Plumb's model of the acceleration of the mean flow by internal waves in the framework of the quasi-biennial oscillation (Plumb 1975,

1977). The principle is to solve for the wave field using a Wentzel-Kramers-Brillouin (WKB) approach (Vallis 2017, chapter 6, appendix A), use this WKB solution to derive an analytical expression of the Reynolds stresses divergence, and use this expression to integrate the zonal flow evolution equation. This modelling is still under investigation, but let us give the main steps and assumptions of its derivation below.

The retroaction of the zonal flow on Rossby waves is due to the fact that, besides the advection (Doppler-shift), the zonal flow itself modifies the potential vorticity gradient necessary for Rossby waves propagation. To see it, let us decompose the velocity into a zonal flow plus fluctuations, as in chapter 3, except that this time we allow for a meridional structure of the zonal flow, $U(y)$:

$$u = \langle u \rangle_x(y,t) + u'(y,x,t) = U + u', \tag{7.1}$$

$$v = \langle v \rangle_x(y,t) + v'(y,x,t) = v', \tag{7.2}$$

$$\zeta = \langle \zeta \rangle_x(y,t) + \zeta'(y,x,t) = -\frac{\partial U}{\partial y} + \zeta'. \tag{7.3}$$

We recall that $\langle \cdot \rangle_x = \frac{1}{2\pi}\int_0^{2\pi} \cdot \, \mathrm{d}x$ is the zonal mean. In the β-plane barotropic vorticity equation (1.31), we substitute the variables with this Reynolds decomposition, and linearise the equation around the background zonal flow, leading to

$$\frac{\partial \zeta'}{\partial t} + U\frac{\partial \zeta'}{\partial x} + \underbrace{\left(\beta - \frac{\partial^2 U}{\partial y^2}\right)}_{\beta^*} v' + \alpha\zeta' = 0. \tag{7.4}$$

We recall that α is the Ekman friction rate. The effective β-effect, denoted β^*, incorporates the modification of the β-effect due to the retroaction of the zonal flow. For instance β^* vanishes in a retrograde flow of curvature β. In other words, a retrograde zonal flow flattens the global potential vorticity gradient (decreases the effective beta-effect) whereas a prograde zonal flow steepens the PV gradient (increases the effective beta-effect). Using the streamfunction ψ' ($u' = -\partial_y\psi'$, $v' = \partial_x\psi'$ and $\zeta' = \nabla^2\psi'$), the Rossby waves equation becomes

$$\frac{\partial}{\partial t}\nabla^2\psi' + U(y)\frac{\partial}{\partial x}\nabla^2\psi' + \beta^*(y)\frac{\partial \psi'}{\partial x} + \alpha\nabla^2\psi' = 0. \tag{7.5}$$

We consider plane wave solutions of zonal wavenumber k and Doppler-shifted zonal phase speed c ($c < U$ for Rossby waves) under the form

$$\psi' = \tilde{\psi}(y)e^{ik(x-ct)} + \text{cc.}, \tag{7.6}$$

where cc. stands for "complex conjugate", and the meridional structure $\tilde{\psi}$ remains to be determined. Substitution into equation (7.5) leads to

$$\frac{\mathrm{d}^2\tilde{\psi}}{\mathrm{d}y^2} + l^2(y)\tilde{\psi} = 0, \tag{7.7}$$

where

$$l^2 = \frac{\beta^*}{U-c}\left(1 + \left(\frac{\alpha}{k(U-c)}\right)^2\right)^{-1}\left(1 + \mathrm{i}\frac{\alpha}{k(U-c)}\right) - k^2 \tag{7.8}$$

represents the meridional structure of the Rossby waves, including their dissipation due to friction accounted for by the imaginary part. The term $\gamma^2 = (\alpha/(k(U-c)))^2$ quantifies the frictional damping of the Rossby waves. In the weak damping limit ($\gamma \ll 1$) and assuming

$l^2 \gg k^2$,

$$l^2 \approx \frac{\beta - \partial_y^2 U}{U-c}\left(1 + \mathrm{i}\frac{\alpha}{k(U-c)}\right). \tag{7.9}$$

The weak damping limit amounts to consider a scale separation between the wavelength of the waves ($(c/\beta)^{1/2}$) and the distance over which they are damped, the so-called attenuation length

$$\Lambda = \frac{c_g}{\alpha} = \frac{kc^{3/2}}{\alpha\beta^{1/2}}, \tag{7.10}$$

where c_g is the characteristic Rossby waves group velocity. In this limit, a Wentzel-Kramers-Brillouin solution of equation (7.7) can be found for the wave field (see Appendix A of chapter 6 in Vallis (2017)). From the WKB solution, an analytical expression for the Reynolds stresses induced by the Rossby wave field can be derived:

$$\langle u'v'\rangle_x(y) = F' \exp\left(-\frac{1}{\Lambda}\int_{y'} \frac{\left[1-\beta^{-1}\partial_{y'}^2 U\right]^{1/2}}{[U/c-1]^{3/2}}\mathrm{d}y'\right). \tag{7.11}$$

This expression readily shows that the Reynolds stresses associated with the wave field will exhibit a particular behaviour close to the critical latitudes (when $U \to c$), and when $\partial_y^2 U \to \beta$. This analytical expression can then be used in the zonal flow evolution equation

$$\frac{\partial U}{\partial t} = -\frac{\partial \langle u'v'\rangle_x}{\partial y} - \alpha U + \nu\frac{\partial^2 U}{\partial y^2}. \tag{7.12}$$

This is an integrodifferential equation, which can be numerically integrated. To use the WKB solution, one has to chose one or several meridional positions at which the Rossby waves are emitted. Preliminary results show that increasing the number of lines of emission can lead to a transition between a regime where each forcing line is independent from the other ones (one prograde jet per latitude of emission), to a regime where the Rossby waves emitted by different forcing latitudes influence each other. Such a model may thus be able to explain the difference between locally and globally forced jets by Rossby waves, i.e. the difference between the saturated states in regime I and II. In the second case, we expect that the retroaction of the zonal flow on the waves may lead to non-trivial stationary states where the zonal jets profile will be equilibrated at a scale different than the forcing scale and predictable as a function of the model parameters. This modelling will be the focus of future work.

7.3.5. Coupling between deep barotropic jets and a stratified layer

We conclude this chapter by suggestions in the broader context of the challenges posed by Jupiter's interior. Zonal jets on Jupiter are not isolated structures, and unclear interactions occur at both their top and bottom boundaries. As sketched in Fig.7.3, it is for instance possible that the barotropic zonal jets penetrate a stratified layer at both boundaries.

At the top boundary, the zonal jets – assumed to be generated deeply in the molecular hydrogen envelope – reach the stratified weather layer. To date, most models decouple the shallow weather layer dynamics and the deep convection. This is also what we did in this thesis, where we studied separately shallow vortices and deep jets. Given the picture drawn by Juno, it now seems necessary to tend towards models that integrate both deep, barotropic zonal jets and shallow, atmospheric processes such as floating lenticular vortices, baroclinic instabilities, moist convection and radiative damping.

In addition to this shallow coupling, jets may also interact with a stratification at their bottom

boundary, deep into Jupiter's interior. The best candidate to account for a deep stratification is the immiscibility between helium and hydrogen under Jupiter's conditions (Debras et al. 2019; Helled 2019). The motivation for including a deep, stably stratified layer in dynamical models comes from the fact that zonal jets dissipated by Lorentz force at their bottom lead to unrealistic jets magnitude and structure (Christensen et al. 2020). In particular, when including Jupiter's electrical conductivity profile, global dynamo simulations exhibit equatorial jets (outside the tangent cylinder) much more predominant compared to midlatitude jets which are too strongly damped (see e.g. Jones 2014; Gastine et al. 2014; Dietrich et al. 2018). This is reminiscent of what is observed in non-magnetic models of Jupiter's convection, where no-slip bottom boundary condition seems to kill mid and high-latitude zonal jets (Aurnou et al. 2004; Heimpel et al. 2020). For these reasons, a deep, stably stratified region that inhibits convection is being considered in addition to the Lorentz forces to limit the depth of zonal jets. We note, however, that the upper limit of the helium rain ($\sim 0.84 R_J$, 11,000 km below the clouds) is located below the inferred termination of the zonal jets ($\sim 3{,}000$ km below the clouds). The origin and location of such a stratification thus remain unclear, but the recent dynamo model of Gastine et al. (2021) shows that it may be one of the keys to understand the structure of Jupiter's magnetic field, namely its dipole-dominated nature.

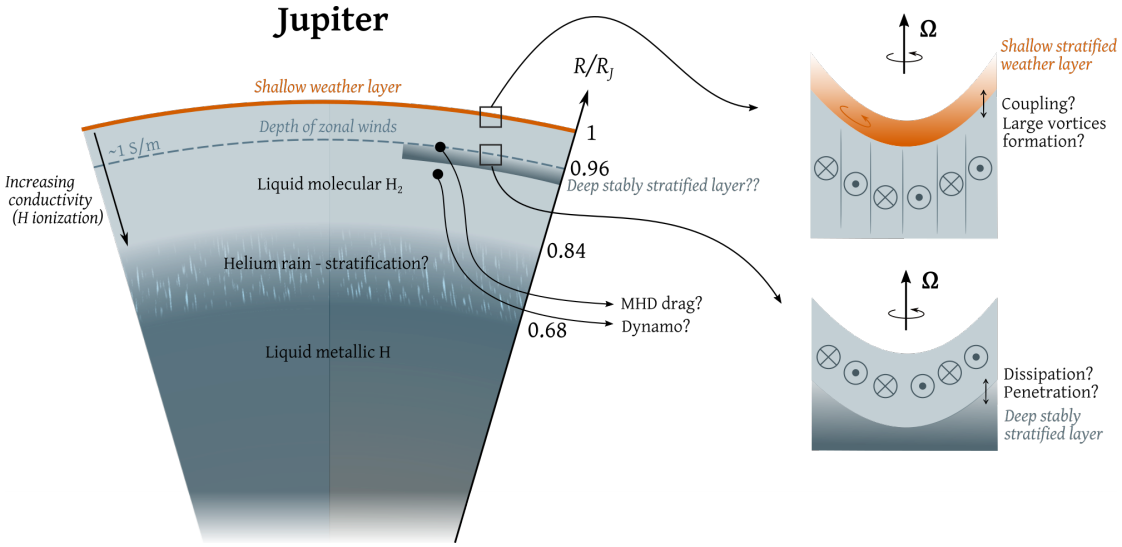

Figure 7.3. – Illustration of possible coupling between zonal jets in the molecular hydrogen envelope and stably stratified layers. The origin of a deep, stratified layer at the base of the zonal jets is unclear since the region of the He rain is expected deeper than the jets dissipation level. Such a basal stratification is nevertheless proposed as an alternative or a complement to Lorentz forces in dynamo models to account for zonal jets quenching. Figure adapted from Fig.5 in Helled (2019).

The inclusion of a stratified layer at the base or at the top of zonal jets could be tackled experimentally. For the case of the coupling with the weather layer, now that we have a barotropic setup where deep zonal jets can be robustly generated, the next step is to add a less dense layer at the top of this zonal jets system to see how the two layers dynamically couple. It may for instance be possible to find a configuration in which baroclinic instabilities can occur at the location of the density jump, leading to the spontaneous formation of baroclinic vortices which would persist as floating vortices in the top layer. Another possibility would be to combine the *Jacuzzi* and *Clusters* setups, and artificially generate vortices in the top layer once the zonal jets are formed. This would allow, for instance, to quantify the persistence of cyclones and anticyclones depending on the direction of the shear, or to study the meridional equilibrium position of the vortices as a function of the zonal flow profile, and compare them

with Jupiter's data.

Regarding the deep stratification, the jets could be generated in the upper layer, and rest onto the bottom denser – or stably stratified – layer. In a similar fashion to the *Clusters* setup, such a configuration would significantly decrease the bottom drag of the jets due to Ekman friction. It would then be possible to study both jets dissipation and penetration in the stratified layer. The challenge is then to be able to force the flow in the upper layer only, which is not possible with the actual setup, forced at the bottom. These two experimental configurations may also be completed by modifying the actual QG numerical code from a single layer to a two-layer system. For a given system of zonal jets forced in one of the two layers, the degree of coupling with the other layer and associated dissipation may be investigated by varying the internal Rossby radius of deformation (equation (1.23)) which quantifies the strength of the stratification.

Jupiter exhibits a wealth of dynamical processes, occurring at very different temporal and spatial scales. Our understanding of Jupiter and the gas giants as global systems is still complicated by numerous sources of uncertainty and technical limitations. As beautifully stated by Vasavada et al. (2005), "Jupiter's atmosphere constitutes an immense fluid dynamics experiment of a scale that could never be achieved in the laboratory, and one that continues to challenge state-of-the-art computers". The combination of simplified studies of experimental, numerical and theoretical nature, which focus on selected phenomena, constitutes one way of improving our understanding of Jupiter's dynamics, and this is the approach that we chose to follow in the present thesis. In addition, the continuous improvement of technical and computational capabilities allows experimental and numerical models to get closer to the planetary regimes. However, understanding Jupiter by forward modelling requires observations of sufficiently good quality and coverage to which the models outputs can be compared. The recent, accurate observations of Jupiter and Saturn from the Juno and Cassini missions constitute a very good opportunity in this regard, while introducing new and exciting challenges for planetary modellers at the same time.

APPENDICES

A. Table listing the parameters of experimental studies of zonal jets

In this appendix, we provide the dimensional and non-dimensional parameters that are used to plot Fig.3.1, where the regimes reached by experiments on zonal jets are compared. Table A.1 lists the corresponding experimental studies. Note that various forcing types are employed. The definition of the Ekman number E, Reynolds number Re and and zonostrophy index R_β are those of Table 4.1.

Ref.	Forcing	u_{rms} ($\mathrm{m\,s^{-1}}$)	h_0 (m)	R (m)	Ω (RPM)	β ($\mathrm{m^{-1}\,s^{-1}}$)	E	Re	$Ro = Re \times E$	R_β^c
Present	Sinks & sources ($L_f \sim 7$cm)	3.40×10^{-2}	0.58	0.49	75	50	3.78×10^{-7}	19720	7.46×10^{-3}	3.88
Burin et al. (2019)	Sinks & sources ($L_f \sim 6.5$cm)	2.50×10^{-2}	0.22	0.13	100	18	1.97×10^{-6}	5500	1.09×10^{-2}	2.30
Cabanes et al. (2017)	Sinks & sources ($L_f \sim 10$cm)	3.50×10^{-2}	0.5	0.5	75	89	5.09×10^{-7}	17500	8.91×10^{-3}	3.88
Read et al. (2015)	Barotropic thermal conv.	4.00×10^{-3}	0.8	7.5	1.5	6.20×10^{-2}	9.95×10^{-6}	3200	3.18×10^{-2}	1.82
Zhang et al. (2014)	Electromag. ($L_f \sim 4.6$cm)	1.40×10^{-2}	0.08	0.55	22	35	6.78×10^{-5}	1120	7.60×10^{-2}	1.55
Smith et al. (2014)	Diff-heated rotating annulus	3.00×10^{-3}	0.15	0.49	38	107	1.12×10^{-5}	450	5.03×10^{-3}	1.91
Di Nitto et al. (2013)	Electromag ($L_f \sim 1.2$cm)	8.00×10^{-3}	0.03	0.5	32	35	3.32×10^{-4}	240	7.96×10^{-2}	0.99
Afanasyev et al. (2013)	Electromag ($L_f \sim 4.6$cm)	5.80×10^{-3}	0.1	0.55	22	35	4.34×10^{-5}	580	2.52×10^{-2}	1.55
Afanasyev et al. (2012)	Local buoyancy source	5.00×10^{-3}	0.12	0.65	22	6	3.01×10^{-5}	600	1.81×10^{-2}	1.38
Espa et al. (2012)	Electromag.($L_f \sim 2$cm)	1.10×10^{-2}	0.01	0.18	24	44	3.98×10^{-3}	110	4.38×10^{-1}	0.67
Wordsworth et al. (2008)	Diff-heated rotating annulus	1.80×10^{-2}	0.22	0.1	37	29	5.33×10^{-6}	3960	2.11×10^{-2}	2.34
Read et al. (2007)	Spray of dense water	3.40×10^{-3}	0.55	7.5	1.5	8	2.10×10^{-5}	1870	3.94×10^{-2}	2.51
Afanasyev et al. (2005)	Electromag.($L_f \sim 2$cm)	5.00×10^{-3}	5.00×10^{-3}	0.15	14	40	2.73×10^{-2}	25	6.82×10^{-1}	0.47
Aubert et al. (2002)	Sinks & sources ($L_f \sim 1.4$cm)	2.00×10^{-2}	0.19	0.32	150	17	1.76×10^{-6}	3800	6.70×10^{-3}	2.11
Bastin et al. (1998)	Diff-heated rotating annulus	3.00×10^{-3}	0.14	0.06	43	91	1.13×10^{-5}	420	4.76×10^{-3}	1.83

Table A.1. – Dimensional and non-dimensional parameters of previous experimental studies of zonal jets. u_{rms} is the total root-mean-squared velocity, h_0 the mean fluid thickness, R the apparatus radius, Ω the rotation rate, and the β-effect arises from the paraboloidal free surface, a sloping bottom, or both depending on the study. When a range of parameters was explored, we indicate the values of the most extreme cases. For rotating annuli, R is the gap width, not the external radius. The non-dimensional parameters definitions are provided in Table 4.1.

B. Forcing details and calibration in the Jacuzzi (zonal jets) experiment

In this appendix, we provide further details on the forcing of the *Jacuzzi* experiment. We provide the forcing calibration results for the two different sets of pumps used in our experiments. We also give further details on the optical calibration of the recorded field of view, and we plot the topographic β-effect in the cases of a curved or flat bottom plate for various rotation rates.

B.1. Forcing details

We force small-scale fluid motions using an hydraulic system located at the base of the tank. This system is inspired from previous setups designed to study turbulent (Bellani et al. 2013; Yarom et al. 2014) and zonal flows (De Verdiere 1979; Aubert et al. 2002; Cabanes et al. 2017; Burin et al. 2019).

A curved bottom plate, made of Acrylonitrile Butadiene Styrene (ABS), is placed at the bottom of the tank. The plate is curved such that at a rotation rate of 75 RPM, the fluid height increases exponentially with radius, which provides a uniform β-effect across the tank. Practically, this gives a bottom topography h_b of

$$h_b(\rho) = h_{\min} + \frac{\Omega^2}{2g}\rho^2 - h_{\min}\exp\left(-\frac{\beta}{2\Omega}\rho\right), \tag{B.1}$$

where g is the gravitational acceleration, $\Omega = 7.854$ rad s^{-1} is the rotation rate, $R = 0.49$ m is the tank radius, $h_{\min} = 0.2$ m is the minimum fluid height in rotation and $\beta = 50.1$ m^{-1} s^{-1}. These parameters were chosen as the best compromise between a large β, a large but reasonable rotation rate, and to minimize the thickness of the bottom plate which is 1m-diameter and needs to be machined (drilled and threaded 128 times). This gives

$$h_b(\rho) = 0.2 + 3.145\rho^2 - 0.2\times\exp\left(3.190\rho\right), \tag{B.2}$$

where ρ and h_b are in meters. The profile of the bottom plate is illustrated on Fig. B.1 *(b)*. It has the shape of a curly bracket, with a maximum depth of 5.33 cm.

This curved bottom plate is drilled with 128 holes (64 inlets and 64 outlets) of 4 mm diameter (Fig. B.1 *(c)*) through which the forcing is performed. The holes are distributed on a polar lattice with 6 rings C_{1-6} located at radii $R_i \in \{0.067, 0.140, 0.214, 0.287, 0.361, 0.434\}$ m as represented by the top-view schematic in Fig. B.1 *(a)*. Each ring counts respectively 6, 12, 18, 24, 30 and 38 holes, half of them being inlets (sucking water from the tank and generating cyclones) and the other half outlets (generating anticyclones). The holes are uniformly distributed along each ring, leading to a minimum separation distance of 7.0 cm (ring C_1) and a maximum separation distance of 7.6 cm (ring C_5). Note that there is also a spatial phase shift between each consecutive rings in order to minimize the variance in the distance between two neighbouring inlets or outlets.

All the holes of a given ring are connected to a submersible pump via a network of flexible tubes. To do so, we use two distributors per ring, one which collects the tubes going to the pump's inlet, and the other one collecting the tubes going to the pump's outlet. Pictures and schematics of the distributors are provided in Fig. B.1 *(d,e)*. Twelve distributors and six submersible pumps are thus located beneath the bottom plate, and circulate water through the six rings. Two different sets of pumps were used, and are detailed in the calibration sections. Pictures of the tubing and pumps beneath the bottom plate are visible in Fig. B.2. The resulting circulation induces no net mass flux, since the water is directly sucked from the working fluid

and released in it. The system was designed to minimize the direct forcing of the zonal mean zonal flow and that only the eddy momentum fluxes should be responsible for its eastward or westward acceleration.

Finally, each ring is controlled by one pump independently of the others which allows us to control the forcing intensity with the radius. The pumps are controlled remotely by linking them to their drivers (TCS EQi Controllers) through the base of the tank (Fig. B.5). The drivers are controlled by an analog signal consisting in a 0-5V voltage coming from a Raspberry Pi. Pictures of the drivers and their connections are provided in Fig. B.3 and B.4 for the two sets of pumps. To communicate remotely with the Raspberry, which is fixed on the rotating table with the drivers, we use a publish-subscribe network protocol called MQTT (Message Queuing Telemetry Transport). In this protocol, the publishers send messages on a given topic, and all the clients that have subscribed to that topic receive the message. The server (called a MQTT broker) that we use to make the link between publishers and subscribers is the open-source broker Mosquitto [1]. Finally, we use Node-RED [2] to generate a graphical interface on a local webpage (Fig. B.6), and to communicate the orders given by the interface to the Raspberry and the drivers through the MQTT broker. We can chose the power of a given pump to be stationary, or to fluctuate randomly within a prescribed power range with a fixed period. For some experiments, we also added the possibility to turn off a given pump periodically.

1. http://mosquitto.org/
2. https://nodered.org/

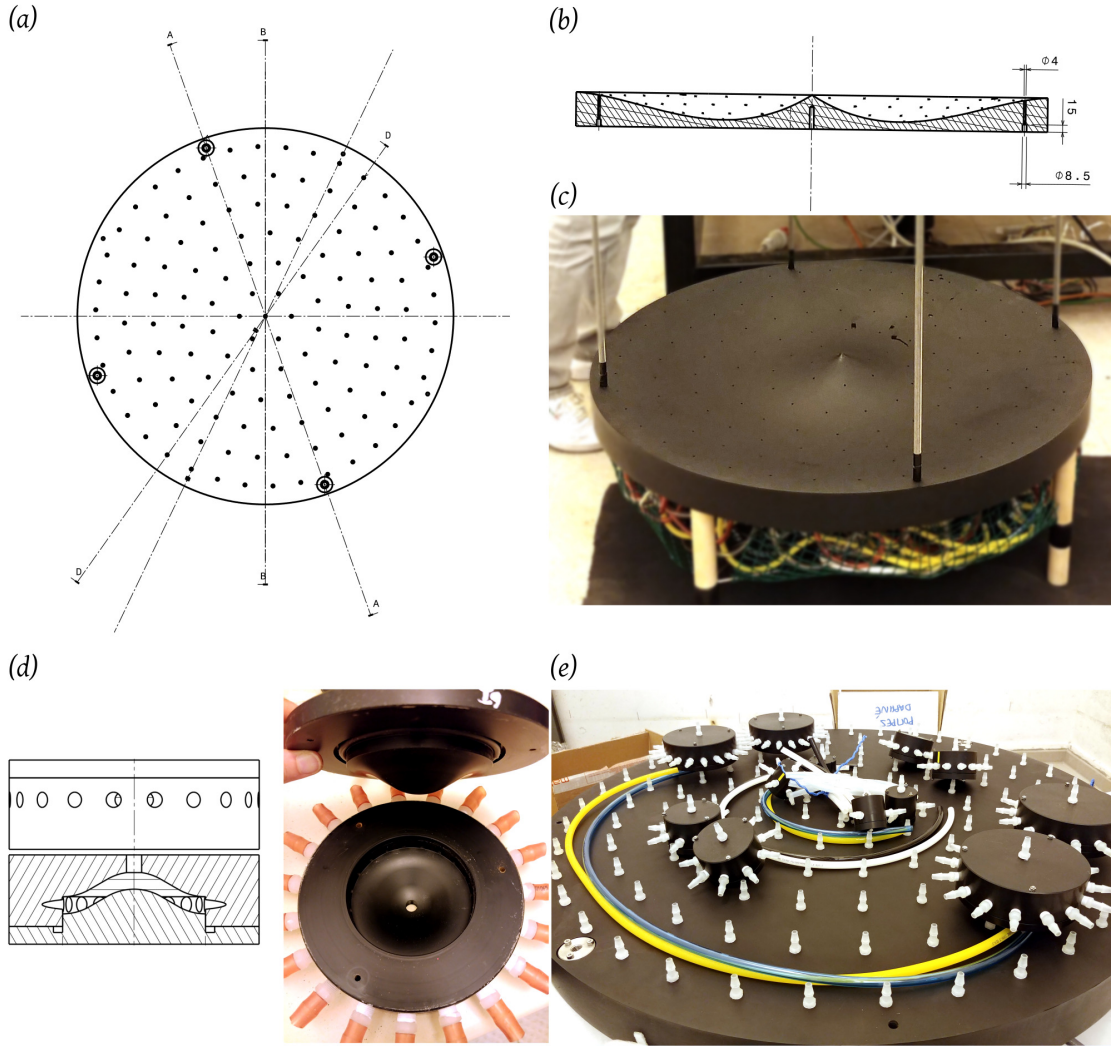

Figure B.1. – Schematics and pictures of the bottom plate and distributors. *(a)* Inlets and outlets distribution on the bottom plate. *(b)* Vertical slice through the bottom plate. *(c)* Picture of the bottom plate. *(d)* Schematic (external view and vertical slice) and picture of a distributor for the sixth ring (19 holes per distributor). *(e)* Picture of the lower side of the bottom plate, before plugging the 128 tubes. Five of the six pairs of distributors are visible.

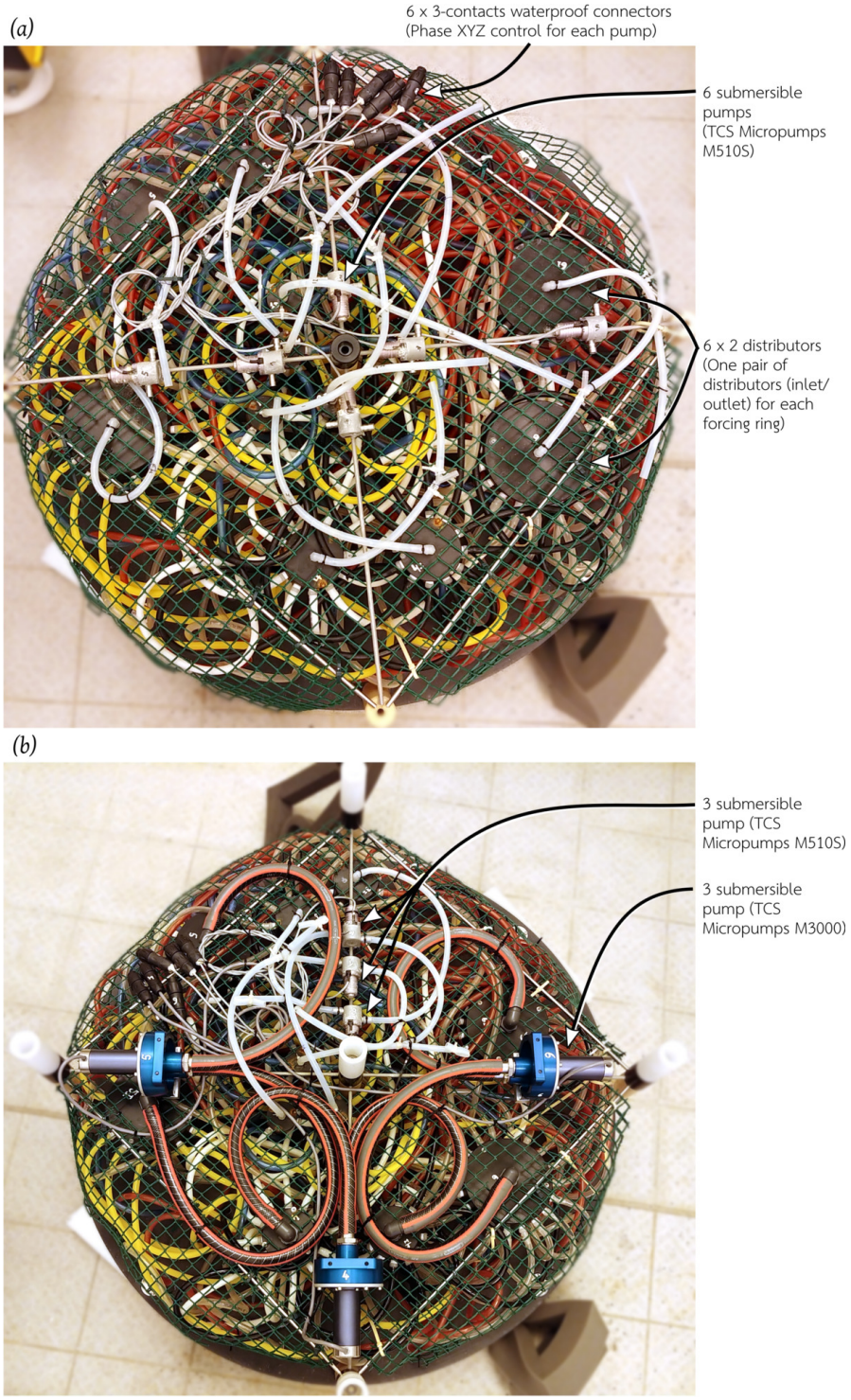

Figure B.2. – Views of the tubing and pumps below the bottom plate through which the forcing is performed. *(a)* First set of pumps. The six pumps are TCS Micropumps M510S. Each pump controls one of the forcing rings, and is linked to two distributors, one for the inlet of the pump, and the second one for the outlet. *(b)* Second set of pumps. The pumps $C_{4,5,6}$ are replaced by TCS Micropumps M3000.

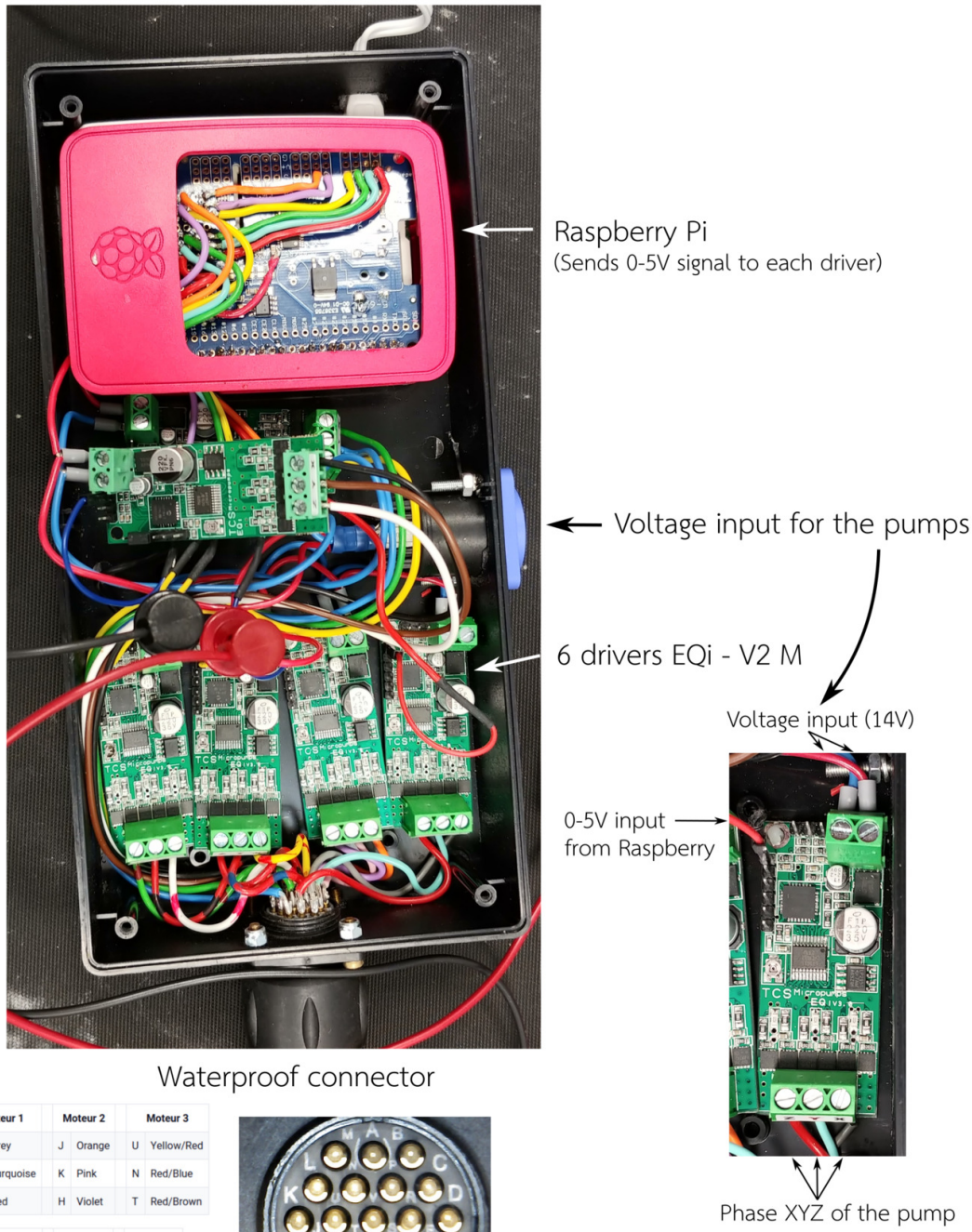

	Moteur 1		Moteur 2		Moteur 3	
X	M	Grey	J	Orange	U	Yellow/Red
Y	L	Turquoise	K	Pink	N	Red/Blue
Z	A	Red	H	Violet	T	Red/Brown

	Moteur 4		Moteur 5		Moteur 6	
X	V	White/Red	C	Green	F	Black
Y	R	Red/Black	B	Blue	G	Brown
Z	P	Green/Red	D	Yellow	E	White

Figure B.3. – Control box for the first set of pumps. The six EQi drivers control each submersible pumps thanks to a 0-5V analog signal coming from the RaspberryPi. The XYZ phase signal is sent to the pumps via a cable which enters the bottom of the tank through a waterproof connector. The total power required when the pumps are at maximum power is of about 180 W. The commands from the drivers are sent to the pumps by passing a cable through the base of the tanks using a waterproof connector (see Fig. B.5).

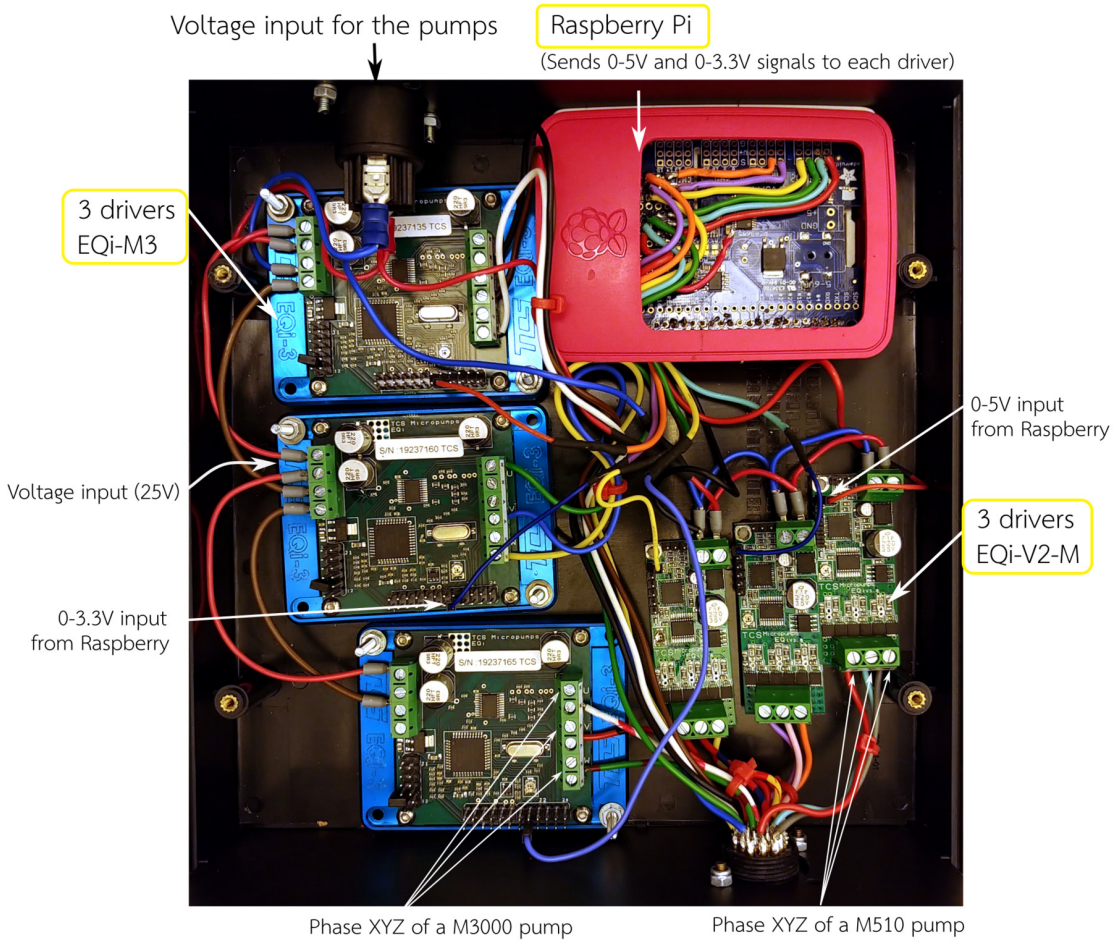

Figure B.4. – Control box for the second set of pumps. The three EQi-V2-M drivers control the three M510S pumps (0-5V signal from the Raspberry), and the three EQi-M3 drivers control the three M3000 pumps (0-3.3V signal from the Raspberry). The XYZ phase signal is sent to the pumps via a cable which enters the bottom of the tank through a waterproof connector. The same power supply as for the first set of pumps is used, but this time, the total power required when the pumps are at maximum power is of about 800 W. The commands from the drivers are sent to the pumps by passing a cable through the base of the tanks using a waterproof connector (see Fig. B.5).

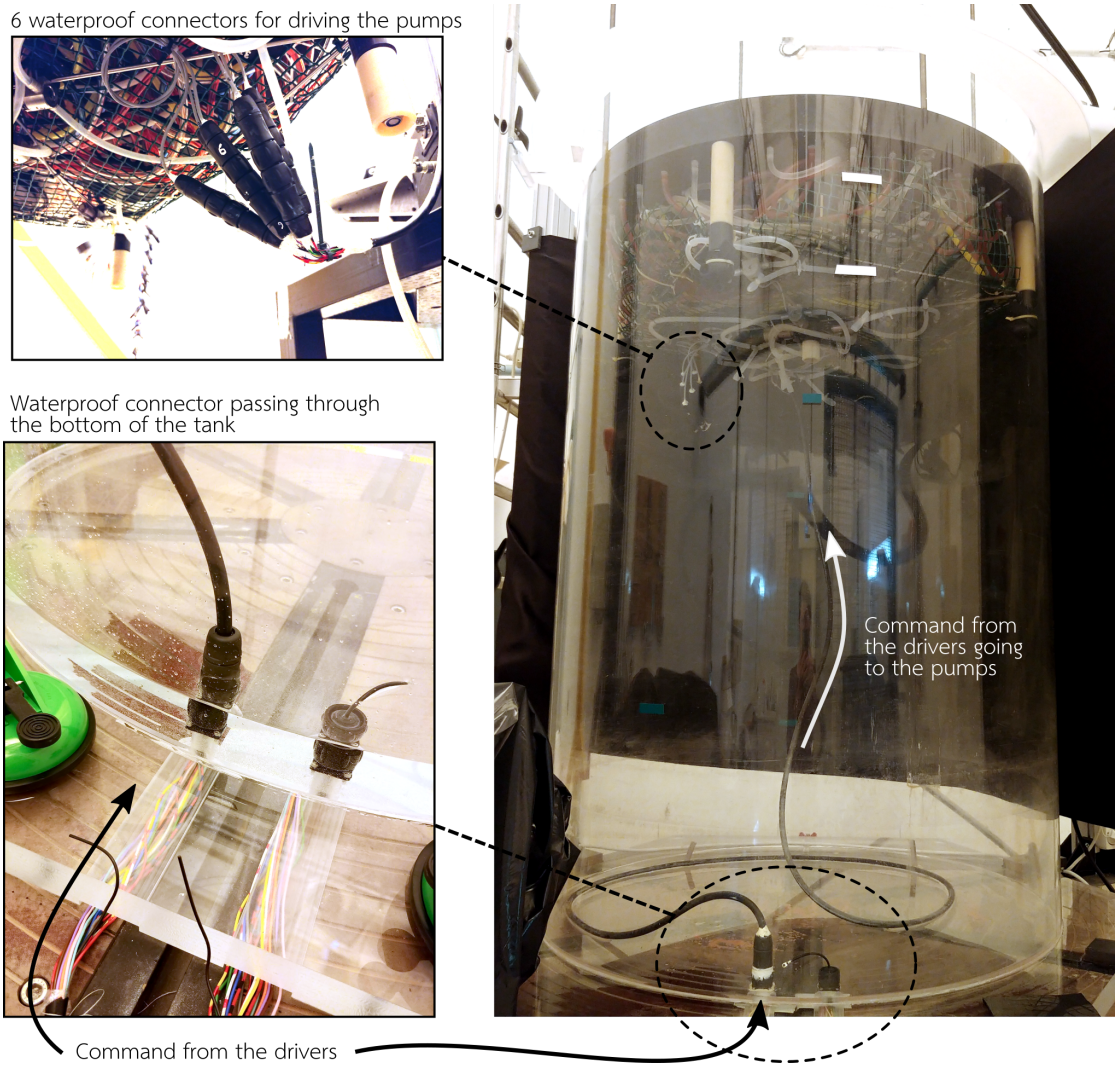

Figure B.5. – Pictures of the waterproof connections between the drivers (Fig. B.3 and B.4) and the submersible pumps which are fixed beneath the bottom plate. The waterproof connectors passing through the bottom of the tank and inside of the tank are SOURIAU Trim Trio UTS Connectors (refs. UTS014E19S, UTFD14B, UTS6JC14E19P).

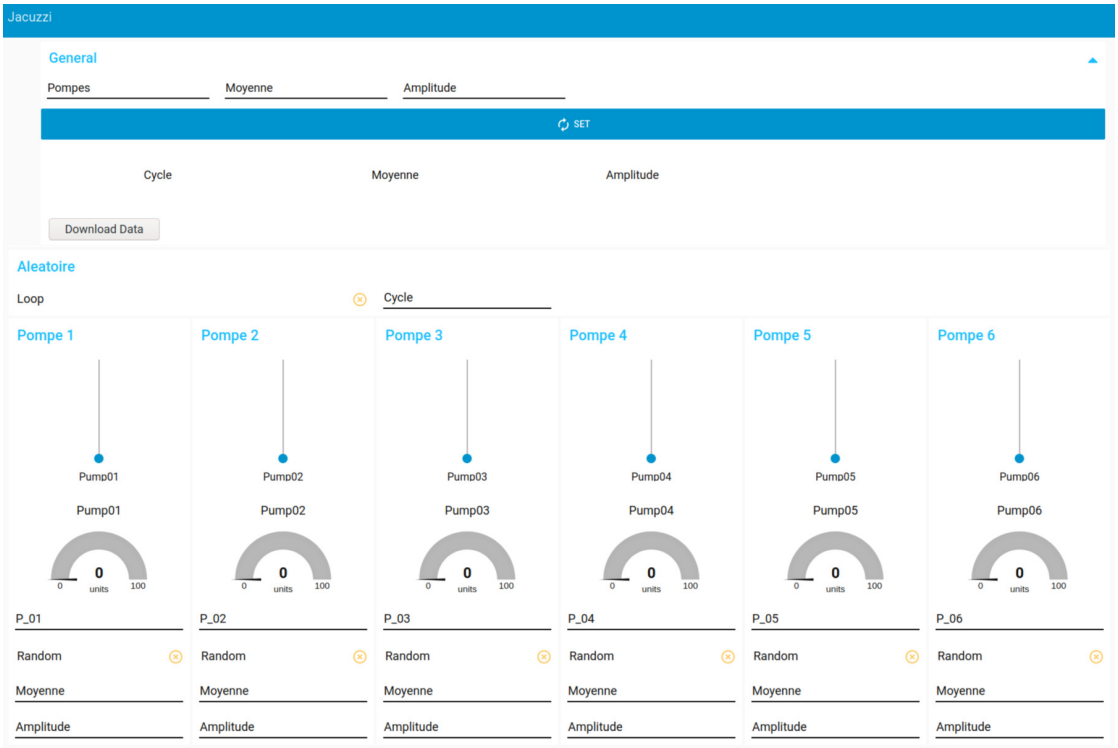

Figure B.6. – Webpage interface generated using Node-RED to remotely control the six forcing pumps. The power of a given pump is chosen between 0 and 100, the message is sent to the Raspberry through a MQTT protocol, and in return the Raspberry sends a signal between 0-5V to the corresponding driver of the pump. A "random" mode can be activated for each pump, in which their power fluctuates around a given mean with a prescribed amplitude and time step. In the latest version, we added an option to completely switch of a given pump periodically (not shown).

B.2. Calibration of the first set of pumps

For the first set of pumps that we used, the six pumps were identical (TCS Micropump, M510S-V), and can be seen in Fig. B.2*(a)*. Their maximum flow rate, without any pressure drop, is of about 8 $\mathrm{mL\,min^{-1}}$. These pumps operate at a maximum current of 2 A and a maximum pressure of 1.5 bar. Each pump is controlled by an EQi-V2 M brushless controller (Fig. B.3).

The forcing is calibrated *in situ* on the horizontal laser plane used for PIV measurements, while the system is in solid-body rotation. For each pump C_i, we turn it on at a given fraction of its maximum power. We measure the corresponding velocity field, and define a region of interest (ROI) around the chosen ring, limited by two circles of radius $R_i + \frac{\Delta R}{2}$ and $R_i - \frac{\Delta R}{2}$ where ΔR is the spacing between two consecutive rings. We measure the total RMS velocity on this ROI, 12 to 15 seconds after the forcing was turned on, i.e. when the forced vortices have reached their maximum vorticity but before the zonal jets fully develop. This measurement was realized for each ring separately and several pump powers. The corresponding data are represented in Fig. B.7 and B.8 for the two different sets of pumps that we used. We then performed a linear fit of the induced RMS velocity as a function of power to obtain a calibration law for each pump. In the main text, the forcing amplitude U_f corresponds to the mean of the six RMS velocity deduced from our calibration, knowing the power fraction for each pump.

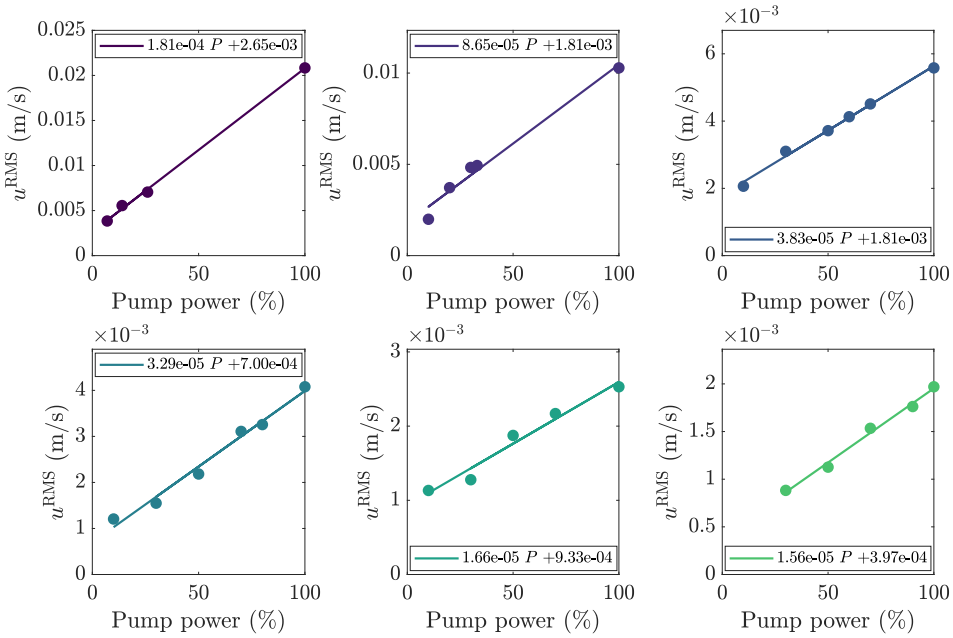

Figure B.7. – Calibration of the experimental forcing for the first set of pumps. Left to right and top to bottom: rings C1 to C6. The total RMS velocity inside of a region of interest is plotted for each pump separately, and several fractions of the pump maximum power (dots). The lines are the result of a linear fit between the induced velocity and the pump power.

B.3. Calibration of the second set of pumps

With the first set of pumps, because of the increased pressure drop due to the increasing number of tubes from ring C_1 to C_6, the forcing is necessarily reduced at large radii. As can be seen from Fig. B.7, the largest RMS velocity reached by C_6 is smaller than the lowest RMS velocity of C_1. Note that their is a minimum velocity for each pump because there is a power threshold below which the pump would not prime. The sixth ring is hence for instance always less forced than the first one. This issue led us to change half of the submersible pumps to ones with higher flow rates (Fig. B.2).

For the second set of pumps that we used, the three pumps controlling C_1, C_2 and C_3 are the previous ones (TCS Micropump, M510S-V). The pumps controlling C_4, C_5 and C_6 are replaced by new models, TCS Micropumps M3000, which maximum flow rate, without any pressure drop, is of about 50 $\mathrm{L\,min^{-1}}$, which is about 6 times larger than the previous pumps (see Fig. B.2 *(b)* for a picture of the new pumps). These pumps operate at a maximum power of 200 W. The three M3000 pumps are controlled by EQi-M3 brushless controllers, controlled by a 0-3.3V input from the Raspeberry Pi (Fig. B.4).

The same process as for the first set of pumps is employed for calibration. The resulting RMS velocities as a function of the pumps power are represented in Fig. B.8. This figure shows that with the new set of pumps, we are able to perform a homogeneous forcing except for ring C_3 which will always be less forced than the others.

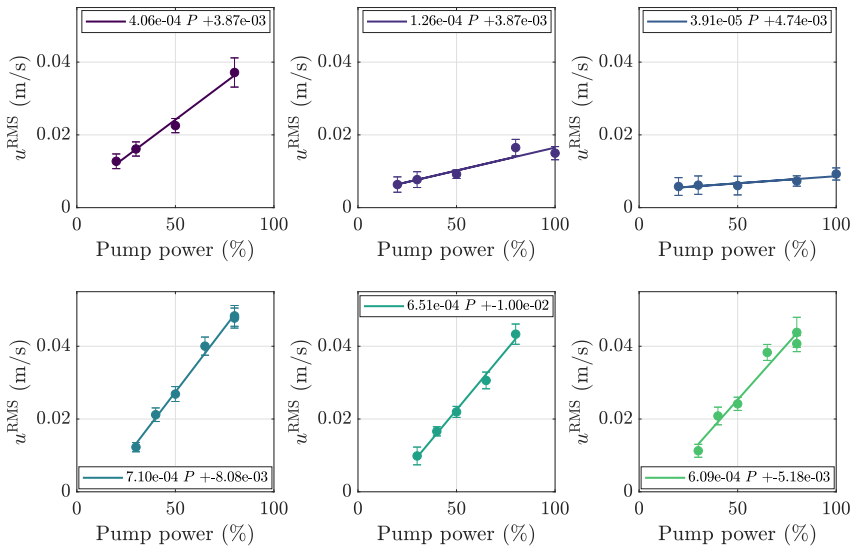

Figure B.8. – Calibration of the experimental forcing for the second set of pumps. Left to right and top to bottom: rings C1 to C6. The total RMS velocity inside of a region of interest is plotted for each pump separately, and several fractions of the pump maximum power (dots). The lines are the result of a linear fit between the induced velocity and the pump power.

B.4. Correction of optical distortion from the free surface

Due to the paraboloidal shape of the water free surface, the images recorded on the horizontal laser plane are distorted. To correct this distortion, we use the calibration tool included in the DANTEC acquisition software, DynamicStudio. We built our own calibration target, represented in Fig. B.9. It consists in a 1 cm-thick disk of Plexiglas, into which we drilled regularly spaced holes on a cartesian grid. The centre marker is larger, and the four adjacent ones are smaller, in order to define the origin and the axes of the coordinate system respectively. The holes were filled with black silicon, and the lower face of the target was painted in white to maximize the contrast with the black markers of the calibration target. This calibration target was placed inside of the tank at the height of the horizontal laser plane (Fig. B.9*(b)*), we filled the tank with water, and we recorded images of the calibration target through the water layer once solid body rotation was reached (Fig. B.9*(c)*).

Once the image of the calibration target was acquired, we used the *Imaging Model Fit* process of DynamicStudio software. We use the third order polynomial model fit, for which the position of each point after the correction (X, Y, Z) is related to the location of each point (x, y) in the image acquired by the camera by the relation:

$$
\begin{aligned}
\begin{pmatrix} x \\ y \end{pmatrix} = \quad & \boldsymbol{A_{000}} \\
+ \quad & \boldsymbol{A_{100}} X + & \boldsymbol{A_{010}} Y + & & \boldsymbol{A_{001}} Z \\
+ \quad & \boldsymbol{A_{110}} XY + & \boldsymbol{A_{101}} XZ + & & \boldsymbol{A_{011}} YZ \\
+ \quad & \boldsymbol{A_{200}} X^2 + & \boldsymbol{A_{020}} Y^2 + & & \boldsymbol{A_{002}} Z^2 \\
+ \quad & \boldsymbol{A_{300}} X^3 + & \boldsymbol{A_{210}} X^2 Y + & & \boldsymbol{A_{201}} Y^2 Z \\
+ \quad & \boldsymbol{A_{030}} Y^3 + & \boldsymbol{A_{120}} XY^2 + & & \boldsymbol{A_{021}} Y^2 Z \\
+ \quad & \boldsymbol{A_{102}} XZ^2 + & \boldsymbol{A_{012}} YZ^2 + & & \boldsymbol{A_{111}} XYZ
\end{aligned}
$$

An example of the coefficients resulting from the calibration is given in Fig. B.9*(d)*. Note that in our case, the calibration target is purely horizontal, thus all the coefficients related to the vertical position Z are null.

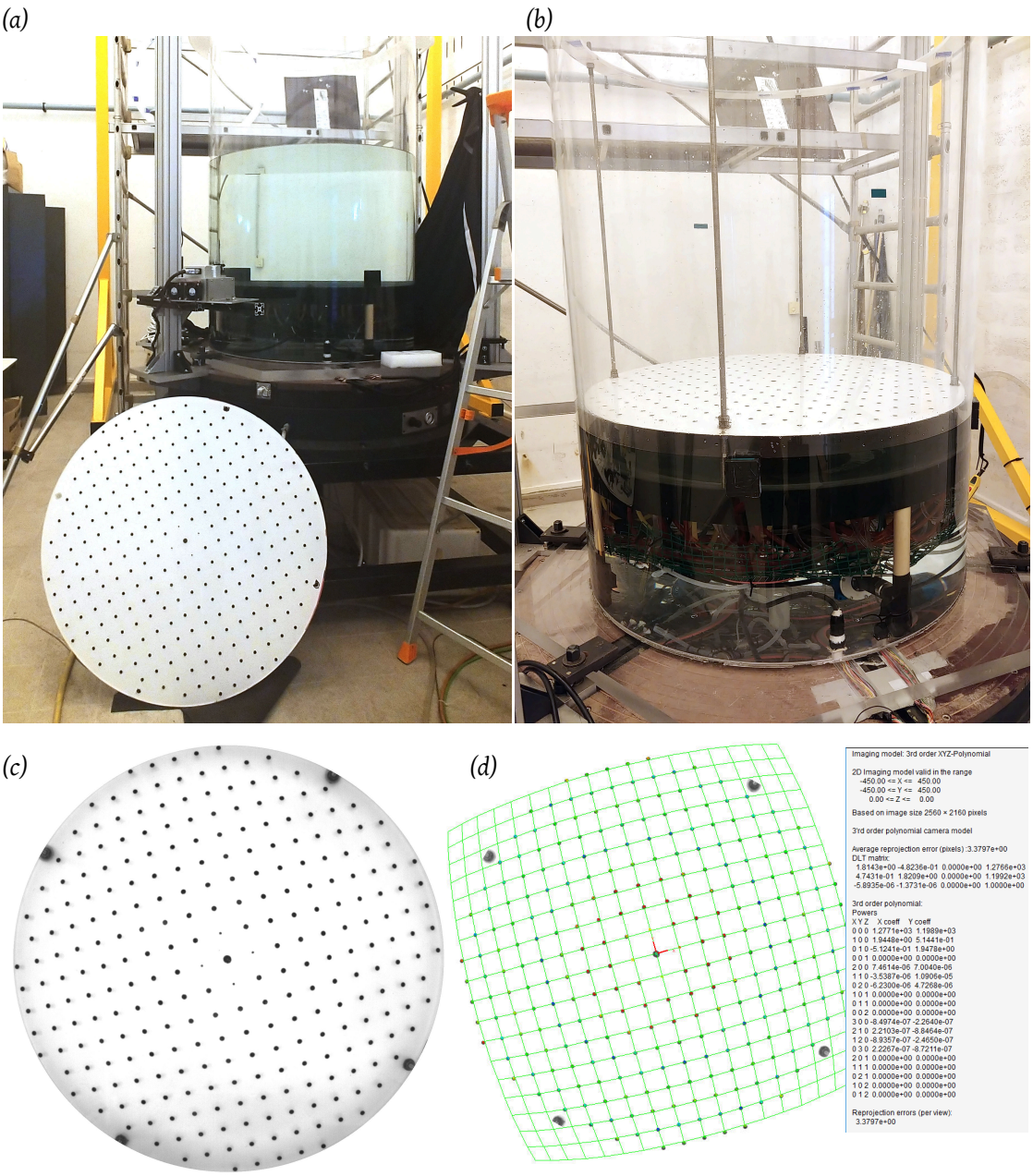

Figure B.9. – Optical calibration. *(a)* Picture of the calibration target. *(b)* Calibration target once placed at the level of the horizontal laser plane used for PIV. *(c)* Picture of the target through the water layer once solid body rotation is reached: the distortion of the initially cartesian pattern is visible. *(d)* Result of the projection of the target markers true position onto the image acquired by the camera using the third order polynomial model fit from DynamicStudio software. The coefficients on the right are the results of the third order polynomial fit.

B.5. Beta-effect for various rotation rates and a curved or flat bottom

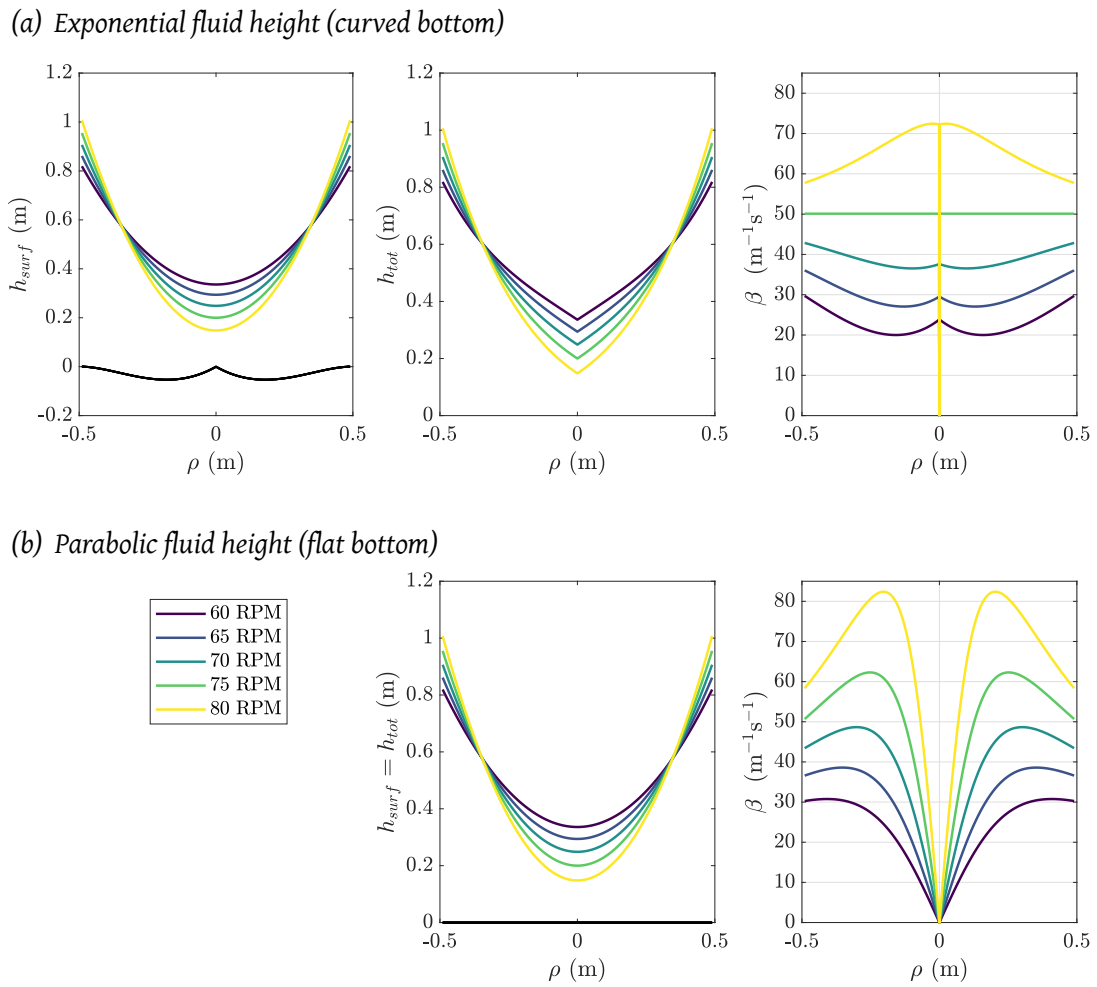

Figure B.10. – Topographic β-effect obtained for various rotation rates and a curved *(a)* or flat *(b)* bottom. From left to right: vertical coordinate of the fluid free surface, total fluid height, and associated topographic β-effect, $\beta = |f/h\, \mathrm{d}_\rho h|$. *(a)* For the curved bottom designed for our experiment, β is exactly constant at 75 RPM, and slightly inhomogeneous for other rotation rates. *(b)* For a flat bottom, the β-effect is always inhomogeneous, and in particular tends to zero at the centre of the tank.

C. Quasi-geostrophic modelling of the Jacuzzi (zonal jets) experiment

C.1. Motivation

Because of fast background rotation, or equivalently the small Rossby number of the system, the geostrophic balance dominates the experimental flow. As a consequence, the flow is quasi two-dimensional, but the curvature of the free-surface as well as the friction over the bottom (Ekman pumping) induce three-dimensional effects. Nevertheless, the weakness of these effects allows their incorporation into quasi-two-dimensional physical models, the so-called "quasi-geostrophic" (QG) models.

These models were first developed in the "shallow-water" community focusing on atmospheric and oceanic dynamics. Starting from the shallow-water equations, the QG approximation consists in this case in expanding variables as asymptotic series using the Rossby number $Ro = U/fL$, where U and L are typical velocity and length scale of the flow, as a small parameter (see e.g. Vallis 2017; Pedlosky 2013). The hypothesis that $Ro \ll 1$ is at the origin of the name of the QG approximation: if the Rossby number is infinitely small, the flow is in geostrophic balance which means that the Coriolis force balances the horizontal gradient of pressure. Shallow water QG models also originally assume that the variations of the fluid free surface height is small compared to the total fluid depth. This is relevant to describe oceans and atmospheres which are thin fluid layer, but in our experiment, this is not the case since the fluid height observes strong variations, of order of the mean fluid height itself. But luckily, another class of QG models has been developed in a "deep" framework by the core dynamics community with a focus on spherical rotating convection (e.g. Busse 1970; Cardin et al. 1994; Aubert et al. 2003; Schaeffer 2004; Gillet et al. 2006; Guervilly et al. 2017). In this framework, it is important to take into account the vertical motions generated at both boundaries: the variation of the fluid height due to the spherical geometry leads to a topographic β-effect, and the vertical Ekman pumping occurring at the solid boundaries allows to properly represent the dissipation in the Ekman boundary layers. In our case, we deal with a simpler geometry where the Ekman boundary layer, situated at the bottom of the tank, is almost horizontal and thus not as complicated as for a spherical interface, and we have a free surface which defines a simple evolution of the fluid height with radius. Nevertheless, the methods are identical.

In sections C.2 and C.3, we derive the conventional quasi-geostrophic model corresponding to our experimental setup, "conventional" meaning that we retain only the linear terms of the β-effect and Ekman pumping. This reduced model allows us to:

- demonstrate that the free-surface curvature leads to a β-effect analogous to a linear variation of the Coriolis parameter with radius (i.e. to a β-plane);
- express the linear friction due to the Ekman pumping.

We use this conventional model in chapter 3 to unveil the physical mechanism of the transition observed experimentally.

Besides theoretical modelling, we also use a slightly different QG model to carry numerical simulations of the experiment. Indeed, in our problem, 3D direct numerical simulations (DNS) are very computationally demanding, namely because the simulation has to resolve both very large scale structures (the jets) and thin Ekman boundary layers that are essential for the long term dynamics. By performing numerical simulations, our goal is to guide and complement the experiment, for instance by exploring the forcing amplitude, scale and spatial heterogeneity, which is difficult to do experimentally because it would require to change the bottom plate and the associated tubing. Additionally, we use simulations as a tool to study extreme regimes that are not reachable experimentally, such as larger β-effects or smaller Ekman numbers which

would require too high rotation rates. For that purpose, DNS are clearly not adapted. Instead, we aim at using a QG model to reduce the momentum equations to a set of 2D equations while incorporating friction by "parametrizing" the effect of the Ekman boundary layers instead of resolving them. In section C.4, we derive the QG equations used in our numerical code. The difference with the conventional QG model is that, following Sansón et al. (2000, 2002) we retain higher order, non-linear terms for the Ekman pumping and β-effect.

C.2. Derivation of the quasi-geostrophic model

We use the cylindrical coordinates (ρ,ϕ,z) with z oriented downward and $(\mathbf{e}_\rho,\mathbf{e}_\phi,\mathbf{e}_z)$ the associated unit vectors (figure 3.2). We consider the flow of an incompressible fluid of constant kinematic viscosity ν and density ρ_f, rotating around the vertical axis at a constant rate $\mathbf{\Omega}=\Omega\,\mathbf{e}_z$. In our setup, $\Omega>0$ since the turntable rotates in the clockwise direction. We denote the velocity field $\mathbf{u}=(u_\rho,u_\phi,u_z)_{\mathbf{e}_\rho,\mathbf{e}_\phi,\mathbf{e}_z}$. The fluid is enclosed inside a cylinder of radius R. The lower boundary is a rigid plate located at $z=0$ and the upper boundary is a free surface defined by $z=-h(\rho)$. Note that here we assume that our experiment, which have a parabolic free-surface and a curved bottom, can be modelled with a flat bottom and an exponential free-surface. Doing so, we neglect the influence of the shape of the bottom topography on the vertical velocity (see equation (C.8)). For a bottom which is almost flat, we expect these effects to be of small amplitude, but one should keep in mind that the presently derived model is only valid for relatively smooth bottom topographies for which we can use the expression of the Ekman pumping over a flat surface.

We start from the continuity and horizontal Navier-Stokes equations in the rotating frame:

$$\frac{\partial u_\rho}{\partial t}+u_\rho\frac{\partial u_\rho}{\partial\rho}+\frac{u_\phi}{\rho}\frac{\partial u_\rho}{\partial\phi}-\frac{u_\phi^2}{\rho}-f u_\phi = -\frac{1}{\rho_f}\frac{\partial P}{\partial\rho}+\nu\left(\nabla^2 u_\rho-\frac{u_\rho}{\rho^2}-\frac{2}{\rho^2}\frac{\partial u_\phi}{\partial\phi}\right), \tag{C.1}$$

$$\frac{\partial u_\phi}{\partial t}+u_\rho\frac{\partial u_\phi}{\partial_\rho}+\frac{u_\phi}{\rho}\frac{\partial u_\phi}{\partial\phi}+\frac{u_\phi u_\rho}{\rho}+f u_\rho = -\frac{1}{\rho_f}\frac{1}{\rho}\frac{\partial P}{\partial\phi}+\nu\left(\nabla^2 u_\phi-\frac{u_\phi}{\rho^2}+\frac{2}{\rho^2}\frac{\partial u_\rho}{\partial\phi}\right), \tag{C.2}$$

$$\frac{1}{\rho}\frac{\partial(\rho u_\rho)}{\partial\rho}+\frac{1}{\rho}\frac{\partial u_\phi}{\partial\phi}+\frac{\partial u_z}{\partial z} = 0, \tag{C.3}$$

where $\nabla^2\cdot=\partial^2_\rho\cdot+\partial^2_\phi\cdot/\rho^2+\partial_\rho\cdot/\rho$. The Coriolis parameter is $f=2\Omega$ and $P=p+\rho_f g z-\rho_f f^2\rho^2/8$ is the reduced pressure incorporating the gravity and centrifugal effects. Note that if we neglect the vertical dependence of the horizontal velocity, we keep it for the vertical velocity w. Indeed, as previously explained, w is expected to strongly vary close to the top and bottom boundaries, and we want to take into account these effects on the horizontal velocity divergence.

The curl of the Navier-Stokes equation leads to the vorticity equation

$$\frac{\partial\zeta}{\partial t}+u_\rho\frac{\partial\zeta}{\partial\rho}+\frac{u_\phi}{\rho}\frac{\partial\zeta}{\partial\phi}+(\zeta+f)\,\boldsymbol{\nabla}_h\cdot\boldsymbol{u}=\nu\nabla^2\zeta, \tag{C.4}$$

where $\zeta=(\boldsymbol{\nabla}\times\boldsymbol{u})\cdot\boldsymbol{e}_z=(\partial_\rho(\rho u_\phi)-\partial_\phi u_\rho)/\rho$ is the vertical component of the vorticity and $\boldsymbol{\nabla}_h\cdot\boldsymbol{u}$ is the horizontal divergence

$$\boldsymbol{\nabla}_h\cdot\boldsymbol{u}=\frac{1}{\rho}\frac{\partial(\rho u_\rho)}{\partial\rho}+\frac{1}{\rho}\frac{\partial u_\phi}{\partial\phi}. \tag{C.5}$$

The last term of the left hand side of equation (C.4), the vortex stretching term, involves the horizontal divergence of the flow which can be estimated from equation (C.3) after integration from $z=-h(\rho)$ to $z=0$ (z oriented downward) to unveil the Ekman pumping through the

vertical velocity:

$$\boldsymbol{\nabla}_h \cdot \boldsymbol{u} = -\frac{1}{h(\rho)} \int_{z=-h}^{0} \frac{\partial u_z}{\partial z}\, \mathrm{d}z = \frac{u_z\big|_{z=-h} - u_z\big|_{z=0}}{h(\rho)}. \tag{C.6}$$

The vertical velocity at the free surface $u_z\big|_{z=-h}$ is given by the kinematic condition

$$u_z\big|_{z=-h} = -\left(\frac{\partial h}{\partial t} + u_\rho \frac{\partial h}{\partial \rho} + \frac{u_\phi}{\rho}\frac{\partial h}{\partial \phi}\right) = -u_\rho \frac{\partial h}{\partial \rho}, \tag{C.7}$$

since h is axisymmetric and we neglect any temporal variations of the fluid height (rigid lid approximation). The vertical velocity at the bottom $u_z\big|_{z=0}$ results from the no-slip boundary condition generating an Ekman pumping. According to linear Ekman theory, for a flat bottom and small Rossby number, the vertical velocity at the top of the boundary layer is proportional to the relative vorticity in the interior flow (see section 5.7 in Vallis 2017):

$$u_z\big|_{z=0} = -\frac{1}{2}\delta\zeta = -\frac{1}{2}E^{1/2} h_0 \zeta, \tag{C.8}$$

where $\delta = \sqrt{2\nu/f}$ is the thickness of the Ekman layer and $E = 2\nu/(f h_0^2)$ is the Ekman number, h_0 being the mean fluid height. The horizontal divergence (C.6) is then

$$\nabla_h \cdot \mathbf{u} = -\frac{u_\rho}{h}\frac{\mathrm{d}h}{\mathrm{d}\rho} + \frac{E^{1/2}}{2}\frac{h_0}{h}\zeta. \tag{C.9}$$

The squeezing and stretching of vorticity is hence due to both the changes in the fluid depth and the vertical velocity induced by the Ekman boundary layer.

Substitution of the horizontal divergence (C.9) in the vorticity equation (C.4) yields

$$\frac{\partial \zeta}{\partial t} + u_\rho \frac{\partial \zeta}{\partial \rho} + \frac{u_\phi}{\rho}\frac{\partial \zeta}{\partial \phi} \underbrace{-(\zeta + f)\frac{u_\rho}{h}\frac{\mathrm{d}h}{\mathrm{d}\rho}}_{\text{Topographic } \beta\text{−effect}} \underbrace{+\frac{E^{1/2}}{2}\frac{h_0}{h}(\zeta + f)\zeta}_{\text{Ekman pumping}} = \nu\nabla^2\zeta, \tag{C.10}$$

C.3. Classical QG model used for theoretical modelling

As stated before, we stand in the limit where the local Rossby number of the flow $Ro_\zeta = \zeta/f$ is small, thus $\zeta \ll f$. Retaining only the linear part of the β-effect and Ekman pumping, we retrieve the classical 2D barotropic vorticity equation in the β-plane approximation:

$$\frac{\mathrm{D}\zeta}{\mathrm{D}t} + \underbrace{\beta\, u_\rho}_{\beta\text{−effect}} + \underbrace{\alpha\zeta}_{\text{Ekman friction}} = \underbrace{\nu\nabla^2\zeta}_{\text{Bulk dissipation}}, \tag{C.11}$$

with β the topographic β parameter resulting from the free-surface radial variations and α the linear Ekman friction parameter:

$$\beta = -\frac{f}{h}\frac{\mathrm{d}h}{\mathrm{d}\rho}, \tag{C.12}$$

$$\alpha = \frac{E^{1/2} f h_0}{2h}. \tag{C.13}$$

This classical quasi-2D model of our experiment is used in section 3.4 of chapter 3 to explain the experimentally observed transition between two regimes on zonal jets.

C.4. Advanced QG model used in numerical simulations

C.4.1. Derivation

As previously explained, we complement and guide the experiment with QG numerical simulations, which, compared to the conventional model (C.11) retains higher order non-linear terms from equation (C.10).

We switch to non-dimensional variables using $1/f$ as the timescale and the radius of the tank, R, as the length-scale, and we denote the non-dimensional variables with a prime, such that

$$\zeta = \zeta' f, \tag{C.14}$$
$$u_\rho = u'_\rho f R \tag{C.15}$$
$$u_\phi = u'_\phi f R \tag{C.16}$$
$$\rho = \rho' R \tag{C.17}$$
$$t = t'/f \tag{C.18}$$
$$h = h' R \tag{C.19}$$

We keep the primes in the following to better identify non-dimensional variables, and to avoid confusion with the experimental variables and parameters which are always given in dimensional forms first. Equation (C.10) becomes

$$\frac{\partial \zeta'}{\partial t'} + u'_\rho \frac{\partial \zeta'}{\partial \rho'} + \frac{u'_\phi}{\rho'}\frac{\partial \zeta'}{\partial \phi'} - \frac{u'_\rho}{h'}\frac{\mathrm{d}h'}{\mathrm{d}\rho'}(\zeta'+1) + \frac{E_R^{1/2}}{2h'}(\zeta'+1)\zeta' = \frac{E_R}{2}\nabla'^2\zeta' + F', \tag{C.20}$$

where E_R is the Ekman number based on the radius of the tank, $E_R = 2\nu/(fR^2) = (h_0/R)^2 E$, and we have introduced a forcing term F'. To close this equation, we now need an expression for the horizontal components of the velocity. To do so, we use the definition of ζ to rewrite the expression of the horizontal divergence (equation (C.9)) as a zero-divergence for a modified velocity field:

$$\frac{1}{\rho'}\frac{\partial(\rho' u'_\rho)}{\partial \rho'} + \frac{1}{\rho'}\frac{\partial u'_\phi}{\partial \phi} = -\frac{u'_\rho}{h'}\frac{\partial h'}{\partial \rho'} + \frac{E_R^{1/2}}{2h'}\zeta' \tag{C.21}$$

$$\implies \frac{\partial}{\partial \rho'}\left(\rho'\left[h' u'_\rho - u'_\phi \frac{E_R^{1/2}}{2}\right]\right) + \frac{\partial}{\partial \phi}\left(h' u'_\phi + u'_\rho \frac{E_R^{1/2}}{2}\right) = 0. \tag{C.22}$$

This allows us to define a streamfunction ψ such that

$$h' u'_\rho - u'_\phi \frac{E_R^{1/2}}{2} = \frac{1}{\rho'}\frac{\partial \psi'}{\partial \phi},$$
$$h' u'_\phi + u'_\rho \frac{E_R^{1/2}}{2} = -\frac{\partial \psi'}{\partial \rho'},$$

or equivalently

$$u'_\rho = \frac{1}{h'}\frac{1}{1+E_R h'^{-2}}\left(\frac{1}{\rho'}\frac{\partial \psi'}{\partial \phi} - \frac{E_R^{1/2}}{2h'}\frac{\partial \psi'}{\partial \rho}\right) = \frac{1}{h'}\left(\frac{1}{\rho'}\frac{\partial \psi'}{\partial \phi} - \frac{E_R^{1/2}}{2h'}\frac{\partial \psi'}{\partial \rho'}\right) + \mathcal{O}(E_R h'^{-2}), \tag{C.23}$$

$$u'_\phi = \frac{1}{h'}\frac{1}{1+E_R h'^{-2}}\left(-\frac{E_R^{1/2}}{2h'\rho'}\frac{\partial \psi'}{\partial \phi} - \frac{\partial \psi'}{\partial \rho'}\right) = \frac{1}{h'}\left(-\frac{E_R^{1/2}}{2h'\rho'}\frac{\partial \psi'}{\partial \phi} - \frac{\partial \psi'}{\partial \rho'}\right) + \mathcal{O}(E_R h'^{-2}), \tag{C.24}$$

where we have neglected terms of order greater or equal to $\mathcal{O}(E_R h'^{-2})$, which is justified in

the limit where we stand since h' is of order unity, and $E_R \ll 1$. Physically, this approximation means that the Ekman boundary layers are very thin compared to the fluid height. Substituting the horizontal velocities with their expressions (C.23) and (C.24) into the vorticity equation (C.20), we obtain in its condensed form the final vorticity equation

$$\frac{\partial \zeta'}{\partial t'} + \mathscr{J}(q', \psi') - \frac{E_R^{1/2}}{2h'} \boldsymbol{\nabla}' \psi' \cdot \boldsymbol{\nabla}' q' = \frac{E_R}{2} \nabla'^2 \zeta - \frac{E_R^{1/2}}{2h'} \zeta' (\zeta' + 1) + F' \tag{C.25}$$

where $\mathscr{J}$ is the non-dimensional Jacobian operator in cylindrical coordinates

$$\mathscr{J}(a, b) = \frac{1}{\rho'} \left(\frac{\partial a}{\partial \rho'} \frac{\partial b}{\partial \phi} - \frac{\partial b}{\partial \rho'} \frac{\partial a}{\partial \phi} \right),$$

and we introduced the potential vorticity

$$q' = \frac{\zeta' + 1}{h'}. \tag{C.26}$$

Taking the curl of (C.23)-(C.24), we obtain the modified Poisson equation that links the vorticity and the streamfunction, which closes the system of equations:

$$\zeta' = -\frac{1}{h'} \nabla'^2 \psi' + \frac{1}{h'^2} \boldsymbol{\nabla}' h' \cdot \boldsymbol{\nabla}' \psi' + \frac{E_R^{1/2}}{h'^2} \mathscr{J}(h', \psi'). \tag{C.27}$$

Note that the potential vorticity q' is a materially conserved quantity if we drop the forcing term and neglect viscous effects. Equation (C.25) can indeed be recast as

$$\frac{\partial q'}{\partial t'} + \frac{1}{h' \rho'} \left(\frac{\partial \psi'}{\partial \phi} \frac{\partial q'}{\partial \rho'} - \frac{\partial \psi'}{\partial \rho'} \frac{\partial q'}{\partial \phi} \right) = 0 \tag{C.28}$$

$$\Leftrightarrow \frac{Dq'}{Dt'} = 0. \tag{C.29}$$

C.4.2. Justification for keeping higher order, non-linear terms

In the case of QG models derived for rotating convection (e.g. Cardin et al. 1994; Aubert et al. 2003; Gillet et al. 2006), the Ekman pumping effects are incorporated the same way as we did, except that their geometry is more complicated and the no-slip boundaries cannot be considered as flat. Apart from these geometrical factors, the main difference lies in the fact that in (C.4), it is common in the rotating convection community to assume that the local vorticity ζ is negligible compared to the planetary vorticity f, and retain only the linear terms for the topographic β-effect and Ekman pumping, exactly as we did for the classical model (C.11). In that case, the terms $E_R^{1/2}/2h' \, \boldsymbol{\nabla}\psi' \cdot \boldsymbol{\nabla} q'$ and $\zeta'^2 E_R^{1/2}/2h'$ are removed from equation (C.25). These two terms hence represent corrections due to nonlinear Ekman effects. The first term corrects the potential vorticity advection, while the second one is a correction of vortex stretching effects. Following Sansón et al. (2000, 2002), we argue that these terms should be kept in our simulations since they are at least of same order as the term $E_R/2\nabla^2\zeta'$ which represents the lateral and bulk viscous effects.

This can be verified by introducing the local Rossby number, based on the local vorticity, $Ro_\zeta = \zeta / f = \zeta'$ and the global Rossby number, based on a typical velocity U and tank radius, $Ro = U/fR$. In our case, we are in a regime where both the Ekman and global Rossby numbers are small, meaning that rotation dominates respectively viscous effects and inertia. Both

conditions are mandatory to legitimately assume a bidimensionalization of the flow. However, the local Rossby number may not be small and the local vorticity ζ associated with small turbulent eddies may be of same order than the rotation rate $f/2$, which is indeed verified in our simulations. This justifies the fact that we keep supplementary non-linear terms compared to other studies. Using the (non-dimensional) Ekman spin-down time scale $E^{-1/2}$ as the reference time scale, the different terms of equation (C.25) are indeed of order

$$\begin{array}{lll} a. & \dfrac{\partial \zeta'}{\partial t'} & \sim Ro_\zeta E^{1/2} \qquad \sim 3\times10^{-5}, \\ b. & \mathscr{J}(q',\psi') & \sim (1+Ro_\zeta)Ro \qquad \sim 1\times10^{-4}, \\ c. & \dfrac{E^{1/2}}{2h'}\nabla\psi'\cdot\nabla q' & \sim \dfrac{E^{1/2}}{2}(1+Ro_\zeta)(Ro) \qquad \sim 3\times10^{-8}, \\ d. & \dfrac{E}{2}\nabla^2\zeta' & \sim \dfrac{E}{2}Ro_\zeta \qquad \sim 1\times10^{-8}, \\ e. & \dfrac{E^{1/2}}{2h'}\zeta'^2 & \sim \dfrac{E^{1/2}}{2}Ro_\zeta^2 \qquad \sim 3\times10^{-6}, \\ f. & \dfrac{E^{1/2}}{2h'}\zeta' & \sim \dfrac{E^{1/2}}{2}Ro_\zeta \qquad \sim 3\times10^{-5}, \end{array} \tag{C.30}$$

where we used $E\sim10^{-7}$, $Ro_\zeta\sim10^{-1}$, $Ro\sim10^{-3}$. The two non-linear terms discussed (c. and e.) are greater or equal to the lateral and bulk viscous effects (d.) and should not be neglected in our case.

C.4.3. Forcing

For now, we have introduced the forcing as an additional source of vorticity (term F' in equation (C.25)). The goal is to reproduce the experimental forcing such that the QG numerical model can be used as a guide and complement the experimental exploration.

In the experiment, because of the Coriolis effect, each inlet or outlet generates respectively a small cyclone or anticyclone right above it. This process can be modelled as a stationary source of vorticity in the form of positive or negative Gaussian sources of vorticity of radius ℓ_f distributed on a prescribed array. We thus define N forcing points distributed over the numerical domain, and at each point, we place a Gaussian source of vorticity such that

$$F'(x',y') = F_0' \sum_{i=1}^{N} (-1)^i \exp\left(-\left[\frac{x'-x_i'}{\ell_f}\right]^2 - \left[\frac{y'-y_i'}{\ell_f}\right]^2 \right), \tag{C.31}$$

where (x',y') are non-dimensional cartesian coordinates, the pairs (x_i',y_i'), $i\in[\![1,N]\!]$ are the centre of each forcing vortex, ℓ_f their radius and F_0 the forcing amplitude. In the simulations presented in the manuscript, these vorticity sources are distributed over a polar array such that the distance between two rings and between two adjacent vortices is approximately the same (this condition cannot be rigorously verified because of the periodicity of the domain in the azimuthal direction). We also performed simulations with a cartesian forcing pattern. In any case, there is the same number of positive or negative vorticity sources such that there is no net angular momentum introduced by our forcing. For the polar pattern, there is also as many positive as negative sources on each ring such that the zonally-averaged forcing term is zero by construction (there is no direct acceleration of the zonal flow).

C.4.4. Zonal flow evolution equation

We perform a Reynolds decomposition of the flow by writing the velocity field as an azimuthal (zonal) average plus some fluctuations:

$$\langle X\rangle_\phi = \frac{1}{2\pi}\int_{\phi=0}^{2\pi} X\,d\phi, \tag{C.32}$$

$$u'_\phi = \langle u'_\phi\rangle_\phi + u''_\phi = U'_\phi(\rho,t) + u''_\phi(\rho,\phi,t) \tag{C.33}$$

$$u'_\rho = \langle u'_\rho\rangle_\phi + u''_\rho = U'_\rho(\rho,t) + u''_\rho(\rho,\phi,t). \tag{C.34}$$

Note that the zonally-averaged radial velocity, U'_ρ, is not zero because of the Ekman pumping. Instead, from (C.21) we have

$$U'_\rho = \frac{E_R^{1/2}}{2h'}U'_\phi. \tag{C.35}$$

Taking the zonal mean of the ϕ-component of the momentum equation (C.2) gives an equation for the mean flow evolution:

$$\frac{\partial U'_\phi}{\partial t'} + U'_\rho\frac{\partial U'_\phi}{\partial \rho'} - \frac{U'_\phi U'_\rho}{\rho'} + U'_\rho = \underbrace{-\left\langle u''_\rho\frac{\partial u''_\phi}{\partial \rho'} - \frac{u''_\phi u''_\rho}{\rho'}\right\rangle_\phi}_{\mathscr{R}(\rho,t)} + \frac{E_R}{2}\left(\nabla^2 U'_\phi - \frac{U'^2_\phi}{\rho'^2}\right). \tag{C.36}$$

Equation (C.36) shows that the zonal flow is driven by non-linear interactions between eddies, $\mathscr{R}$. This term corresponds to the divergence of horizontal Reynolds stresses, sometimes referred to as the eddy momentum flux.

C.4.5. Numerical methods

We solve the vorticity-stream-function system (C.25)-(C.27) with a no-slip boundary condition at the outer boundary, and a free-slip condition at the inner boundary, the latter being introduced at $\rho'_i = 0.05$ to avoid the singularity at the centre of the domain. The unknown ψ' and ζ' are decomposed into their Fourier components up to degree $m = 2048$ and we use a pseudo-spectral method in the azimuthal direction with the $2/3^{\text{rd}}$-rule dealiasing method. In the radial direction, we use centred finite differences of fourth-order on 1024 points. Time integration is performed with an implicit Crank-Nicolson scheme for the linear operator, applied directly in the Fourier space. An explicit third-order Adams Bashforth scheme is used for the non-linear terms. We use an adaptative time-step so that the CFL stability condition is verified, with a safety factor of 0.1. The code is parallelized using MPI, and we typically ran the simulations over 64 CPUs. Except when explicitly stated, the simulations presented in this thesis were realized with an Ekman number $E_R = 1.25\times10^{-7}$. The typical computational time is then of ~20 hours.

D. Bessel-Fourier decomposition for kinetic energy spectra

In this appendix, we first describe the idea of the Bessel-Fourier transform with the example of a continuous function on a polar domain (Wang et al. 2008). We then briefly explain the methods used to compute the associated discrete transform, given that our velocity fields are measured on discrete grids.

D.1. Principle for continuous functions

The following description for continuous functions is a summary of the methods described in Wang et al. (2008) relevant for our experimental flows.

Basis functions Given the rotational symmetry of the experimental 2D velocity fields obtained from PIV, we perform a Fourier-like analysis relevant in the polar system of coordinates (ρ, ϕ). The basis functions, that is the eigenfunctions of the Laplacian, are separable in polar coordinates:

$$\Psi(\rho, \phi) = R(\rho)\Phi(\phi). \tag{D.1}$$

Owing to the periodicity in ϕ, i.e. the single-value requirement $\Phi(\phi) = \Phi(\phi + 2\pi)$, the angular part of these basis functions is

$$\Phi_m(\phi) = \frac{1}{\sqrt{2\pi}} e^{im\phi}, \tag{D.2}$$

where m is an integer. This angular part satisfy the orthogonality relation

$$\int_{-\infty}^{+\infty} e^{ik_1 x} \left[e^{ik_2 x}\right]^* dx = 2\pi\delta(k_1 - k_2). \tag{D.3}$$

The associated transform in angular coordinate is thus the classical 1D Fourier transform.

The radial basis functions are Bessel functions of order m, $J_m(k\rho)$ where the parameter k can take either continuous or discrete values depending on whether the considered domain is infinite of finite. In our case the functions are defined on a domain of finite maximum radius R and we have zero-value boundary conditions for the basis functions. A set of k values can be determined such that the radial basis functions are mutually orthogonal on the finite interval $[0, R]$. More precisely, the zero-value boundary condition leads to $k_{nm} = \alpha_{nm}/R$, where α_{nm} are the positive zeros of the Bessel function of order m, denoted J_m. The normalized radial basis functions can then be expressed as

$$R_{nm}(\rho) = \frac{1}{\sqrt{N_{nm}}} J_m(k_{nm}\rho), \tag{D.4}$$

with

$$N_{nm} = \frac{R^2}{2} J_{m+1}^2(\alpha_{nm}). \tag{D.5}$$

$\{R_{nm} | n = 1, 2, \cdots\}$ form an orthonormal basis on the interval $[0, R]$, and each R_{nm} has $n-1$ zeros on $[0, R]$. Similarly to the complex exponential, these basis functions satisfy an orthogonality relation

$$\int_0^R J_m(k_{nm}\rho) J_m(k_{n'm}\rho)\rho d\rho = N_{nm}\delta_{nn'} \tag{D.6}$$

A function $f(\rho)$ defined on this interval can thus be expanded as

$$f(\rho) = \sum_{n=1}^{\infty} \left[\int_0^R f(\rho') R_{nm}(\rho')\rho' d\rho'\right] R_{nm}(\rho), \tag{D.7}$$

which is usually known as the m-th order Fourier-Bessel series of f.

Transform and expansion The total basis functions are the product of the radial and angular parts :

$$\Psi_{n,m}(\rho,\phi) = R_{nm}(\rho)\Phi_m(\phi). \tag{D.8}$$

The orthogonality relation is given by

$$\int_0^R \int_0^{2\pi} \Psi^*_{nm}(\rho,\phi)\Psi_{n'm'}(\rho,\phi)\rho\, d\rho\, d\phi = \delta_{nn'}\delta_{mm'}. \tag{D.9}$$

By definition, they satisfy the Helmoltz differential equation

$$\nabla^2\Psi_{nm} + k^2_{nm}\Psi_{nm} = 0, \tag{D.10}$$

along with the corresponding boundary conditions (zero-value in our case). The set Ψ_{nm} with $n = 1,2,\cdots$ and $m = \cdots,-2,-1,0,1,2,\cdots$ constitutes an orthonormal basis on the region $\rho \le R$. For each Ψ_{nm}, $|m|$ is the number of periods in the angular direction, and $n-1$ corresponds to the number of zero crossings in the radial direction. The value of k_{nm} is thus an indication of the scale of the basic patterns, similarly to the normal Fourier transform. The spatial structure of Ψ_{nm} for some pairs (n,m) is represented in Fig.D.1.

A 2D function $f(\rho,\phi)$ defined on $\rho \le R$ can hence be expanded with respect to $\{\Psi_{nm}\}$:

$$f(\rho,\phi) = \sum_{n=1}^{\infty}\sum_{m=-\infty}^{+\infty} \hat{\hat{f}}_{nm}\Psi_{nm}(\rho,\phi), \tag{D.11}$$

where the coefficients

$$\hat{\hat{f}}_{nm} = \int_0^R \int_0^{2\pi} f(\rho,\phi)\Psi^*_{nm}(\rho,\phi)\rho\, d\rho\, d\phi, \tag{D.12}$$

are the Fourier-Bessel transform coefficients.

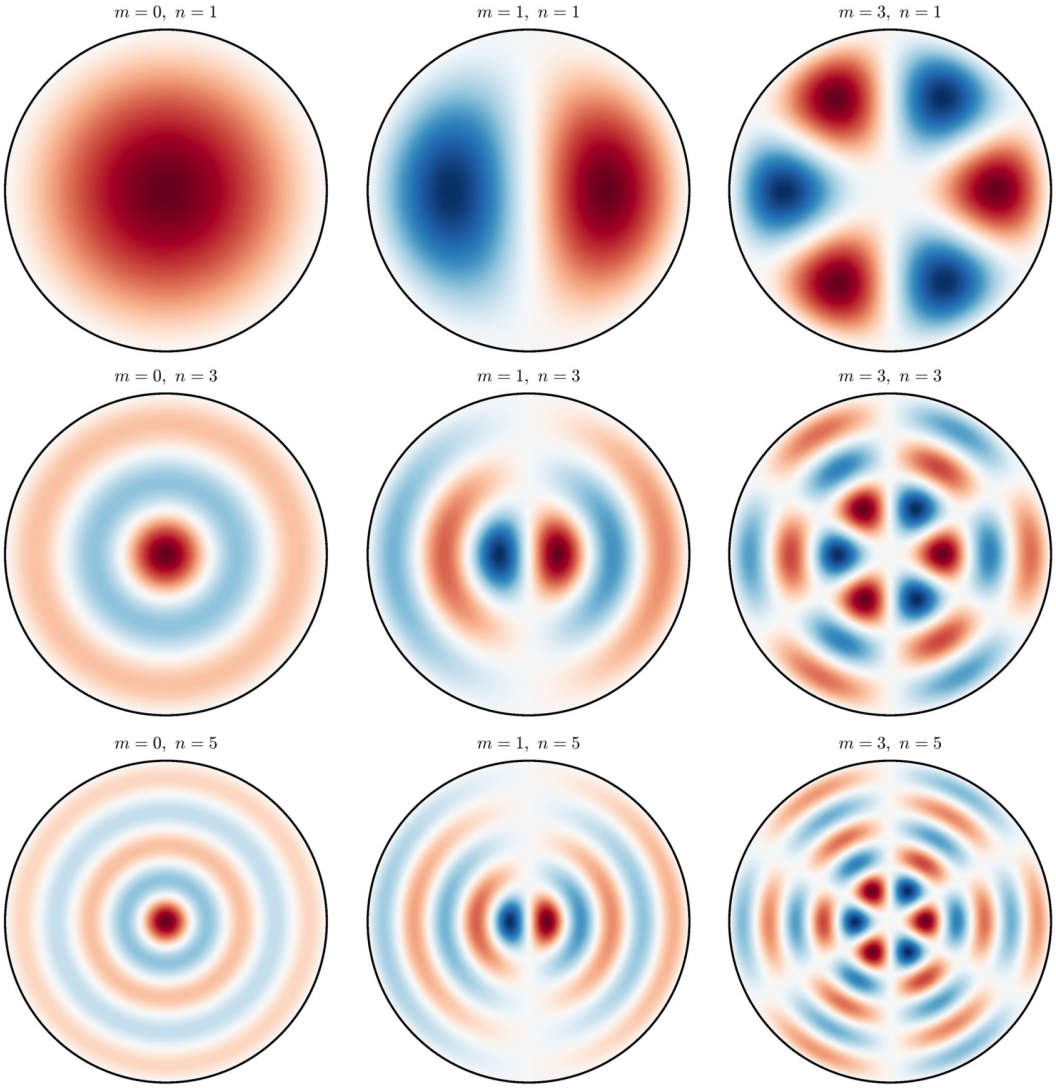

Figure D.1. – Structure of the real part of the basis functions (equation (D.8)) for different values of the radial and azimuthal indices (n, m).

D.2. Discrete transform

The experimental velocity fields being obtained on a discrete grid, the transform coefficients need to be computed using numerical quadrature, and we will thus obtain a finite set of discrete coefficients $\{\hat{u}_{nm} | n = 1, 2, \cdots, N_\rho$ and $m = -N_\phi/2+1, \cdots, 0, 1, 2, \cdots, N_\phi/2\}$. For simplicity, we denote $f_{ji} = f(\rho_i, \phi_j)$ where ρ_i and ϕ_j are the discrete radial and azimuthal positions respectively ($i \in [[1, N_\rho]]$, $j \in [[1, N_\phi]]$).

Discrete Fourier transform The angular part of the transform is performed using the Matlab *fft* function. For each radius, we thus compute a discrete FFT in the azimuthal direction. The

direct and inverse discrete transforms read respectively

$$\hat{f}_m(\rho) = \sum_{j=1}^{N_\phi} f_j(\rho) e^{-2i\pi m \frac{j-1}{N_\phi}}, \tag{D.13}$$

$$f_j(\rho) = \frac{1}{N_\phi} \sum_{m=1}^{N_\phi} \hat{f}_m(\rho) e^{2i\pi(j-1)\frac{m-1}{N_\phi}}. \tag{D.14}$$

The associated discrete version of the Parseval relation is

$$\sum_{j=1}^{N_\phi} |f_j|^2 = \frac{1}{N_\phi^2} \sum_{m=1}^{N_\phi} \hat{f}_m \hat{f}_m^*. \tag{D.15}$$

The kinetic energy per azimuthal wavenumber can then be computed as

$$E_m(\rho) = \frac{1}{N_\phi^2} \left[\hat{u}_m \hat{u}_m^* + \hat{v}_m \hat{v}_m^* \right] \tag{D.16}$$

(see Durran et al. 2017, for more details).

Discrete Hankel transform For each azimuthal mode m, its Fourier transform coefficient $\hat{f}_m(\rho)$ has a radial structure onto which we perform a discrete Hankel transform of order m. We use the Matlab algorithm described in García-Melendo et al. (2011b). Briefly, for each mode m, the discrete Hankel transform coefficients are computed following

$$\hat{\hat{f}}_{nm} = \frac{1}{\pi V^2} \sum_{i=1}^{N_\rho} \frac{\hat{f}_{mi}}{J_{m+1}^2(\alpha_{mi})} J_m\left(\frac{\alpha_{nm}\alpha_{mi}}{S}\right), \tag{D.17}$$

$$\hat{f}_m(\rho) = \frac{1}{\pi R^2} \sum_{n=1}^{N_\rho} \frac{\hat{\hat{f}}_{nm}}{J_{m+1}^2(\alpha_{mn})} J_m\left(\frac{\alpha_{nm}\alpha_{mi}}{S}\right) \tag{D.18}$$

where R is the maximum radius, V is the maximum radial wavenumber, which is different for each mode m ($V_m = \alpha_{N_\rho+1,m}/(2\pi R)$), and $S = 2\pi RV$. Here again, α_{nm} is the n^{th} zero of the Bessel function of the first kind of order m, J_m. The corresponding discrete Parseval relation is

$$\sum_{i=1}^{N_\rho} \frac{|\hat{f}_{mi}|^2}{2\pi^2 V^2 J_{m+1}^2(\alpha_{mi})} = \sum_{n=1}^{N_\rho} \frac{|\hat{\hat{f}}_{mn}|^2}{2\pi^2 R^2 J_{m+1}^2(\alpha_{mn})}. \tag{D.19}$$

Taking into account both the Fourier and Hankel transforms, the kinetic energy for each mode (m,n) can then be expressed as

$$E_{nm} = \frac{1}{N_\phi^2} \frac{1}{2\pi^2 R^3 J_{m+1}^2(\alpha_{nm})} \left[\hat{u}_{nm} \hat{u}_{nm}^* + \hat{v}_{nm} \hat{v}_{nm}^* \right]. \tag{D.20}$$

Note that $\hat{u}_{nm}$ is in $\mathrm{m^3 s^{-1}}$ (equation (D.12)), and thus E_{nm} is in $\mathrm{m^3 s^{-2}}$, which is homogeneous to a kinetic energy per wavenumber. The corresponding wavenumber is $k_{nm} = \alpha_{nm}/(2\pi R)$. The zonal kinetic energy spectra E_Z is then that of the axisymmetric mode $m = 0$ only, and the residual energy spectra E_R is what remains:

$$E_Z = E_{n0}, \tag{D.21}$$

$$E_R = \sum_{m,m\neq 0} E_{nm}. \tag{D.22}$$

E. Very long time experiments in the Jacuzzi setup

In this appendix, we plot the Hovmöller diagrams for two long-time experiments (experiments 1L and 2K in Table 5.1). Images were recorded for 3 minutes every 30 minutes. The corresponding plots of the zonal flow profile through time are available in Fig.5.5.

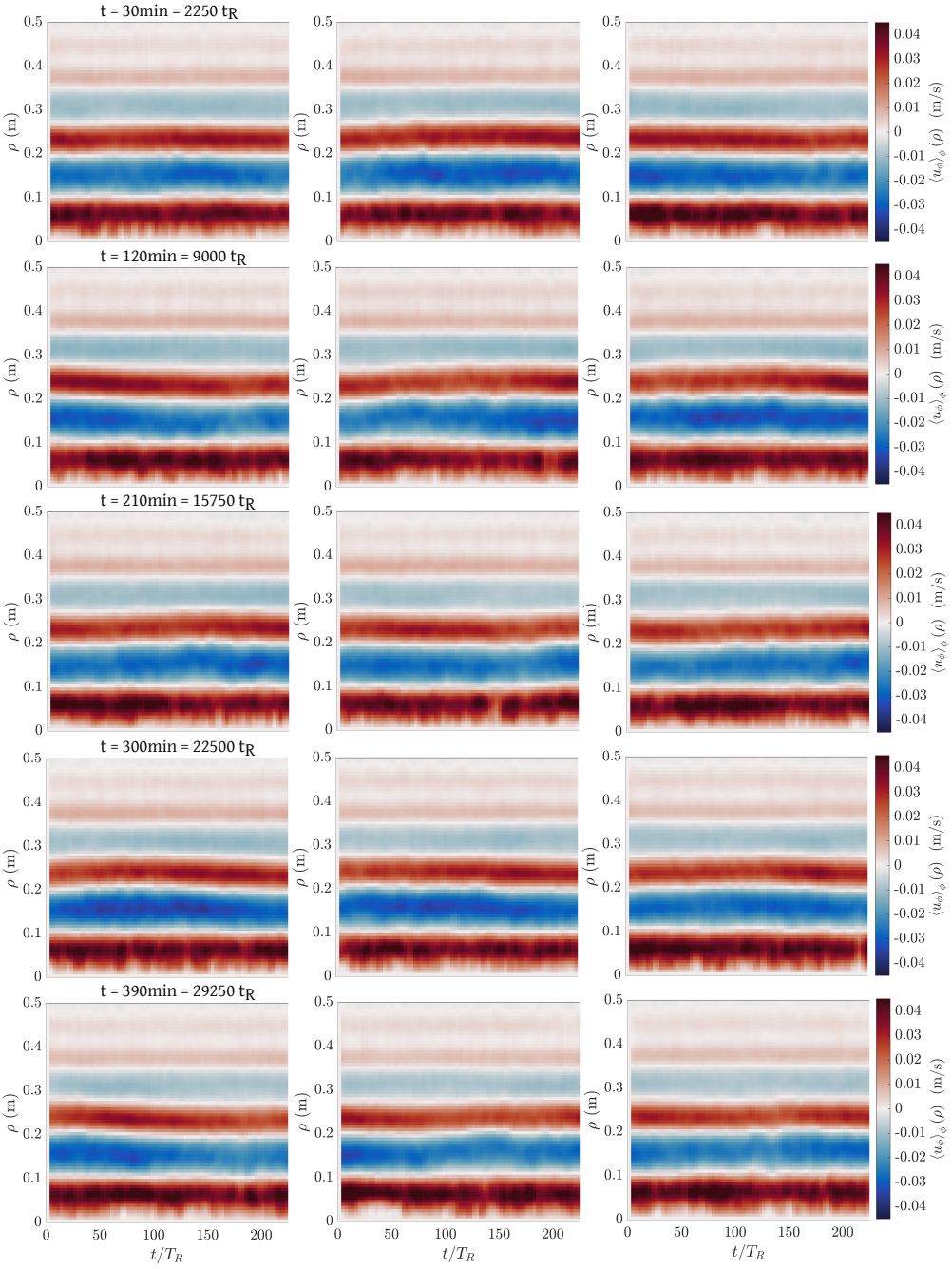

Figure E.1. – Experiment 1L (see Table 5.1). Space-time diagrams of the zonal flow measured for 3 minutes every 30 minutes.

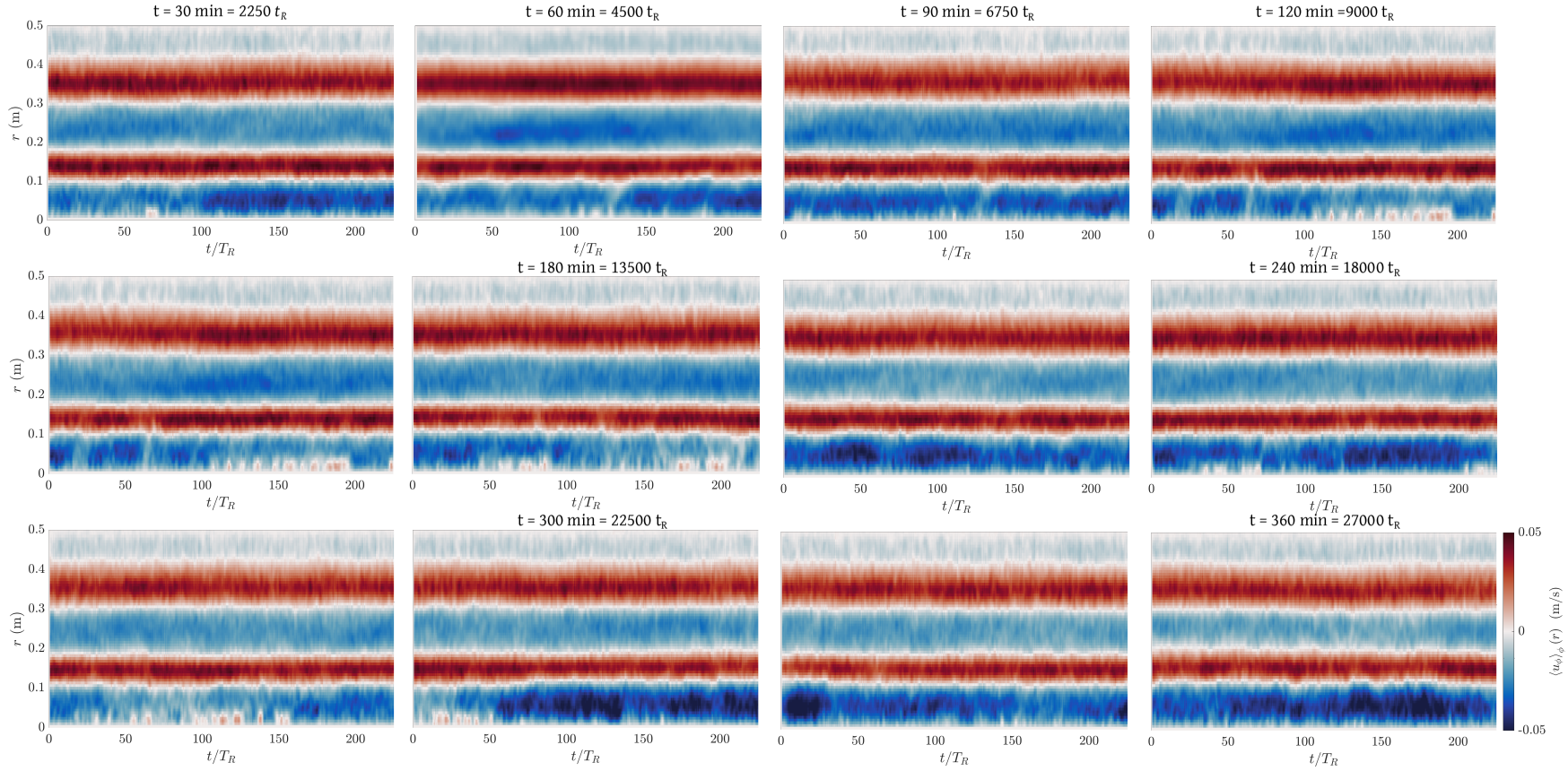

Figure E.2. – Experiment 2K (see Table 5.1). Space-time diagrams of the zonal flow measured for 3 minutes every 30 minutes.

Bibliography

ABE-OUCHI, A. et al. (2013). "Insolation-Driven 100,000-Year Glacial Cycles and Hysteresis of Ice-Sheet Volume". *Nature* **500**: (7461), 190–193. DOI: 10.1038/nature12374 (cit. on p. 177).

ACHTERBERG, R. K. and INGERSOLL, A. P. (1994). "Numerical Simulation of Baroclinic Jovian Vortices". *Journal of the atmospheric sciences* **51**: (4), 541–562 (cit. on p. 45).

ADRIANI, A. et al. (2018). "Clusters of Cyclones Encircling Jupiter's Poles". *Nature* **555**: (7695), 216–219. DOI: 10.1038/nature25491 (cit. on pp. 45, 64, 196, 198).

ADRIANI, A. et al. (2020). "Two-Year Observations of the Jupiter Polar Regions by JIRAM on Board Juno". *Journal of Geophysical Research: Planets* **125**: (6), e2019JE006098. DOI: 10.1029/2019JE006098 (cit. on pp. 45, 196, 198).

AFANASYEV, Y. D. and CRAIG, J. D. C. (2013). "Rotating Shallow Water Turbulence: Experiments with Altimetry". *Physics of Fluids* **25**: (10), 106603. DOI: 10.1063/1.4826477 (cit. on p. 235).

AFANASYEV, Y. D., O'LEARY, S., RHINES, P. B., and LINDAHL, E. (2012). "On the Origin of Jets in the Ocean". *Geophysical & Astrophysical Fluid Dynamics* **106**: (2), 113–137. DOI: 10.1080/03091929.2011.562896 (cit. on pp. 99, 235).

AFANASYEV, Y. D. and WELLS, J. (2005). "Quasi-Two-Dimensional Turbulence on the Polar Beta-Plane: Laboratory Experiments". *Geophysical & Astrophysical Fluid Dynamics* **99**: (1), 1–17. DOI: 10.1080/03091920412331319513 (cit. on pp. 99, 235).

AFANASYEV, Y. D. and IVANOV, L. M. (2019). "β-Plume Mechanism of Zonal Jet Creation by a Spatially Localized Forcing". In: *Zonal Jets: Phenomenology, Genesis, and Physics*. Ed. by B. GALPERIN and P. L. READ. Cambridge: Cambridge University Press, pp. 266–283. ISBN: 978-1-107-35822-5. DOI: 10.1017/9781107358225.017 (cit. on p. 120).

ANTIPOV, S. V., NEZLIN, M. V., SNEZHKIN, E. N., and TRUBNIKOV, A. S. (1986). "Rossby Autosoliton and Stationary Model of the Jovian Great Red Spot". *Nature* **323**: (6085), 238–240. DOI: 10.1038/323238a0 (cit. on p. 64).

ARNOLD, N. P., TZIPERMAN, E., and FARRELL, B. (2011). "Abrupt Transition to Strong Superrotation Driven by Equatorial Wave Resonance in an Idealized GCM". *Journal of the Atmospheric Sciences* **69**: (2), 626–640. DOI: 10.1175/JAS-D-11-0136.1 (cit. on pp. 134, 189).

ARREGI, J., ROJAS, J. F., SÁNCHEZ-LAVEGA, A., and MORGADO, A. (2006). "Phase Dispersion Relation of the 5-Micron Hot Spot Wave from a Long-Term Study of Jupiter in the Visible". *Journal of Geophysical Research: Planets* **111**: (E9), DOI: 10.1029/2005JE002653 (cit. on p. 135).

ASAY-DAVIS, X. S., MARCUS, P. S., WONG, M. H., and DE PATER, I. (2009). "Jupiter's Shrinking Great Red Spot and Steady Oval BA: Velocity Measurements with the 'Advection Corrected Correlation Image Velocimetry' Automated Cloud-Tracking Method". *Icarus* **203**: (1), 164–188. DOI: 10.1016/j.icarus.2009.05.001 (cit. on pp. 44, 85).

AUBERT, J., GILLET, N., and CARDIN, P. (2003). "Quasigeostrophic Models of Convection in Rotating Spherical Shells". *Geochemistry, Geophysics, Geosystems* **4**: (7), DOI: 10.1029/2002GC000456 (cit. on pp. 248, 252).

AUBERT, J., JUNG, S., and SWINNEY, H. L. (2002). "Observations of Zonal Flow Created by Potential Vorticity Mixing in a Rotating Fluid". *Geophysical Research Letters* **29**: (18), 23-1-23–4. DOI: 10.1029/2002GL015422 (cit. on pp. 99, 102, 235, 236).

AUBERT, O., LE BARS, M., LE GAL, P., and MARCUS, P. S. (2012). "The Universal Aspect Ratio of Vortices in Rotating Stratified Flows: Experiments and Observations". *Journal of Fluid Mechanics* **706**: 34–45. DOI: 10.1017/jfm.2012.176 (cit. on pp. 4, 5, 61, 65, 68, 81, 223).

AURNOU, J. M., HEIMPEL, M., ALLEN, L., KING, E., and WICHT, J. (2008). "Convective Heat Transfer and the Pattern of Thermal Emission on the Gas Giants". *Geophysical Journal International* **173**: (3), 793–801. DOI: 10.1111/j.1365-246X.2008.03764.x (cit. on p. 199).

AURNOU, J. M. and OLSON, P. L. (2001). "Strong Zonal Winds from Thermal Convection in a Rotating Spherical Shell". *Geophysical Research Letters* **28**: (13), 2557–2559. DOI: 10.1029/2000GL012474 (cit. on p. 56).

AURNOU, J. M. and HEIMPEL, M. H. (2004). "Zonal Jets in Rotating Convection with Mixed Mechanical Boundary Conditions". *Icarus* **169**: (2), 492–498. DOI: 10.1016/j.icarus.2004.01.013 (cit. on p. 232).

BAKAS, N. A. and IOANNOU, P. J. (2013). "Emergence of Large Scale Structure in Barotropic β-Plane Turbulence". *Physical Review Letters* **110**: (22), 224501. DOI: 10.1103/PhysRevLett.110.224501 (cit. on p. 190).

BARBOSA AGUIAR, A. C., READ, P. L., WORDSWORTH, R. D., SALTER, T., and HIRO YAMAZAKI, Y. (2010). "A Laboratory Model of Saturn's North Polar Hexagon". *Icarus* **206**: (2), 755–763. DOI: 10.1016/j.icarus.2009.10.022 (cit. on pp. 98, 191).

BASTIN, M. E. and READ, P. L. (1998). "Experiments on the Structure of Baroclinic Waves and Zonal Jets in an Internally Heated, Rotating, Cylinder of Fluid". *Physics of Fluids* **10**: (2), 374–389. DOI: 10.1063/1.869530 (cit. on pp. 99, 235).

BELLANI, G. and VARIANO, E. A. (2013). "Homogeneity and Isotropy in a Laboratory Turbulent Flow". *Experiments in Fluids* **55**: (1), 1646. DOI: 10.1007/s00348-013-1646-8 (cit. on pp. 102, 236).

BERHANU, M. et al. (2007). "Magnetic Field Reversals in an Experimental Turbulent Dynamo". *Europhysics Letters (EPL)* **77**: (5), 59001. DOI: 10.1209/0295-5075/77/59001 (cit. on pp. 177, 178).

BERON-VERA, F. J. et al. (2008). "Zonal Jets as Transport Barriers in Planetary Atmospheres". *Journal of the Atmospheric Sciences* **65**: (10), 3316–3326. DOI: 10.1175/2008JAS2579.1 (cit. on pp. 140, 173).

BIESCAS, B. et al. (2008). "Imaging Meddy Finestructure Using Multichannel Seismic Reflection Data". *Geophysical Research Letters* **35**: (11), DOI: 10.1029/2008GL033971 (cit. on p. 65).

BILLANT, P. and CHOMAZ, J.-M. (2001). "Self-Similarity of Strongly Stratified Inviscid Flows". *Physics of Fluids* **13**: (6), 1645–1651. DOI: 10.1063/1.1369125 (cit. on p. 64).

BIN, W., YUQING, W., LIGUANG, W., and ELSBERRY, R. (1999). "Dynamics in Tropical Cyclone Motion: A Review". *Chinese Journal of Atmospheric Sciences* **22**: (4), 416–434 (cit. on p. 209).

BOFFETTA, G. and ECKE, R. E. (2012). "Two-Dimensional Turbulence". *Annual Review of Fluid Mechanics* **44**: (1), 427–451. DOI: 10.1146/annurev-fluid-120710-101240 (cit. on pp. 42, 145, 148, 151).

BOLTON, S. J. et al. (2017). "The Juno Mission". *Space Science Reviews* **213**: (1-4), 5–37. DOI: 10.1007/s11214-017-0429-6 (cit. on pp. 47, 64).

BORRERO-ECHEVERRY, D., CROWLEY, C. J., and RIDDICK, T. P. (2018). "Rheoscopic Fluids in a Post-Kalliroscope World". *Physics of Fluids* **30**: (8), 087103. DOI: 10.1063/1.5045053 (cit. on p. 207).

BOUCHET, F., NARDINE, C., and TANGARIFE, T. (2019a). "Kinetic Theory and Quasi-Linear Theories of Jet Dynamics". In: *Zonal Jets: Phenomenology, Genesis, and Physics*. Ed. by B. GALPERIN and P. L. READ. Cambridge: Cambridge University Press, pp. 368–379. ISBN: 978-1-107-35822-5. DOI: 10.1017/9781107358225.024 (cit. on p. 189).

BOUCHET, F., ROLLAND, J., and SIMONNET, E. (2019b). "Rare Event Algorithm Links Transitions in Turbulent Flows with Activated Nucleations". *Physical Review Letters* **122**: (7), 074502. DOI: 10.1103/PhysRevLett.122.074502 (cit. on pp. 177, 178, 189, 225).

BOUCHET, F. and VENAILLE, A. (2012). "Statistical Mechanics of Two-Dimensional and Geophysical Flows". *Physics Reports*. Statistical Mechanics of Two-Dimensional and Geophysical Flows **515**: (5), 227–295. DOI: 10.1016/j.physrep.2012.02.001 (cit. on pp. 55, 98).

– (2019c). "Zonal Flows as Statistical Equilibria". In: *Zonal Jets*. Ed. by B. GALPERIN and P. L. READ. Cambridge University Press, pp. 347–359. ISBN: 978-1-107-04388-6. DOI: 10.1017/9781107358225.022 (cit. on p. 98).

BRUESHABER, S. R., SAYANAGI, K. M., and DOWLING, T. E. (2019). "Dynamical Regimes of Giant Planet Polar Vortices". *Icarus* **323**: 46–61. DOI: 10.1016/j.icarus.2019.02.001 (cit. on p. 199).

BRYGOO, S. et al. (2021). "Evidence of Hydrogen-Helium Immiscibility at Jupiter-Interior Conditions". *Nature* **593**: (7860), 517–521. DOI: 10.1038/s41586-021-03516-0 (cit. on p. 21).

BURIN, M. J. et al. (2019). "Turbulence and Jet-Driven Zonal Flows: Secondary Circulation in Rotating Fluids Due to Asymmetric Forcing". *Physical Review E* **99**: (2), 023108. DOI: 10.1103/PhysRevE.99.023108 (cit. on pp. 99, 102, 235, 236).

BUSSE, F. H. (1970). "Thermal Instabilities in Rapidly Rotating Systems". *Journal of Fluid Mechanics* **44**: (3), 441–460 (cit. on p. 248).

– (1976). "A Simple Model of Convection in the Jovian Atmosphere". *Icarus* **29**: (2), 255–260. DOI: 10.1016/0019-1035(76)90053-1 (cit. on pp. 32, 48).

CABANES, S., AURNOU, J., FAVIER, B., and LE BARS, M. (2017). "A Laboratory Model for Deep-Seated Jets on the Gas Giants". *Nature Physics* **13**: (4), 387–390. DOI: 10.1038/nphys4001 (cit. on pp. 4, 5, 61, 97, 99–102, 127, 138, 139, 143, 145, 151, 223, 224, 235, 236).

CABANES, S., ESPA, S., GALPERIN, B., YOUNG, R. M. B., and READ, P. L. (2020a). "Revealing the Intensity of Turbulent Energy Transfer in Planetary Atmospheres". *Geophysical Research Letters* **47**: (23), e2020GL088685. DOI: 10.1029/2020GL088685 (cit. on p. 140).

CABANES, S., SPIGA, A., and YOUNG, R. M. B. (2020b). "Global Climate Modeling of Saturn's Atmosphere. Part III: Global Statistical Picture of Zonostrophic Turbulence in High-Resolution 3D-Turbulent Simulations". *Icarus* **345**: 113705. DOI: 10.1016/j.icarus.2020.113705 (cit. on p. 56).

CADOT, O., EVRARD, A., and PASTUR, L. (2015). "Imperfect Supercritical Bifurcation in a Three-Dimensional Turbulent Wake". *Physical Review E* **91**: (6), 063005. DOI: 10.1103/PhysRevE.91.063005 (cit. on p. 178).

CAI, T., CHAN, K. L., and MAYR, H. G. (2021). "Deep, Closely Packed, Long-Lived Cyclones on Jupiter's Poles". *The Planetary Science Journal* **2**: (2), 81. DOI: 10.3847/PSJ/abedbd (cit. on p. 199).

CAO, H. and STEVENSON, D. (2017). "Zonal Flow Magnetic Field Interaction in the Semi-Conducting Region of Giant Planets". *Icarus* **296**: 59–72. DOI: 10.1016/j.icarus.2017.05.015 (cit. on p. 47).

CARDIN, P. and OLSON, P. (1994). "Chaotic Thermal Convection in a Rapidly Rotating Spherical Shell: Consequences for Flow in the Outer Core". *Physics of the Earth and Planetary Interiors* **82**: (3-4), 235–259 (cit. on pp. 43, 248, 252).

CARNEVALE, G. F., KLOOSTERZIEL, R. C., and VAN HEIJST, G. J. F. (1991). "Propagation of Barotropic Vortices over Topography in a Rotating Tank". *Journal of Fluid Mechanics* **233**: 119–139. DOI: 10.1017/S0022112091000411 (cit. on pp. 204, 207–209, 219).

CARTON, X., DANIAULT, N., ALVES, J., CHERUBIN, L., and AMBAR, I. (2010). "Meddy Dynamics and Interaction with Neighboring Eddies Southwest of Portugal: Observations and Modeling". *Journal of Geophysical Research* **115**: (C6), C06017. DOI: 10.1029/2009JC005646 (cit. on p. 57).

CARTON, X. (2001). "Hydrodynamical Modeling of Oceanic Vortices". *Surveys in Geophysics* **22**: (3), 179–263. DOI: 10.1023/A:1013779219578 (cit. on pp. 57, 64).

CARTON, X., LE CANN, B., SERPETTE, A., and DUBERT, J. (2013). "Interactions of Surface and Deep Anticyclonic Eddies in the Bay of Biscay". *Journal of Marine Systems* **109**: S45–S59 (cit. on pp. 57, 65).

CHAN, J. C. L. and WILLIAMS, R. T. (1987). "Analytical and Numerical Studies of the Beta-Effect in Tropical Cyclone Motion. Part I: Zero Mean Flow". *Journal of the Atmospheric Sciences* **44**: (9), 1257–1265. DOI: 10.1175/1520-0469(1987)044<1257:AANSOT>2.0.CO;2 (cit. on p. 118).

CHANG, K.-I. et al. (2004). "Circulation and Currents in the Southwestern East/Japan Sea: Overview and Review". *Progress in Oceanography* **61**: 105–156. DOI: 10.1016/j.pocean.2004.06.005 (cit. on p. 57).

CHARNEY, J. G., SHUKLA, J., and MO, K. C. (1981). "Comparison of a Barotropic Blocking Theory with Observation". *Journal of the Atmospheric Sciences* **38**: (4), 762–779. DOI: 10.1175/1520-0469(1981)038<0762:COABBT>2.0.CO;2 (cit. on pp. 134, 189).

CHARNEY, J. G. and DEVORE, J. G. (1979). "Multiple Flow Equilibria in the Atmosphere and Blocking". *Journal of the Atmospheric Sciences* **36**: (7), 1205–1216. DOI: 10.1175/1520-0469(1979)036<1205:MFEITA>2.0.CO;2 (cit. on pp. 116, 129, 134, 189).

CHEKHLOV, A., ORSZAG, S., SUKORIANSKY, S., GALPERIN, B., and STAROSELSKY, I. (1996). "The Effect of Small-Scale Forcing on Large-Scale Structures in Two-Dimensional Flows". *Physica D: Nonlinear Phenomena* **98**: (2-4), 321–334. DOI: 10.1016/0167-2789(96)00102-9 (cit. on pp. 52, 145).

CHEMKE, R. and KASPI, Y. (2016). "The Effect of Eddy–Eddy Interactions on Jet Formation and Macroturbulent Scales". *Journal of the Atmospheric Sciences* **73**: (5), 2049–2059. DOI: 10.1175/JAS-D-15-0375.1 (cit. on p. 98).

CHO, J. Y.-K. and POLVANI, L. M. (1996). "The Emergence of Jets and Vortices in Freely Evolving, Shallow-water Turbulence on a Sphere". *Physics of Fluids* **8**: (6), 1531–1552. DOI: 10.1063/1.868929 (cit. on pp. 55, 196).

CHOI, D., BANFIELD, D., GIERASCH, P., and SHOWMAN, A. (2007). "Velocity and Vorticity Measurements of Jupiter's Great Red Spot Using Automated Cloud Feature Tracking". *Icarus* **188**: (1), 35–46. DOI: 10.1016/j.icarus.2006.10.037 (cit. on pp. 84, 85, 94).

CHOI, D. S. and SHOWMAN, A. P. (2011). "Power Spectral Analysis of Jupiter's Clouds and Kinetic Energy from Cassini". *Icarus* **216**: (2), 597–609. DOI: 10.1016/j.icarus.2011.10.001 (cit. on p. 48).

CHOI, D. S., SHOWMAN, A. P., and VASAVADA, A. R. (2010). "The Evolving Flow of Jupiter's White Ovals and Adjacent Cyclones". *Icarus* **207**: (1), 359–372. DOI: 10.1016/j.icarus.2009.10.013 (cit. on pp. 43, 44, 80, 81, 84, 86, 94).

CHOMAZ, J.-M., ORTIZ, S., GALLAIRE, F., and BILLANT, P. (2010). "Stability of Quasi-Two-Dimensional Vortices". In: *Fronts, Waves and Vortices in Geophysical Flows*. Ed. by J.-B. FLOR. Lecture Notes in Physics. Berlin, Heidelberg: Springer Berlin Heidelberg, pp. 35–59. ISBN: 978-3-642-11587-5. DOI: 10.1007/978-3-642-11587-5_2 (cit. on p. 77).

CHRISTENSEN, U. R. (2002). "Zonal Flow Driven by Strongly Supercritical Convection in Rotating Spherical Shells". *Journal of Fluid Mechanics* **470**: 115–133. DOI: 10.1017/S0022112002002008 (cit. on p. 56).

CHRISTENSEN, U. R., WICHT, J., and DIETRICH, W. (2020). "Mechanisms for Limiting the Depth of Zonal Winds in the Gas Giant Planets". *The Astrophysical Journal* **890**: (61), 1–14. DOI: 10.3847/1538-4357/ab698c (cit. on p. 232).

CIANI, D., CARTON, X., and VERRON, J. (2016). "On the Merger of Subsurface Isolated Vortices". *Geophysical & Astrophysical Fluid Dynamics* **110**: (1), 23–49. DOI: 10.1080/03091929.2015.1135430 (cit. on p. 220).

CONDIE, S. A. and RHINES, P. B. (1994). "A Convective Model for the Zonal Jets in the Atmospheres of Jupiter and Saturn". *Nature* **367**: (6465), 711–713. DOI: 10.1038/367711a0 (cit. on p. 99).

CONRATH, B. J., FLASAR, F. M., PIRRAGLIA, J. A., GIERASCH, P. J., and HUNT, G. E. (1981). "Thermal Structure and Dynamics of the Jovian Atmosphere. 2. Visible Cloud Features". *Journal of Geophysical Research: Space Physics* **86**: (A10), 8769–8775. DOI: 10.1029/JA086iA10p08769 (cit. on pp. 45, 82).

CONSTANTINOU, N. C. (2019). "Formation of Large-Scale Structures by Turbulence in Rotating Planets". PhD thesis (cit. on pp. 54, 55).

CONSTANTINOU, N. C., FARRELL, B. F., and IOANNOU, P. J. (2014). "Emergence and Equilibration of Jets in Beta-Plane Turbulence: Applications of Stochastic Structural Stability Theory". *Journal of the Atmospheric Sciences* **71**: (5), 1818–1842. DOI: 10.1175/JAS-D-13-076.1 (cit. on pp. 55, 133, 225).

CORRADO, R., LACORATA, G., PALATELLA, L., SANTOLERI, R., and ZAMBIANCHI, E. (2017). "General Characteristics of Relative Dispersion in the Ocean". *Scientific Reports* **7**: (1), 46291. DOI: 10.1038/srep46291 (cit. on p. 158).

COUMOU, D., PETOUKHOV, V., RAHMSTORF, S., PETRI, S., and SCHELLNHUBER, H. J. (2014). "Quasi-Resonant Circulation Regimes and Hemispheric Synchronization of Extreme Weather in Boreal Summer". *Proceedings of the National Academy of Sciences* **111**: (34), 12331–12336. DOI: 10.1073/pnas.1412797111 (cit. on p. 134).

CRAVATTE, S., KESSLER, W. S., and MARIN, F. (2012). "Intermediate Zonal Jets in the Tropical Pacific Ocean Observed by Argo Floats". *Journal of Physical Oceanography* **42**: (9), 1475–1485. DOI: 10.1175/JPO-D-11-0206.1 (cit. on pp. 57, 98).

DANILOV, S. and GRYANIK, V. M. (2004a). "Barotropic Beta-Plane Turbulence in a Regime with Strong Zonal Jets Revisited". *Journal of the Atmospheric Sciences* **61**: (18), 2283–2295. DOI: 10.1175/1520-0469(2004)061<2283:BBTIAR>2.0.CO;2 (cit. on p. 142).

DANILOV, S. and GURARIE, D. (2004b). "Scaling, Spectra and Zonal Jets in Beta-Plane Turbulence". *Physics of Fluids* **16**: (7), 2592–2603. DOI: 10.1063/1.1752928 (cit. on p. 142).

DAVEY, M. K. and KILLWORTH, P. D. (1989). "Flows Produced by Discrete Sources of Buoyancy". *Journal of Physical Oceanography* **19**: (9), 1279–1290. DOI: 10.1175/1520-0485(1989)019<1279:FPBDSO>2.0.CO;2 (cit. on p. 118).

DE PATER, I. et al. (2010). "Persistent Rings in and around Jupiter's Anticyclones – Observations and Theory". *Icarus* **210**: (2), 742–762. DOI: 10.1016/j.icarus.2010.07.027 (cit. on pp. 45, 82, 85).

DE VERDIERE, A. C. (1979). "Mean Flow Generation by Topographic Rossby Waves". *Journal of Fluid Mechanics* **94**: (1), 39–64. DOI: 10.1017/S0022112079000938 (cit. on pp. 99, 102, 108, 109, 236).

DEBRAS, F. and CHABRIER, G. (2019). "New Models of Jupiter in the Context of Juno and Galileo". *The Astrophysical Journal* **872**: (1), 100. DOI: 10.3847/1538-4357/aaff65 (cit. on pp. 21, 232).

DI NITTO, G., ESPA, S., and CENEDESE, A. (2013). "Simulating Zonation in Geophysical Flows by Laboratory Experiments". *Physics of Fluids* **25**: (8), 086602. DOI: 10.1063/1.4817540 (cit. on pp. 99, 235).

DIETRICH, W. and JONES, C. A. (2018). "Anelastic Spherical Dynamos with Radially Variable Electrical Conductivity". *Icarus* **305**: 15–32. DOI: 10.1016/j.icarus.2018.01.003 (cit. on pp. 43, 232).

DOWLING, T. E. and INGERSOLL, A. P. (1988a). "Jupiter's Great Red Spot as a Shallow Water System". *Journal of the Atmospheric Sciences* **46**: (21), 3256–3278. DOI: 10.1175/1520-0469(1989)046<3256:JGRSAA>2.0.CO;2 (cit. on pp. 43, 64).

– (1988b). "Potential Vorticity and Layer Thickness Variations in the Flow around Jupiter's Great Red Spot and White Oval BC". *Journal of the Atmospheric Sciences* **45**: (8), 1380–1396. DOI: 10.1175/1520-0469(1988)045<1380:PVALTV>2.0.CO;2 (cit. on p. 64).

DRITSCHEL, D. and MCINTYRE, M. (2008). "Multiple Jets as PV Staircases: The Phillips Effect and the Resilience of Eddy-Transport Barriers". *Journal of the Atmospheric Sciences* **65**: (3), 855–874 (cit. on pp. 53, 98, 108, 110, 139, 140, 173).

DUNKERTON, T. and SCOTT, R. (2008). "A Barotropic Model of the Angular Momentum–Conserving Potential Vorticity Staircase in Spherical Geometry". *Journal of the Atmospheric Sciences* **65**: (4), 1105–1136. DOI: 10.1175/2007JAS2223.1 (cit. on pp. 53, 139).

DURRAN, D., WEYN, J. A., and MENCHACA, M. Q. (2017). "Practical Considerations for Computing Dimensional Spectra from Gridded Data". *Monthly Weather Review* **145**: (9), 3901–3910. DOI: 10.1175/MWR-D-17-0056.1 (cit. on p. 258).

ESLER, J. G. (2004). "Benjamin–Feir instability of Rossby waves on a jet". *Quarterly Journal of the Royal Meteorological Society* **130**: (600), 1611–1630. DOI: 10.1256/qj.03.74 (cit. on p. 193).

ESPA, S., NITTO, G. D., and CENEDESE, A. (2010). "The Emergence of Zonal Jets in Forced Rotating Shallow Water Turbulence: A Laboratory Study". *Europhysics Letters (EPL)* **92**: (3), 34006. DOI: 10.1209/0295-5075/92/34006 (cit. on p. 162).

ESPA, S. et al. (2012). "Zonal Jets and Cyclone–Anticyclone Asymmetry in Decaying Rotating Turbulence: Laboratory Experiments and Numerical Simulations". *Geophysical & Astrophysical Fluid Dynamics* **106**: (6), 557–573. DOI: 10.1080/03091929.2011.637301 (cit. on pp. 99, 235).

ESTRADA, A. O., GÓMEZ, R. C. C., CROS, A., and GAL, P. L. (2020). "Coalescence of Lenticular Anticyclones in a Linearly Stratified Rotating Fluid". *Geophysical & Astrophysical Fluid Dynamics* **114**: (4-5), 504–523. DOI: 10.1080/03091929.2020.1734199 (cit. on pp. 213, 219, 220).

FACCHINI, G. (2017). “Some Aspects of the Dynamics of Rotating, Stratified and Shear Flows”. PhD thesis. Aix-Marseille Université (cit. on p. 70).

FACCHINI, G. and LE BARS, M. (2016). “On the Lifetime of a Pancake Anticyclone in a Rotating Stratified Flow”. *Journal of Fluid Mechanics* **804**: 688–711. DOI: 10.1017/jfm.2016.549 (cit. on pp. 4, 5, 61, 65, 72, 90–94, 223).

FACCHINI, G., FAVIER, B., LE GAL, P., WANG, M., and LE BARS, M. (2018). “The Linear Instability of the Stratified Plane Couette Flow”. *Journal of Fluid Mechanics* **853**: 205–234. DOI: 10.1017/jfm.2018.556 (cit. on p. 70).

FARRELL, B. F. and IOANNOU, P. J. (2003). “Structural Stability of Turbulent Jets”. *Journal of the Atmospheric Sciences* **60**: (17), 2101–2118. DOI: 10.1175/1520-0469(2003)060<2101:SSOTJ>2.0.CO;2 (cit. on p. 55).

FAVIER, B., GUERVILLY, C., and KNOBLOCH, E. (2019). “Subcritical Turbulent Condensate in Rapidly Rotating Rayleigh–Bénard Convection”. *Journal of Fluid Mechanics* **864**: DOI: 10.1017/jfm.2019.58 (cit. on p. 178).

FERRARI, R. and NIKURASHIN, M. (2010). “Suppression of Eddy Diffusivity across Jets in the Southern Ocean”. *Journal of Physical Oceanography* **40**: (7), 1501–1519. DOI: 10.1175/2010JPO4278.1 (cit. on pp. 171, 172).

FEUDEL, U., PISARCHIK, A. N., and SHOWALTER, K. (2018). “Multistability and Tipping: From Mathematics and Physics to Climate and Brain—Minireview and Preface to the Focus Issue”. *Chaos: An Interdisciplinary Journal of Nonlinear Science* **28**: (3), 033501. DOI: 10.1063/1.5027718 (cit. on p. 177).

FINE, K. S., CASS, A. C., FLYNN, W. G., and DRISCOLL, C. F. (1995). “Relaxation of 2D Turbulence to Vortex Crystals”. *Physical Review Letters* **75**: (18), 3277–3280. DOI: 10.1103/PhysRevLett.75.3277 (cit. on p. 198).

FIRING, E. and BEARDSLEY, R. C. (1976). “The Behavior of a Barotropic Eddy on a β-Plane”. *Journal of Physical Oceanography* **6**: (1), 57–65. DOI: 10.1175/1520-0485(1976)006<0057:TBOABE>2.0.CO;2 (cit. on pp. 118, 204, 219).

FISCHER, P. F., LOTTES, J. W., and KERKEMEIER, S. G. (2008). *Nek5000 Web Page*. http://nek5000.mcs.anl.gov (cit. on p. 74).

FLASAR, F. M. et al. (1981). “Thermal Structure and Dynamics of the Jovian Atmosphere 1. The Great Red Spot”. *Journal of Geophysical Research: Space Physics* **86**: (A10), 8759–8767. DOI: 10.1029/JA086iA10p08759 (cit. on p. 82).

FLETCHER, L. N. et al. (2010). “Thermal Structure and Composition of Jupiter’s Great Red Spot from High-Resolution Thermal Imaging”. *Icarus* **208**: (1), 306–328. DOI: 10.1016/j.icarus.2010.01.005 (cit. on p. 82).

FLÓR, J.-B. and EAMES, I. (2002). “Dynamics of Monopolar Vortices on a Topographic Beta-Plane”. *Journal of Fluid Mechanics* **456**: 353–376. DOI: 10.1017/S0022112001007728 (cit. on pp. 204, 207, 208, 210, 219).

FOX-KEMPER, B., LUMPKIN, R., and BRYAN, F. O. (2013). “Chapter 8 - Lateral Transport in the Ocean Interior”. In: *International Geophysics*. Ed. by G. SIEDLER, S. M. GRIFFIES, J. GOULD, and J. A. CHURCH. Vol. 103. Ocean Circulation and Climate. Academic Press, pp. 185–209. DOI: 10.1016/B978-0-12-391851-2.00008-8 (cit. on p. 171).

FOX-KEMPER, B. et al. (2019). “Challenges and Prospects in Ocean Circulation Models”. *Frontiers in Marine Science* **6**: DOI: 10.3389/fmars.2019.00065 (cit. on pp. 140, 158, 171).

FRÜH, W.-G. and READ, P. L. (1999). “Experiments on a Barotropic Rotating Shear Layer. Part 1. Instability and Steady Vortices”. *Journal of Fluid Mechanics* **383**: 143–173. DOI: 10.1017/S0022112098003930 (cit. on p. 98).

GALANTI, E. et al. (2019a). “Saturn’s Deep Atmospheric Flows Revealed by the Cassini Grand Finale Gravity Measurements”. *Geophysical Research Letters* **46**: (2), 616–624. DOI: 10.1029/2018GL078087 (cit. on pp. 21, 47).

GALANTI, E. et al. (2019b). "Determining the Depth of Jupiter's Great Red Spot with Juno: A Slepian Approach". *The Astrophysical Journal* **874**: (2), L24. DOI: 10.3847/2041-8213/ab1086 (cit. on p. 87).

GALLEGO, D., RIBERA, P., GARCIA-HERRERA, R., HERNANDEZ, E., and GIMENO, L. (2005). "A New Look for the Southern Hemisphere Jet Stream". *Climate Dynamics* **24**: (6), 607–621. DOI: 10.1007/s00382-005-0006-7 (cit. on pp. 58, 59).

GALPERIN, B. et al. (2006). "Anisotropic Turbulence and Zonal Jets in Rotating Flows with a β-Effect". *Nonlinear Processes in Geophysics* **13**: (1), 83–98. DOI: 10.5194/npg-13-83-2006 (cit. on pp. 52, 53, 98, 99, 139, 142, 145, 151, 153).

GALPERIN, B., HOEMANN, J., ESPA, S., DI NITTO, G., and LACORATA, G. (2016). "Anisotropic Macroturbulence and Diffusion Associated with a Westward Zonal Jet: From Laboratory to Planetary Atmospheres and Oceans". *Physical Review E* **94**: (6), 063102. DOI: 10.1103/PhysRevE.94.063102 (cit. on p. 162).

GALPERIN, B., HOEMANN, J., ESPA, S., and NITTO, G. D. (2014a). "Anisotropic Turbulence and Rossby Waves in an Easterly Jet: An Experimental Study". *Geophysical Research Letters* **41**: (17), 6237–6243. DOI: 10.1002/2014GL060767 (cit. on pp. 99, 140, 154, 170).

GALPERIN, B. and READ, P. L. (2019a). *Zonal Jets: Phenomenology, Genesis, and Physics*. Cambridge: Cambridge University Press. ISBN: 978-1-107-04388-6. DOI: 10.1017/9781107358225 (cit. on pp. 48, 58, 98).

GALPERIN, B., SUKORIANSKY, S., and DIKOVSKAYA, N. (2010). "Geophysical Flows with Anisotropic Turbulence and Dispersive Waves: Flows with a β-Effect". *Ocean Dynamics* **60**: (2), 427–441. DOI: 10.1007/s10236-010-0278-2 (cit. on pp. 142, 190).

GALPERIN, B. et al. (2014b). "Cassini Observations Reveal a Regime of Zonostrophic Macroturbulence on Jupiter". *Icarus* **229**: 295–320. DOI: 10.1016/j.icarus.2013.08.030 (cit. on pp. 46, 48, 49, 53, 98, 143, 145).

GALPERIN, B. et al. (2019b). "Barotropic and Zonostrophic Turbulence". In: *Zonal Jets: Phenomenology, Genesis, and Physics*. Ed. by B. GALPERIN and P. L. READ. Cambridge: Cambridge University Press, pp. 220–237. ISBN: 978-1-107-35822-5. DOI: 10.1017/9781107358225.013 (cit. on pp. 53, 54, 98, 99, 127, 139, 143, 153).

GARCÍA-MELENDO, E., PÉREZ-HOYOS, S., SÁNCHEZ-LAVEGA, A., and HUESO, R. (2011a). "Saturn's Zonal Wind Profile in 2004–2009 from Cassini ISS Images and Its Long-Term Variability". *Icarus* **215**: (1), 62–74. DOI: 10.1016/j.icarus.2011.07.005 (cit. on p. 190).

GARCÍA-MELENDO, E. et al. (2011b). "Dynamics of Jupiter's Equatorial Region at Cloud Top Level from Cassini and HST Images". *Icarus* **211**: (2), 1242–1257. DOI: 10.1016/j.icarus.2010.11.020 (cit. on pp. 135, 258).

GARGETT, A. and GARNER, T. (2008). "Determining Thorpe Scales from Ship-Lowered CTD Density Profiles". *Journal of Atmospheric and Oceanic Technology* **25**: (9), 1657–1670. DOI: 10.1175/2008JTECHO541.1 (cit. on p. 140).

GASTINE, T. and WICHT, J. (2012). "Effects of Compressibility on Driving Zonal Flow in Gas Giants". *Icarus* **219**: (1), 428–442. DOI: 10.1016/j.icarus.2012.03.018 (cit. on p. 43).

– (2021). "Stable Stratification Promotes Multiple Zonal Jets in a Turbulent Jovian Dynamo Model". *Icarus*, 114514. DOI: 10.1016/j.icarus.2021.114514 (cit. on pp. 43, 232).

GASTINE, T., WICHT, J., DUARTE, L. D. V., HEIMPEL, M., and BECKER, A. (2014). "Explaining Jupiter's Magnetic Field and Equatorial Jet Dynamics". *Geophysical Research Letters* **41**: (15), 5410–5419. DOI: 10.1002/2014GL060814 (cit. on p. 232).

GILL, A. E. (1974). "The Stability of Planetary Waves on an Infinite Beta-plane". *Geophysical Fluid Dynamics* **6**: (1), 29–47. DOI: 10.1080/03091927409365786 (cit. on p. 55).

GILLET, N. and JONES, C. (2006). "The Quasi-Geostrophic Model for Rapidly Rotating Spherical Convection Outside the Tangent Cylinder". *Journal of Fluid Mechanics* **554**: 343–369. DOI: 10.1017/S0022112006009219 (cit. on pp. 43, 248, 252).

GILLET, N., BRITO, D., JAULT, D., and NATAF, H. C. (2007). "Experimental and Numerical Studies of Convection in a Rapidly Rotating Spherical Shell". *Journal of Fluid Mechanics* **580**: 83–121. DOI: 10.1017/S0022112007005265 (cit. on p. 99).

GISSINGER, C. (2012). "A New Deterministic Model for Chaotic Reversals". *The European Physical Journal B* **85**: (4), 137. DOI: 10.1140/epjb/e2012-20799-5 (cit. on p. 177).

GRASSI, D. et al. (2018). "First Estimate of Wind Fields in the Jupiter Polar Regions From JIRAM-Juno Images". *Journal of Geophysical Research: Planets* **123**: (6), 1511–1524. DOI: 10.1029/2018JE005555 (cit. on p. 203).

GREICIUS, T. (2017). *NASA's Juno Probes the Depths of Jupiter's Great Red Spot*. http://www.nasa.gov/feature/jpl/nasas-juno-probes-the-depths-of-jupiters-great-red-spot (cit. on pp. 87, 88).

GRIFFITHS, R. W. and HOPFINGER, E. J. (1987). "Coalescing of Geostrophic Vortices". *Journal of Fluid Mechanics* **178**: 73–97. DOI: 10.1017/S0022112087001125 (cit. on pp. 213, 219).

GROESKAMP, S., LACASCE, J. H., MCDOUGALL, T. J., and ROGÉ, M. (2020). "Full-Depth Global Estimates of Ocean Mesoscale Eddy Mixing From Observations and Theory". *Geophysical Research Letters* **47**: (18), e2020GL089425. DOI: 10.1029/2020GL089425 (cit. on pp. 171, 174).

GUERVILLY, C. and CARDIN, P. (2016). "Subcritical Convection of Liquid Metals in a Rotating Sphere Using a Quasi-Geostrophic Model". *Journal of Fluid Mechanics* **808**: 61–89. DOI: 10.1017/jfm.2016.631 (cit. on p. 133).

– (2017). "Multiple Zonal Jets and Convective Heat Transport Barriers in a Quasi-Geostrophic Model of Planetary Cores". *Geophysical Journal International* **211**: (1), 455–471. DOI: 10.1093/gji/ggx315 (cit. on pp. 58, 59, 173, 177, 248).

GUILLOT, T. et al. (2018). "A Suppression of Differential Rotation in Jupiter's Deep Interior". *Nature* **555**: (7695), 227–230. DOI: 10.1038/nature25775 (cit. on pp. 47, 64).

GUIMBARD, D., LE DIZÈS, S., LE BARS, M., LE GAL, P., and LEBLANC, S. (2010). "Elliptic Instability of a Stratified Fluid in a Rotating Cylinder". *Journal of Fluid Mechanics* **660**: 240–257. DOI: 10.1017/S0022112010002636 (cit. on p. 77).

GUIZAR-SICAIROS, M. and GUTIÉRREZ-VEGA, J. C. (2004). "Computation of Quasi-Discrete Hankel Transforms of Integer Order for Propagating Optical Wave Fields". *JOSA A* **21**: (1), 53–58. DOI: 10.1364/JOSAA.21.000053 (cit. on p. 148).

GUNNARSON, J. L. et al. (2018). "Saturn's New Ribbons: Cassini Observations of Planetary Waves in Saturn's 42N Atmospheric Jet". *Geophysical Research Letters* **45**: (15), 7399–7408. DOI: 10.1029/2018GL078156 (cit. on p. 135).

GUYON, É., HULIN, J.-P., and PETIT, L. (2012). *Hydrodynamique Physique*. Third. EDP Sciences, CNRS Editions. ISBN: 978-2-7598-0561-7. DOI: 10.1051/978-2-7598-0893-9 (cit. on p. 41).

HASSANZADEH, P., MARCUS, P. S., and LE GAL, P. (2012). "The Universal Aspect Ratio of Vortices in Rotating Stratified Flows: Theory and Simulation". *Journal of Fluid Mechanics* **706**: 46–57. DOI: 10.1017/jfm.2012.180 (cit. on pp. 65, 81, 89).

HEIMPEL, M., AURNOU, J., and WICHT, J. (2005). "Simulation of Equatorial and High-Latitude Jets on Jupiter in a Deep Convection Model". *Nature* **438**: (7065), 193–196. DOI: 10.1038/nature04208 (cit. on pp. 33, 56).

HEIMPEL, M., GASTINE, T., and WICHT, J. (2016). "Simulation of Deep-Seated Zonal Jets and Shallow Vortices in Gas Giant Atmospheres". *Nature Geoscience* **9**: (1), 19–23. DOI: 10.1038/ngeo2601 (cit. on pp. 43, 56).

HEIMPEL, M., YADAV, R., FEATHERSTONE, N., and AURNOU, J. (2020). *Polar and Mid-Latitude Vortices and Zonal Flows on Jupiter and Saturn*. Preprint. In Review. DOI: 10.21203/rs.3.rs-85026/v1 (cit. on pp. 199, 232).

HELD, I. M. (1983). "Stationary and Quasi-Stationary Eddies in the Extratropical Troposphere: Theory". In: *Large-Scale Dynamical Processes in the Atmosphere*. Ed. by B. HOSKINS and R. PEARCE, pp. 127–168 (cit. on p. 116).

HELLED, R. (2019). "The Interiors of Jupiter and Saturn". *Oxford Research Encyclopedia of Planetary Science*. DOI: 10.1093/acrefore/9780190647926.013.175 (cit. on pp. 20, 21, 46, 232).

HELLED, R. et al. (2014). "Giant Planet Formation, Evolution, and Internal Structure". In: *Protostars and Planets VI*. Ed. by H. BEUTHER, R. KLESSEN, C. DULLEMOND, and T. HENNING. University of Arizona Press, p. 643 (cit. on p. 20).

HERBERT, C., CABALLERO, R., and BOUCHET, F. (2020). "Atmospheric Bistability and Abrupt Transitions to Superrotation: Wave–Jet Resonance and Hadley Cell Feedbacks". *Journal of the Atmospheric Sciences* **77**: (1), 31–49. DOI: 10.1175/JAS-D-19-0089.1 (cit. on pp. 116, 134, 189).

HIDE, R. (1961). "Origin of Jupiter's Great Red Spot". *Nature* **190**: (4779), 895–896. DOI: 10.1038/190895a0 (cit. on pp. 45, 64).

– (1968). "On Source-Sink Flows in a Rotating Fluid". *Journal of Fluid Mechanics* **32**: (4), 737–764. DOI: 10.1017/S002211206800100X (cit. on p. 99).

HIDE, R. and MASON, P. J. (1975). "Sloping Convection in a Rotating Fluid". *Advances in Physics* **24**: (1), 47–100. DOI: 10.1080/00018737500101371 (cit. on p. 99).

HUANG, H.-P., GALPERIN, B., and SUKORIANSKY, S. (2000). "Anisotropic Spectra in Two-Dimensional Turbulence on the Surface of a Rotating Sphere". *Physics of Fluids* **13**: (1), 225–240. DOI: 10.1063/1.1327594 (cit. on pp. 52, 145).

IESS, L. et al. (2018). "Measurement of Jupiter's Asymmetric Gravity Field". *Nature* **555**: (7695), 220–222. DOI: 10.1038/nature25776 (cit. on p. 64).

INGERSOLL, A. P. et al. (1981). "Interaction of Eddies and Mean Zonal Flow on Jupiter as Inferred from Voyager 1 and 2 Images". *Journal of Geophysical Research: Space Physics* **86**: (A10), 8733–8743. DOI: 10.1029/JA086iA10p08733 (cit. on p. 49).

INGERSOLL, A. P. et al. (2007). "Dynamics of Jupiter's Atmosphere". In: *Jupiter: The Planet, Satellites and Magnetosphere*. Ed. by F. BAGENAL, T. E. DOWLING, and W. B. MCKINNON. Vol. 1. Cambridge University Press, pp. 105–128. ISBN: 978-0-521-03545-3 (cit. on p. 98).

INGERSOLL, A. P. (1990). "Atmospheric Dynamics of the Outer Planets". *Science* **248**: (4953), 308–315. DOI: 10.1126/science.248.4953.308 (cit. on pp. 49, 57).

JANSSEN, M. A. et al. (2017). "MWR: Microwave Radiometer for the Juno Mission to Jupiter". *Space Science Reviews* **213**: (1-4), 139–185. DOI: 10.1007/s11214-017-0349-5 (cit. on p. 87).

JONES, C. A. (2014). "A Dynamo Model of Jupiter's Magnetic Field". *Icarus* **241**: 148–159. DOI: 10.1016/j.icarus.2014.06.020 (cit. on pp. 43, 232).

KAPLAN, E. J., SCHAEFFER, N., VIDAL, J., and CARDIN, P. (2017). "Subcritical Thermal Convection of Liquid Metals in a Rapidly Rotating Sphere". *Physical Review Letters* **119**: (9), 094501. DOI: 10.1103/PhysRevLett.119.094501 (cit. on p. 133).

KASPI, Y. et al. (2018). "Jupiter's Atmospheric Jet Streams Extend Thousands of Kilometres Deep". *Nature* **555**: (7695), 223–226. DOI: 10.1038/nature25793 (cit. on pp. 21, 47, 64, 98).

KASPI, Y. et al. (2020). "Comparison of the Deep Atmospheric Dynamics of Jupiter and Saturn in Light of the Juno and Cassini Gravity Measurements". *Space Science Reviews* **216**: (84), DOI: 10.1007/s11214-020-00705-7 (cit. on pp. 21, 47, 98).

KIM, D. et al. (2012). "Impact of an Anticyclonic Eddy on the Summer Nutrient and Chlorophyll a Distributions in the Ulleung Basin, East Sea (Japan Sea)". *ICES Journal of Marine Science* **69**: (1), 23–29. DOI: 10.1093/icesjms/fsr178 (cit. on pp. 57, 64).

KLOCKER, A., FERRARI, R., and LACASCE, J. H. (2012). "Estimating Suppression of Eddy Mixing by Mean Flows". *Journal of Physical Oceanography* **42**: (9), 1566–1576. DOI: 10.1175/JPO-D-11-0205.1 (cit. on pp. 171–173).

KLOCKER, A. and MARSHALL, D. P. (2014). "Advection of Baroclinic Eddies by Depth Mean Flow". *Geophysical Research Letters* **41**: (10), 3517–3521. DOI: 10.1002/2014GL060001 (cit. on pp. 134, 135).

KLOOSTERZIEL, R. C. (1990). "On the Large-Time Asymptotics of the Diffusion Equation on Infinite Domains". *Journal of Engineering Mathematics* **24**: (3), 213–236. DOI: 10.1007/BF00058467 (cit. on p. 72).

KOLMOGOROV, A. N., LEVIN, V., HUNT, J. C. R., PHILLIPS, O. M., and WILLIAMS, D. (1991). "The Local Structure of Turbulence in Incompressible Viscous Fluid for Very Large Reynolds Numbers". *Proceedings of the Royal Society of London. Series A: Mathematical and Physical Sciences* **434**: (1890), 9–13. DOI: 10.1098/rspa.1991.0075 (cit. on p. 40).

KONG, D., ZHANG, K., SCHUBERT, G., and ANDERSON, J. D. (2018). "Origin of Jupiter's Cloud-Level Zonal Winds Remains a Puzzle Even after Juno". *Proceedings of the National Academy of Sciences* **115**: (34), 8499–8504. DOI: 10.1073/pnas.1805927115 (cit. on p. 47).

LACASCE, J. H. (2008). "Statistics from Lagrangian Observations". *Progress in Oceanography* **77**: (1), 1–29. DOI: 10.1016/j.pocean.2008.02.002 (cit. on pp. 158, 162).

LACORATA, G. and ESPA, S. (2012). "On the Influence of a β-Effect on Lagrangian Diffusion". *Geophysical Research Letters* **39**: (11), L11605. DOI: 10.1029/2012GL051841 (cit. on pp. 158, 162).

LEE, S. and HELD, I. M. (1993). "Baroclinic Wave Packets in Models and Observations". *Journal of the Atmospheric Sciences* **50**: (10), 1413–1428. DOI: 10.1175/1520-0469(1993)050<1413:BWPIMA>2.0.CO;2 (cit. on p. 193).

LEGARRETA, J. and SANCHEZLAVEGA, A. (2008). "Vertical Structure of Jupiter's Troposphere from Nonlinear Simulations of Long-Lived Vortices". *Icarus* **196**: (1), 184–201. DOI: 10.1016/j.icarus.2008.02.018 (cit. on pp. 82, 83, 85).

LEMASQUERIER, D., FACCHINI, G., FAVIER, B., and BARS, M. L. (2020a). "Remote Determination of the Shape of Jupiter's Vortices from Laboratory Experiments". *Nature Physics*, 1–6. DOI: 10.1038/s41567-020-0833-9 (cit. on p. 63).

LEMASQUERIER, D., FAVIER, B., and LE BARS, M. (2021). "Zonal Jets at the Laboratory Scale: Hysteresis and Rossby Waves Resonance". *Journal of Fluid Mechanics* **910**: A18. DOI: 10.1017/jfm.2020.1000 (cit. on pp. 97, 104, 105, 110, 190, 191).

LEMASQUERIER, D., FAVIER, B., and LE BARS, M. (2020b). "Gas Giant–like Zonal Jets in the Laboratory". *Physical Review Fluids* **5**: (11), 110506. DOI: 10.1103/PhysRevFluids.5.110506 (cit. on p. 97).

LEWEKE, T., LE DIZÈS, S., and WILLIAMSON, C. H. (2016). "Dynamics and Instabilities of Vortex Pairs". *Annual Review of Fluid Mechanics* **48**: (1), 507–541. DOI: 10.1146/annurev-fluid-122414-034558 (cit. on pp. 213, 219).

LI, C., INGERSOLL, A. P., KLIPFEL, A. P., and BRETTLE, H. (2020). "Modeling the Stability of Polygonal Patterns of Vortices at the Poles of Jupiter as Revealed by the Juno Spacecraft". *Proceedings of the National Academy of Sciences* **117**: (39), 24082–24087. DOI: 10.1073/pnas.2008440117 (cit. on pp. 199, 202–204, 220, 221).

LI, C. et al. (2017). "The Distribution of Ammonia on Jupiter from a Preliminary Inversion of Juno Microwave Radiometer Data". *Geophysical Research Letters* **44**: (11), 5317–5325. DOI: 10.1002/2017GL073159 (cit. on p. 64).

LI, L. et al. (2004). "Life Cycles of Spots on Jupiter from Cassini Images". *Icarus*. Special Issue: Cassini-Huygens at Jupiter **172**: (1), 9–23. DOI: 10.1016/j.icarus.2003.10.015 (cit. on pp. 43, 45).

LIAN, Y. and SHOWMAN, A. P. (2010). "Generation of Equatorial Jets by Large-Scale Latent Heating on the Giant Planets". *Icarus* **207**: (1), 373–393. DOI: 10.1016/j.icarus.2009.10.006 (cit. on pp. 48, 56).

LIGHTHILL, S. J. (1978). "Acoustic Streaming". *Journal of Sound and Vibration* **61**: (3), 391–418. DOI: 10.1016/0022-460X(78)90388-7 (cit. on p. 55).

LIMAYE, S. S. (1986). "Jupiter: New Estimates of the Mean Zonal Flow at the Cloud Level". *Icarus* **65**: (2), 335–352. DOI: 10.1016/0019-1035(86)90142-9 (cit. on pp. 81, 84).

LINDEN, P. F. and VAN HEIJST, G. J. F. (1984). "Two-Layer Spin-up and Frontogenesis". *Journal of Fluid Mechanics* **143**: 69–94. DOI: 10.1017/S0022112084001269 (cit. on p. 221).

LIU, J., GOLDREICH, P. M., and STEVENSON, D. J. (2008). "Constraints on Deep-Seated Zonal Winds inside Jupiter and Saturn". *Icarus*. Mars Polar Science IV **196**: (2), 653–664. DOI: 10.1016/j.icarus.2007.11.036 (cit. on p. 47).

LORENZ, E. N. (1972). "Barotropic Instability of Rossby Wave Motion". *Journal of the Atmospheric Sciences* **29**: (2), 258–265. DOI: 10.1175/1520-0469(1972)029<0258:BIORWM>2.0.CO;2 (cit. on p. 55).

MALGUZZI, P., SPERANZA, A., SUTERA, A., and CABALLERO, R. (1996). "Nonlinear Amplification of Stationary Rossby Waves Near Resonance. Part I." *Journal of the Atmospheric Sciences* **53**: (2), 298–311. DOI: 10.1175/1520-0469(1996)053<0298:NAOSRW>2.0.CO;2 (cit. on p. 133).

– (1997). "Nonlinear Amplification of Stationary Rossby Waves near Resonance. Part II". *Journal of the Atmospheric Sciences* **54**: (20), 2441–2451. DOI: 10.1175/1520-0469(1997)054<2441:NAOSRW>2.0.CO;2 (cit. on p. 133).

MANLEY, T. O. and HUNKINS, K. (1985). "Mesoscale Eddies of the Arctic Ocean". *Journal of Geophysical Research: Oceans* **90**: (C3), 4911–4930. DOI: 10.1029/JC090iC03p04911 (cit. on pp. 57, 65).

MARCUS, P. S., KUNDU, T., and LEE, C. (2000). "Vortex Dynamics and Zonal Flows". *Physics of Plasmas* **7**: (5), 1630–1640. DOI: 10.1063/1.874045 (cit. on p. 43).

MARCUS, P. S. (1988). "Numerical Simulation of Jupiter's Great Red Spot". *Nature* **331**: (6158), 693–696. DOI: 10.1038/331693a0 (cit. on p. 64).

– (1990). "Vortex Dynamics in a Shearing Zonal Flow". *Journal of Fluid Mechanics* **215**: (-1), 393–430. DOI: 10.1017/S0022112090002695 (cit. on p. 64).

MASUDA, A., MARUBAYASHI, K., and ISHIBASHI, M. (1990). "A Laboratory Experiment and Numerical Simulation of an Isolated Barotropic Eddy in a Basin with Topographic β". *Journal of Fluid Mechanics* **213**: (-1), 641. DOI: 10.1017/S0022112090002488 (cit. on p. 219).

MAXIMENKO, N. A., BANG, B., and SASAKI, H. (2005). "Observational Evidence of Alternating Zonal Jets in the World Ocean". *Geophysical research letters* **32**: (12), (cit. on pp. 57, 59, 98).

MCDOWELL, S. E. and ROSSBY, H. T. (1978). "Mediterranean Water: An Intense Mesoscale Eddy off the Bahamas". *Science* **202**: (4372), 1085–1087. DOI: 10.1126/science.202.4372.1085 (cit. on p. 57).

MCEWAN, A. D., THOMPSON, R. O. R. Y., and PLUMB, R. A. (1980). "Mean Flows Driven by Weak Eddies in Rotating Systems". *Journal of Fluid Mechanics* **99**: (3), 655–672. DOI: 10.1017/S002211208000081X (cit. on p. 108).

MCINTYRE, M. (2008). "Potential-Vorticity Inversion and the Wave-Turbulence Jigsaw: Some Recent Clarifications". *Advances in Geosciences* **15**: 47–56. DOI: 10.5194/adgeo-15-47-2008 (cit. on pp. 53, 139).

MCWILLIAMS, J. C. and FLIERL, G. R. (1979). "On the Evolution of Isolated, Nonlinear Vortices". *Journal of Physical Oceanography* **9**: (6), 1155–1182. DOI: 10.1175/1520-0485(1979)009<1155:OTEOIN>2.0.CO;2 (cit. on p. 208).

MESCHANOV, S. and SHAPIRO, G. (1998). "A Young Lens of Red Sea Water in the Arabian Sea". *Deep Sea Research Part I: Oceanographic Research Papers* **45**: (1), 1–13. DOI: 10.1016/S0967-0637(97)00018-6 (cit. on p. 57).

MEUNIER, P. and LEWEKE, T. (2003). "Analysis and Treatment of Errors Due to High Velocity Gradients in Particle Image Velocimetry". *Experiments in fluids* **35**: (5), 408–421. DOI: 10.1007/s00348-003-0673-2 (cit. on pp. 71, 104).

MICHEL, G., HERAULT, J., PÉTRÉLIS, F., and FAUVE, S. (2016). "Bifurcations of a Large-Scale Circulation in a Quasi-Bidimensional Turbulent Flow". *Europhysics Letters (EPL)* **115**: (6), 64004. DOI: 10.1209/0295-5075/115/64004 (cit. on p. 178).

MITCHELL, J. L., BEEBE, R. F., INGERSOLL, A. P., and GARNEAU, G. W. (1981). "Flow Fields within Jupiter's Great Red Spot and White Oval BC". *Journal of Geophysical Research: Space Physics* **86**: (A10), 8751–8757. DOI: doi.org/10.1029/JA086iA10p08751 (cit. on pp. 65, 80, 81, 84, 85).

MITCHELL, J. L. et al. (2019). "Terrestrial Atmospheres". In: *Zonal Jets: Phenomenology, Genesis, and Physics*. Ed. by B. GALPERIN and P. L. READ. Cambridge: Cambridge University Press, pp. 9–45. ISBN: 978-1-107-35822-5. DOI: 10.1017/9781107358225.002 (cit. on p. 58).

MIYAZAKI, T. (1993). "Elliptical Instability in a Stably Stratified Rotating Fluid". *Physics of Fluids A: Fluid Dynamics* **5**: (11), 2702–2709. DOI: 10.1063/1.858733 (cit. on p. 77).

MOORE, K. M. et al. (2019). "Time Variation of Jupiter's Internal Magnetic Field Consistent with Zonal Wind Advection". *Nature Astronomy* **3**: (8), 730–735. DOI: 10.1038/s41550-019-0772-5 (cit. on p. 47).

MORALES-JUBERIAS, R., SANCHEZ-LAVEGA, A., LECACHEUX, J., and COLAS, F. (2002). "A Comparative Study of Jovian Anticyclone Properties from a Six-Year (1994–2000) Survey". *Icarus* **157**: (1), 76–90. DOI: 10.1006/icar.2001.6819 (cit. on p. 43).

MORALES-JUBERIAS, R., SÁNCHEZ-LAVEGA, A., and DOWLING, T. E. (2003). "EPIC Simulations of the Merger of Jupiter's White Ovals BE and FA: Altitude-Dependent Behavior". *Icarus* **166**: (1), 63–74. DOI: 10.1016/j.icarus.2003.08.009 (cit. on p. 82).

MORBIDELLI, A. (2018). "Accretion Processes". *Oxford Research Encyclopedia of Planetary Science* (cit. on p. 20).

NIINO, H. and MISAWA, N. (1984). "An Experimental and Theoretical Study of Barotropic Instability". *Journal of the Atmospheric Sciences* **41**: (12), 1992–2011. DOI: 10.1175/1520-0469(1984)041<1992:AEATSO>2.0.CO;2 (cit. on p. 98).

O'NEILL, M. E., EMANUEL, K. A., and FLIERL, G. R. (2015). "Polar Vortex Formation in Giant-Planet Atmospheres Due to Moist Convection". *Nature Geoscience* **8**: (7), 523–526. DOI: 10.1038/ngeo2459 (cit. on pp. 196, 198).

– (2016). "Weak Jets and Strong Cyclones: Shallow-Water Modeling of Giant Planet Polar Caps". *Journal of the Atmospheric Sciences* **73**: (4), 1841–1855. DOI: 10.1175/JAS-D-15-0314.1 (cit. on pp. 196, 198).

OLLITRAULT, M., GABILLET, C., and VERDIÈRE, A. C. D. (2005). "Open Ocean Regimes of Relative Dispersion". *Journal of Fluid Mechanics* **533**: 381–407. DOI: 10.1017/S0022112005004556 (cit. on p. 158).

OLSON, D. B. and BACKUS, R. H. (1985). "The Concentrating of Organisms at Fronts: A Cold-Water Fish and a Warm-Core Gulf Stream Ring". *Journal of Marine Research* **43**: (1), 113–137. DOI: 10.1357/002224085788437325 (cit. on p. 57).

OZMIDOV, R. V. (1965). "On the Turbulent Exchange in a Stably Stratified Ocean." *Izv. Acad. Sci. USSR, Atmos. Oceanic Phys.* **1**: (8), 861–871 (cit. on p. 52).

PANETTA, R. L. (1993). "Zonal Jets in Wide Baroclinically Unstable Regions: Persistence and Scale Selection". *Journal of the Atmospheric Sciences* **50**: (14), 2073–2106. DOI: 10.1175/1520-0469(1993)050<2073:ZJIWBU>2.0.CO;2 (cit. on p. 177).

PEDLOSKY, J. (1967). "The Spin up of a Stratified Fluid". *Journal of Fluid Mechanics* **28**: (03), 463. DOI: 10.1017/S0022112067002228 (cit. on p. 204).

– (1981). "Resonant Topographic Waves in Barotropic and Baroclinic Flows". *Journal of the Atmospheric Sciences* **38**: (12), 2626–2641. DOI: 10.1175/1520-0469(1981)038<2626:RTWIBA>2.0.CO;2 (cit. on p. 116).

– (2013). *Geophysical Fluid Dynamics*. Second. Springer-Verlag New York. ISBN: 978-0-387-96387-7 (cit. on pp. 22, 248).

PETOUKHOV, V., RAHMSTORF, S., PETRI, S., and SCHELLNHUBER, H. J. (2013). "Quasiresonant Amplification of Planetary Waves and Recent Northern Hemisphere Weather Extremes". *Proceedings of the National Academy of Sciences* **110**: (14), 5336. DOI: 10.1073/pnas.1222000110 (cit. on p. 134).

PHILLIPS, O. M. (1972). "Turbulence in a Strongly Stratified Fluid—Is It Unstable?" *Deep Sea Research and Oceanographic Abstracts* **19**: (1), 79–81. DOI: 10.1016/0011-7471(72)90074-5 (cit. on pp. 53, 139).

PLUMB, R. A. (1975). "Momentum Transport by the Thermal Tide in the Stratosphere of Venus". *Quarterly Journal of the Royal Meteorological Society* **101**: (430), 763–776. DOI: 10.1002/qj.49710143005 (cit. on p. 229).
– (1977). "The Interaction of Two Internal Waves with the Mean Flow: Implications for the Theory of the Quasi-Biennial Oscillation". *Journal of the Atmospheric Sciences* **34**: (12), 1847–1858. DOI: 10.1175/1520-0469(1977)034<1847:TIOTIW>2.0.CO;2 (cit. on p. 229).

POLVANI, L. M., MCWILLIAMS, J. C., SPALL, M. A., and FORD, R. (1994). "The Coherent Structures of Shallow-water Turbulence: Deformation-radius Effects, Cyclone/Anticyclone Asymmetry and Gravity-wave Generation". *Chaos: An Interdisciplinary Journal of Nonlinear Science* **4**: (2), 177–186. DOI: 10.1063/1.166002 (cit. on p. 45).

PORCO, C. C. et al. (2003). "Cassini Imaging of Jupiter's Atmosphere, Satellites, and Rings". *Science* **299**: (5612), 1541–1547. DOI: 10.1126/science.1079462 (cit. on pp. 46, 98).

QUINN, B. E., NAZARENKO, S. V., CONNAUGHTON, C. P., GALLAGHER, S., and HNAT, B. (2019). "Modulational Instability in Basic Plasma and Geophysical Models". In: *Zonal Jets: Phenomenology, Genesis, and Physics*. Ed. by B. GALPERIN and P. L. READ. Cambridge: Cambridge University Press, pp. 255–265. ISBN: 978-1-107-35822-5. DOI: 10.1017/9781107358225.016 (cit. on pp. 55, 98).

RAVELET, F., MARIÉ, L., CHIFFAUDEL, A., and DAVIAUD, F. (2004). "Multistability and Memory Effect in a Highly Turbulent Flow: Experimental Evidence for a Global Bifurcation". *Physical Review Letters* **93**: (16), 164501. DOI: 10.1103/PhysRevLett.93.164501 (cit. on p. 178).

READ, P. L. and HIDE, R. (1984). "An Isolated Baroclinic Eddy as a Laboratory Analogue of the Great Red Spot on Jupiter". *Nature* **308**: (5954), 45–48. DOI: 10.1038/308045a0 (cit. on pp. 43, 64).

READ, P. L. et al. (2015). "An Experimental Study of Multiple Zonal Jet Formation in Rotating, Thermally Driven Convective Flows on a Topographic Beta-Plane". *Physics of Fluids* **27**: (8), 085111. DOI: 10.1063/1.4928697 (cit. on pp. 99, 235).

READ, P. (1986). "Stable, Baroclinic Eddies on Jupiter and Saturn: A Laboratory Analog and Some Observational Tests". *Icarus* **65**: (2-3), 304–334. DOI: 10.1016/0019-1035(86)90141-7 (cit. on p. 43).

READ, P. L. (2019). "Zonal Jet Flows in the Laboratory: An Introduction". In: *Zonal Jets: Phenomenology, Genesis, and Physics*. Ed. by B. GALPERIN and P. L. READ. Cambridge: Cambridge University Press, pp. 119–134. ISBN: 978-1-107-35822-5. DOI: 10.1017/9781107358225.006 (cit. on p. 99).

READ, P. L. et al. (2007). "Dynamics of Convectively Driven Banded Jets in the Laboratory". *Journal of the Atmospheric Sciences* **64**: (11), 4031–4052. DOI: 10.1175/2007JAS2219.1 (cit. on pp. 99, 235).

READ, P. and HIDE, R. (1983). "Long-Lived Eddies in the Laboratory and in the Atmospheres of Jupiter and Saturn". *Nature* **302**: (5904), 126–129. DOI: 10.1038/302126a0 (cit. on pp. 43, 64).

READ, P. et al. (2004). "Jupiter's and Saturn's Convectively Driven Banded Jets in the Laboratory". *Geophysical Research Letters* **31**: (22), DOI: 10.1029/2004GL020106 (cit. on p. 99).

REDEKOPP, L. G. (1977). "On the Theory of Solitary Rossby Waves". *Journal of Fluid Mechanics* **82**: (4), 725–745. DOI: 10.1017/S0022112077000950 (cit. on p. 193).

REZNIK, G. M. (1992). "Dynamics of Singular Vortices on a Beta-Plane". *Journal of Fluid Mechanics* **240**: (-1), 405–432. DOI: 10.1017/S0022112092000144 (cit. on p. 208).

REZNIK, G. M. and KIZNER, Z. (2007). "Two-Layer Quasi-Geostrophic Singular Vortices Embedded in a Regular Flow. Part 2. Steady and Unsteady Drift of Individual Vortices on a Beta-Plane". *Journal of Fluid Mechanics* **584**: 203–223. DOI: 10.1017/S0022112007006404 (cit. on p. 210).

RHINES, P. B. (2007). "Jets and Orography: Idealized Experiments with Tip Jets and Lighthill Blocking". *Journal of the Atmospheric Sciences* **64**: (10), 3627–3639. DOI: 10.1175/JAS4008.1 (cit. on p. 39).

RHINES, P. B. (1975). "Waves and Turbulence on a Beta-Plane". *Journal of Fluid Mechanics* **69**: (03), 417. DOI: 10.1017/S0022112075001504 (cit. on pp. 48, 50, 52, 98, 125, 145).

RICHARDSON, P. L. (1993). "Tracking Ocean Eddies". *American Scientist* **81**: (3), 261–271 (cit. on pp. 57, 58).

ROGERS, J. (1995). *The Giant Planet Jupiter*. Vol. 6. Cambridge University Press (cit. on pp. 43, 177).

RYPINA, I. I. et al. (2007). "On the Lagrangian Dynamics of Atmospheric Zonal Jets and the Permeability of the Stratospheric Polar Vortex". *Journal of the Atmospheric Sciences* **64**: (10), 3595–3610. DOI: 10.1175/JAS4036.1 (cit. on p. 173).

SALYK, C., INGERSOLL, A. P., LORRE, J., VASAVADA, A., and DEL GENIO, A. D. (2006). "Interaction between Eddies and Mean Flow in Jupiter's Atmosphere: Analysis of Cassini Imaging Data". *Icarus* **185**: (2), 430–442. DOI: 10.1016/j.icarus.2006.08.007 (cit. on p. 49).

SÁNCHEZ-LAVEGA, A. et al. (2019). "Gas Giants". In: *Zonal Jets: Phenomenology, Genesis, and Physics*. Ed. by B. GALPERIN and P. L. READ. Cambridge: Cambridge University Press, pp. 72–103. ISBN: 978-1-107-35822-5. DOI: 10.1017/9781107358225.004 (cit. on pp. 48, 57).

SANSÓN, L. Z. and VAN HEIJST, G. (2000). "Nonlinear Ekman Effects in Rotating Barotropic Flows". *Journal of Fluid Mechanics* **412**: 75–91 (cit. on pp. 115, 249, 252).

– (2002). "Ekman Effects in a Rotating Flow over Bottom Topography". *Journal of Fluid Mechanics* **471**: 239–255. DOI: 10.1017/S0022112002002239 (cit. on pp. 249, 252).

SAYANAGI, K. M. et al. (2018). "Saturn's Polar Atmosphere". In: *Saturn in the 21st Century*. Ed. by F. M. FLASAR, K. H. BAINES, N. KRUPP, and T. STALLARD. Cambridge Planetary Science. Cambridge: Cambridge University Press, pp. 337–376. ISBN: 978-1-107-10677-2. DOI: 10.1017/9781316227220.012 (cit. on pp. 193, 196).

SCHAEFFER, N. (2004). "Instabilités, Turbulence et Dynamo Dans Une Couche de Fluide Cisaillée En Rotation Rapide. Importance de l'aspect Ondulatoire". PhD thesis. Université Joseph-Fourier-Grenoble I (cit. on p. 248).

SCHECTER, D. A., DUBIN, D. H. E., FINE, K. S., and DRISCOLL, C. F. (1999). "Vortex Crystals from 2D Euler Flow: Experiment and Simulation". *Physics of Fluids* **11**: (4), 905–914. DOI: 10.1063/1.869961 (cit. on p. 198).

SCHNEIDER, T. (2006). "The General Circulation of the Atmosphere". *Annual Review of Earth and Planetary Sciences* **34**: (1), 655–688. DOI: 10.1146/annurev.earth.34.031405.125144 (cit. on p. 98).

SCHNEIDER, T. and LIU, J. (2009). "Formation of Jets and Equatorial Superrotation on Jupiter". *Journal of the Atmospheric Sciences* **66**: (3), 579–601. DOI: 10.1175/2008JAS2798.1 (cit. on p. 56).

SCOTT, R. K. (2011). "Polar Accumulation of Cyclonic Vorticity". *Geophysical & Astrophysical Fluid Dynamics* **105**: (4-5), 409–420. DOI: 10.1080/03091929.2010.509927 (cit. on p. 196).

SCOTT, R. K. and POLVANI, L. M. (2007). "Forced-Dissipative Shallow-Water Turbulence on the Sphere and the Atmospheric Circulation of the Giant Planets". *Journal of the Atmospheric Sciences* **64**: (9), 3158–3176. DOI: 10.1175/JAS4003.1 (cit. on pp. 33, 55, 196).

– (2008). "Equatorial Superrotation in Shallow Atmospheres". *Geophysical Research Letters* **35**: (24), DOI: 10.1029/2008GL036060 (cit. on p. 56).

SCOTT, R. K. and TISSIER, A.-S. (2012a). "The Generation of Zonal Jets by Large-Scale Mixing". *Physics of Fluids* **24**: (12), 126601. DOI: 10.1063/1.4771991 (cit. on pp. 53, 139).

SCOTT, R. K. and DRITSCHEL, D. G. (2012b). "The Structure of Zonal Jets in Geostrophic Turbulence". *Journal of Fluid Mechanics* **711**: 576–598. DOI: 10.1017/jfm.2012.410 (cit. on pp. 54, 98, 105).

– (2019). "Zonal Jet Formation by Potential Vorticity Mixing at Large and Small Scales". In: *Zonal Jets: Phenomenology, Genesis, and Physics*. Ed. by B. GALPERIN and P. L. READ. Cambridge: Cambridge University Press, pp. 238–246. ISBN: 978-1-107-35822-5. DOI: 10.1017/9781107358225.014 (cit. on pp. 98, 153).

SEIFF, A. et al. (1998). "Thermal Structure of Jupiter's Atmosphere near the Edge of a 5-Micrometer Hot Spot in the North Equatorial Belt". *Journal of Geophysical Research: Planets* **103**: (E10), 22857–22889. DOI: 10.1029/98JE01766 (cit. on pp. 22, 46, 82, 83).

SEMIN, B., GARROUM, N., PÉTRÉLIS, F., and FAUVE, S. (2018). "Nonlinear Saturation of the Large Scale Flow in a Laboratory Model of the Quasibiennial Oscillation". *Physical Review Letters* **121**: (13), 134502. DOI: 10.1103/PhysRevLett.121.134502 (cit. on p. 133).

SHAPIRO, G. I., ZENK, W., MESCHANOV, S. L., and SCHULTZ TOKOS, K. L. (1995). "Self-Similarity of the Meddy Family in the Eastern North Atlantic". *Oceanologica Acta* **18**: (1), 29–42 (cit. on p. 65).

SHETTY, S., ASAY-DAVIS, X. S., and MARCUS, P. S. (2007). "On the Interaction of Jupiter's Great Red Spot and Zonal Jet Streams". *Journal of the Atmospheric Sciences* **64**: (12), 4432–4444. DOI: 10.1175/2007JAS2097.1 (cit. on pp. 81, 84, 86).

SHETTY, S. and MARCUS, P. S. (2010). "Changes in Jupiter's Great Red Spot (1979–2006) and Oval BA (2000–2006)". *Icarus* **210**: (1), 182–201. DOI: 10.1016/j.icarus.2010.06.026 (cit. on pp. 44, 83, 94).

SHI, Y. et al. (2018). "One Possible Mechanism for Eddy Distribution in Zonal Current with Meridional Shear". *Scientific Reports* **8**: (1), 10106. DOI: 10.1038/s41598-018-28465-z (cit. on p. 65).

SHOWMAN, A. P. (2007). "Numerical Simulations of Forced Shallow-Water Turbulence: Effects of Moist Convection on the Large-Scale Circulation of Jupiter and Saturn". *Journal of the Atmospheric Sciences* **64**: (9), 3132–3157. DOI: 10.1175/JAS4007.1 (cit. on p. 55).

SIMON, A. A., BEEBE, R. F., GIERASCH, P. J., VASAVADA, A. R., and BELTON, M. J. S. (1998). "Global Context of the Galileo-E6 Observations of Jupiter's White Ovals". *Icarus* **135**: (1), 220–229. DOI: 10.1006/icar.1998.5970 (cit. on p. 84).

SIMON, A. A., WONG, M. H., and ORTON, G. S. (2015). "First Results from the Hubble OPAL Program: Jupiter in 2015". *The Astrophysical Journal* **812**: (1), 55. DOI: 10.1088/0004-637X/812/1/55 (cit. on p. 178).

SIMON, A. A. et al. (2018). "Historical and Contemporary Trends in the Size, Drift, and Color of Jupiter's Great Red Spot". *The Astronomical Journal* **155**: (4), 151. DOI: 10.3847/1538-3881/aaae01 (cit. on pp. 43, 80, 84–87).

SIMONNET, E., ROLLAND, J., and BOUCHET, F. (2021). "Multistability and Rare Spontaneous Transitions in Barotropic β-Plane Turbulence". *Journal of the Atmospheric Sciences* **78**: (6), 1889–1911. DOI: 10.1175/JAS-D-20-0279.1 (cit. on pp. 177, 178, 189, 190, 224).

SINDONI, G. et al. (2017). "Characterization of the White Ovals on Jupiter's Southern Hemisphere Using the First Data by the Juno/JIRAM Instrument". *Geophysical Research Letters* **44**: (10), 4660–4668. DOI: 10.1002/2017GL072940 (cit. on pp. 21, 43).

SLAVIN, A. G. and AFANASYEV, Y. D. (2012). "Multiple Zonal Jets on the Polar Beta Plane". *Physics of Fluids* **24**: (1), 016603. DOI: 10.1063/1.3678017 (cit. on p. 99).

SMITH, C. A., SPEER, K. G., and GRIFFITHS, R. W. (2014). "Multiple Zonal Jets in a Differentially Heated Rotating Annulus". *Journal of Physical Oceanography* **44**: (9), 2273–2291. DOI: 10.1175/JPO-D-13-0255.1 (cit. on pp. 99, 177, 235).

SOLOMON, T. H., HOLLOWAY, W. J., and SWINNEY, H. L. (1993). "Shear Flow Instabilities and Rossby Waves in Barotropic Flow in a Rotating Annulus". *Physics of Fluids A: Fluid Dynamics* **5**: (8), 1971–1982. DOI: 10.1063/1.858824 (cit. on p. 99).

SOMMERIA, J., MEYERS, S. D., and SWINNEY, H. L. (1989). "Laboratory Model of a Planetary Eastward Jet". *Nature* **337**: (6202), 58–61. DOI: 10.1038/337058a0 (cit. on p. 99).

SOMMERIA, J., MEYERS, S. D., and SWINNEY, H. L. (1988). "Laboratory Simulation of Jupiter's Great Red Spot". *Nature* **331**: (6158), 689–693. DOI: 10.1038/331689a0 (cit. on pp. 43, 64).

SPIGA, A. et al. (2020). "Global Climate Modeling of Saturn's Atmosphere. Part II: Multi-Annual High-Resolution Dynamical Simulations". *Icarus* **335**: 113377. DOI: 10.1016/j.icarus.2019.07.011 (cit. on pp. 56, 193).

STEGNER, A. and ZEITLIN, V. (1998). "From Quasi-Geostrophic to Strongly Nonlinear Monopolar Vortices in a Paraboloidal Shallow-Water-Layer Experiment". *Journal of Fluid Mechanics* **356**: 1–24 (cit. on pp. 204, 208, 219).

STEVENS, R. J. A. M., ZHONG, J.-Q., CLERCX, H. J. H., AHLERS, G., and LOHSE, D. (2009). "Transitions between Turbulent States in Rotating Rayleigh-Bénard Convection". *Physical Review Letters* **103**: (2), 024503. DOI: 10.1103/PhysRevLett.103.024503 (cit. on p. 178).

STOMMEL, H. (1982). "Is the South Pacific Helium-3 Plume Dynamically Active?" *Earth and Planetary Science Letters* **61**: (1), 63–67. DOI: 10.1016/0012-821X(82)90038-3 (cit. on p. 118).

SUGIYAMA, K. et al. (2010). "Flow Reversals in Thermally Driven Turbulence". *Physical Review Letters* **105**: (3), 034503. DOI: 10.1103/PhysRevLett.105.034503 (cit. on p. 178).

SUKORIANSKY, S., DIKOVSKAYA, N., and GALPERIN, B. (2007). "On the Arrest of Inverse Energy Cascade and the Rhines Scale". *Journal of the Atmospheric Sciences* **64**: (9), 3312–3327. DOI: 10.1175/JAS4013.1 (cit. on pp. 52, 53, 98, 99, 127, 139, 142, 145, 148, 151, 153).

– (2008). "Nonlinear Waves in Zonostrophic Turbulence". *Physical Review Letters* **101**: (17), DOI: 10.1103/PhysRevLett.101.178501 (cit. on pp. 176, 190).

– (2009). "Transport of Momentum and Scalar in Turbulent Flows with Anisotropic Dispersive Waves". *Geophysical Research Letters* **36**: (14), DOI: 10.1029/2009GL038632 (cit. on pp. 140, 159, 166).

SUKORIANSKY, S., DIKOVSKAYA, N., GRIMSHAW, R., and GALPERIN, B. (2012). "Rossby Waves and Zonons in Zonostrophic Turbulence". *AIP Conference Proceedings* **1439**: (1), 111–122. DOI: 10.1063/1.3701355 (cit. on pp. 190, 193).

SUKORIANSKY, S., GALPERIN, B., and DIKOVSKAYA, N. (2002). "Universal Spectrum of Two-Dimensional Turbulence on a Rotating Sphere and Some Basic Features of Atmospheric Circulation on Giant Planets". *Physical Review Letters* **89**: (12), DOI: 10.1103/PhysRevLett.89.124501 (cit. on pp. 52, 59, 98, 127, 139, 145, 151).

SUTYRIN, G. G. (1988). "Motion of an Intense Vortex on a Rotating Globe". *Fluid Dynamics* **23**: (2), 215–223. DOI: 10.1007/BF01051890 (cit. on pp. 208, 210, 219).

SUTYRIN, G. G. and FLIERL, G. R. (1994). "Intense Vortex Motion on the Beta Plane: Development of the Beta Gyres". *Journal of the Atmospheric Sciences* **51**: (5), 773–790. DOI: 10.1175/1520-0469(1994)051<0773:IVMOTB>2.0.CO;2 (cit. on p. 209).

SUTYRIN, G. G. and MOREL, Y. G. (1997). "Intense Vortex Motion in a Stratified Fluid on the Beta-Plane: An Analytical Theory and Its Validation". *Journal of Fluid Mechanics* **336**: 203–220. DOI: 10.1017/S0022112096004685 (cit. on p. 210).

TERRY, P. W. (2000). "Suppression of Turbulence and Transport by Sheared Flow". *Reviews of Modern Physics* **72**: (1), 109–165. DOI: 10.1103/RevModPhys.72.109 (cit. on p. 58).

THEISS, J. (2004). "Equatorward Energy Cascade, Critical Latitude, and the Predominance of Cyclonic Vortices in Geostrophic Turbulence". *Journal of Physical Oceanography* **34**: (7), 1663–1678. DOI: 10.1175/1520-0485(2004)034<1663:EECCLA>2.0.CO;2 (cit. on p. 196).

THOMPSON, A. F. (2008). "The Atmospheric Ocean: Eddies and Jets in the Antarctic Circumpolar Current". *Philosophical Transactions of the Royal Society A: Mathematical, Physical and Engineering Sciences* **366**: (1885), 4529–4541. DOI: 10.1098/rsta.2008.0196 (cit. on p. 59).

– (2010). "Jet Formation and Evolution in Baroclinic Turbulence with Simple Topography". *Journal of Physical Oceanography* **40**: (2), 257–278. DOI: 10.1175/2009JPO4218.1 (cit. on pp. 140, 173).

THOMPSON, R. O. R. Y. (1980). "A Prograde Jet Driven by Rossby Waves". *Journal of the Atmospheric Sciences* **37**: (6), 1216–1226. DOI: 10.1175/1520-0469(1980)037<1216:APJDBR>2.0.CO;2 (cit. on p. 108).

THORPE, S. A. (2005). *The Turbulent Ocean*. Cambridge: Cambridge University Press. ISBN: 978-0-521-83543-5. DOI: 10.1017/CBO9780511819933 (cit. on pp. 140, 154).

TIAN, Y. et al. (2001). "Experimental and Numerical Studies of an Eastward Jet over Topography". *Journal of Fluid Mechanics* **438**: 129–157. DOI: 10.1017/S0022112001004372 (cit. on pp. 116, 133, 189).

TOLLEFSON, J. et al. (2017). "Changes in Jupiter's Zonal Wind Profile Preceding and during the Juno Mission". *Icarus* **296**: 163–178. DOI: 10.1016/j.icarus.2017.06.007 (cit. on pp. 46, 47, 81, 84, 98, 177, 178, 190).

TYCHENSKY, A. and CARTON, X. (1998). "Hydrological and Dynamical Characterization of Meddies in the Azores Region: A Paradigm for Baroclinic Vortex Dynamics". *Journal of Geophysical Research: Oceans* **103**: (C11), 25061–25079. DOI: 10.1029/97JC03418 (cit. on pp. 57, 58).

VALCKE, S. and VERRON, J. (1997). "Interactions of Baroclinic Isolated Vortices: The Dominant Effect of Shielding". *Journal of Physical Oceanography* **27**: (4), 524–541. DOI: 10.1175/1520-0485(1997)027<0524:IOBIVT>2.0.CO;2 (cit. on p. 220).

VALLIS, G. K. (2017). *Atmospheric and Oceanic Fluid Dynamics: Fundamentals and Large-Scale Circulation*. Second. Cambridge: Cambridge University Press. ISBN: 978-1-107-06550-5. DOI: 10.1017/9781107588417 (cit. on pp. 22, 30, 36, 39, 41, 42, 108, 120, 200, 210, 230, 231, 248, 250).

VALLIS, G. K. and MALTRUD, M. E. (1993). "Generation of Mean Flows and Jets on a Beta Plane and over Topography". *Journal of Physical Oceanography* **23**: (7), 1346–1362. DOI: 10.1175/1520-0485(1993)023<1346:GOMFAJ>2.0.CO;2 (cit. on pp. 50, 51).

VAN HEIJST, G. and CLERCX, H. (2009). "Laboratory Modeling of Geophysical Vortices". *Annual Review of Fluid Mechanics* **41**: (1), 143–164. DOI: 10.1146/annurev.fluid.010908.165207 (cit. on pp. 198, 202).

VAN SEBILLE, E. et al. (2018). "Lagrangian Ocean Analysis: Fundamentals and Practices". *Ocean Modelling* **121**: 49–75. DOI: 10.1016/j.ocemod.2017.11.008 (cit. on pp. 140, 158, 171, 173).

VASAVADA, A. R. et al. (2006). "Cassini Imaging of Saturn: Southern Hemisphere Winds and Vortices". *Journal of Geophysical Research: Planets* **111**: (E5), DOI: 10.1029/2005JE002563 (cit. on pp. 193, 197).

VASAVADA, A. R. and SHOWMAN, A. P. (2005). "Jovian Atmospheric Dynamics: An Update after *Galileo* and *Cassini*". *Reports on Progress in Physics* **68**: (8), 1935–1996. DOI: 10.1088/0034-4885/68/8/R06 (cit. on pp. 21, 22, 32, 43, 45, 47, 48, 57, 64, 65, 85, 98, 134, 233).

WANG, Q., RONNEBERGER, O., and BURKHARDT, H. (2008). "Fourier Analysis in Polar and Spherical Coordinates". *Albert-Ludwigs-Universität Freiburg, Institut für Informatik* (cit. on p. 255).

WARNEFORD, E. S. and DELLAR, P. J. (2014). "Thermal Shallow Water Models of Geostrophic Turbulence in Jovian Atmospheres". *Physics of Fluids* **26**: (1), 016603. DOI: 10.1063/1.4861123 (cit. on p. 56).

WEEKS, E. R. et al. (1997). "Transitions Between Blocked and Zonal Flows in a Rotating Annulus with Topography". *Science* **278**: (5343), 1598–1601. DOI: 10.1126/science.278.5343.1598 (cit. on pp. 116, 133, 189).

WHITEHEAD, J. A. (1975). "Mean Flow Generated by Circulation on a β-Plane: An Analogy with the Moving Flame Experiment". *Tellus* **27**: (4), 358–364. DOI: 10.1111/j.2153-3490.1975.tb01686.x (cit. on pp. 99, 108).

WILLIAMS, G. P. (2002). "Jovian Dynamics. Part II: The Genesis and Equilibration of Vortex Sets". *Journal of the Atmospheric Sciences* **59**: (8), 1356–1370. DOI: 10.1175/1520-0469(2002)059<1356:JDPITG>2.0.CO;2 (cit. on p. 45).

– (2003). "Jovian Dynamics. Part III: Multiple, Migrating, and Equatorial Jets". *Journal of the Atmospheric Sciences* **60**: (10), 1270–1296. DOI: 10.1175/1520-0469(2003)60<1270:JDPIMM>2.0.CO;2 (cit. on p. 55).

WILLIAMS, G. P. and WILSON, R. J. (1988). "The Stability and Genesis of Rossby Vortices". *Journal of the atmospheric sciences* **45**: (2), 207–241. DOI: 10.1175/1520-0469(1988)045%3C0207:TSAGOR%3E2.0.CO;2 (cit. on p. 64).

WIRTH, V., RIEMER, M., CHANG, E. K. M., and MARTIUS, O. (2018). "Rossby Wave Packets on the Midlatitude Waveguide—A Review". *Monthly Weather Review* **146**: (7), 1965–2001. DOI: 10.1175/MWR-D-16-0483.1 (cit. on p. 191).

WONG, M. H., DE PATER, I., ASAY-DAVIS, X., MARCUS, P. S., and GO, C. Y. (2011). "Vertical Structure of Jupiter's Oval BA before and after It Reddened: What Changed?" *Icarus* **215**: (1), 211–225. DOI: 10.1016/j.icarus.2011.06.032 (cit. on p. 85).

WORDSWORTH, R. D., READ, P. L., and YAMAZAKI, Y. H. (2008). "Turbulence, Waves, and Jets in a Differentially Heated Rotating Annulus Experiment". *Physics of Fluids* **20**: (12), 126602. DOI: 10.1063/1.2990042 (cit. on pp. 98, 99, 235).

YADAV, R. K. and BLOXHAM, J. (2020). "Deep Rotating Convection Generates the Polar Hexagon on Saturn". *Proceedings of the National Academy of Sciences* **117**: (25), 13991–13996. DOI: 10.1073/pnas.2000317117 (cit. on pp. 43, 56, 193).

YAROM, E. and SHARON, E. (2014). "Experimental Observation of Steady Inertial Wave Turbulence in Deep Rotating Flows". *Nature Physics* **10**: (7), 510–514. DOI: 10.1038/nphys2984 (cit. on pp. 102, 236).

YIM, E. (2015). "Stability of Columnar and Pancake Vortices in Stratified-Rotating Fluids". PhD thesis. École Polytechnique (cit. on p. 76).

YIM, E., BILLANT, P., and MÉNESGUEN, C. (2016). "Stability of an Isolated Pancake Vortex in Continuously Stratified-Rotating Fluids". *Journal of Fluid Mechanics* **801**: 508–553. DOI: 10.1017/jfm.2016.402 (cit. on p. 76).

YOUNG, R. M. B. and READ, P. L. (2017). "Forward and Inverse Kinetic Energy Cascades in Jupiter's Turbulent Weather Layer". *Nature Physics* **13**: (11), 1135–1140. DOI: 10.1038/nphys4227 (cit. on pp. 31, 48, 98, 143, 227).

YOUNG, R. M. B., READ, P. L., and WANG, Y. (2019). "Simulating Jupiter's Weather Layer. Part I: Jet Spin-up in a Dry Atmosphere". *Icarus* **326**: 225–252. DOI: 10.1016/j.icarus.2018.12.005 (cit. on pp. 56, 193).

YOUSSEF, A. and MARCUS, P. S. (2003). "The Dynamics of Jovian White Ovals from Formation to Merger". *Icarus* **162**: (1), 74–93. DOI: 10.1016/S0019-1035(02)00060-X (cit. on p. 177).

ZEMAN, O. (1994). "A Note on the Spectra and Decay of Rotating Homogeneous Turbulence". *Physics of Fluids* **6**: (10), 3221–3223. DOI: 10.1063/1.868053 (cit. on p. 51).

ZHANG, Y. and AFANASYEV, Y. D. (2014). "Beta-Plane Turbulence: Experiments with Altimetry". *Physics of Fluids* **26**: (2), 026602. DOI: 10.1063/1.4864339 (cit. on pp. 99, 235).

Résumé

Dans cette thèse, nous nous attachons à modéliser certains aspects de la dynamique des fluides à l'œuvre sur Jupiter. Notre étude est axée autour de trois dispositifs expérimentaux en rotation, de simulations numériques idéalisées et d'analyses théoriques. L'objectif est de mieux comprendre les processus fondamentaux qui gouvernent la dynamique de la géante gazeuse, et ainsi compléter les modèles numériques globaux et les observations de Jupiter. Le premier type de structure que nous étudions sont les grands vortex Joviens. En tirant profit de leur état de quasi-équilibre au sein d'un environnement tournant, stratifié et cisaillé par les jets zonaux, nous montrons que les anticyclones des moyennes latitudes sont des structures superficielles, restreintes à l'atmosphère de la géante gazeuse. Aux hautes latitudes, où les jets zonaux sont moins puissants, les cyclones sont libres de migrer vers le pôle sous l'effet de la variation de la force de Coriolis avec la latitude (effet-β). Nous reproduisons cette migration au laboratoire, et proposons quelques pistes pour comprendre leur équilibre autour du pole sous forme de polygones, récemment révélé par la mission Juno. Le deuxième type de structure à grande échelle auquel nous nous intéressons sont les jets zonaux, qui correspondent à de puissants vents est-ouest qui s'étendent en profondeur dans Jupiter. Nous avons mis en place un dispositif expérimental capable de reproduire l'émergence spontanée de jets zonaux intenses au sein d'un écoulement turbulent en rotation rapide. Nous mettons en évidence le rôle primordial des ondes de Rossby dans la formation initiale des jets zonaux, mais aussi lors de leur saturation non-linéaire, au travers d'une transition entre deux régimes de jets, accompagnée de bistabilité. Nous étudions les propriétés – inhomogènes et anisotropes – de l'écoulement turbulent ainsi obtenu, dans un régime expérimental extrême pertinent pour les géantes gazeuses, et nous interrogeons sa stabilité à long terme. L'ensemble des résultats présentés se veut générique, et applicable à tout système fluide – planétaire ou non – soumis à des effets physiques analogues.

Abstract

In this thesis, we aim at modelling selected aspects of Jupiter's fluid dynamics. The present work relies on three rotating experimental setups, complemented by idealised numerical simulations and theoretical analyses. The goal is to better understand the fundamental physical processes governing the dynamics of the gas giants, thereby completing global scale simulations and observations of Jupiter. The first type of large-scale structures which we focus on are Jovian vortices. By taking advantage of their quasi-equilibrium state in a rotating stratified shear flow, we show that midlatitude anticyclones are very shallow structures, confined near the weather layer. At high latitudes, where the zonal jets are weaker, the cyclones are free to drift poleward due to the variation of the Coriolis force with latitude (so-called β-effect). We reproduce experimentally this β-drift, and provide avenues in order to model their equilibration into circumpolar clusters of cyclones, as revealed by the Juno mission. The second type of large-scale structures which we focus on are zonal jets, the strong and deep east-west winds responsible for the banded aspect of Jupiter. We design a setup where dominant zonal flows emerge spontaneously from a rapidly-rotating turbulent flow. Our experiments demonstrate the essential role of Rossby waves in the emergence of the jets, but also in their nonlinear saturation through a transition between two regimes of jets involving bistability and Rossby waves resonance. We study the inhomogeneous and anisotropic properties of the associated turbulent flow, in an extreme regime relevant to the gas giants. We additionally investigate its long-term behaviour, characterized by multistability. The present work aims at being generic and applicable to other fluid systems – planetary or not – subject to analogous physical effects.